Laser-based measurements of liquid-liquid mixing in horizontal pipes by transverse jets

Stuart Fraser Wright

Department of Chemical Engineering
Imperial College London

A dissertation submitted in partial fulfilment for the degree of
Doctor of Philosophy and the Diploma of Imperial College London

January 2021

Declaration of Originality

This work presented in this thesis is a description of the work carried out by the author within the Department of Chemical Engineering, Imperial College London, under the supervision and guidance of Professor Omar K. Matar and Professor Christos N. Markides. I hereby declare the content is the original work of the author, except where acknowledged and suitably referenced, and no part has been submitted in support of an application for a degree with any other university.

Copyright Declaration

The copyright of this thesis rests with the author. Unless otherwise indicated, its contents are licensed under a Creative Commons Attribution-Non-Commercial 4.0 International Licence (CC BY-NC). Under this licence, you may copy and redistribute the material in any medium or format. You may also create and distribute modified versions of the work. This is on the condition that you credit the author and do not use it, or any derivative works, for a commercial purpose. When reusing or sharing this work, ensure you make the licence terms clear to others by naming the licence and linking to the licence text. Where a work has been adapted, you should indicate that the work has been changed and describe those changes. Please seek permission from the copyright holder for uses of this work that are not included in this licence or permitted under UK Copyright Law.

Abstract

Low pipeline velocities lead to stratification of liquid-liquid flows, resulting in phase slip where the *in situ* phase fractions differ from the input fractions. This prevents samples being obtained that are representative of these flow's phase fractions, and thus, mixing is used to overcome stratification. This work investigates pipeline jet mixers, obtaining measurements for comparison with theory.

A review of jets for mixing is presented which establishes that few studies have been published on liquid-liquid jet mixing. Additionally, a review of prior refractive index matching experimental techniques is included, covering the techniques used within liquid-liquid and liquid-solid experimental systems. Importantly, only two liquid-liquid-solid experimental systems are found to be triply refractive index-matched and none are used for studying pipeline flows.

A refractive index-matched facility is developed, consisting of a 10 mm^2/s silicone oil, a 51 wt/wt % water/glycerol solution and an ETFE pipe. This allowed the mixing processes to be observed through using laser-based optical techniques, namely Particle Image Velocimetry to measure 2- and 3-component velocity fields and Planar Laser-Induced Fluorescence to measure phase distributions, interface heights and droplet sizes. Measurements are made of the incoming flows, the jet interactions and the resulting dispersions for a range of flow conditions, jet velocities and pipeline positions.

Results demonstrate that mixing occurs in two zones: the first during initial jet interaction where Kelvin-Helmholtz instabilities dominate; the second occurs downstream due to secondary flows. Mixing is found to decreases as the jet velocity decreases and the aqueous phase fraction increases. Increasing the crossflow velocity decreases mixing while simultaneously pushing the point of optimum mixing downstream. Coalescence is found to dominate breakup by ten pipes diameter downstream of the jet.

The results presented within will aid the understanding of these flows and provide sufficient detail to improve the predictive accuracy of computational models.

Acknowledgements

I would like to thank everyone who has been involved in this long, difficult but rewarding journey. Firstly, I would like to thank my family, Alison Wright who had to reduce her working hours as a nurse to look after our four children, Koby, Dakota, Talon and Meadow. They have all had far less time from me than they all deserved. I am extremely thankful to Professor Omar Matar and Professor Christos Markides for their faith in me and with all the advice and help they gave me throughout the project. I would like to thank Professor Geoff Hewitt who introduced me to Imperial College London through prior work on the Mixmeter. I would also like to thank Robert Gediking who helped build my complex parts in the machine shop.

I am indebted to numerous people at Cameron, Schlumberger and Sensia. Gary Potten, Jon Moreau for their help in setting up, continual involvement, development and faith in the project. Mark Jiskoot who was instrumental in the setup and running of the project and as well as my original employment for whom I will be forever grateful. I would like to thank Nigel McGee, James Baker and Brandon Antoine for their mechanical knowledge and support during the project. I would like to thank Ian Startup for his support and continuous mentorship. I would like to thank Thomas Madden and Kathy Metzer who put a lot of effort into managing the project. I would also like to thank my colleagues John McLane, Mark Foster and David Kind for filling in for me while I was frequently out of the office.

I would like to thank Dr Ivan Zadrazil for his help in the laboratory particularly with the laser-based measurements and processing even after he had left the laboratory. I would like to thank my colleges Dr Jae S. An, Dr Roberto J. Ibarra-Hernandez and Andrius Patapas for the close work, help and friendship they have given me while working in the laboratory. Dr Alexandros Charogiannis for his help with the processing of images and PIV. Finally, I would like to thank Dr Victor Voulgaropoulos for his support both with the experiments, analysis and for having a continuously positive outlook something for which I will be forever grateful.

"It doesn't matter how beautiful your theory is, it doesn't matter how smart you are. If it doesn't agree with experiment, it's wrong."

Richard Feynman

"Not only is the Universe stranger than we think, it is stranger than we can think."

Werner Heisenberg

Contents

Declaration of Originality 2
Copyright Declaration 3
Abstract 4
Acknowledgements 5
Contents 7
List of Figures 11
List of Tables 29
Nomenclature 31
Chapter 1 Introduction 34
1.1 Jet mixing background 37
1.2 Objectives 40
1.3 Thesis structure 41
Chapter 2 Review of literature 42
2.1 Multiphase flows 42
2.2 Liquid-liquid flows in horizontal pipes 42
2.3 Jets 44
2.4 Classical jet work 45
2.5 Jet breakup 46
2.6 Jets in crossflows 48
2.7 Buoyant jet studies 49
2.8 Liquid-liquid dispersion modelling 53
2.9 Jet mixing of immiscible liquid-liquid flows 58
2.10 Static mixing of immiscible liquid-liquid flows 72
2.11 Refractive index matching 73
2.12 Refractive index, density and viscosity tuning 78
2.13 Contact angle and wettability 83
Chapter 3 Experimental methods 86
3.1 Degrees of freedom 86
3.2 Two fluid model 92

3.3 Experimental facility 92
3.3.1 Storage, metering and control section 95
3.3.2 Separation 97
3.3.3 Inlet Design 98
3.3.4 Test section 99
3.3.5 Meter calibration 101
3.3.6 Jet nozzles 102
3.3.7 LabVIEW control system 103
3.4 Optical measurement techniques 105
3.5 Stereo-PIV calculations and error estimations 108
3.6 Graticule calibration target 110
3.7 Fluids, dye, and test section materials 112
3.7.1 Liquid selections 112
3.7.2 Test section materials 115
3.7.3 Tracer particles 116
3.8 Density measurements 119
3.9 Viscosity measurements 120
3.10 Refractive index measurements 121
3.11 Contact angle measurements 122
3.12 Interfacial and surface tension measurements 123
3.13 Experimental test matrix 123
3.14 Image processing 125
3.14.1 Calibration and image correction 125
3.14.2 Extraction of the region of interest 126
3.14.3 Binarization for phase data 129
3.14.4 Stratified flow heights 137
3.14.5 Vertical phase profiles and the C_1/C_2 metric 140
3.14.6 Aqueous droplet detection 143
3.14.7 Droplet size calculations 151
3.14.8 Droplet probability distributions 153
3.14.9 Velocity field analysis 154
Chapter 4 Integral measurements 157
4.1 Material and fluid measurements 157
4.1.1 Refractive index 157

4.1.2 Density 159
4.1.3 Viscosity 162
4.1.4 Contact angles 163
4.1.5 Surface and interfacial tension measurements 166
4.1.6 Summary of experimental liquids and particles 167
4.2 Crossflow measurements 167
4.2.1 Observations of experimental crossflows 167
4.2.2 Crossflows pressure drops 168
4.2.3 Interface heights 170
4.3 Jet nozzle pressure drop and power usage 172
4.4 Phenomenological observations 174
4.4.1 Overview of jets and mixing 175
4.4.2 Near jet processes and effects 179
4.4.3 Compound droplets 182
4.5 Flow pattern maps 186
4.5.1 Flow pattern map classifications 186
4.5.2 Flow pattern maps for U-jet 187
4.5.3 Comparison of jet types 194
4.6 Summary 197
Chapter 5 Mixing characteristics: Phase Concentrations 199
5.1 Concentration profiles 199
5.1.1 Low mixing levels and varying phase fractions 199
5.1.2 Varying jet velocities and phase fractions 201
5.1.3 Varying crossflow velocities and phase fractions 204
5.1.4 Effect of varying distance from the jet 208
5.1.5 Concentration profile for different jet types 212
5.2 Industrial mixing parameter, C_1/C_2 214
5.2.1 Distance, phase fraction and jet velocity effects 215
5.2.2 Residence time 219
5.2.3 Effect of jet type 223
5.3 Summary 227
Chapter 6 Mixing characteristics: Droplet sizes 229
6.1 Droplet chord lengths 229
6.2 Evolution of droplet chord lengths 236

6.3 Jet type effect on droplet chord length 254
6.4 Summary 256
Chapter 7 Velocity field measurements 259
7.1 Incoming velocity fields before jet interaction 259
7.2 Velocity fields downstream of jet interaction 262
7.2.1 Aqueous phase fraction effect downstream 262
7.2.2 Crossflow velocity effect downstream 264
7.2.3 Jet velocity effect downstream 265
7.3 Two-component PIV jet velocity fields 267
7.3.1 Varying aqueous phase fraction 270
7.3.2 Varying crossflow velocity 277
7.3.3 Varying jet velocity 284
7.4 Three-component stereo-PIV jet velocity fields 286
7.5 Summary 292
Chapter 8 Conclusions 295
8.1 Overview and further discussion 295
8.2 Key findings 301
8.3 Suggestions for future research 303
References 306
Appendix A: Refractive index matching systems 329
A.1 Common plastics 329
A.2 Silicone and urethane rubbers 337
A.3 Custom polymers, resins and hydrogels 340
A.4 Glasses 342
A.5 Liquid-liquid systems 348
A.6 Organic liquids 351
A.7 Aqueous and hydrophilic liquids 354
Appendix B: Preliminary modelling work 361

List of Figures

Figure 1.1 Six profile tests demonstrating the variation in vertical water distribution against decreasing pipeline velocity where P_0 is the highest velocity and P_5 is the lowest velocity (ISO 1999). 35
Figure 1.2 Mixing elements of the Sulzer SMX mixer which are used for creating fine liquid-liquid dispersions (Rama Rao et al., 2007). 36
Figure 1.3 A jet mixer system known as a "CoJetix" that uses a nozzle and quill that is inserted into pipelines that are 6-inches or greater in diameter, (Cameron, 2013). 38
Figure 1.4 An example wall originating jet mixer design which is used for pipelines that are 8 inches or smaller (Jiskoot et al., 2018) 39
Figure 2.1 Views of oil and water flow regimes, adapted from Trallero (1995). 44
Figure 2.2 The four regimes of jet breakup plotted on a map of Reynolds number against Weber number Sirignano and Mehring (2000). 46
Figure 2.3 The four regimes of a liquid jet breakup plotted on a map of Reynolds number against Ohnesorge number (Bravo and Kweon, 2014). 47
Figure 2.4 A schematic of a jet in crossflow (Galeazzo et al., 2011) 48
Figure 2.5 Schematic of jet breakup in a crossflow highlighting both primary and secondary droplet breakup (Pai et al., 2009). 49
Figure 2.6 Sketch of a buoyant jet in stratified crossflow from Wright (1984) 49
Figure 2.7 Three regimes for immiscible negatively buoyant jets Geyer et al., (2011). 50
Figure 2.8 Dimensionless maps of immiscible negatively buoyant jets Geyer et al. (2011); Top: 3-D map of Ri versus Re versus We; Bottom: map of Ri versus We. 51
Figure 2.9 Buoyant jets undergoing breakup: a) Regime 1: atomization, b) Regime 2A: pinch-off, c) Regime 2B: skirt breakup, (Berard et al., 2013). 52

Figure 2.10 Scatter plot of jet breakup results of Berard et al. (2013) for Ohnesorge number versus Reynolds number of the jet. 53
Figure 2.11 Schematic of the pipe concentrations used to calculate the C_1/C_2 concentration ration used in industrial liquid-liquid mixing calculations. 54
Figure 2.12 Balance between droplet settling and turbulent dispersion (Baker, 1986). 55
Figure 2.13 Schematic of pipeline liquid-liquid jet mixer proposed by Slater (1983) making use of a rotor-stator pump that both drives and emulsify the liquids. 60
Figure 2.14 Schematic of the Jiskoot jet mixer with the jet mix loop containing a pump, an integral sampler and a static mixer Jiskoot (1986). 61
Figure 2.15 The three regions of jet mixing as defined by Fernando (1990), Region 1 is penetration, Region 2 is the near-field, and region 3 is the far-field. 62
Figure 2.16 Experimental setup used by Fernando (1990) for studying a single jet breaking up a static stratified layer of water (bottom) and kerosene (top). 63
Figure 2.17 Jet breakup of a stratified layer of water and kerosene Fernando (1990); left, a close-up image of the jet; right, a schematic of jet droplet formation. 63
Figure 2.18 Structure and stages of breakup and entrainment for a jet penetrating two stratified immiscible liquids, Fernando (1990). 64
Figure 2.19 Two nozzle designs used by Fernando (1990); left, single upward nozzle; right, a copy of the Jiskoot multiple jet nozzle. 65
Figure 2.20 Cross-section of the forward-facing jet mix nozzle with three jet exits around the circumference of the nozzle, (Jiskoot and Jiskoot, 2001). 66
Figure 2.21 The horizontally oriented nozzle of Verloop and Verloop (2010b). 67
Figure 2.22 Schematic of an eductor (Hosseinzadeh et al., 2018). 68
Figure 2.23 Dual jet nozzle created by Mohajer (2013). 69
Figure 2.24 A typical CoJetix sampling system with a jet nozzle and a quill in the main pipe as well as a flowmeter, a controller and a pump in the jet

mixer loop and a bypass loop containing a sampling cabinet (Potten and Wright, 2014)..... 70
Figure 2.25 Dual jet concept of the SmartMix jet mixer where the two feed lines are used to supply jets of two different sizes (Maru et al., 2018)..... 71
Figure 2.26 A nozzle implementation of the weak and strong jet concept of the "SmartMix" (Maru and Waters, 2018)..... 72
Figure 2.27 Refraction of a light ray at an interface as it passes from a high to a low refractive index medium: (a) no refraction/reflection occurs when the light direction is perpendicular to the interface; (b) slight refraction at low angles; (c) increasing refraction at higher angles; (d) critical angle between refraction and reflection; and (e) total internal reflection. 74
Figure 2.28 Two droplets on a solid surface in a lighter emersion fluid making contact angles θ with a solid. The liquid of droplet (a) has a lower affinity for the surface than the immersion fluid and a larger contact angle, while the liquid of droplet (b) has a greater affinity for the solid than the immersion fluid and a smaller contact angle. 83
Figure 2.29 Contact angle for a droplet of an 80% glycerol solution immersed in Exxsol D80 on a borosilicate glass surface (Morgan, 2012). 83
Figure 2.30 Water-in-oil contact angle for several steel surfaces measured against time (Tang et al., 2009). 84
Figure 3.1 Schematic illustrating the two angles of jet originating from a pipe wall. 87
Figure 3.2 Schematic illustrating a single jet in a liquid-liquid stratified crossflow and the resulting downstream droplets. 88
Figure 3.3 P&ID of the TOWER facility as it was in January 2015 before modifications were made to accommodate the jet mixing experimental campaign. 93
Figure 3.4 P&ID of the TOWER facility including all modifications for the jet mixing experimental campaign during April 2018..... 94
Figure 3.5 3-D model of the inlet conditioner design with independent inlets, a separation plate, mesh elements and flow straighteners..... 98

Figure 3.6 Inlet as installed and filled with experimental liquids. The bottom section contains the aqueous solution that is dyed pink with Eosin Y while the top section is filled with clear silicone oil. 99
Figure 3.7 Overview diagram showing all components of the test section, including inlet conditioner, flow development section and observation box with jet entry. 100
Figure 3.8 Images of the observation box. Top: Observation box empty of liquids demonstrating the usual distortion of a mismatched refractive index system. Bottom: Beginning of the observation box highlighting the nozzle entry point and the calibration graticule immersed in the index-matched silicone oil. 100
Figure 3.9 Reading of the uncalibrated large oil turbine meter versus the calibrated Khrone Optimass 6000 Coriolis meter. 101
Figure 3.10 Nozzles used in the experimental campaign and the direction of the resulting jets. Top row: Vertically up U-jet. Middle row: forward-facing F-jet. Bottom row: Twin V-jet. Left column: 3-D drawing of nozzles. Middle column: the direction of the jet in the cross-section of the pipe. Right column: the direction of the jet in pipe axial direction. 102
Figure 3.11 The LabVIEW interface of the control and data logging system used to make measurements during the experimental campaign. 104
Figure 3.12 Dual camera setup used for the simultaneous PLIF, PIV and stereo-PIV during the experimental campaign. 108
Figure 3.13 General setup for a dual camera (DaVis, 2017). 109
Figure 3.14 Image of three-dimensional graticule calibration target used for spatial calibration and optical correction. 111
Figure 3.15 Graticule calibration target inside a part filled ETFE pipe located in the oil-filled observation box. 112
Figure 3.16 Eosin Y absorption and emission spectra in water. 115
Figure 3.17 Close up of the ETFE pipe filled with silicone oil and located within the observation box also filled with silicone oil. 116
Figure 3.18 An 8 m/s silicone oil jet penetrating the aqueous phase of a crossflow with a velocity of V_m = 0.4 m/s and an aqueous phase fraction of ϕ = 0.20 at 60 ms after the jet's first appearance into the flow. The

flows non-dimensional numbers are Re_j = 3700, Re_{aq} = 1200, Re_o = 1900 and We_j = 7300. 119
Figure 3.19 Stanton Redcroft / Paar calculating density meter (densitometer) used to measure fluid densities within the laboratory..... 120
Figure 3.20 The HAAKE falling ball viscometer type C used to perform laboratory measurements of the liquid viscosity, Left: the viscometer tube encased in a water jacket used for temperature control; Right: the calibrated measurement balls, where the middle left ball (ball 2) was used..... 121
Figure 3.21 CETI Prisma 8300 benchtop refractometer used to perform refractive index measurement of the liquids used experimentally during the campaign. 122
Figure 3.22 A time and spatially-averaged normalized intensity plot of a dispersed crossflow of V_m = 0.6 m/s and an aqueous phase fraction of ϕ = 0.20..... 127
Figure 3.23 Example extraction of the region of interest from an image of crossflow of V_m = 0.4 m/s and an aqueous phase fraction of ϕ = 0.20 that was mixed by a U-Jet with a velocity of V_j = 4 m/s. Top: the original image; Bottom: the extracted region of interest..... 128
Figure 3.24 Example stratified flow image (top left) with the associated binarized image (top right) and the probability distribution of the pixel intensity..... 129
Figure 3.25 Top: An image of a crossflow with a velocity of V_m = 0.6 m/s and an aqueous phase fraction of ϕ = 0.10 mixed by a 4 m/s jet containing a range of scales with droplets visible both in and out of the plane. Bottom: Probability distribution of the pixel intensity for the same flow..... 131
Figure 3.26 Binarization Stage-1 to capture the largest objects. Left column sensitivity 0.3; middle column: 0.4; right column: 0.5; Top row: 1260×580 window; Middle row: 630×290 window; Bottom row: 420×193 windows. 133
Figure 3.27 Second binarization stage to capture the smaller objects. Left column sensitivity 0.2; middle column: 0.3; right column: 0.4; Top row: 21×19 window; Middle row: 11×9 window; Bottom row: 7×7 windows..... 134

Figure 3.28 Combined binarization of the second stage with the first stage to capture all objects, with a stage-1 sensitivity of 0.2 and window size of 260×580. Left column: stage-2 sensitivity 0.2; middle column: stage-2 sensitivity 0.3; right column: stage-2 sensitivity 0.4; Top row: stage-2 window 21×19; Middle row: stage-2 window11×9; Bottom row: stage-2 windows 7×7..... 135
Figure 3.29 Four example cases demonstrating the binarization of stratified flows. Left column: the original image; Right column: binarized images. 139
Figure 3.30 Example photo of a stratified flow showing the detected height of the interface in green at a thickness pixel..... 140
Figure 3.31 Outline of the steps used to compute the vertical phase profile from the images of a crossflow of V_m = 0.4 m/s and an aqueous phase fraction of ϕ = 0.10 at a distance of L = 4 D with a U-Jet with a velocity of V_j = 4 m/s. Top: Image following extraction; Middle: Binarized image; Bottom left: Spatially averaged aqueous phase profile for a single frame; Bottom right: Aqueous phase profile averaged over 1000 frames..... 142
Figure 3.32 Example showing the stages of droplet detection for a crossflow of V_m = 0.6 m/s and an aqueous phase fraction of ϕ = 0.10 at a distance of L = 10 D with a U-Jet with a velocity of V_j = 8 m/s. (a) original image; (b) binarized image; (c) droplets detected by imfindimage range 3 to 8 pixels ; (d) droplets detected by imfindimage range 8 to 23 pixels; (e) droplets detected by imfindimage range 23 to 60 pixels; (f) droplets detected by imfindimage range 60 to 150 pixels; (g) droplets detected by regionprops; (h) all detected candidate droplets; (i) after first filter; (j) after second filter; (k) after third filter; (l) after the third filter on the original image..... 146
Figure 3.33 The effect on droplet chord length statistics for a crossflow with a velocity of V_m = 0.4 m/s and an aqueous phase fraction of ϕ = 0.05 interacting with a jet of V_j = 12 m/s at a downstream position of L = 10 D. Top: the effect of axial distance on D_{10} and D_{32}. Bottom: effect of the frames count on the mean (D_{10}), Sauter Mean Diameter (D_{32}) and standard deviation (S)..... 151

Figure 4.1 Refractive index versus temperature for three viscosity silicone oils 5 mm^2/s (BC5), 10 mm^2/s (BC10) and 20 mm^2/s (BC20) sourced from Basildon Chemicals..... 158
Figure 4.2 Refractive index of a range of glycerol solution concentrations 49, 50, 51 and 52 wt/wt %, compared with BC10 silicone oil..... 159
Figure 4.3 Density versus temperature, showing both the benchtop Stanton Redcroft / Paar DMA 46 measurements and the measurements made by the Coriolis meters during the experimental campaigns. Top: BC10 Silicone oil; Bottom: Aqueous phase..... 161
Figure 4.4 Laboratory measured dynamic viscosity versus temperature. Top: BC10 silicone oil; Bottom: glycerol-based aqueous phase..... 163
Figure 4.5 Droplets glycerol water solutions in BC10 silicone oil. Top row: on glass; Bottom row: on Acrylic; Left column: 43% glycerol; Right column 60% glycerol..... 165
Figure 4.6 Images of contact angles formed by various liquids on steel surfaces, (i) 43% glycerol solution in BC10 silicone oil on mild steel Plate 1; (ii) 60% glycerol in BC10 silicone oil on mild steel Plate 1; (iii) Tap water in D140 mineral oil on mild steel Plate 1; (iv) 60% glycerol solution in BC10 silicone oil on mild steel Plate 2..... 166
Figure 4.7 A V_m = 0.6 m/s stratified crossflow with a ϕ = 0.20 aqueous phase fraction located upstream of the jet at $L = -2\ D$ while the jet is inactive. 168
Figure 4.8 Pressure drops against velocity including experimental measured by differential pressure transmitters at two positions from the inlet and the two-fluid model for both laminar and turbulent flows of Taitel and Dukler (1976). Top: located between 2 m and 6 m; Bottom: located between 4 m and 6 m..... 169
Figure 4.9 Aqueous phase heights and those predicted by the two-fluid model of Taitel and Dukler et al. (1976), plotted as height (H_{aq}) versus aqueous phase fraction (ϕ). Top: all crossflow velocities; Bottom: crossflow velocities V_m < 0.4 m/s..... 171
Figure 4.10 Pressure losses and power usages measured during the experimental campaign for the three type jet nozzle against the jet velocity. Top: ΔP versus V_j; Bottom: P_j versus V_j 173

Figure 4.11 Characteristic effects of liquid jets formed by a U-type jet interacting with stratified flows with $0.2 \leq V_m \leq 0.6$ m/s, $0.05 \leq \phi \leq 0.50$ and $4 \leq V_j \leq 12$ m/s. Rows from top to bottom show increasing levels of mixing while columns from left to right are increasing in downstream distance from the jet. 177

Figure 4.12 An 8 m/s silicone oil jet penetrating the aqueous phase of a crossflow with a velocity of $V_m = 0.4$ m/s and an aqueous phase fraction of $\phi = 0.20$ at 60 ms after the jet's first appearance into the flow. The flows non-dimensional numbers are $Re_j = 3700$, $Re_{aq} = 1200$, $Re_o = 1900$, $We_j = 7300$. 180

Figure 4.13 An 8 m/s silicone oil jet penetrating the aqueous phase of a crossflow with a velocity of $V_m = 0.4$ m/s and an aqueous phase fraction of $\phi = 0.20$ at 5200 ms after the jet's first appearance into the flow. The flows non-dimensional numbers are $Re_j = 3700$, $Re_{aq} = 1200$, $Re_o = 1900$, $We_j = 7300$. 182

Figure 4.14 A 10 mm diameter compound droplet created during the mixing process with a jet velocity of $V_j = 4$ m/s, a crossflow of $V_m = 0.4$ m/s and an aqueous phase fraction of $\phi = 0.50$ at a distance of $L = 4\ D$ with $Re_j = 1900$, $Re_{aq} = 2700$, $Re_o = 1400$ and $We_j = 1800$. 183

Figure 4.15 Large compound droplets formed by a U-jet with a velocity of $V_j = 4$ m/s interacting with an incoming stratified flow with a pipeline velocity of $V_m = 0.2$ m/s and an aqueous phase fraction of $\phi = 0.50$. 183

Figure 4.16 Significant numbers of compound droplet formed by a U-jet with a velocity of $V_j = 8$ m/s interacting with an incoming stratified flow with a velocity of $V_m = 0.2$ m/s and an aqueous phase fraction of $\phi = 0.50$. 184

Figure 4.17 Small compound droplets formed in a U-jet with a velocity of $V_j = 4$ m/s interacting with an incoming stratified flow with a velocity of $V_m = 0.8$ m/s and an aqueous phase fraction of $\phi = 0.50$. 185

Figure 4.18 Compound droplets formed in an incoming stratified flow with droplets at the interface for a pipeline velocity of $V_m = 0.8$ m/s and an aqueous phase fraction of $\phi = 0.50$ 185

Figure 4.19 A U-jet with a velocity of V_j = 8 m/s interacting with an incoming stratified flow with a velocity of V_m = 0.8 m/s and an aqueous phase fraction of ϕ = 0.50 187
Figure 4.20 Flow pattern map from mixing with the U-jet at L = 1 D showing inlet mixture velocity versus phase fraction. Top: V_j = 4 m/s, Re_j = 1900, We_j = 1800; middle: V_j = 8 m/s, Re_j = 3700, We_j = 7300; bottom: V_j = 12 m/s, Re_j = 5600, We_j = 17000. 189
Figure 4.21 Flow pattern map from mixing with the U-jet at L = 4 D showing inlet mixture velocity versus phase fraction. Top: V_j = 4 m/s, Re_j = 1900, We_j = 1800; middle: V_j = 8 m/s, Re_j = 3700, We_j = 7300; bottom: V_j = 12 m/s, Re_j = 5600, We_j = 17000. 190
Figure 4.22 Flow pattern map from mixing with the U-jet at L = 10 D showing inlet mixture velocity versus phase fraction. Top: V_j = 4 m/s, Re_j = 1900, We_j = 1800; middle: V_j = 8 m/s, Re_j = 3700, We_j = 7300; bottom: V_j = 12 m/s, Re_j = 5600, We_j = 17000. 191
Figure 4.23 Flow pattern map from mixing with the U-jet showing velocity ratio versus phase fraction. Top: V_j = 4 m/s, Re_j = 1900, We_j = 1800; middle: V_j = 8 m/s, Re_j = 3700, We_j = 7300; bottom: V_j = 12 m/s, Re_j = 5600, We_j = 17000. 192
Figure 4.24 Flow pattern from mixing with the U-jet showing residence time versus phase fraction. Top: V_j = 4 m/s, Re_j = 1900, We_j = 1800; middle: V_j = 8 m/s, Re_j = 3700, We_j = 7300; bottom: V_j = 12 m/s, Re_j = 5600, We_j = 17000. 193
Figure 4.25 Flow pattern map from mixing with the F-jet at L = 10 D showing inlet mixture velocity versus phase fraction. Top: V_j = 4 m/s, Re_j = 1900, We_j = 1800; middle: V_j = 8 m/s, Re_j = 3700, We_j = 7300; bottom: V_j = 12 m/s, Re_j = 5600, We_j = 17000. 195
Figure 4.26 Flow pattern map from mixing with the V-jet at L = 10 D showing inlet mixture velocity versus phase fraction. Top: V_j = 4 m/s, Re_j = 1300, We_j = 1300; middle: V_j = 8 m/s, Re_j = 2600, We_j = 5100; bottom: V_j = 12 m/s, Re_j = 3900, We_j = 12000. 196
Figure 5.1 Concentration profiles at L = 10 D for a U-jet with a velocity of V_j = 4 m/s, Re_j = 1900 and We_j = 1800 interacting with crossflows with

aqueous phase fractions of ϕ = 0.05, ϕ = 0.10 and ϕ = 0.20 and a velocity of V_m = 0.4 m/s. 200

Figure 5.2 Concentration profiles at L = 10 D for U-jet with velocities of V_j = 4 m/s, V_j = 6 m/s, V_j = 8 m/s, V_j = 10 m/s, V_j = 12 m/s, V_j = 14 m/s and V_j = 16 m/s interacting with a crossflow with varying aqueous phase fraction and a velocity of V_m = 0.4 m/s. Top: ϕ = 0.20, Re_{aq} = 1200 and Re_o = 1900; Middle: ϕ = 0.10, Re_{aq} = 700 and Re_o = 2100; Bottom: ϕ = 0.05, Re_{aq} = 380 and Re_o = 2200. 203

Figure 5.3 Concentration profiles at L = 10 D for a U-jet with a velocity of V_j = 4 m/s and Re_j = 1900, We_j = 1800 interacting with crossflows with varying aqueous phase fraction and velocities of V_m = 0.1 m/s, V_m = 0.2 m/s, V_m = 0.4 m/s and V_m = 0.6 m/s. Top: ϕ = 0.20; Middle: ϕ = 0.10; Bottom: ϕ = 0.05. 205

Figure 5.4 Concentration profiles at L = 10 D for a U-jet interacting with crossflows with an aqueous phase fraction of ϕ = 0.05 and velocities of V_m = 0.1 m/s, V_m = 0.2 m/s, V_m = 0.4 m/s and V_m = 0.6 m/s. Top: V_j = 4 m/s, Re_j = 1900, We_j = 1800; Middle: V_j = 8 m/s, Re_j = 3700, We_j = 7300; Bottom: V_j = 12 m/s, Re_j = 5600, We_j = 17000. 207

Figure 5.5 Concentration profiles for a U-jet with a velocity of V_j = 4 m/s and Re_j = 1900, We_j = 1800 interacting with crossflows with an aqueous phase fraction of ϕ = 0.10 and velocities of V_m = 0.1 m/s, V_m = 0.2 m/s, V_m = 0.4 m/s and V_m = 0.6 m/s. Top: L = 4 D; Bottom: L = 10 D. 209

Figure 5.6 Concentration profiles for a U-jet with a velocity of V_j = 8 m/s and Re_j = 3600, We_j = 7300 interacting with crossflows with an aqueous phase fraction of ϕ = 0.10 and velocities of V_m = 0.1 m/s, V_m = 0.2 m/s, V_m = 0.4 m/s and V_m = 0.6 m/s. Top: L = 4 D; Bottom: L = 10 D. 210

Figure 5.7 Concentration profiles for a U-jet with a velocity of V_j = 12 m/s and Re_j = 5600, We_j = 17000 interacting with crossflows with an aqueous phase fraction of ϕ = 0.10 and velocities of V_m = 0.1 m/s, V_m = 0.2 m/s, V_m = 0.4 m/s and V_m = 0.6 m/s. Top: L = 4 D; Bottom: L = 10 D. 211

Figure 5.8 Concentration profiles at L = 10 D for the three jet types with a velocity of V_j = 4 m/s interacting with crossflows with a varying aqueous

phase fraction of $\phi = 0.05$ and velocity of $V_m = 0.4$ m/s. Top: $\phi = 0.20$, $Re_{aq} = 1200$ and $Re_o = 1900$; Middle: $\phi = 0.10$, $Re_{aq} = 690$ and $Re_o = 2100$; Bottom: $\phi = 0.05$, $Re_{aq} = 380$ and $Re_o = 2200$. 213

Figure 5.9 Concentration profiles at $L = 10\ D$ for the three jet types with a velocity of $V_j = 8$ m/s interacting with crossflows with an aqueous phase fraction of $\phi = 0.05$ and velocity of $V_m = 0.4$ m/s with $Re_{aq} = 380$ and $Re_o = 2200$. 214

Figure 5.10 C_1/C_2 ratio against distance from jet for a U-jet with jet interacting with a $V_m = 0.2$ m/s crossflow with inlet aqueous phase fractions of $\phi = 0.05$ ($Re_{aq} = 190$, $Re_o = 1100$), $\phi = 0.10$ ($Re_{aq} = 340$, $Re_o = 1100$) and $\phi = 0.20$ ($Re_{aq} = 620$, $Re_o = 1000$). Top: $V_j = 4$ m/s, $Re_j = 1900$, $We_j = 1800$; Middle: $V_j = 8$ m/s, $Re_j = 3600$, $We_j = 7300$; Bottom: $V_j = 12$ m/s, $Re_j = 5600$, $We_j = 17000$..... 216

Figure 5.11 C_1/C_2 ratio against distance from jet for the U-jet with a jet velocity of $V_j = 12$ m/s and $Re_j = 5600$, $We_j = 17000$ interacting with a $V_m = 0.4$ m/s crossflow with inlet aqueous phase fractions of $\phi = 0.05$ ($Re_{aq} = 380$, $Re_o = 2200$), $\phi = 0.10$ ($Re_{aq} = 690$, $Re_o = 2100$) and $\phi = 0.20$ ($Re_{aq} = 1200$, $Re_o = 1900$). 218

Figure 5.12 C_1/C_2 ratio against distance from jet for the U-jet with a jet interacting with a $V_m = 0.6$ m/s crossflow with inlet aqueous phase fractions of $\phi = 0.05$ ($Re_{aq} = 590$, $Re_o = 3300$), $\phi = 0.10$ ($Re_{aq} = 1100$, $Re_o = 3200$) and $\phi = 0.20$ ($Re_{aq} = 1900$, $Re_o = 2900$). Top: $V_j = 4$ m/s, $Re_j = 1900$, $We_j = 1800$; Bottom: $V_j = 12$ m/s, $Re_j = 5600$, $We_j = 17000$. 219

Figure 5.13 C_1/C_2 ratio against pipeline residence times for the U-jet with jet velocities of $V_j = 4$, 8 and 12 m/s interacting with crossflow velocities between $V_m = 0.1 – 0.6$ m/s with varying inlet aqueous phase fraction. Top: $\phi = 0.05$; Middle: $\phi = 0.10$; Bottom: $\phi = 0.20$. Linear fitting trend lines..... 221

Figure 5.14 C_1/C_2 ratio against pipeline residence times for the U-jet with jet velocities of $V_j = 4$, 8 and 12 m/s interacting with crossflow velocities between $V_m = 0.1 – 0.6$ m/s with varying inlet aqueous phase fraction. Top: $\phi = 0.05$; Middle: $\phi = 0.10$; Bottom: $\phi = 0.20$. Exponential fitting trend lines..... 222

Figure 5.15 C_1/C_2 ratio against distance from jet for the three different jet types interacting with varying crossflow with inlet aqueous phase fractions of $\phi = 0.20$. Left column: $V_j = 4$ m/s; Middle column: $V_j = 8$ m/s; Right columns: $V_j = 12$ m/s. Top row: $V_m = 0.2$ m/s; Middle row: $V_m = 0.4$ m/s; Bottom row: $V_m = 0.6$ m/s. 224

Figure 5.16 C_1/C_2 ratio against distance from jet for the three different jet types interacting with a crossflow with inlet aqueous phase fractions of $\phi = 0.05$. Left column: $V_j = 4$ m/s; Middle column: $V_j = 8$ m/s; Right column: $V_j = 12$ m/s. Top row: $V_m = 0.2$ m/s; Middle row: $V_m = 0.4$ m/s; Bottom row: $V_m = 0.6$ m/s. 226

Figure 6.1 Droplet chord lengths relationships: Top left: D_{32} and mean (D_{10}); Top right: D_{32} and Dv_{10}; Bottom left: D_{32} and Dv_{50}; Bottom right: D_{32} and Dv_{90}. 231

Figure 6.2 Droplet chord lengths against height for a U-jet interacting with a crossflow velocity of $V_m = 0.4$ m/s and an aqueous phase fraction of $\phi = 0.05$ with Reynolds number of $Re_{aq} = 380$, $Re_o = 2200$ at a distance of $L = 10\ D$. Left column: D_{10}, D_{32}, Dv_{50}; Right column: D_{32}; Top Row: $V_j = 4$ m/s, $Re_j = 1900$, $We_j = 1800$; 2nd row: $V_j = 6$ m/s, $Re_j = 2800$, $We_j = 4100$; 3rd row: $V_j = 8$ m/s, $Re_j = 3700$, $We_j = 7300$; Bottom row: $V_j = 12$ m/s, $Re_j = 5600$, $We_j = 17000$. 233

Figure 6.3 D_{32} droplet chord lengths against height for a U-jet interacting with a crossflow velocity of $V_m = 0.4$ m/s at a distance of $L = 10\ D$ where the jet velocities and inlet aqueous phase fractions are varying. Left column: $\phi = 0.10$, $Re_{aq} = 690$, $Re_o = 2100$; right column: $\phi = 0.20$, $Re_{aq} = 1200$, $Re_o = 1900$; top row: $V_j = 4$ m/s, $Re_j = 1900$, $We_j = 1800$; 2nd row: $V_j = 8$ m/s, $Re_j = 3700$, $We_j = 7300$; bottom row: $V_j = 12$ m/s, $Re_j = 5600$, $We_j = 17000$. 235

Figure 6.4 Droplet chord length distributions against height for a U-jet interacting with a crossflow velocity of $V_m = 0.4$ m/s at a distance of $L = 10\ D$ where the jet velocities and inlet aqueous phase fractions are varying. Left column: $V_j = 4$ m/s, $Re_j = 1900$, $We_j = 1800$; middle column: $V_j = 8$ m/s, $Re_j = 3600$, $We_j = 7300$; right column: $V_j = 12$ m/s, $Re_j = 5600$, $We_j = 17000$; Top row: $\phi = 0.05$, $Re_{aq} = 380$, $Re_o = 2200$;

2nd row: ϕ = 0.10, Re_{aq} = 690, Re_o = 2100; bottom row: ϕ = 0.20, Re_{aq} = 1200, Re_o = 1900. 236
Figure 6.5 D_{32} droplet chord lengths against height for a U-jet interacting with a crossflow of ϕ = 0.20, a jet velocity of V_j = 12 m/s and Re_j = 5600, We_j = 17000. Left column: L = 4 D; right column: L = 10 D; top row: V_m = 0.1 m/s, Re_{aq} = 290, Re_o = 480; 2nd row: V_m = 0.2 m/s, Re_{aq} = 620, Re_o = 1000; 3rd row: V_m = 0.4 m/s, Re_{aq} = 1200, Re_o = 1900; bottom row: V_m = 0.6 m/s, Re_{aq} = 1900, Re_o = 2900. 239
Figure 6.6 D_{32} droplet chord lengths distributions for a U-jet interacting with a crossflow of ϕ = 0.20, a jet velocity of V_j = 12 m/s and Re_j = 5600, We_j = 17000. Left column: L = 4 D; right column: L = 10 D; top row: V_m = 0.1 m/s, V_m = 0.1 m/s, Re_{aq} = 290; 2nd row: V_m = 0.2 m/s, Re_{aq} = 620, Re_o = 1000; 3rd row: V_m = 0.4 m/s, Re_{aq} = 1200, Re_o = 1900; bottom row: V_m = 0.6 m/s, Re_{aq} = 1900, Re_o = 2900..... 240
Figure 6.7 D_{32} droplet chord lengths distributions for a U-jet with a velocity of V_j = 12 m/s (Re_j = 5600, We_j = 17000) interacting with a crossflow with a velocity of V_m = 0.6 m/s and an aqueous phase fraction of ϕ = 0.20 (Re_{aq} = 1900, Re_o = 2900). Left top: top 3rd at 4 D; Right top: pipe top 3rd at 10 D; Left middle: pipe middle 3rd at 4 D; Right middle: pipe middle 3rd at 10 D; Left bottom: pipe bottom 3rd at 4 D; Right bottom: pipe bottom 3rd at 10 D. 243
Figure 6.8 D_{32} droplet chord lengths distributions for a U-jet with a velocity of V_j = 12 m/s (Re_j = 5600, We_j = 17000) interacting with a crossflow with a velocity of V_m = 0.4 m/s and an aqueous phase fraction of ϕ = 0.20 (Re_{aq} = 1200, Re_o = 1900). Left top: top 3rd at 4 D; Right top: pipe top 3rd at 10 D; Left middle: pipe middle 3rd at 4 D; Right middle: pipe middle 3rd at 10 D; Left bottom: pipe bottom 3rd at 4 D; Right bottom: pipe bottom 3rd at 10 D. 244
Figure 6.9 D_{10} droplet chord lengths against residence time from a U-jet interacting with crossflows with aqueous phase fractions of ϕ = 0.05, ϕ = 0.10 and ϕ = 0.20, where linear fits have been applied to the data. Top: V_j = 4 m/s, Re_j = 1900, We_j = 1800; Middle: V_j = 8 m/s, Re_j = 3600, We_j = 7300; Bottom: V_j = 12 m/s, Re_j = 5600, We_j = 17000. 247

Figure 6.10 D_{10} droplet chord lengths against residence time from a U-jet interacting with crossflows with aqueous phase fractions of $\phi = 0.05$, $\phi = 0.10$ and $\phi = 0.20$, where second-order polynomials have been fitted to the data. Top: $V_j = 4$ m/s, $Re_j = 1900$, $We_j = 1800$; Middle: $V_j = 8$ m/s, $Re_j = 3600$, $We_j = 7300$; Bottom: $V_j = 12$ m/s, $Re_j = 5600$, $We_j = 17000$..... 248

Figure 6.11 D_{32} droplet chord lengths against residence time from the jet for a U-jet interacting with crossflows with inlet aqueous phase fractions of $\phi = 0.05$, $\phi = 0.10$ and $\phi = 0.20$, where linear fits have been applied to the data. Top: $V_j = 4$ m/s, $Re_j = 1900$, $We_j = 1800$; Middle: $V_j = 8$ m/s, $Re_j = 3600$, $We_j = 7300$; Bottom: $V_j = 12$ m/s, $Re_j = 5600$, $We_j = 17000$..... 249

Figure 6.12 D_{32} droplet chord lengths against residence time from the jet for a U-jet interacting with crossflows with inlet aqueous phase fractions of $\phi = 0.05$, $\phi = 0.10$ and $\phi = 0.20$, where second-order polynomials have been fitted to the data. Top: $V_j = 4$ m/s, $Re_j = 1900$, $We_j = 1800$; Middle: $V_j = 8$ m/s, $Re_j = 3600$, $We_j = 7300$; Bottom: $V_j = 12$ m/s, $Re_j = 5600$, $We_j = 17000$..... 250

Figure 6.13 D_{32} droplet chord lengths against distance from a U-jet with jet velocity $V_j = 12$ m/s ($Re_j = 5600$, $We_j = 17000$) interacting crossflow with inlet aqueous phase fractions of $\phi = 0.05$, $\phi = 0.10$ and $\phi = 0.20$. Top left: $V_m = 0.1$ m/s; Top right: $V_m = 0.2$ m/s; Bottom left: $V_m = 0.4$ m/s; Bottom right: $V_m = 0.6$ m/s..... 251

Figure 6.14 D_{32} droplet chord lengths against distance from a U-jet with jet velocity $V_j = 8$ m/s ($Re_j = 3600$, $We_j = 7300$) interacting crossflow with inlet aqueous phase fractions of $\phi = 0.05$, $\phi = 0.10$ and $\phi = 0.20$. Top left: $V_m = 0.1$ m/s; Top right: $V_m = 0.2$ m/s; Bottom left: $V_m = 0.4$ m/s; Bottom right: $V_m = 0.6$ m/s..... 252

Figure 6.15 D_{32} droplet chord length model including the processes of break up, coalescence and interface absorption..... 253

Figure 6.16 D_{32} droplet chord lengths against height for jets interacting with a crossflow of $\phi = 0.20$ and a jet velocity of $V_j = 12$ m/s at a downstream distance of $L = 10\ D$. Left column: $V_m = 0.2$ m/s, $Re_{aq} = 620$, $Re_o = 1000$; right column: $V_m = 0.4$ m/s, $Re_{aq} = 1200$, $Re_o = 1900$; top: U-jet,

Re_j = 5600, We_j = 17000; 2nd row: F-jet, Re_j = 5600, We_j = 17000; bottom row: V-jet, Re_j = 3900, We_j = 12000. 255

Figure 6.17 D_{32} droplet chord lengths distributions for jets interacting with a crossflow of $\phi = 0.20$ and a jet velocity of $V_j = 12$ m/s at a downstream distance of $L = 10\ D$. Left column: $V_m = 0.1$ m/s, Re_{aq} = 100, Re_o = 540; middle column: $V_m = 0.4$ m/s, Re_{aq} = 380, Re_o = 2200; Right column: $V_m = 0.6$ m/s, Re_{aq} = 590, Re_o = 3300; top row: U-jet, Re_j = 5600, We_j = 17000; 2nd row: F-jet, Re_j = 5600, We_j = 17000; bottom row: V-jet, Re_j = 3900, We_j = 12000. 256

Figure 7.1 PIV measurement of a time-averaged velocity field for a laminar single-phase crossflow velocity of $V_m = 0.198$ m/s and a Reynolds number of Re = 1380 compared with its reflection in $r = 0$ and an ideal parabolic laminar flow profile for the same velocity. 260

Figure 7.2 Illustration of the method used to integrate the velocity profile of an almost symmetrical laminar flow to calculate the overall flow rate..... 261

Figure 7.3 PIV measurement of a time-averaged velocity field for a two-phase crossflow with a velocity of $V_m = 0.2$ m/s and four aqueous phase fractions of $\phi = 0.05$, $\phi = 0.10$, $\phi = 0.20$, and $\phi = 0.50$, at a distance of $L = -2\ D$. 262

Figure 7.4 Top: PIV measurement of a time-averaged velocity field at a downstream position of $L = 10\ D$ for F-jet with a velocity of $V_j = 8$ m/s and Re_j = 3600, We_j = 7300 interacting with a crossflow velocity of $V_m = 0.2$ m/s and aqueous phase fractions of $\phi = 0.05$ (Re_{aq} = 190, Re_o = 1100) and $\phi = 0.20$ (Re_{aq} = 620, Re_o = 1000)..... 263

Figure 7.5 PLIF view at a downstream position of $L = 10\ D$ for F-jet with a velocity of $V_j = 8$ m/s and Re_j = 3600, We_j = 7300 interacting with a crossflow velocity of $V_m = 0.2$ m/s and various aqueous phase fractions. Left: $\phi = 0.05$ (Re_{aq} = 190, Re_o = 1100); Right: $\phi = 0.20$ (Re_{aq} = 620, Re_o = 1000). 263

Figure 7.6 PIV measurement of a time-averaged velocity field at $L = 10\ D$ for different jet types with a velocity of $V_j = 8$ m/s interacting with an aqueous phase fraction of $\phi = 0.20$ and two crossflow velocities of $V_m = 0.2$ m/s and $V_m = 0.6$ m/s. Top: F-jet, Re_j = 3600, We_j = 7300; Bottom: V-jet, Re_j = 2500, We_j = 5100. 265

Figure 7.7 PIV measurement of a time-averaged velocity field for different jet types with velocities of V_j = 4 m/s, V_j = 8 m/s and V_j = 12 m/s interacting with a crossflow with a velocity of V_m = 0.2 m/s and an aqueous phase fraction of ϕ = 0.20 with Reynold numbers Re_{aq} = 620, Re_o = 1000. Top: F-jet; Bottom: V-jet. 267
Figure 7.8 PIV measurement of a time-averaged velocity field for a U-jet with a velocity of V_j = 4 m/s and Re_j = 1900, We_j = 1800 interacting with a crossflow of V_m = 0.2 m/s and an aqueous fraction of ϕ = 0.20 with Re_{aq} = 620, Re_o = 1000. 268
Figure 7.9 Inferred cross-sectional average velocity field of the U-jet, with an aqueous phase layer at the bottom which acts as a barrier to mixing when present. 270
Figure 7.10 PIV measurement of a time-averaged velocity field for jet a with a velocity of V_j = 4 m/s and Re_j = 1900, We_j = 1800 interacting with a crossflow of V_m = 0.2 m/s and a varying aqueous fraction. Top row: ϕ = 0.05, Re_{aq} = 190, Re_o = 1100; Middle row: ϕ = 0.20, Re_{aq} = 620, Re_o = 1000; Bottom row: ϕ = 0.50, Re_{aq} = 1300, Re_o = 660. 272
Figure 7.11 PIV measurement of the time-averaged vorticity fields for jet with a velocity of V_j = 4 m/s and Re_j = 1900, We_j = 1800 interacting with a crossflow of V_m = 0.2 m/s and a varying aqueous fraction. Top row: ϕ = 0.05, Re_{aq} = 190, Re_o = 1100; Middle row: ϕ = 0.20, Re_{aq} = 620, Re_o = 1000; Bottom row: ϕ = 0.50, Re_{aq} = 1300, Re_o = 660. 273
Figure 7.12 PIV measurement a vertical time-space plot of vorticity field for a jet with a velocity of V_j = 4 m/s and Re_j = 1900, We_j = 1800 interacting with a crossflow of V_m = 0.2 m/s and a varying aqueous phase fraction. Top row: ϕ = 0.05, Re_{aq} = 190, Re_o = 1100; Middle row: ϕ = 0.20, Re_{aq} = 620, Re_o = 1000; Bottom row: ϕ = 0.50, Re_{aq} = 1300, Re_o = 660. 275
Figure 7.13 PIV measurement the horizontal time-space plot of vorticity field at a height of r = 0.8 R between a distance of L = 0.5 and 1.0 D for a jet with a velocity of V_j = 4 m/s and Re_j = 1900, We_j = 1800 interacting with a crossflow of V_m = 0.2 m/s and an aqueous fraction ϕ = 0.20 and Re_{aq} = 620, Re_o = 1000. 276

Figure 7.14 PIV measurement of a time-averaged velocity field for jet a with a velocity of V_j = 4 m/s and Re_j = 1900, We_j = 1800 interacting with a varying crossflow velocity with an aqueous phase fraction of ϕ = 0.20. Top row: V_m = 0.1 m/s; 2nd row: V_m = 0.2 m/s; 3rd row: V_m = 0.4 m/s; Bottom row: V_m = 0.6 m/s. 278

Figure 7.15 PIV measurement of a time-averaged vorticity field for jet a with a velocity of V_j = 4 m/s and Re_j = 1900, We_j = 1800 interacting with a varying crossflow velocity with an aqueous phase fraction of ϕ = 0.20. Top row: V_m = 0.1 m/s; 2nd row: V_m = 0.2 m/s; 3rd row: V_m = 0.4 m/s; Bottom row: V_m = 0.6 m/s. 279

Figure 7.16 PLIF image of an U-jet with a velocity of V_j = 4 m/s and Re_j = 1900, We_j = 1800 interacting with a V_m = 0.6 m/s crossflow velocity and an aqueous phase fraction of ϕ = 0.20 with Re_{aq} = 1900, Re_o = 2900, showing trough followed by a peak of the aqueous layer height of the incoming flow. 280

Figure 7.17 PLIF image of a U-jet a with a velocity of V_j = 4 m/s and Re_j = 1900, We_j = 1800 interacting with a V_m = 0.6 m/s crossflow velocity and an aqueous phase fraction of ϕ = 0.20 with Re_{aq} = 1900, Re_o = 2900. Showing several changes in the jet angle of deflection during a single experimental run. Left column: high jet angle of deflection; Right column: low jet angle of deflection. 281

Figure 7.18 PIV measurement of time-space vorticity field for a jet with a velocity of V_j = 4 m/s and Re_j = 1900, We_j = 1800 interacting with a varying crossflow velocity with an aqueous phase fraction of ϕ = 0.20. Top row: V_m = 0.1 m/s; 2nd row: V_m = 0.2 m/s; 3rd row: V_m = 0.4 m/s; Bottom row: V_m = 0.6 m/s. 283

Figure 7.19 PIV measurement of a time-averaged velocity field for a jet with a varying velocity interacting with a crossflow velocity of V_m = 0.2 m/s with an aqueous phase fraction of ϕ = 0.20 with Re_{aq} = 620, Re_o = 1000. Top: V_j = 4 m/s, Re_j = 1900, We_j = 1800; Middle: V_j = 6 m/s, Re_j = 2800, We_j = 4000; Bottom: V_j = 8 m/s, Re_j = 3700, We_j = 7300. 285

Figure 7.20 Stereo-PIV measurements showing a time-averaged velocity field measurements for a jet with a velocity of V_j = 4 m/s and Re_j = 1900, We_j = 1800 interacting with a crossflow velocity of

V_m = 0.1 m/s with an aqueous phase fraction of ϕ = 0.10 with Re_{aq} = 170, Re_o = 530. 286
Figure 7.21 Stereo-PIV measurements plotting the contour map of the three separate components of the time-averaged velocity field for a jet with a velocity of V_j = 4 m/s and Re_j = 1900, We_j = 1800 interacting with a crossflow velocity of V_m = 0.1 m/s with an aqueous phase fraction of ϕ = 0.10 (Re_{aq} = 170, Re_o = 530). Top: *u*-component; Middle: *v*-component; Bottom: *w*-component. 287
Figure 7.22 Stereo-PIV measurements of three instantaneous velocity field for a jet with a velocity of V_j = 4 m/s and Re_j = 1900, We_j = 1800 interacting with a crossflow velocity of V_m = 0.1 m/s with an aqueous phase fraction of ϕ = 0.10, Re_{aq} = 170, Re_o = 530. The time interval between each of these frames is 300 ms 289
Figure 7.23 Calculation of the kinetic energy for a jet with a velocity of V_j = 4 m/s and Re_j = 1900, We_j = 1800 interacting with a crossflow of V_m = 0.1 m/s and an aqueous fraction ϕ = 0.10 with Re_{aq} = 170, Re_o = 530. Top: 2-component PIV; Bottom: 3-component stereo-PIV. 291
Figure 7.24 Calculation of the turbulent kinetic energy for a jet with a velocity of V_j = 4 m/s and Re_j = 1900, We_j = 1800 interacting with a crossflow of V_m = 0.1 m/s and an aqueous fraction ϕ = 0.10 with Re_{aq} = 170, Re_o = 530. Top: 2-component PIV; Bottom: 3-component stereo-PIV. 292
Figure A.1 Variation of refractive index with viscosity for Dow Corning 200 (polydimethylsiloxane) silicone oils (Dow Corning datasheets). 354
Figure A.2 Refractive index variation for two temperatures of 25 ºC and 60 ºC over a full range of glycerol solutions; data from Leron (2012) 356
Figure B.1 Upstream, interaction and downstream modelling sections 361
Figure B.2 CFD Simulations showing water-oil crossflow being mixed by jets. Left: single vertically upward jet; Right: twin impinging jets, one arranged vertically up and the other vertically down. 362
Figure B.3 The C_1/C_2 ratio against distance from jet. Left: single upward jet C_1/C_2 at 1.000 s and 1.284 s.; Right: two vertically impinging jets at 1.000 s and 1.229 s. 362

List of Tables

Table 1.1 Range over which crude oil sampling water dispersion model has been validated as stated by the ASTM (2010). 37
Table 2.1 List of selected solid-liquid-liquid refractive index-matched systems. 78
Table 2.2 Surface contact angle measurements demonstrating how the initial solid wetting can affect the results, (Angeli and Hewitt 1999)..... 85
Table 3.1 Depth of field calculations..... 107
Table 3.2 Minimum length scales that can be tracked by particles with an error of less than 1% in both the oil and aqueous phases. 118
Table 3.3 Ranges of properties used in the experimental campaigns as well as those seen in industrial applications. 124
Table 3.4 Fraction of aqueous phase that is detected in the binarization Stage-1 when changing window sizes and the sensitivity 133
Table 3.5 Fraction of aqueous phase detected in binarization Stage-2 when it is combined with a stage-1 using a sensitivity of 0.2 and window size of 260×580. 135
Table 3.6 Fraction of aqueous phase detected in the combined binarization stage when using the stage-1 window size of 1260×580 and stage-2 window size of 11×9 and varying the sensitivity of the two stages. 135
Table 3.7 Comparison of the metered phase fraction against the phase fraction calculated from the binarized image for 100 frames of highly dispersed flows at a location of $L = 4D$ from the jet. 137
Table 3.8 Comparison of the metered phase fraction against the phase fraction calculated from the binarized image for 100 frames of highly dispersed flows at a location of $L = 4D$ from the jet. 143
Table 3.9 Change in measurement during the various stages of the droplet detection method for a crossflow of $V_m = 0.6$ m/s and an aqueous phase fraction of $\phi = 0.10$ at a distance of $L = 10\ D$ with a U-Jet with a velocity of $V_j = 8$ m/s. 147

Table 3.10 Comparison of automatic droplet detections versus hand droplet detections from sample images. 149
Table 3.11 Calculation of the number of histogram bins for the experimental test cases used in Chapter 6. 153
Table 4.1 Optical contact angle measurements. 164
Table 4.2 Properties of the experimental fluids and particles. 167
Table 6.1 Drop chord length statistics for a subset of the experimental test cases. 230
Table 6.2 Droplet chord length statistics and associated residence times for a U-jet with a velocity of V_j = 12 m/s jet with Re_j = 5600 and We_j = 17000. 237
Table 7.1 Vortex measurements for a jet with V_j = 4 m/s velocity, Re_j = 1900 and We_j = 1800 interacting with V_m = 0.2 m/s crossflow of varying aqueous phase fraction. 274
Table 7.2 Vortex measurements for a jet with V_j = 4 m/s velocity, Re_j = 1900 and We_j = 1800 interacting with a varying crossflow with an aqueous fraction ϕ = 0.20. 282
Table A.1 List of plastics and polymer-based refractive index-matched systems including FEP, THV, ETFE, PVDF, PVA, PMMA, Nylon and PS. 331
Table A.2 List of rubber-based refractive index-matched systems. 339
Table A.3 List of custom-polymer, resin and hydrogel refractive index-matched systems. 341
Table A.4 List of glass-based refractive index-matched systems including fused-quartz, silica-gel, borosilicate and soda-lime glass, as the solid phase. 343
Table A.5 List of selected liquid-liquid refractive index-matched systems. 349
Table A.6 List of organic liquids previously in refractive index-matched experiments, with their RI, surface tension, dynamic viscosity and density. 352
Table A.7 Hydrophilic liquids previously used in refractive index-matched experiments, with their refractive index, surface tension, dynamic viscosity and density. 357
Table A.8 List of solids used for refractive index tuning of aqueous solutions. 358

Nomenclature

Latin Letters

A	Cross-sectional area [m^3]
c	Speed of light in a vacuum [m/s] or camera circle of confusion [mm]
c_x	The position of a droplet centre in the x-axis
c_y	The position of a droplet centre in the y-axis
C	Aqueous phase concentration [–]
C_0	Average aqueous phase concentration in the pipe [–]
C_1	Average aqueous phase concentration in the top half of the pipe [–]
C_2	Average aqueous phase concentration in the bottom half of the pipe [–]
D	Pipe internal diameter [m]
D_h	Hydraulic diameter [m]
D_j	Jet exit internal diameter [m]
D_{10}	Mean diameter [m]
D_{32}	Sauter mean diameter [m]
D_{max}	Maximum droplet diameter [m]
Dv_{10}	Droplet diameter for 10% of the cumulative mass [m]
Dv_{50}	Droplet diameter for 50% of the cumulative mass [m]
Dv_{90}	Droplet diameter for 90% of the cumulative mass [m]
e	Pipe roughness [m]
E	The rate of energy dissipation [W/kg]
E_0	The rate of energy dissipation in a long straight pipe [W/kg]
Eo	Eötvös number [–]
Fr	Froude number [–]
d	Droplet diameter [m]
f_F	Fanning friction factor [–]
f	Darcy friction factor [–] or lens focal length [mm]
F	Force [N]
g	Gravitational acceleration [m/s^2]
h_0	Initial jet radius [m]
H_{aq}	Height of the aqueous phase [m]
h_{min}	The minimum height the jet penetrates [m]
h_{max}	The maximum height the jet penetrates [m]
k	Turbulent kinetic energy [m^2/s^2]
K	Viscometer ball calibration constant [mPa]
KE	Kinetic energy [J/kg]
Q	Volumetric flow [m^3/s]
l	Laser sheet thickness [m]
L	Characteristic length or axial distance from the jet [m]
M	Number of component vectors [–]
n	Refractive index [–]
N	The number of droplets [–] or lens F-number. [–]
Oh	Ohnesorge number [–]
p	Wetted perimeter [m]
P	Pressure [Pa]
P_0, P_1, P_2, P_3, P_4, P_5	Water concentration profiles at heights 0,1,2,3,4,5 [–]
P_j	Power of a jet [W]
r	Distance from pipe centre [m]
R	Pipe internal radius [m]
Re	Reynolds number [–]
Ri	Richardson number [–]
S	Standard deviation [–]
St	Stokes number [–]

t	Time
t_0	Particle relaxation time [s]
T	Temperature [°C]
TKE	Turbulent kinetic energy [J/kg]
$t_{res,}$	Residence time from jet [s]
$t_{res,4}$	Residence time at 4 diameters from jet [s]
$t_{res,10}$	Residence time at 10 diameters from jet [s]
u	Streamwise or axial velocity component [m/s] or distance from CCD to laser plane [mm]
U^*	Pipe friction velocity [m/s]
V	Velocity component [m/s]
v	Vertical velocity component [m/s]
W	Water droplet settling rate due to gravity [m/s]
$W_{>5\%}$	Water droplet settling rate due to gravity for water fractions over 5% [m/s]
W_{corr}	Corrected water droplet settling rate due to gravity [m/s]
w	3rd velocity component, travelling perpendicular the laser plane [m/s]
We	Weber number [–]
x	The horizontal component of the measurement plane
y	The vertical component of the measurement plane
z	Component through the measurement plane, i.e. perpendicular to the laser sheet
Z_m	Maximum height rise of a jet [m]

Greek Letters

β	The characteristic parameter of a piping element [–]
δ	A small change in parameter
Δ	Change in parameter
ε	Eddy viscosity [m^2/s]; Turbulent dissipation [m^2/s^3]
ζ	Dimensionless constant with a value of 0.36
μ	Dynamic viscosity [Pa·s]
ν	Kinematic viscosity [m^2/s]
ρ	Density [kg/m^3]
σ	Interfacial or surface tension [N/m]
ϕ	Aqueous phase fraction in crossflow [–]
ϕ_j	Aqueous phase fraction in jet [–]
ϕ_i	The fraction of phase i [–]
θ	Contact angle in aqueous phase [°] or angle around a circle [°]
ψ	The angle of the jet in the pipe cross-section [°]
Ω	The angle of the jet from the pipe wall from facing forward [°]

Subscripts

aq	Aqueous phase
b	Ball
c	Continuous phase
d	Droplet; Dispersed phase
h	Hydraulic
i	General formula index
int	Interface between phases
j	Jet
j_o	Jet oil
j_aq	Jet aqueous phase
L	Liquid
m	The liquid mixture before the jet
mj	The liquid mixture after jet
o	Oil
p	Particle
res	Residence time
so	Silicone oil
s	Sample standard deviation
w	Water
x	The horizontal component of the measurement plane
y	The vertical component of the measurement plane

z	The component through the measurement plane, i.e. perpendicular to the laser sheet

Abbreviations

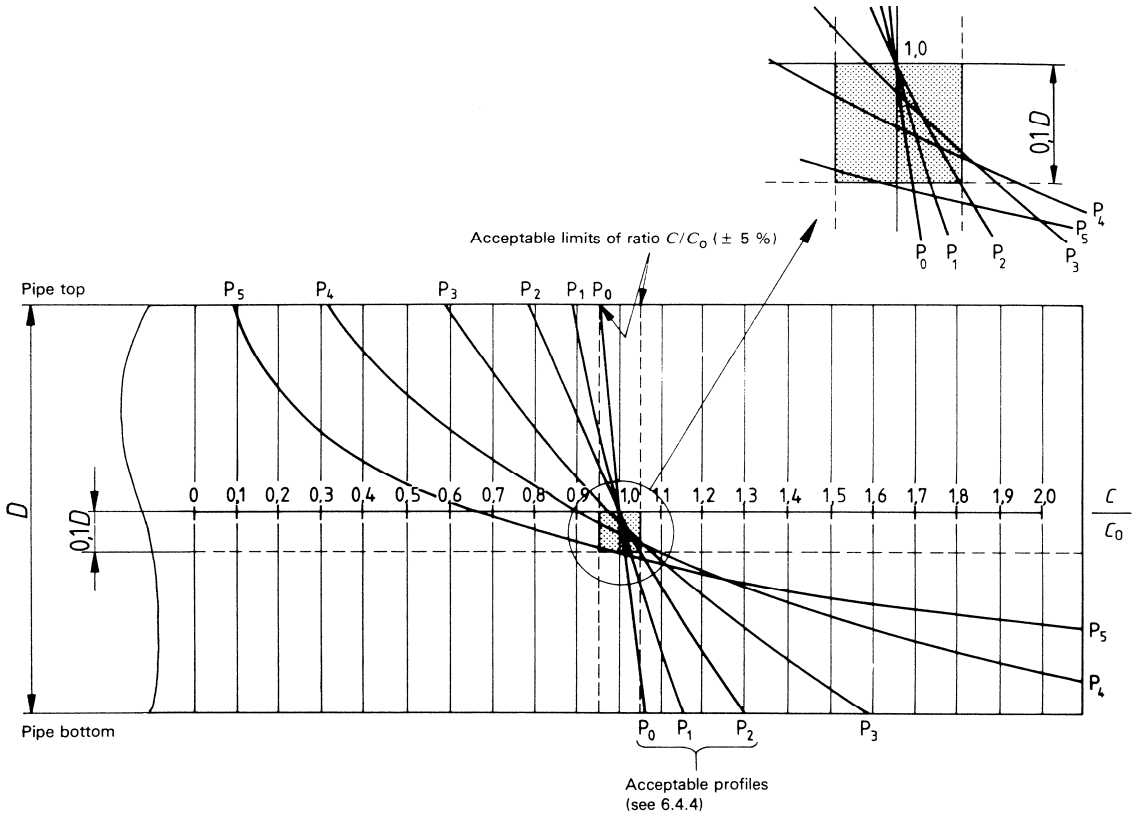
2-D	Two-dimensional
3-D	Three-dimensional
CFD	Computational fluid dynamics
CVP	Counter-rotating vortex pair
D O/W	Flow with a dispersion layer of oil-in-water
D O/W&W	Flow with a dispersion layer of oil-in-water and water layer
D O/W&W/O	Two dispersion layers one oil-in-water and the other water-in-oil
DES	Detached eddy simulation
DNS	Direct numerical simulation
F-jet	Forward-facing 4 mm jet
ISO	International Organization for Standardization
LES	Large-eddy simulation
OD	Outside diameter
PBM	Population balance model
PFEM	Particle finite element method
RANS	Reynolds Averaged Navier-Stokes
RI	Refractive index
RIM	Refractive index-matched
ST	Stratified flow
ST&MI	Stratified flow with a mixing layer
RSM	Reynolds stress model
U-jet	Vertically upward 4 mm jet
V-jet	Twin 2.8 mm jets arranged in a V shape in the pipes cross-section
VOF	Volume of fluid
W/O	Water-in-oil dispersions

Chapter 1

Introduction

Crude oil production is a multiphase process involving oil, water, gas and sediments. The initial stages of production separate these phases to varying extents, resulting in the crude oil in pipelines for export and transportation typically containing average free water percentages of 5% or less. Large crude oil shipments are of the order of a million barrels, which, at a nominal $50 US dollars a barrel, are valued at $50 million US dollars. The high value of these crude oil transactions is therefore affected by small errors in the water fractions. Financial losses are compounded through the additional costs involved in the processing and removing water and associated dissolved salts along with the added taxation incurred by treating water as oil. These potential losses lead to the desire to ascertain the phase fraction and properties of the crude oils through obtaining physical liquids samples which can then be subsequently analysed within a laboratory. The samples are collected by both the supplier and customer so that transactions properties and values can be agreed and confirmed following crude oil transfers.

These sampling systems obtain a representative composite sample of crude oil batches through an automatic collection of between 2000 and 10000 flow proportional sub-samples taken during pipeline transfers. The samples need to be representative of current pipeline contents and hence sampling systems require the water to be evenly dispersed throughout the cross-section of the pipe. However, horizontal liquid-liquid flows with low pipeline velocities undergo gravitationally induced stratification due to liquid density differences, see the profile tests in Figure 1.1. In typical process conditions, the water fraction also undergoes temporal changes both short duration changes, occurring due to the formation of water slugs and longer duration changes occurring through stratification in holding tanks. These temporal and spatial phase fraction changes make flow homogenisation a design requirement of sampling systems.



NOTE — The ratio C/C_0 is the ratio of the water concentration at a point to the mean water concentration at the the sampling location.

Profiles P_3, P_4 and P_5 are not acceptable because the ratio C/C_0 is outside the range 0,95 to 1,05 for at least part of the recommended region for the sample withdrawal point (see figures 2 and 3).

Figure 1.1 Six profile tests demonstrating the variation in vertical water distribution against decreasing pipeline velocity where P_0 is the highest velocity and P_5 is the lowest velocity (ISO 1999).

Adequate mixing can be obtained by using either passive or active mixing techniques. Passive mixing techniques extract energy from the flow for mixing, examples of which, include pipe elements like valves, Venturi, orifice plates and static mixers. Indeed, static mixers can be purposefully designed to create liquid-liquid dispersions (see Figure 1.2), examples include the SMX (Legrand et al., 2001; Rama Rao et al., 2007; Theron et al., 2010), SMX+ (Theron and Sauze, 2011), SMV (Sembira et al., 1986; Lobry et al., 2011) and KSM (Middleman, 1974; Yamamoto et al., 2007; Voulgaropoulos and Angeli, 2017). These static mixers provide adequate liquid-liquid dispersions over a restricted operating range of velocities, viscosities and densities, however, extending this range leads to excessive pressure drops which can be both undesirable and impractical.

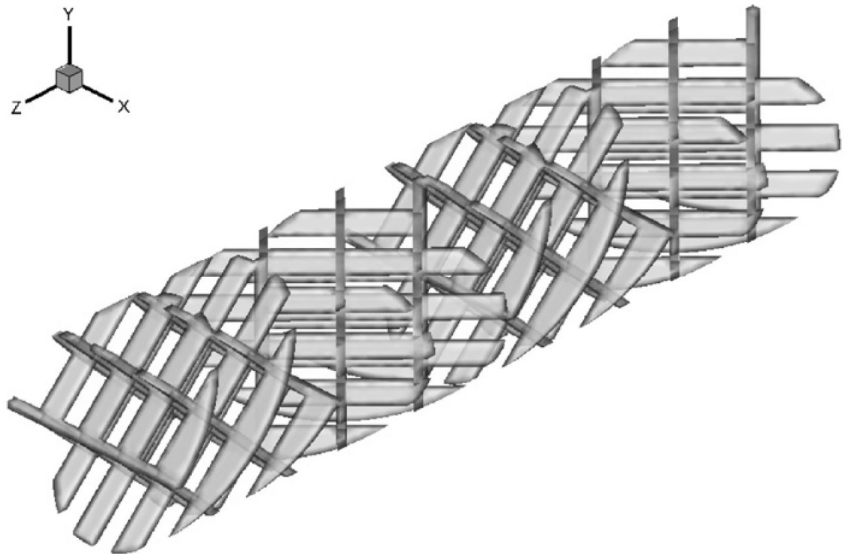


Figure 1.2 Mixing elements of the Sulzer SMX mixer which are used for creating fine liquid-liquid dispersions (Rama Rao et al., 2007).

In contrast, active mixing uses external sources of energy, like pumps, through adding energy to the flows to homogenize the fluids rather than extracting it from the flow thus alleviating the tight restrictions of static mixers. These active mixers have the advantage that the degree of energy inputted to the flows can be varied which allows mixing levels to be varied, which is desirable when trying to prevent the formation of difficult to separate tight emulsions. In the oil industry, the most common installed active mixer for crude oil sampling systems uses a pump to create high velocity transverse and impinging jets. These jets typically have velocities of up to 30 m/s, where this limit is due to the consideration of pipe walls erosion. The jet lower limits vary and depend on geometrical conditions, fluid properties and flow conditions. Understanding these high-velocity transverse jets is therefore critically important in sampling system designs.

Mixing elements are located upstream of the sampling system so the liquids will be thoroughly dispersed at the point of sampling when working as intended. However, the level of mixing varies with the liquid proprieties including density, viscosity and interfacial tension as well as with the process's conditions including water fraction and pipeline mixture velocity. Importantly, entrained process water must remain resident long enough following mixing so that samples are representative of the average cross-sectional water concentration at the point and time of sampling. However, it is undesirable to mix the fluids to the point where they become a stabilized

or tight emulsion given the added costs associated with water separation from crude oil. Therefore, it is vital to understand the incoming liquid-liquid flow and the resulting outgoing dispersion when designing any mixing technology.

To predict the water distribution in crude oils, designers of sampling systems currently use the analytical model of ISO 3171:1999 Annex A (ISO, 1999). This model is used to estimate the distribution in a variety of pipeline conditions, liquid properties and mixer variants. This Annex A model was developed during the 1970s and 1980s, but subsequent changes in the properties of traded crude oils and process requirements have led to this model being used significantly beyond its original design limits. The similar ASTM (2010) standard includes the ranges over which the calculations have been validated, Table 1.1, and expresses caution when extrapolating beyond this ranges. This has rightly led to concerns about model validity and an industrial desire to develop newer models and computational fluid dynamics (CFD) techniques.

Table 1.1 Range over which crude oil sampling water dispersion model has been validated as stated by the ASTM (2010).

Relative density	0.8927 – 0.8550 (27°– 34°API)
Pipe diameter	40 cm – 130 cm (16 in – 53 in)
Kinematic Viscosity	6 mm^2/s – 25 mm^2/s at 40 °C
Flow velocity	<3.7 m/s
Water concentration	<5% v/v

This thesis develops the understanding of the behaviour of horizontal pipeline jet mixers through a series of experimental campaigns. Providing insights so designers can optimize jet mixers to reduce energy requirements while providing engineers and operators increased confidence in the physical samples taken from pipelines.

1.1 Jet mixing background

Jet mixers for crude oil and process water were developed during the late 1970s and early 1980s (Jiskoot, 1979; Slater, 1983; Peerless and Jiskoot, 1978; Freeman, 1980; Peerless and Walker, 1985), becoming commercialized in the 1980s (Slater 1983; Jiskoot, 1984). This coincided with the demand for accurate systems for sampling water in crude oils and the associated development of standards. These jet mixing systems quickly became the dominant form of mixing for these fluids flows.

Only a small number of companies were involved in early jet mixer development and a single company, Jiskoot Autocontrol Ltd, became the market leader of these jet mixing systems leading to a drop in the number of manufacturers and suppliers. Over the next two decades, competition remained limited due to the existence of commercial patents (Jiskoot, 1979; Jiskoot, 1984; Jiskoot 1999) that inhibited competition. Then, as the patents expired towards the end of the 2000s, new competitors began to emerge which resulted in a new era of development of jet mixers and their associated engineering tools.

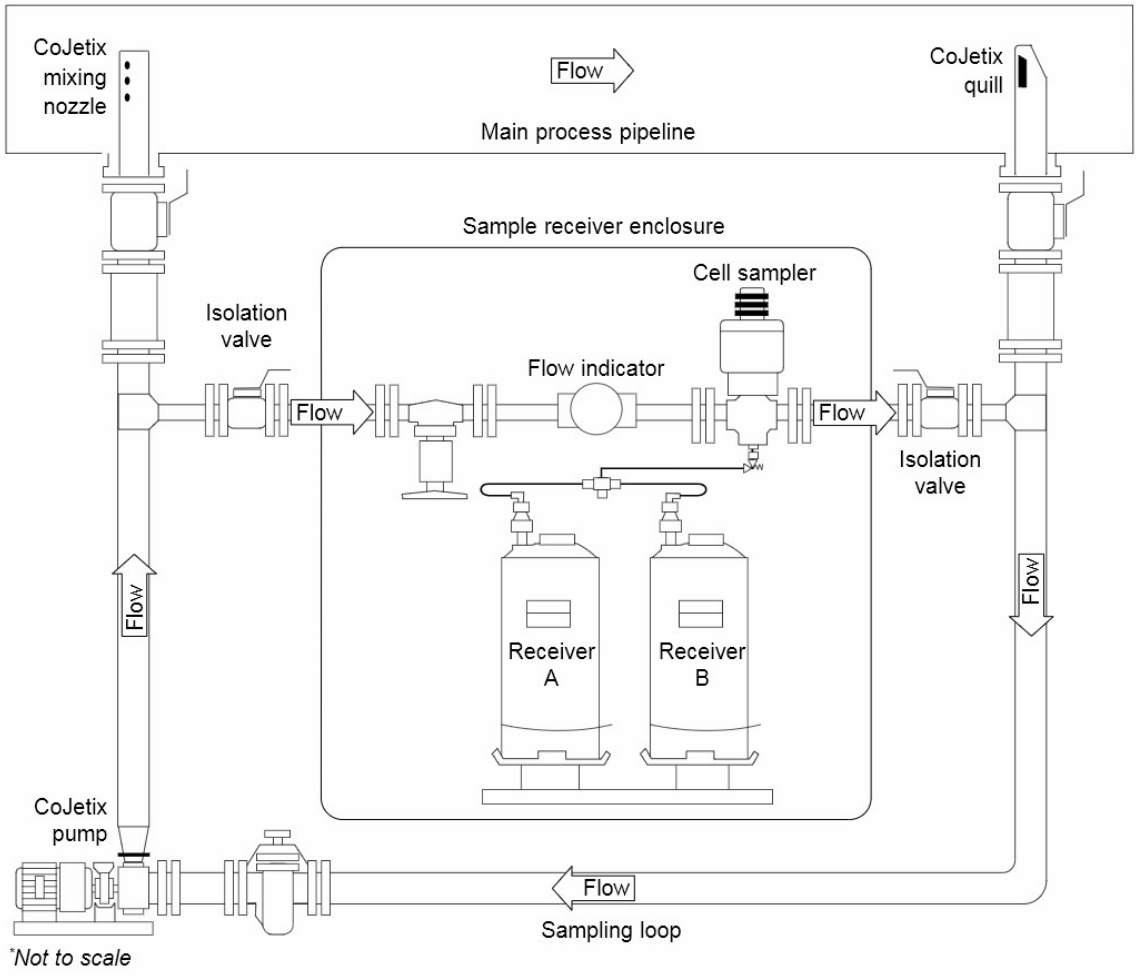


Figure 1.3 A jet mixer system known as a "CoJetix" that uses a nozzle and quill that is inserted into pipelines that are 6-inches or greater in diameter, (Cameron, 2013).

Current designs of jet mixers typical have several jets that originate from either the walls or from a probe inserted into the flow known as a nozzle (Jiskoot, 1984; Jiskoot, 1999). An example of the nozzle system design is presented in Figure 1.3. This

nozzle design reduces the required jet penetration depth in larger diameter pipelines, where they have been successfully used on pipelines as large as 56-inches in diameter. However, the insertion of a nozzle into smaller pipelines can create a large cross-sectional obstruction to the flow which creates an excessive pressure drop. This pressure drop results in nozzle designs typically only being used on pipelines of 6-inch or greater (Wright et al., 2020). Penetration depth is less of a concern for small diameter pipelines and therefore flow obstructions are eliminated through using wall jet mixer designs like that in Figure 1.4 and detailed in Jiskoot et al. (2018).

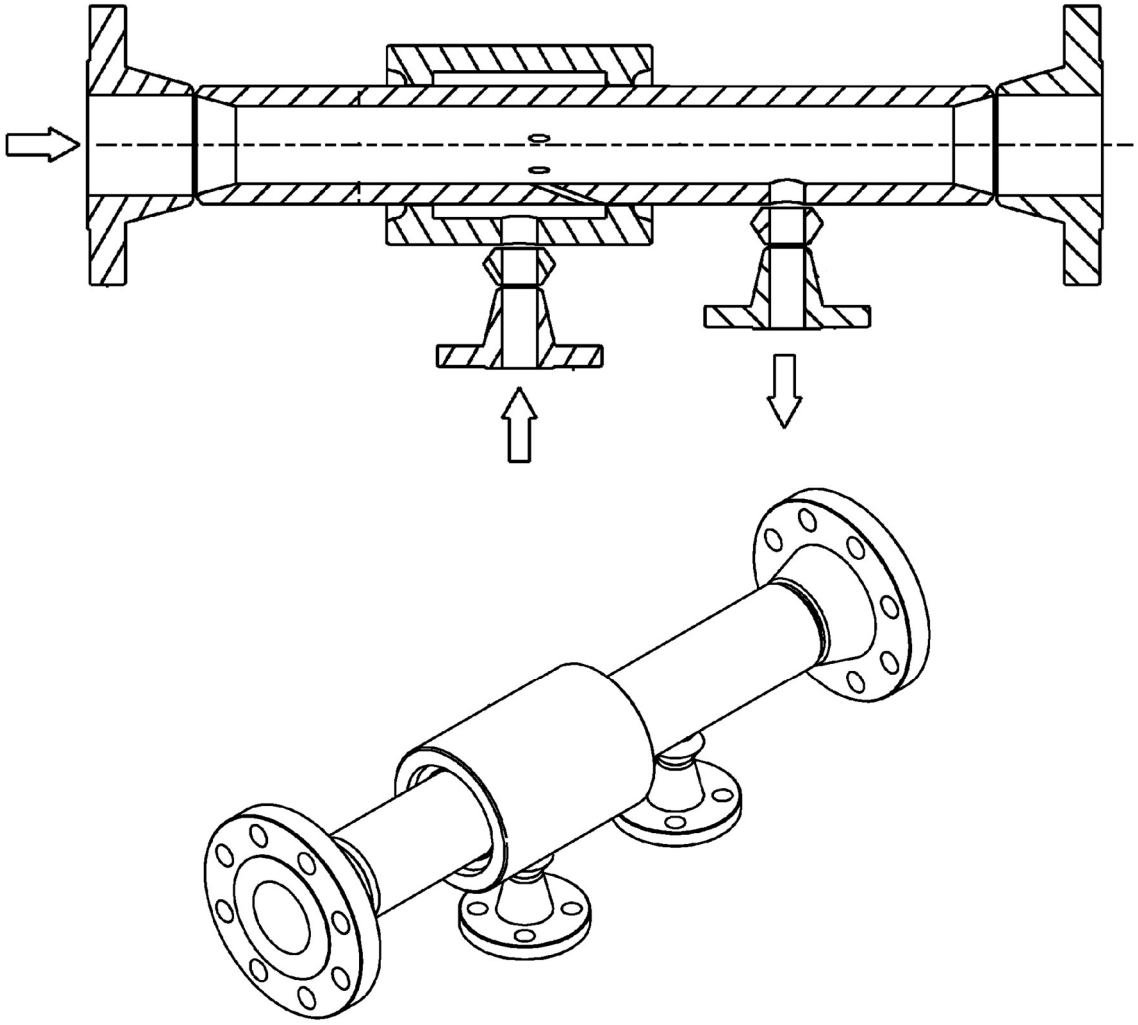


Figure 1.4 An example wall originating jet mixer design which is used for pipelines that are 8 inches or smaller (Jiskoot et al., 2018).

In horizontal pipelines, the nozzle and wall jets are situated towards the bottom of the pipe where a higher water fraction is expected, while for vertical

based systems the jets are distributed across the entire pipe diameter or circumference. Wall-based jet mixers in horizontal flows were selected as the focus of this thesis, even though many of the principles that have been developed in this work apply to the larger horizontal nozzle designs.

The jets are formed from the same liquids as those flowing through the pipeline and as such the jets are a two-phase mixture that is predominately crude oil along with a varying fraction of water. The jet liquids are extracted downstream of the jet location at a position where the water is expected to be thoroughly dispersed within the oil so that the fluids are representative of the average.

The extraction point typically uses a probe known as a "quill" although occasionally a side T may be used instead. In general, this liquid extraction point is simultaneously used as the location where the samples are extracted for analysis and, therefore, its placement is critical when sampling for the accuracy of the phase fraction. The axial displacement along the pipeline between the jets and the sample extraction point is loosely constrained within ISO (1999), therefore, current designs have used distances based more on engineering experience rather than modelling.

The insights gained into mixing performance contained within this thesis are important, particularly at low velocities, where the spatial and temporal variations in dispersed phase concentration after mixing can be significant.

1.2 Objectives

The PhD investigation can be summarized as "what processes lead to mixing of liquid-liquid pipeline flows when using transverse jets, and how do the flows subsequently develop following jet interaction?" The project, therefore, investigates the mixing effect of jets in horizontal pipes, forcing segregated flows of water and oil into unstable water in oil dispersions. The project collects data experimentally on the flow fields and the spatiotemporal distribution of water and droplet sizes. These results can then be used to test and develop numerical and analytical models to predict the mixing behaviour of jet mixer designs.

The objectives of this PhD project are the following:

1. To design, construct and commission a liquid-liquid horizontal pipe flow facility that allows for mixing using several transverse jet configurations.

2. To develop advanced spatiotemporally-resolved laser-based diagnostics to measure the phase fractions, (phase distribution, interface height and droplet sizes) and both the 2- and 3-component velocity fields for both phases.
3. To design and run an experimental campaign covering a wide range of conditions for various jet geometries and arrangements.
4. To analyse the results to obtain insights into the complex flow, understand the relevant fluid dynamics phenomena, develop simple predictive tools, as well as create a database of results that can aid the development and validation of advanced computational fluid dynamics models.

1.3 Thesis structure

This thesis has eight chapters. Chapter 1 contains this introduction, motivation and study objectives. Chapter 2 reviews the literature for liquid-liquid flows and jets highlighting a lack of prior work. Chapter 3 describes the experimental flow facility and the techniques used to investigate the flows. Chapter 4 details classical experimental measurements including liquid properties, pressure drops, interface heights, phenomenological observations and flow pattern maps. Chapter 5 examines the PLIF measurements of phase concentration profiles and the associated industrial mixing parameter C_1/C_2. Chapter 6 discusses the development of droplet sizes and distributions and how these are affected by the experimental configuration. Chapter 7 discusses the velocity field measurements made using PIV and stereo-PIV and how these fields contribute to the mixing processes. Finally, Chapter 8 presents conclusions and suggestions for future work. Following this, we have appendices including a detailed review of refractive index-matched systems created during this project.

Chapter 2

Review of literature

This literature review focuses on prior liquid-liquid multiphase flows, jets, mixing and refractive index matching experimental systems. We start with multiphase flows then continue onto jets and finally cover refractive index matching (RIM).

2.1 Multiphase flows

Multiphase flows comprise of two or more immiscible phases, wherein a phase can be either a gas, liquid or solid where an interface is present between the phases. These multiphase flows are central to many diverse scales, settings and applications which include, but are not limited to, biomedical and biological systems, geological processes such as landslides, river and volcanic flows, planetary atmospherics, as well as industrial processes in the petrochemical, energy, nuclear, transport, automotive, manufacturing and food production sectors. Multiphase flows are often linked to important processes such as evaporation, condensation, boiling, mixing, reaction, cavitation, erosion, sedimentation and extraction. Despite this pervasive and important practical relevance, these flows are inherently complex, nonlinear and multiscale and remain an area of extensive research (Ibarra, 2017; Voulgaropoulos et al., 2019; Hosseinzadeh et al., 2018).

2.2 Liquid-liquid flows in horizontal pipes

In the case of multiphase flow where only two phases are present, the combinations reduce to liquid-solid, gas-solid, liquid-liquid, and liquid-gas. Immiscible liquid-liquid flows are therefore a type of multiphase flow that consists of two immiscible liquids, most commonly, an aqueous phase and an organic phase. The study of horizontal

liquid-liquid flows is of significance to this work as these studies provide insights into the expected flow conditions before encountering the mixing jets. Amundsen (2011) lists 63 horizontally liquid-liquid flow studies which have taken place over five decades, demonstrating that this subject has been studied in some detail.

In these horizontal liquid-liquid flows the two liquids typically differ in numerous properties like colour, refractive index, density and viscosity. Even relatively small differences in properties like density are frequently large enough for the flows to undergo gravitationally-induced separation and stratification. In turn, this stratification leads to a variation in the bulk velocity of the two phases, particularly during low flow velocities (Angeli and Hewitt, 2000; Voulgaropoulos 2018). Most generally, these horizontal flows can be considered to range from stratified flows to fully dispersed emulsions and these occur in many processes, for example, stratified flows are frequently encountered in low-velocity oil and gas transportation lines while fully dispersed emulsions are common in processing foods like dairy and chocolate, as well as in chemical processing and paint production.

More specifically complex interactions lead to several geometric configurations, known as “flow regimes” or “flow patterns” as reviewed in Ibarra et al. (2014). Flow regimes are dependent on many factors, including the liquid fractions and velocities, the liquid properties like density, viscosity and interfacial tension as well as the piping configuration, diameter, inclination, roughness and wetting properties. The different flow regimes have characteristics that can also differ including relative fluid velocities, hold up and pressure gradients.

Trallero et al. (1997) and Trallero (1997) attempted to standardize the classifications of flow patterns into the three basic groups presented in Figure 2.1, these groups are, 1) segregated flows, 2) water dominated dispersed flows, and 3) oil dominated dispersed flows. Segregated flows are stratified (ST) or stratified with mixing at the interface (ST&MI).

In stratified flows (ST), the water and oil phases are separated by an interface with the denser phase, normally water, on the bottom. Interfacial waves can be visibly present between the phases. Stratified flows with mixing at the interface (ST&MI) have separate oil and water phases at the top and bottom along with a mixing zone between the two liquids that can be complex and significant in size.

Water-dominated dispersed flows are categorized as either a dispersion of oil-in-water (D O/W) or a dispersion of oil-in-water with water (D O/W&W). In a

D O/W&W, a layer of the water phase exists, normally on the bottom, while the oil is dispersed in the continuous water phase, normally at the top. In contrast, for D O/W the oil is dispersed throughout the continuous water phase.

Oil-dominated dispersed flows are categorized as either dual dispersions of water-in-oil and oil-in-water (D O/W&W/O) or as water-in-oil dispersions (W/O). In D O/W&W/O two continuous phases are present in layers, in one layer the water is dispersed within a continuous oil phase, normally on the top, and a second layer where oil is dispersed in a continuous phase of water, normally on the bottom. It is important to remember that flow pattern maps are somewhat subjective especially close to transitions between regimes.

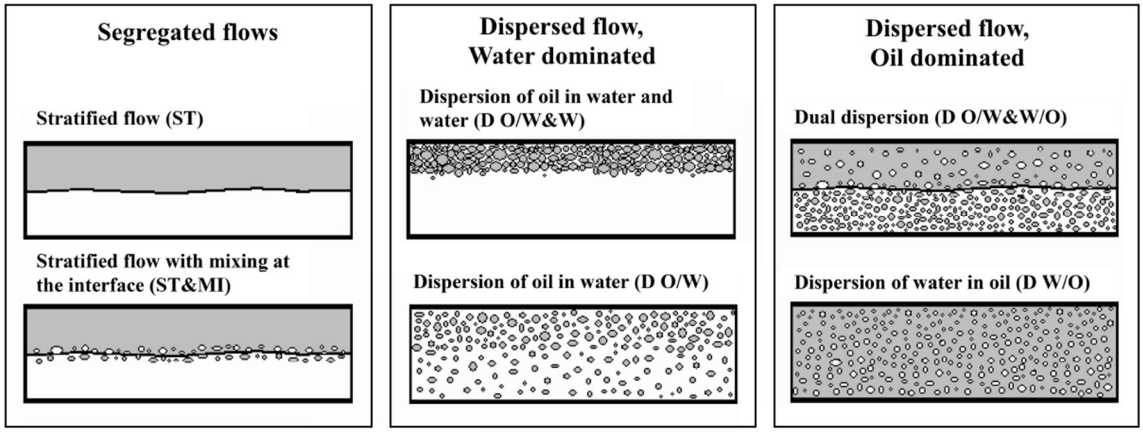


Figure 2.1 Views of oil and water flow regimes, adapted from Trallero (1995).

Sampling systems perform poorly in regimes other than homogeneous dispersions either of water in oil (D W/O) or oil in water (D O/W). When operating correctly, a jet mixer should, therefore, force a transition from one of these regimes into a dispersed flow (D W/O) or (D O/W). The transition from a fully-stratified flow into a fully-homogeneous flow is the most extreme and difficult for a jet mixer to achieve.

2.3 Jets

Jets are collimated flows of matter that are typically circular or planar in shape. Jets occur in many natural phenomena and over an enormous range of scales ranging from the subatomic jets formed by the atomic decays in particle accelerators due (Fries et al., 2016) up to galactic scale jets emitted from the centre

of active galaxies nuclei (Beall, 2014). Jets, therefore, have a wide range of applications and are particularly important within industrial sectors where they are used in processes like fuel injection, printing, propulsion, mixing, cleaning, and sprays. In many of these processes, the physics behind jets breakup is vitally important and a detailed review of the physics of jets including jet breakup can be found in Eggers and Villermaux (2008). The review of Eggers and Villermaux demonstrates that jets are a deeply studied phenomenon.

A single-phase jet is a flow of material that is injected into the same surrounding material, for example, a fast stream entering a lake. However, jets are often a multiphase phenomenon where the material of the jet is different from that of the surrounding medium, for example, a water fountain jet entering the air or oil injecting into water. Thus, if the jet and surrounding material consist of two immiscible fluids then they are a multiphase phenomenon. For this review, only jets consisting of liquid-gas and liquid-liquid shall be considered further for discussion.

2.4 Classical jet work

The earliest recorded studies of jets were conducted by Leonardo da Vinci in the Codex Leicester, (Eggers and Villermaux, 2008). Da Vinci realized that the detachment of a falling drop from a jet required gravity to overcome the cohesive surface tension forces that were holding the jet together. Laplace and Young realized that surface tension acted to both hold fluid particles together and to drive the breakup of the jet. The surface tension forces cause the jet to become narrower in the troughs of surface waves and this eventually leads to its breakup. In can be concluded therefore that the greater the bonding is between particles the faster a jet will break up (Eggers and Villermaux, 2008).

Savart performed experimental work on jets using a sheet of light where he observed undulations growing on the jet surface and realized that jet droplet formation was spontaneous and intrinsic to jets (Eggers and Villermaux, 2008). Plateau realized that surface tension was the source of jet breakup and that jets were unstable to any jet surface instability that exceeded a critical wavelength. This critical wavelength was calculated to be $2\pi h_0$, where h_0 is the initial radius of the jet (Eggers and Villermaux, 2008). Even still, Plateau calculated the optimal wavelength to be $8.76h_0$ from Savarts work.

Rayleigh realized jet dynamics were important over a critical wavelength. In doing so, Rayleigh introduced linear stability analyses of inviscid jets, which highlighted the importance of the most unstable surface wavelength, where the instabilities demonstrated the most rapid growth rate. Linear stability analysis eventually calculated that the optimal wavelength was $9.01h_0$ agreeing with Savarts results (Eggers and Villermaux, 2008).

2.5 Jet breakup

Sirignano and Mehring (2000) reviewed the theory of liquid jet disintegration where they found that there are four regimes or modes of a liquid jet breakup, there are; Rayleigh mechanism, first wind-induced, second wind-induced and atomisation.

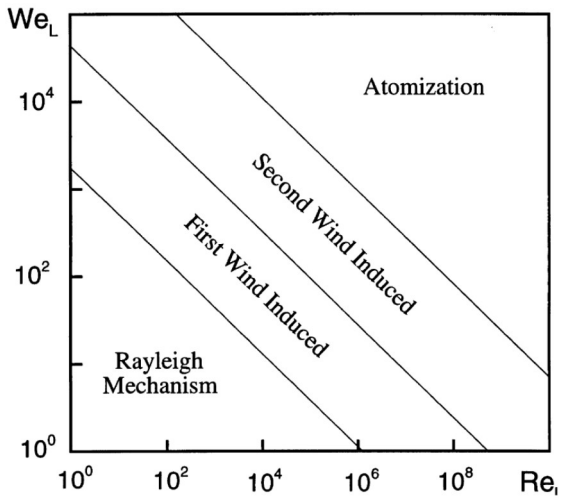


Figure 2.2 The four regimes of jet breakup plotted on a map of Reynolds number against Weber number Sirignano and Mehring (2000).

Figure 2.2 highlights that these four regimes are dependent on the Reynolds number (Eq. 2.1) and Weber number (Eq. 2.2). Alternatively, the Ohnesorge number (Eq. 2.3) is often used in place of the Weber number, see Figure 2.3:

$$\mathrm{Re} = \frac{\rho u L}{\mu} \qquad \text{Equation 2.1}$$

$$\mathrm{We} = \frac{\rho u^2 L}{\sigma} \qquad \text{Equation 2.2}$$

$$\mathrm{Oh} = \frac{\mu}{\sqrt{\mu\sigma L}} = \frac{\sqrt{\mathrm{We}}}{\mathrm{Re}} \qquad \text{Equation 2.3}$$

The Rayleigh mechanism is caused through Plateau-Rayleigh instability where surface tension amplifies the initial distortions on the jet which eventually lead to a pinch-off that forms droplets larger than the jet's exit diameter. In the first wind-induced regime, the inertia of the surrounding fluid causes undulations to be formed on the surface of the jet. These undulations subsequently lead to the breakup of the jet, forming droplets with a diameter of the order of that of the jet outlet. In the second wind-induced regime, the inertia of the surrounding fluid results in the jet breakup forming droplets that are smaller than the jet exit diameter. In the atomization regime, the jet forms the smallest droplets, essentially as soon as the jet exits the nozzle. Figure 2.3 provides a schematic of these four regimes.

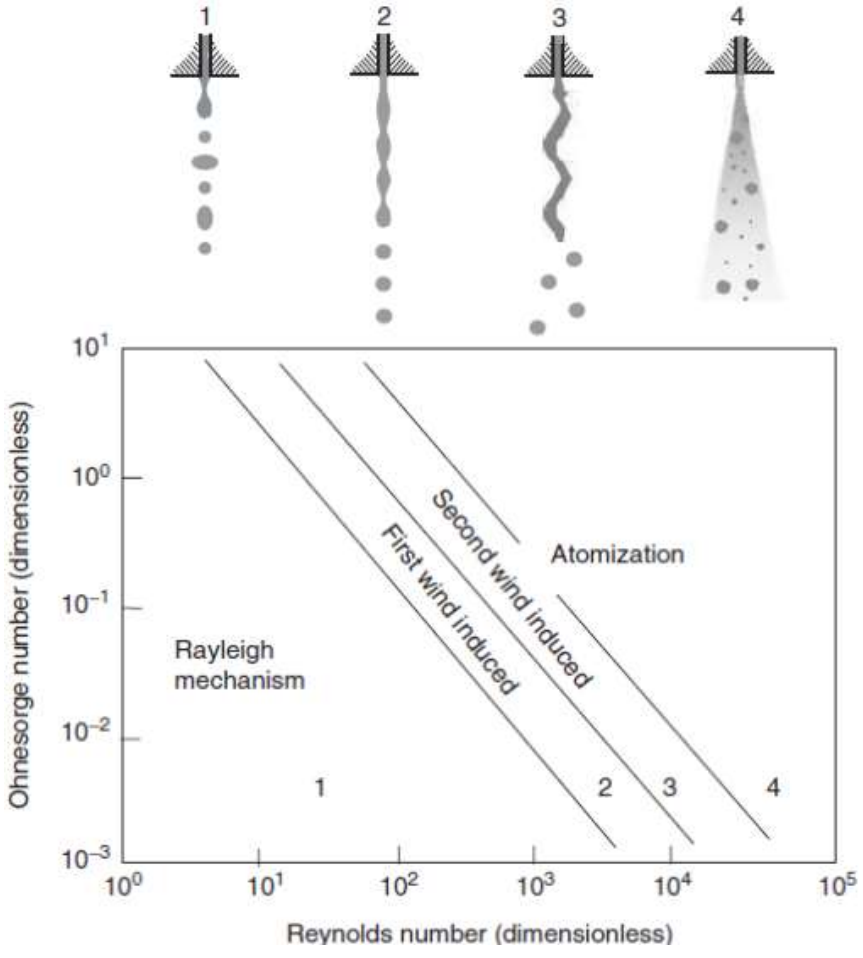


Figure 2.3 The four regimes of a liquid jet breakup plotted on a map of Reynolds number against Ohnesorge number (Bravo and Kweon, 2014).

2.6 Jets in crossflows

When jets are injected into a crossflow the jet is accelerated into the direction of the crossflow causing the jet to appear to turn. Vortices are formed on both the windward side (leading-edge vortices) and the leeward side (lee-side vortices) of the jet. These vortices lead to the breakup and mixing of the jet with the surrounding fluid. Downstream of the jet's exit, a counter-rotating vortex pair (CVP) develops, where one side of this counter-rotating pair is drawn in Figure 2.4. The CVP aids both mixing and droplet breakup as it helps to entrain the surrounding fluid into the core of jet where it experiences higher shear.

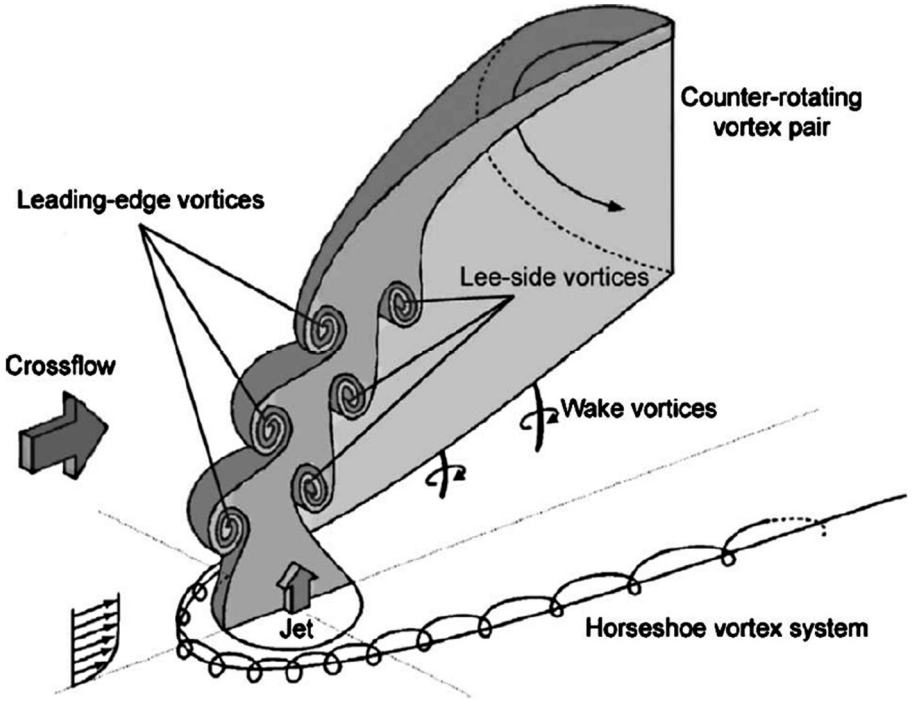


Figure 2.4 A schematic of a jet in crossflow (Galeazzo et al., 2011).

The breakup of the jet can be divided into the two stages labelled in Figure 2.5, primary breakup and secondary breakup. Primary breakup is the first stage and occurs when the droplets break off from the ligaments that are formed on a jet. Whereas, the secondary breakup occurs when the larger droplets formed during the primary breakup are subsequently broken up further.

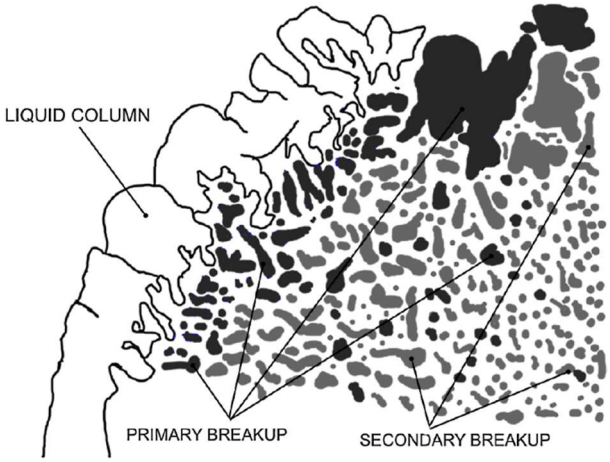


Figure 2.5 Schematic of jet breakup in a crossflow highlighting both primary and secondary droplet breakup (Pai et al., 2009).

2.7 Buoyant jet studies

Buoyant round jets which were emitted vertically into a stratified crossflow, schematically in Figure 2.6, have been investigated by Wright (1977) and Wright (1984). Wright (1984) developed simple power laws that describe both the jet height rise and its dilution relation in stratified crossflows.

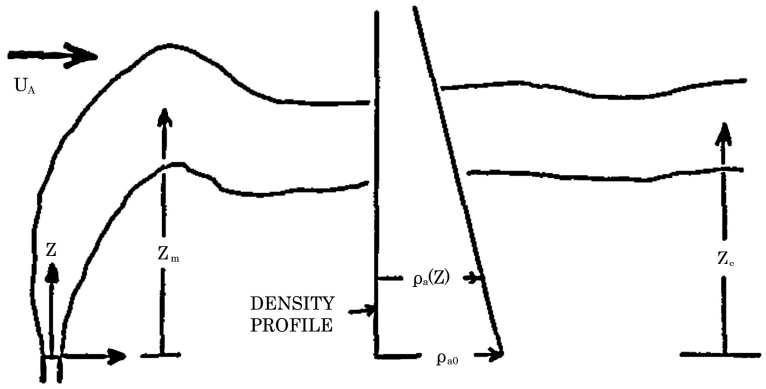


Figure 2.6 Sketch of a buoyant jet in stratified crossflow from Wright (1984).

Hwang and Chiang (1986) studied the relationship between the maximum rise and the emission conditions for buoyant jets in a stratified crossflow. The experiments were performed in stratified saltwater by injecting negatively buoyant jets of diameter 1.85, 3.05, 5.01 mm from at the top of a tank through a horizontally moving nozzle. A height fitting function was then developed that was found to closely match the height of

the plume. Computational modelling of buoyant jets in a stratified crossflow using a k-ε RANS model was performed by Yang and Hwang (2001) to predict a jet's evolution. The model was claimed to represent experimental data well. Stratification was found to limit the height rise and therefore the degree of mixing.

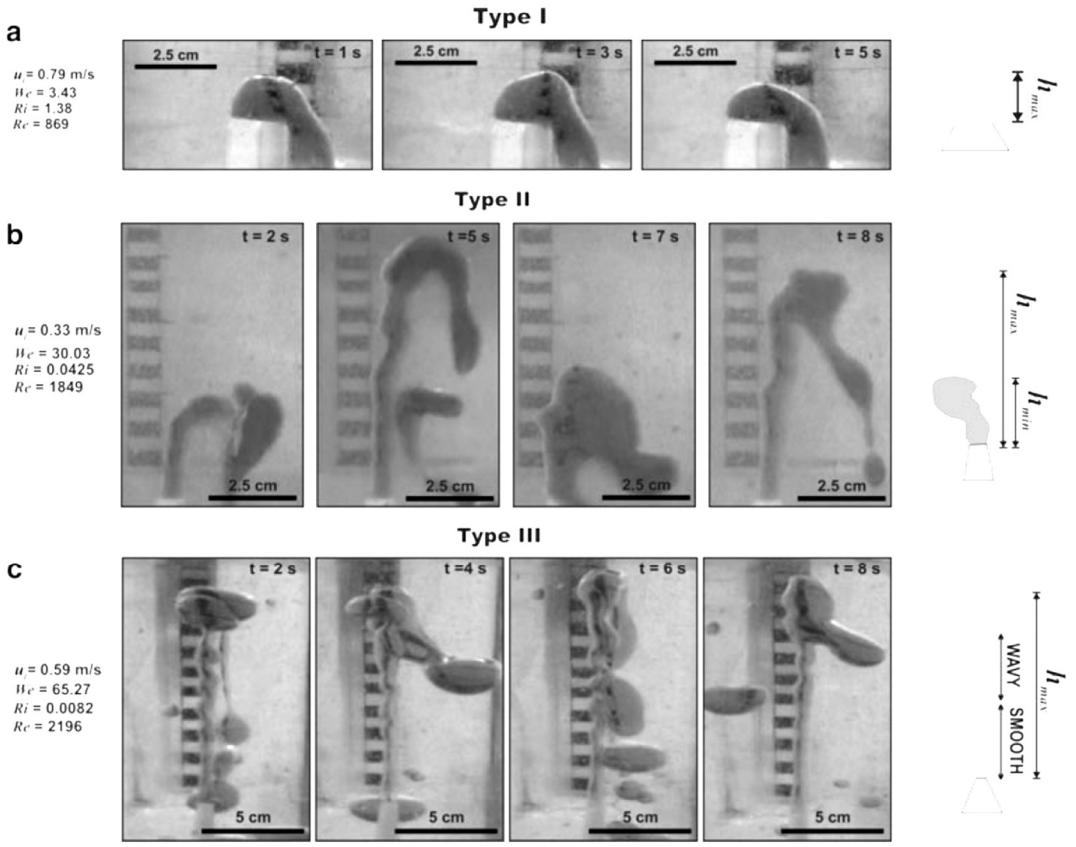


Figure 2.7 Three regimes for immiscible negatively buoyant jets Geyer et al., (2011).

Geyer et al. (2011) performed experiments on negatively buoyant immiscible jets through injecting dyed water into a static tank of rapeseed oil. They found three types of jet regimes, presented in Figure 2.7. In type I, the jet reaches a constant height, whereas, in type II, the jet pulses, and the height was found to be inconsistent. Finally, in type III, the jets reached a maximum height where the fluid built up, then once a critical volume was reached, a blob of fluid separates and falls.

Various regime maps like that displayed in Figure 2.8 were then developed using various dimensionless numbers. Geyer et al. then found that the Richardson number, Eq. 2.4, or equivalently the Froude number, Eq. 2.5 played the greatest role in determining the jet height, while the Reynolds and Weber numbers determined the behaviour of the flow.

$$\mathrm{Ri} = \frac{gL}{\sqrt{u^2}}\left(\frac{\rho_w - \rho_o}{\rho_o}\right) \qquad \text{Equation 2.4}$$

$$\mathrm{Fr} = \frac{1}{\sqrt{\mathrm{Ri}}} \qquad \text{Equation 2.5}$$

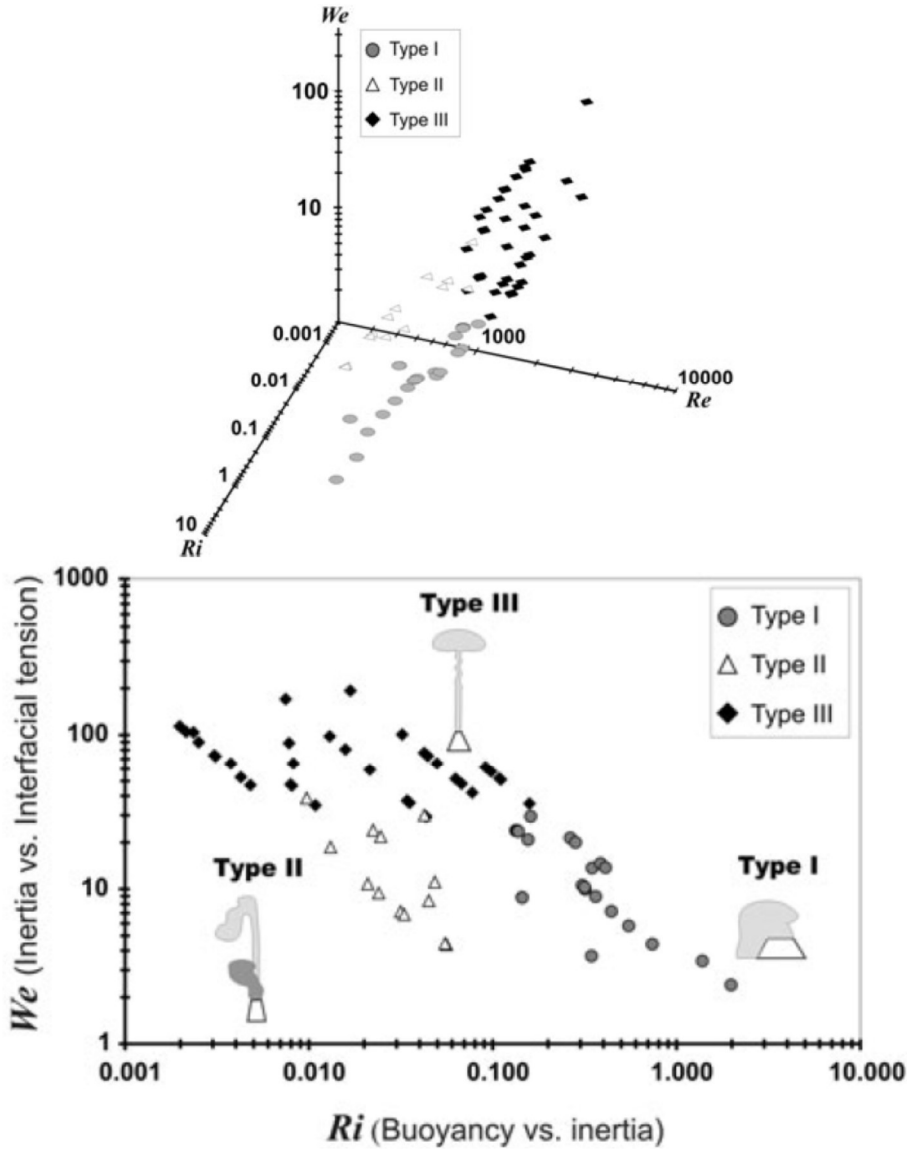


Figure 2.8 Dimensionless maps of immiscible negatively buoyant jets Geyer et al. (2011); Top: 3-D map of Ri versus Re versus We; Bottom: map of Ri versus We.

Mier-Torrecilla et al. (2012) performed simulations of negatively buoyant jets in immiscible fluids using the particle finite element method (PFEM) based on the work of Geyer et al. (2011). They found the simulation was able to reproduce the main features of all three flow types shown in Figure 2.7 and fitted the regime map of Figure 2.8, concluding that PFEM is a useful tool for this type of simulation.

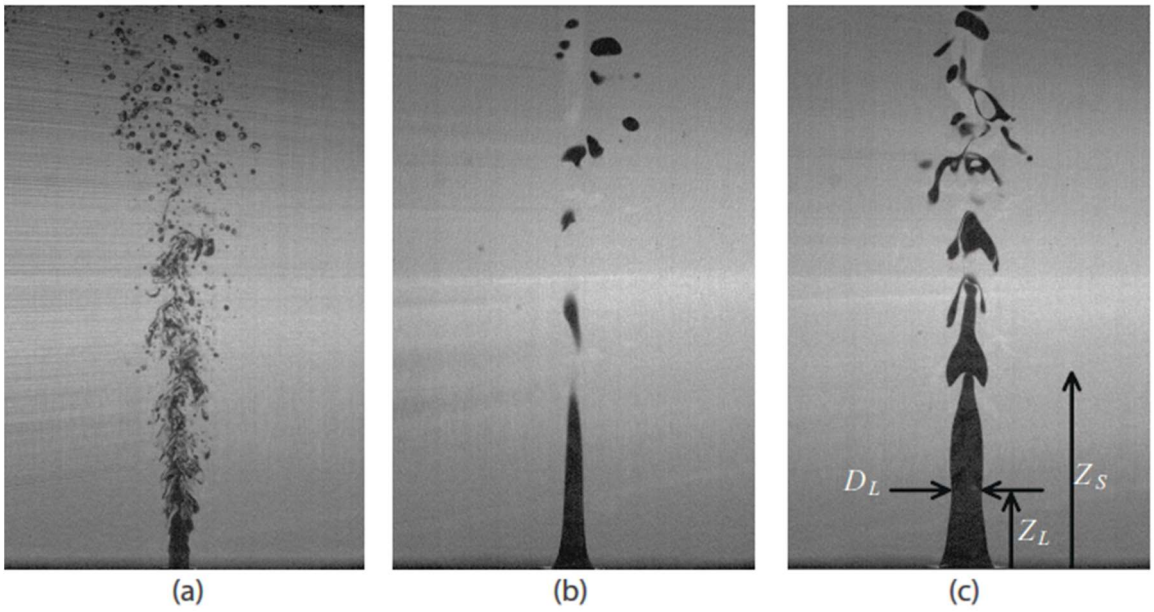


Figure 2.9 Buoyant jets undergoing breakup: a) Regime 1: atomization, b) Regime 2A: pinch-off, c) Regime 2B: skirt breakup, (Berard et al., 2013).

Liquid-liquid experiments and simulations examining the breakup of two-phase buoyant jets using the optical observational techniques of PLIF and PIV have been conducted by Berard et al. (2013). Optical distortions were minimised through matching the refractive index of the silicone oils to glycerol solutions. Berard et al. (2013) divided jet breakup into three regimes, presented in Figure 2.9. Regime 1 is 'atomization', where the drops rapidly break into droplets that are smaller than the jet plumes diameter. Regime 2A is called 'pinch-off', where jet instabilities were found to produce droplets that were larger than the plume. Regime 2B is called skirt breakup, which occurs when droplets break off and the pinch-off points roll up into the droplets.

Berard et al. (2013) concluded that the breakup regimes could be characterized using flow maps like Figure 2.10, where the different plots were parameterized using the Reynolds number, Weber number, Richardson number, Ohnesorge number and Eötvös number (Eq. 2.6):

$$\mathrm{Eo} = \frac{g(\rho_w - \rho_o)L^2}{\sigma} = \mathrm{Ri} \times \mathrm{We} \qquad \text{Equation 2.6}$$

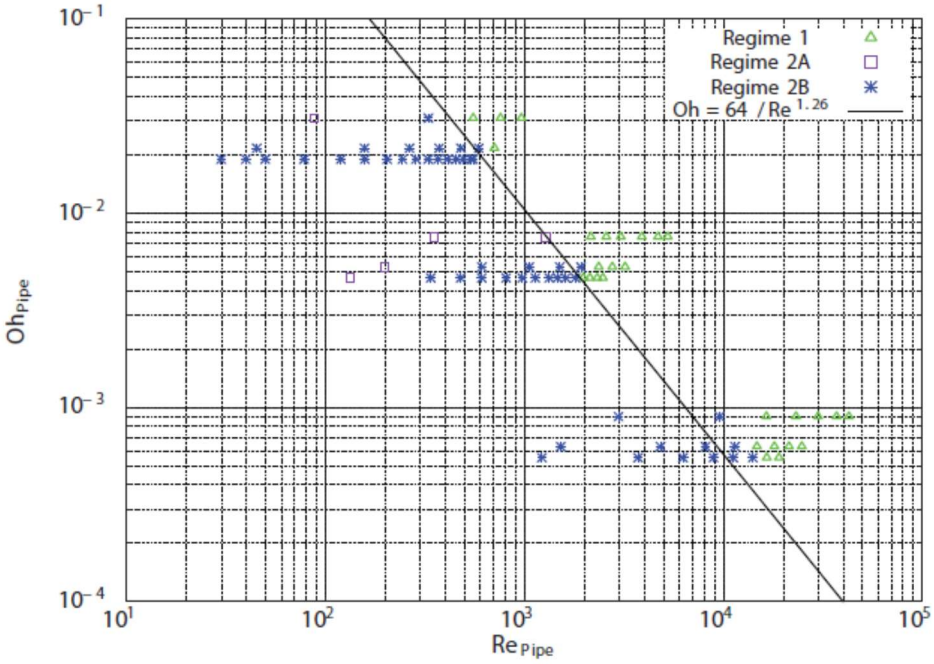


Figure 2.10 Scatter plot of jet breakup results of Berard et al. (2013) for Ohnesorge number versus Reynolds number of the jet.

Berard et al. (2013) created simulations of four of the jets using a finite volume solver and the Volume of Fluid (VOF) method. These simulations were found to closely resemble the experiments. The simulations were accelerated by a factor between three and six through using GPU accelerator cards.

2.8 Liquid-liquid dispersion modelling

The International standard "ISO3171:1999 Petroleum liquids – automatic pipeline sampling" (ISO, 1999) contains the mechanistic model used throughout industry for estimating the dispersion of water within crude oils and further details can be found within Hayward (1983). These calculations are known colloquially as "Annex A" due to their location within Annex A of the standard. The Annex A dispersion model builds upon the earlier work of Karabelas (1977, 1978a, 1978b) who studied the vertical phase and droplet size distributions of dilute liquid-liquid dispersions with varying pipeline velocity with a focus on the application of crude oil sampling. A critical analysis of the ISO3171:1999 Annex A calculation is given within Baker (1986).

$$\frac{C_1}{C_2} = exp\left(\frac{-W}{\varepsilon/D}\right) \qquad \text{Equation 2.7}$$

The principle calculation used within the Annex A (ISO, 1999) is given in Eq. 2.7. This equation estimates the ratio of the water fraction in the top of the pipe,C_1, to the water fraction contained in the bottom of the pipe, C_2, which is illustrated schematically in Figure 2.11.

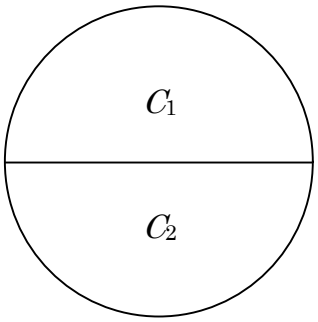


Figure 2.11 Schematic of the pipe concentrations used to calculate the C_1/C_2 concentration ration used in industrial liquid-liquid mixing calculations.

Inputs to the calculation include W, which is the settling rate of the water droplets due to gravity, and ε/D, which is the rate of turbulent dispersion, ε being the eddy viscosity and D is the internal diameter of the pipe.

The settling rate of the water droplets, W, is given by Eq. 2.8 where g is the acceleration due to gravity, ρ_d is the density of the dispersed water phase, ρ_c is the density of the continuous oil phase, v is the oil's kinematic viscosity and D_{32} is Sauter mean diameter of the water droplets:

$$W = \frac{g}{18}\left(\frac{\rho_d - \rho_c}{\rho_c}\right)\frac{{D_{32}}^2}{v} \qquad \text{Equation 2.8}$$

$$D_{32} = 0.3625\left(\frac{\sigma}{\rho_c}\right)E^{-0.4} \qquad \text{Equation 2.9}$$

The droplets are assumed to be spherical in Eq. 2.8. Baker (1986) states that experimental evidence suggested this is a reasonable assumption. Drag is generally increased with non-spherical particles and is reduced by up to of 5% for ellipsoidal droplets (Clift et al., 2005).

Eq. 2.8 is based upon Stokes Law which is valid for low Reynolds numbers. Baker (1986) argues using the experimental results of Mosri and Alexander (1972) that Eq. 2.8 is only valid for droplets with Re < 0.5; above this Reynolds number, the droplet settling rate predicted by Eq. 2.8 will be too high. The experimental drag coefficient of Mosri and Alexander (1972) was found to be 44% higher for Reynolds numbers of 5.

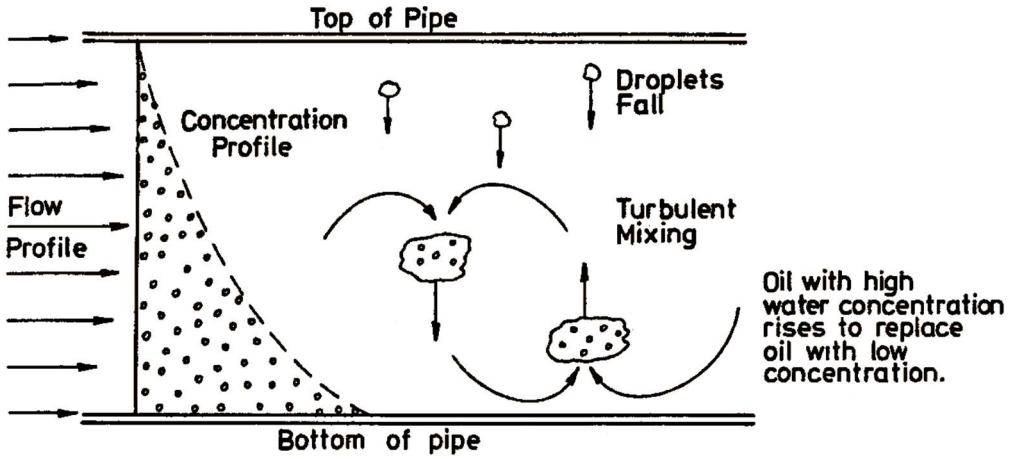


Figure 2.12 Balance between droplet settling and turbulent dispersion (Baker, 1986).

This balance of these forces is schematically illustrated in Figure 2.12, where the settling of the water droplets leads to stratification, while the turbulence leads to the dispersion of the droplet. The ISO3171:1999 Annex A standard states that a flow has an excellent dispersion when the water concentration ratio, C_1/C_2, is between the range of 0.9 to 1.0.

$$\varepsilon = \zeta R U^* \qquad \text{Equation 2.10}$$

$$U^* = u\left(\frac{f_F}{2}\right)^{1/2} \qquad \text{Equation 2.11}$$

$$f_F = \frac{0.079}{\mathrm{Re}^{0.25}} \qquad \text{Equation 2.12}$$

$$f = 4f_F \qquad \text{Equation 2.13}$$

The eddy viscosity is given by Eq. 2.10, where ζ is a dimensionless constant given to be the value 0.36, R is the internal pipe radius and U^* is the pipe friction velocity. The pipe friction velocity is in turn given by Eq. 2.11, where u is the pipeline mean velocity and f_F is the Fanning friction factor and is related to the Darcy friction factor (f) by Eq. 2.13. The Fanning friction factor is based on the Blasius approximation of a smooth pipe, Eq. 2.12, where Re is the Reynolds number (Hager, 2003).

The Sauter mean diameter (D_{32}) is in turn estimated from Eq. 2.9, where σ is the interfacial tension which is generally assumed to be 0.025 N/m, and E is the energy dissipation rate per unit mass. Baker (1986) considered that the assumed value

for interfacial tension of 0.025 N/m to be low and stated that if the interfacial tension were 0.035 N/m then the resulting droplets would be larger and, therefore, the settling rate would increase by 50%. Eq. 2.9 originated from the work of Hinze (1955), where the ISO calculations assume that D_{32} is half the size of the maximum droplet diameter, D_{max}. There are numerous variations of Eq. 2.9 where an overview of these can be found within the work of Paul et al. (2004).

The energy dissipation rate is estimated from the pressure drop using Eq. 2.14:

$$E = \frac{\Delta P\, V}{\Delta L\, \rho_c} \qquad \text{Equation 2.14}$$

where ΔP is the pressure drop and ΔL is the characteristic length over which the pressure and hence energy is dissipated:

$$\frac{\Delta P}{\Delta L} = \frac{2\, f_F \rho_c\, V^2}{D} \qquad \text{Equation 2.15}$$

This is the general condition of the pressure drop for a long straight pipe is, which results in an energy dissipation E_0 equal to that of Eq. 2.16:

$$E_0 = \frac{2\, f_F\, V^3}{D} \qquad \text{Equation 2.16}$$

In the case of piping elements other than a straight pipe either the pressure drop, $\Delta P/\Delta L$, is provided for, or a correction is made through Eq. 2.17, where β is a characteristic parameter of each piping element:

$$E = \beta E_0 \qquad \text{Equation 2.17}$$

A small subset of these characteristic parameters is provided within ISO (1999), for common piping elements including bends, enlargements, contraction, orifices and valves. However, it should be noted that ISO (1999) does not contain a specific formula for jet mixing and so energy dissipation needs to be calculated using alternative formulae. Baker (1986) notes that ΔL can be uncertain and that larger values of ΔL will lead to larger droplets. This can therefore be a source of error when calculating C_1/C_2 ratios.

The calculation used in ISO (1999) assumes that the water fraction is low enough that the coalescence is negligible. However, Eq. 2.18 is used as a step-change correction to the water settling rate when the water concentration exceeds 5% to compensate for increased coalescence.

$$W_{>5\%} = 1.2W \qquad \text{Equation 2.18}$$

Baker (1986) noted in his critic that Hayward (1983) had suggested Eq. 2.19 is used rather than Eq. 2.18 for coalescence corrections but that this was not adopted:

$$W_{\text{cor}} = W(1 + 5.4C_0) \qquad \text{Equation 2.19}$$

Dispersed concentrations are divided into three ranges by Paul et al. (2004). Range one is dilute, where the dispersion concentration is less than 1% and droplets can be treated as individuals which only interact with the continuous fluid. Range two is a moderate concentration a dispersion of less than 20%. Range two systems can sometimes be treated as a dilute system, but generally, for concentrations above 5%, coalescence becomes significant and needs to be accounted for. Range three is concentrated, where the dispersed phase is more than 20%, in this regime coalescence is significant, and the behaviour is highly complex. The ISO assumes that coalescence is negligible and therefore this needs to be treated with care when applied to concentrations that above 5%.

In addition to the ISO standard, there are alternatives like ASTM D4177-95 Chapter 8.2, Standard Practice for Automatic Sampling of Petroleum and Petroleum Products (ASTM, 2010). These alternatives standards have more or less adopted the calculations within the ISO (1999). Importantly, these additional standards indicate that a C_1/C_2 lower than 0.7 can indicate the presence of coalescence and any result should be treated with caution.

The formula used in the ISO's Annex A calculation assumes that the average droplet size has reached equilibrium immediately after the element. Paul et al. (2004) state that droplets of twice the equilibrium size are normally reached rapidly within tank mixers, but it takes a long time for the droplets to reach equilibrium dimensions. Consequently, it likely that the ISO's assumption that droplets have reached equilibrium size is poor for elements like bends and valves. Further, the Annex A assumes the element with the highest energy dissipation rate should be used to determine the level mixing. This can be justified if the droplets have reached equilibrium dimensions however as previously stated this is unlikely to be true for some of the element types specified.

A three-dimensional model for assessing the evolution of water distribution within oils following a mixing element was developed by Segev (1984). This model found that the uniformity of water concentration is improved when the continuous fluid's viscosity, density or pipeline velocity are larger and when the surface tension, pipe diameter, fluid density difference or pipe angle from vertical are smaller.

Baker (1988) developed the model of Segev (1984) further into a three-dimensional computational model for assessing water concentration distribution within crude oils following a mixing element. The model allowed for the evolution of the distribution following mixing and incorporated secondary swirl and the decay of turbulence. Baker's model was tested at BP and generally found to underestimate the uniformity of the water concentration.

Scaling laws for optimum mixing for both confined and unconfined single or double jets in crossflows have been developed by Forliti (2012). The models include the entrainment rate and drag effects on jet momentum and are found to correlate well with experimental evidence of unconfined jets. After reviewing the literature, they concluded that current models do not work well between two and eight jets and that this scaling issue needs further work for the issues to be resolved.

2.9 Jet mixing of immiscible liquid-liquid flows

Early simulated liquid-liquid jet mixing experiments were performed by Peerless and Jiskoot (1978). Here a 45 mm diameter pipe was used, with the continuous liquid being water and a dispersed phase represented by solid polystyrene chips. The flow, containing both the water and polystyrene chips, was developed over an 1800 mm length at which point water jets of 1, 2, 3 or 4 mm were injected to disperse the chips in the flow. A splitter plate was then located at 120, 150, 180, 200 and 250 mm downstream of the jets to discover how well the polystyrene chips had been dispersed with distance.

Peerless and Jiskoot (1978) found that mixing was maximised when the ratio of the velocity of the jet u_j to that of the pipeline mixture velocity u_m was in the range 10 to 20, and that ratios higher than 20 produced little improvement in distribution. The most homogenous distribution was generally achieved when the splitter plate was at the closest distance of 120 mm, or equivalently 2.7 test section diameters.

Peerless and Jiskoot (1978) calculated the pressure loss, ΔP, needed to accelerate a jet of ideal fluid using Eq. 2.20, where ρ is fluid density and u_j is the average jet exit velocity. They then combined Eq. 2.20 with the volumetric flow of the jet, Q_j, to calculate the jet power, P_j, Eq. 2.21, where d_j is the jet diameter.

$$\Delta P = \frac{\rho {u_j}^2}{2} \qquad \text{Equation 2.20}$$

$$P_j = Q_j \Delta P = \frac{\pi}{8} \rho {d_j}^2 {u_j}^3 \qquad \text{Equation 2.21}$$

Jiskoot (1979) filed a patent for a jet mixer for mixing water in crude oil in 1978. This jet mixer included a nozzle, a take-off quill, a pump to power the jets and a bypass line which had the capability of manually withdrawing a physical sample. This patent became the basis of future designs of jet mixers.

A study into the effectiveness of using a jet mixing system for dispersing water in oil within horizontal pipes for subsampling was performed by NEL (1980). The study was performed in a test section with a 102 mm internal diameter where both 4 mm and 8 mm diameter jets were used to disperse water concentrations of between one and four per cent in oil flows of between 3 and 8 L/s. The jet mixers were compared with the results produced using an orifice plate with an area ratio of 0.1. The orifice plate had been found to produce excellent homogenisation but with unacceptably high-pressure losses.

The study at NEL (1980) found that the jet mixer performed as well as the orifice plate while having negligible pressure losses. The optimum sampling point was determined during the NEL experiments to be at six pipe diameters downstream of the jet, which is more than twice that predicted by Peerless and Jiskoot (1978). Similar levels of mixing were found when 2% of the pipeline flow rate was recirculated through a 4mm jet as when 5% of the pipeline flow was recirculated through an 8mm jet. It was claimed that the jet diameter should be scaled with pipe diameter and that the two most important factors were the jet power and sample position. It was found that the kinetic energy needs to be increased as the water fraction increased to achieve the same level of homogeneity.

Slater (1983) registered a patent for a pipeline liquid-liquid mixing device which made use of a rotor-stator design which then created jets, see Figure 2.13.

This design pulls the fluids from the bottom of the pipeline through a central feed-pipe located in a probe that travels the entire length of the pipeline. The suction is created by the centrifugal forces from the spinning rotor which is driven by a motor located on top of the mixer. The emulsion is then created as the liquids are sheared between the rotor and stator assembly. The mixed fluids are then returned to the pipeline through a return-pipe that encloses the feed-pipe. The return pipe created transverse jets of the premixed fluid to created further pipeline mixing.

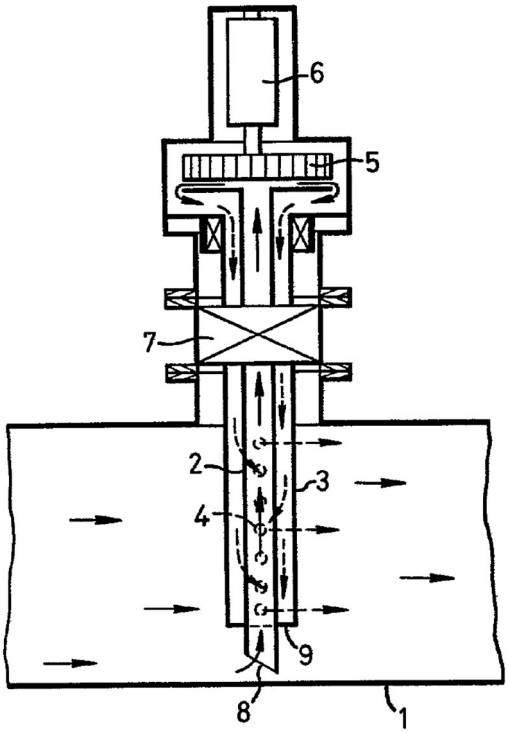


Figure 2.13 Schematic of pipeline liquid-liquid jet mixer proposed by Slater (1983) making use of a rotor-stator pump that both drives and emulsify the liquids.

Jiskoot (1986) filed a patent for the jet mixer with, what is now, the standard nozzle and quill design, see Figure 2.14. The fluids are drawn from the downstream quill (labelled scoop) using a pump which is then reinjected upstream through a nozzle to create the jets for mixing. The quill is located in the centre of the pipe and is expected to obtain fully mixed liquids. The nozzle is located towards the bottom of the pipe so that the jets interacted with the water which is expected to be located at the bottom for most crude oils. The patent included several variations and options including i) a static mixer after the pump; ii) a flow-through sampler located after the pump; iii) a sampler located on bypass stream; iv) a flow velocity reducer.

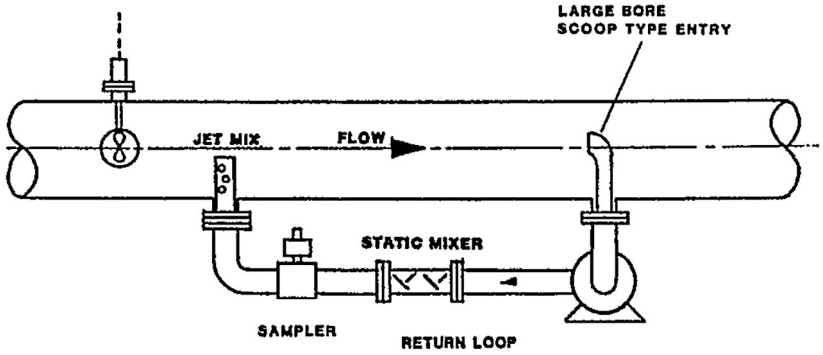


Figure 2.14 Schematic of the Jiskoot jet mixer with the jet mix loop containing a pump, an integral sampler and a static mixer Jiskoot (1986).

A model was developed by Peerless and Walker (1985) to calculate the length and cross-sectional area of a jet needed to obtain a specified droplet size in unconfined static conditions. The model, therefore, has no preference for geometric orientation or between transverse and axial jets. It was estimated that the sampling location should be located two to five jet lengths from jet entry as no further mixing is predicted after this length. The calculations estimated the change in droplet surface energy after the breakup had ceased. It was calculated that this energy required to break up the droplets was ten times greater than that needed to maintain a uniform pipe profile and it was therefore concluded that if sufficient jet energy was present to create the required small droplets it will simultaneously ensure that the concentration profile is uniform. It was also concluded that the droplets should maintain their size for a long-distance following break up. Peerless and Walker (1985) claimed the droplet distribution from jet mixing is significantly more complex than those studied by Karabelas (1977).

A detailed study on jet mixing of water within crude oils was performed by Fernando (1990) and was published as the short note Fernando and Lenn (1990). The process of jet mixing was divided into the three regions labelled in Figure 2.15. The penetration region, Region 1, is a complex area covering entrainment and primary breakup. The near-field region, Region 2, is dominated by swirl generated from the jets. In the far-field region, Region 3, separation dominates due to gravity and is approximately two-dimensional.

The study of Fernando (1990) was split into three stages, the first stage was experimental and used a 2 mm jet of kerosene to penetrate a non-flowing stratified system, where water was located on the bottom and kerosene, on the top. The

experiments were conducted in a short section of steel pipe with an internal diameter of 140 mm with clear acrylic covers attached to both ends of the pipe. Backlighting was then applied at one end of the pipe while a high-speed camera was used at the other end to capture high-speed shadowgraphy observations of the jet and subsequent mixing process. A frame from one of these experiments can be seen in Figure 2.16.

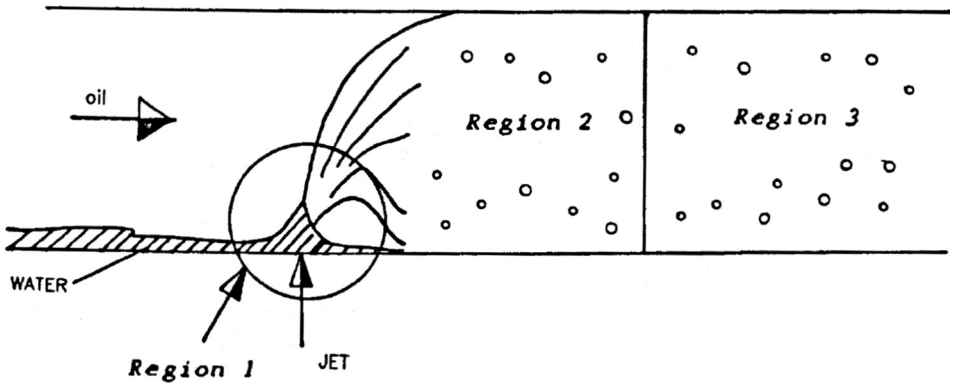


Figure 2.15 The three regions of jet mixing as defined by Fernando (1990), Region 1 is penetration, Region 2 is the near-field, and region 3 is the far-field.

Fernando (1990) experimentally measured the water entrainment rate of the oil jet during stage 1. The entrainment rate was calculated by measuring the change in height of the water layer as the jet passed through the water layer. The water layer depth was measured using ultrasonic transducers and the layer was barely disturbed unless it was less than 8 mm deep. Experiments were varied through changing water height, viscosity, interfacial tension and jet velocity.

Fernando (1990) investigated how the resulting droplet sizes varied with changing parameters, through measuring the water droplet diameters on the shadowgraphy photos at the outer edges of the jets. However, the interior of the jet was opaque due to mismatches in the refractive index of the liquids, see Figure 2.17 (left), and this prevented the measurement of droplets diameters away from the edges. All experimental droplets were found to be roughly spherical apart from the droplets created at low jets velocities.

In addition to the droplet sizes, the droplet breakup and entrainment processes were studied using the shadowgraphy images. The processes leading to the droplet breakup were determined using subsequent frames. A schematic of two such frames is given on the right Figure 2.17. Using these images, a detailed theory of this complex process of the jet breakup was devised, a schematic of these processes is given in

Figure 2.18. The jet initially entrains an outer sheath of water as it passes through the water layer. This water sheath then subsequently undergoes breakup once it enters the oil layer. In between the water sheath and the oil core of the jet, there is a two-component interface containing both droplets of water and droplets of oil.

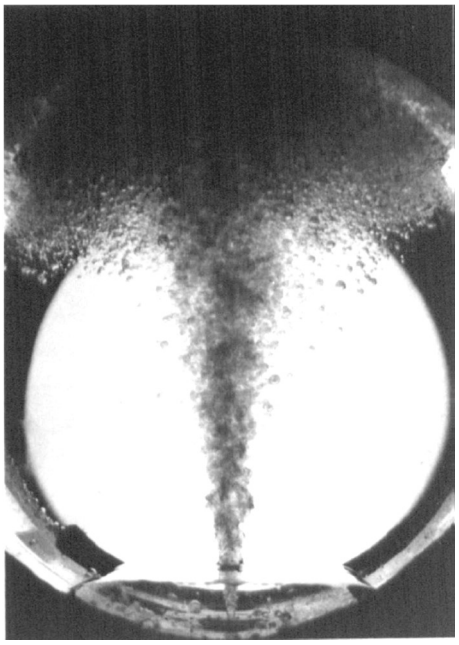


Figure 2.16 Experimental setup used by Fernando (1990) for studying a single jet breaking up a static stratified layer of water (bottom) and kerosene (top).

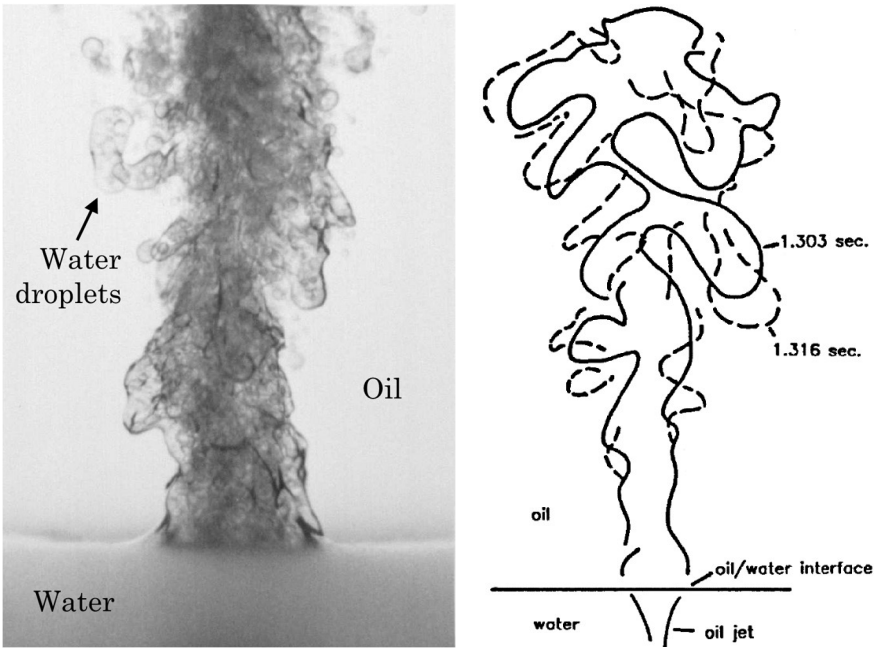


Figure 2.17 Jet breakup of a stratified layer of water and kerosene Fernando (1990); left, a close-up image of the jet; right, a schematic of jet droplet formation.

Fernando (1990) claimed that within the water, Region 1, the jet breakup undergoes the same four regimes as a liquid jet breaking up in the air, (see Figure 2.2). In the oil (Region 2), low-speed jets appeared to follow breakup processes that were comparable to that of a model of an idealized fan spray nozzle. Whereas, high-speed jets presented more complex breakup process and no longer fitted with the breakup model of a fan spray nozzle.

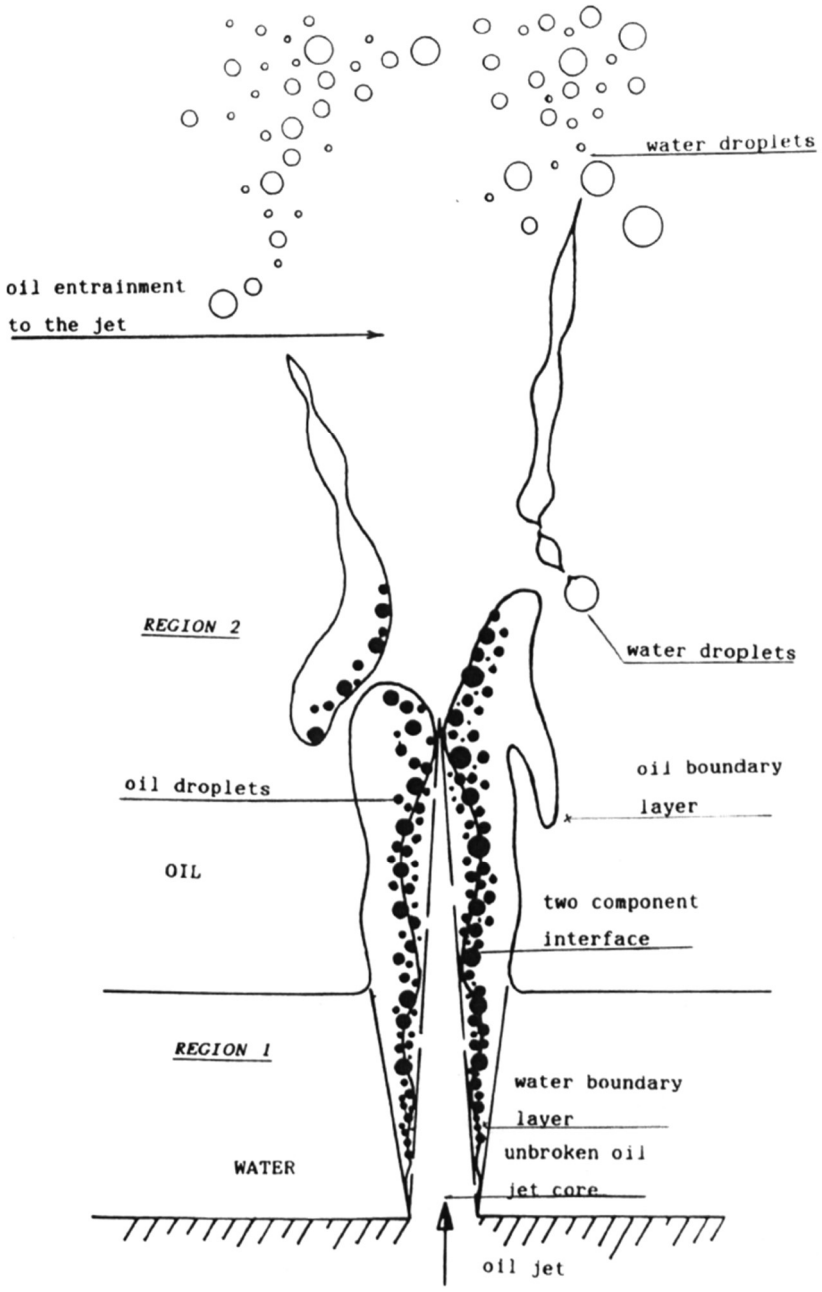


Figure 2.18 Structure and stages of breakup and entrainment for a jet penetrating two stratified immiscible liquids, Fernando (1990).

Stage two of Fernando's (1990) work involved steady-state modelling of a single jet using a commercial CFD package called PHOENICS CFD. PHOENICS used a finite volume discretization with k-ε RANS turbulence model, using two different multiphase models. Simulations were made for 70 mm diameter horizontal pipe of length 25 pipe diameters (1750 mm) with a water layer height of 10 mm from the pipe bottom. A coarse cylindrical coordinate grid of $r = 20$, $\theta = 16$, $z = 60$ was used where the jet entered at the bottom at cell $z = 8.5$. The first model used was the homogeneous model where there is assumed to be no slip between the phases. The second model used an Eulerian model with a fixed water droplet size.

Fernando (1990) found that the jet penetration trajectory compared reasonably with prior experimental results of Maruyama et al. (1981) and Fitzgerald and Holley (1979). He found that water distribution could be made uniform by varying the jet diameter and velocity ratio between pipeline and jet. Fernando (1990) also found that the standard measure of C_1/C_2 greater than 0.9 can be in error as distributions vary across the pipe cross-section horizontally as well as vertically. He found that the homogeneous model became uniform faster than the Eulerian model. Fernando (1990) concluded however that the grid refinement was needed for quantitative validation of these simulations.

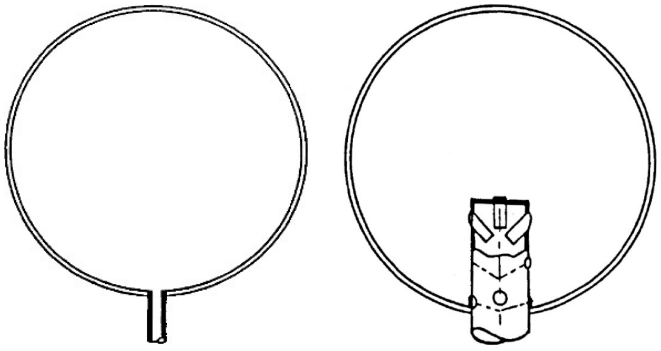


Figure 2.19 Two nozzle designs used by Fernando (1990); left, single upward nozzle; right, a copy of the Jiskoot multiple jet nozzle.

Stage three of Fernando's (1990) was a set of single-phase water jet experiments to study the mixing and velocity decays in a flowing pipe. The Perspex pipe had an internal diameter of 80 mm and had two interchangeable nozzles fitted, a single vertical 4.24 mm jet or a scaled-down Jiskoot multi-jet nozzle with eight 1.5 mm jets. The single jet was designed to have the same cross-sectional area as the

combined eight multi-jet nozzle so that total power of the two nozzles were comparable. These two nozzles are illustrated in Figure 2.19.

Fernando (1990) first set of experiments used small amounts of fluorescent dye to obtain the mixing patterns of the two jets. These experiments were made at multiple positions downstream of the jet nozzle using a camera with a UV flash for short exposures and a UV light for longer exposures. It was concluded that the multi-jet nozzle mixed faster than the single jet nozzle.

The second set of experiments used laser Doppler anemometry (LDA) to obtain the velocity field and the decay of the swirl following the jet. It was found that the swirl from the jets mostly decays by three pipe diameters and that the flow can be treated as two dimensional after four pipe diameters. The decay of the swirl was found to only be weakly dependant on the pipe Reynolds number.

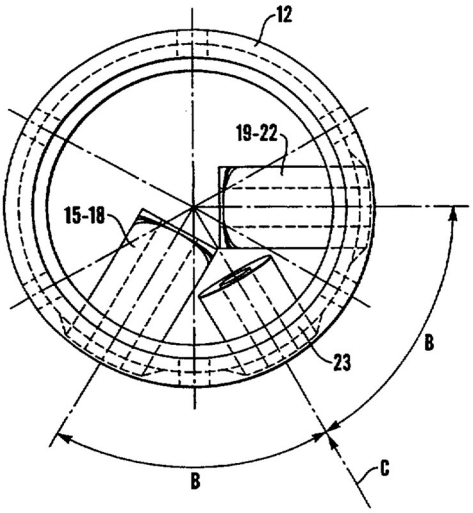


Figure 2.20 Cross-section of the forward-facing jet mix nozzle with three jet exits around the circumference of the nozzle, (Jiskoot and Jiskoot, 2001).

In related work, Lenn et al. (1993) used LDA to study velocity profiles and mixing formed downstream of a T-Junction in water. The results were used to estimate water distribution and droplet sizes in crudes oils following at a T junction using the computational model of Baker (1988). It was found experimentally that energy dissipation was higher than that predicted by the model, leading to smaller droplets and improved mixing. It was concluded that the model was improved by the study but that further laboratory liquid-liquid experiments were needed and that the model needed an extension to high water fractions. A T-Junction, and indeed other elements, can be

regarded as a type of static mixer. Jiskoot and Jiskoot (2001) filed a patent for a jet mixer design where the jets were arranged forward facing into the crossflow rather than at right angles to the flow. This design helped to increase shear in the flow and hence increase the level of mixing, see the nozzle cross-section in Figure 2.20.

Verloop and Verloop (2010a) and Verloop and Verloop (2010b) presented the design of jet mixer nozzle which enters through the top of the pipe but is then angled horizontally along the bottom of the pipe. This design allowed large jets to be directed vertically to lift the water from the bottom of the pipe, while smaller jets were included on the nozzle end to encourage the dispersion of water on the pipe bottom.

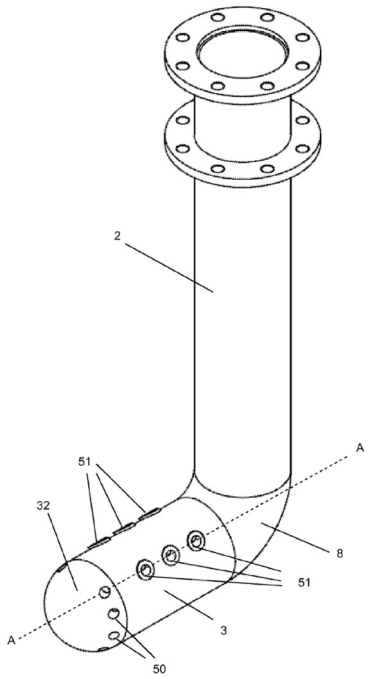


Figure 2.21 The horizontally oriented nozzle of Verloop and Verloop (2010b).

Verloop and Verloop (2012) introduced the design of an eductor-jet pump to mix pipeline liquid-liquid flows. Eductor-jet pumps use the Venturi effect to produce fluid flow through forcing a high-pressure motive fluid through the opening of Venturi, creating a pressure drop, see Figure 2.22. The pressure drop leads to the fluid surrounding the Venturi opening becoming entrained and driven through the eductor-jet pump. Eductors are commonly used in tank mixing applications and are available commercially by suppliers like Schutte & Koerting, Venturi Jet Pumps Ltd and Primetech. However, the use of eductors for mixing liquid-liquid pipeline flows appears novel in Verloop and Verloop (2012).

The design of eductor presented in Verloop and Verloop (2012) and Verloop et al. (2019) is such that the opening on the inductor is located at the bottom of the pipe whereby the bottom liquid is drawn into the Eductor for mixing and then ejected. The design of the inductor assumes that the water is located at the bottom of the pipe and therefore passes through the inductor. However, the assumption that water is located at the bottom liquid-liquid system may not be true following bends (Ayala et al., 2016) and therefore the eductor would seem to require a suitable flow development length to function optimally. Given the water is assumed to pass through the eductor it would seem probable that the design would be limited by the volumetric flow of water that can pass through eductor. Benjamin (2001) states that the entrained flow of eductors-jet pumps is typical 50% to 80% of the motive flow and that although entrained flows can be higher it results in the loss of head.

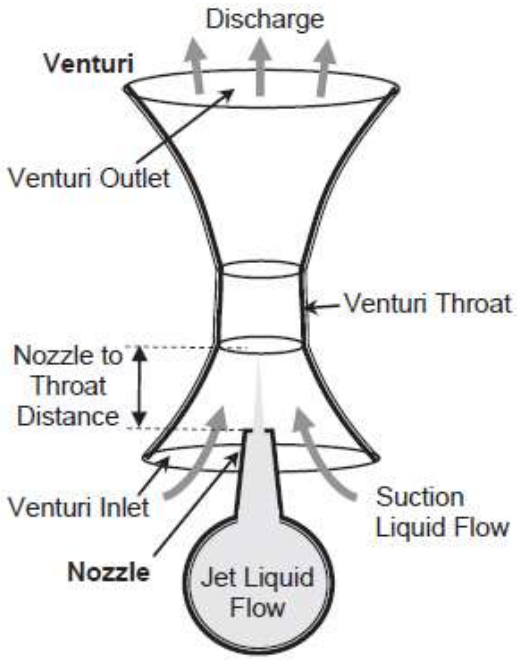


Figure 2.22 Schematic of an eductor (Hosseinzadeh et al., 2018).

Verloop et al. (2019) indicate that their eductor design is suitable for vertical orientation however they do not state where the eductor opening should be located to successfully entrain the water in this orientation. Further Verloop et al. (2019) provide no vertical designs for either their eductor or their "traditional" jet mix indicating that the same asymmetrical designs may have been used for both orientations.

Verloop et al. (2019) claim that their eductor design requires less energy than that of their "traditional" jet mixer design by comparing the error in sampled water fraction to that of the volumetric flow through their two nozzle designs. However, while volumetric flow appears lower, Verloop et al. (2019) do not state pressure losses or power needed to drive the two nozzles and as such power requirement of the two systems could not be confirmed. Hosseinzadeh et al. (2017) perform simulations and Hosseinzadeh et al. (2018) perform measurements of the resulting droplet sizes of an eductor used for mixing two immiscible liquids where they found that the resulting droplets sizes depend on the size of the Venturi's throat, where smaller throat results in smaller droplet sizes.

Mohajer (2013) created a jet mix nozzle design as part of a system that produced two large jets, one on either side of the nozzle, see Figure 2.23. This nozzle is similar to the earliest jet mix designs produced by Jiskoot which were designed with two large jets on either side of a nozzle located at the bottom of the pipe.

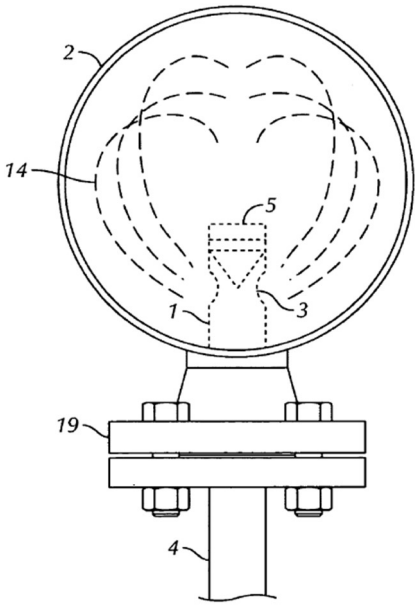


Figure 2.23 Dual jet nozzle created by Mohajer (2013).

The industrial performance of jet mixers over 25 years is presented in Potten and Wright (2014), they demonstrate that the evolution of jet mixers and the associated sampling systems have resulted in a steady increase in the mixing performance. The evolution has resulted in the current larger-scale design known as a "CoJetix", which incorporate a sampling system within a bypass loop around the pump of the jet mix, see Figure 2.24.

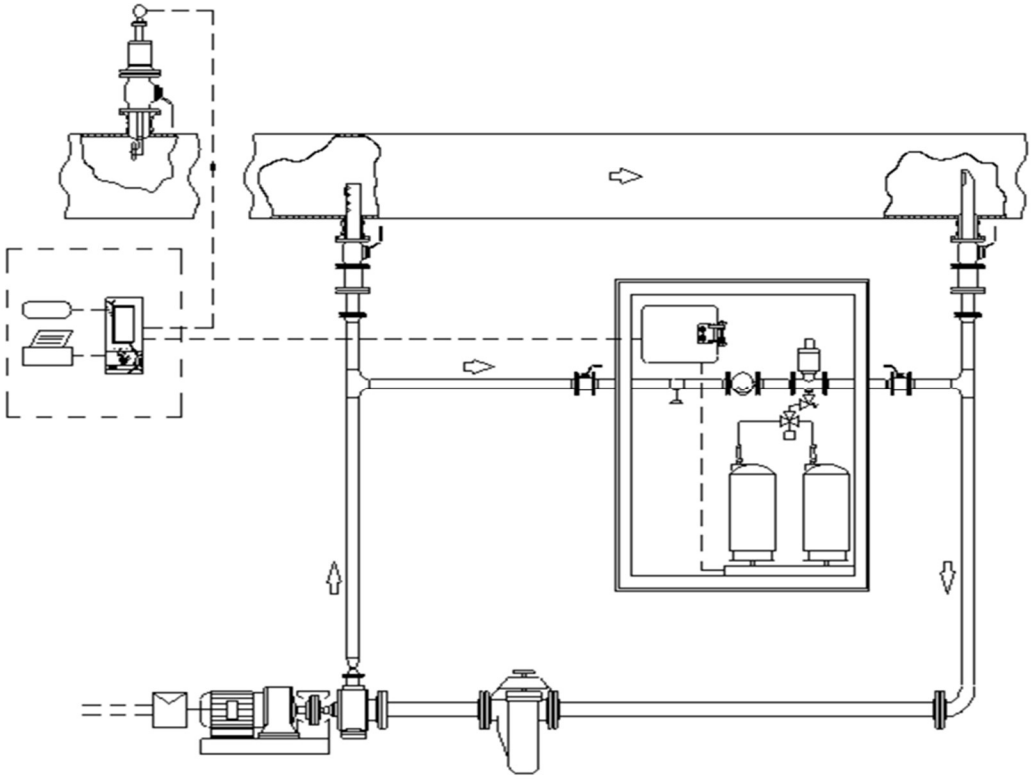


Figure 2.24 A typical CoJetix sampling system with a jet nozzle and a quill in the main pipe as well as a flowmeter, a controller and a pump in the jet mixer loop and a bypass loop containing a sampling cabinet (Potten and Wright, 2014).

Lakshmanan et al. (2015) presented results for Large Eddy Simulations using OpenFOAM and magnetic resonance measurements of mixing a 2.5" diameter liquid-liquid flow using a new design of jet mixer known as the "SmartMix", illustrated in Figure 2.25. Lakshmanan et al. (2015) present the pipeline water fraction profiles against height following mixing where they found evidence of stratification. Lakshmanan et al. (2015) concluded that the C_1/C_2 ratio was not a good measure of how well a flow is mixed due to this stratification. However, their suggested calculation of C_1 and C_2 only makes use of the water fraction at two pipe positions rather than an average over the upper and lower cross-section as intended by the standards (Baker, 1986). Lakshmanan et al. (2017a) state that the measurement uncertainty in the water fraction of the magnetic resonance technique used was ±0.5%.

The OpenFOAM simulations are detailed in Huang (2017) where it is stated that they used the twoLiquidMixingFoam (2LM) which they modified to improve performance. Importantly, Huang (2017) states that the OpenFOAM simulations were found to agree well with the magnetic resonance measurements.

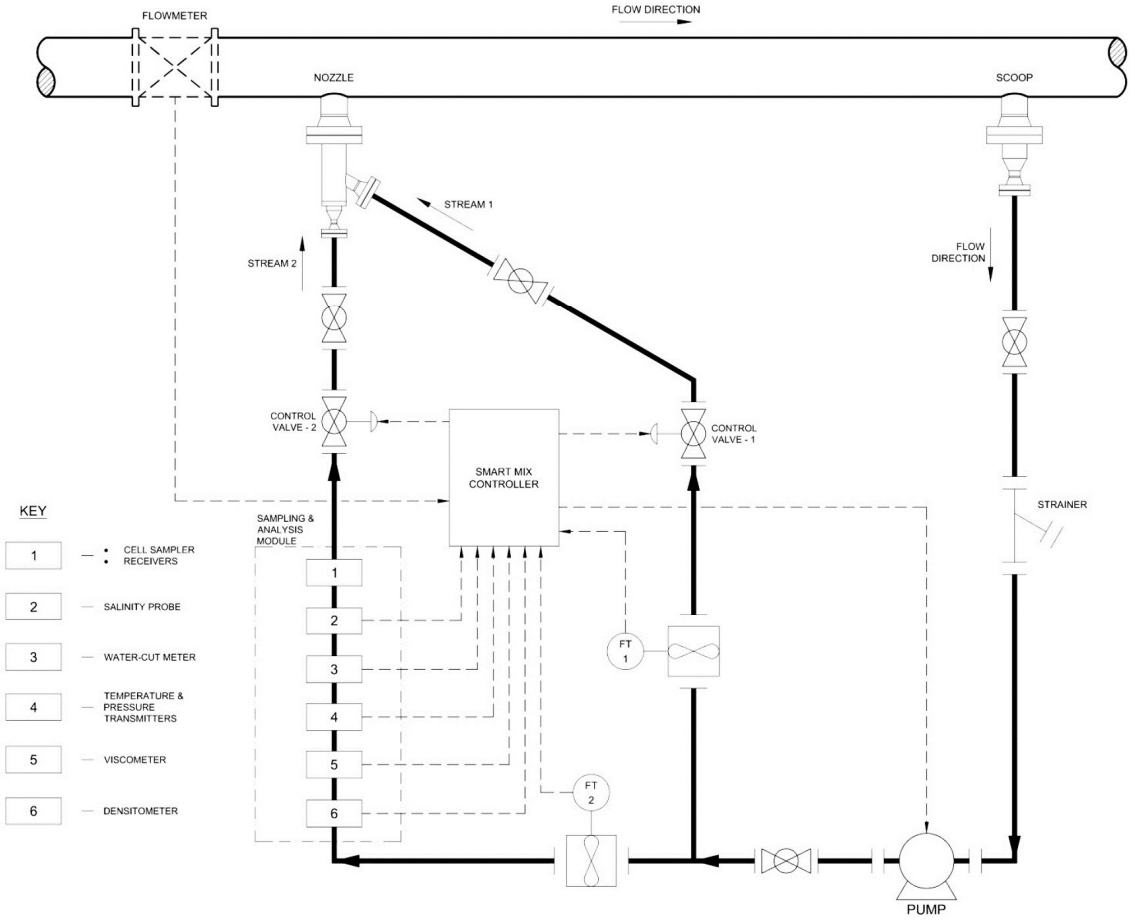


Figure 2.25 Dual jet concept of the SmartMix jet mixer where the two feed lines are used to supply jets of two different sizes (Maru et al., 2018).

The installation of the SmartMix is illustrated in Figure 2.25 (Maru et al., 2018). The SmartMix makes use of two feeds which supply a nozzle with jets of two differing strengths (Lakshmanan et al., 2017b). Maru and Lakshmanan (2018) claim that the interaction of these two differing strength jets allows the system to control the turbulent dissipation rate of the mixer using two control valves. The sampling system is located on one of the feedlines to the nozzle known as "Stream-2". This should imply that this stream is always flowing at a high enough velocity to prevent water dropout for the sampler. The operation of the control system is detailed in Maru et al. (2018) and Maru et al. (2019) where it is stated the control of the jets is automatic. Maru et al. (2019) state there are two different types of nozzle known as "NJ4" and the "SLIT" but provides no further details on their construction. Maru and Waters (2018) provide the design of one such nozzle showing the dual inlets of

their weak and strong jet concept in Figure 2.26. Figure 2.26(right) presents in the internals of the nozzle which contains separate feeds for the weak and strong jets.

Maru et al. (2019) use a six-point probe to test the "NJ4" and the "SLIT" nozzle designs in a 10-inch facility, where the two nozzles designs are claimed to result in C_1/C_2 ratios that exceed 0.97 in all test cases. However, it is unclear how the C_1/C_2 ratio was calculated from these experiments and the individual water fractions measured from the six-point probe are not included. This is especially important given Lakshmanan et al. (2015) earlier conclusion that the C_1/C_2 ratio was not a good measure of how well the flow was mixed.

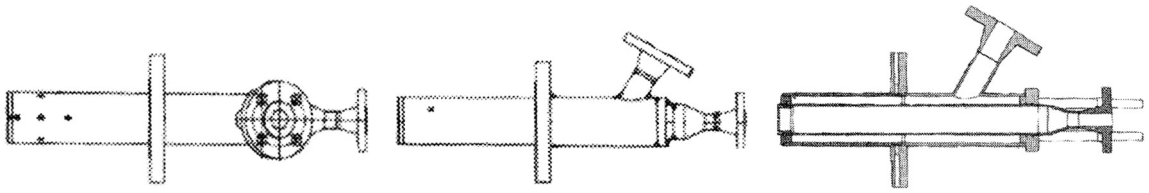


Figure 2.26 A nozzle implementation of the weak and strong jet concept of the "SmartMix" (Maru and Waters, 2018).

A flow-through mixing-chamber was patented by Jiskoot et al. (2018) for smaller line sizes, see Figure 1.4. This jet mixing system creates jets from small holes drilled into the pipeline wall instead of from a nozzle protruding into the pipe. This system is suitable for line sizes of 8" and smaller, where a nozzle protruding into the pipe can create excessive pressure loses which can lead to a gas breakout in some crude oils (Wright et al., 2020). The design extracts the mixing fluid downstream using a pump and pumps the fluid into a chamber with surrounds the pipe that has the wall holes that created the jet pattern to mix the flow.

2.10 Static mixing of immiscible liquid-liquid flows

In contrast to the limited amount of work on jet mixing liquid-liquid flows, previous work applying static mixers to such flows is much more extensive. A general review of static mixers and their industrial applications can be found within Thakur et al. (2003). Even more detailed descriptions of the operation and sizing of static mixers can be found in Paul et al. (2004).

A review of the literature indicates that the various Sulzer mixers (SMV, SMX, SMX+) and the Kenics mixers (KM, HEV, KSM) have the greatest amount of published work. SMV mixers have been studied by Lobry et al., 2011, Theron and Sauze, (2011), Sembira et al., (1986), Sembira et al., (1988). SMX and SMX+ mixers have been studied by Das et al.,(2005), Fradette et al., (2007), Hirschberg et al., (2009), Legrand et al., (2001), Liu et al., (2005), Rama Rao et al., (2007), Theron and Sauze, (2011), Theron et al., (2010). HEV mixers have been studied by Bakker and LaRoche, (2000), Lemenand et al., (2003), Lemenand et al., (2005). The KM mixer has been studied by Voulgaropoulos and Angeli, (2017) and Voulgaropoulos et al., (2019).

Most liquid-liquid static mixer studies have concentrated on measuring and modelling the resulting droplet sizes based on hydrodynamic, physical and dimensionless numbers. A summary of the static mixer models can be found in Lobry et al. (2011) and Paul et al. (2004).

2.11 Refractive index matching

The main challenge when implementing optical techniques is the requirement for optically undisturbed or fully known optical paths throughout the interrogated region, covering all fluid phases and any suspensions that may be of interest, including of the illumination and/or the observation or detection (e.g., reflected, scattered, fluorescent) light. Specifically, optical distortions and intensity variations in the fluid domains under observation can arise due to the refraction and/or reflection of light when this passes through materials with differing refractive indices (RIs), i.e., solid-gas, liquid-gas, solid-liquid and liquid-liquid, depending on the fluids/flows of interest. These distortions lead to unwanted optical warping, displacement and rotation of the measuring plane or volume, giving rise to increased errors in the measurement of interfacial topologies, velocities or other scalars.

The technique of refractive index matching (RIM) limits the physical process that causes refraction and reflection between differing materials. When applied to multiphase flows, the technique matches the refractive index of a primary liquid to secondary liquids or solids, for liquid-liquid, solid-liquid, solid-liquid-liquid flows.

The refraction of light at an interface is caused by a variation in the optical speed in the two adjacent transmission media, which creates a directional change in the propagation light-path. The degree of change of the light path direction

depends on the angle of incidence and the relative difference in the optical speeds in the two transmission media. The speed of light in a transmission medium u can be stated relative to the speed of light in a vacuum c, through the refractive index (RI), as defined by Eq. 2.22:

$$n = \frac{c}{u} \qquad \text{Equation 2.22}$$

Eq. 2.23 which is referred to as Snell's law and is also known as is the law of refraction, relates a light ray's angle of incidence to its angle of refraction at the interface between two transmission media of differing RI (n_1 n_2; see Figure 2.27):

$$\frac{\sin(\theta_1)}{\sin(\theta_2)} = \frac{n_2}{n_1} \qquad \text{Equation 2.23}$$

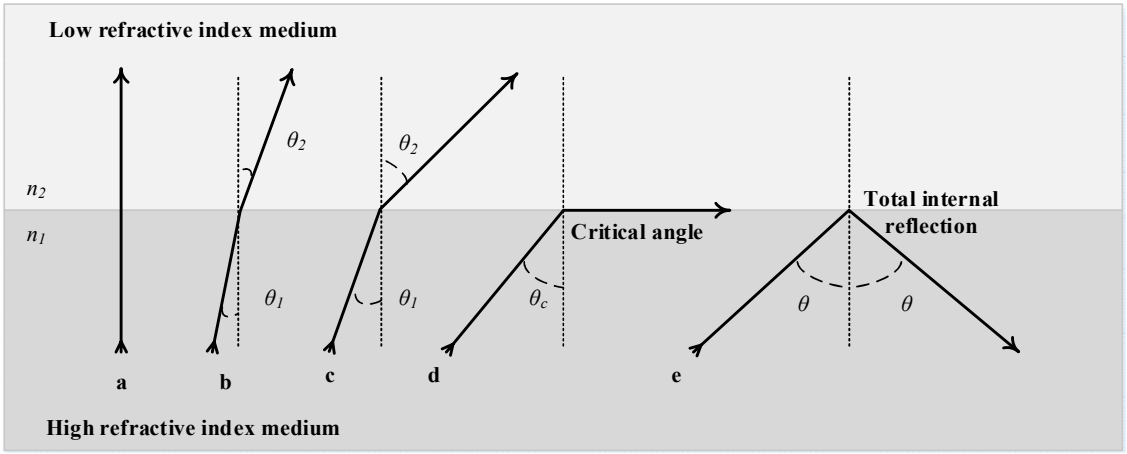


Figure 2.27 Refraction of a light ray at an interface as it passes from a high to a low refractive index medium: (a) no refraction/reflection occurs when the light direction is perpendicular to the interface; (b) slight refraction at low angles; (c) increasing refraction at higher angles; (d) critical angle between refraction and reflection; and (e) total internal reflection.

It emerges from Snell's law that larger directional changes (distortions) occur at an interface when: (i) there are greater relative RI mismatches between the two transmission media; and (ii) the incident angle (relative to the interface normal direction) is large, as illustrated in Figure **2.27**(a-c). Importantly, this also means that a higher RI mismatch or incident angle can lead to greater measurement errors if not fully corrected. Furthermore, if light travels from a material of higher RI (n_1) to one of lower RI (n_2) then a critical angle θ_c exists at which light travels along the direction of the interface, Figure **2.27**(d), and above which the light is fully reflected,

Figure **2.27**(e), creating optically inaccessible areas. Snell's law can be used to determine this critical angle θ_c, as given by Eq. 2.24:

$$\theta_c = \arcsin\left(\frac{n_2}{n_1}\right) \qquad \text{Equation 2.24}$$

In summary, the optical illumination of a targeted region of interest or its observation through interfaces (liquid-liquid or solid-liquid) associated with mismatched RIs can introduce positional or intensity uncertainty, and even lead to the observation of multiple images or optically inaccessible regions, especially if the interfaces are moving or curved. Such problems were reported, e.g., by Lowe and Kutt (1992), who were motivated to develop a spatial correction method using images from two cameras and ray-tracing equations.

It should be noted that the RI and thus the angle of refraction are wavelength-dependent, and this can lead to varying degrees of optical distortion depending on the wavelength of monochromatic light used, or dispersion if mixed wavelength light is used; in fact, this forms the basis of some measurement methods. For example, in the case of the most common liquid, pure water, the RI shows rational function dependency on the wavelength in the visible part of the electromagnetic spectrum, with values in the range 1.330 – 1.343 for wavelengths 405 – 707 nm at 20 °C/1 bar(a) (Thormahlen et al., 1985).

By convention, reported RIs are often measured using the sodium D-line at 598 nm, however, common lasers employed in optical-based measurements emit at different wavelengths (e.g., λNd:YAG = 266, 532, 1064 nm; λNd:YLF = 527 nm). This can induce errors in RI matching, since the RI of a solid or liquid phase generally decreases with increasing wavelength (Forziati, 1950), even in RIM systems that have been matched at their literature-reported values. Patil and Liburdy (2012) found that the use of fluorescent-dye-doped seeding-particles introduced a further source of error because the emitted fluorescent-light wavelengths differed to that of the laser source, and for which the system was optimized.

Beyond the illumination and/or observation wavelengths, several experimental parameters can lead to changes in the RIs of individual materials/substances in optical fluid-flow measurements, thus increasing errors even for initially matched systems in quiescent and laboratory-controlled environments, in particular, variations in temperature or pressure.

Mondy et al. (1986) reported that the temperature had to be kept within ±1 ºC to observe through 0.15 m of a 30% concentrated solid suspension, due to the temperature dependence of the RI of the fluid. This is an important consideration given that, unless controlled, the temperature can vary during experiments due to changes to the ambient conditions or the presence of heat sources or sinks in the flow loop (e.g., pumps or uninsulated walls). Significant temperature gradients leading to RI variations that introduce measurement errors were mentioned by Schmidt et al. (1984) who needed to create a laser-path correction curve to reduce positional errors in their LDA measurements in a fluid with a large temperature gradient.

RI deviations can also occur through processes such as hygroscopicity or evaporation causing relative changes to the components within fluid mixtures. In one example, Miller et al. (2006) found that the RI of their DEP and ethanol mixture changed over time due to the differential evaporation of the ethanol, highlighting the need for closed systems and fluid loops, especially when dealing with volatile fluids. Similarly, changes can occur when the solid materials can absorb the liquid phase(s), leading to RI changes over time (Dijksman et al., 2012), or due to the chemical instability or reactivity of the materials employed, again, unless these are controlled by the experimental design and procedure. For instance, Averbakh et al. (1997) and Shauly et al. (1997) utilized a mixture of 14.1 wt.% 1,1,2,2-tetrabromoethane, 35.7 wt.% polyalkylene glycol oil, 50.3 wt.% Triton X100 and 0.1 wt.% Tinuvin 328 to match the RI of PMMA. In this example, the Tinuvin 328 was specifically added to the mixture to reduce the rate of UV breakdown of tetrabromoethane. Finally, the RIs of solid components can also vary due to non-uniformities introduced during their manufacture, such as material impurities, inclusions, etc.

Four comprehensive papers have been published on RIM systems (Smedley and Coles, 1990; Budwig, 1994; Wiederseiner et al., 2011; Dijksman et al., 2012). Smedley and Coles (1990) created 121 pure single-component immiscible liquid-liquid pairs, some of which had closely matched RIs, however, none of these RIM liquid pairs were based on the common fluids of water, glycerol or silicone oil, and neither were they RI tuned as were single-component liquids. Budwig (1994) detailed the principles of RIM liquid flows covering both single-phase liquid and two-phase liquid-liquid flows. Wiederseiner et al. (2011) reviewed the RIM literature for flows containing concentrated particle suspensions and covered solid-liquid systems in great detail, including techniques for matching the RI of

solid particles and liquids. Dijksman et al. (2012) reviewed dense granular RIM systems for use with 3-D tomographic techniques, whilst detailing the optical effect of RI mismatches in such systems. The tomographic method relied on laser scanning to build 3-D data of the granular material through the RIM system.

During this work, a detailed review of the literature of prior refractive index systems was performed resulting in Wright et al. (2017). A summary of the liquid matches for plastics, rubbers, glasses, liquid-liquid matches as well as typical liquids and additives used has been included in Appendix A. This review found that RIM systems have been used predominantly for experiments featuring solid-liquid systems, and that while liquid-liquid RIM systems are relatively common, full three-phase solid-liquid-liquid RIM systems are rare, with only a few cases reported in the literature (see Table 2.1).

In one such effort, Burdett et al. (1981) investigated a solid-liquid-liquid RIM system for studying dispersed flows, holdup and axial mixing in packed extraction columns. The matching of liquid-liquid systems with PMMA was considered, but this was disregarded as the aqueous-phase consisted of concentrated salt solutions that were deemed too corrosive. Glycerol solutions were also considered, but the viscosity of these solutions was considered too high when over 70 wt.% of glycerol was added, limiting the maximum achievable RI to ≈ 1.430. Several solids below this limit were then considered including polytetrafluoroethylene (PTFE), polyformaldehyde (PFA), polychlorotrifluoroethylene (PCTFE) and silicone rubber, with respective RIs of 1.380, 1.410, 1.430 and 1.420. Ultimately, silicone rubber was selected as this was fairly transparent and chemically inert. The silicone rubber was then RI matched to two immiscible fluids, where the aqueous-phase was a 67.9 wt.% glycerol solution and the organic phase was methlcyclohexane. In another study, by Stöhr et al. (2003), two-phase liquid flows through porous media were investigated using PLIF and a fully matched RIM system. The porous medium consisted of fused-quartz matched to two immiscible fluid combinations. The first immiscible fluid was a mixture of silicone oils (98 wt.% Dow Corning 556 fluid and 2 wt.% Dow Corning 200 fluid), while the second fluid was an aqueous solution of 58 wt.% $ZnCl_2$.

Table 2.1 List of selected solid-liquid-liquid refractive index-matched systems.

n	Phase	Material	Density [kg/m³]	Dynamic viscosity* [mPa s]	Interfacial tension [mN/m]	References
1.422	Solid	Silicone rubber			n/a	Burdett et al. (1981)
	Organic	Methylcyclohexane	772		41.3	
	Aqueous	67.9 wt.% glycerol 32.1 wt.% water	1173	19.3		
1.460	Solid	Fused-quartz	2200	n/a	n/a	Stöhr et al. (2003)
	Organic	98 wt.% Dow Corning 556 fluid (silicone oil) 2 wt.% Dow Corning 200 fluid (silicone oil)	970	21		
	Aqueous	58 wt.% $ZnCl_2$ 42 wt.% water	1700	4		

* Temperature for viscosity is provided when stated, otherwise, it is assumed this is in ambient laboratory conditions between 20 ºC and 25 ºC.

2.12 Refractive index, density and viscosity tuning

While some liquids are naturally close optical matches to other liquids or solids, the RI of liquids in general can to be tuned to obtain a required RI matching degree by mixing miscible liquids or adding soluble solids. This practice also requires the ability to predict the RI of the resulting liquid mixtures or solutions. The RI of such mixtures can be predicted by numerous relations, with the most common of these listed below; here: n is the RI and ϕ is the volume fraction while the subscripts indicate the component.

A simple prediction of the RI of a multicomponent liquid can be made using the empirical Arago-Biot (AB) equation (Arago and Biot, 1806; Reis et al., 2010), which is based on linear volumetric additivity for each component in the mixture:

$$n = \sum_i \phi_i n_i \qquad \text{Equation 2.25}$$

and is similar to the empirical Gladstone-Dale (GD) equation (Dale and Gladstone, 1863; Sharma et al. 2006):

$$n - 1 = \sum_i \phi_i (n_i - 1) \qquad \text{Equation 2.26}$$

Another empirical relation is the Lichtenecker (L) or Lichtenecker-Rother equation (Lichtenecker, 1926; Lichtenecker and Rother, 1931; Heller, 1945) which, as Simpkin (2010) showed, has a theoretical basis derivable from Maxwell's equations:

$$\ln n = \sum_i \phi_i \ln n_i \qquad \text{Equation 2.27}$$

while relatively common Newton (N) equation (Newton, 1704; Kurtz and Ward, 1936; Reis et al., 2010) also has a theoretical foundation:

$$n^2 = \sum_i \phi_i n_i^2 \qquad \text{Equation 2.28}$$

Proceeding now to more complex models, the more involved theoretical Oster (O) equation (Oster, 1948; Sharma et al. 2006) is:

$$\frac{(n^2-1)(2n^2+1)}{n^2} = \sum_i \phi_i \frac{\left(n_i^2-1\right)\left(2n_i^2+1\right)}{n_i^2} \qquad \text{Equation 2.29}$$

while the theoretical model of the Lorentz-Lorenz (LL) equation is based on material polarizability (Lorentz, 1906; Pacák and Kodejš, 1988), has a similar form:

$$\frac{n^2-1}{n^2+2} = \sum_i \phi_i \frac{n_i^2-1}{n_i^2+2} \qquad \text{Equation 2.30}$$

as does the empirical Eykman (E) equation (Eykman, 1895; Dreisbach, 1948; Sharma et al., 2006):

$$\frac{n-1}{n+0.4} = \sum_i \phi_i \frac{n_i^2-1}{n_i+0.4} \qquad \text{Equation 2.31}$$

Furthermore, the RIs of binary mixtures can be calculated by the Eyring-Jhon (EJ) equation (Eyring and Jhon, 1969):

$$n = n_1\phi_1^2 + 2(n_1 n_2)^{1/2}\phi_1\phi_2 + n_2\phi_2^2 \qquad \text{Equation 2.32}$$

and for dilute binary mixtures, where component-2 is denoted here as the dilute component, the RI can be calculated by using the theoretical Wiener (W) equation (Wiener, 1910; Heller, 1945; Wiederseiner et al., 2011):

$$\frac{n-1}{n^2+2n_1^2} = \phi_2 \frac{n_2^2-n_1^2}{n_2^2-2n_1^2} \qquad \text{Equation 2.33}$$

or by using the theoretically derived Heller (H) equation (Heller, 1945; Mehra, 2003):

$$\frac{n - n_1}{n_1} = \frac{3}{2}\phi_2 \frac{n_2^2 - n_1^2}{n_2^2 - 2n_1^2} \qquad \text{Equation 2.34}$$

In all of the above expressions, the volume fraction of a component-*i*, ϕ_i, is defined using Eq. 2.35, where V and x are molar volumes and molar fractions, respectively (Sharma et al., 2006):

$$\phi_i = \frac{x_i V_i}{\sum_j x_j V_j} \qquad \text{Equation 2.35}$$

The theory behind the RI of liquid mixtures is discussed by Reis et al. (2010), who explains that differences between the AB and N equations, which are amongst the simplest of the above relations, stem from the rigorous definitions of RI before and after mixing, respectively.

In trying to establish which relation appears better suited for the prediction of the RI of liquid mixtures, we examined comparisons performed by several authors. In one such effort that focussed on binary mixtures, Tasić et al. (1992) compared the AB, GD, LL, W and H equations concluding that LL predictions agreed well with RI measurements, whereas the AB relation was found to be the poorest predictor. Mehra (2003) compared the equations GD, LL, W and H with binary mixtures of hexadecane and heptadecane with a series of alcohols, and concluded that the GD and W equations did not perform as well as the LL or H equations. The authors also noted that the GD equation gave the same results as the W equation in dilute mixtures but that neither worked well at higher concentrations. In their extensive study, Sharma et al. (2006) compared the AB, GD, N, O, LL, E, EJ, W and H equations, and considered the H equation to be most accurate for their specific binary test-mixtures of eucalyptol with hydrocarbons. The authors noted small deviations between the AB and GD predictions and reported that the W equation exhibited larger deviations from experimental RI values than the E, EJ and H equations.

In another comprehensive study involving multiple empirical and theoretical relations, Mandava et al. (2015) compared the AB, GD, N, O, LL, E, EJ, W and H equations and found that the O relation was the worst-performing for their mixtures, while the N equation performed the best. Isehunwa et al. (2015) compared predictions of the RIs of selected binary mixtures from the AB, GD, LL, W and H equations, and found that their own modified AB equation had the widest temperature applicability.

From the above variability over the best performing relation(s), but also a large number of similar studies in the literature, it is clear that these equations should be treated as a guide and that RI should be measured whenever possible, but also that it is a great challenge to identify one relation that can be generally accepted as being best with different relations performing better with different liquid phases and their relative mixture concentrations. Nevertheless, Mehra (2003) states that the most frequently used equation is LL equation, and although in the above comparisons only Tasić et al. (1992) and Mehra (2003) found LL to be the most accurate approach, none found that it was the worst-performing. Based on this observation, the present authors consider that the LL equation appears to be the most promising starting point for RI tuning.

Importantly, combining three or more liquids or additives allows for the matching or tuning of parameters over and above the RI, i.e., density, viscosity, surface and interfacial tensions, to achieve flow similarity. Density tuning is desirable when gravitational effects need to be considered in both solid-liquid and liquid-liquid systems and is particularly important when trying to establish neutrally buoyant solids (Bailey and Yoda, 2003). Viscosity tuning is important when trying to obtain direct matches to actual liquids or when matching Reynolds numbers. Likewise, the interfacial tension can be important in liquid-liquid systems when investigating interfacial phenomena (droplet breakup, atomization, etc.). The prediction of density, viscosity and surface tension is beyond the scope of this report, so the reader is referred to Polling et al. (2001) which is an excellent reference source covering a range of methods for estimating these properties for a wide range of liquids, and their mixtures. Combinations can also allow RI tuning at two wavelengths simultaneously, for example, the wavelengths of laser emission and dye fluorescence (Saksena et al. 2015).

Further, many physio/biological, petrochemical and other flows involve complex non-Newtonian fluids for which it is often desirable to tune additional properties in RIM experiments, such as the fluid rheology, to achieve dynamic similarity with flows of interest. For example, the shear thinning and viscoelastic behaviour of blood is often modelled by adding xanthan gum, and the further addition of NaI or NaSCN can be used to reduce the viscosity of the resultant xanthan gum mixtures (Najjari et al., 2016).

Tuning for dynamic similarity in two-phase flow systems where (Newtonian) viscosity, density and interfacial tension are important can be achieved by satisfying

Eqs. 2.36 to 2.38 for the liquid phases of interest *A* and *B*, and the surrogate/model liquids *SA* and *SB* (Saksena et al. 2015). Eqs. 2.36 and 2.37 equate the density and viscosity ratios of the surrogate and actual liquids, while Eq. 2.38 is required for matching dimensionless numbers concerning interfacial tension including the Weber number, Bond number, capillary number, Eötvös number and Ohnesorge number:

$$\frac{\rho_{SA}}{\rho_{SB}} = \frac{\rho_A}{\rho_B} \qquad \text{Equation 2.36}$$

$$\frac{\mu_{SA}}{\mu_{SB}} = \frac{\mu_A}{\mu_B} \qquad \text{Equation 2.37}$$

$$\frac{\sigma_{SA:SB}^3 \rho_{SA}}{\mu_{SA}^4} = \frac{\sigma_{A:B}^3 \rho_A}{\mu_A^4} \qquad \text{Equation 2.38}$$

A highly tunable liquid-liquid RIM system with a RI covering the range from 1.395 and 1.436 was created by Saksena et al. (2015). This system simultaneously allowed control over RI, viscosity, density as well as a potential 4th parameter. This flexibility was achieved through having two liquid-mixture phases: an aqueous-solution containing 1,2-propanediol and Caesium Bromide (CsBr), and an organic phase comprising a light (5×10^{-6} m^2/s) and heavy (5×10^{-5} m^2/s) silicone oil blended with 1-bromooctane. The system was extended for wider viscosity and density ratios by Cadillion et al. (2016) by replacing the silicone oils with ones with even larger viscosity differences (1×10^{-6} m^2/s and 5×10^{-3} m^2/s) to obtain a system with an RI in the range 1.382 – 1.436.

An experimental system will typically define a working temperature range. Temperature variations can, however, give rise to RI variations, meaning that RI tuning may be required even for what superficially appears to be a RIM system. In one example, Fort et al. (2015) demonstrated that para-cymene closely matched PMMA at 291.7 K, but noted that a cooling system may be required if heat sources, such as pumps, exist within a flow-loop. It was therefore suggested that para-cymene's RI could be tuned through adding a small amount of cinnamaldehyde with an RI of 1.562 to allow RI matching with PMMA at higher temperatures.

2.13 Contact angle and wettability

A contact angle is an angle made at the interface between two fluids on a surface. Figure 2.28 demonstrates the definition of the contact angle for two-fluid droplets on a solid surface in an immersion fluid. The fluid of droplet (a) on the left is more phobic of the surface than the immersion fluid and therefore has a larger contact angle, while the fluid of droplet (b) on the right has a greater affinity for the surface than the immersion fluid and so has a smaller contact angle. In particular, surface and interfacial tension should be taken into account when selecting fluids for liquid-liquid flow studies to match the experimental conditions in a given application (e.g., the flow of water and oil through crude-oil transport pipelines).

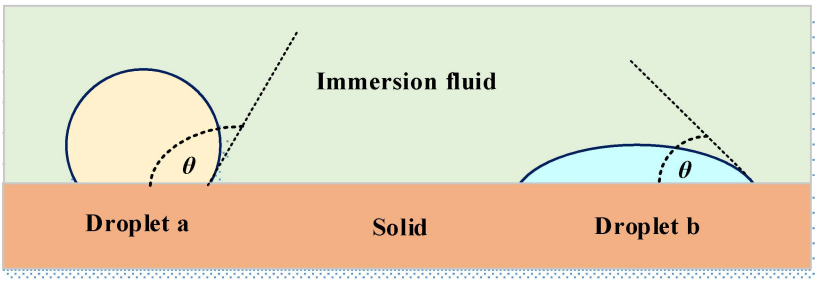


Figure 2.28 Two droplets on a solid surface in a lighter emersion fluid making contact angles θ with a solid. The liquid of droplet (a) has a lower affinity for the surface than the immersion fluid and a larger contact angle, while the liquid of droplet (b) has a greater affinity for the solid than the immersion fluid and a smaller contact angle.

The contact angle quantifies the wettability of the surface where for water it is either hydrophobic or hydrophilic, or similarly, for oil, it is oleophobic or oleophilic. Figure 2.29 shows the contact angle formed between Exxsol D80 mineral oil, and a droplet of 80% glycerol-water solution on borosilicate glass where the contact angle is measured through the aqueous phase, Morgan (2012).

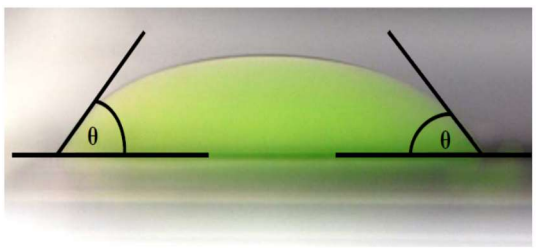


Figure 2.29 Contact angle for a droplet of an 80% glycerol solution immersed in Exxsol D80 on a borosilicate glass surface (Morgan, 2012).

Tang et al. (2009) performed contact angle measurement on several mild steel surfaces with crude oils and 1% NaCl solution. Tang et al. (2009) demonstrated that the surface roughness increases the aqueous contact angle making the surface more hydrophobic, while also demonstrating that an Iron carbonate film makes the surface more hydrophilic. Tabrizi (2012) however found that 316 stainless steel contact angle increased with surface roughness but then decreased. Tang et al. (2009) found that the contact takes of the order of 100 s to settle into equilibrium changing from a hydrophobic state into a hydrophilic state, see Figure 2.30.

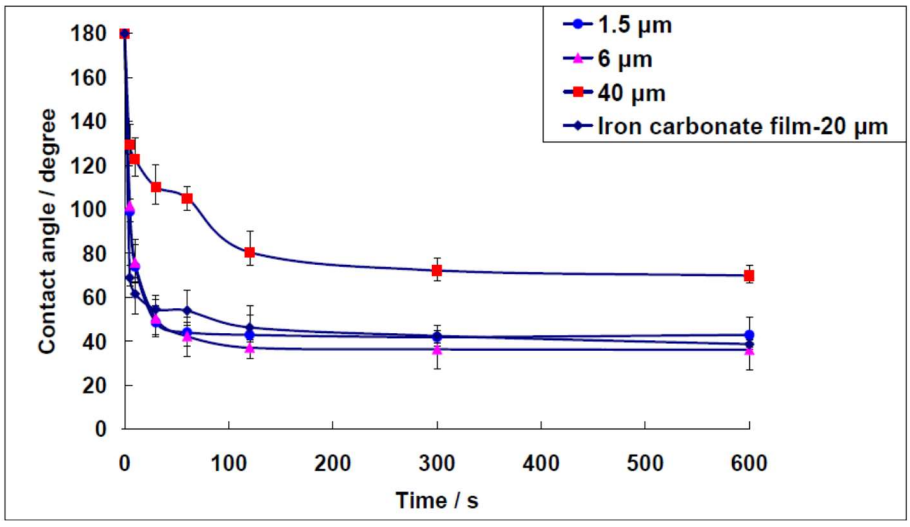


Figure 2.30 Water-in-oil contact angle for several steel surfaces measured against time (Tang et al., 2009).

Schmitt and Stradmann (1998) analysed the effect of CO_2 corrosion and demonstrated that the surface-active compounds affect the contact angle. Compounds of Alcohol Ethoxylates and quaternary ammonium increased the hydrophilic properties of the steel while fatty amines and imidazolines produced hydrophobic surfaces. Li (2009) demonstrated that a corrosion inhibitor can change the steel surface from hydrophilic to hydrophobic.

Angeli and Hewitt (1999) refer to experiments conducted by Norsk Hydro which found that steel can be preferentially wetted by either water or oil depending on the history of the sample while acrylic is always oil wetted, see results in Table 2.2.

Table 2.2 Surface contact angle measurements demonstrating how the initial solid wetting can affect the results, (Angeli and Hewitt 1999).

Surface material	Oil drops in water, water wetted	Oil drops in water, oil wetted	Water drops in oil, water wetted	Water drops in oil, oil wetted
Steel	143.3°	0.0°	0.0°	128.7°
Acrylic	87.6°	84.4°	106.0°	121.6°

Chapter 3

Experimental methods

This chapter describes the experimental facility and its design along with the techniques used in obtaining the detailed measurements of the jet mixing of stratified pipeline flows. Several experimental techniques were used including both classical measurements, like pressure, temperature, flow, density and viscosity as well as advanced laser-based optical techniques using refractive index matching, including PLIF, PIV and stereo-PIV. The experimental system, therefore, allows the acquisition of flow regimes, pressure gradients, phase fractions, droplet sizes and velocity profiles so that mixing efficiency at multiple positions along the test section can be established and compared.

3.1 Degrees of freedom

An analysis of the degrees of freedom within jet mixer systems was conducted before starting the design of the experimental system and test matrices. This study found there is a considerable range of physical design parameters for jet mixers, including:

- Main pipeline diameter;
- Location of the jet outlets, e.g. from the wall or a nozzle located inside the pipe cross-section;
- Number of jets;
- Jet diameter, that could differ for each jet;
- Jet exit shape, e.g. circular, planar, etc.;
- Jet collimation length;
- Jet angles, in both the flow and transverse flow directions;
- Relative positions of the jet or jets;
- Jet exit velocity;
- Steady or pulsating jet;

Indeed, a more detailed dimensional analysis on an immiscible two-fluid pipeline flows found that, with a single round jet originating from the bottom of the pipe wall, 16 independent variables can be defined, which are:

1. The density of the oil phase, ρ_o
2. The density of the aqueous phase, ρ_{aq}
3. The viscosity of the oil phase, μ_o
4. The viscosity of the aqueous phase, μ_{aq}
5. The internal diameter of the jet, D_j
6. The internal diameter of the pipe test section, D
7. The volumetric flow of oil in the mainline, Q_o
8. The volumetric flow in the aqueous phase in the mainline, Q_{aq}
9. The volumetric flow of oil in the jet Q_{j_o}
10. The volumetric flow of aqueous phase in the jet, Q_{j_aq}
11. The interfacial tension between the oil and aqueous phase, σ
12. The contact angle between pipe material and aqueous phase, θ
13. The test section pipe material roughness, e
14. The jet angle in pipe cross-section ψ see Figure 3.1(left)
15. The jet angle in direction of flow, Ω, see Figure 3.1(right)
16. Local gravitational acceleration,

Using the Buckingham π theorem (Buckingham, 1914) we can conclude from the variables and fundamental dimensions that there are 13 independent dimensional groups required to describe this relatively simple jet mixing problem.

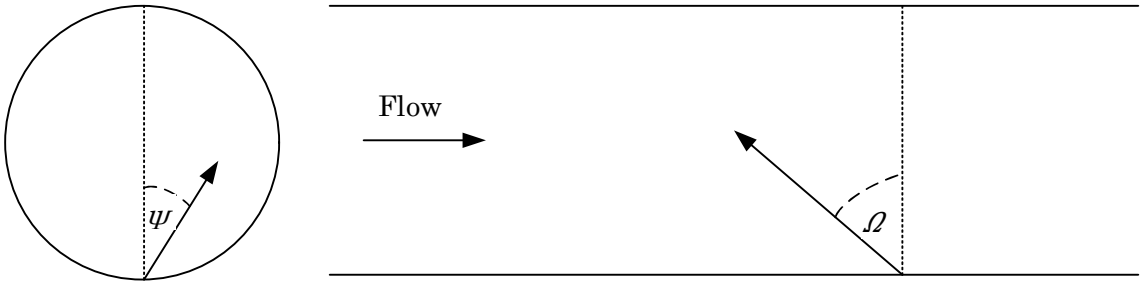


Figure 3.1 Schematic illustrating the two angles of jet originating from a pipe wall.

.

Some of these physical properties are represented in Figures 3.1 and 3.2. Figure 3.1 is an illustration of the two angles that the jet can take relative to the incoming flow, the angle forward into the flow from the vertical, Ω, and the angle from the vertical in the cross-section of the pipe ψ. Whilst Figure 3.2 illustrates the incoming stratified flows and the jet, showing the interface height, H_{aq}, the internal diameter of the pipe, D, and the exit diameter of the jet, D_j.

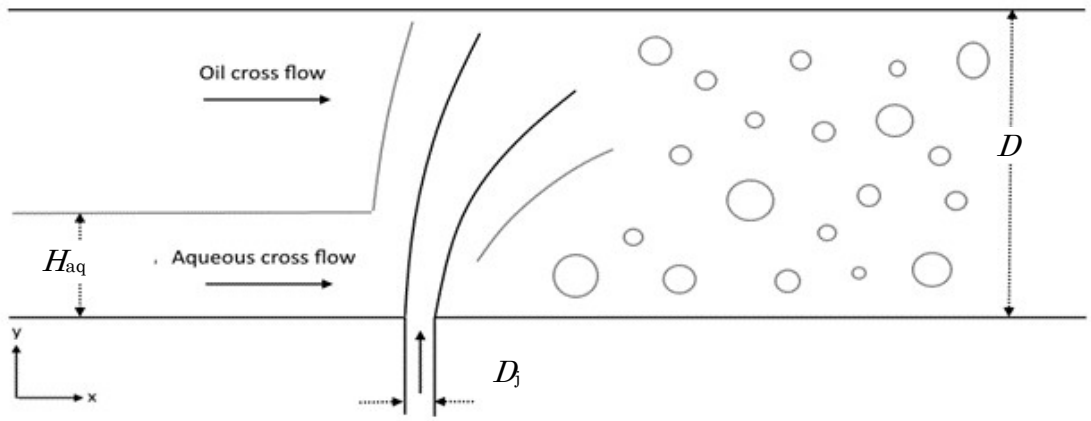


Figure 3.2 Schematic illustrating a single jet in a liquid-liquid stratified crossflow and the resulting downstream droplets.

The height of the interface between the aqueous crossflow and oil crossflow is a function of:

$$H_{aq} = f(Q_o, Q_{aq}, D, \mu_o, \mu_{aq}, \rho_o, \rho_{aq}, \theta, e, \sigma, g) \qquad \text{Equation 3.1}$$

The velocity of the crossflow mixture is a function of:

$$u_m = f(Q_o, Q_{aq}, D, \mu_o, \mu_{aq}, \rho_o, \rho_{aq}, \theta, e, \sigma, g) \qquad \text{Equation 3.2}$$

A fully stratified oil and water flow implies that the density and viscosity of the crossflow are given by the functions:

$$\rho_m = \begin{cases} y < H_{aq} & \rho_{aq} \\ y > H_{aq} & \rho_o \end{cases} \qquad \mu_m = \begin{cases} y < H_{aq} & \mu_{aq} \\ y > H_{aq} & \mu_o \end{cases} \qquad \text{Equation 3.3}$$

The average density and viscosity of the combined crossflows can be approximated by assuming a no-slip condition and then averaging based on the pipe input volumetric fractions, giving:

$$\langle \rho_{\mathrm{m}} \rangle = (\phi - 1)\rho_{\mathrm{o}} + \phi_{\mathrm{j}}\rho_{\mathrm{aq}} \qquad \langle \mu_{\mathrm{m}} \rangle = (\phi - 1)\mu_{\mathrm{o}} + \phi_{\mathrm{j}}\mu_{\mathrm{aq}} \qquad \text{Equation 3.4}$$

The average velocity of the combined crossflows on the jet can be approximated through:

$$\langle V_{\mathrm{m}} \rangle = \frac{4\left(Q_{\mathrm{aq}} + Q_{\mathrm{o}}\right)}{\pi D^2} \qquad \text{Equation 3.5}$$

The density and viscosity of the jet can be approximated by averaging based on the input jet volumetric fractions, giving:

$$\rho_{\mathrm{j}} = \left(\phi_{\mathrm{j}} - 1\right)\rho_{\mathrm{o}} + \phi_{\mathrm{j}}\rho_{\mathrm{aq}} \qquad \mu_{\mathrm{j}} = \left(\phi_{\mathrm{j}} - 1\right)\mu_{\mathrm{o}} + \phi_{\mathrm{j}}\mu_{\mathrm{aq}} \qquad \text{Equation 3.6}$$

The average velocity of the jet is

$$\langle V_{\mathrm{j}} \rangle = \frac{4\left(Q_{\mathrm{j_aq}} + Q_{\mathrm{j_o}}\right)}{\pi {D_{\mathrm{j}}}^2} \qquad \text{Equation 3.7}$$

All the variables are based upon the three fundamental dimensions of length, mass and time. Using the parameters above the following dimensional groups can be defined as:

1. Wettability; θ
2. Relative roughness; $\frac{e}{D}$
3. Jet to crossflow density ratio; $\frac{\rho_{\mathrm{j}}}{\langle \rho_{\mathrm{m}} \rangle}$
4. Jet to crossflow viscosity ratio; $\frac{\mu_{\mathrm{j}}}{\langle \mu_{\mathrm{m}} \rangle}$
5. Velocity ratio; $\frac{\langle V_{\mathrm{j}} \rangle}{\langle V_{\mathrm{m}} \rangle}$
6. Momentum flux ratio; $q = \frac{\rho_{\mathrm{j}}}{\langle \rho_{\mathrm{m}} \rangle}\left(\frac{\langle V_{\mathrm{j}} \rangle}{\langle V_{\mathrm{m}} \rangle}\right)^2$
7. Pipe input water fraction; $\phi = \frac{Q_{\mathrm{aq}}}{Q_{\mathrm{aq}} + Q_{\mathrm{o}}}$

8. Jet input water fraction; $\phi_{\mathrm{j}} = \frac{Q_{\mathrm{j_aq}}}{Q_{\mathrm{j_aq}} + Q_{\mathrm{j_o}}}$

9. Jet to Pipe diameter ratio; $\frac{D_{\mathrm{j}}}{D}$

10. Jet flow Weber number; $\mathrm{We_j} = \frac{\rho_{\mathrm{j}}\langle V_{\mathrm{j}}\rangle^2 D_{\mathrm{j}}}{\sigma} = \frac{jet\ inertia}{interfacial\ tension}$

11. Crossflow Weber number; $\mathrm{We_m} = \frac{\langle\rho_{\mathrm{m}}\rangle\langle V_{\mathrm{m}}\rangle^2 D_{\mathrm{j}}}{\sigma} = \frac{\mathrm{We_j}}{q} = \frac{cross\ flow\ inertia}{interfacial\ tension}$

12. Jet flow Reynolds number; $\mathrm{Re_j} = \frac{\rho_{\mathrm{j}}\langle V_j\rangle D_j}{\mu_j} = \frac{jet\ inertia}{jet\ viscosity}$

13. Crossflow Reynolds number; $\mathrm{Re_m} = \frac{\langle\rho_{\mathrm{m}}\rangle\langle V_{\mathrm{m}}\rangle D_{\mathrm{j}}}{\langle\mu_{\mathrm{m}}\rangle} = \frac{\mathrm{Re_j}\tilde{\mu}}{\sqrt{q\times\tilde{\rho}}} = \frac{cross\ flow\ inertia}{cross\ flow\ viscosity}$

14. Ohnesorge number; $\mathrm{Oh} = \frac{V_{\mathrm{j}}}{\sqrt{\rho_{\mathrm{j}} D_j \sigma}} = \frac{\sqrt{\mathrm{We_j}}}{\mathrm{Re_j}} = \frac{jet\ viscosity}{interfacial\ tension}$

15. Richardson number; $\mathrm{Ri} = \frac{gD_{\mathrm{j}}}{\langle V_{\mathrm{j}}\rangle^2}\left(\frac{\langle\rho_{\mathrm{m}}\rangle - \rho_{\mathrm{j}}}{\rho_{\mathrm{j}}}\right) = \frac{jet\ buoyancy}{jet\ inertia}$

16. Eötvös number; $\mathrm{Eo} = \frac{g\left(\langle\rho_{\mathrm{m}}\rangle - \rho_{\mathrm{j}}\right){D_{\mathrm{j}}}^2}{\sigma} = \mathrm{Ri}\cdot\mathrm{We_j} = \frac{jet\ buoyancy}{interfacial\ tension}$

17. The jet angle in the axial direction of the flow; Ω

18. The jet angle in the pipe cross-section; Ψ

The momentum flux ratio (6), crossflow Weber number (10), crossflow Reynolds number (13), Ohnesorge number (14) and Eötvös number (16) can all be

created from other dimensionless groups. Therefore, seven of the above 18 dimensionless groups are not independent.

The mainline pipe diameter of industrial crude oil pipelines is normally between 2 and 48 inches (Transportation Research Board, 2004). An industrial pipe size was desirable but had to fit within the limited experimental laboratory space so a 2-inch pipe was selected for this work. Jet mixing designs with mainline pipeline diameters below 6-inches typically have jets that originate from the wall to minimise pressure losses (Wright et al., 2020), and hence wall originating jets were selected for the 2-inch pipework used in the experimental campaign.

Current industrial jet mixers have between one and twenty jets where the number of jets increases with the pipeline diameter. Given the experimental pipelines internal diameter was to be 2-inches, it was decided that the use of one or two jets would reduce the system complexity, and would allow for a clearer view of the processes leading to the jet breakup of the stratified flows.

In an industrial environment, the jet nozzle exit varies with implementation although all current implementations use round jets. These round jets typically have exit diameters, D_j, between 5 mm and 20 mm, where the 5 mm limit is chosen to prevent blockages and so irrelevant in the laboratory systems. In the industrial systems, the internal collimation length, which is the tube leading up to the jet exit, ranges from one to four D_j. In the 2-inch laboratory system, round jets with $D_j = 2.8 - 4$ mm and collimation lengths of one D_j were selected for the experimental system.

The angles and positioning of the jets are varied so it was decided that only simple jet configurations would be used to minimise experimental complexity. The velocity of industrial jet mixing systems is normally within the range of 10 m/s to 30 m/s where the upper limit increases with the main pipeline diameter. Given a jet velocity of 30 m/s would lead to high-pressure losses and could be a safety hazard, the maximum laboratory jet velocity was restricted to 16 m/s.

Finally, the velocity of jet mixers can be steady or vary in time and it was decided that the experimental system would choose steady jets to limit complexity leaving unsteady jets for future work. The complexity of jet mixing system can be vast and thus the choices made to limit the system complexity allowed the experimental campaigns to be completed with the given timeframe of the project.

3.2 Two fluid model

Stratified two-phase flows are typically given independent Reynolds numbers for each phase. A common one-dimensional model used to calculate these Reynolds numbers is the "two-fluid model" that was initially developed for liquid-gas systems by Taitel and Dukler (1976) and then adapted for liquid-liquid systems by Brauner et al (1989), Brauner and Moalem Maron (1989) and Kurban (1997). The model assumes that the flows are parallel, horizontal, steady-state and fully developed with a flat interface where there is no heat transfer or diffusion. The resulting Reynolds numbers are:

$$\mathrm{Re}_{aq} = \frac{\rho_{\mathrm{aq}} \langle V_{\mathrm{aq}} \rangle D_{\mathrm{H_aq}}}{\mu_{\mathrm{aq}}} \qquad \text{Equation 3.8}$$

$$\mathrm{Re}_{o} = \frac{\rho_{\mathrm{o}} \langle V_{\mathrm{o}} \rangle D_{\mathrm{H_o}}}{\mu_{\mathrm{o}}} \qquad \text{Equation 3.9}$$

where the hydraulic diameters, $D_{\mathrm{H_aq}}$ and $D_{\mathrm{H_o}}$, are given by:

$$D_{\mathrm{H_aq}} = \frac{4A_{\mathrm{aq}}}{p_{\mathrm{aq}} + p_{\mathrm{int}}} \qquad D_{\mathrm{H_o}} = \frac{4A_{\mathrm{o}}}{p_{\mathrm{o}}} \qquad \text{when } V_{\mathrm{aq}} > V_{\mathrm{o}} \qquad \text{Equation 3.10}$$

$$D_{\mathrm{H_aq}} = \frac{4A_{\mathrm{aq}}}{p_{\mathrm{aq}}} \qquad D_{\mathrm{H_o}} = \frac{4A_{\mathrm{o}}}{p_{\mathrm{o}} + p_{\mathrm{int}}} \qquad \text{when } V_{\mathrm{aq}} < V_{\mathrm{o}} \qquad \text{Equation 3.11}$$

$$D_{\mathrm{H_aq}} = \frac{4A_{\mathrm{aq}}}{p_{\mathrm{aq}}} \qquad D_{\mathrm{H_o}} = \frac{4A_{\mathrm{o}}}{p_{\mathrm{o}} + p_{\mathrm{int}}} \qquad \text{when } V_{\mathrm{aq}} \approx V_{\mathrm{o}} \qquad \text{Equation 3.12}$$

A is the cross-sectional area occupied by the phase and p_{aq}, p_{o} and p_{int} are the wetted perimeters of the aqueous phase pipe wall, oil pipe wall and the interface between phases, respectively.

3.3 Experimental facility

The jet mixing experimental investigations were conducted at Imperial College London's two-phase oil and water experimental rig (TOWER). TOWER is a liquid-liquid facility that was designed to study co-current flows of immiscible liquids and was constructed in the early 1990s by Panagiota Angelli (Angeli, 1996) and Adib Kurban (Kurban, 1997). Since 1990, the TOWER facility has undergone several significant revisions, accommodating differing liquid-liquid experiments including those of Soleimani (1999), Hussain (2004), Morgan (2012) and Ibarra (2017).

In January 2015, the facility was configured for the experimental work of Ibarra (2017) for studying co-current stratified oil-water flows in horizontal and inclined pipes using water and the oil Exxsol D140. A piping and instrumentation diagram (P&ID) of Ibarra's configuration at this time is presented in Figure 3.3.

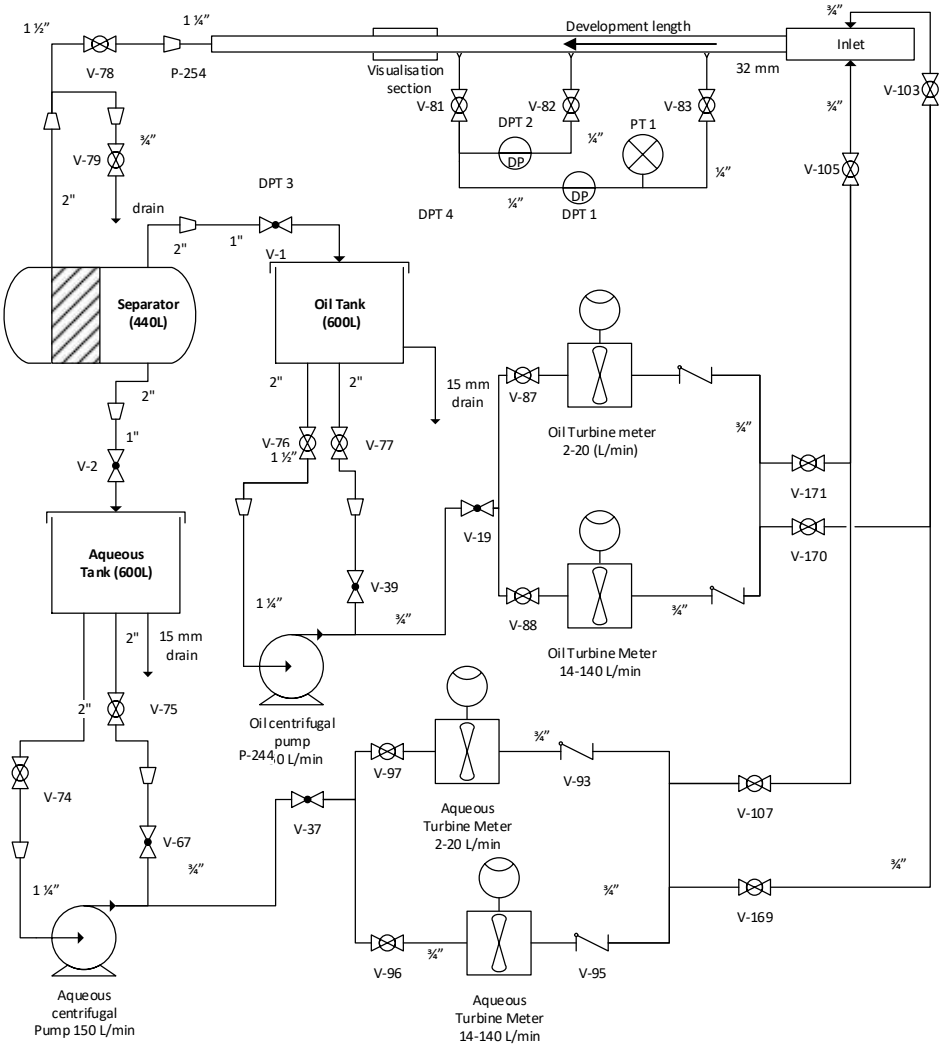


Figure 3.3 P&ID of the TOWER facility as it was in January 2015 before modifications were made to accommodate the jet mixing experimental campaign.

In accommodating this jet mixing experimental work the TOWER facility required extensive modifications as can be seen in Figure 3.4 which presents the P&ID used during the experimental campaigns. The design and construction of TOWER modifications were performed over about two years while the facility was being used by Ibarra. This required careful planning, implementation and testing of modifications, including the creation of a parallel test section, to minimise disruption

to Ibarra's ongoing experimental campaign. The following sections describe the details of the TOWER facility as used during the jet mixing experimental campaign.

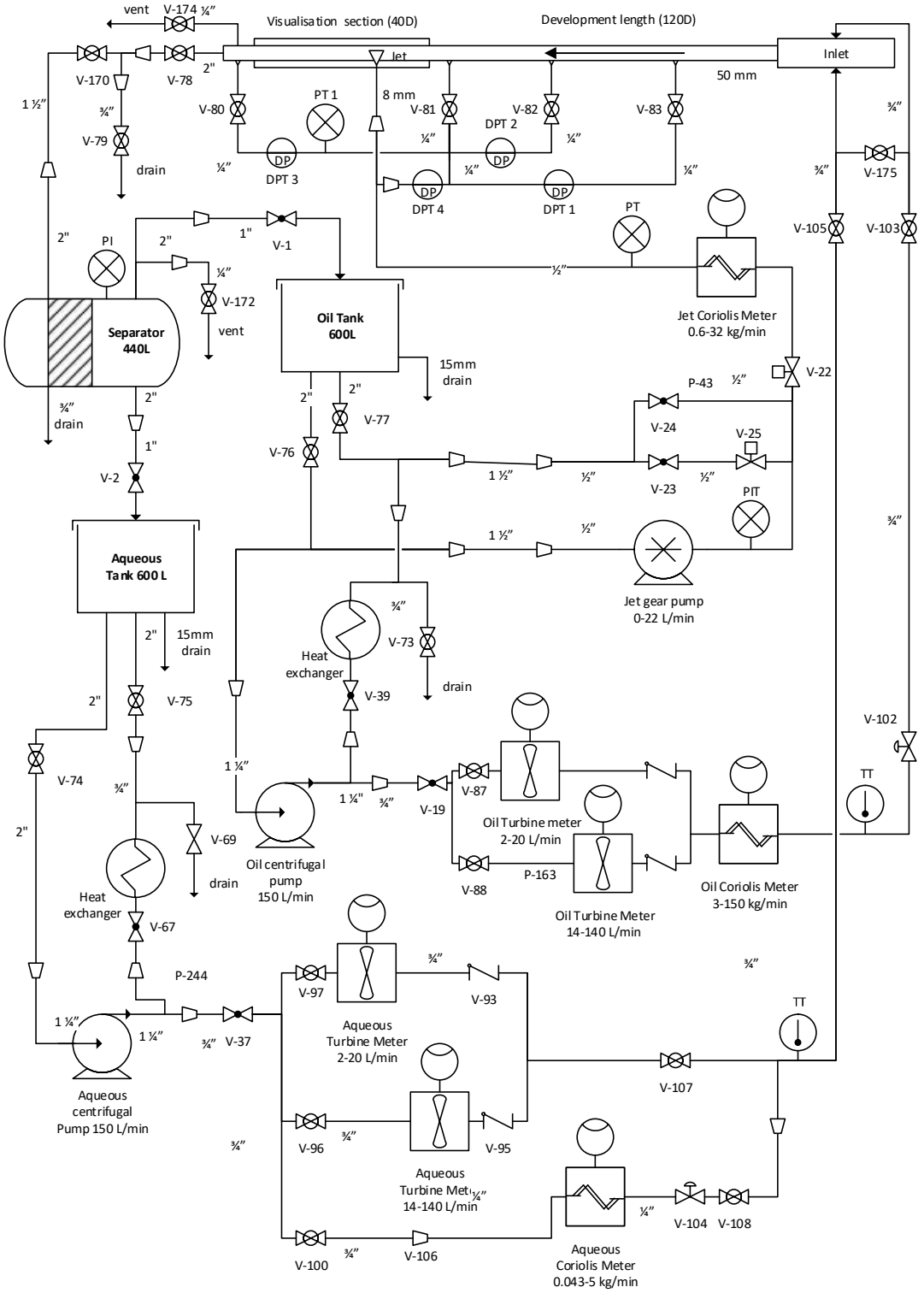


Figure 3.4 P&ID of the TOWER facility including all modifications for the jet mixing experimental campaign during April 2018.

3.3.1 Storage, metering and control section

The oil and aqueous phase are stored in two 600 L fibreglass resin tanks which have removable unsealed lids. The tanks are filled from the outlets of the 440 L liquid-liquid separator. The top separator outlet flows into the oil tank while the bottom outlet flows into the aqueous tank. The tank filling rates are controlled manually using two globe valves, one on each of the two separator outlet lines. These valves are controlled so that the separator maintains an approximate 50:50 ratio of each phase.

The height of the separator was controlled though adjusting the rate the aqueous phase drained, whereby opening or closing aqueous phase globe valve increased or decreased the drain rate, respectively. The globe valve of the oil outlet was normally fully open, except during high experimental flow rates when the globe valve was partially closed to prevent aqueous phase overflowing into the oil tank.

The outlets from the two tanks feed into Grundfos CRN 10-5 vertical multiple-stage centrifugal pumps. Each of the Grundfos CRN 10-5 pumps can produce a flow of up to 166 L/min, however, system pressure losses have reduced the maximum achievable flow to 70 L/min for oil phase pump and 55 L/min for the aqueous phase pump. The Grundfos CRN 10-5 pumps are single speed, which results in the pump giving maximum flow for the given backpressure. Therefore, the flow from the pump is split between the required experimental flow and a recirculation flow, using two manual globe valves. The recirculation flow for both phases returns to the tanks via water-cooled Hrale stainless steel 50 plate 285 kW heater exchangers.

It was discovered early in testing that heat exchangers were required as that the temperature of the fluids would rise to 37 ºC within 5 hours of experimental operation without any cooling installed. Temperature control was therefore needed to prevent changes in properties like viscosity, interfacial tension and refractive index with experimental run time. One side of the heat exchangers flowed the experimental fluids, while on the other side a flow of tap water with a temperature of 10 – 15 °C was used. The flow of tap water through the heat exchangers was controlled by globe valves and then sent to drain after exiting. These heat exchangers allowed the precise control of the temperature of the experimental liquids which were maintained at 23 °C.

The oil flows into the test section inlet are measured with two LFT Turbine Flowmeters manufactured by BELL flow systems and both use F110 flow rate indicator totalizers manufactured by Fluidwell BV. One meter is ranged 2 – 20 L/min

while the second meter is ranged 14 – 140 L/min. The oil flows were also measured with a Khrone Optimass 6000 Coriolis meter ranged 3 – 150 kg/min which corresponds to a volumetric flow of approximately 3.2 – 162 L/min given an oil density of 930 kg/m^3. In addition to flow, the Coriolis meter simultaneously provides density and temperature measurement of the oil flows. The Optimass 6000 was combined with a pneumatic valve using a Bronkhorst three-term proportional-integral-derivative (PID) controller so that flow rates could be set and maintained automatically.

The aqueous phase flows into the test section inlet are measured by three meters, two LFT Turbine Flowmeters with F110 flow rate indicator totalizers which are again ranged 2 – 20 L/min and 14 – 140 L/min. While the third meter is a Bronkhorst mini CORI-FLOW M15 Coriolis meter with a range of 5.00 kg/hr and 300.0 kg/hr, which corresponding to a volumetric flow of approximately 0.074 – 4.4 L/min given an aqueous density of 1130 kg/m^3. When the aqueous phase Coriolis meter is used the desired flow set-point is entered into a PID controller which uses a pneumatic valve along with feedback from the Coriolis meter to control the flow. The CORI-FLOW M15 simultaneously provides temperature and density measurements of the aqueous flows.

The jet system is feed from the 600 L oil tank using a Midland MOD100 positive displacement pump with a maximum flow of 22 L/min. The pump is attached to a 3-phase motor which is powered using a Parker 650 inverter drive which allows control of the speed of the pump's motor using an input 4 – 20 mA signal, hence allowing the control of the flows to the jet. Jet flow rates are measured using a Cameron CC010 Coriolis meter ranged 1 – 20 kg/min, which is equivalent of 1.1 – 21 L/min given the oil density of 930 kg/m^3. In addition to flow, the CC010 Coriolis meter simultaneously measures the jet's oil density and temperature.

The pressure at the pump outlet and differential pressure over the jet nozzles is measured using pressure transmitters. These pressures are used to set up the jet within the LabVIEW control system. The jet control within LabVIEW has two modes of operation "recirculation" and "jetting". In the recirculation mode, the flow from the jet pump is recirculated back to the oil tank, while in the jetting mode the flow from the jet pump exits the jet nozzle into the test section. These two jet modes are switched using a pair of fast-acting pneumatic ball valves which are electronically activated via a solenoid from the LabVIEW control system. Before each experimental test point, the required jet velocity is set up into the jetting mode and the pressure at the pump's

outlet is recorded. The jet system is then set back into the recirculation mode, where the pressure of recirculation mode is matched to that of the jetting mode using a needle valve. This balancing of pressure between the two modes minimises the effect on the pump's flow and pressure when switching between modes.

The electronic timing of two pneumatic valves used to switch between the jet modes was configured during the commissioning of the experimental facilities so that the flow path was never blocked so ensuring pressures were minimally affected during the rapid switchover.

In addition to the temperatures measured at the Coriolis meters, the temperatures of the oil and aqueous solution entering the inlet of the experimental test section are also measured by two platinum resistance thermometers (PRT) that are connected to a Pico technology TC-08 thermocouple data logger which is then connected to the LabVIEW control system.

3.3.2 Separation

The separation of the oil phase and the aqueous phase is performed with a dedicated liquid-liquid separator manufactured by ACS Separations & Mass-Transfer Products. The separator is 1.94 m long, has an internal diameter of 0.54 m corresponding to a volume of 440 L. The separator contains a dedicated liquid-liquid "KnitMesh" coalescer manufactured by KnitMesh Ltd, the coalescer has an axial length of 0.30 m and has the same diameter of 0.54 m as the separator's internal diameter. The bi-material coalescer intertwines filaments of metal and plastic which are hydrophilic and oleophilic, respectively. The two-materials aid coalescence of both phases, increasing the efficiency at which the coalescer can operate to the point of allowing continuous experimental operation with an operational jet mixer.

The operation of the separator is regulated by adjusting the outward flows using globe valves located on both the oil and aqueous outlets pipes. These outward flows are controlled so that the interface level viewed through the observation window of the separator is held as close to halfway as practicable for each experimental run.

3.3.3 Inlet Design

A 3-D model of the test section inlet conditioner is shown in Figure 3.5. This inlet conditioner was specifically designed to encourage stratified flows to develop as rapidly as practicable within the constrained laboratory environment.

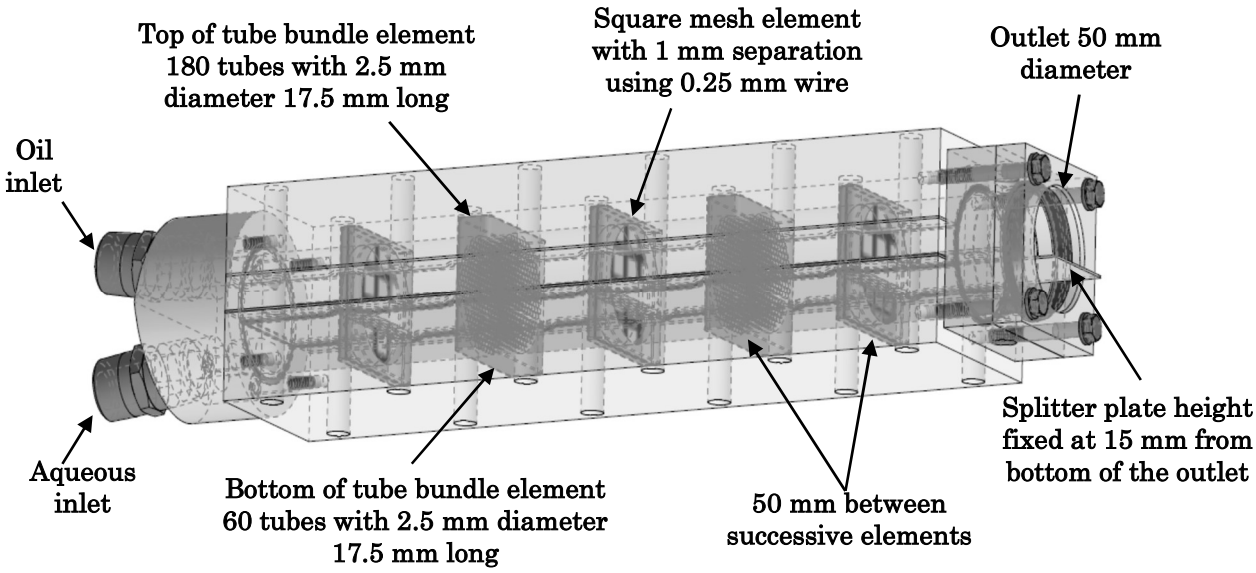


Figure 3.5 3-D model of the inlet conditioner design with independent inlets, a separation plate, mesh elements and flow straighteners.

The inlet has an internal diameter of 50 mm which is split with a phase separation plate. The phase separation plate is fixed at a height of 15 mm from the bottom of the pipe. This phase separation plate prevents the oil and aqueous phases from interacting until they leave the inlet conditioner and hence limit mixing. The fluids enter at the two fittings on the left, where the lighter oil phase enters the inlet at the top fitting above the separation plate while the heavier pink aqueous phase enters through the bottom fitting below the separation plate, see Figure 3.6.

In addition to the separation plate, the inlet conditioner has several elements, three meshes and two tube bundles (or flow straighteners) which create homogeneous turbulence and remove swirl, respectively. Each of these five elements is split into two parts, one part above the separation plate, and the other part below the separation plate. The tube bundles are drilled from a single piece of PMMA and have a total of 240 holes each with a 2.5 mm diameter and a 17.5 mm length, of which 180 holes are in the top section and the remaining 60 holes are in the bottom

section. The resulting tube bundle has a beta ratio of 0.60. The tube bundles were designed using the work of Bell and Mehta (1989) who suggested that the length of the tube bundle should be 6 – 8 times the diameter and so the tubes bundles have a length of 17.5 mm. The mesh elements use a square mesh with a separation distance of 1 mm between wires in both directions and a wire thickness of 0.25 mm and therefore, the mesh has a beta ratio of 0.64. Each of the elements is separated by 50 mm as suggested by Brown et al. (2006), who stated that the separation distance of mesh elements should be at least 20 times the length of the largest openings.

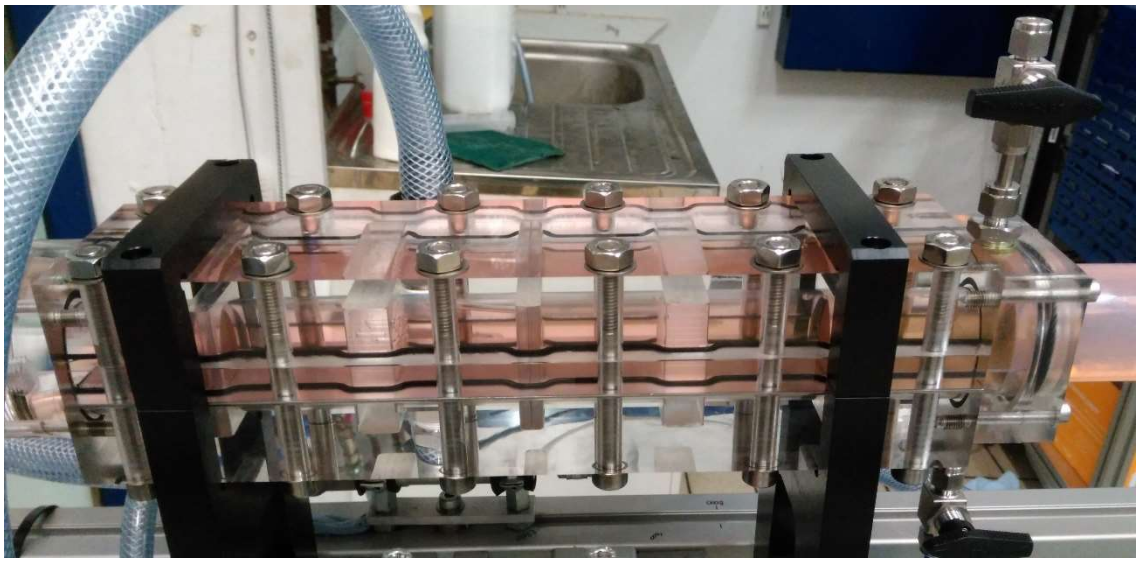


Figure 3.6 Inlet as installed and filled with experimental liquids. The bottom section contains the aqueous solution that is dyed pink with Eosin Y while the top section is filled with clear silicone oil.

3.3.4 Test section

An overview of the main test section is given in Figure 3.7. It consists of an 8 m long ETFE pipe which has a 50 mm internal diameter. The test section contains a pressure sensor, three differential pressure transmitters and the observational section enclosing the jet nozzle. The observation section is located at 6.0 m from the inlet and consists of a 2.1 m long PMMA box surrounding the ETFE pipe. The jet nozzle is located at 6.3 m from the inlet, 0.3 m inside the observation box, and is accessed from the bottom of the observation box.

The space between the observation box walls and ETFE is filled with silicone oil to minimise optical distortion. The observation section is shown in Figure 3.8(top), it

contains an air-filled ETFE pipe where optical distortions are present and this can be contrasted with Figure 3.8(bottom) where the same pipe is now filled with refractive index-matched silicone oil. To install the calibration target in the observation box, the flow development pipe section needed to be removed. The calibration target was then inserted through the opening created by the removal of the flow development section and its location was set with a positioning rod, see Figure 3.8(bottom).

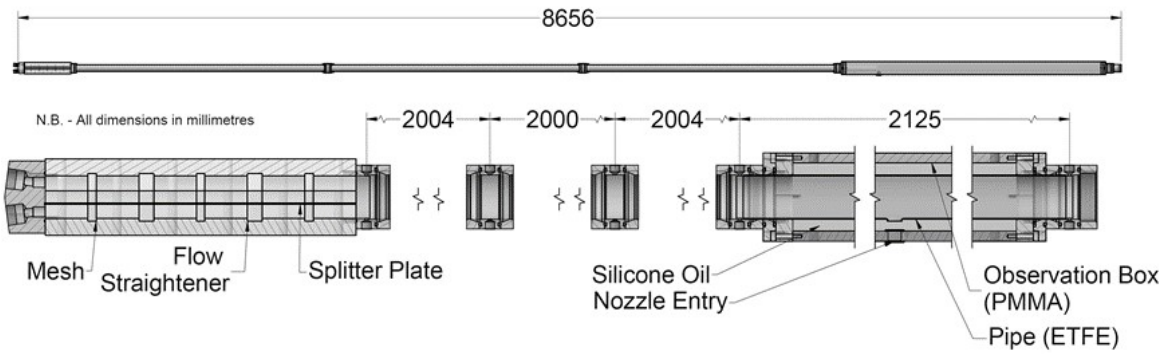


Figure 3.7 Overview diagram showing all components of the test section, including inlet conditioner, flow development section and observation box with jet entry.

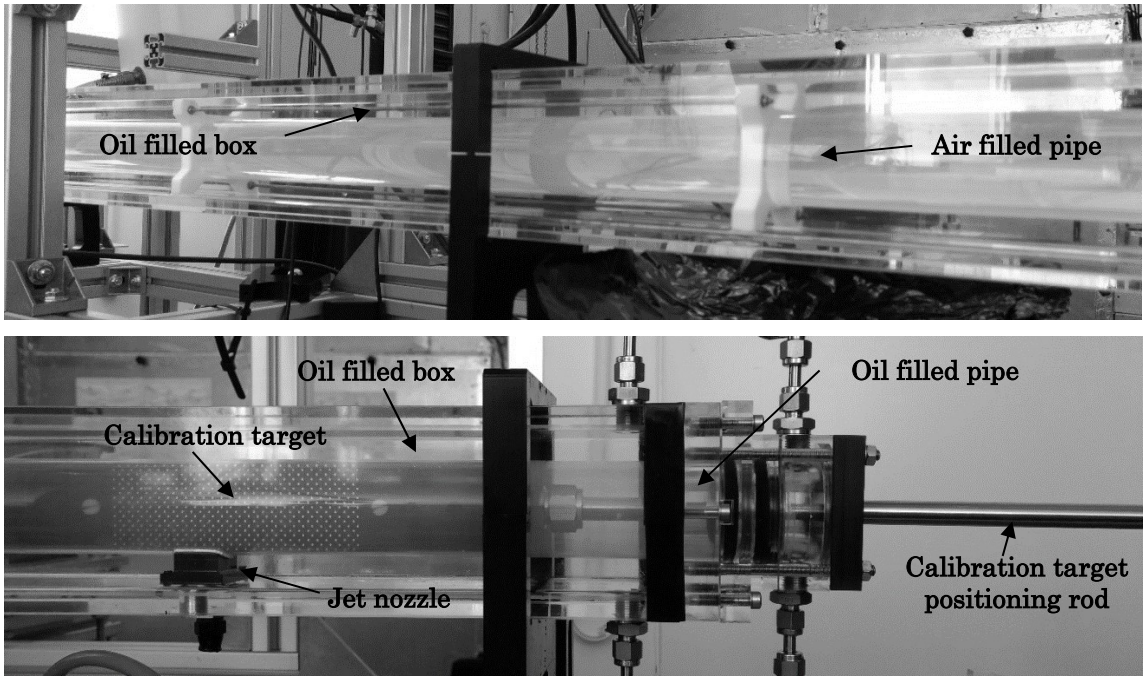


Figure 3.8 Images of the observation box. Top: Observation box empty of liquids demonstrating the usual distortion of a mismatched refractive index system. Bottom: Beginning of the observation box highlighting the nozzle entry point and the calibration graticule immersed in the index-matched silicone oil.

3.3.5 Meter calibration

Calibration of the instruments was performed before any experimental measurements were taken. Firstly, the electronics of each instrument were calibrated to set the slope and intercept of the analogue input loop and these were stored in the calibration of the LabVIEW control system. Once the analogue loops were calibrated the instruments themselves were calibrated. The differential pressure meters were calibrated using the zero-calibration method. This involves filling the experimental setup with the liquids, removing all the gas through bleeding, then zeroing the differential pressure reading once the system has fully stabilized. This was particularly important for the differential pressure transmitters used in the main test section where the pressure range was −2000 to 4000 Pa and thus sensitive to changes in height and liquid density.

The newly purchased Khrone Optimass 6000 Coriolis flowmeter came with a factory calibration certificate for its full range and was therefore used as a master meter to calibrate the turbine flow meters. Calibration was achieved by simultaneously flowing through a turbine and the Coriolis meter in series, while stepping through the turbine meter's calibration range, see the example in Figure 3.9. Once the readings were taken the turbine meter's K factor, in pulses per unit volume, could be corrected, for example, it was found that the large oil turbine needed the K factor to be decreased by 1.25%, see Figure 3.9.

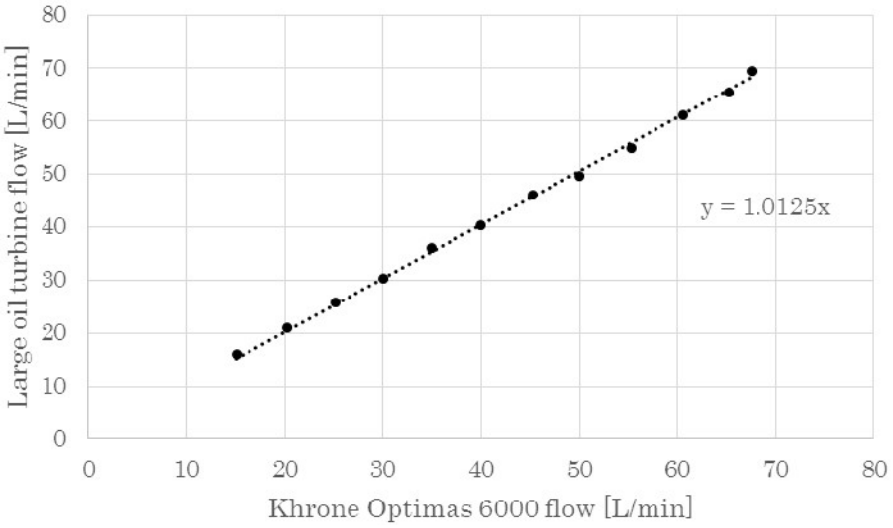


Figure 3.9 Reading of the uncalibrated large oil turbine meter versus the calibrated Khrone Optimass 6000 Coriolis meter.

3.3.6 Jet nozzles

The experimental campaign used three simplified nozzle designs where in all cases the jets originated at the edge of the pipe wall. Each of these jets has the same total exit area but vary in geometry. The first and simplest nozzle is the U-jet type, Figure 3.10(top), which has a 4 mm diameter opening and exits in a vertically upward direction. The second nozzle is the F-jet type, Figure 3.10(middle), which also has a 4 mm diameter nozzle but is directed into the oncoming pipe flow at an angle of 40° from the vertical. The third nozzle is the V-jet type, Figure 3.10(bottom), which has two 2.8 mm diameters holes which are separated by an angle of 60°, where each jet is angled at 30° from the vertical within the same pipe cross-sectional plane.

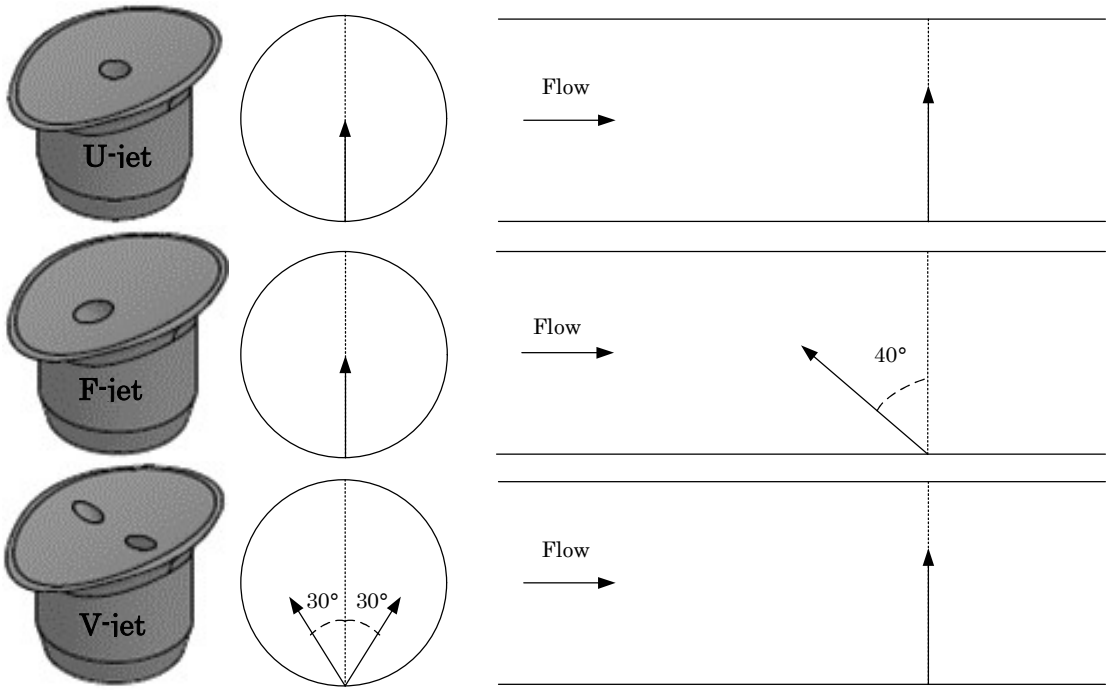


Figure 3.10 Nozzles used in the experimental campaign and the direction of the resulting jets. Top row: Vertically up U-jet. Middle row: forward-facing F-jet. Bottom row: Twin V-jet. Left column: 3-D drawing of nozzles. Middle column: the direction of the jet in the cross-section of the pipe. Right column: the direction of the jet in pipe axial direction.

3.3.7 LabVIEW control system

An extensive LabVIEW control system was designed and constructed to monitor and record the measurements from the experimental test section. In addition to providing data logging, the LabVIEW simultaneously provides control of several instruments including the control valves for the oil and aqueous phase, the jet pump speed, the ball valves controlling the jet mode and the camera trigger. Importantly, the LabVIEW control system provides synchronisation between the jet flows, camera and laser activation. This synchronisation ensures that the jet is activated through the timed switching of the two ball valves followed by the activation of the camera which in turn synchronizes the pulses of laser light from the laser with each camera frame.

The interface of the LabVIEW control system is shown in Figure 3.11. This control system provides extensive experimental runtime details including plots of flow rates, velocities, phase fractions, pressures, temperatures, densities, tank heights, pump speeds, valve positions and experimental durations. Thus allowing the instruments and behaviour of the experiment system to be monitored and adjusted in real-time. The sampling of data was performed at a rate of 500 Hz, and these measurements where then averaged every 0.1 s and subsequently recorded into a comma-separated value file for later processing.

Interfacing of LabVIEW to the instrumentation was performed in several ways. The 4 – 20 mA input and output loops, as well as the digital inputs and outputs, were interfaced using two National Instruments multifunction data acquisition cards a NI USB-6009 and a NI USB-6211. The Pico technology TC-08 thermocouple data logger, as well as the two Bronkhorst Coriolis controllers, were interfaced using manufacturer supplied LabVIEW interface libraries. While the Cameron Coriolis meter was interfaced using the Modicon Modbus RTU protocol running over a RS 485 serial port.

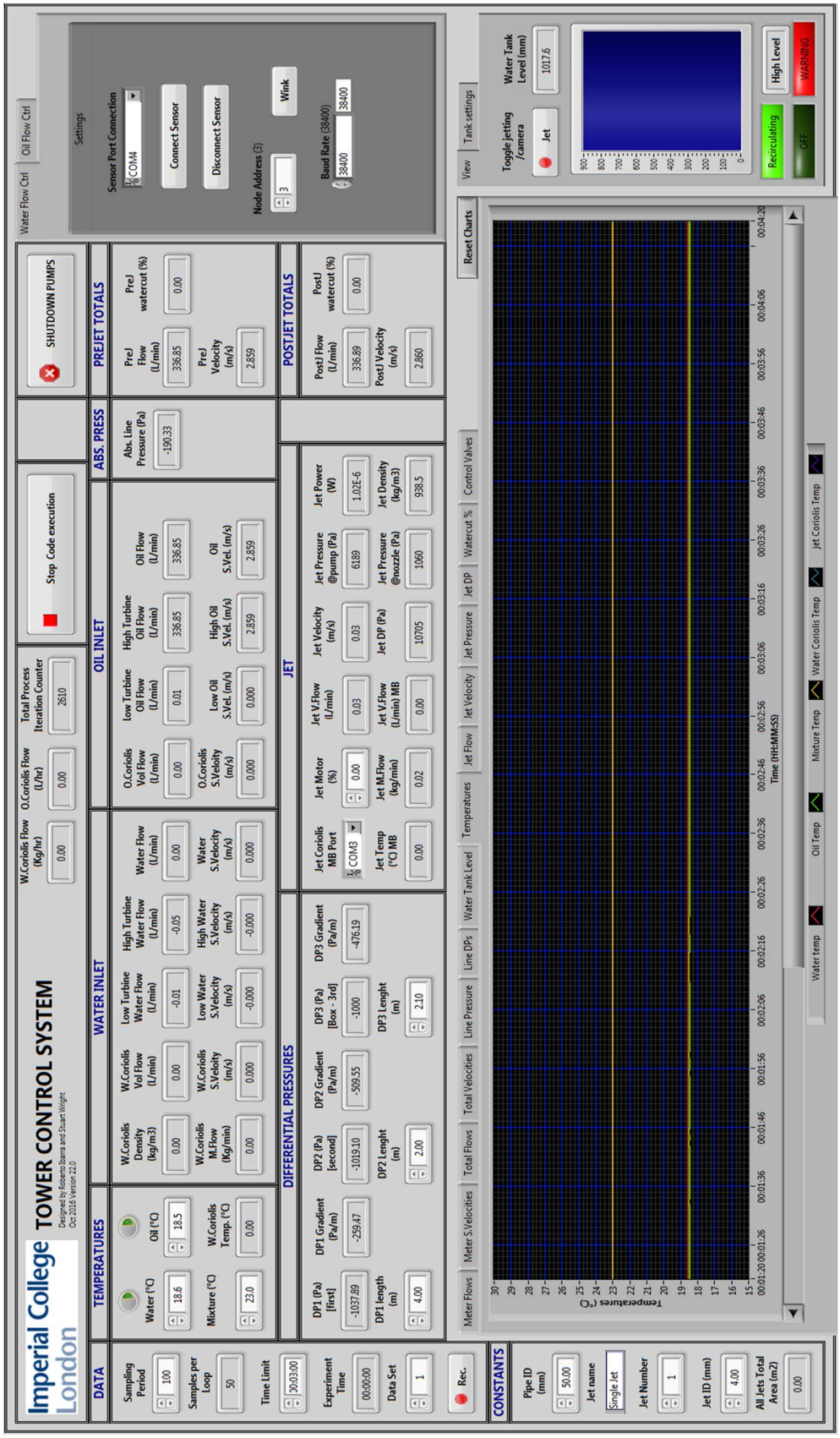


Figure 3.11 The LabVIEW interface of the control and data logging system used to make measurements during the experimental campaign.

3.4 Optical measurement techniques

The volume fractions, phase distribution, droplet sizes and velocity fields are obtained using the advanced visualisation techniques of Planar Laser-Induced Fluorescence (PLIF), Particle Image Velocimetry (PIV), and stereo particle velocimetry (stereo-PIV). PLIF uses a pulsed laser sheet to illuminate a thin sheet within the pipe that then excites a fluorescent dye which emits light that has been spectrum-shifted to a lower frequency. Importantly, the dye is only soluble in one phase, and therefore the presence of this phase can be detected through the emission of the dye, whilst the other phase(s) remain dark. Images are obtained through synchronising the camera capture rate with the laser pulsation frequency. Once the images have been captured, they are processed to obtain the *in situ* volume fractions, droplet sizes and phase distribution.

The techniques of PIV and stereo-PIV use images from the camera(s) to capture the positions of tracers (particles, droplets or bubbles) where the tracers can be assumed to be small enough that they closely follow the fluid motions without disturbing the flows. Successive images are then processed to establish the velocity fields between frames, this then allows the calculation of properties like turbulence kinetic energy and shear stresses. PIV follows a group of tracers in a small area between frames to calculate the average velocity of the tracer group and hence area. The tracer particles can be either reflective or fluorescent, although fluorescent particles are generally only suitable for small-scale systems as their cost can be prohibitive. The PIV analysis uses the results from the one camera to produce a two-dimensional array of two-component velocity meaurements in the x- and y-direction. Stereo-PIV builds upon the technique of PIV by combining the results of two (or more) cameras to produce a two-dimensional array of the three components of velocity in the x-, y- and z-directions.

Illumination is provided through a dual cavity neodymium-doped yttrium lithium fluoride (Nd:YLF) laser (Litron Lasers LDY 304). This laser produces light at a 1054 nm wavelength which is in the infrared spectrum. Internally to the laser, this infrared wavelength is converted into visible green 527 nm wavelength by passing through a frequency doubling crystal. At the 527 nm wavelength, the laser produces a maximum of 30 mJ per pulse at a frequency of 1 kHz while the maximum repetition rate is 20 kHz albeit with lower power laser pulses. After exiting the laser, the 527 nm laser light first passes through a Dantec Dynamics laser preconditioner

and focuser before passing onto the laser-guiding arm which feeds the roughly circular laser beam into a sheet-optics generator provided by Dantec Dynamics.

Sheet-optics convert the circular laser beam into a laser sheet at the measurement location. The focal point, thickness and width of the laser sheet can be configured through adjustment of the sheet generator. In the case of high contrast PLIF measurements, the sheet was set to be ≈ 1.5 mm thick to capture sharp interfaces between the phase fractions.

The 3rd velocity component was large at the top of the pipe where the high-velocity jets impacted on the wall. In this location, the flows could potentially be travelling in both direction relative to the laser plane in this 3rd velocity component. Eq. 3.13 calculates the maximum velocity for a given sheet thickness of l and a Δt between frames, where the particles start from the centre and propagate outwards. Applying the cameras' minimum Δt between image frames of 0.5 ms to Eq. 3.13, the maximum velocity that can be measured is 5 m/s if a 5 mm thick laser sheet is used. Hence the laser sheet was set to a thickness of ≈ 5 mm to ensure that sufficient volume was present to capture the large 3rd velocity components.

$$V_{z_max} = \frac{l}{2}\frac{1}{\Delta t} = \frac{0.005\ \text{m}}{2}\frac{1}{0.0005\ \text{s}} = 5\ \text{m/s} \qquad \text{Equation 3.13}$$

To maximise the field of view, the width of the laser sheet along the pipe was set to ≈ 150 mm or three pipe diameters for all experimental conditions. After exiting the laser sheet generator, the laser sheet enters through the top of the pipe in a vertical plane that passes through the centreline of the pipe and is oriented along the pipe axis. This laser sheet excites a fluorescent dye, Eosin Y, which is dissolved in the aqueous phase while simultaneously illuminating tracer particles that are suspended within both liquid phases.

Images are captured using two monochromatic Olympus iSpeed3 cameras. Each iSpeed3 camera contains a CMOS sensor with a resolution of 1280 × 1024 at frame rates of up to 2 kHz. Each of these camera pixels corresponded to a length of ≈ 80 µm in the experimental field of view of the 2-D horizontal laser plane throughout the experimental campaign. The shutters of the two cameras were synchronized together and to the laser so that a single laser pulse illuminates the same flow phenomena in the image of both cameras simultaneously.

The cameras are arranged so that the primary camera is located perpendicular to the observation box to minimise distortion, while the secondary camera was angled to make stereo measurements, see Figure 3.12. The primary camera collects the particle and PLIF information and uses a Nikon AF Micro NIKKOR 60 mm f/2.8D lens set to an f-number of 4. When higher contrast PLIF measurements are performed, a 540 nm long-pass filter (LP540) is used to increase the contrast between the phases. When performing combined PLIF and PIV or stereo-PIV measurements no filter is used on the primary camera as this would have excluded the laser light reflected by the particles.

The secondary camera is tilted from the perpendicular of the laser sheet and uses a Sigma 105 mm f/2.8 EX DG Macro lens set to an f-number of 8. This lens is then attached to a Scheimpflug mount to optimize focusing on the laser sheet on the tilted sensor. This secondary angled camera collects the particle position data so that the stereo velocity component can be extracted when making stereo-PIV measurements.

The depth of field (DOF) can be estimated using Eq. Equation 3.14, where N is the selected f-number of the lens, f, is the focal length of the lens, c, is the circle of confusion for the CCD and u, is the distance of the laser sheet to the CCD, (Allen and Triantaphillidou, 2011). The estimated depth of field for both camera and lens configurations used during the experimental campaign is presented in Table 3.1.

$$\mathrm{DOF} \approx \frac{2u^2 Nc}{f^2} \qquad \text{Equation 3.14}$$

Table 3.1 Depth of field calculations

Selected lens f-number, *N*	Lens focal length, *f*, [mm]	Circle of confusion, *c*, [mm]	CCD distance to laser sheet, *u*, [mm]	Depth of field, DOF, [mm]
4	60	0.02	380	5.4
8	105	0.02	470	6.4

The arrangement of the camera, lens and Scheimpflug for the desired two pipe diameter field of view, along with the difference in refractive indices at the surface of observation box limited the angle at which focus could be maintained on the laser sheet to a maximum of 23° to the perpendicular. Therefore to minimise the stereo-PIV uncertainty, a camera angle of 23° was used.

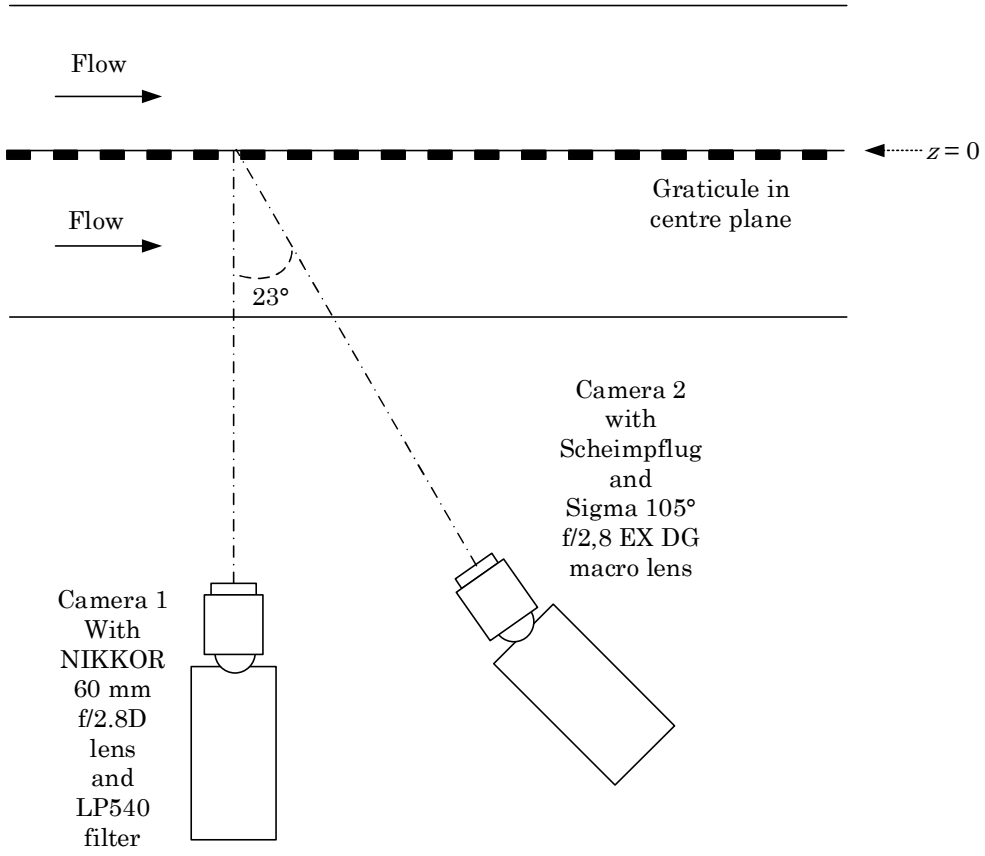


Figure 3.12 Dual camera setup used for the simultaneous PLIF, PIV and stereo-PIV during the experimental campaign.

3.5 Stereo-PIV calculations and error estimations

This section discusses the calculation of velocities in a stereo-PIV system as well as the expected errors. Figure 3.13 illustrates the possible angles for a stereo-PIV setup, where the two cameras are located on the same *y*-plane, but camera 1 and camera 2 are separated by angles of α_1 and α_2 from the perpendicular in the *x*-plane.

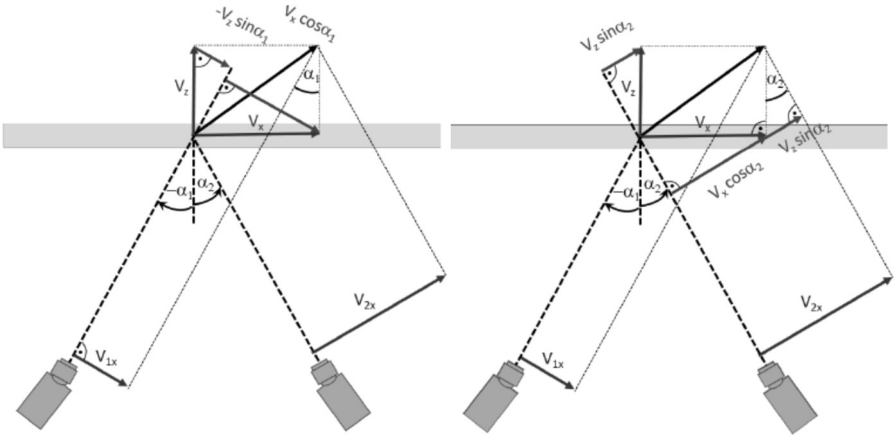


Figure 3.13 General setup for a dual camera (DaVis, 2017).

In this setup, each camera captures two velocities, where these velocities are given by Eqs. 3.15, 3.16 and 3.17 (DaVis, 2017).

$$V_{1x} = V_x \cos\alpha_1 - V_z \sin\alpha_1 \qquad \text{Equation 3.15}$$

$$V_{2x} = V_x \cos\alpha_2 + V_z \sin\alpha_2 \qquad \text{Equation 3.16}$$

$$V_{1y} = V_{2y} = V_y \qquad \text{Equation 3.17}$$

Combing these and solving will give the three velocity components in Eqs. 3.18, 3.19 and 3.20, (DaVis, 2017).

$$V_x = \frac{V_{1x}\sin\alpha_2 - V_{2x}\sin\alpha_1}{\sin(\alpha_2 - \alpha_1)} \qquad \text{Equation 3.18}$$

$$V_z = \frac{V_{1x}\cos\alpha_2 - V_{2x}\cos\alpha_1}{\sin(\alpha_2 - \alpha_1)} \qquad \text{Equation 3.19}$$

$$V_y = \frac{V_{1y} + V_{2y}}{2} \qquad \text{Equation 3.20}$$

Assuming the errors are equal in each direction for each camera, then the errors in the velocity calculations are given by Eqs. 3.21, 3.22 and 3.23 (DaVis, 2017).

$$\mathrm{rms}(V_x) = \mathrm{rms}\left(V_{1x,2x}\right)\frac{\sqrt{\sin^2\alpha_1 + \sin^2\alpha_2}}{|\sin(\alpha_2 - \alpha_1)|} \quad \text{Equation 3.21}$$

$$\mathrm{rms}(V_z) = \mathrm{rms}\left(V_{1x,2x}\right)\frac{\sqrt{\cos^2\alpha_1 + \cos^2\alpha_2}}{|\sin(\alpha_2 - \alpha_1)|} \quad \text{Equation 3.22}$$

$$\mathrm{rms}\left(V_y\right) = \frac{\mathrm{rms}\left(V_{1x,2x}\right)}{\sqrt{2}} \quad \text{Equation 3.23}$$

In the case of the experimental configuration used for the stereo-PIV jet experiments, we have $\alpha_1 = 0$ and $\alpha_2 = 23°$ and thus get the following simplified equations for velocity and error estimations:

$$V_x = V_{1x} \quad \text{Equation 3.24}$$

$$V_z = \frac{V_{1x}\cos 23° - V_{2x}}{\sin 23°} \quad \text{Equation 3.25}$$

$$V_y = \frac{V_{1y} + V_{2y}}{2} \quad \text{Equation 3.26}$$

$$\mathrm{rms}(V_x) = \mathrm{rms}\left(V_{1x,2x}\right) \quad \text{Equation 3.27}$$

$$\mathrm{rms}(V_z) = \mathrm{rms}\left(V_{1x,2x}\right)\frac{\sqrt{1 + \cos^2 23°}}{\sin 23°} \approx 3.5\ \mathrm{rms}\left(V_{1x,2x}\right) \quad \text{Equation 3.28}$$

$$\mathrm{rms}\left(V_y\right) = \frac{\mathrm{rms}\left(V_{1x,2x}\right)}{\sqrt{2}} \approx 0.7\ \mathrm{rms}\left(V_{1x,2x}\right) \quad \text{Equation 3.29}$$

These equations indicate that with the camera angles used experimentally the velocity in the *y*-component has the smallest error and this is approximately five times lower than highest error which is in the *z*-component. These equations also suggest that when the *z*-component is small compared to the *x*-component that the uncertainty in the *z*-component will be high.

3.6 Graticule calibration target

A high accuracy graticule was needed for stereo-PIV calibration in the three spatial dimensions. Given the graticule needed to be accurately located in a circular pipe a custom design was built, see Figure 3.14 and Figure 3.15. This design is similar to the commercially available 'Type 7' plate provided by LaVision but is designed to calibrate the entire field of view and to automatically centre at the pipe axis.

The graticule was machined using computer numerical control (CNC) from aluminium to create 2 mm wide ridges and 3 mm wide vertical troughs, where there is a 1 mm difference in depth between the ridges and troughs. The graticule was then anodized black to minimise laser reflection. After the black anodization, 1 mm diameter circular dots were formed through removing the thin anodized layer by milling on the CNC machine. The plate was machined to an accuracy greater than 10 µm which ensures that the graticule can be used for optical correction and spatial calibration.

The dots on the graticule are formed from two offset layers. The first layer is located on the top of the ridges while the second layer is located in the troughs, thus the two layers of dots are separated by 1 mm in the z-direction. On each layer, the centres of each dot are then spaced 5 mm apart in both the x- and y-directions to form a grid. In addition, the ridge layer of dots is offset/staggered to the trough layer by 2.5 mm in both the x- and y-directions. This arrangement of dots ensures that there are ten spatial calibration markers present in the vertical y-direction for both the ridges and troughs.

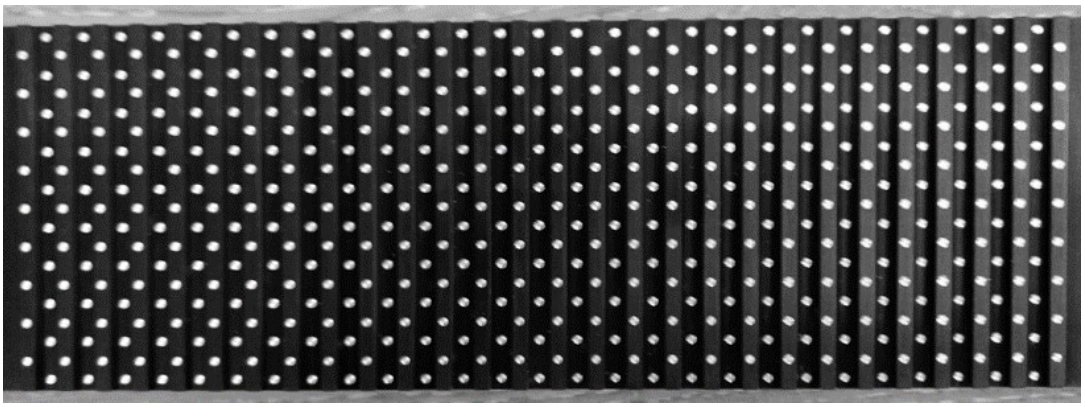


Figure 3.14 Image of three-dimensional graticule calibration target used for spatial calibration and optical correction.

The graticule was placed onto a positioning rod, sealed into the pipe, which was then filled with oil. After filling, images were taken from each camera position to allow spatial calibrations to be performed as detailed in 3.14.1. Figures 3.15 presents the graticule calibration target within the observation box when the pipe is half-filled with the refractive index-matched silicone oil. The difference between the unfilled top of the pipe and the bottom of the pipe highlights the importance of filling the pipe with a refractive index matching liquid before calibrations are performed.

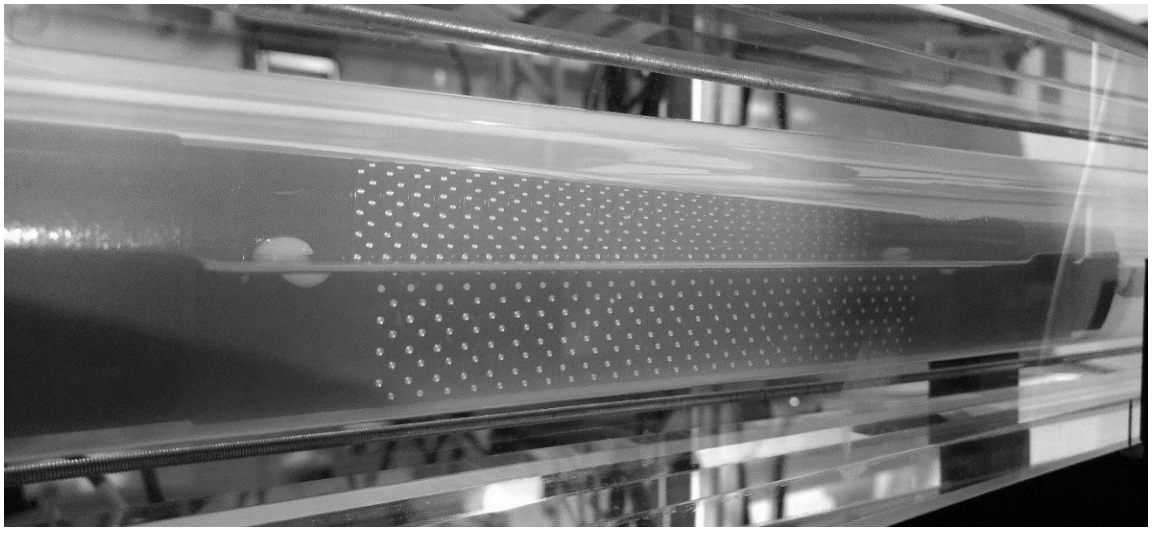


Figure 3.15 Graticule calibration target inside a part filled ETFE pipe located in the oil-filled observation box.

3.7 Fluids, dye, and test section materials

This section outlines the selection process for the two immiscible liquids, the materials used in the observation section as well as the tracer particles.

3.7.1 Liquid selections

Differences in the refractive indices of materials cause images to suffer from warping, translations, rotations and hidden volumes (Wright et al., 2017). These distortions occur when traversing material interface boundaries which are common in multiphase flows. Dispersed flows have many such interfaces which render them obscure to accurate observations, as a result, optical observations deep within jets are generally impossible. These optical effects can be limited through the matching the refractive index of the two liquids. Consequently, refractive index matching was considered a primary consideration for liquid selection for this experimental campaign.

In addition to refractive index matching, the two liquids needed to meet the requirements that they were immiscible and optically transparent as well as having low toxicity, low flammability and low corrosivity while simultaneously being stable for the duration of the experimental campaign. The design guidelines for liquid-liquid flow systems of Smedley and Coles (1990) are particularly useful here. Generalizing these guidelines, it is suggested: (i) not to use any system

components, liquids or solids, that are unstable, reactive either between themselves or with the environment (air, flow loop components, etc.); (ii) not to use liquids that either damage, absorb or dissolve any experimental solids or components of solids like plasticizers; (iii) not to use chemicals or optical components that undergo photodissociation or damage especially at wavelengths and powers used in light sources/lasers; (iv) to use safe, low-toxicity and low-flammability chemicals whenever practicably possible; (v) to use materials that are optically transparent at all experimental wavelengths; (vi) to avoid liquids with low vapour-pressures or that are hygroscopic, thus reducing refractive index changes due to evaporation or absorption; (vii) to select low-cost fluid options; (viii) to select liquids that match the refractive index of the observations solids (walls, particles); and (ix) to select solids and liquids that give any desired contact angles. In the case of liquid-liquid systems, specifically, select the components for each phase to: (i) have low interphase solubility; (ii) allow matching over the required range of viscosities and densities; (iii) allow matching over a wide range of refractive indices to extend the options for the observational solid; and (iv) provide the desired interfacial tension between the liquids.

It was also important to the project sponsors that the liquids selected were representative of industrial jet mixing conditions, where industrial crude oil densities range between of 700 kg/m^3 to 1000 kg/m^3 and viscosities 0.5 mPa/s to 100 mPa/s, while the aqueous phase commonly has densities ranging between 1000 kg/m^3 to 1200 kg/m^3 and a viscosity of around 1 mPa/s. The interfacial tension was also considered important but is rarely known during crude oil transport and indeed varies between crude oil batches. However, the interfacial tension is generally assumed to be 25 mN/m (ISO 1999).

Water is an obvious choice for one liquid, but it has a refractive index of 1.33 which is relatively low when compared to mineral oils which typically have refractive indices of 1.45 or greater. Glycerol, however, has a refractive index of ≈ 1.47 and importantly, is soluble in water while being insoluble in oils. Glycerol can, therefore, be used to raise the refractive index the aqueous phase in oil/water systems, as performed by Morgan (2012) who matched the refractive index of Exssol D80 with an 81.7 wt/wt % glycerol solution. However, the high concentration of glycerol used by Morgan resulted in the viscosity of the glycerol solution being ≈ 60 mPa·s at 25 ºC which was is much higher than that of the Exssol D80 which was 1.7 mPa·s at 25 ºC.

Given that crude oils generally have lower densities and higher viscosities than the process water, it was felt that alternative fluids needed to be selected to create more realistic experimental conditions.

In contrast to mineral oils, polydimethylsiloxane silicone oils have a refractive index of ≈ 1.40 which is lower than that of mineral oils (Wright et al., 2017). This lower refractive index means that less glycerol of ≈ 50 wt/wt% must be added to water to match the refractive index of these silicone oils.

The combination of silicone oil and a glycerol solution as the two immiscible liquids has been used in several previous experimental systems including Ninomiya and Yasuda (2006) as well as Berard et al. (2013). Given these liquids met all the requirements for this experimental campaign they were chosen for this experimental work. A polydimethylsiloxane silicone oil called BC10 supplied by Basildon chemicals was selected for the oil phase. While the aqueous phase was then tuned, by adding glycerol to water, until the aqueous phase was matched in refractive index to that of the oil.

The fluorescent dye needed for making PLIF measurements needed to be selected so that it was only soluble in one of the two phases. In addition, it was also important to take into consideration both the absorption and emission spectra of the dye. Ideally, the peak of the dye's absorption spectra should be close to that of the laser light wavelength to maximise the absorption efficiency and hence maximise the dye emission brightness to enable clear phase identification. Further, the toxicity of the dye should be considered important when significant quantities of liquid are being used and where exposure is likely. The non-toxic fluorescent dye Eosin Y, used by Morgan (2012) and Ibarra (2017), is soluble in water-glycerol solutions and has an absorption peak at 524 nm which is close to the laser emission wavelength of 527 nm, see Figure 3.16. Eosin Y dye was therefore selected for the experimental campaign and a 5 wt/wt% water solution of Eosin Y was sourced from Sigma-Aldrich.

Morgan (2012) used a concentration of 0.2 mL per litre of this Eosin Y solution but this had resulted in significant differences in brightness between the top and bottom of the aqueous phase. Following a short investigation, a concentration of 0.035 mL per litre of this Eosin Y solution was dispersed into the experimental glycerol solution. At this lower concentration, the brightness levels were found to be suitable for PLIF analysis with clear images that showed a minimal reduction in intensity from the top to the bottom of the pipe.

Additional measurements had found that at the concentration employed during the experimental campaign, the Eosin Y dye had no measurable effect on the fluid properties of density, viscosity, refractive index or interfacial tension.

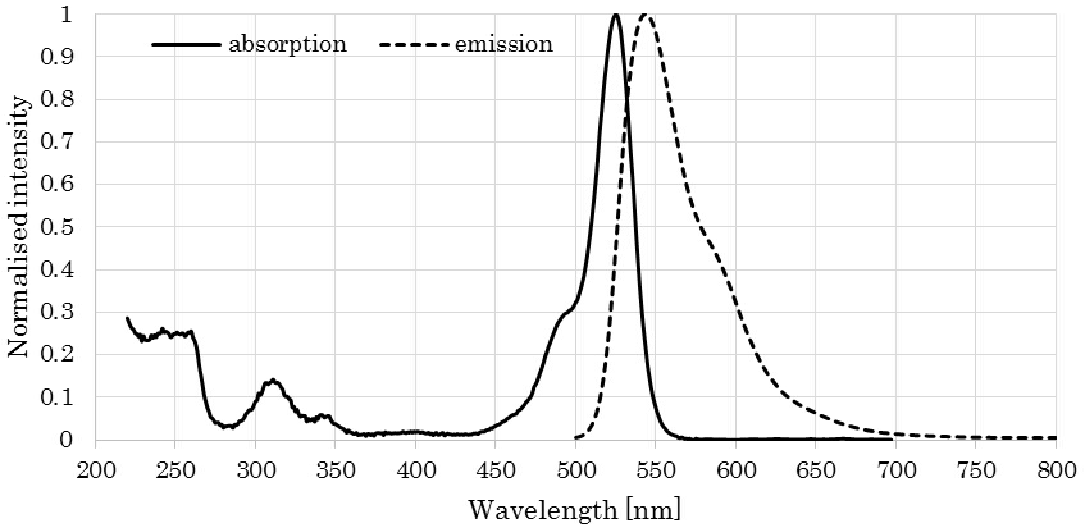


Figure 3.16 Eosin Y absorption and emission spectra in water.

3.7.2 Test section materials

In addition to selecting the liquids and dyes, the test section materials needed to be selected. In all cases, the materials of the seals and test section needed to withstand long-term exposure to the selected liquids, where silicone oil acts as a solvent to many sealants and rubbers. Both the pipe material and observation box needed to be accessible at the optical wavelengths emitted by both the laser and any fluorescent dyes. In the case of the observation box PMMA was selected as this can be easily machined, was strong and has been widely used in experimental systems, see Appendix A.1 and Wright et al. (2017).

The liquid-liquid refractive index-matched systems had a refractive index of 1.400 and so a refractive indexing matching solid was sought that would not be attacked by any of the chemical used in this experimental campaign. The review of the literature performed in Wright et al. (2017) did not find any prior matching experimental material for these liquids. However, Ethylene tetrafluoroethylene (ETFE), with an RI of 1.402 was identified as a RI matching material. Given ETFE's

similarity to the fluorinated ethylene propylene (FEP) successfully used by Zadrazil et al. (2014) among others, ETFE was selected for the pipe material.

The matching of the pipe wall's refractive index to the liquids further reduces distortions when the light passes through the inner and outer interfaces of the curved pipe walls. In principle, this allows the experimentalist to obtain data closer to the pipe wall, while reducing the corrections that need to be applied, Zadrazil et al. (2014).

ETFE, also known as Tefzel, is a soft fluoroplastic that is similar to the more familiar fluoroplastic of polytetrafluoroethylene (PTFE), also known as Teflon. Being a fluoroplastic, ETFE is relatively chemically inert and can withstand a wide range of chemicals. ETFE can be considered translucent, as can be seen in Figure 3.17, rather than clear which results in some limited diffusion of the light.

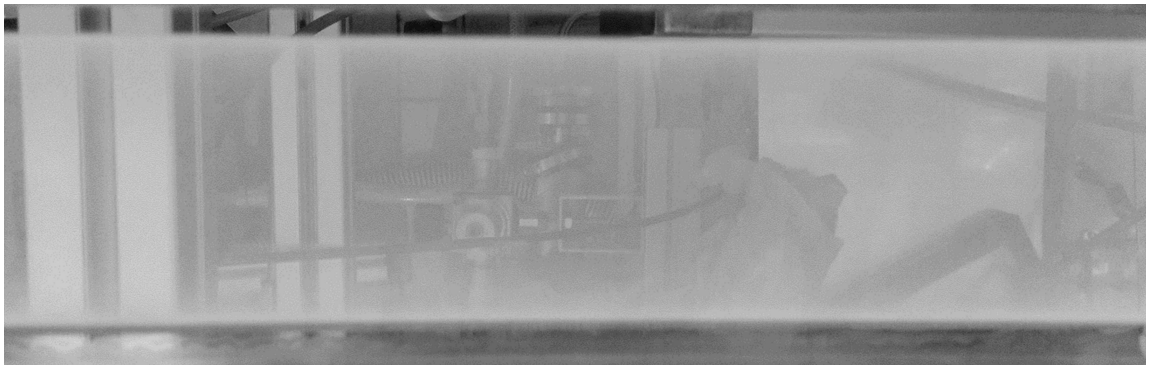


Figure 3.17 Close up of the ETFE pipe filled with silicone oil and located within the observation box also filled with silicone oil.

3.7.3 Tracer particles

The techniques of PIV and stereo-PIV require tracer particles so that their displacement can be measured and fluid velocity calculated. The selection of the tracer particles depended on the wettability in the liquid, the density relative to suspension liquid, the particles size and the apparent particle size, the Stokes number and cost. Each tracer particle should have a high enough affinity to the phase they are suspended within to remain entrained for the period of the experimental run. Similarly, the density and size of the particles should be small enough that they remain in suspension for the duration of the experiment. While the size of the particles should not be too large and concentrated to influence the results of the experiment itself.

The apparent size of a particle in an image differs from the actual size. The ideal apparent PIV tracer size in an image is two to three pixels. If a particle's apparent size is one pixel or less it can result in what known as "pixel-locking" (also known as "peak-locking") where velocities appear to be integer multiples of the pixels themselves (Overmars et al., 2010). Whereas apparent particle sizes of larger than three pixels are generally unnecessary and result in wasted image resolution or phenomenon obscurity.

A short experimental investigation of tracer particles suggested that reflective particles would need to be ≈ 100 µm in diameter to get a large enough apparent size through the ETFE pipe, whereas fluorescent particles could be much smaller. However, in the quantities needed for the TOWER facility, fluorescent particles were prohibitively expensive to purchase while there was insufficient time to design and make custom fluorescent particles during this project. Consequently, 100 µm diameter reflective particles were needed.

The oil phase was seeded with 100 µm diameter oleophilic silver-coated hollow ceramic spheres (SHCS) sourced from Hart materials (AGSL 150-16-16-TRD). These SHCS had a nominal density of 900 kg/m^3 which was similar to that of the oil's 930 kg/m^3. The aqueous phase was seeded with 100 µm diameter hydrophilic polyamide spheres sourced from LaVision. These polyamide spheres had a nominal density of 1100 kg/m^{3}which was similar to that of the aqueous phase's 1130 kg/m^3.

The Stokes number (St), given by Eq. 3.30, is used to calculate the behaviour of suspended particles in a flow. It is defined as the ratio of the characteristic time of the particle, t_0, known as 'particle relaxation time', to the characteristic time of the flow u_0/l_0. When a particles Reynolds number is less than unity, we have a Stokes flow where the particle relaxation time is given by Eq. 3.31 and is dependent on the particle density, ρ_p, the particle diameter d_p, and the liquid dynamic viscosity, μ_L. The characteristic time of the flow u_0/l_0, is taken to be the ratio of the liquid velocity u_L to that of a characteristic length L. For the purposes of PIV measurements and particle selection, the Stokes number is given by Eq. 3.32. This number should be less than 0.1 for the experimental conditions to ensure any error in the particle's tracking of the flow is less than 0.1% (Tropea et al., 2007).

$$\mathrm{St} = \frac{t_0 u_0}{l_0} \qquad \text{Equation 3.30}$$

$$t_0 = \frac{\rho_\mathrm{p} {d_\mathrm{p}}^2}{18\mu_\mathrm{L}} \qquad \text{Equation 3.31}$$

$$\mathrm{St} = \frac{\rho_\mathrm{p} {d_\mathrm{p}}^2}{18\mu_\mathrm{L}} \frac{u_\mathrm{L}}{L} < 0.1 \qquad \text{Equation 3.32}$$

$$L = \frac{\rho_\mathrm{p} {d_\mathrm{p}}^2 u_\mathrm{L}}{1.8\mu_\mathrm{L}} \qquad \text{Equation 3.33}$$

The minimum length scales that can be tracked by a particle with less than 1% error for a given velocity can be found by rearranging Eq. 3.32 into Eq. 3.33. Table 3.2 lists the length scales that can be resolved with less than 1% error for the two liquid particle combinations over a range of experimental velocities.

Table 3.2 Minimum length scales that can be tracked by particles with an error of less than 1% in both the oil and aqueous phases.

Fluids at 23°C	Density, ρ, [kg/m³]	Viscosity, μ, [mPa s]	Particle diameter [µm]	Particle density [kg/m3]	Liquid velocity [m/s]	Minimum length scale, L, [mm]
Silicone Oil	930	8.4	100	900	12	11.32
					6	5.66
					2	1.89
					0.1	0.09
Glycerol solution	1130	5.3	100	900	12	8.73
					6	4.37
					2	1.46
					0.1	0.07

Figure 3.18 presents a jet penetrating the interface with an associated length scale to the right. The highest velocities are located near to the exit of the jet and this velocity can be up to ≈ 12 m/s. At the highest velocities, the selected liquid/particle combinations are only able to track structures of the order of ≈ 10 mm and larger with less than a 1% error. However, as Figure 3.18 shows there are many fine structures much smaller than 10 mm close to the jet and so the particles are unable to track them closely. As we move away from the jet, the velocity decreases and so smaller structures can be tracked by the particles. Once the velocity has decreased to 2 m/s the particles can track structures with lengths scales of 2 mm with less than a 1% error.



Figure 3.18 An 8 m/s silicone oil jet penetrating the aqueous phase of a crossflow with a velocity of V_m = 0.4 m/s and an aqueous phase fraction of ϕ = 0.20 at 60 ms after the jet's first appearance into the flow. The flows non-dimensional numbers are Re_j = 3700, Re_{aq} = 1200, Re_o = 1900 and We_j = 7300.

3.8 Density measurements

Liquid density measurements were performed using both benchtop laboratory equipment and during the experimental campaign runs. The benchtop density measurements were made using a Stanton Redcroft / Paar DMA-46 densitometer, see Figure 3.19. The measurements were performed over a temperature range of 15 – 35 ºC.

During experimental runs, the liquid density measurements were performed using the various Coriolis meters. The density of the silicone oil was measured using the Cameron CC010 Coriolis meter; whereas the measurement of aqueous phase density was obtained using the Bronkhorst mini CORI-FLOW M15 Coriolis meter.

Initially, the density measurements of the Bronkhorst mini CORI-FLOW M15 Coriolis meter were found to be somewhat dependant on the velocity within the Coriolis meter. This dependency on velocity was compensated for through using a velocity correction factor that was applied to the results during processing.

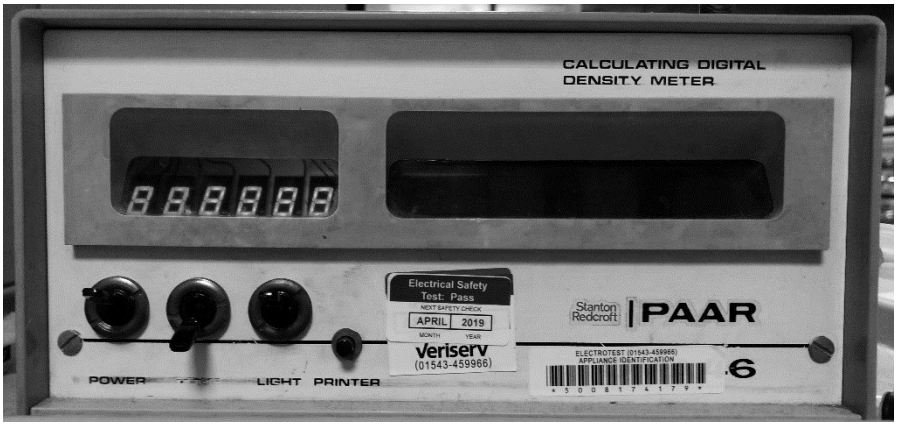


Figure 3.19 Stanton Redcroft / Paar calculating density meter (densitometer) used to measure fluid densities within the laboratory.

3.9 Viscosity measurements

Viscosity measurements were performed using a laboratory HAAKE falling ball viscometer type C, see Figure 3.20, where all measurements were performed using the boron-silica glass calibration ball 2, part number 800-0003. Measurements were performed over a temperature range of 15 – 35 °C.

This HAAKE viscometer works by measuring the time (t) which the ball falls between two lines when filled with the measurement liquid. This time is then used with the balls calibration value (K) and ball density (ρ_b) to calculate the dynamic viscosity of the liquid (μ) using Eq. 3.34, where (ρ_L) is the liquid density. This dynamic viscosity can then be converted into a kinematic viscosity using Eq. 3.35.

$$\mu = \mathrm{t} \times (\rho_\mathrm{b} - \rho_\mathrm{L}) \times K \qquad \text{Equation 3.34}$$

$$\nu = \frac{\mu}{\rho_\mathrm{L}} \qquad \text{Equation 3.35}$$



Figure 3.20 The HAAKE falling ball viscometer type C used to perform laboratory measurements of the liquid viscosity, Left: the viscometer tube encased in a water jacket used for temperature control; Right: the calibrated measurement balls, where the middle left ball (ball 2) was used.

3.10 Refractive index measurements

Refractive index measurements of the liquids were made using a CETI Prisma 8300 benchtop refractometer shown in Figure 3.21. The refractive index measurements were performed over a temperature range of 15 – 35 °C. The sample's temperature was controlled using a temperature bath while the temperature was measured using a Hanna instruments HI 935005 K-type thermocouple. Refractive index measurements were made to an accuracy of ±0.0001.

Refractive index measurements were made before the start of each experimental campaign as well as at regular intervals during the campaigns. These RI measurements were used to make adjustments to the glycerol solution's RI to compensate for the changes caused by evaporation in the open storage tanks.



Figure 3.21 CETI Prisma 8300 benchtop refractometer used to perform refractive index measurement of the liquids used experimentally during the campaign.

3.11 Contact angle measurements

The optical measurements of contact angles were performed using KRÜSS EasyDrop contact angle instrument at ambient temperatures. The EasyDrop instrument uses a black and white CCD camera manufactured by TELI with a microscope lens to obtain a close-up shadowgraph image of the resulting drop.

A purpose-built glass cuvette was used with the surface material under analysis being attached to the bottom of the cuvette. The cuvette was then filled with the silicone oil to a height that would more than cover the droplets sitting on the surface of the solid under investigation. An auto-micropipette was then used to carefully create up to ten droplets of glycerol solution each with a volume of 20 µL within the silicone oil. These droplets then settled to the material surface under investigation at the bottom of the cuvette. The droplets were then left to stabilize for three to four hours after the droplets had been deposited. The contact measurements were then performed in the cuvette using the KRÜSS EasyDrop.

The images of droplets captured by the camera are processed by the EasyDrop software (version 1.90.0.14) by fitting a sessile drop curve to the droplet's perimeter. The tangent of this curve at the contact point between the droplet and the surface is then used to calculate the contact angle for the solid-liquid-liquid interface.

The 51 wt/wt% glycerol solution used in the flow experiments was refractive index-matched to the silicone oil. However, if this concentration of glycerol solution had been used for contact angle measurements in the silicone oil then no shadows of the droplet edges would have been present. To overcome this, two concentrations of glycerol solution were used, one above (43 wt/wt% glycerol) and one below (60 wt/wt% glycerol) the concentration used in the flow experiments. In all cases, the results measured for the contact angles of these two glycerol solutions were within the tolerance of the measurement equipment. Therefore, an average of these contact angles was assumed for the glycerol solution used in the experimental campaign.

3.12 Interfacial and surface tension measurements

The surface and interfacial tension measurements were performed using the Wilhelmy plate method on an "Attention sigma 700/701 force tensiometer" at a room temperature of ≈ 23 °C. The instrument measures the force (F) on the platinum plate as it is drawn through the interface between the two fluids. The interfacial tension (σ) is then given by Eq. 3.36 where the contact angle θ is assumed to be zero since the intentionally roughened platinum plate is designed to ensure almost complete wetting of the plate's surface.

$$\sigma = \frac{F}{l \times \cos(\theta)} \qquad \text{Equation 3.36}$$

3.13 Experimental test matrix

The experimental campaign was designed to maximise the capabilities of the revised TOWER facility, which placed limits on the upper and lower flow capabilities of the system. In designing the test matrix, it was deemed desirable that the experiments should test liquid-liquid regimes which are the worst-case regimes for mixing, i.e. flows which were either stratified or stratified with an interface layer. In the 50 mm internal dimension of the test section pipe, these desired flow regimes occur when the mixture velocities are below 0.8 m/s (Trallero et al., 1997).

Table 3.3 Ranges of properties used in the experimental campaigns as well as those seen in industrial applications.

	Experimental Range	Industrial Range
Pipe velocity, V_m	0.1 – 0.8 m/s	0.1 – 5 m/s
Pipe ID	50 mm	50 – 1350 mm
Oil density	935 kg/m^3	700 – 1000 kg/m^3
Aqueous density	1128 kg/m^3	1010 – 1140 kg/m^3
Density ratio, ρ_o/ρ_{aq}	0.83	0.61 – 0.99
Oil viscosity	8.4 mPa s	0.5 – 1000 mPa s
Aqueous viscosity	5.3 mPa s	≈ 1 mPa s
Viscosity ratio, μ_o/μ_{aq}	1.6	0.5 – 1000
Jet velocity, V_j	4 – 16 m/s	10 – 30 m/s
Jet Flow, Q_j	3 – 12 L/min	100 – 7000 L/min
Jet Reynolds numbers, Re_j	1300 – 7400	50 – 650000
Jet Weber number, We_j	1300 – 28000	9000 – 1500000
Jet momentum flux ratio, q	24 – 25000	4 – 90000
Jet number	1 – 2	6 – 20
Mixture Flow rate	0 – 94 L/min	0 – 400000 L/min
Mixture Reynolds numbers, Re_m	650 – 6600	1 – 10000000
Inlet silicone oil flow, Q_o	0 – 70 L/min	
Inlet silicone oil Reynolds numbers, Re_o	200 – 3300	
Inlet aqueous phase flow, Q_{aq}	0 – 55 L/min	
Inlet aqueous phase Reynolds numbers, Re_{aq}	60 – 5100	
Inlet aqueous fraction, ϕ	0.01 – 0.50	0.005 – 0.95
Relative pipe roughness, e/D	2×10^{-5}	1×10^{-5} – 2×10^{-4}
Contact angle, θ	144°	95° – 134°

Crude oil sampling and mixing are typically concerned with flows that have low aqueous fractions of around 0.01. However, TOWER's capabilities allowed the experimental investigation to test over a wider range of aqueous fractions of up to 0.50. The experiments were conducted over a small range of jets velocities between 4 m/s and 16 m/s where the jet was silicone oil. Differing jet nozzle designs were compared by matching the flow rate and jet velocity through ensuring the total jet outlet area was the same for all the jet nozzles. The Reynolds number of the jets were only matched between the U-jet and F-jet as the V-jet had two outlets with the same total area as the single opening in the U-jet and F-jet.

The final experimental test matrix used inlet mixture velocities between 0.1 m/s and 0.8 m/s, whilst the aqueous phase fractions were set to 0.01, 0.05, 0.20 and 0.50. Table 3.3 summarizes the experimental ranges used during the campaign and compares these to the wide range in industrial installations. In comparing the dimensionless numbers of Table 3.3, the majority of the dimensionless numbers of the experimental campaign fits within a wide range of industrial applications. The exceptions are the contact angle which is higher than that generally seen in industrial applications and the jet number which is smaller in the experimental setup to facilitate clear observations.

The incoming stratified oil flows were either laminar, $Re < 2100$, or transitional $2100 < Re < 4000$, while the incoming aqueous phase and the jet flows ranged from laminar to turbulent, $Re > 4000$. The Weber number of the jets ranged from 1300 to 28000 indicating that the kinetic forces will dominate interfacial tension.

3.14 Image processing

Image processing is performed using several software tools including commercial software, open-source and custom codes developed for the project. This section describes these tools and their use.

3.14.1 Calibration and image correction

Image correction and spatial calibration are performed using LaVision DaVis 8.4 software. Images of the graticule calibration target at the intended measurement position immersed in an oil-filled pipe are obtained for each experimental camera. These images are then imported into DaVis where for stereo-PIV measurements, where there are two sets of images, one set at each camera position.

To perform the calibration, the dimensions of the graticule calibration target are set within the DaVis program. Then the user manually selects three reference calibration marks from the graticule images arranged in an L shape, where the three circular dots were selected in roughly the centre of the images. In the case of stereo-PIV systems, the selected reference calibrations marks had to be the same marks for both cameras. DaVis then uses these references marks to automatically detect all the remaining calibration marks within the images. Once the detection is completed, a 3rd

order polynomial calibration fitting is calculated for each configuration of the camera view of the graticule and hence the measurement plane.

Once created the calibration fittings are then applied to every experimental image to correct for any optical distortion, while simultaneously providing a length reference in all three dimensions. In the case of stereo-PIV measurements, a further calibration refinement can be accomplished using the DaVis software function "stereoscopic PIV Self-Calibration" which pre-processes the set of experimental images to reduce the calibration errors further. Once the images have been corrected, they can be exported for further processing in other software packages.

Measurements of the graticule images give a spatial resolution of 0.085 ±0.005 mm per pixel (mm/px) in the camera angled perpendicular to the laser sheet. While the angled camera used in the stereo-PIV measurements had a spatial resolution that ranged from 0.069 ±0.005 mm/px to 0.077 ±0.005 mm/px.

3.14.2 Extraction of the region of interest

The area within the inner pipe walls were the limits of the region of interest. Therefore, to speed up processing and reduce the storage of data it was desirable to remove the areas above and below the liquids early in processing.

The pipe walls were bright and prominent objects within the images due to the diffusion and glow of the laser light in the ETFE pipe. This allowed their position to be detected through software processing. The first step in wall detection was through time averaging all the experimental images of an experimental test run into a single image. This time-averaged image was then averaged in the horizontal/axial direction to give a single dimensional array containing image intensity with height. Figure 3.22 presents a normalized intensity plot of a dispersed crossflow with a velocity of V_m = 0.6 m/s and an aqueous phase fraction of ϕ = 0.2. The top and bottom pipe walls are highlighted along with the region of interest.

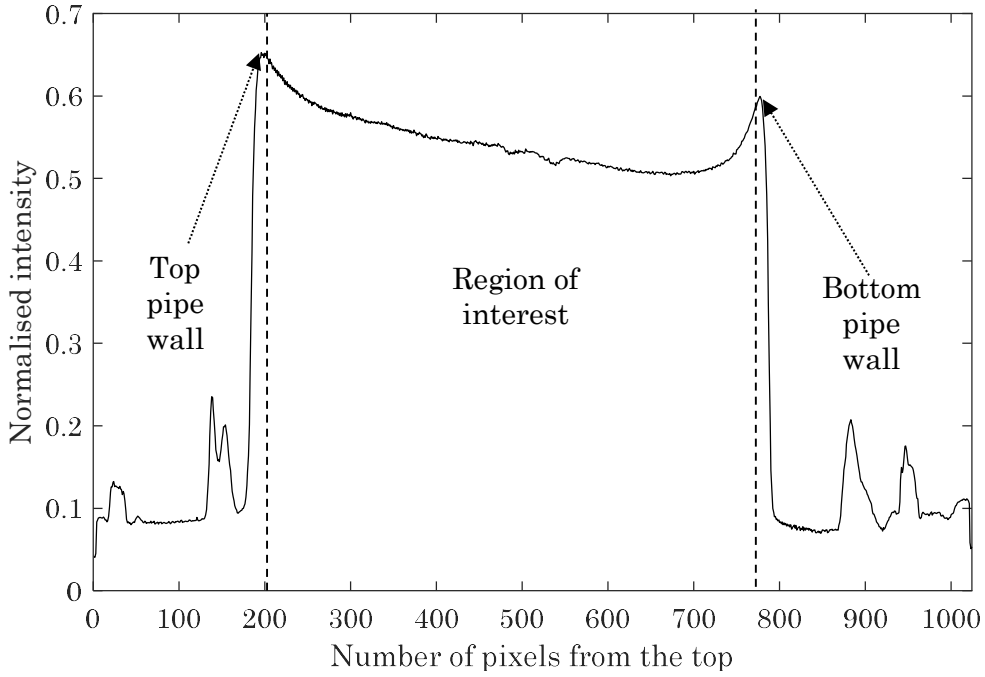


Figure 3.22 A time and spatially-averaged normalized intensity plot of a dispersed crossflow of V_m = 0.6 m/s and an aqueous phase fraction of ϕ = 0.20.

The two vertical intensity peaks correspond to the pipe walls at the top and bottom of the pipe. Combining the position of these two intensity peaks with the known thickness of the pipe wall allowed the areas above and below the region of interest to be cropped from images resulting in an image that only contained the liquid region for further processing. An example is presented in Figure 3.23, where the top figure is the original image, and the bottom figure is the extracted region of interest.

Once the region had been extracted the resulting images were 1280 pixels wide and ranged from approximately 571 to 582 pixels high. A visual inspection of the images indicates that the walls were detected to within an accuracy of ±3 pixels (±0.5%) for the top pipe wall and within ±5 pixels (±0.9%) for the bottom pipe wall making the error in height ±8 pixels (±1.4%). The height of the extracted region of interest is one pipe diameter, 1 D, which is 50 mm. Therefore, each camera pixel has an apparent height of 0.087±0.01 mm/px. When compared with measurement of spatial resolution made with the static graticule of 0.085 ±0.005 mm/px in Subsection 3.14.1, the extracted region of interest from the flow was ≈ 2% smaller than that predicted by the graticule measurements.

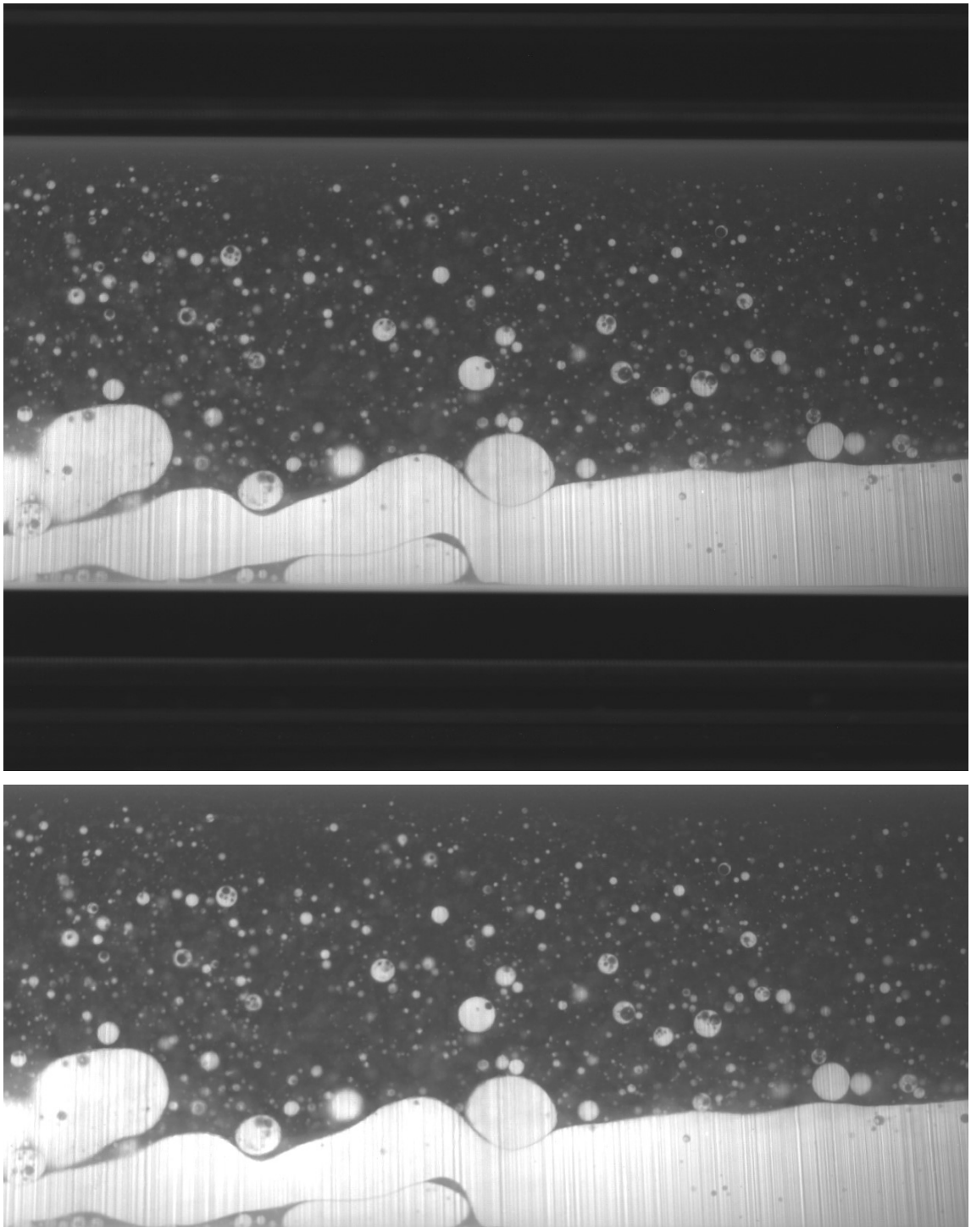


Figure 3.23 Example extraction of the region of interest from an image of crossflow of V_m = 0.4 m/s and an aqueous phase fraction of ϕ = 0.20 that was mixed by a U-Jet with a velocity of V_j = 4 m/s. Top: the original image; Bottom: the extracted region of interest.

3.14.3 Binarization for phase data

The extraction of the phase data is performed through the binarization of the images using a custom MATLAB code. The binarization process converts the pixels containing the illuminated aqueous phase into one and the darker pixels where the oil phase is present into zero.

The binarization of stratified flow is presented in Figure 3.24, along with the original camera image and the pixel intensity probability distribution of the camera image. The probability distribution shows that for this case the aqueous phase and the oil phase have a distinct illumination ranges, where the aqueous phase has an intensity of more than 150 while the oil phase has an intensity below 60. Setting the binarization threshold within the range of 60 to 150 results in binarizations that are all similar to that shown in Figure 3.24.

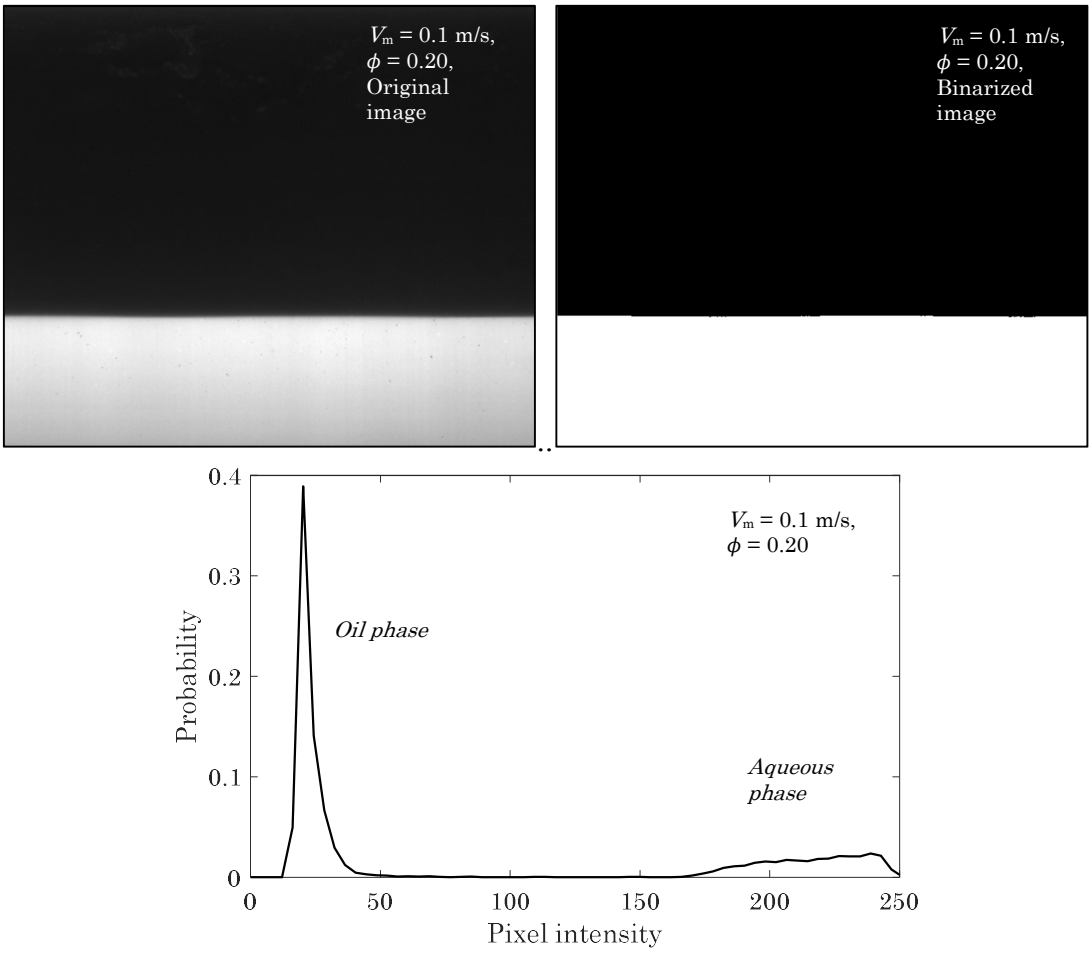


Figure 3.24 Example stratified flow image (top left) with the associated binarized image (top right) and the probability distribution of the pixel intensity.

It is worth noting that the intensity also changes from the top of the pipe to the bottom as the laser is absorbed by the Eosin-Y dye. This leads to the aqueous phase peak spreading in the probability distribution of Figure 3.24. This change in fluorescent intensity with height can also be seen in Figure 3.22 as a decreasing intensity gradient between 250 and 700 pixels from the top. This gradient is dependent on the amount of dye the laser sheet passes through and the dye is proportional to the aqueous phase and thus the gradient in intensity increases as the water fraction increases.

Whilst the experimental campaign produced stratified flows like that shown in Figure 3.24, more complex flows were also produced following the mixing of the jet. Figure 3.25(top) shows a camera image of a crossflow with a velocity of V_m = 0.6 m/s and an aqueous phase fraction of ϕ = 0.10 mixed by a 4 m/s jet. This image contains a range of object scales with varying intensities.

The brightest and largest objects are within the laser sheet while it is less clear where the fainter and smaller objects lie. Some objects will be slightly in front or behind the laser sheet, where they are illuminated by reflected or diffused laser light and thus appear fainter. While smaller droplets in the laser plane will appear fainter due to due to their smaller volume combined with the diffusion of their emitted fluorescent light through the interfaces of the emulsion. In addition, the intensity gradient from top to bottom results in droplets varying in intensity with height even within the laser plane. Given the range of object intensities, it was not possible to determine which droplets were within the laser plane.

Figure 3.25(bottom) presents the associated probability distribution for Figure 3.25(top). In contrast with Figure 3.24(bottom), the probability distribution of Figure 3.25(bottom) has a continuous intensity range between the two peaks, which is caused by the change in intensity with height, faint smaller droplets and droplets out of the plane. This continuous range in intensity of the objects is thus more challenging for the binarization process and given it was not possible to reliably determine where droplets were in respect to the laser plane, all detected droplets were included in the binarization process.

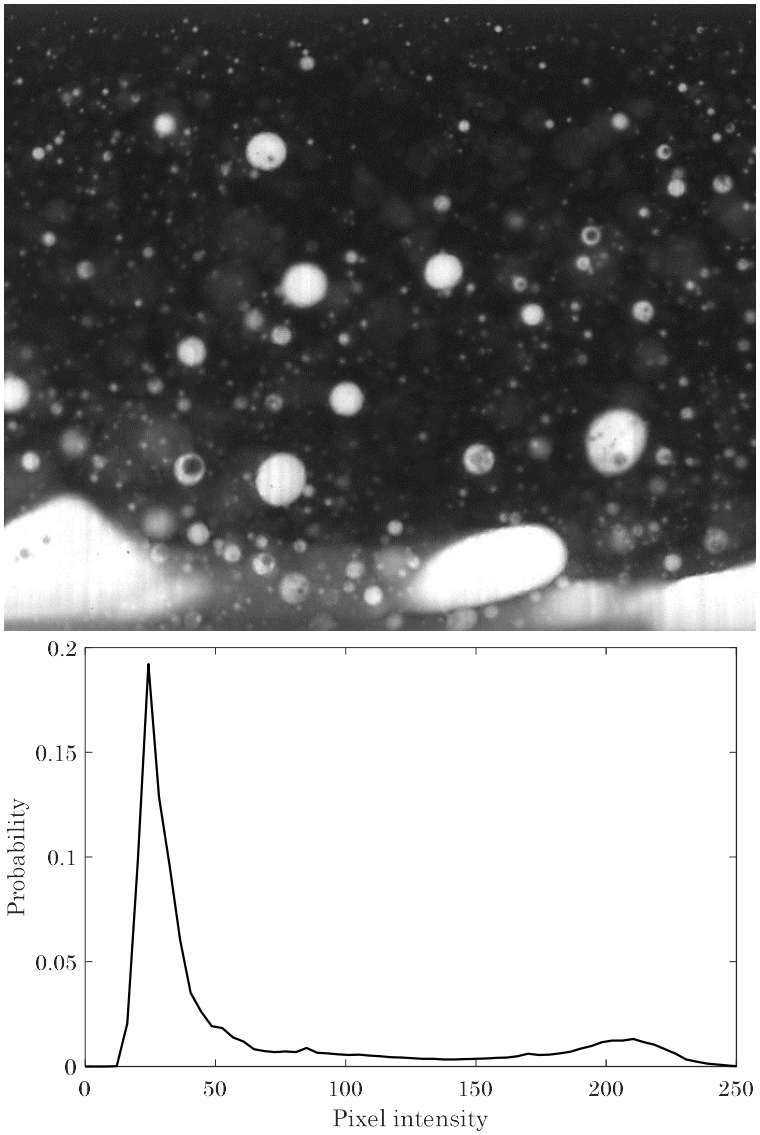


Figure 3.25 Top: An image of a crossflow with a velocity of V_m = 0.6 m/s and an aqueous phase fraction of ϕ = 0.10 mixed by a 4 m/s jet containing a range of scales with droplets visible both in and out of the plane. Bottom: Probability distribution of the pixel intensity for the same flow.

The binarization technique for phase detection has been used on numerous occasions including Morgan (2012) and Ibarra (2017) for pipeline stratified flows and Charogiannis et al. (2017) for falling films. Voulgaropoulos and Angeli (2017) however applied the technique to refractive index-matched liquid-liquid dispersed pipeline flows. Their techniques made use of an adaptive threshold to binarize their flows using MATLAB's "adaptthresh" function. Voulgaropoulos and Angeli (2017) state that the largest uncertainty in their binarization method is in the selection of the adaptive threshold sensitivity which creates uncertainty of ±20%.

The binarization technique of Voulgaropoulos and Angeli (2017) has two steps the MATLAB "adaptthresh" function is used to automatically create a threshold map from the image based on user-defined "sensitivity" parameter which can range 0 to 1. The "adaptthresh" function calculates the mean intensity range for a local neighbourhood, where the size of this neighbourhood can also be defined by the user. The sensitivity is then used to compute the threshold for this pixel, where a higher sensitivity value results in moving the pixels local threshold to lower intensities. Voulgaropoulos and Angeli (2017) do not state the size of the neighbourhood used but the default breaks the images into ≈ 64 equal size rectangles.

The binarization method used in this experimental work is based upon that of Voulgaropoulos and Angeli (2017). This experimental work has a wider range of droplet sizes than that of Voulgaropoulos and Angeli (2017) and it was found that small neighbourhood sizes were needed to detect the smallest visible droplets, but small neighbourhood sizes erased the insides of large objects. The solution to this problem was to have two sets of the neighbourhood sizes and thresholds to binarize the small and large objects and then to combine the two binarized images to capture all visible objects.

The steps used in binarization were as follows; (i) create adaptive-threshold-1 from sensitivity-1 and neighbourhood-size-1; (ii) create binary-image-1 using adaptive-threshold-1; (iii) create adaptive-threshold-2 from sensitivity-2 and neighbourhood-size-2; (iv) create binary-image-2 using adaptive-threshold-2; (v) logical OR together binary-image-1 and binary-image-2 to produce a final binary image.

The selection of the parameters was performed by comparing the original images to the binary images for several sets of results. The same thresholds and windows sizes were then used for all image binarizations. The first binarization stage "Stage-1" was designed to detect the objects with diameters over ≈ 5% of the image height. The effect of changing the parameter for Stage-1 on Figure 3.25(top) are presented in Figure 3.26 and Table 3.4. All the images in Figure 3.26 managed to capture the large objects. The change in threshold from left to right tends to increase the outline of the droplets, while a reduction in window size increases the number of smaller droplets detected. However, the use of a smaller window size below a full-frame fails to completely binarize all stratified flows and thus a full-frame window of 1260×580 was used for neighbourhood-size-1. The effect of smaller window sizes on the binarization of larger objects is apparent in Figure 3.27 where large objects are either not present or become hollowed out.

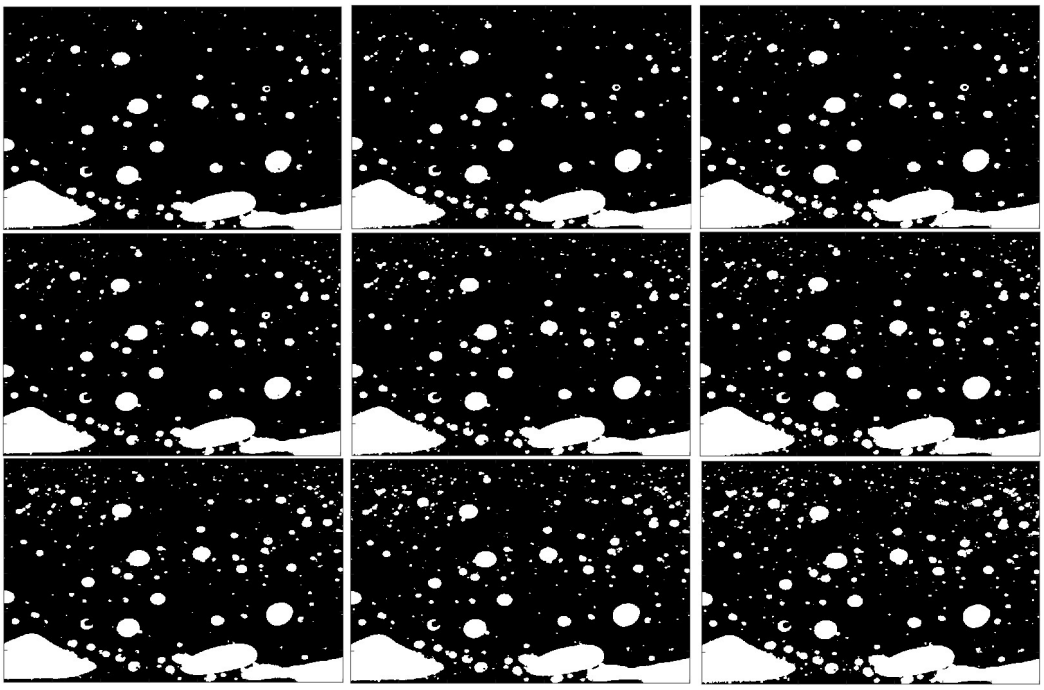


Figure 3.26 Binarization Stage-1 to capture the largest objects. Left column sensitivity 0.3; middle column: 0.4; right column: 0.5; Top row: 1260×580 window; Middle row: 630×290 window; Bottom row: 420×193 windows.

A comparison of the resulting binarized images with that of the original images resulted in the selection of 0.4 for the sensitivity in stage-1. This value was found to detect all the large objects while limiting the merging of what appeared to be unlinked objects. Table 3.4 has a mean value of 0.152 and a standard deviation of 0.0133, estimating the aqueous phase fraction is 0.152 ±0.027 (±18%) with 95% confidence. When using a 1260×580 window a change in sensitivity of ±0.1 from 0.4 results in a ±6% change in the aqueous phase fraction. The objects increase in diameter with increased sensitivity and the change in measured aqueous phase indicates that a change in sensitivity of ±0.1 corresponds to a change in object diameter of up to ≈ ±3%.

Table 3.4 Fraction of aqueous phase that is detected in the binarization Stage-1 when changing window sizes and the sensitivity

Window size stage-1	Sensitivity stage-1 0.3	Sensitivity stage-1 0.4	Sensitivity stage-1 0.5
1260×580	0.1323	0.1399	0.1485
630×290	0.1421	0.1509	0.1613
420×193	0.1507	0.1617	0.1763

The effect on the image of Figure 3.25(top) from changing the sensitivity and window size for the second binarization Stage-2, are presented in Figure 3.27. The top row of Figure 3.27 shows the binarization using a 21×19 window size. It was considered that the 21×19 window size was unable to capture the smallest objects. The two stages of binarization needed to overlap to ensure all object sizes were binarized. However, smaller window sizes like the 7×7 window shown in the bottom row of Figure 3.27, hollowed out the droplet centres of objects with a diameter of ≈ 5% of the image height. Therefore, a window size of 11×9 was selected for the second binarization stage, see the middle row of Figure 3.27.

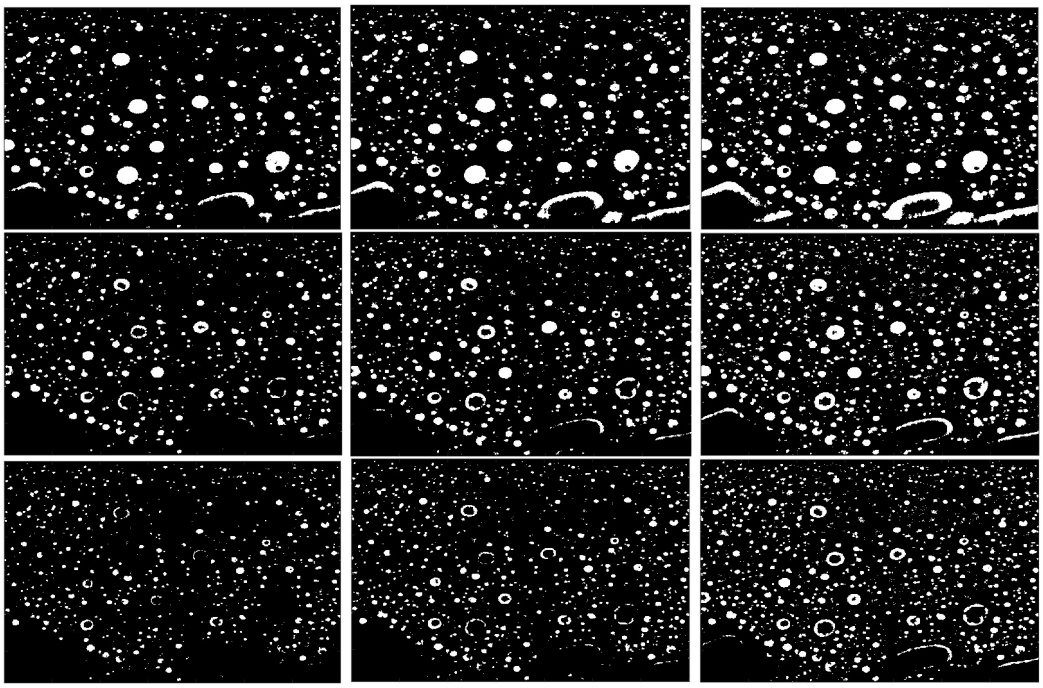


Figure 3.27 Second binarization stage to capture the smaller objects. Left column sensitivity 0.2; middle column: 0.3; right column: 0.4; Top row: 21×19 window; Middle row: 11×9 window; Bottom row: 7×7 windows.

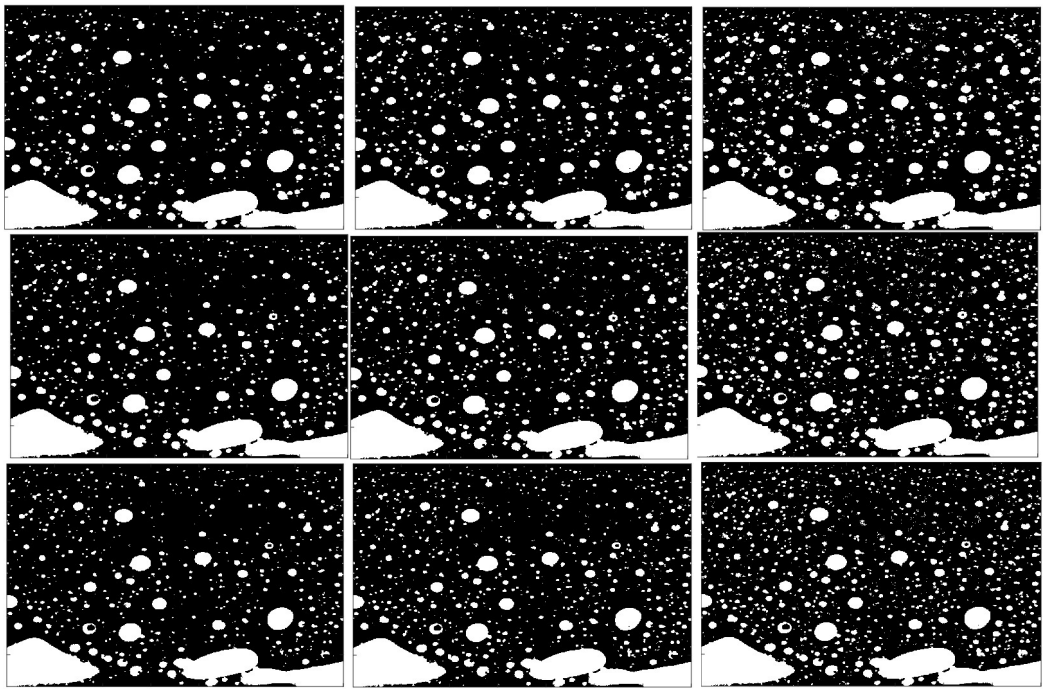


Figure 3.28 Combined binarization of the second stage with the first stage to capture all objects, with a stage-1 sensitivity of 0.2 and window size of 260×580. Left column: stage-2 sensitivity 0.2; middle column: stage-2 sensitivity 0.3; right column: stage-2 sensitivity 0.4; Top row: stage-2 window 21×19; Middle row: stage-2 window11×9; Bottom row: stage-2 windows 7×7.

Table 3.5 Fraction of aqueous phase detected in binarization Stage-2 when it is combined with a stage-1 using a sensitivity of 0.2 and window size of 260×580.

Window size stage-2	Sensitivity stage-2 0.2	Sensitivity 0.3	Sensitivity 0.4
21×19	0.1778	0.1906	0.2107
11×9	0.1734	0.1865	0.2097
7×7	0.1665	0.1691	0.1889

Table 3.6 Fraction of aqueous phase detected in the combined binarization stage when using the stage-1 window size of 1260×580 and stage-2 window size of 11×9 and varying the sensitivity of the two stages.

Sensitivity	Stage-2 0.2	Stage-2 0.3	Stage-2 0.4
Stage-1 0.3	0.1684	0.1818	0.2054
Stage-1 0.4	0.1734	0.1865	0.2097
Stage-1 0.5	0.1789	0.1917	0.2145

Figure 3.28 presents the combined binarization of the two stages where it has captured the wide range of scales present in the flows. A greater number of smaller droplets are detected as the window size is reduced and the sensitivity is increased which increases the fraction of aqueous phase detected. The combined effect of the two binarization stages is detailed in Table 3.5, where the first stage used a window size of 1260×580 and a sensitivity of 0.4. Table 3.5 had a mean value of 0.186 and a standard deviation of 0.0161, estimating the aqueous phase fraction to be 0.186 ±0.032 (±17%) with 95% confidence. The overall effect of the sensitivity of ±0.10 of Stage-2 is a change of ≈ ±10%, when the stage-2 windows size is 11×9, see Table 3.5.

Table 3.6 combines the sensitivities from the two stages and demonstrates that the greatest effect on the sensitivity is in the second stage. Table 3.6 has a mean value of 0.165 and a standard deviation of 0.0190, estimating the aqueous phase fraction to be 0.190 ±0.033 (±17%). A change in sensitivity of ±0.10 to both stages results in a change of up to ±14% of aqueous phase fraction. When combined with the changes to the window size it is estimated that there is an overall sensitivity of ±20% to the aqueous phase due to the binarization process.

In stratified flows, the interface between the phases is clear and allows the phase-detection algorithm to work well, whereas the binarization of dispersed flows is expected to see the largest errors due to (i) the inclusion of out of the laser plane droplets that cannot be separated and (ii) a greater number of emulsion interfaces blurring images. Given the velocities of the two phases are close in dispersed flows, the *in situ* phase fractions of the dispersed flows will be closer to that of the inlet phase fractions than that of more stratified flows. Therefore, the following analysis assumes that the *in situ* phase fractions are the same as the inlet phase fractions.

A comparison of the inlet phase fraction recorded by the flow meters with that of the phase fraction detected by the binarization process of dispersed flows is presented in Table 3.7. The root mean square of the relative errors in Table 3.7 is ±28%. These results indicate that the binarization process tends to overestimate the water fraction at the lower water fractions, $\phi < 0.20$, while underestimating the aqueous phase fractions at the highest aqueous phase fractions, $\phi > 0.20$.

Table 3.7 Comparison of the metered phase fraction against the phase fraction calculated from the binarized image for 100 frames of highly dispersed flows at a location of $L = 4D$ from the jet.

Oil inlet flow [L/min]	Aqueous inlet flow [L/min]	Oil jet flow [L/min]	Metered aqueous phase fraction	Binarized aqueous phase fraction	Absolute. error	Relative error
22.4	1.18	9.05	0.036	0.050	1.4%	39%
44.8	2.36	9.05	0.041	0.048	0.70%	17%
64.7	3.34	8.59	0.044	0.040	−0.40%	−9.0%
10.6	1.18	9.05	0.057	0.076	1.9%	33%
21.2	2.36	9.06	0.072	0.111	3.9%	54%
42.4	4.71	9.05	0.084	0.080	−0.40%	−4.8%
63.6	7.07	9.04	0.089	0.124	3.5%	39%
9.42	2.36	9.04	0.112	0.132	2.0%	18%
18.8	4.71	9.05	0.145	0.188	4.3%	30%
37.7	9.42	9.05	0.168	0.183	1.5%	8.9%
56.0	14.0	9.02	0.177	0.207	3.0%	17%
5.89	5.89	9.05	0.283	0.217	−6.6%	−23%
11.6	11.6	9.16	0.358	0.278	−8.0%	−22%
23.6	23.6	9.04	0.412	0.298	−11%	−28%

3.14.4 Stratified flow heights

This experimental work uses the same techniques as those used by Morgan (2012) and Ibarra (2017) to calculate the interface height of pipeline stratified flows from PLIF results. The two phases are first binarized and then the interface is then detected through finding the intensity change either from the top or bottom of the pipe.

The following steps were performed to extract the interface height: (i) the region of interest was extracted using the method outlined in the Subsection 3.14.2; (ii) the flows were binarized using the method outlined in Subsection 3.14.3; (iii) the binarized images were filtered to remove all objects smaller than 100 pixels; (iv) holes in the detected aqueous phase were filled; (v) the interface height was detected in pixels; (vi) the interface height was scaled to mm.

The first filtering step removed all objects containing fewer than 100 pixels, using MATLAB's "bwareaopen" function. This resulted in images with only the largest continuous aqueous regions. The second filtering step filled all holes within the remaining continuous aqueous regions using MATLAB's "imfill" function. This second filtering stage eliminated all oil bubbles that were entirely contained within the

aqueous phase after binarization. In combination these two filtering steps eliminated areas caused through several effects including (i) noise, (ii) dust and dirt on walls, (iv) fine aqueous droplets suspended in the oil phase, (iv) fine oil droplets suspended in the aqueous phase (v) illumination issues and (i) damaged camera pixels.

Figure 3.29 presents the binarization and filtering of four stratified flow examples where the complexity of the flows increases from top to bottom. In the top two examples, the interface is well defined and the binarization closely follows the interface, whereas in the third and fourth cases the presence of droplets results in a less defined interface. These less defined interfaces have droplets that are separated by a thin film between the two phases which cannot be reliably detected. Therefore, the presence of droplets at the interface increases the uncertainty in the interface height calculation. Importantly, the number of droplets at the interface increases with crossflow velocity and aqueous phase fraction and hence so does the uncertainty.

The interface position in pixels is then ascertained through finding the distance to the first change in intensity from top to bottom at a single vertical location of pixel column 50. The interface height is then scaled from pixels to mm, where the scale is calculated by dividing the internal height of the pipe, 50 mm, by the number of vertical pixels of the image which contains the region of interest between the walls. The process is then repeated for 150 successive frames, which were recorded at a frame rate of 50 Hz, to calculate the mean interface height over three seconds.

Pipeline stratified flows are a three-dimensional flow with a complex velocity profile that is dependent on numerous properties including the relative viscosity of the two liquids and the contact angle the two fluids make with the wall, as described in the work of Ng (2002). These complex velocity profiles typically result in the input phase fractions differing from that of the *in situ* phase fractions even in stratified laminar flows without waves. Thus, if a flow is isolated the phase fractions are that of the *in situ* phase fractions rather than that of the measured input phase fractions. Therefore, it was not possible to integrate the phase fractions of a flow with that of the input phase fractions without obtaining more data than that obtained during this or the previous experimental works.

Even still, the interface detection method employed within here and by Morgan (2012) and Ibarra (2017) is similar to that of the simpler falling film interface detection used by Charogiannis et el. (2017). Charogiannis et el. (2017) integrated PLIF film thickness measurements with PIV velocity profiles and compared these with

measured flow rates as well as DNS simulations. Charogiannis et el. (2017) concluded that the technique of using PLIF to measure interface height had an error of 2% when measuring the average film thickness of a gas free falling film.

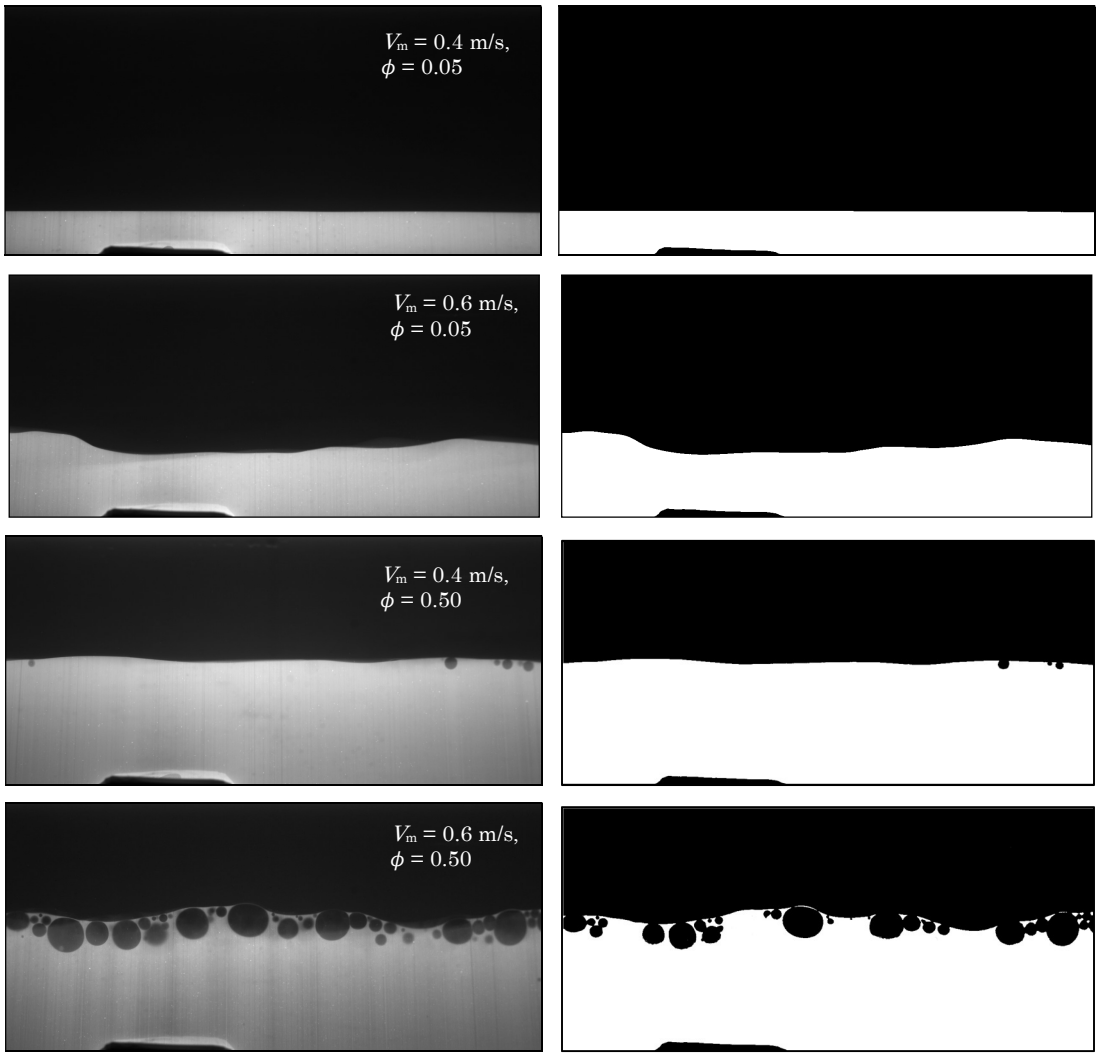


Figure 3.29 Four example cases demonstrating the binarization of stratified flows. Left column: the original image; Right column: binarized images.

Figure 3.30 shows the detected interface in green superimposed upon the image from the first row of Figure 3.29. Visual inspection of the interface indicates that the interface is within ±1 pixel for this simple flow. The image has a height of 576 pixels, and so ±1 pixel corresponds to an error of ≈ ±0.2% which is an order of magnitude smaller than the error in extracting the region of interest. Therefore, we have a height uncertainty of <2% in these simple flows principally caused through detection of the two pipe walls. Uncertainty will increase as the waviness of the flow increases due to the

three-dimensional nature of the flow however the 2% error calculated by Charogiannis et el. (2017) appears to be reasonable estimation when droplets are excluded. Droplets at the interface increase the errors still further and the scatter in interface heights at aqueous phase fractions of $\phi = 0.5$ indicate the uncertainty could be as ±7% in some high aqueous phase fraction cases, see Figure 4.9(top).

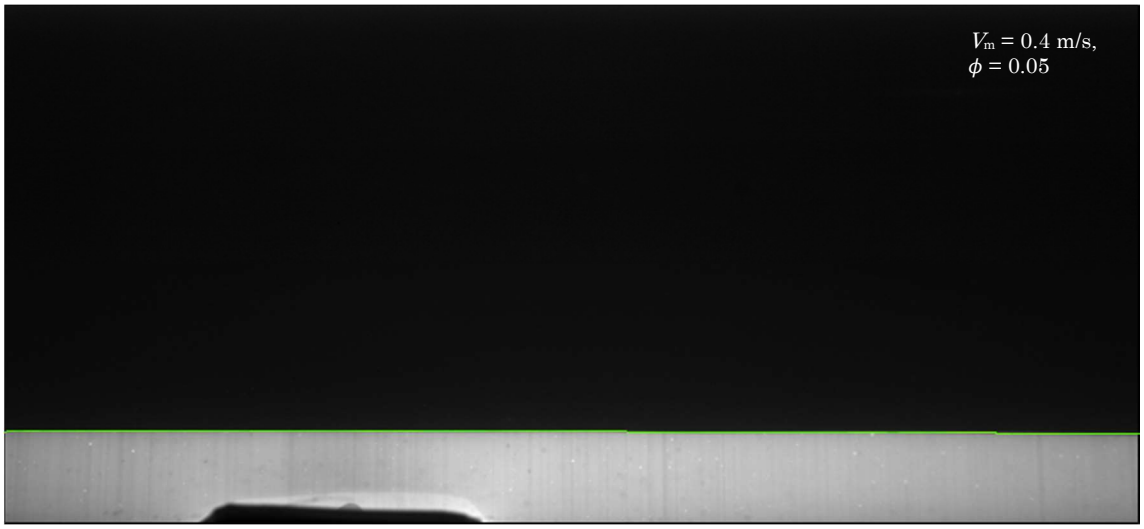


Figure 3.30 Example photo of a stratified flow showing the detected height of the interface in green at a thickness pixel.

3.14.5 Vertical phase profiles and the C_1/C_2 metric

The PLIF images were used to extract a vertical aqueous phase fraction profiles to establish the dispersion of the aqueous phase following mixing. The following steps were taken in the extraction of the vertical phase profile:

(i) The region of interest was extracted using the method outlined in Subsection 3.14.2, see Figure 3.31(top).

(ii) The images were binarized using the techniques outlined in Subsection 3.14.3, to establish the presence of either the oil or aqueous phase in each pixel of the image, see Figure 3.31(middle).

(iii) The binary representations of the images are then converted into real numbers such that the 0 for oil and the 1 for the aqueous phase become 0.0 and 1.0, respectively.

(iv) The real representations were then spatial averaged in the horizontal direction ±0.5D either side of the stated measurement position, between

the lines in Figure 3.31(middle). This created an average aqueous phase fraction between 0.0 – 1.0, see Figure 3.31(bottom left).

(v) A time- and spatially-averaged profile was then created over 1000 frames captured at 100 Hz to create the vertical phase fraction over a 10 second period, see Figure 3.31(bottom right).

Figure 3.31(bottom left) shows the profile for a single frame horizontally averaged over a window width of ±0.5D either side of the measurement point $L = 10\ D$. While the profile is visible it still has a high amount of scattering. Once the profile has been averaged over the 100 frames of the 10 second period, the profile appears smoother, see Figure 3.31(bottom right).

In addition to showing the profile, Figure 3.31(bottom right) also shows the standard deviation. Throughout much of the profile, the standard deviation is of the order 0.015. There are two peaks in the standard deviation which occur where there are large changes in aqueous phase fraction. The largest peak is near the wavy interface at $r/R \approx -0.6$ while a smaller peak occurs close to the lower pipe wall at $r/R = -1$. The mean aqueous phase fraction measured in the binarization of this image is 0.17 while the metered inlet aqueous phase fraction is 0.10, this can, in part be explained due to the stratification of the aqueous phase.

The PLIF images capture the aqueous phase fraction in the plane of the laser sheet and, therefore, we calculate a C_1/C_2 metric through taking a ratio of the concentrations in the top half of the laser plane to that in the bottom half of the laser plane. The C_1/C_2 metric in the plane of the laser sheet is calculated through time and spatially averaging the vertical phase profile calculated earlier. The following steps are used: (i) the mean concentration in the top of the pipe, C_1, is calculated through spatial averaging the vertical phase profile from the pipe centre, $r/R = 0$, to the pipe top, $r/R = 1$, above the dotted line in Figure 3.31(bottom left); (ii) the mean concentration in the bottom of the pipe, C_2, is calculated through averaging the vertical phase profile from the pipe centre, $r/R = 0$, to the pipe bottom, $r/R = -1$, below the dotted line in Figure 3.31(bottom left); (iii) the C_1/C_2 metric is then calculated from the ratio of these two concentrations.

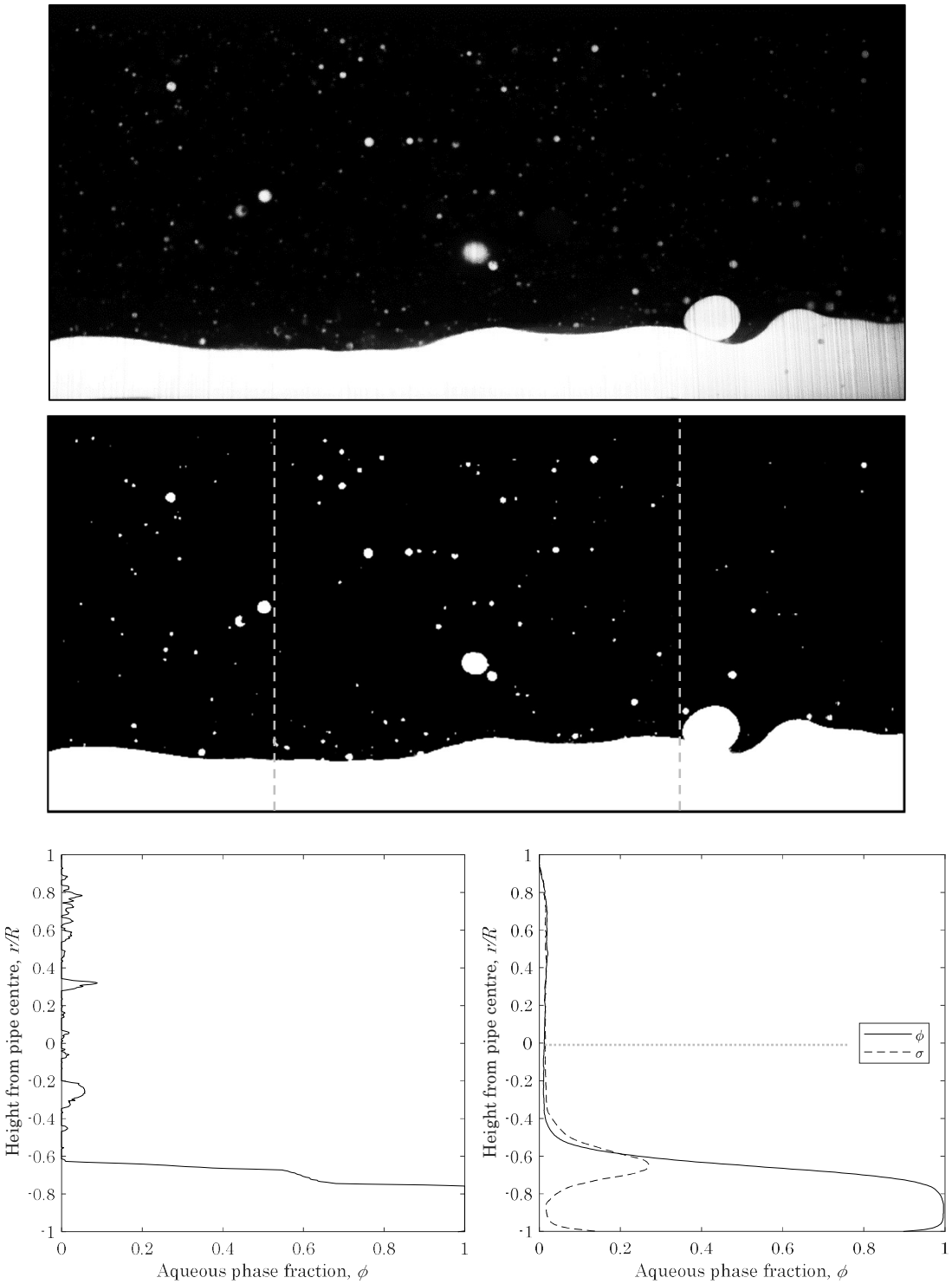


Figure 3.31 Outline of the steps used to compute the vertical phase profile from the images of a crossflow of $V_m = 0.4$ m/s and an aqueous phase fraction of $\phi = 0.10$ at a distance of $L = 4\ D$ with a U-Jet with a velocity of $V_j = 4$ m/s. Top: Image following extraction; Middle: Binarized image; Bottom left: Spatially averaged aqueous phase profile for a single frame; Bottom right: Aqueous phase profile averaged over 1000 frames.

The uncertainty in the C_1/C_2 metric can be large when the aqueous phase fraction is low $\phi \leq 0.05$ as large errors in the denominator lead to large errors in ratios. However, as stated in Subsection 3.14.3 the binarization process tends to overestimate the aqueous fraction for $\phi < 0.20$ and underestimate the aqueous fraction for $\phi > 0.20$, which given the higher aqueous phase fraction is expected to be in the bottom half of the pipe, causes the C_1/C_2 ratio to tend to one. Through using the binarization results presented in Table 3.7, several example C_1/C_2 have been calculated and compared with the metered values in Table 3.8. Taking the root mean square of the results in Table 3.8 the error in C_1/C_2 is estimated to be ±0.12.

Table 3.8 Comparison of the metered phase fraction against the phase fraction calculated from the binarized image for 100 frames of highly dispersed flows at a location of $L = 4D$ from the jet.

Metered values			Binarized values			Error
Aqueous phase fraction, C_1	Aqueous phase fraction, C_2	C_1/C_2	Aqueous phase fraction, C_1	Aqueous phase fraction, C_2	C_1/C_2	
0.036	0.412	0.09	0.05	0.298	0.17	0.08
0.041	0.358	0.11	0.048	0.278	0.17	0.06
0.044	0.283	0.16	0.04	0.217	0.18	0.03
0.057	0.177	0.32	0.076	0.207	0.37	0.05
0.072	0.168	0.43	0.111	0.183	0.61	0.18
0.084	0.145	0.58	0.08	0.188	0.43	−0.15
0.089	0.112	0.79	0.124	0.132	0.94	0.14

3.14.6 Aqueous droplet detection

The majority of the droplets were automatically detected using a custom-designed MATLAB code, which is based upon the techniques used in Voulgaropoulos (2017) to detect liquid-liquid droplets in a similar multiphase flow. The implementation within this work uses two independent methods to detect candidate droplets.

The first method detects circular droplets using the MATLAB "imfindcircles" function where a Hough transform is used to find the curvature of the circular droplets based upon pixel intensity gradients (Atherton and Kerbyson, 1999). The parametric equations are given by:

$$x = c_x + \frac{d_p}{2}\sin(\theta) \qquad \text{Equation 3.37}$$

$$y = c_y + \frac{d_p}{2}\sin(\theta) \qquad \text{Equation 3.38}$$

where c_x and c_y are the locations of the centre of a circle with a diameter of d_p and θ is the angle around the circle. The "imfindcircles" function locates the pixels of droplets it detects that lie on a circle with the parameters c_x, c_y and d_p, where c_x c_y correspond to the centre of the droplet with a chord length of d_p.

The second method uses the MATLAB "bwconncomp" and "regionprops" functions to provide statistics on the binary image, where the droplet detection algorithm uses three of the statistics provided by "regionprops". The first statistic gives the centroid or centre of mass of each discontinuous aqueous phase region, where the centroid is the centre of a candidate droplet. The second statistic is the length of the major and minor axis of an ellipse fitted to each discontinuous aqueous phase region. The third statistic of "regionprops" provides the extent in pixels of the candidate droplet in the images *x* and *y* directions. This second droplet detection method was able to detect smaller droplets than that found in "imfindcircles".

The droplet detection method used the following steps to extract the droplet chord lengths:

(i) The region of interest was extracted using the method outlined in Subsection 3.14.2, see Figure 3.32(a).

(ii) The images were binarized using the techniques outlined in Subsection 3.14.3, to establish the presence of either the oil or aqueous phase in each pixel of the image, see Figure 3.32(b).

(iii) Candidate droplets were detected using the "imfindcircles" function using four overlapping radius ranges measured in pixels, see Figure 3.32(c-f).

(iv) Further candidate droplets were detected using the MATLAB "bwconncomp" and "regionprops" functions. Objects smaller than two pixels in either axis were discarded as too small. Objects with a semimajor axis greater than three times than the semiminor axis was considered too asymmetrical and discarded. These candidates are shown in Figure 3.32(g).

(v) The five sets of candidate droplets were then combined into a single list of centres and radii, see Figure 3.32(h).

(vi) Irregular objects were then removed. The area occupied by each candidate droplet was checked if it contained ≥0.80 aqueous phase fraction. If it contained less than 0.80 the radius was shrunk by 5% and retested. This step was repeated twice and if the candidate droplet still contained less than 0.80 the droplet was removed, see Figure 3.32(i).

(vii) Curved objects like wave crests were removed next. The aqueous phase fraction was calculated for a perimeter two pixels outside the radius of the droplet. If this perimeter contained more than 0.50 aqueous phase fraction the candidate was not considered to be a separate droplet and removed, see Figure 3.32(j).

(viii) When a large droplet overlapped more than 30% the radius of a smaller droplet, the smaller droplet was removed, see Figure 3.32(k-l).

(ix) Once automatic detection was completed, a few large droplets with large asymmetries were measured manually and added to the total.

In addition to the binary image two parameters were provided to the "imfindcircles" function, the range of radii over which circles were detected and the "sensitivity factor" in finding circles. MATLAB recommends that the "imfindcircles" function's search range is less than three times the minimum. To accommodate this requirement "imfindcircles" method was repeated over four overlapping ranges which were 3 to 8 pixels, 8 to 23 pixels, 23 to 60 pixels and 60 to 150 pixels. Where these 4 ranges were selected to cover the sizes of all the spherical droplet diameters within the images. Figure 3.32(c-f) shows the droplets detected in each of these ranges. However, the size of these ranges has a negligible effect on the measurement, for instance, the use of a single range of 3 to150 in the example shown in Figure 3.32 changes the D_{10} and D_{32} measurements by −3% and +0.3%, respectively.

The "imfindcircles" function sensitivity factor is the sensitivity used by the circular Hough transform accumulator array. Increasing this value increases the number of circles detected through the detection of increasingly weak or partially obscured circles. In this work, a sensitivity factor of 0.95 was used. If the sensitivity factor is reduced to the default value of 0.85 then the D_{10} and D_{32} measurements in the example are changed by −5% and+7%, respectively.

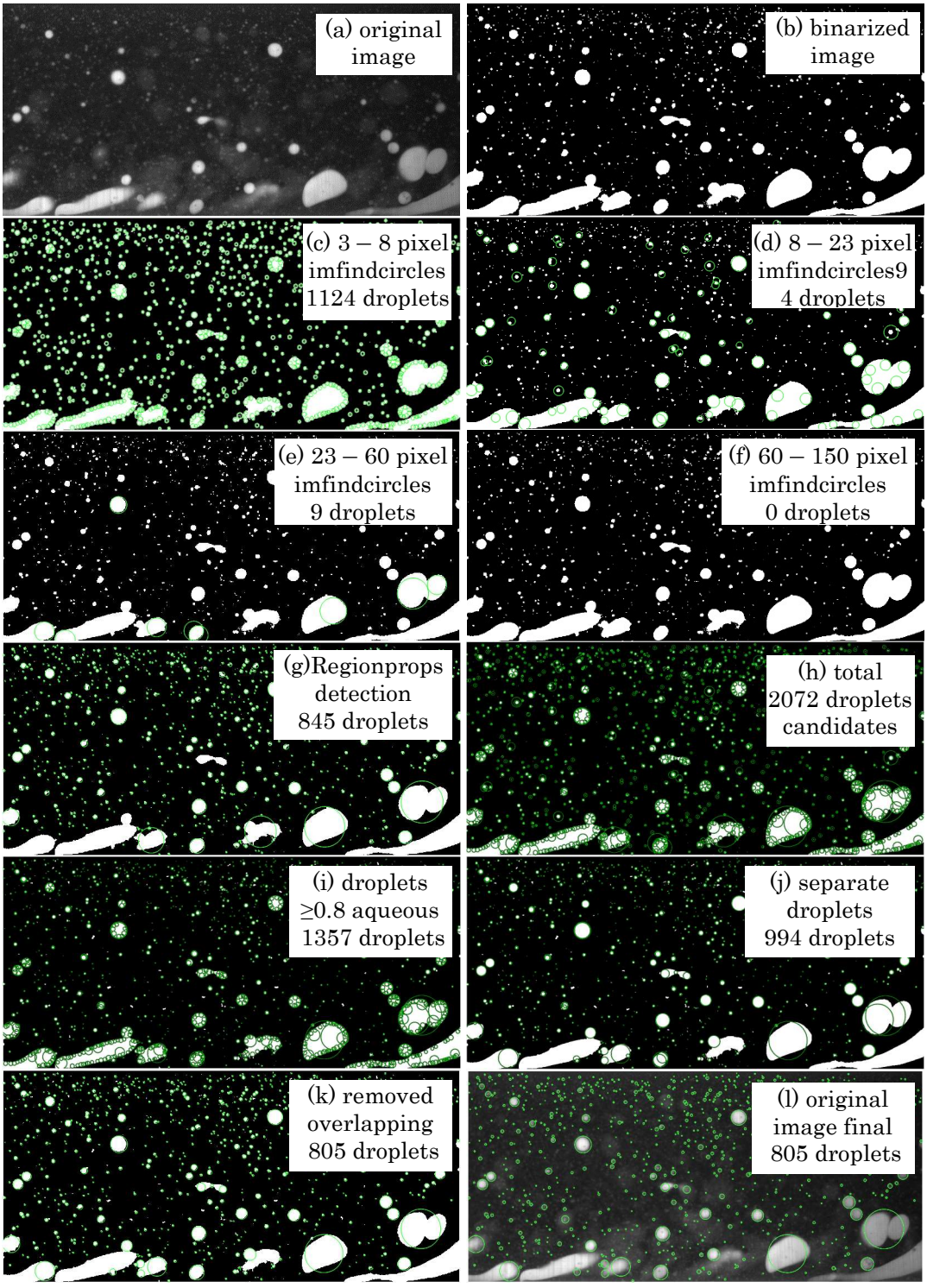


Figure 3.32 Example showing the stages of droplet detection for a crossflow of V_m = 0.6 m/s and an aqueous phase fraction of ϕ = 0.10 at a distance of L = 10 D with a U-Jet with a velocity of V_j = 8 m/s. (a) original image; (b) binarized image; (c) droplets detected by imfindimage range 3 to 8 pixels ; (d) droplets detected by imfindimage range 8 to 23 pixels; (e) droplets detected by imfindimage range 23 to 60 pixels; (f) droplets detected by imfindimage range 60 to 150 pixels; (g) droplets detected by regionprops; (h) all detected candidate droplets; (i) after first filter; (j) after second filter; (k) after third filter; (l) after the third filter on the original image.

The second droplet detection method makes use of MATLAB's "bwconncomp" and "regionprops" functions. The "bwconncomp" function finds all the binary objects in the image that are connected within the 4-connected neighbourhood of each pixel i.e. connected at the surface of each pixel. Once these objects are identified by "bwconncomp", the "regionprops" function is used to calculate the candidate droplet centroid, radii, semimajor and semiminor axis, and the length in the x- and y-directions. If an object is smaller than two pixels in either direction, they are discarded as too small for detection. Increasing this limit to 3 pixels in either direction in the example causes a +18% and +1% changes to D_{10} and D_{32}, respectively. Objects with a semimajor axis that is more than three times greater than the semiminor axis are considered too asymmetrical and discarded. Discarding objects with a semimajor axis that is greater than four times the semiminor axis does not affect the final D_{10} and D_{32} measurements in the example. The minimum of two pixels in both directions sets the lower limit of droplet size detection to be ≈ 0.17 mm.

The two droplet detection methods produced a large list of candidate droplets some of which were detected multiple times. Some of the candidate droplets were misdetections, while others had high levels of overlap making their size difficult to determine. Therefore, the candidate droplets were filtered to minimise these problems. Table 3.9 presents the change in candidate droplet numbers and the associated effect on the D_{10} and D_{32} measurements after applying each filtering stage to the example shown in Figure 3.32.

Table 3.9 Change in measurement during the various stages of the droplet detection method for a crossflow of V_m = 0.6 m/s and an aqueous phase fraction of ϕ = 0.10 at a distance of L = 10 D with a U-Jet with a velocity of V_j = 8 m/s.

Droplet filtering stage	Droplet candidates	Droplet size, D_{10}, [mm]	Droplet size, D_{32}, [mm]
Initial droplet candidates	2072	0.673	2.94
Removal of droplets <0.80 aqueous phase fraction	1372	0.643	3.03
Removal of attached curved surfaces that are not droplets	994	0.550	3.66
Removal of overlapping droplets	805	0.478	4.36

In the first filter, the droplets were tested based on their aqueous phase fraction. This involved calculating the aqueous phase fraction within the area of the

droplet where the assumption was made that all droplets were circular. If the aqueous phase fraction was greater than 0.80 the droplet was kept, while if the calculated aqueous fraction was less than 0.80 the diameter of the droplet was reduced by 5% and the aqueous phase fraction test was repeated. The process was repeated a further two times, and then if the droplet was still found to contain less than 0.80 phase fraction it was discarded as misdetection. To maximise the effectiveness of the filter the phase fraction limit needed to be as high as possible without removing too many large asymmetrical droplets that needing to be manually added later. The upper limit of 0.80 was found by comparing the detection rate of several test cases. The effect of this first filter can be seen in the difference between the first and second row of Table 3.9 and Figure 3.32(h) and Figure 3.32(i). The number of droplets is reduced by 33% and the D_{10} and D_{32} measurements change by −10% and +3%, respectively. Reducing the droplets phase fraction limit from 0.8 to 0.7 results in the final D_{10} and D_{32} measurements changing by 0.1% and 8%, respectively.

The second filter removed misdetections on curved objects like wave crests and large droplets. These misdetections can be seen around the perimeter of the large droplets in Figure 3.32(i) and the effectiveness of the filter in removing them can be seen in Figure 3.32(j). To remove these misdetections, the aqueous phase fraction was calculated on a circular annulus one pixel thick centred on the droplet but two pixels outside the radius of the droplet. If this perimeter contained an aqueous phase fraction more than 0.60 the candidate was considered part of a larger object and discarded. The effect of this second filter can be seen in the difference between the second and third row of Table 3.9. The number of droplets is reduced by 28% and the measurements of D_{10} and D_{32} change by −15% and +21%, respectively. Visual inspection of several test cases showed that increasing the limit of the perimeter aqueous phase fraction to 0.7 results in an increasing number of misdetections while reducing the value below 0.5 removes overlapping droplets. Decreasing the phase fraction limit from 0.6 to 0.5 results in the final D_{10} and D_{32} measurements changing by −0.1% and −1%, respectively. Increasing this to 0.7 results in the final D_{10} and D_{32} measurements changing by +5% and +5%, respectively.

The third filter removed any droplets with a high degree of overlap. The droplets were assumed to be circular and the distance between the centres of every pair of droplets was calculated. Then the radius of the larger droplet was subtracted and if the remaining distance was less than the 70% of the radius of the smaller droplet

then the smaller droplet was removed. Changing the allowed overlap of the smaller droplets from 70% by ±10% had <0.1% effect on the final measurements of D_{10} and D_{32}.

While most droplets especially smaller spherical ones were detected automatically by the MATLAB procedure described above, up to ≈ 10, irregular or clustered droplets like those to the bottom left of Figure 3.32 needed to be added manually for each frame as it was found these contained a significant fraction of the aqueous phase. The manual addition was performed using a software package called ImageJ (version 1.52a) where a corrected greyscale image was manually opened that highlighted the automatically detected droplets, as in Figure 3.32. The ImageJ ellipse selection tool was then used to manually place the best-fit ellipse around each of the large droplets that had not been automatically detected. Once all the manually fitted droplets for the image under analysis were selected, the centres, areas, perimeters and the major and minor axis of each ellipse were recorded. Finally, these manually detected droplets were then added to the automatically detected droplets to produce the overall droplet detection for a single image.

Table 3.10 Comparison of automatic droplet detections versus hand droplet detections from sample images.

Automatic droplets			Manual droplets			Abs. Error	Rel. Error	Abs. Error	Rel. Error
N	D_{10}, [mm]	D_{32}, [mm]	N	D_{10}, [mm]	D_{10}, %	D_{10}, [mm]	D_{10}, %	D_{32}, [mm]	D_{32}, %
36	0.484	1.086	35	0.499	0.996	−0.015	−3%	0.090	9%
38	0.423	0.652	33	0.432	0.589	−0.009	−2%	0.063	11%
117	0.280	0.442	89	0.336	0.399	−0.056	−17%	0.043	11%
89	0.467	0.800	112	0.562	0.767	−0.095	−17%	0.033	4%

A study was performed to compare the automatic detection of droplets with that of manual detection. This involved analysing small windows of experimental camera images by hand by using ImageJ to manually select the droplets from the images as outlined above followed by the calculation of D_{10} and D_{32}. Then the automatic droplet size detection method outlined above was applied to the same small camera window and D_{10} and D_{32} were again calculated. The image windows covered the entire pipe height (≈ 580 px) and were 31 px wide. The window size provided a droplet count ranging from 32 to 117. Several images and flow conditions were compared and the

results of this study are presented in Table 3.10. The root mean square of the absolute errors in D_{10} and D_{32} are both ≈ 0.06 mm which is less than one pixel. The root mean square of the relative errors is 12% and 9% for D_{10} and D_{32}, respectively.

During the development of the image processing techniques, an analysis was performed on the averaging effects on the statistics of the droplet chord lengths. Figure 3.33 shows the effects on averaging a crossflow with a velocity of V_m = 0.4 m/s and an aqueous phase fraction of ϕ = 0.05 interacting with a jet of V_j = 12 m/s at a downstream position of L = 10 D. The measurements were averaged over an area of 2500 mm^2 i.e. 1 D vertically and horizontally. Figure 3.33(top) shows the effect of spatial averaging on the results where the D_{32} varies from 2.9 mm to 3.5 mm over the 1 D due to droplet coalescence where the mean value is 3.2 mm and the standard deviation is 0.18 mm. The mean droplet diameter, D_{10}, varies from 0.43 mm to 0.45 mm with a mean of 0.44 mm and a standard deviation of 0.008 mm.

Figure 3.33(bottom) shows the effect of the frame count ranging from one to ten frames. Comparing the values at four frames and ten frames there is a difference of 0.5% and 10% for D_{10} and D_{32}, respectively. Therefore, four frames were considered a reliable estimation of the experimental value and the measurements presented in Chapter 6 were time-averaged from four frames collected over nine seconds.

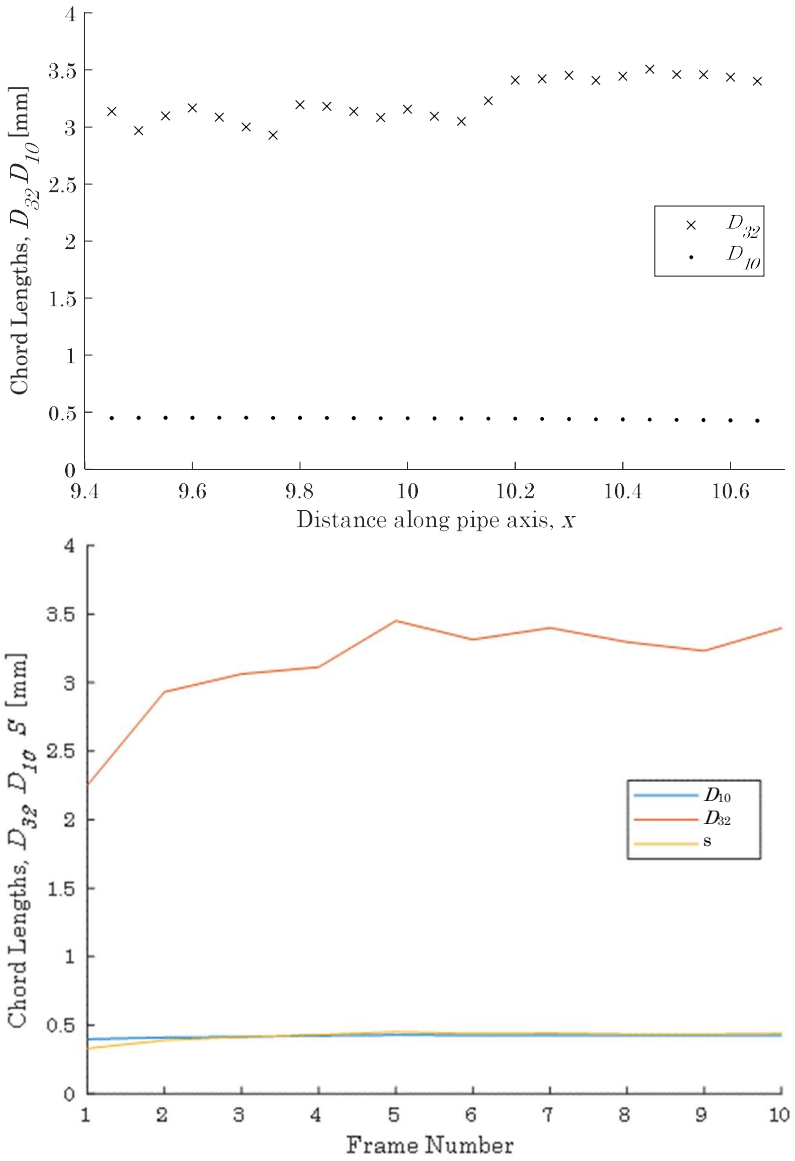


Figure 3.33 The effect on droplet chord length statistics for a crossflow with a velocity of V_m = 0.4 m/s and an aqueous phase fraction of ϕ = 0.05 interacting with a jet of V_j = 12 m/s at a downstream position of L = 10 D. Top: the effect of axial distance on D_{10} and D_{32}. Bottom: effect of the frames count on the mean (D_{10}), Sauter Mean Diameter (D_{32}) and standard deviation (S).

3.14.7 Droplet size calculations

The radii extracted in Subsection 3.14.6 are half the droplet chord lengths. While various correction can be applied to the chord length to estimate the actual droplet diameters from the chord length, this work does not apply these corrections and uses these chord lengths directly to calculate the droplet diameters.

Several droplet diameters measurement can be calculated from the droplet chord lengths including the arithmetic mean or D_{10}, the Sauter Mean Diameter, D_{32}, as well as Dv_{10}, Dv_{50} and Dv_{90}, which corresponds to the droplet chord lengths for 10%, 50% and 90% of the cumulative droplet mass, respectively, while D_{min} and D_{max} are the minimum and maximum sizes of the detected droplets, respectively.

The mean, D_{10}, is calculated in Eq. 3.39, by taking the arithmetic mean of the droplet chord lengths, d_i, and the total number of droplets N, while the Sauter Mean Diameter is calculated from the droplet chord lengths using Eq. 3.40.

$$D_{10} = \frac{\sum_{i=0}^{N} d_i}{N} \qquad \text{Equation 3.39}$$

$$D_{32} = \frac{\sum_{i=1}^{N} d_i^3}{\sum_{i=1}^{N} d_i^2} \qquad \text{Equation 3.40}$$

The steps used to calculate of Dv_{10}, Dv_{50} and Dv_{90} are all similar. The droplets are ordered by the size of chord length from smallest to largest. The total volume occupied by the droplets V_{100} is then calculated using Eq. 3.41 where $i = 1$ is the smallest droplet and $i = N$ is the largest droplet. In the case of Dv_{10}, the volumes of the ordered droplet are summed using Eq. 3.42 until the V_x exceeds 10% of V_{100}, at droplet number n. Dv_{10} is then estimated from the two closest droplet chord lengths at droplet numbers n and $n-1$ and volumes at $V_{x,i=n}$ and $V_{x,i=n-1}$ using Eq. 3.44, where the weighting between the chord lengths, W, is given by Eq. 3.43. Dv_{50} and Dv_{90} can be calculated in the same way except using Eq. 3.42 until the V_x exceeds 50% and 90%, respectively. These calculations make the assumption that the density of the droplets are all the same.

$$V_{100} = \sum_{i=1}^{N} d_i^3 \qquad \text{Equation 3.41}$$

$$V_x = \sum_{i=1} d_i^3 \qquad \text{Equation 3.42}$$

$$W = \frac{V_{x,i=n-1} - V_{100}}{V_{x,i=n} - V_{100}} \qquad \text{Equation 3.43}$$

$$Dv_x = W d_n + (1 - W) d_{n-1} \qquad \text{Equation 3.44}$$

3.14.8 Droplet probability distributions

The bin number and size used in the creation of droplet chord length probability distribution were selected following an analysis of the test cases used in this manuscript. Table 3.11 presents three calculations commonly used to estimate the number of bins needed for a histogram (Sturges, 1926; Dogăn and Dogăn, 2010). It was felt that Sturge's formula produced too few bins to see the level of detail desired while the Square root choice created excess bins for the data. To keep all the probability distribution alike, all histograms presented in this manuscript use 50 equally-spaced bins with a width of 0.05 mm over a 2.5 mm range.

Table 3.11 Calculation of the number of histogram bins for the experimental test cases used in Chapter 6.

N	Sturge's formula $1 + \log_2 N$	Rice rule $2\sqrt[3]{N}$	Square root choice $\sqrt{N}$
2917	12.5	28.6	54.0
3385	12.7	30.0	58.2
3545	12.8	30.5	59.5
3695	12.9	30.9	60.8
3732	12.9	31.0	61.1
3790	12.9	31.2	61.6
4418	13.1	32.8	66.5
4742	13.2	33.6	68.9
4843	13.2	33.8	69.6
5097	13.3	34.4	71.4
5749	13.5	35.8	75.8
6025	13.6	36.4	77.6
6283	13.6	36.9	79.3
6573	13.7	37.5	81.1
6815	13.7	37.9	82.6
6918	13.8	38.1	83.2
7067	13.8	38.4	84.1
7335	13.8	38.9	85.6
7357	13.8	38.9	85.8
7384	13.9	38.9	85.9
10597	14.4	43.9	102.9

3.14.9 Velocity field analysis

Velocity field analysis is performed using PIVLab toolbox version 2.20 developed by Thielicke and Stamhuis (2014), LaVision's DaVis 8.4 software package, along with custom MATLAB codes for both pre- and post-processing. The PIV processing for 2-component velocity vectors was predominantly implemented using PIVLab version 2.20, while the stereoscopic-PIV for 3-component velocity vectors was completed using LaVision's DaVis 8.4 software package.

In the case of 2-component PIV processing, the upper and lower pipe walls were then detected, and the region of interest was extracted from the images as detailed in Subsection 3.14.2. The pre-processed images were then imported into PIVLab, where the time step, δt, between successive frames was set, where the minimum δt was 0.5 ms due to the camera having a maximum frame rate of 2 kHz.

The spatial calibration in PIVLab was performed through importing images of the graticule calibration target located in the oil-filled pipe at the location of the laser sheet, see Section 3.6. Once imported, two points with a known separation distance were selected on the image and their separation distance entered into PIVLab. The spatial length was then calculated and stored for use in all further length calculations.

Next, several pre-processing options were selected within PIVLab, included Wiener2 denoising with a pixel size of three, a high pass filter with a pixel size of 15. The contrast was stretched and enhanced using contrast-limited adaptive histogram (CLAHE) with a pixel size of 20.

The PIV processing was then configured in PIVLab where multi-pass processing was selected. The first pass typically used an interrogation window of 70×70 pixels, while the final pass used a windows 32×32 pixels and had a particle density of ≈ 7. In all cases a 50% overlap was used between interrogation windows, resulting in a typical velocity vector array of ≈ 35 high by ≈ 70 wide. Given the spatial resolution of the camera was measured to be 0.085 mm/px (see Subsection 3.14.1), the spatial width of each 32-pixel wide window was 2.7 mm and the area covered by 1024 pixels was 7.4 mm^2. However, the thickness of the laser sheet was ≈ 5 mm which reduces the spatial resolution to ≈ 5 mm.

The FFT window deformation PIV algorithm was selected and Gauss 2 × 3 sub-pixel estimator was used, while the correlation quality was set to extreme. PIV processing then proceeded.

Post-processing in PIVLab is used to filter erroneous velocity vectors through limiting the allowable ranges and a local median filter is applied with a threshold of three and epsilon 0.1. In the case of instantaneous measurements, the missing vectors can then be interpolated to complete the vector fields.

In the case of stereo-PIV measurements, the uncorrected images were imported into DaVis and the calibration was applied. However, in contrast to the standard PIV processing, image correction and de-warping are an integral part of the stereoscopic PIV algorithm and are thus not performed during pre-processing stages.

Pre-processing involves the subtraction of a minimum filter which uses the minimum pixel intensity of the five frames around the current one. This minimum filter removes most of the image background from the image leaving the bright moving objects like the particles, droplets as well as some noise.

PIV processing within DaVis proceeds to make use of DaVis' adaptive multi-pass algorithm to refine the velocity field. The algorithm started with a window size of 96 × 96 and ended with 32 × 32 while using a 50% overlap and a particle velocity vector array of ≈ 35 high by ≈ 70 wide. The window sizes were selected to extract as much data as possible given the particle density of ≈ 7. The camera with the lowest spatial resolution was the camera parallel to the laser sheet, which was measured to be 0.085 mm/px (see Subsection 3.14.1). Each window was 32 pixels wide, had a spatial width of 2.7 mm and the area covered by the 2304 pixels was 7.4 mm^2. However, the thickness of the laser sheet was ≈ 5 mm reducing the spatial resolution to ≈ 5 mm. The overall spatial volume covered by each stereoscopic window was ≈ 37 mm^3.

In the case of stereo-PIV measurements, the "stereoscopic PIV Self-Calibration" is run through the images refining the calibration for the test point. Then the minimum time filter is subtracted to remove the image background. This is followed by the DaVis stereo-PIV velocity field processing which incorporates dewarping and spatial calibration as an integral part of the velocity field algorithm. Then in all cases, DaVis' adaptive multi-pass stereoscopic algorithm is used to refine the velocity field starting with a window sizes of 96 × 96 and ending with windows sizes of 48 × 48 using a 50% overlap. Post-processing is then used to filter erroneous velocity vectors through limiting allowable ranges, using a cross-correlation peak intensity filter and removing groups with less than five vectors.

Post-processing then filtered out erroneous velocity vectors through, discarding results with large stereoscopic uncertainty, limiting the allowable velocity ranges, using a cross-correlation peak intensity filter and removing groups with less than five vectors.

In the high-velocity region at the exit from the jet, a mask needed to be applied in both PIVLab and DaVis. This mask obscures the area that produces erroneous results with the PIV algorithms employed by PIV and stereo-PIV. To create the mask the images were initially processed and regions with excessive velocity were identified. These regions were then masked and the process was repeated until the mask was found to cover only the regions where the velocity was too high for PIV processing to be successfully applied.

Chapter 4

Integral measurements

This chapter provides traditional measurements and observations of the liquids and flows in the experimental campaigns of this thesis. Section 4.1 provides details on the fundamental measurements of the liquids, Section 4.2 provide observation into the incoming stratified flows, Section 4.3 provides a traditional measurement of the jet flows, Section 4.4 provides phenomenological observations and insights to jets interacting with flows and Section 4.5 presents the resultant flow pattern maps from jet mixing stratified flows.

4.1 Material and fluid measurements

This section provides the fundamental measurements of the liquids used throughout the experimental campaign, including refractive indices, densities, viscosities, contact angles, as well as interfacial and surface tensions.

4.1.1 Refractive index

Measurements were performed on the refractive indices for three different viscosity grade polydimethylsiloxane silicone oils sold by Basildon chemicals, known as BC5, BC10 and BC20, with nominal kinematic viscosities of 5 mm^2/s, 10 mm^2/s and 20 mm^2/s, respectively. The refractive index measurements were taken over the temperature range of 15 to 40°C, and are plotted in Figure 4.1. The refractive index of the silicone oils BC5, BC10 and BC20 increases as their nominal kinematic viscosities increase. Whilst the refractive indices of all three liquids decrease as the temperature increases. The density of the oils decrease with temperature and a decrease in density typically leads to a lower refractive index (Mathews, 1914).

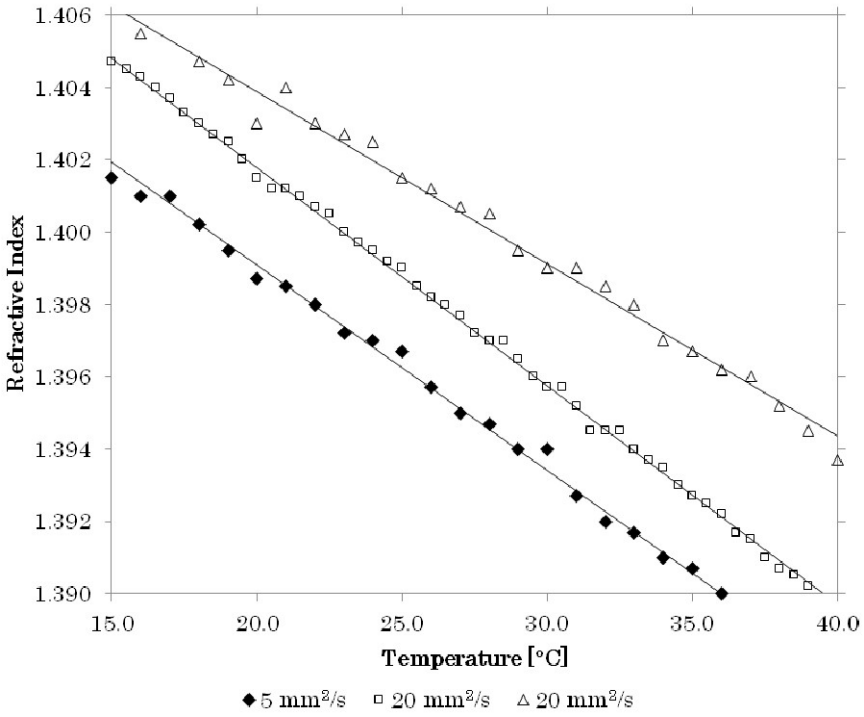


Figure 4.1 Refractive index versus temperature for three viscosity silicone oils 5 mm²/s (BC5), 10 mm²/s (BC10) and 20 mm²/s (BC20) sourced from Basildon Chemicals.

Ninomiya and Yasuda (2006) matched the refractive index of a 6 mm²/s silicone oil with that of 50 wt/wt % glycerol solution with the same viscosity. Given the narrow range of refractive indices, the BC10 silicone oil was selected for experimental purposes as this would ensure the viscosity of the oil (10 mm²/s) was greater than the intended glycerol-based aqueous solution.

Several aqueous solutions were prepared with 49, 50 51 and 52 wt/wt % of glycerol to measure how closely they matched the BC10 silicone oil over the 15 °C – 40 °C temperature range. The refractive indices for these concentrations of glycerol solution are plotted together with that of the BC10 silicone oil in Figure 4.2. At the anticipated 23 °C operating temperature of experimental liquids, a 51 to 52 wt/wt % glycerol solution was found to closely match that of the BC10 silicone oil.

In addition to measuring the refractive index of the pure glycerol solution, the refractive index was also measured with the Eosin Y dye at up to 10 times the concentration used during the experiments. No measurable changes in the refractive indices were found due to the addition of Eosin Y dye.

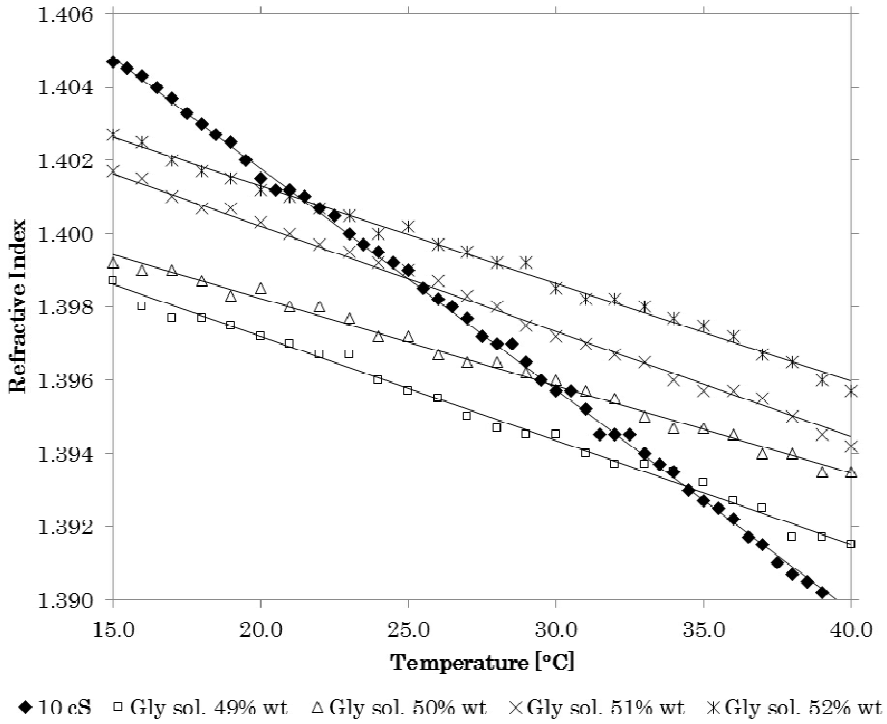


Figure 4.2 Refractive index of a range of glycerol solution concentrations 49, 50, 51 and 52 wt/wt %, compared with BC10 silicone oil.

4.1.2 Density

The silicone oil's density was measured on the benchtop using a Stanton Redcroft / Paar DMA-46 densitometer, giving a value of 932 kg/m^3 at a temperature of 24 °C. During the experimental campaign, the silicone oil's density was measured using the Khrone Optimass 6000 Coriolis meter. Figure 4.3(top) plots these two sets of density measurements against temperature, where the temperature range is from 15 °C to 35 °C. The silicone oil density measurements from the experimental Coriolis meter agree well with the benchtop laboratory measurements, where the majority of the experimental results are within ±2 kg/m^3. The straight-line fit to the Coriolis measurement reveals the density of the silicone oil changes by −1.02 kg/m^3 per °C which is ≈ 0.1% per °C. The density measurements highlight the importance of controlling the oil temperature for accurate flow measurement during the experimental campaign.

The density of the aqueous phase, a 51 wt/wt % glycerol solution, was measured on the benchtop using a Stanton Redcroft/Paar DMA-46 densitometer to be 1131 kg/m^3 at a temperature of 24°C. Therefore, the ratio of density between the silicone oil to the aqueous phase is 0.82 to 2 significant figures.

During the experimental campaign, the density of the aqueous phase was measured using the Bronkhorst mini CORI-FLOW M15 Coriolis meter. Figure 4.3(bottom) plots both sets of aqueous phase density measurements against temperature. A best-fit line to the experimental data reveals that the aqueous phase changes by −0.54 kg/m^3 per ºC or ≈ 0.05% per °C, which is half that of the silicone oil.

The scatter for the experimental Coriolis density measurements for the glycerol solution is ±4 kg/m^3, which is approximately twice that seen in the Coriolis measurements of the silicone oil's density. The difference in scatter between these two sets of Coriolis density measurements can be attributed to the significant difference in the two sizes of meter as well as the potentially different measurement implementations used by the two manufacturers of the Coriolis meters.

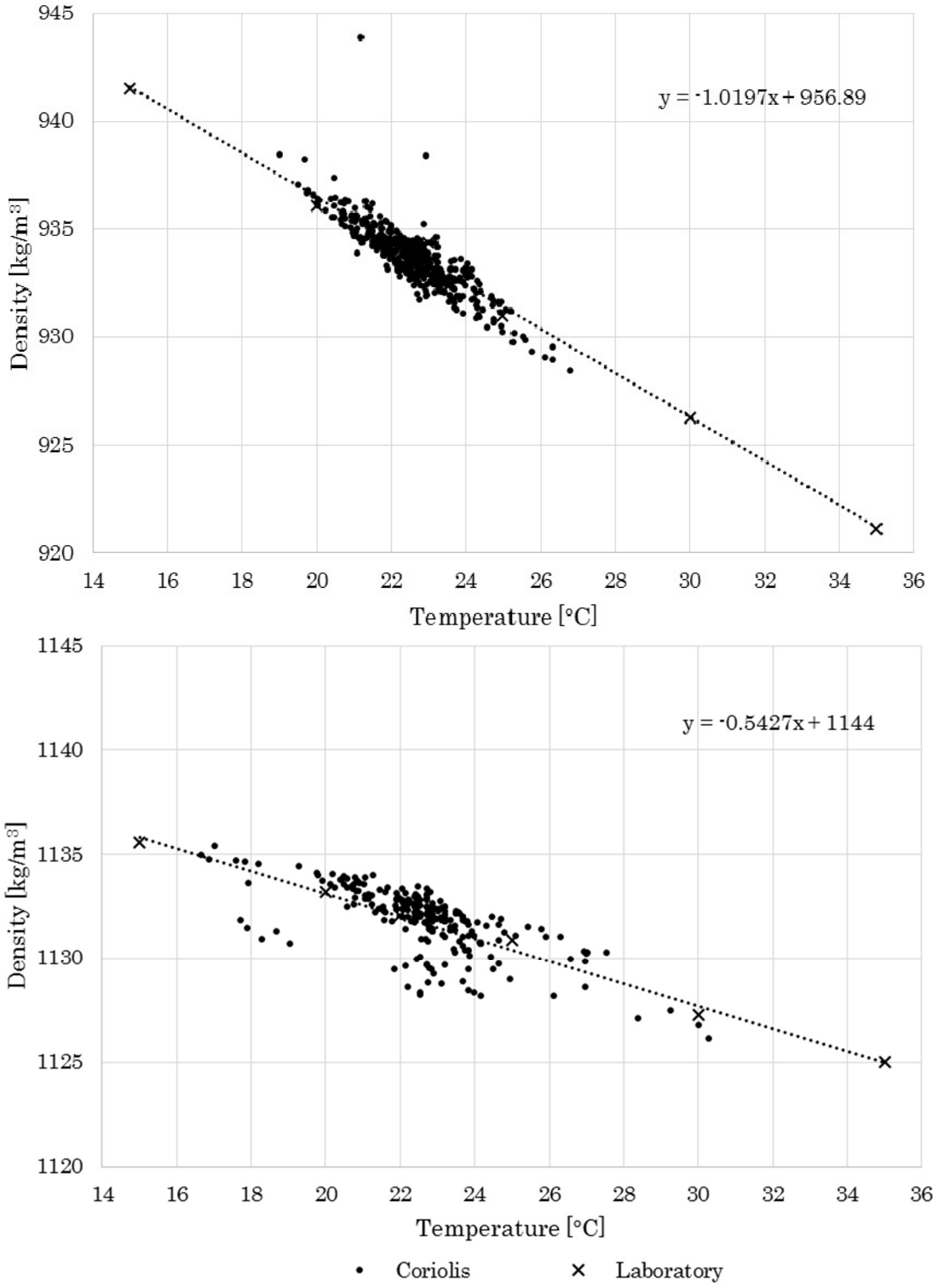


Figure 4.3 Density versus temperature, showing both the benchtop Stanton Redcroft / Paar DMA 46 measurements and the measurements made by the Coriolis meters during the experimental campaigns. Top: BC10 Silicone oil; Bottom: Aqueous phase.

4.1.3 Viscosity

The benchtop laboratory measurements of viscosity were performed using a HAAKE falling ball viscometer type C. The viscosity measurements for the BC10 silicone oil over a temperature range of 15 °C to 35 °C are plotted in Figure 4.4(top). The dynamic viscosity of the silicone oil is shown to be ≈ 8.2 mPa·s at 24 °C, and the viscosity was found to change by approximately 1.5 mPa·s over the measured 20 °C temperature range, i.e. ≈ 0.08 mPa·s/°C.

Benchtop laboratory viscosity measurements for the aqueous phase are plotted against temperature in Figure 4.4(bottom). The dynamic viscosity of aqueous phase is ≈ 5.2 mPa·s at 24 °C but the change in viscosity over the 20 °C temperature range is 2.0 mPa·s (0.10 mPa·s/°C), which is 25% higher than the more viscous silicone oil. The viscosity ratio for the silicone oil to the aqueous phase is 1.6 to 2 significant figures.

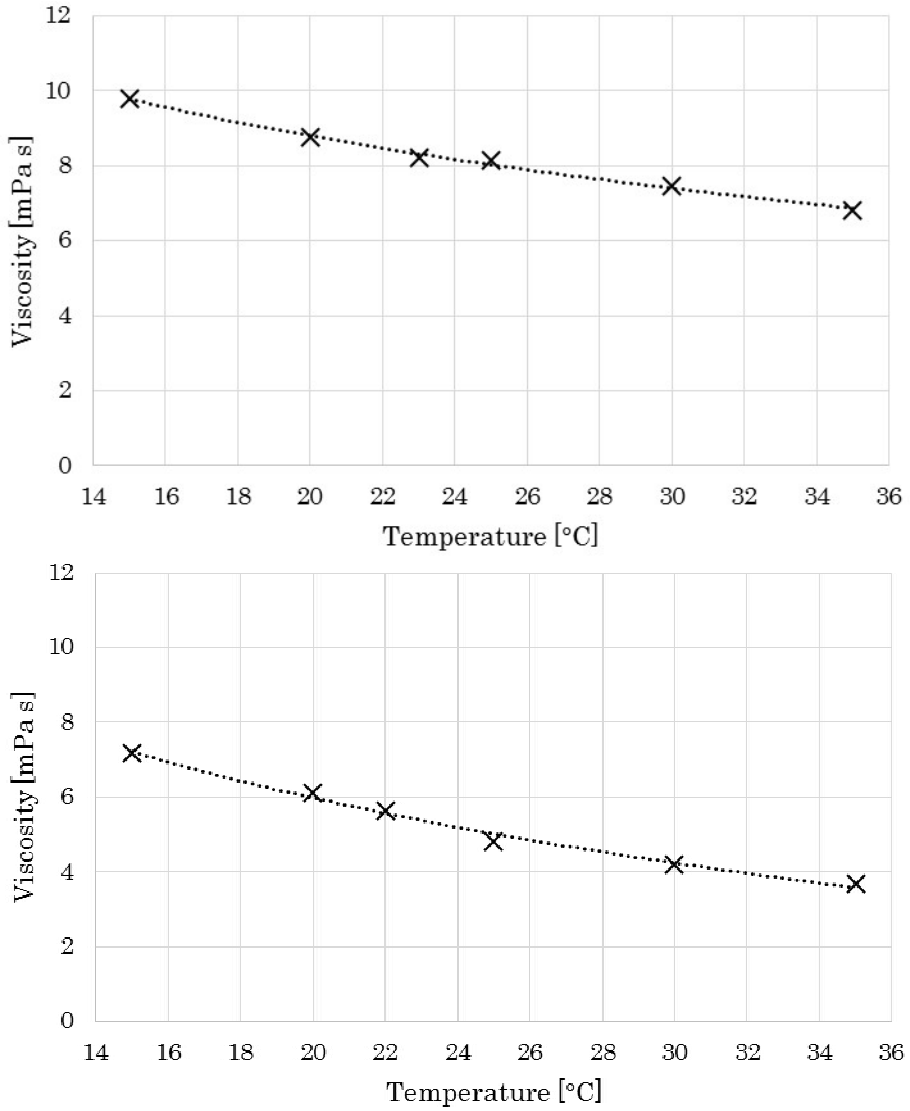


Figure 4.4 Laboratory measured dynamic viscosity versus temperature. Top: BC10 silicone oil; Bottom: glycerol-based aqueous phase.

4.1.4 Contact angles

Contact angle measurements were performed using the KRÜSS EasyDrop contact angle instrument. This instrument makes use of the shadow created around a drop due to the mismatch in refractive indices common in liquids. This shadow is then used to detect the edge of the droplet, which is in turn used to calculate the contact angle with the surface under investigation.

Contact angle measurements were made at ambient temperatures of ≈ 21 °C on a selection of solids with a selection of immiscible liquids. The aqueous phase was either water or a water/glycerol solution. While the oil phase was either the BC10

silicone oil used during the main experimental campaign or an Exxsol D140 mineral oil used in the previous TOWER experimental campaign of Ibarra (2017). A summary of the contact angle measurements on several potential experimental and industrial pipeline surface materials are presented in Table 4.1.

The refractive index matching of the experimental liquids, the BC10 fluid and the 51% by weight glycerol solution, made the droplet interface invisible to the camera. This prevented the optical measurements of contact angles for this combination of liquids. As a result, contact angle measurements were performed using two glycerol concentrations above (60 wt/wt %) and below (43 wt/wt %) the 51 wt/wt % used in the main experiments. The contact angles measured using these two glycerol solutions were found to be within one standard deviation of each other and therefore an average of these two measurements were used to predict the contact angle of the actual experimental liquids.

Table 4.1 Optical contact angle measurements.

Oil	Solid	Glycerol [wt/wt %]	θ, [°]	S, [°]
BC10	Glass	60%	57.0°	6.8°
BC10	Glass	43%	58.5°	7.4°
BC10	Mild steel 1	60%	133.7°	13.3°
BC10	Mild steel 1	43%	134.9°	12.5°
D140	Mild steel 1	0%	107.1°	7.4°
BC10	Mild steel 2	60%	96.7°	3.7°
BC10	PMMA	60%	121.5°	2.9°
BC10	PMMA	43%	133.0°	7.2°
BC10	ETFE	60%	143.8°	12.4°
BC10	ETFE	43%	145.3°	11.2°

The top row of Figure 4.5 show images of droplets formed from the two glycerol solutions within the silicone oil on a glass surface. The droplets have a small contact angle, of ≈ 58°, demonstrating that glass is wetted by the water/glycerol solutions and is oleophobic. In contrast, the bottom row of Figure 4.5 shows the same liquids located on an oleophilic PMMA surface where the contact angle is larger at ≈ 126°.

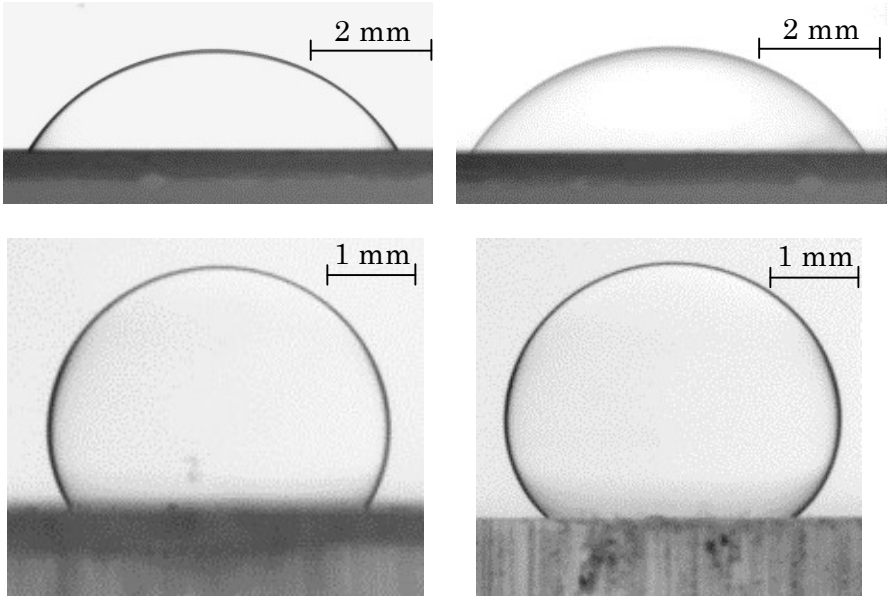


Figure 4.5 Droplets glycerol water solutions in BC10 silicone oil. Top row: on glass; Bottom row: on Acrylic; Left column: 43% glycerol; Right column 60% glycerol.

Given crude oil is transported in steel pipelines, experiments were performed on two steel plates to ascertain the contact angle seen in industrial systems. Importantly, mild steel is generally regarded as water wetted although it is dependent on both the roughness of the surface Tang et al. (2009) and Tabrizi et al. (2012) and the type of corrosion Schmitt et al. (1998). Figures 4.6(i) and Figures 4.6(ii) show the glycerol solutions and silicone oil located on an unpolished mild steel plate (Plate-1) where it can be seen that this mild steel plate was wetted by the silicone oil solution rather than the glycerol solution.

To rule out liquid effects, the contact angle was measured for tap water in Exxsol D140, see Figures 4.6(iii), this again showed that the mild steel plate was oil wetted, although to a smaller extent at 107.1° when compared with the silicone oil and the two glycerol solution 133.7° and 134.9°. A second mild steel plate was then sourced, this is labelled as 'Plate-2'. This plate was sanded using 80-grit sandpaper to remove any surface finish and corrosion. The plate was then tested using the BC10 silicone oil and 60% glycerol solution, an image of which can be seen in Figures 4.6(iv).

It was found that steel Plate-2 was less oil wetted than that of steel Plate-1 with a contact angle of 96.7° versus 133.7°. It was therefore concluded that industrial steel pipes have a wide range of contact angles where they can potentially change from hydrophilic to hydrophobic over their useful lifetime (Angeli and Hewitt 1999).

The contact angle of the two concentration glycerol solutions and an ETFE sample were measured to be 143.8° and 145.3°, and a nominal value of 144° was therefore assumed for the experimental fluids.

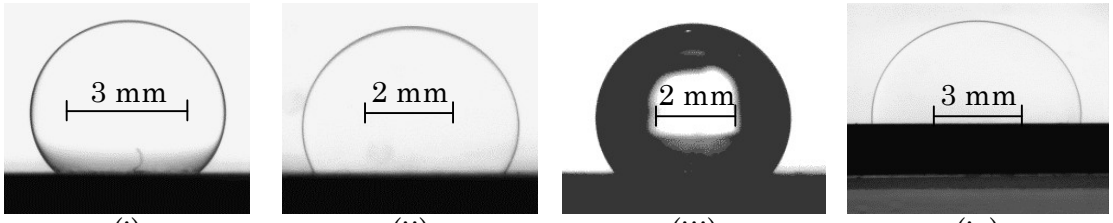


Figure 4.6 Images of contact angles formed by various liquids on steel surfaces, (i) 43% glycerol solution in BC10 silicone oil on mild steel Plate 1; (ii) 60% glycerol in BC10 silicone oil on mild steel Plate 1; (iii) Tap water in D140 mineral oil on mild steel Plate 1; (iv) 60% glycerol solution in BC10 silicone oil on mild steel Plate 2.

4.1.5 Surface and interfacial tension measurements

The surface and interfacial tension measurements were performed using the Wilhelmy plate method on an Attention sigma 700/701 force tensiometer at a room temperature of approximately 23 °C.

The glycerol solution was measured to have a surface tension of 48.8 ± 0.2 mN/m at 23 °C, while the BC10 silicone oil had a surface tension of 18.8 ± 0.1 mN/m at 23 °C. The interfacial tension between these two liquids (without dye) was measured to be 32.5 ± 2.4 mN/m at 23 °C. The measurement of the interfacial tension was particularly difficult due to the liquids matching refractive indices which contributed to the large measurement uncertainty.

The measurement of the interfacial tension was repeated with the addition of the Eosin Y dye and was found to be 33.2 ± 1.5 mN/m at 23 °C. The deviation between the interfacial tension measurements with and without dye was within the measurement uncertainty, and it was therefore concluded, that the dye had a negligible effect on the interfacial tension.

4.1.6 Summary of experimental liquids and particles

A summary of the properties of the liquids and particles used during the experimental campaign is provided in Table 4.2.

Table 4.2 Properties of the experimental fluids and particles.

Fluids at 23°C	Density, ρ_L, [kg/m^3]	Viscosity, μ_L, [mPa s]	Refractive index, n	Particles type	Particle density, ρ_p, [kg/m^3]	Stokes number, St	Surface tension [mN/m]	Interfacial tension, σ, [mN/m]	Contact angle, θ, with ETFE
Silicone Oil	935.3 ±0.2	8.4 ±0.3	1.400 ±0.001	100 µm SHGS	900	<0.02	18.1±0.1	32.5±2.4	144°
Glycerol solution	1128.8 ±0.3	5.3 ±0.3	1.400 ±0.001	100 µm poly-amide	1100	<0.03	48.2±0.2		

4.2 Crossflow measurements

This section presents observations and traditional fluids flow measurements of the incoming stratified flows that are subsequently introduced to the jet for mixing. Measurements include the pressure drops over the flow development section as well as the interface heights of the incoming flow.

4.2.1 Observations of experimental crossflows

The combination of the inlet conditioner and flow development sections produce a range of incoming stratified flow conditions for presentation to the jets for mixing.

A typical PLIF image for a stratified wavy flow can be seen in Figure 4.7 which shows a 0.6 m/s crossflow with an aqueous phase fraction of 0.20, where the aqueous phase appears bright and the oil phase dark. The interface is visible in this image at about a quarter of the way up from the bottom of the pipe.

The three-dimensionality of this flow is visible in the background of the image, appearing as a shadow above and below the true interface. This shadow is formed by the slight illumination of the interface outside the measurement plane. This out of plane illumination is caused by the diffusion of laser light by the ETFE pipe walls as well as secondary reflections of the laser light.

The interface height increases with the inlet aqueous phase fraction. While the magnitude of the interface waves increase with mixture velocity, eventually, as the velocities continue to increase, droplets form at the interface (Ibarra RJ, 2017).

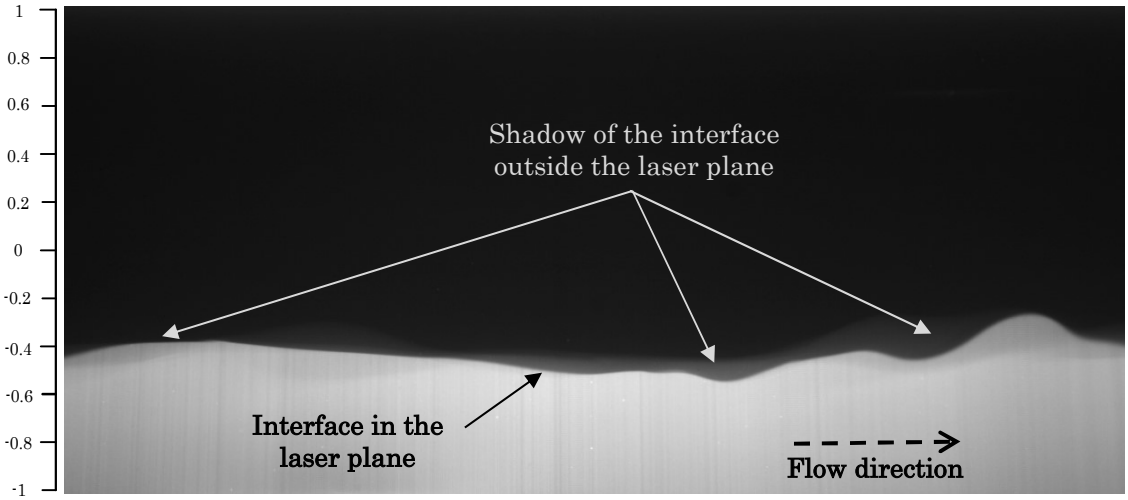


Figure 4.7 A V_m = 0.6 m/s stratified crossflow with a ϕ = 0.20 aqueous phase fraction located upstream of the jet at $L = -2\ D$ while the jet is inactive.

4.2.2 Crossflows pressure drops

The differential pressure drops of the crossflows are measured along the 6 m flow development section. Differential pressure transmitter one is positioned between 2 m and 6 m from the inlet, while differential pressure transmitter two is located between 4 m and 6 m from the inlet. The differential pressures measured by these transmitters during the experimental campaign are plotted in Figure 4.8. In both pressure transmitters, the measurements cluster together into four groups, which correspond to the four inlet mixture velocities used throughout the experimental campaign.

The two differential pressure transmitters show close agreement, which is an indication that the flow is not undergoing significant development between the two measurement points of the differential pressure transmitters.

In addition to the measured pressure drops, the predicted pressure drops of the two-fluid model of Taitel and Dukler (1976) are also plotted for comparison, where, the dotted fitting line is for the lower velocity laminar flows and the dashed fitting line is for the higher velocity turbulent flows. The agreement between the two pressure transmitters and model indicates that the flow inlet conditioner and flow development length are successfully developing the stratified liquid-liquid flow before its presentation to the jet for the mixing experimental campaign.

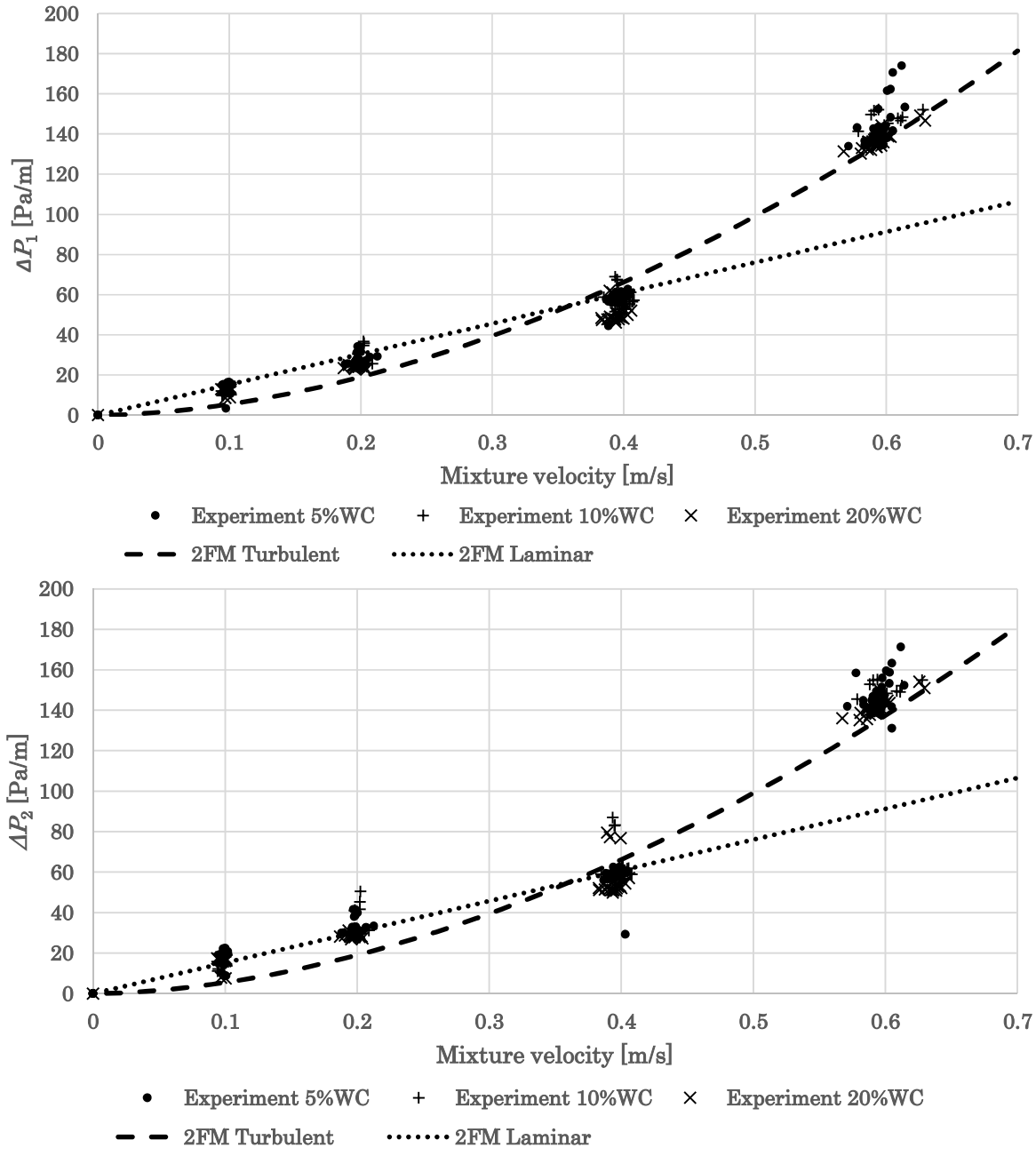


Figure 4.8 Pressure drops against velocity including experimental measured by differential pressure transmitters at two positions from the inlet and the two-fluid model for both laminar and turbulent flows of Taitel and Dukler (1976). Top: located between 2 m and 6 m; Bottom: located between 4 m and 6 m.

4.2.3 Interface heights

The liquid-liquid interface height of the incoming unmixed crossflows was measured during the experimental campaign from the PLIF images using the interface detection method outlined in Subsection 3.14.4. The time average of these interface heights for the experimental crossflows is plotted against the experimental inlet aqueous phase fraction in Figure 4.9. The top figure includes all crossflow velocities while the bottom figure includes crossflows with velocities $V_m < 0.4$ m/s. The interface heights are clustered into five groups which correspond to the five aqueous phase fractions used during the campaign. In addition to the experimental measurements, the two-fluid-model of Taitel and Dukler et al. (1976) is plotted for comparison, where this model shows a reasonably close agreement with the experimental data.

The spread in the interface heights seen in Figure 4.9(top) when $\phi = 0.50$ is principally due to the presence of droplets at the interface at higher crossflow velocities which make the interface height less defined, see Figure 3.24. In contrast, Figure 4.9(bottom) only includes crossflows with velocities $V_m < 0.4$ m/s, which excludes the experimental cases with droplets at the interface. This results in a significant reduction in the amount of scattering in the interface heights when the aqueous phase fraction is $\phi = 0.50$.

Figure 4.9(top) has a higher average interface height than that in Figure 4.9(bottom) when $\phi \geq 0.20$. At these higher water fractions, there are visibly more oil droplets in the aqueous phase than there are aqueous droplets in the oil phase, this results in the interface rising, see Figure 3.24. Therefore, this higher average interface is consistent with the interface rising due to the presence of oil droplets within the aqueous phase.

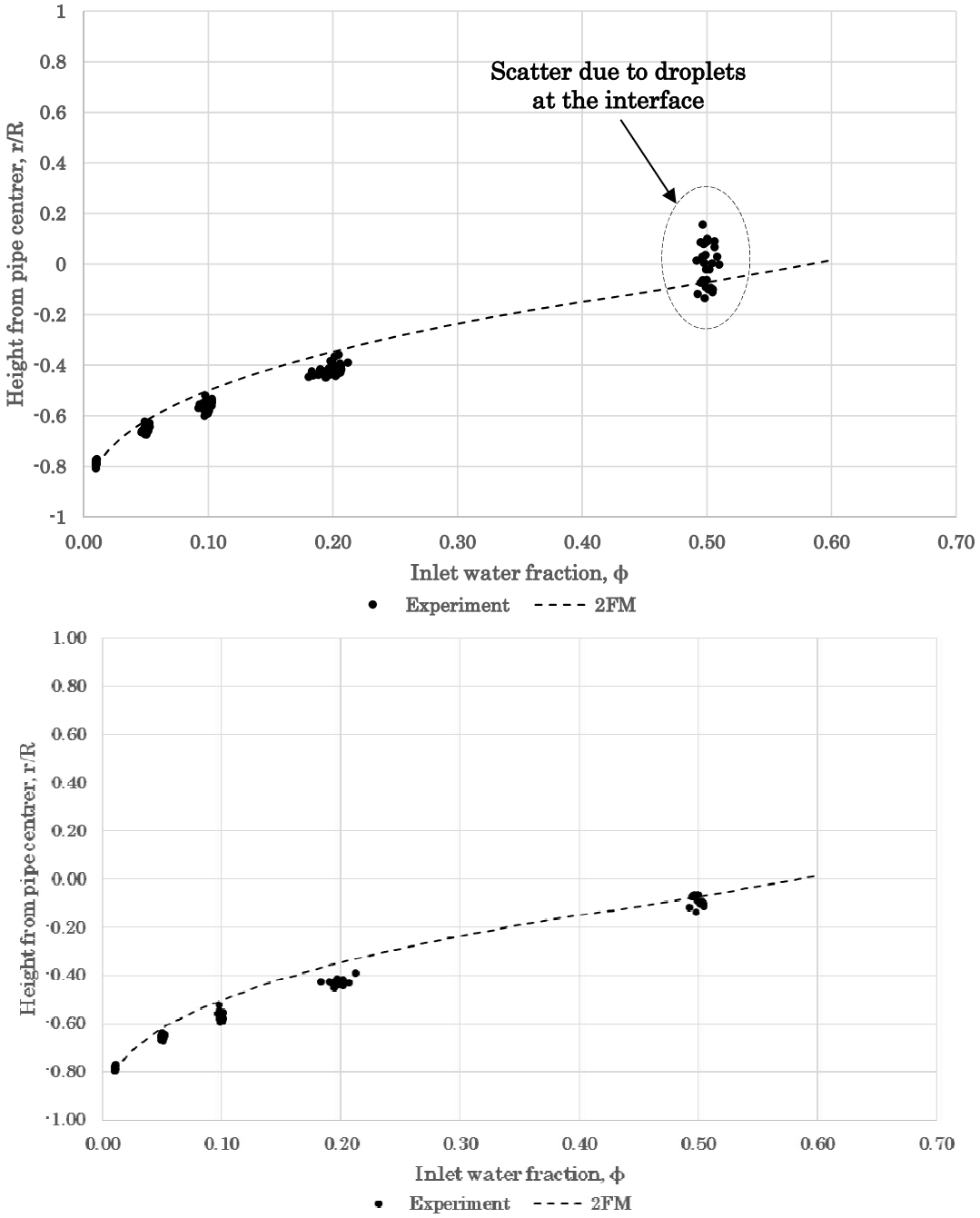


Figure 4.9 Aqueous phase heights and those predicted by the two-fluid model of Taitel and Dukler et al. (1976), plotted as height (H_{aq}) versus aqueous phase fraction (ϕ). Top: all crossflow velocities; Bottom: crossflow velocities $V_m < 0.4$ m/s.

4.3 Jet nozzle pressure drop and power usage

Measurements of the pressure loss and power requirements between the nozzle feed pipe and the main test section were made throughout the experimental campaign. These measurements are plotted in Figure 4.10, where Figure 4.10 (top) and Figure 4.10 (bottom) present measured pressure losses and power usage, respectively. The power usage is calculated from the measured pressure drop and the flow rate using Eq. 2.21. The change in power requirements calculated by Eq. 2.21 is proportional to the pressure loss because the nozzle exit area, flow rates and velocities were all matched between the nozzles.

All three of the jet nozzles have a different relationship between the jet velocity and the pressure loss or power usage. However, the two 4 mm diameter single jet nozzles are relatively close, where the pressure loss and power usage of the forward-facing F-jet are ≈ 10% higher than the vertically oriented U-jet. The small differences in pressure loss and power usage between these two jet nozzle types could be due to differences in the internal geometry of nozzles or because of the angle of the jets relative to the crossflows. Where the U-jet has a vertical exit while the F-jet exit is oriented into the crossflow at an angle of 40°. Further investigation is needed to confirm the magnitude of these effects on pressure loss and power usage.

In contrast, the measured pressure drops and power usages of the V-jet nozzle are significantly higher than the other two jet nozzles, where the V-jet is ≈ 80% greater than the U-jet for the same jet velocities and hence flow rates. These higher-pressure losses and power requirements for the V-jet can be attributed to the significantly different internal nozzle geometry required to create the twin 2.8 mm jets when compared to the U-jet.

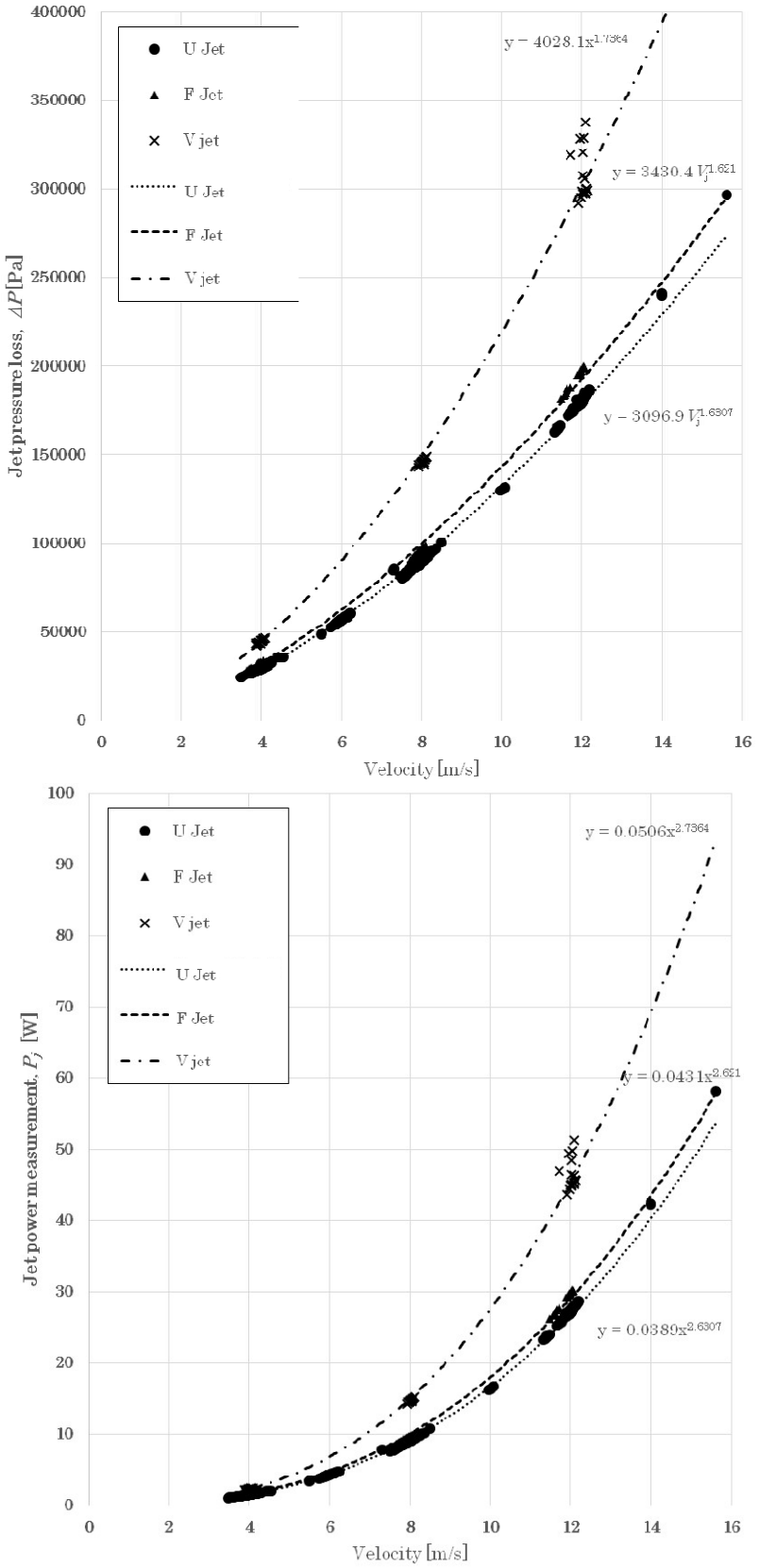


Figure 4.10 Pressure losses and power usages measured during the experimental campaign for the three type jet nozzle against the jet velocity. Top: ΔP versus V_j; Bottom: P_j versus V_j.

The relationship between pressure loss and velocity for fully-developed flows is given by Eq. 4.1, where for laminar flows the Darcy friction factor is given by the Darcy-Weisbach equation (Brown, 2002) (Eq. 4.2), while for turbulent flows the Colebrook-White (Colebrook, 1939) empirical relation can be used (Eq. 4.3). Hence for laminar flows, the change in pressure loss is proportional to velocity (Eq. 4.4) while for turbulent flows it is proportional to the square of velocity (Eq. 4.5).

$$\Delta P = f\frac{L}{D}\frac{\rho\bar{V}^2}{2} \qquad \text{Equation 4.1}$$

$$f = \frac{64}{\mathrm{Re}} = \frac{64\mu}{\rho V D} \qquad \text{Equation 4.2}$$

$$\frac{1}{\sqrt{f}} = -2\log_{10}\left(\frac{e}{3.7D_{\mathrm{h}}} + \frac{2.51}{\mathrm{Re}\sqrt{f}}\right) \qquad \text{Equation 4.3}$$

$$\Delta P \propto V \text{ (for laminar flows)} \qquad \text{Equation 4.4}$$

$$\Delta P \propto V^2 \text{ (for turbulent flows)} \qquad \text{Equation 4.5}$$

A simple power-law fitting has been applied to the pressure drops of the three different jet types and each has an exponent in the range from 1.6 to 1.7. These exponents are lower than the value of two expected for turbulent flows but higher than the value of one that is expected for laminar flows. However, as the flow passes through the nozzle the geometry varies and so do the velocities. This variation in geometry and velocity results in the Reynolds number inside the jet nozzles varying between 1000 and 6000, which indicates that the flow within the nozzles can undergo transitions from laminar to turbulent within the nozzle.

4.4 Phenomenological observations

This section details the phenomenological observations and insights of the jets and the mixing processes close to the jets as well as the development downstream of the unstable liquid-liquid dispersions obtained during the experimental campaign.

The experimental measurements were performed in a steady-state condition where the jet was on for a long period before the data was collected. However, some

images were also captured as the jet was activated as this allowed clearer images to be captured around the jet as fewer interfaces were present to blur the images.

4.4.1 Overview of jets and mixing

A comprehensive spectrum of PLIF observations of the conditions seen during the experimental campaigns is presented in Figures 4.11(a–b, i–iii), where the aqueous phase appears white while the oil phase appears black. In Figures 4.11(a–b, i–iii) the level of mixing increases as the rows (a–g) progress down while the distance downstream from the jet entry increases as the columns, (i–iii), move from left to right. Each image captures the plane that passes through the centre of the pipe, passing from top to bottom and along the axis. The mainline flow enters from the left and exits from the right, while the jet enters from the bottom of each image in the left column. Each image shows the entire 50 mm height of the pipe's internal diameter and provides a width of ≈ 100 mm or two pipe diameters (2 D) in the pipes axial direction.

The first row of Figure 4.11 shows a V_j = 4 m/s jet, with a crossflow velocity of V_m = 0.2 m/s and an aqueous phase fraction of ϕ = 0.50 with associated non-dimensional numbers of Re_j = 1900, Re_{aq} = 1300, Re_o = 660, We_j = 1800. In Figure 4.11(a, i) the oil jet can be seen to penetrate the aqueous phase, disturbing the interface and creating many fine droplets even at the lowest jet Weber number. The zone between the fine droplets and the aqueous layer is mixed having ligaments that stretch from the aqueous phase to the mixed zone at the top. These ligaments eventually stretch so far that they break and create much larger droplets than those formed at the jet interface. Even though the jet flow before the exit is within the laminar regime with Re_j < 2100, as are the incoming crossflows, the resulting disturbance after the jet exits the nozzle looks chaotic. At a distance of four diameters downstream from the jet, L = 4 D, Figure 4.11(a, ii), the largest droplets can already be seen to be undergoing stratification. Once the flow reaches ten diameters downstream, Figure 4.11(a, iii), the largest droplets are either all located at the interface or have already coalesced with the interface. An aqueous phase layer at the bottom contains a few oil droplets which are present throughout all the images in the first row of Figures 4.11(a, i–iii).

The second row of Figure 4.11 increases the crossflow from 0.2 m/s to 0.6 m/s and Reynolds numbers to Re_{aq} = 3900 and Re_o = 2100. Contrasting the second row

with the first row, the jet is turned more rapidly in the axial direction as it exits the nozzle. Indeed in the second row, the jet has been turned so far in the direction of the crossflow that the interface is barely penetrated by the jet, figure 4.11(b, i). This increase in crossflow velocity and Reynold's numbers appears to suppress the creation of the finest droplets. At a distance of $L = 4\ D$ downstream, Figure 4.11(b, ii), the upper half of the pipe is seen to have many large complex structures, including large droplets and long stretched ligaments. At a distance of ten diameters downstream, Figure 4.11(b, iii), the liquids have undergone significant stratification with the largest, predominantly oil droplets, located at the interface. The aqueous layer is again present throughout all the images in the second row of Figures 4.11(b, i–iii).

When compared to first and second rows, the third row increases the jet velocity from 4 m/s to 8 m/s with a Reynolds number of $Re_j = 3700$ and Weber number of $We_j = 7300$. This jet velocity increase results in the jet penetrating the interface while the interface height in the centre plane immediately downstream of the jet rises almost to the top of the pipe, see Figure 4.11(c, ii). When comparing rows two and three the jet appears to break up faster which is consistent with the increase in Weber number. At a distance of four diameters downstream, Figure 4.11(c, ii), the jet has created a highly mixed zone, in which a large number of complex droplets are present along with distorted ligaments, some of which stretch the entire 100 mm of the image. Towards the bottom of Figure 4.11(c, ii), the ligaments appear to be coalescing and stratifying. At a distance of ten diameters downstream, Figure 4.11(c, iii), some stratification is occurring but there are still many complex zones of both oil-in-water and water-in-oil. At the bottom of the pipe, an aqueous layer is now present although this still contains many small droplets of oil.

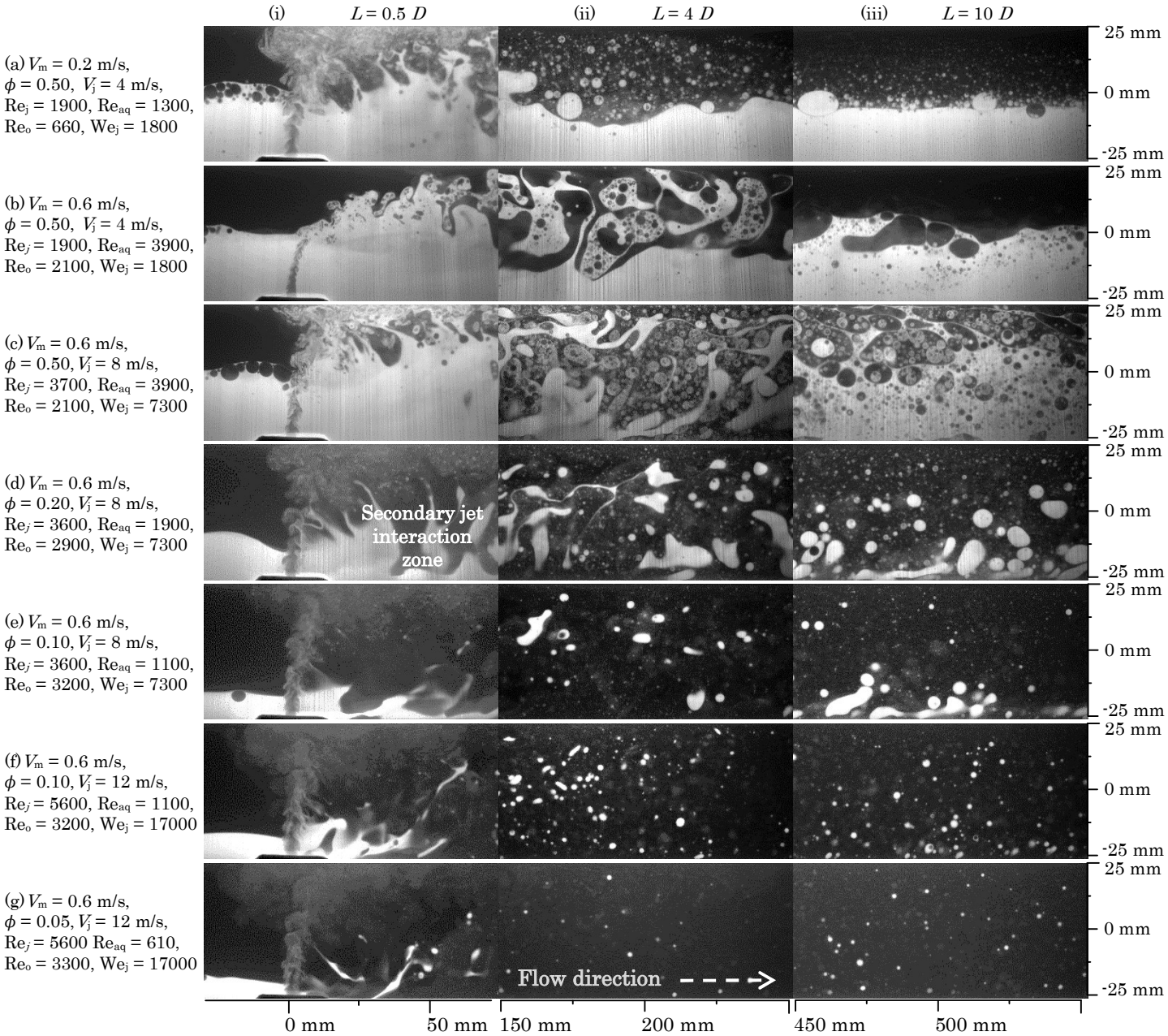


Figure 4.11 Characteristic effects of liquid jets formed by a U-type jet interacting with stratified flows with $0.2 \leq V_m \leq 0.6$ m/s, $0.05 \leq \phi \leq 0.50$ and $4 \leq V_j \leq 12$ m/s. Rows from top to bottom show increasing levels of mixing while columns from left to right are increasing in downstream distance from the jet.

The fourth row reduces the aqueous phase fraction from 0.50 to 0.20 compared to the first three rows, this decreases Re_{aq} to 1900 and increases Re_o to 2900. The reduction in aqueous phase fraction results in the jet more cleanly penetrating the interface than the third row and in doing so forms many fine droplets around both sides of the jet see Figure 4.11(d, i). Immediately downstream of the jet, the aqueous phase is lifted, and from this lifted interface, some small ligaments of aqueous phase

are stretched towards the jet flow at the top of the pipe as it travels downstream. The oil phase is seen passing through the aqueous phase at about one diameter downstream of the jet. This highlights the 3-dimensional nature of these mixing processes, where the flows from the jet are propelled to the top of the pipe where they impinge the pipe wall and then flow around the circumference of the pipe and eventually through the aqueous layer. This "secondary jet interaction zone" is discussed in further detail in Subsection 4.4.2. By four diameters downstream, Figure 4.11(d, ii), the flow has developed a wide range of droplet sizes as well as several stretched ligaments. However by ten diameters downstream, Figure 4.11(d, iii), the ligaments have largely disappeared, and the larger droplets have fallen to the bottom of the pipe and are starting to coalesce.

The fifth row reduces the aqueous phase fraction further from 0.20 to 0.10 when compared to that of the fourth row, this decreases Re_{aq} to 1100 and increases Re_o to 3200. In Figure 4.11(e, i) the jet is seen to create fine droplets while the interface layer is starting to break up in less than half a pipe diameter downstream of the jet. At four diameters downstream, Figure 4.11(e, ii), there are fewer large droplets when compared with the fourth row, and the maximum droplet sizes are smaller, while the remaining ligaments are more tenuous. At ten diameters downstream, Figure 4.11(e, iii), the largest droplets have again mostly settled towards the bottom of the pipe and some have coalesced.

The sixth row increases the jet velocity from 8 m/s to 12 m/s compared to the fifth row resulting in Reynolds number of $Re_j = 5600$ and Weber number of $We_j = 17000$. Now when we compared Figures 4.11(e, i) to 4.11(f, i) the jet turns less in the direction of the crossflow and appears to create even finer droplets than the fifth row while the interface downstream of the jet undergoes immediate breakup. By four diameters downstream, Figure 4.11(f, ii), the maximum droplet sizes are significantly smaller than in the fifth row due to the increase in Weber number. Even still, by ten diameters downstream, Figure 4.11(f, iii), these smaller droplets still appear to be in greater numbers at the bottom half of the pipe indicating stratification is still occurring.

Finally, the seventh row decreases the aqueous phase fraction further from 0.10 to 0.05 which decreases Re_{aq} to 610 and increases Re_o to 3300. The decrease in aqueous phase fraction results in the jet creating fine droplets at the jet while the remaining aqueous phase layer is stretched into fine ligaments see Figure 4.11(g, i). At four diameters downstream, the droplets are fine and well dispersed, Figure 4.11(g, ii). At

ten diameters downstream the droplets still appear to be well dispersed, however, they also appear to be slightly larger indicating that coalescence may be occurring.

The experimental campaign uses jet velocities ranging from 4 m/s to 16 m/s which corresponds to jet Reynolds numbers (Re_j) in the range of 1900 to 7600 and jet Weber numbers (We_j) in the range of 1800 to 29000. Comparing these numbers to the work of Sirignano and Mehring (2000) (Figure 2.2) indicates that the jet breakup regime should range from the upper end of the "First Wind Induced" to the "Second Wind Induced". However, all images in the first column of Figure 4.11 create droplets smaller than the exit nozzle which is consistent with the "Second Wind Induced" even for jets with the lowest Reynolds and Weber number.

In summary, observations of images indicate that as the crossflow velocity or aqueous phase fraction increases the level of mixing decreases whilst the largest droplet diameters increase. In contrast, an increase in jet velocity or the jet Weber number results in an increase in mixing and subsequent decrease in the largest droplet diameters.

4.4.2 Near jet processes and effects

This subsection discusses several of the processes that occur near the jet. Figure 4.12 shows the development of an oil jet with a velocity of $V_j = 8$ m/s penetrating a crossflow with a velocity of $V_m = 0.4$ m/s and an aqueous phase fraction of $\phi = 0.20$ after a period of 60 ms from when the jet first starts to enter the crossflow with non-dimensional numbers of $Re_j = 3700$, $Re_{aq} = 1200$, $Re_o = 1900$, $We_j = 7300$. The jet development is shown here because the initial images are clearer due to the presence of fewer droplet interfaces in front of the laser plane. However, it should be noted that measurements were performed once the jet was in a steady state.

The most obvious effect is the asymmetry of the image, this is caused by the left to right direction of the crossflow and results in the jet turning into the axial direction of the crossflow after it exits the nozzle. The degree of penetration depends on the ratio of the momentum of the jet to that of the momentum of the crossflow, where a higher momentum crossflow will result in more rapid jet turning, whereas a higher jet momentum will result in a less rapid jet turning (Gutmark, 2008). In some experimental cases, the jet is turned so much that it fails to impinge upon the top pipe wall and so becomes a classical jet in crossflow.

A second observable phenomenon is the Kelvin-Helmholtz instabilities which are present in both the aqueous layer and the oil layer on the outer edges of the jet flow as it travels vertically upwards. These Kelvin-Helmholtz instabilities rapidly form after the oil jet exits the nozzle into the aqueous phase due to the significant difference in velocity between the oil of the jet and the aqueous phase in the bottom of the pipe.

The Kelvin-Helmholtz instabilities result in the outer edges of the jet's oil mixing with of the aqueous layer where ligaments and droplets are stretched and sheared inside eddies. The Kelvin-Helmholtz instabilities then continue to develop as the jet reaches the interface and in doing so, carry a significant amount of the aqueous phase along with the jet. These instabilities have become pronounced by the time jet reaches the interface layer, where the core of the silicone oil jet has become pinched between two eddies formed by this process. As the jet passes through the interface layer, into the oil phase, the mixing between the layers becomes pronounced as now the crossflow oil also becomes entrained into the jet flow. The droplets formed through these Kelvin-Helmholtz instabilities are the finest droplets created by the jet.

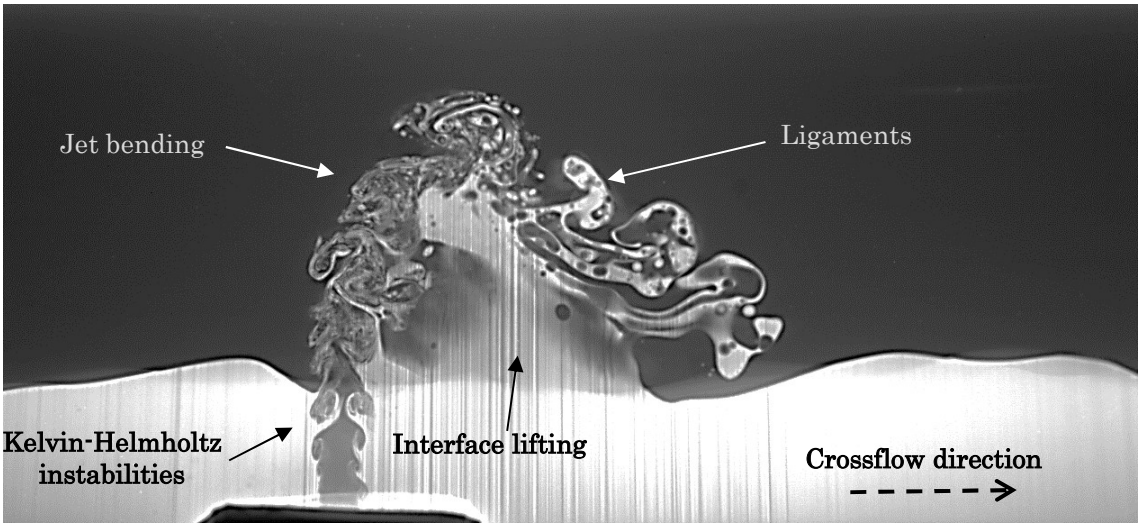


Figure 4.12 An 8 m/s silicone oil jet penetrating the aqueous phase of a crossflow with a velocity of V_m = 0.4 m/s and an aqueous phase fraction of ϕ = 0.20 at 60 ms after the jet's first appearance into the flow. The flows non-dimensional numbers are Re_j = 3700, Re_{aq} = 1200, Re_o = 1900, We_j = 7300.

A third visible process is the lifting of the aqueous phase interface which occurs on the downstream side of the jet as highlighted in Figure 4.12. This lifting of the aqueous interface is caused by the secondary flow around the pipe walls and forms ligament and sheets that stretch from the interface to the underside of the jet. Once

these stretched ligaments and sheets break, they produce droplets that are larger than those created by the Kelvin-Helmholtz instabilities. These larger droplets then subsequently undergo further breakup in the flow as it travels downstream.

As the jet becomes more established several further processes become apparent close to the jet. These new processes are illustrated in Figure 4.13 which shows the same conditions as shown in Figure 4.12 but after 5200 ms from when the jet first appeared in the crossflow when the jet is established.

Some processes only occur when the jet has sufficient momentum compared to that of the crossflow to allow the jet to impinge upon the top of the pipe. This causes the jet's flow to spread in all directions along the pipe wall from the centre of the impingement region of the jet. When impingement happens, a jet recirculation zone or vortex develops upstream of the jet and towards the top of the pipe, where small droplets can be seen to circulating while larger droplets breakup. This vortex is formed by the upstream jet flow decelerating into the crossflows, both flows then continue downwards and then back towards the jet creating the recirculation. In addition, this vortex captures many of the vortices from the upstream side of the jet.

Observing the recirculation zone over a longer period with the jet in a pseudo steady-state has shown that the recirculation zone has a transient behaviour where its size and position can ebb and flow, where for some conditions it can dissipate for short periods. The average size and position of this vortex depend upon the momentum of both the crossflow and jet, where an increase in crossflow momentum weakens and pushes the vortex further downstream while an increase in jet momentum pushes the vortex upstream and increases the vortex size and intensity. If the crossflow velocity is high enough the momentum of the crossflow will prevent the jet impinging on the top pipe wall and forming the vortex, while windward vortices created by the jet flow downstream rather than become trapped.

The jet flows that impinge upon the top pipe wall, flow around the circumference of the pipe, where they can then disrupt the aqueous layer in a secondary zone of jet interaction. When the jet has sufficient momentum, the flows around the pipe penetrate the interface at the secondary jet interaction zone. The bottom right of Figure 4.13 is the result of the aqueous phase being penetrated, lifted and broken up in this secondary jet interaction zone. However, if the jet has insufficient energy the interface layer will not be penetrated but can still become distorted, lifted and stretched, at the plane of the laser sheet.



Figure 4.13 An 8 m/s silicone oil jet penetrating the aqueous phase of a crossflow with a velocity of V_m = 0.4 m/s and an aqueous phase fraction of ϕ = 0.20 at 5200 ms after the jet's first appearance into the flow. The flows non-dimensional numbers are Re_j = 3700, Re_{aq} = 1200, Re_o = 1900, We_j = 7300.

4.4.3 Compound droplets

The mixing leads to droplets that have complex structures, where smaller droplets are contained within the larger droplets. An example of one of these compound droplets is given in Figure 4.14, where the 7 mm aqueous droplet contains numerous smaller oil droplets, some of which themselves contain further aqueous droplets.

As these compound-droplets contain varying amounts of the two-phases, their effective density difference with the continuous phase is less than that of any single-phase droplet. Given the settling or rising rate of a droplet is dependent on its density difference we can conclude that these compound droplets will settle or rise at a slower rate than equivalently sized single-phase droplets. The average droplet settling / rising rates are therefore expected to be lower than that predicted by calculations based on single phase droplet size alone. Any droplet size will have a range of effective densities, and thus the settling / rising rates for any given droplet size will range up to the maximum rate of a single phase droplet.

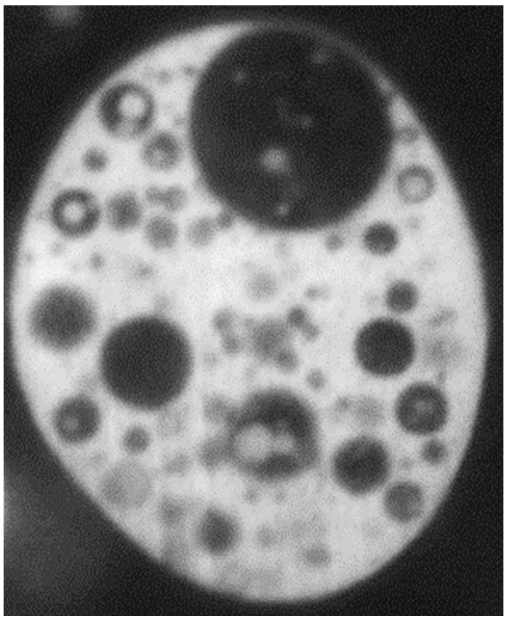


Figure 4.14 A 10 mm diameter compound droplet created during the mixing process with a jet velocity of $V_j = 4$ m/s, a crossflow of $V_m = 0.4$ m/s and an aqueous phase fraction of $\phi = 0.50$ at a distance of $L = 4\ D$ with $Re_j = 1900$, $Re_{aq} = 2700$, $Re_o = 1400$ and $We_j = 1800$.

The largest compound droplets were formed for high water fractions and low jet velocities. A high compound droplet production rate can be seen in the example presented in Figure 4.15 of a crossflow with a velocity of $V_m = 0.2$ m/s and a water fraction of $\phi = 0.5$ interacting with a jet with a velocity of $V_j = 4$ m/s.



Figure 4.15 Large compound droplets formed by a U-jet with a velocity of $V_j = 4$ m/s interacting with an incoming stratified flow with a pipeline velocity of $V_m = 0.2$ m/s and an aqueous phase fraction of $\phi = 0.50$.

As the water fraction decreases from $\phi = 0.5$ the compound droplets become smaller and they contain increasing finer droplets. At the lowest water fractions of $\phi = 0.05$ and below, compound droplets were not visibly present, however, this could be the result of the experimental resolution not having sufficient detail to discern them. Increasing the jet velocity decreases the droplet size while increasing the number of compound droplets, compare Figure 4.16 with Figure 4.15.

The largest compound droplets were formed when the jet velocity was at $V_j = 4$ m/s and the crossflow velocities were between $V_m = 0.2$ m/s and $V_m = 0.4$ m/s. At lower crossflow velocities the jet created smaller droplets while at greater crossflow velocities the jet struggled to penetrate the interface. Increasing the jet velocity increases the crossflow velocities where the largest compound droplets form. So that when the jet velocity was at $V_j = 8$ m/s the largest compound droplets formed when the crossflow velocities were between $V_m = 0.4$ m/s and $V_m = 0.6$ m/s.

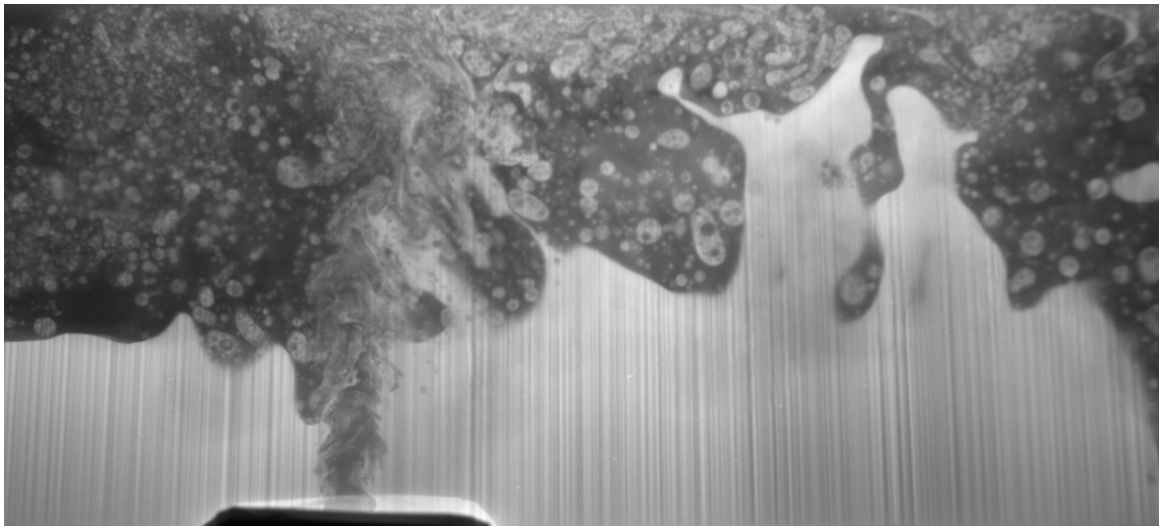


Figure 4.16 Significant numbers of compound droplet formed by a U-jet with a velocity of $V_j = 8$ m/s interacting with an incoming stratified flow with a velocity of $V_m = 0.2$ m/s and an aqueous phase fraction of $\phi = 0.50$.

Compound droplets were found even when the jet was not seen to break through the interface layer, as occurs when the jet velocity is low and the water fraction and crossflow are high. Small examples of these compound droplets can be seen in Figure 4.17. Therefore, compound droplets can form when a liquid jet of one phase is injected into a liquid crossflow of another phase.

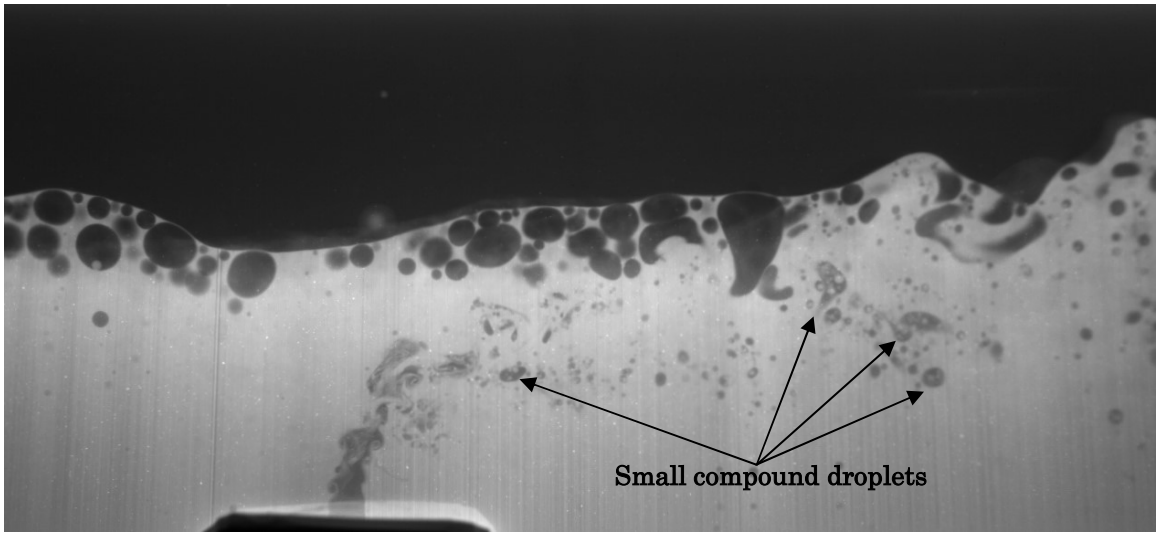


Figure 4.17 Small compound droplets formed in a U-jet with a velocity of V_j = 4 m/s interacting with an incoming stratified flow with a velocity of V_m = 0.8 m/s and an aqueous phase fraction of ϕ = 0.50.

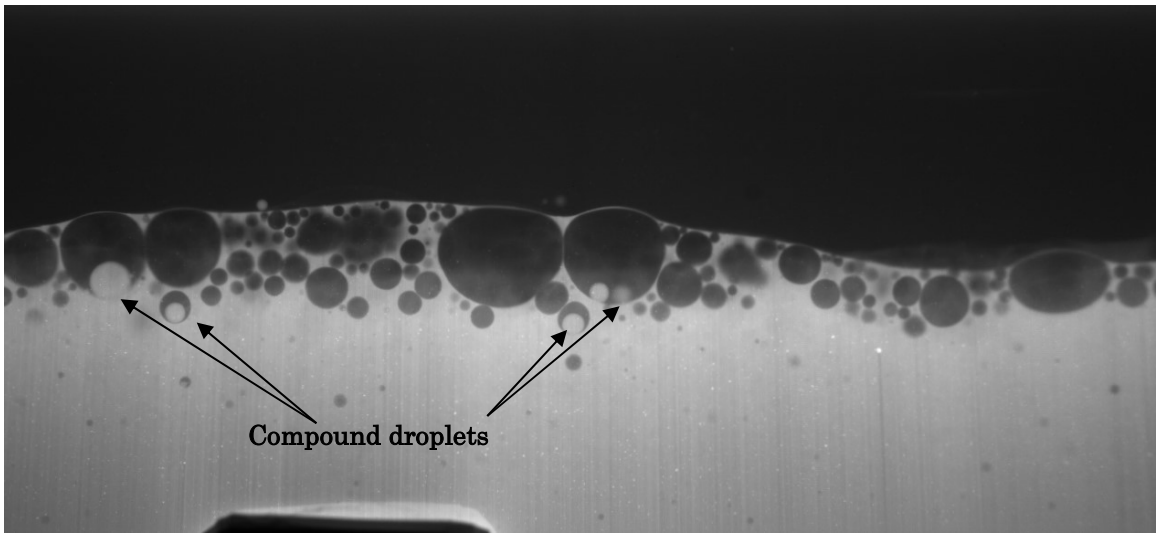


Figure 4.18 Compound droplets formed in an incoming stratified flow with droplets at the interface for a pipeline velocity of V_m = 0.8 m/s and an aqueous phase fraction of ϕ = 0.50

Whilst the jet created the complex compound droplets, simpler compound droplets were visible in the incoming stratified flows and are similar to the compound droplets seen in the work of Morgan (2012). In this experimental campaign, the compound droplet occurred in the incoming stratified flows when the pipe velocity was high enough to form a large number of droplets at the interface, i.e. when $V_m \geq 0.4$ m/s. The number and complexity of these compound droplets were seen to increase with the pipe velocity and aqueous phase fraction where the highest number of compound droplets were seen when

the velocity was V_m = 0.8 m/s and aqueous phase fraction was ϕ = 0.50, see Figure 4.18. Indicating that the formation of these droplet increases with the level of mixing.

Unfortunately, it was not possible to establish if these compound droplets formed at all scales due to insufficient image resolution. Therefore, the effect of these compound droplets on settling velocities is an area for future investigation.

4.5 Flow pattern maps

The observation of the experimental images allows the development of flow pattern maps like those suggested by Trallero et al. (1997) and Trallero (1997). These flow pattern maps can be grouped into different regimes to evaluate the level of liquid-liquid mixing, where it is important to remember that liquid-liquid mixing involves creating a homogenous distribution of the phases throughout the cross-section of the pipe.

4.5.1 Flow pattern map classifications

The regimes defined for our purposes are listed as follows;

- *Dispersions*

Many of the experimental cases have an aqueous phase fraction that is below 0.2. When these flows become sufficiently well mixed by the jets, the resulting flows become water-in-oil dispersions (WOD) like those presented in Figures 4.11(g, ii) and 4.11(g, iii).

- *Complex mixtures*

The resulting mixed flows can be highly complex when the aqueous phase fraction of the mixture ranges between 0.3 – 0.5. These complex flows have many zones that can be either water-continuous or oil-continuous, and these zones undergo rapid temporal and spatial variation and mergers, an example of such a flow is shown in Figure 4.19. While these flows are mixed they are not a fine dispersion of one phase within another. These complex mixtures are labelled M.

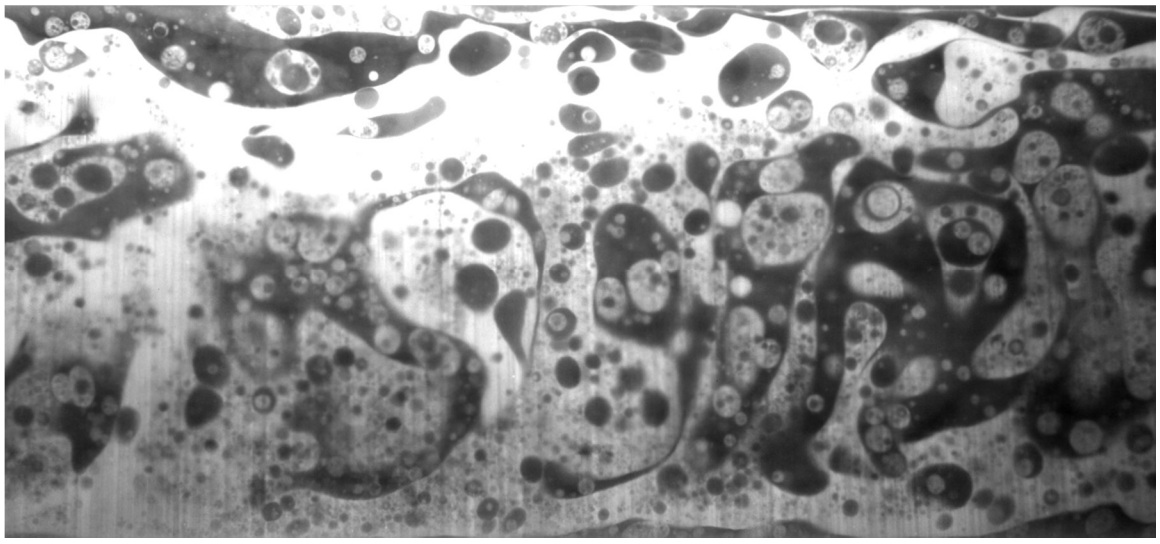


Figure 4.19 A U-jet with a velocity of V_j = 8 m/s interacting with an incoming stratified flow with a velocity of V_m = 0.8 m/s and an aqueous phase fraction of ϕ = 0.50

- ***Stratifying Dispersions***

The flows created by the jets can be highly unstable due to the presence of relatively large droplets that undergo rapid re-stratification, see Figure 4.11(e, iii). These flows are considered to be transitional and in the process of stratifying when a water layer is beginning to form underneath the water-in-oil dispersion. These stratifying flow are labelled as RSW WOD.

- ***Unmixed stratified flows***

All the remaining flows regimes contain a stratified layer or layers and are therefore grouped into an unmixed category. These unmixed/stratified flows are labelled U.

4.5.2 Flow pattern maps for U-jet

The flow pattern maps for the upward jet (U-jet) are presented in Figures 4.20, 4.21 and 4.22, corresponding to downstream positions from the jet of $L = 1\ D$, $L = 4\ D$ and $L = 10\ D$, respectively. The inlet velocity is on the x-axis, the aqueous phase fraction is on the y-axis, and the jet velocity changes from 4 m/s, to 8 m/s and then to 12 m/s as you go from top to bottom.

Analysis of these plots highlights three conditions where mixing is found to be insufficient. Firstly, conditions exist where there is insufficient jet energy to create a

mixed system for a given aqueous phase fraction and mixture velocity regardless of axial distance from the jet. These conditions of insufficient mixing were only found to occur in the slowest velocity 4 m/s jet and only occurred at the highest aqueous phase fractions and the lowest crossflow velocity. These test points were found to be located above the solid line in the top left of Figures 4.20(top), 4.21(top) and 4.22(top).

Secondly, conditions exist where mixing was unstable due to the presence of large droplets, as a result, these unstable flows quickly begin to separate and re-stratify. These re-stratifying flows are located in the top left above the dashed line in Figures 4.21(top) and 4.22(top, middle). The flow pattern maps demonstrate that the number of re-stratifying test points increase with the axial distance from the jet and aqueous phase fraction and decrease with crossflow and jet velocities.

Thirdly, we have a condition where the crossflow velocity is high enough that a jet has insufficient time for mixing to occur, but these flows become mixed as the flow moves further downstream from the jet. These initially unmixed regions can be seen to the right of the dotted line in Figure 4.20(top, middle). Contrasting these with Figure 4.21 (top, middle) several test points with mixture velocities between 0.4 and 0.6 m/s can be seen to have changed from unmixed to water in oil dispersions. The flow pattern maps indicate that the number of test points that have insufficient time to mix increase with an aqueous phase fraction and crossflow velocity while decreasing with jet velocity and axial distance from the jet.

The flow pattern maps from Figures 4.20, 4.21 and 4.22 are combined in Figure 4.23 for all downstream locations L, where on the x- and y-axis there is the jet velocity ratio and the aqueous phase fraction, respectively. While both dimensionless parameters impact the degree of mixing they do so in a complex way resulting in some overlap. Even still, the mixing in Figure 4.23 generally increases at a given downstream location when the velocity ratio increases or the aqueous phase fraction decreases.

Figure 4.24 plots the same data with the mixture residence time (L/V_{mj}) on the x-axis and the aqueous phase fraction (ϕ) on the y-axis for the three jet velocity of V_j = 4 m/s, 8 m/s and 12 m/s. Again there is some overlap but generally increasing the jet velocity increases the mixing and extends the time and hence distance over which a flow is mixed for a given aqueous phase fraction.

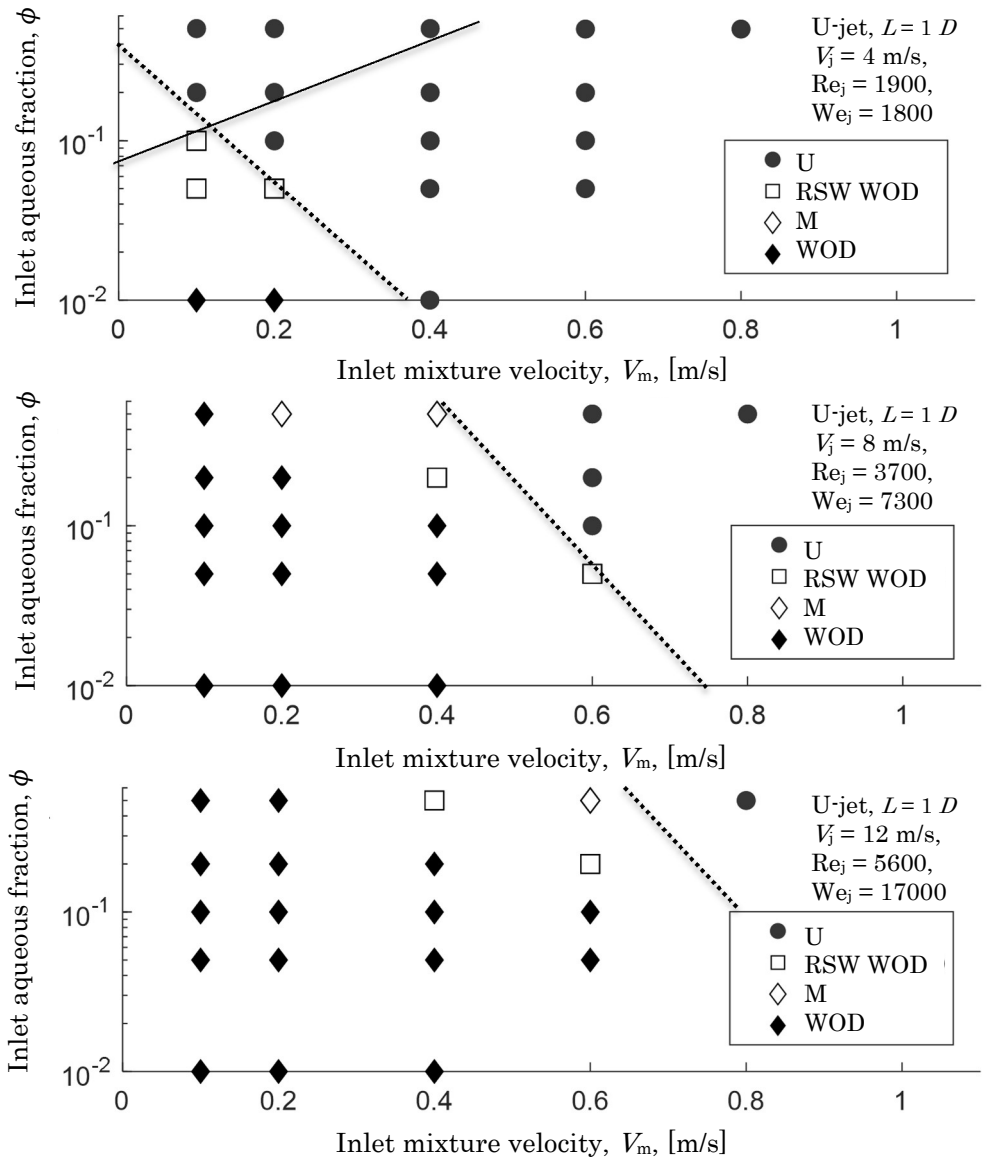


Figure 4.20 Flow pattern map from mixing with the U-jet at $L = 1\ D$ showing inlet mixture velocity versus phase fraction. Top: V_j = 4 m/s, Re_j = 1900, We_j = 1800; middle: V_j = 8 m/s, Re_j = 3700, We_j = 7300; bottom: V_j = 12 m/s, Re_j = 5600, We_j = 17000.

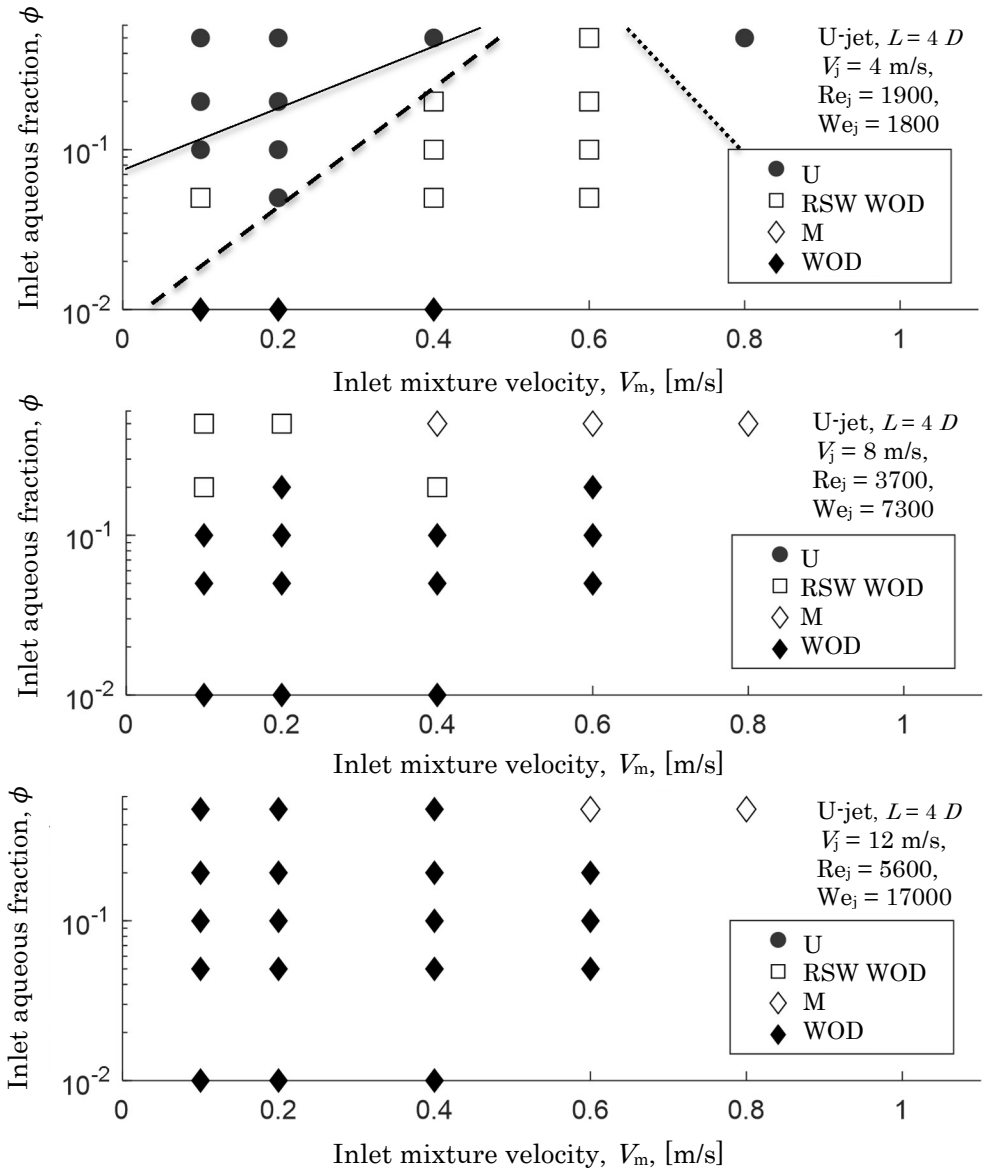


Figure 4.21 Flow pattern map from mixing with the U-jet at $L = 4\ D$ showing inlet mixture velocity versus phase fraction. Top: V_j = 4 m/s, Re_j = 1900, We_j = 1800; middle: V_j = 8 m/s, Re_j = 3700, We_j = 7300; bottom: V_j = 12 m/s, Re_j = 5600, We_j = 17000.

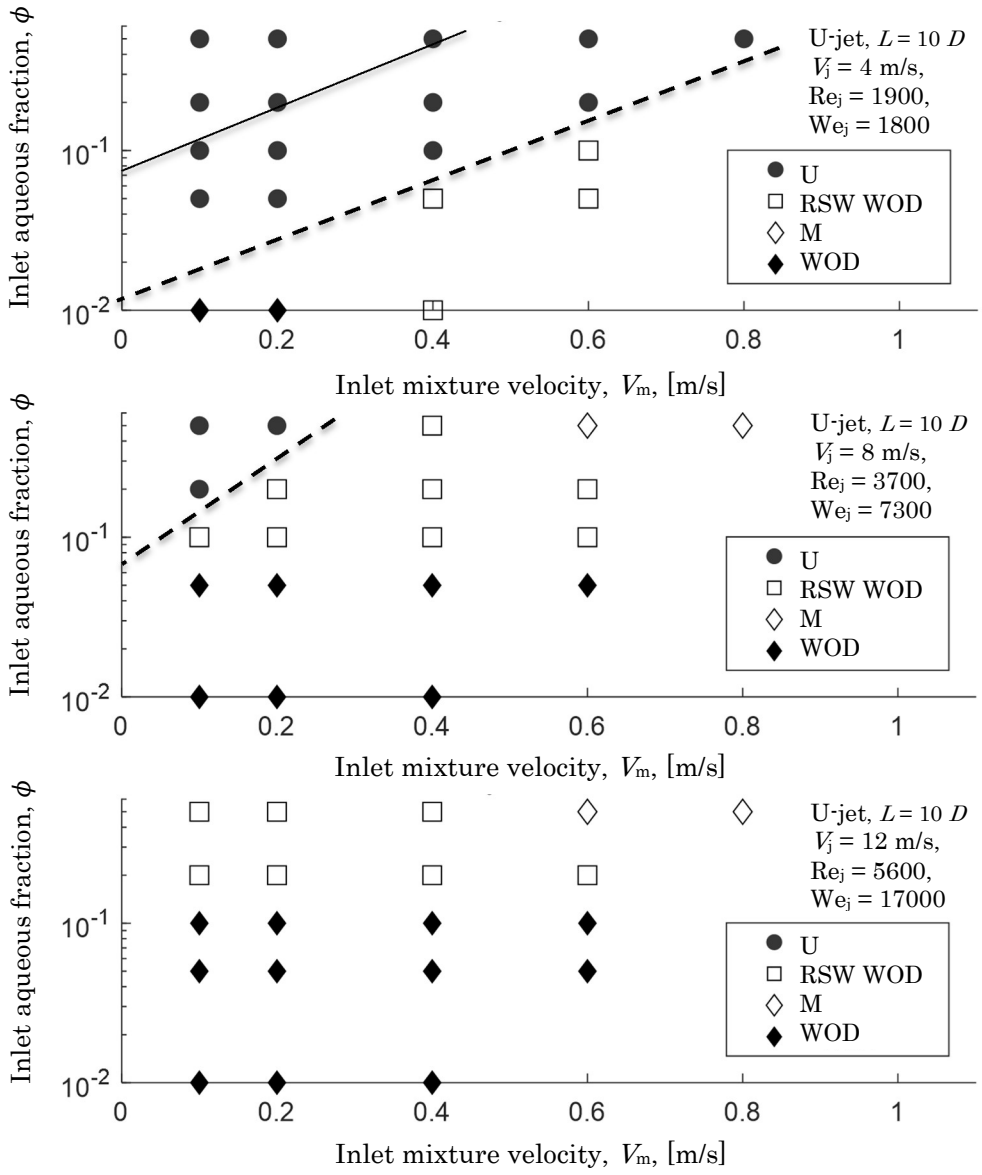


Figure 4.22 Flow pattern map from mixing with the U-jet at $L = 10\ D$ showing inlet mixture velocity versus phase fraction. Top: $V_j = 4$ m/s, $Re_j = 1900$, $We_j = 1800$; middle: $V_j = 8$ m/s, $Re_j = 3700$, $We_j = 7300$; bottom: $V_j = 12$ m/s, $Re_j = 5600$, $We_j = 17000$.

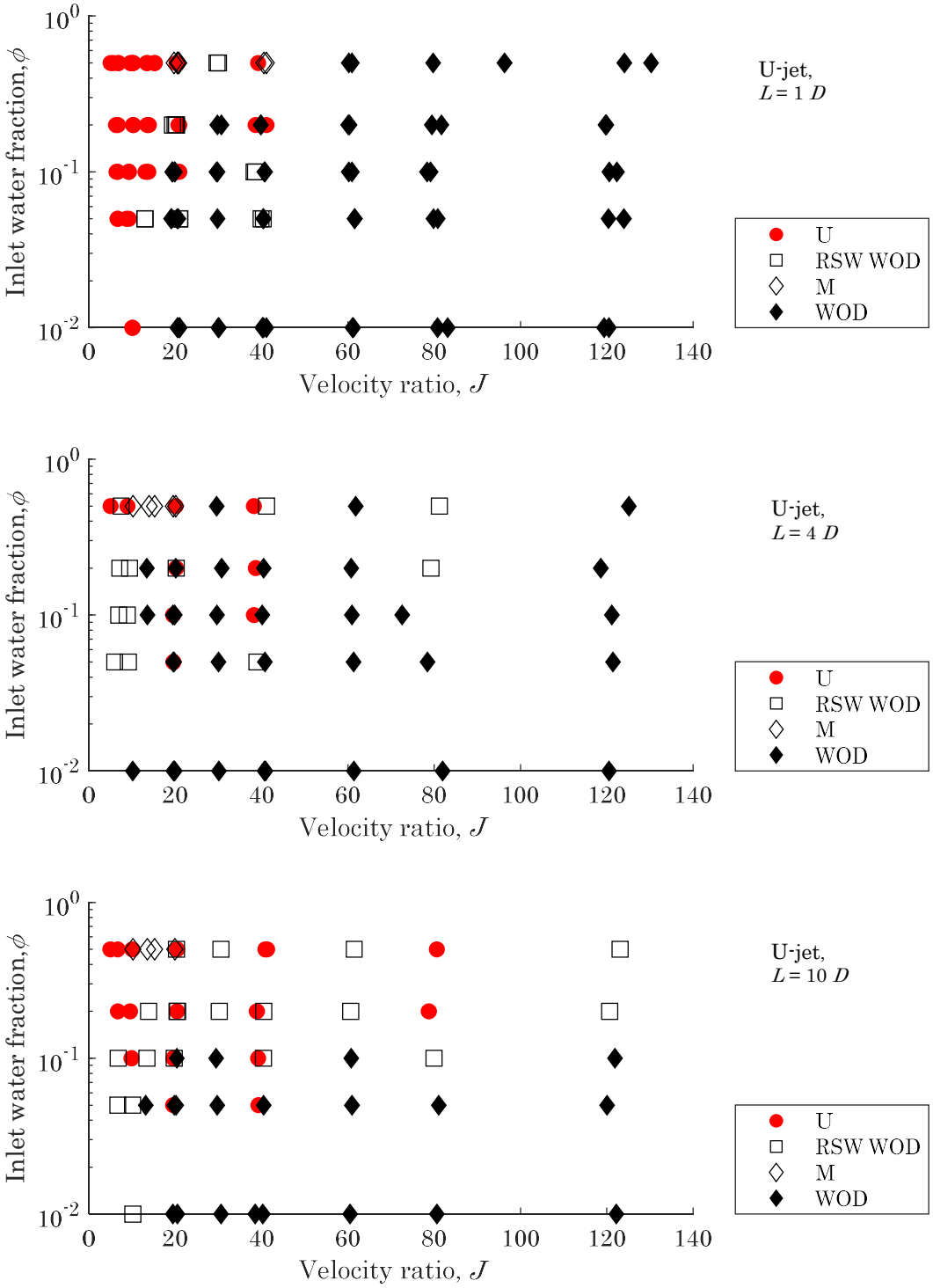


Figure 4.23 Flow pattern map from mixing with the U-jet showing velocity ratio versus phase fraction. Top: V_j = 4 m/s, Re_j = 1900, We_j = 1800; middle: V_j = 8 m/s, Re_j = 3700, We_j = 7300; bottom: V_j = 12 m/s, Re_j = 5600, We_j = 17000.

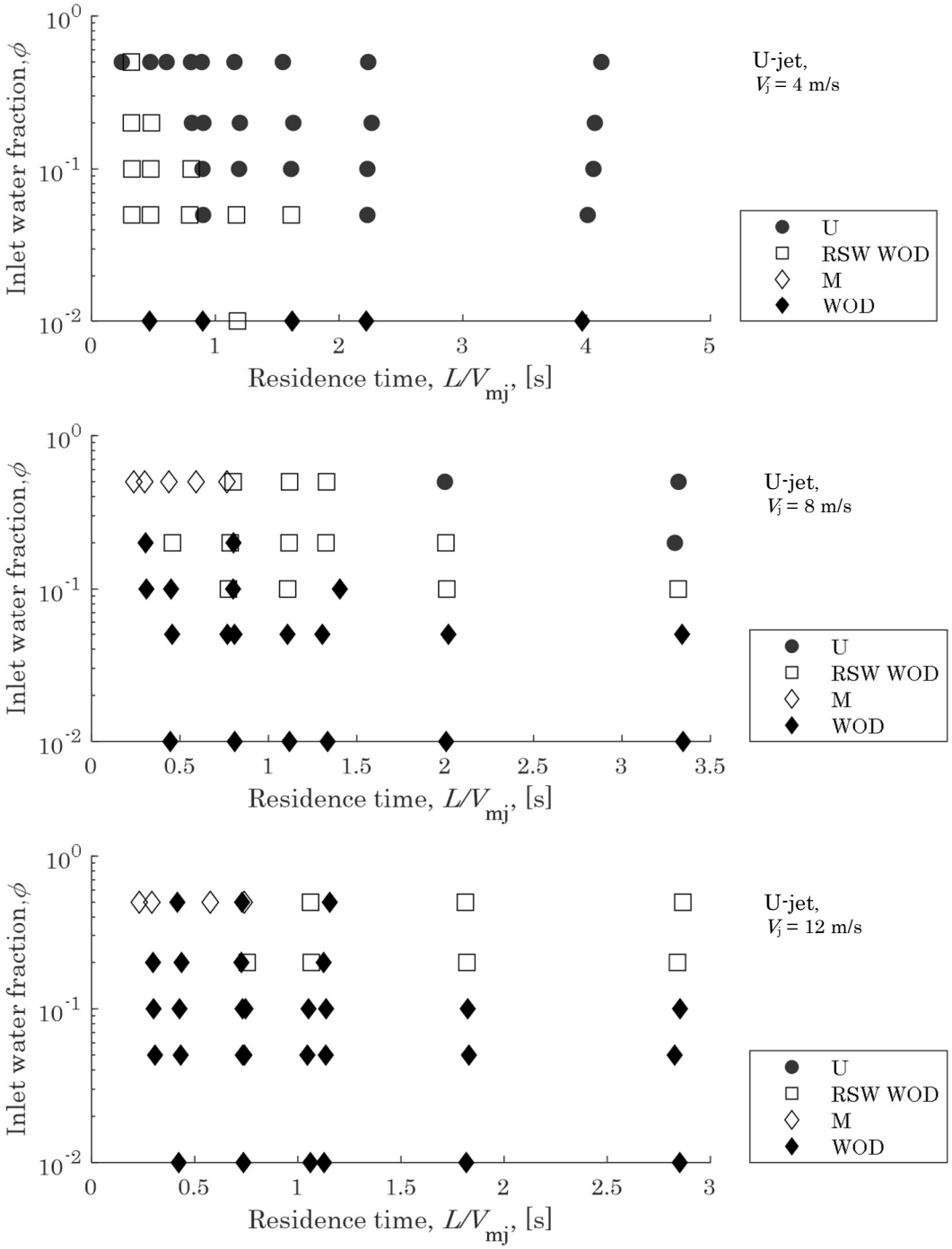


Figure 4.24 Flow pattern from mixing with the U-jet showing residence time versus phase fraction. Top: V_j = 4 m/s, Re_j = 1900, We_j = 1800; middle: V_j = 8 m/s, Re_j = 3700, We_j = 7300; bottom: V_j = 12 m/s, Re_j = 5600, We_j = 17000.

4.5.3 Comparison of jet types

Flow pattern maps for the forward jet (F-jet) and the twin V-jet at a distance of $L = 10\ D$ downstream are presented in Figure 4.25 and Figure 4.26, these can be compared with the flow pattern maps of the upward jet (U-jet) in Figure 4.22.

The F-jet (Figure 4.25) and U-jet (Figure 4.22) are comparable although the F-jet appears to have a marginally poorer level of mixing, which is highlighted by the larger number of unmixed flow conditions in dots where the two flow maps overlap. Whereas the V-jet, Figure 4.26 has a higher fraction of water-in-oil dispersions (WOD) which suggests it provides an increased level of mixing than that of either the F-jet or U-jet. The apparent better mixing of the V-jet is notwithstanding having the Weber and Reynolds numbers that are 70% of the F-jet or U-jet. However, it should be remembered that the V-jet has two smaller jets with the same overall flow as the F-jet and U-jet. These smaller jets have a greater surface area at the expense of an 80% increase in pressure loss and power requirements.

The increase in power requirement for the V-jet means a larger pump motor is required compared with that of the F-jet or U-jet to maintain the mixing advantage. Alternatively, the level of mixing of the V-jet could be reduced to match that of the U-jet by lowering the flowrate to the V-jet. This could potentially lead to smaller installation pipework and fittings thereby reducing the initial cost of the equipment. Even still, the advantage of the V-jet does not appear to be so great and the running costs of this nozzle are still likely to be higher for the operator. Importantly, no attempt was made to optimize the pressure losses through the nozzles. Therefore, more work is needed to establish if the advantages of the V-jet could be maintained through careful optimisation of the nozzle design to reduce pressure losses and power requirements.

Importantly, none of the experimental test cases ever created dispersions that were so fine and tight that the liquid-liquid separator was unable to separate the two phases on a continual operating basis. This is an important consideration for the industry as it indicates that overmixing was not occurring and that the velocity of the jets could have been increased further to create finer dispersions.

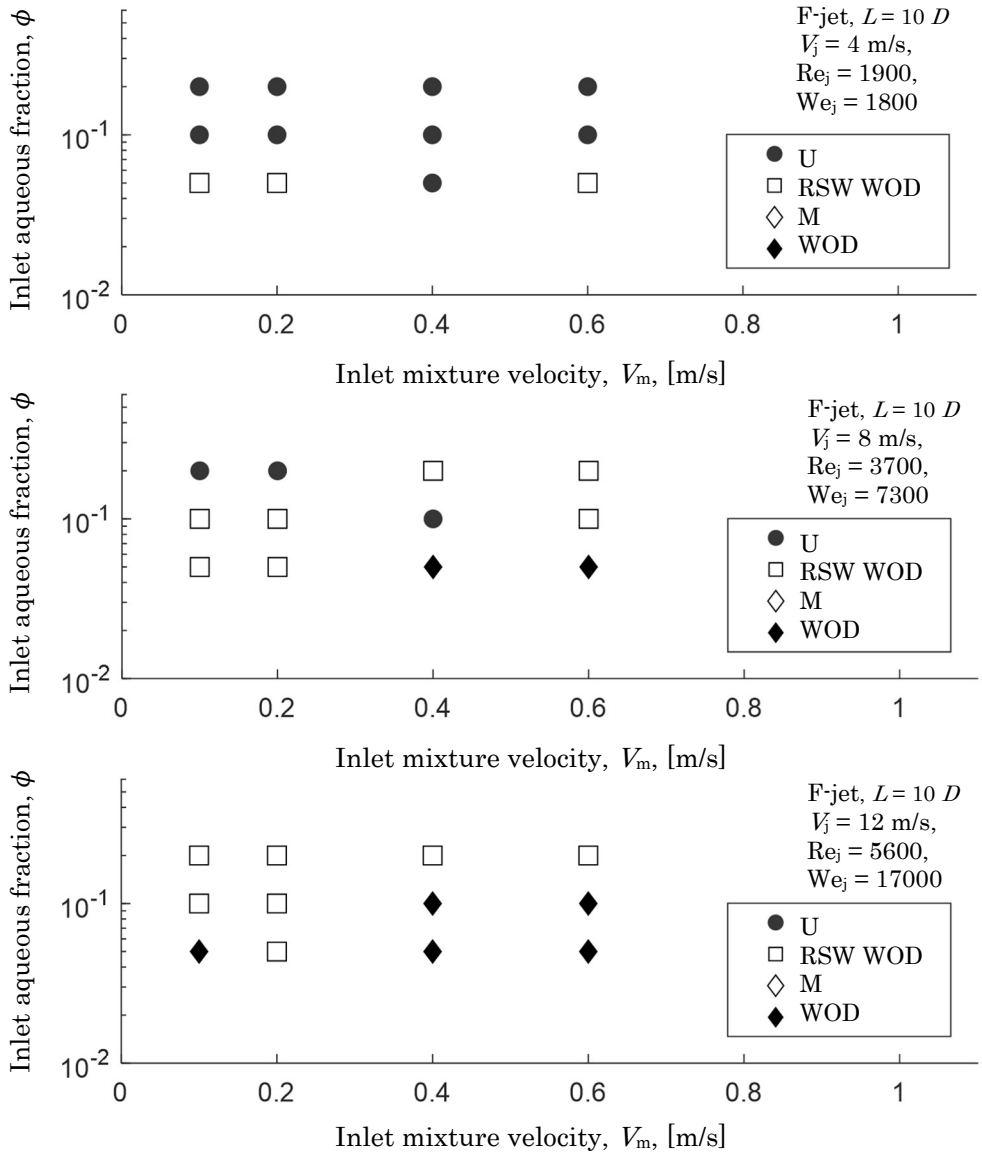


Figure 4.25 Flow pattern map from mixing with the F-jet at $L = 10\ D$ showing inlet mixture velocity versus phase fraction. Top: V_j = 4 m/s, Re_j = 1900, We_j = 1800; middle: V_j = 8 m/s, Re_j = 3700, We_j = 7300; bottom: V_j = 12 m/s, Re_j = 5600, We_j = 17000.

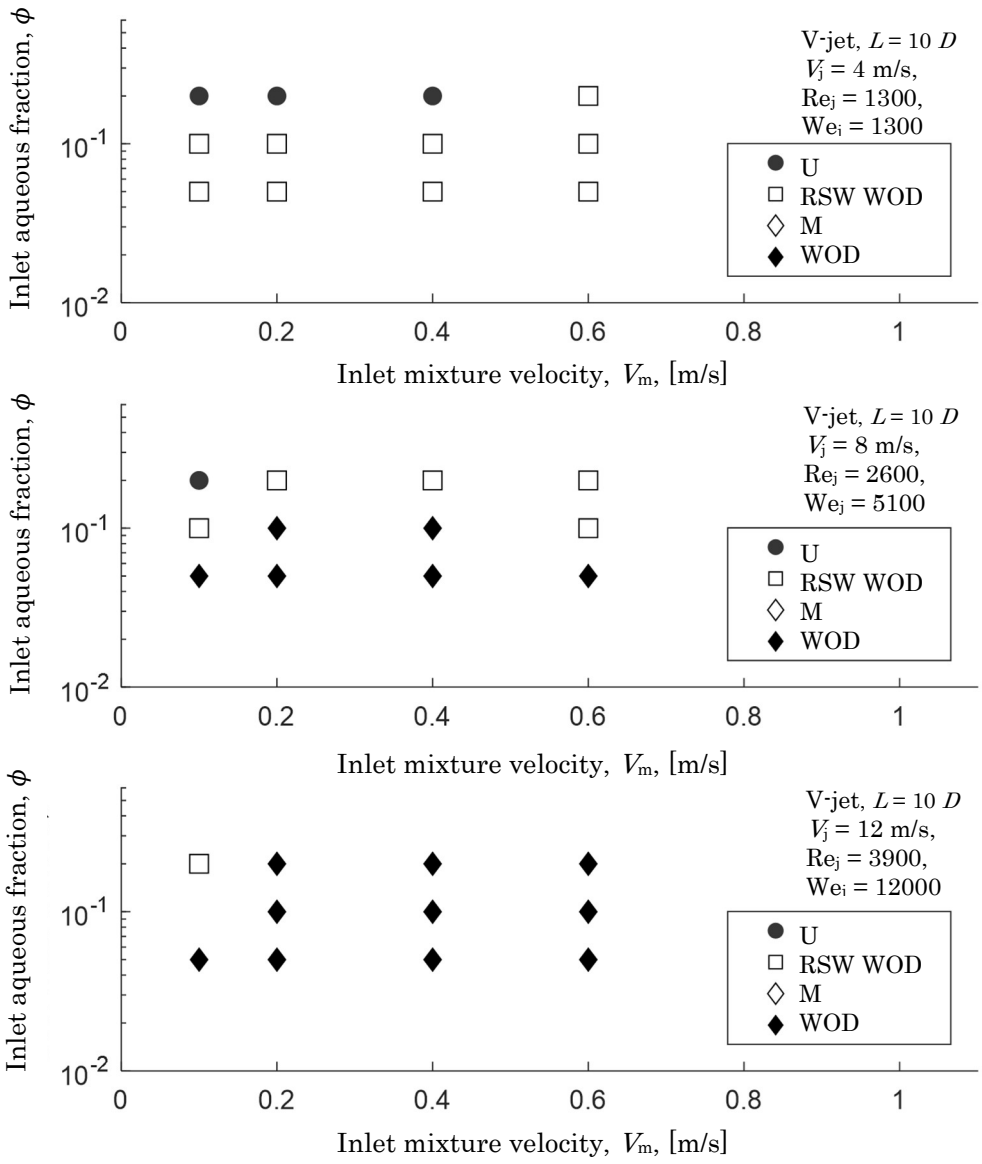


Figure 4.26 Flow pattern map from mixing with the V-jet at $L = 10\ D$ showing inlet mixture velocity versus phase fraction. Top: V_j = 4 m/s, Re_j = 1300, We_j = 1300; middle: V_j = 8 m/s, Re_j = 2600, We_j = 5100; bottom: V_j = 12 m/s, Re_j = 3900, We_j = 12000.

4.6 Summary

This chapter presented the measurements of the experimental liquids, pressure drops, incoming interface heights, phenomenological observations and flow pattern maps. The key point from this chapter are:

- Observations of the flows indicate that the level of mixing increases as the aqueous phase fraction, ϕ, decreases, and the jet velocity, V_j, increases relative to the crossflow velocity V_m. The level of mixing tends to increase with the jet velocity ratio at a given axial position. Increasing the crossflow reduces the residency time which, in turn, increases the distance at which a flow remains mixed. In general, this distance increases with jet velocity and decreases with aqueous phase fraction.
- Stratification of the resulting downstream flows from the jet is frequently visible, especially at ten pipe diameters. A stratified layer rapidly forms for the lowest jet velocities and highest aqueous phase fractions.
- Comparing the three jet types the flow pattern maps indicate that the V-jet was the best mixer, producing the greatest number of mixed flow regimes while the F-jet is marginally poorer than that of the U-jet. However, the power requirements of the V-jet are 80% higher than that of the U-jet, which counterbalances its mixing efficiency. Further work is required to optimize the mixing configuration in terms of choice of jets and operating conditions.

Additional points of interest include:

- Incoming stratified flows have clear visible interfaces between the oil and aqueous phase. However, objects out of the plane can be seen as dim shadows due to the diffusion of laser light by the ETFE pipe wall.
- The incoming crossflows range from laminar to turbulent flow regimes. The lower viscosity of the aqueous phase results in it transitioning to a turbulent flow regime at lower crossflow velocities compared to the oil phase.
- The interface height and pressure drops of the incoming flows match well with that predicted by the two-fluid model of Taitel and Dukler et al. (1976).
- The pressure losses and power usage of the U-jet and F-jet are similar, where the F-Jet is ≈ 10% greater. In contrast, the pressure losses and power usage of the V-jet are ≈ 80% greater than the U-jet.

- Comparison of the pressures losses between the first two differential pressure transmitters and the two-fluid model suggests the incoming flows are developed by the time they reach the measurement section.
- The jet Reynolds numbers (Re_j) are in the range of 1900 to 7600 while the jet Weber numbers (We_j) are in the range of 1800 to 29000. This indicates that upon leaving the exit of the jet nozzle, the jets are in the upper part of the "First Wind Induced" and the bottom of the "Second Wind Induced" breakup regime. However, droplets are always much smaller than the exit of the jet nozzle which suggests the jets are always in the "Second Wind Induced" breakup regime.
- The jet is turned by the momentum of crossflow into the downstream axial direction. The degree with which the jet is turned is dependent on the momentum of the jet to that of the crossflow.
- The aqueous phase is seen to be lifted, stretched and broken up downstream of the jet. This lifted aqueous phase can then be broken up by the jet flows as they travel around the pipe's circumference following the jets impingement on the top wall of the pipe. This creates a secondary zone of jet interaction downstream from the jet nozzle exit.
- Kelvin-Helmholtz instabilities create much of the mixing near to the jets while creating the smallest droplet sizes.
- A recirculation zone can form upstream of the jet and towards the top of the pipe. The recirculation zone only forms when the momentum of the jet is high enough compared to that of the crossflow for the jet to impinge upon the top of the pipe.
- Complex compound droplets are found to exist within the flow. This indicates that the calculated pure droplet settling rate will be higher than the average droplet settling rate due to the lower density difference of the compound droplets.
- Flow pattern maps reveal that (i) there are downstream positions where the jet has had insufficient time to mix; (ii) downstream stratification of the flows can occur rapidly; (iii) conditions exist where the jet has insufficient energy to mix.
- The liquid-liquid separator had no problem separating the two liquids continuously for all the experimental conditions. This demonstrates that overmixing of two liquids was not occurring and that the velocity of the jet could have been increased if further mixing was required.

Chapter 5

Mixing characteristics: Phase Concentrations

This chapter presents the PLIF results for mixing and includes the resultant phase concentration profiles in Section 5.1 and the industrial mixing parameter (C_1/C_2) in Section 5.2. The effect of distance, crossflow velocity, inlet aqueous phase fraction, residence time and jet type are presented and analysed. Importantly, the measurement plane formed by the laser sheet is centred along the axis of the pipe and passes from the top to the bottom of the pipe. Therefore, the results contained within this chapter are all based upon this 2-dimensional measurement plane.

5.1 Concentration profiles

This section presents the experimental PLIF measurements of the aqueous phase concentration profiles. These concentration profiles provide a quantitative measurement of the phase distributions in the centre plane. The measurements close to the jet provide insights into the overall dispersal and mixing of the phases in the liquid-liquid stratified crossflows. The measurements downstream, on the other hand, provide insights into the subsequent separation of the phases that occurs once the jet interaction has decayed sufficiently.

5.1.1 Low mixing levels and varying phase fractions

Figure 5.1 presents the aqueous phase fraction at $L = 10\ D$ downstream of an upward U-jet with a velocity of $V_j = 4$ m/s interacting with a crossflow of $V_m = 0.4$ m/s for three

test cases of crossflows with aqueous phase fractions of $\phi = 0.05$, $\phi = 0.10$ and $\phi = 0.20$, resulting in the downstream mixture phase fractions of $\phi_{mj} = 0.05$, $\phi_{mj} = 0.09$ and $\phi_{mj} = 0.19$, respectively. These three test cases all have low levels of mixing and a high degree of separation. They demonstrate that the aqueous phase height increases with an increase in the incoming aqueous phase fraction. In addition, it shows that at ten diameters downstream from the jet the amount of aqueous phase that is entrained within the oil increases as the aqueous phase fraction increases.

Towards the bottom of the pipe's wall, the aqueous phase fraction decreases, three effects contribute to this. The first is a lift force which causes moving droplets to migrate away from the pipe wall as discussed in Voulgarpoulos (2019). The second effect is the high contact angle of 144° for the aqueous phase droplets on the ETFE pipe wall, which causes droplets to bead-up and sit away from the pipe wall. The third effect is an experimental bias which is caused by the slight dimming of the laser sheet's power from the top to the bottom of the pipe. The dimming occurs when the laser sheet encounters the aqueous phase where some of the laser light is absorbed by the Eosin Y dye so reducing the intensity of the laser.

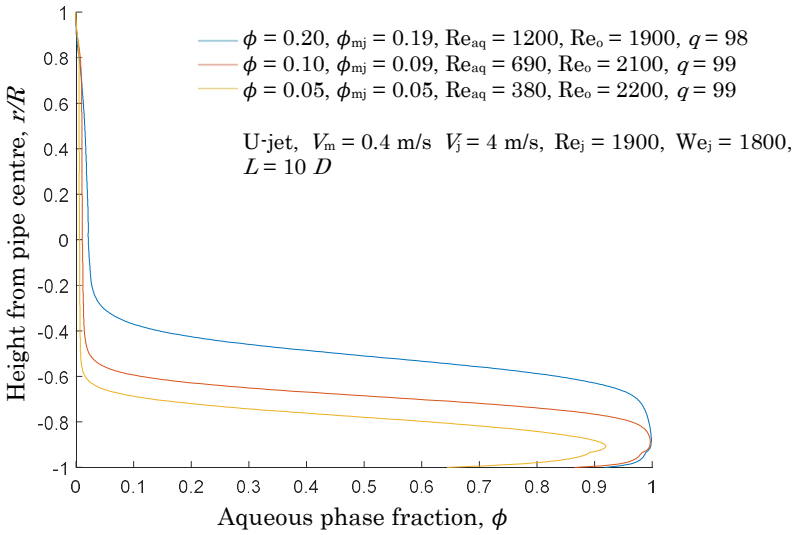


Figure 5.1 Concentration profiles at $L = 10\ D$ for a U-jet with a velocity of $V_j = 4$ m/s, $Re_j = 1900$ and $We_j = 1800$ interacting with crossflows with aqueous phase fractions of $\phi = 0.05$, $\phi = 0.10$ and $\phi = 0.20$ and a velocity of $V_m = 0.4$ m/s.

5.1.2 Varying jet velocities and phase fractions

Examining experimental cases with the same inlet conditions and varying the jet velocity provides insights into the effect the jet velocity has on the mixing processes. Figure 5.2(top) presents three flows with a crossflow velocity of V_m = 0.4 m/s and an inlet aqueous phase fraction of ϕ = 0.20, at a distance of L = 10 D downstream from a U-jet with velocities of V_j = 4, 8 and 12 m/s. As the jet velocity increases the height of the stratified aqueous phase layer decreases while at the same time the aqueous phase distribution above the stratified layer increases. Although, the aqueous phase fraction at the bottom of the pipe never decreases to the vertical average. The aqueous phase fraction at the top of the pipe becomes higher than the pipe average once the jet velocity reaches V_j = 12 m/s.

Figure 5.2(middle) presents seven flows with a crossflow velocity of V_m = 0.4 m/s, and a lower inlet aqueous phase fraction of ϕ = 0.10, at a distance of L = 10 D downstream from the U-jet with velocities of V_j = 4, 6, 8, 10, 12, 14 and 16 m/s. In these lower aqueous phase fraction cases the stratified layer again decreases with increasing jet velocity. However, for all jet velocities, there is a higher fraction of the aqueous phase at the bottom of the pipe than the average of each experimental case. Therefore, we can conclude that for these jet velocities either some of the aqueous phase is never dispersed into the oil phase or that the aqueous phase has already partially stratified. Given the distance is ten pipe diameters from the jet exit and the crossflow is 0.4 m/s this would mean that the droplets would have to fall to the bottom of the pipe within less than 1.25 s.

The profiles in Figure 5.2(middle) again show that there is an increase in the aqueous phase at the top of the pipe as the jet velocity increases. This indicates that the jet maybe lifting some of the aqueous-phase to the top of the pipe but it is failing to distribute it evenly throughout the pipe. The aqueous-phase fractions do not all overlap and this may be in part explained by the smallest droplets becoming sub-pixel size causing some of the aqueous phase to become lost into the background noise. This effect becomes more significant as the jet velocity increases, and the average droplet size reduces. In particular, the jet velocities of 14 m/s and above appear to be missing some of the aqueous phase fraction in Figure 5.2(middle).

Figure 5.2(bottom) presents a further six flows with a crossflow velocity of V_m = 0.4 m/s, and a lower inlet aqueous phase fraction of ϕ = 0.05, at a distance of

$L = 10\ D$ downstream of the U-jet with velocities of V_j = 4, 6, 8, 10, 12, and 14 m/s. The stratified layer again decreases with increasing jet velocity. Once the jet velocity reaches V_j = 8 m/s the proportion of the aqueous phase at the top and bottom of the pipe is similar, however, the middle section of the pipe has a lower aqueous phase fraction. While for jet velocities higher than V_j = 8 m/s the aqueous phase fraction becomes inverted with a higher fraction at the top of the pipe. At this lower aqueous phase fraction, the loss of the aqueous phase to the background becomes significant at a jet velocity of 10 m/s, which is a lower velocity than in Figure 5.2(middle).

In summary, an increase in jet velocity and Weber number leads to increases in the level of mixing due to the increase in energy into the flow. Increasing the aqueous phase fraction leads to a decrease in mixing even for the same jet velocity and Weber number. The decrease in mixing as the aqueous fraction is increased occurs due to the greater droplet surface area that is required to achieve the same level of mixing. Droplet surface area is created when capillary forces, due to the interfacial tension between the oil and the aqueous phases, are overcome, which, in turn, requires an increase in energy from the jet.

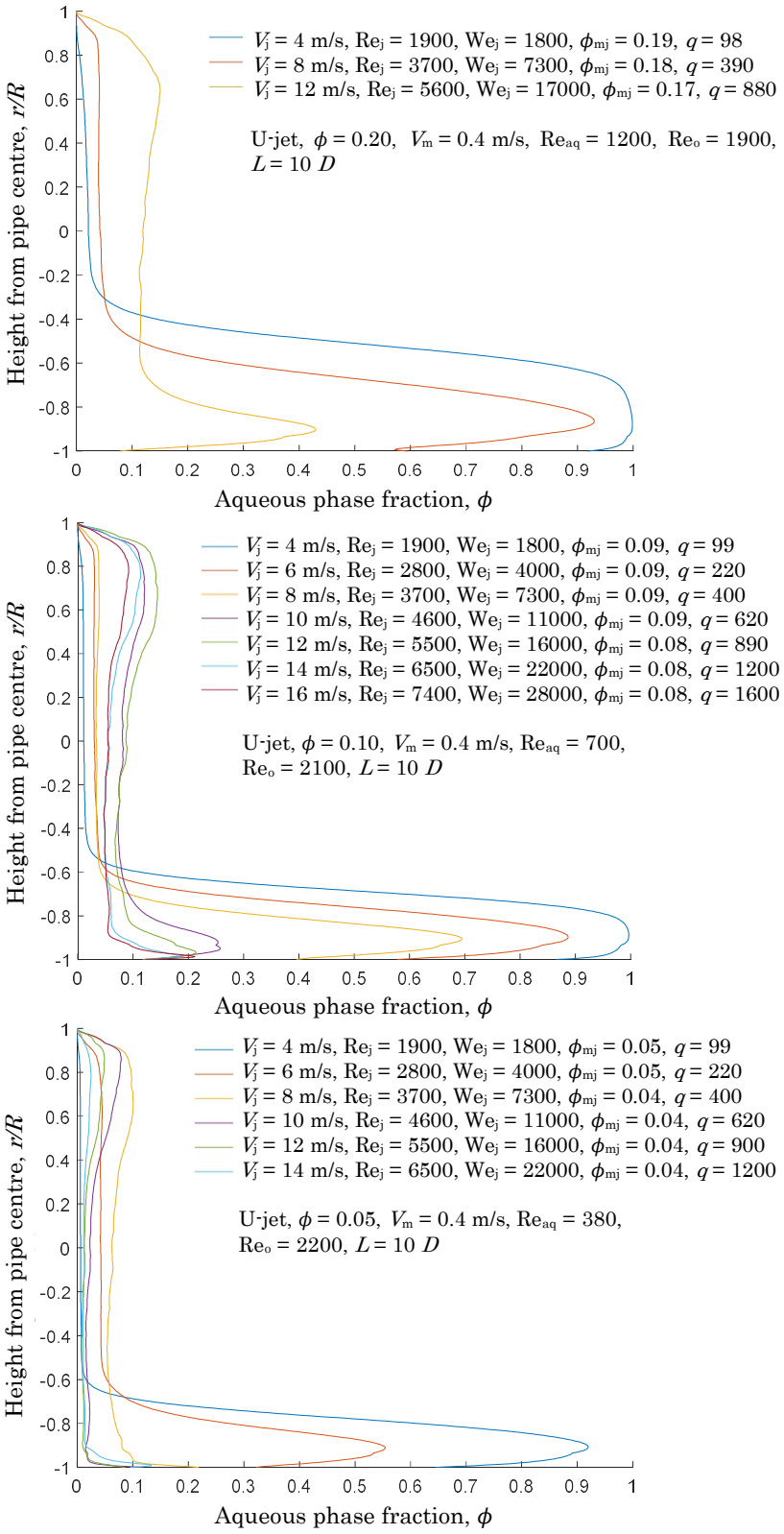


Figure 5.2 Concentration profiles at $L = 10\ D$ for U-jet with velocities of V_j = 4 m/s, V_j = 6 m/s, V_j = 8 m/s, V_j = 10 m/s, V_j = 12 m/s, V_j = 14 m/s and V_j = 16 m/s interacting with a crossflow with varying aqueous phase fraction and a velocity of V_m = 0.4 m/s. Top: ϕ = 0.20, Re_{aq} = 1200 and Re_o = 1900; Middle: ϕ = 0.10, Re_{aq} = 700 and Re_o = 2100; Bottom: ϕ = 0.05, Re_{aq} = 380 and Re_o = 2200.

5.1.3 Varying crossflow velocities and phase fractions

The effects of varying the crossflow velocity at a distance of $L = 10\ D$ with a U-jet with a velocity of $V_j = 4$ m/s, are presented in Figures 5.3 where the input aqueous phase fraction are $\phi = 0.20$, $\phi = 0.10$ and $\phi = 0.05$, corresponding top, middle and bottom, respectively. In cases where the crossflow velocity is above $V_m = 0.2$ m/s, it is apparent that the aqueous phase is present throughout the height of the pipe. While for lower crossflow velocities at or below $V_m = 0.2$ m/s, the sharp oil to aqueous phase transition indicates the flow s have had the time to stratify significantly.

A comparison of the $V_m = 0.1$ m/s and $V_m = 0.2$ m/s crossflows shows that there are small differences in the height in the oil-aqueous-phase transition layer which is dependent on the crossflow. This occurs because while the aqueous phase fractions of the inlet crossflows, ϕ, are the same, the aqueous phase fractions following mixing with the jet, ϕ_{mj}, are lower in the slower crossflow where the jet has contributed proportionally more oil to the resultant mixture. Given the mixture's aqueous phase fraction decreases as crossflow velocity decreases, the interface height would also be expected to decrease.

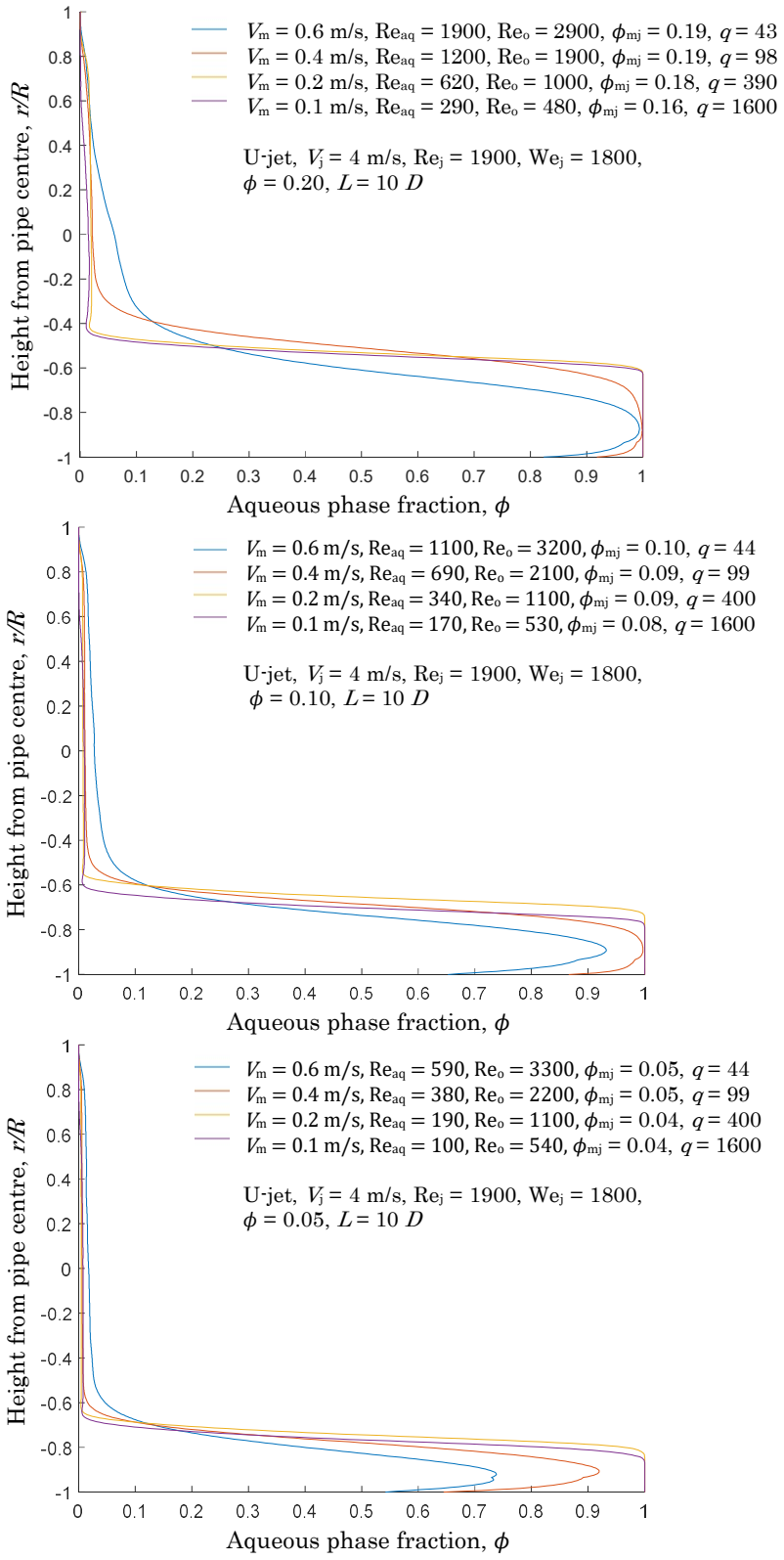


Figure 5.3 Concentration profiles at $L = 10\ D$ for a U-jet with a velocity of $V_j = 4$ m/s and $Re_j = 1900$, $We_j = 1800$ interacting with crossflows with varying aqueous phase fraction and velocities of $V_m = 0.1$ m/s, $V_m = 0.2$ m/s, $V_m = 0.4$ m/s and $V_m = 0.6$ m/s. Top: $\phi = 0.20$; Middle: $\phi = 0.10$; Bottom: $\phi = 0.05$.

The effect of increasing the jet velocity to V_j = 8 m/s on crossflows with an aqueous phase fraction of ϕ = 0.05 and velocities of 0.1 to 0.6 m/s are shown in Figure 5.4(middle). In all cases, the layer of stratification is reduced when compared with the lower jet velocity of V_j = 4 m/s in Figure 5.4(top). In addition, the vertical concentration increases further as the crossflow velocity increases until a crossflow of V_m = 0.4 m/s is reached, where again see an increase in concentration at the top of the pipe. As the crossflow increases to V_m = 0.6 m/s, the concentration profile starts to increase in the stratification layer at the bottom. This indicates that the 8 m/s jet does not have sufficient energy to break up and disperse the flows at these higher crossflows.

A further increase in the jet velocity to V_j = 12 m/s on crossflows with an aqueous phase fraction of ϕ = 0.05 and velocities of 0.1 to 0.6 m/s are presented in Figure 5.4(bottom). The stratification layer decreases further when compared with the lower jet velocity results of Figures 5.4(top, middle), while the vertical concentration increases further with increasing crossflow velocity. When the crossflow velocity reaches V_m = 0.4 m/s there is again an increase in concentration at the top of the pipe. However, in contrast to Figure 5.4(middle), Figure 5.4(bottom) does not see the stratification layer increase again indicating that the 12 m/s velocity jet retains sufficient energy for mixing even at the highest crossflow velocity.

In summary, increasing the crossflow velocity can maintain a dispersion by leaving a shorter duration for stratification. However, increasing the crossflow velocity decreases the amount of energy per unit mass and hence may result in a requirement to increase the jet velocity to maintain mixing.

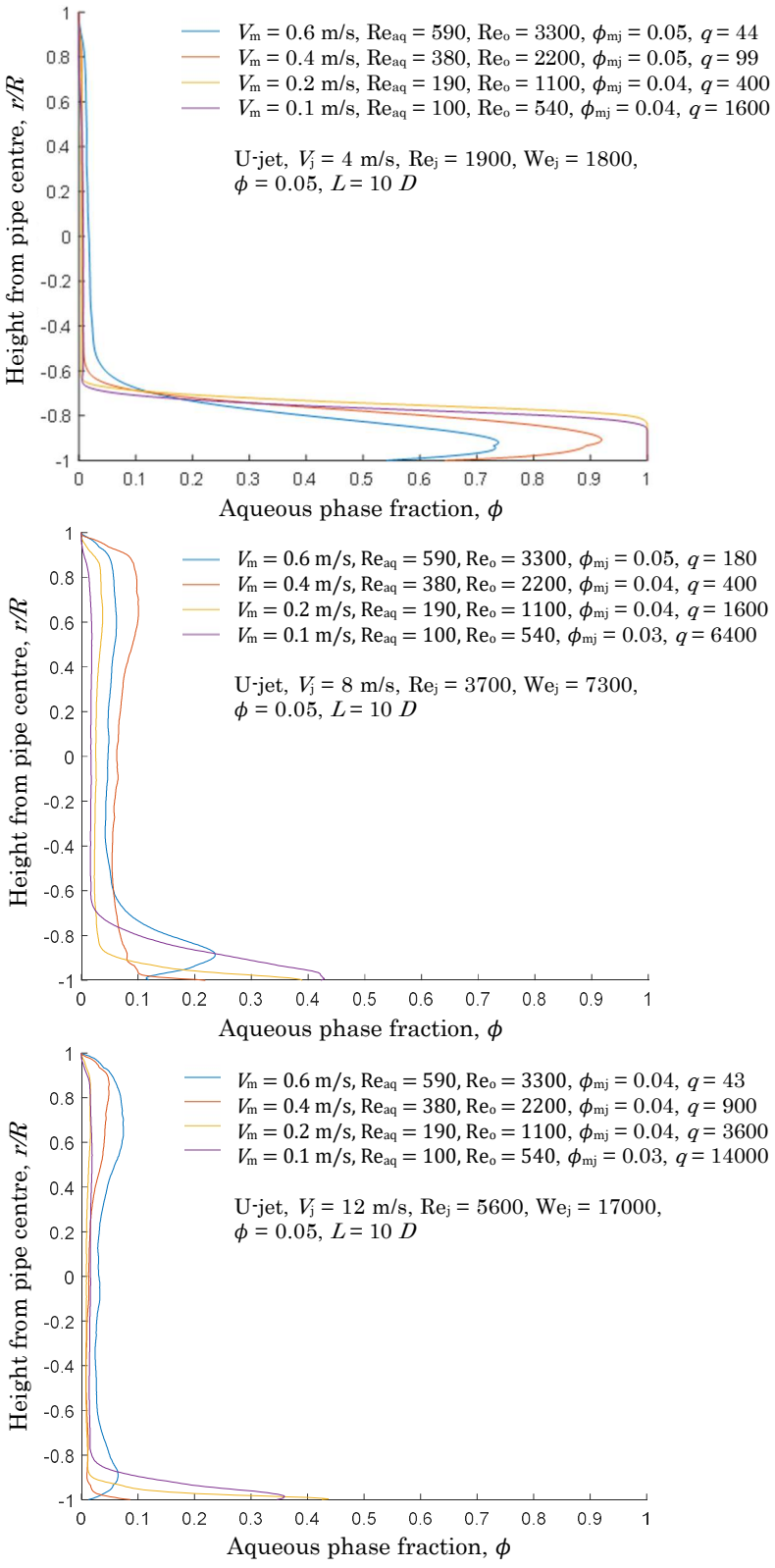


Figure 5.4 Concentration profiles at $L = 10\ D$ for a U-jet interacting with crossflows with an aqueous phase fraction of $\phi = 0.05$ and velocities of V_m = 0.1 m/s, V_m = 0.2 m/s, V_m = 0.4 m/s and V_m = 0.6 m/s. Top: V_j = 4 m/s, Re_j = 1900, We_j = 1800; Middle: V_j = 8 m/s, Re_j = 3700, We_j = 7300; Bottom: V_j = 12 m/s, Re_j = 5600, We_j = 17000.

5.1.4 Effect of varying distance from the jet

The effect of varying the distance from the jet between $L = 4\ D$ and $L = 10\ D$ are presented in the following pairs of figures. Figure 5.5(top, bottom) show the effects of a jet with a velocity of $V_j = 4$ m/s interacting with a crossflow with an aqueous fraction of $\phi = 0.10$ and velocities of $V_m = 0.6,\ 0.4,\ 0.2$ and 0.1 m/s crossflow. Figure 5.5(top) and Figure 5.5(bottom) are at a distance of $L = 4\ D$ and $L = 10\ D$, respectively. At a distance of $L = 4\ D$, crossflows that were at or below $V_m = 0.2$ m/s have already stratified, while the higher crossflow velocities of $V_m = 0.4$ and $V_m = 0.6$ m/s contain partially stratified mixtures. Once the flows reach a distance of $L = 10\ D$ all crossflows are stratified and have a clearly defined interface layer.

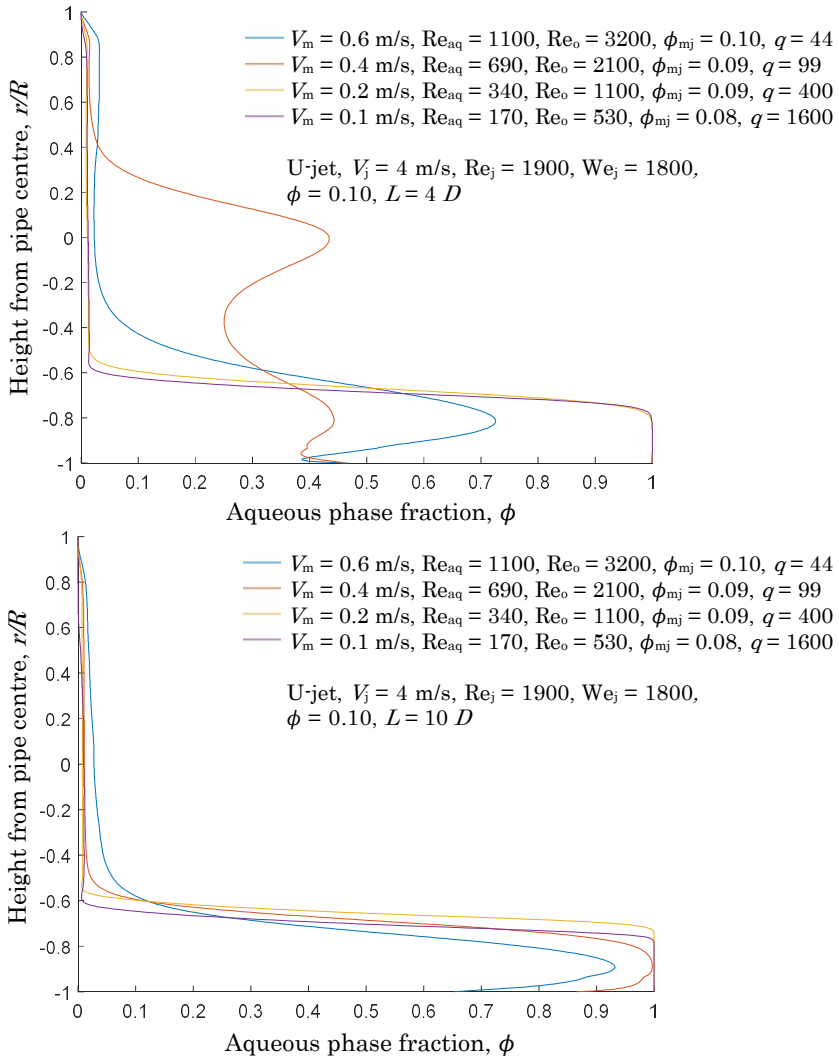


Figure 5.5 Concentration profiles for a U-jet with a velocity of V_j = 4 m/s and Re_j = 1900, We_j = 1800 interacting with crossflows with an aqueous phase fraction of ϕ = 0.10 and velocities of V_m = 0.1 m/s, V_m = 0.2 m/s, V_m = 0.4 m/s and V_m = 0.6 m/s. Top: L = 4 D; Bottom: L = 10 D.

Figure 5.6(top, bottom) presents the same conditions as in Figure 5.5, with the exception that the jet velocity is increased from V_j = 4 m/s to V_j = 8 m/s. Figure 5.6(top) is at a distance of L = 4 D from the jet while Figure 5.6(bottom) is at a distance of L = 10 D. At a distance of L = 4 D, the crossflow velocity of V_m = 0.1 m/s is mostly dispersed with some stratification at the pipe bottom, while the crossflows above a velocity of V_m = 0.1 m/s have an evenly dispersed vertical aqueous phase fraction. At a distance of L = 10 D, all flows have increased stratification, and therefore, have a better level of mixing at L = 4 D.

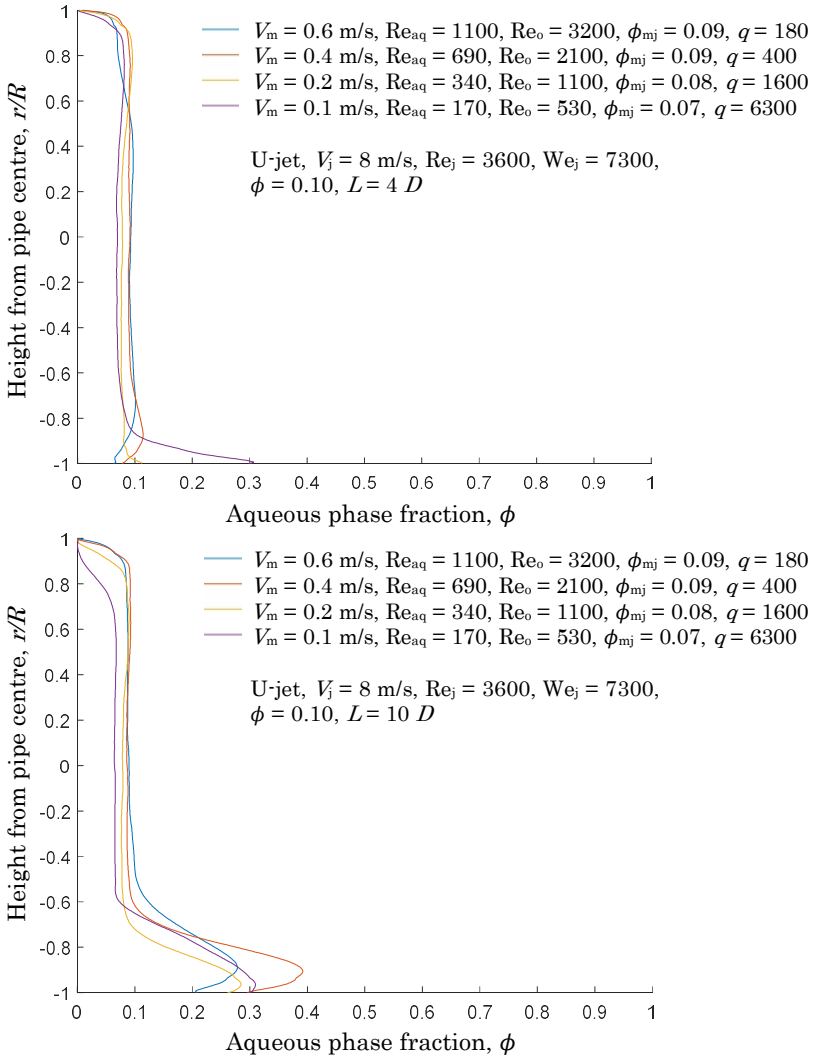


Figure 5.6 Concentration profiles for a U-jet with a velocity of V_j = 8 m/s and Re_j = 3600, We_j = 7300 interacting with crossflows with an aqueous phase fraction of ϕ = 0.10 and velocities of V_m = 0.1 m/s, V_m = 0.2 m/s, V_m = 0.4 m/s and V_m = 0.6 m/s. Top: L = 4 D; Bottom: L = 10 D.

Figure 5.7(top, bottom) present the same conditions as Figures 5.5 and 5.6 with the exception that the jet velocity is now increased to V_j = 12 m/s. Figure 5.7(top) is at a distance of L = 4 D from the jet while Figure 5.7(bottom) is at a distance of L = 10 D. At L = 4 D, all crossflows are now evenly dispersed vertically throughout the pipe, with a slight amount of stratification for the V_m = 0.1 m/s crossflow. Once the flows reach a distance of L = 10 D, all the crossflows have signs of stratification. Again better mixing occurs at L = 4 D than at L = 10 D.

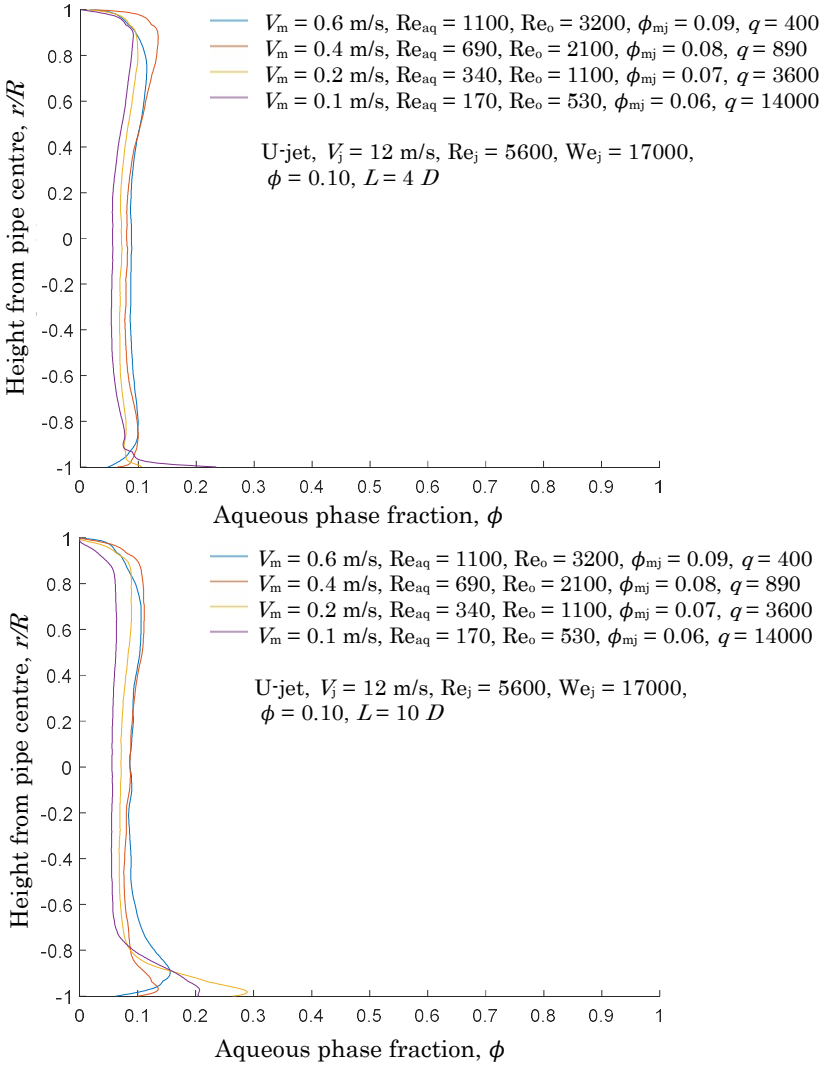


Figure 5.7 Concentration profiles for a U-jet with a velocity of V_j = 12 m/s and Re_j = 5600, We_j = 17000 interacting with crossflows with an aqueous phase fraction of ϕ = 0.10 and velocities of V_m = 0.1 m/s, V_m = 0.2 m/s, V_m = 0.4 m/s and V_m = 0.6 m/s. Top: L = 4 D; Bottom: L = 10 D.

5.1.5 Concentration profile for different jet types

The phase profiles of the three jet types at a distance of $L = 10\ D$ are presented in Figure 5.8. All these experimental cases have jet velocities of $V_j = 4$ m/s and crossflows of $V_m = 0.4$ m/s where the inlet aqueous phase fraction is $\phi = 0.20$, $\phi = 0.10$ and $\phi = 0.05$ for Figures 5.8, top, middle and bottom, respectively. In all three cases, the V-jet performs the best having the lowest interface height of the three types of jet, indicating that the V-jet creates a more stable phase distribution despite it also having the lowest Reynolds and Weber numbers. Whereas the F-jet has the highest interface level with the most abrupt concentration change, indicating that this jet has seen the least dispersion and/or most rapid re-stratification. The U-jet's mixing performance is generally around halfway between the two other jet types.

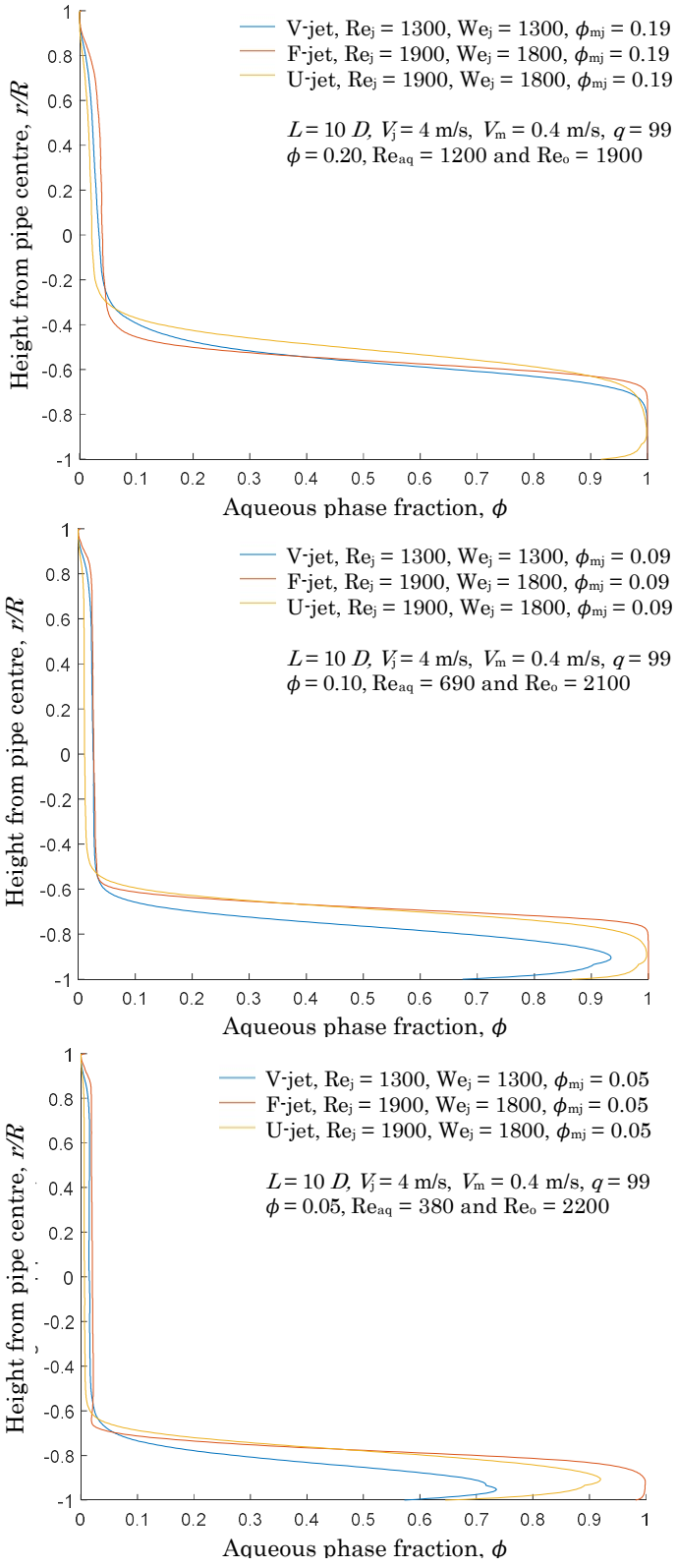


Figure 5.8 Concentration profiles at $L = 10\ D$ for the three jet types with a velocity of $V_j = 4$ m/s interacting with crossflows with a varying aqueous phase fraction of $\phi = 0.05$ and velocity of $V_m = 0.4$ m/s. Top: $\phi = 0.20$, $Re_{aq} = 1200$ and $Re_o = 1900$; Middle: $\phi = 0.10$, $Re_{aq} = 690$ and $Re_o = 2100$; Bottom: $\phi = 0.05$, $Re_{aq} = 380$ and $Re_o = 2200$.

Figure 5.9 presents the phase profiles of the three different jets types with an increased jet velocity of $V_j = 8$ m/s, and the same crossflow velocity of $V_m = 0.4$ m/s and inlet aqueous phase fraction of $\phi = 0.10$. Compared with the equivalent crossflow conditions of Figure 5.8(middle) all three jet types produce more even concentration profiles, where the V-jet again produces the most evenly distributed phase concentration profile. The aqueous phase fraction towards the top of the pipe is again above that in the centre of the pipe.

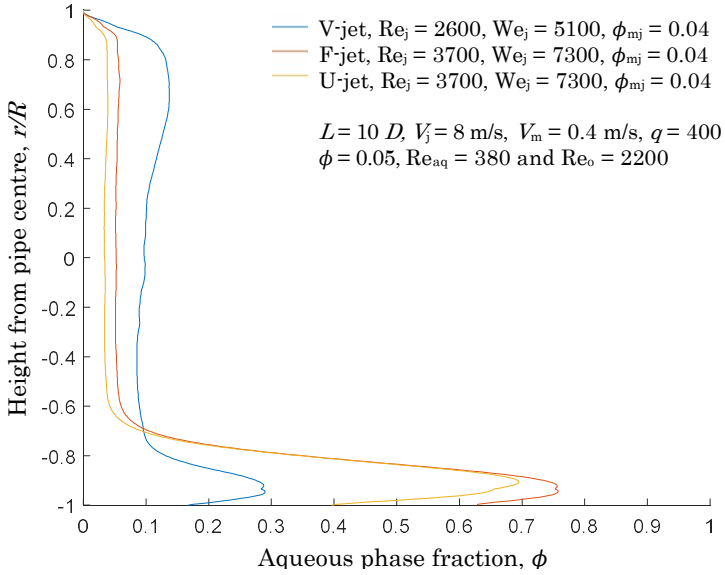


Figure 5.9 Concentration profiles at $L = 10\ D$ for the three jet types with a velocity of $V_j = 8$ m/s interacting with crossflows with an aqueous phase fraction of $\phi = 0.05$ and velocity of $V_m = 0.4$ m/s with $Re_{aq} = 380$ and $Re_o = 2200$.

5.2 Industrial mixing parameter, C_1/C_2

Experimental measurements of the industrial liquid-liquid mixing metric known as the C_1/C_2 ratio (ISO 1999) are presented within this section. This metric provides a quantitative single value measurement of the phase distribution that has occurred following the jet's interaction with the stratified crossflow. This metric is included here for comparison with similar industrial processing literature like that of (Lakshmanan et al. 2015; Maru et al., 2019; Verloop et al., 2019). The C_1/C_2 ratio is calculated form the concentration profile as outlined in Subsection 3.14.5.

5.2.1 Distance, phase fraction and jet velocity effects

Figure 5.10(top) presents the C_1/C_2 ratio for a low crossflow of V_m = 0.2 m/s being perturbed by a jet velocity of V_j = 4 m/s at several positions downstream of the jet's exit, for three inlet aqueous fractions of, ϕ = 0.05, ϕ = 0.10 and ϕ = 0.20. In all cases, the C_1/C_2 ratio is less than 0.2 which indicates that little of the aqueous phase is present in the top half of the measurement plane and that therefore the mixing, distribution and dispersion of the aqueous phase is poor.

Figure 5.10(middle) shows the measurement of C_1/C_2 ratio when the jet velocity is increased to V_j = 8 m/s and all other conditions are the same as 5.10 (top). This increase in jet velocity causes the C_1/C_2 ratio to increase substantially, particularly within the distance of one to five pipe diameters downstream of the jet, where the C_1/C_2 ratios of between 0.8 and 1.2 indicate that the distribution of the aqueous phase is similar for both the top and bottom halves of the measurement plane. At these distances, it is also apparent that the highest aqueous phase fraction of ϕ = 0.20 has lower C_1/C_2 ratio than the ϕ = 0.05 and ϕ = 0.10 aqueous phase fractions. Once the flow reaches nine to eleven diameters downstream of the jet we see that the C_1/C_2 ratios decrease significantly for the case with an aqueous phase fraction of ϕ = 0.20. This decrease in the C_1/C_2 ratios is not as pronounced for the case with an aqueous phase fraction of ϕ = 0.10, while the case with an aqueous phase fraction of ϕ = 0.05 experiences little if any decrease in the C_1/C_2 ratio. This indicates that an increase in the aqueous phase fraction increases the rate at which the mixture re-stratifies.

Figure 5.10(bottom) presents the measurement of C_1/C_2 ratios when the jet velocity is increased still further to V_j = 12 m/s while keeping all other parameters constant. All the measurement of C_1/C_2 ratio before a distance of five diameters downstream of the jet now have a similar C_1/C_2 ratio of ≈ 1.2, with the one exception being for an aqueous phase fraction of ϕ = 0.05 at a distance of L = 1 D where the C_1/C_2 value is ≈ 1.5. These C_1/C_2 ratios greater than one indicate that there is a higher concentration of the aqueous phase in the top half of the measurement plane than the bottom half. Once the flow reaches nine diameters downstream of the jet the C_1/C_2 ratios fall to between 0.8 and 0.9 which suggests that the flow is still reasonably evenly dispersed between the top and bottom of the pipe.

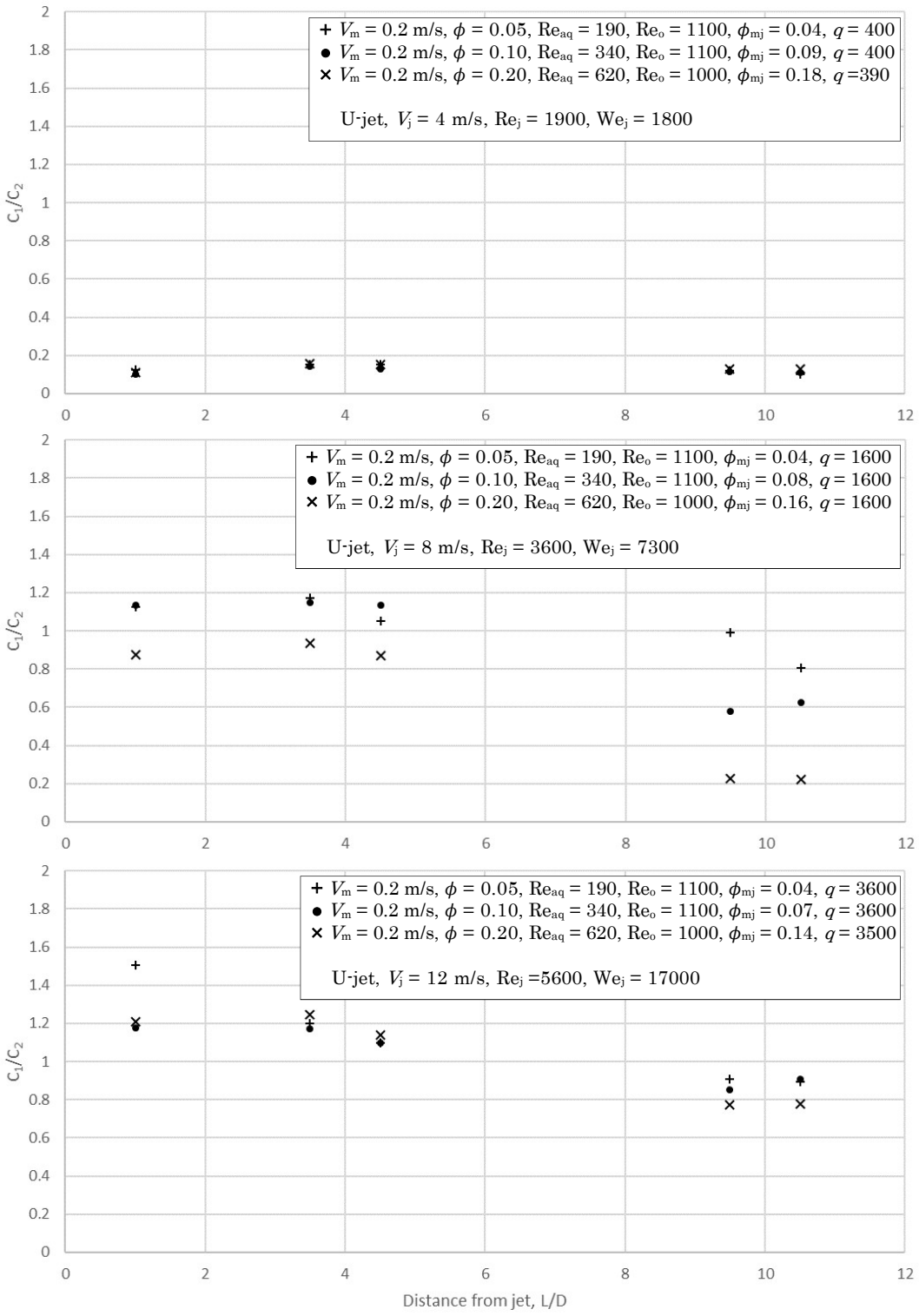


Figure 5.10 C_1/C_2 ratio against distance from jet for a U-jet with jet interacting with a V_m = 0.2 m/s crossflow with inlet aqueous phase fractions of ϕ = 0.05 (Re_{aq} = 190, Re_o = 1100), ϕ = 0.10 (Re_{aq} = 340, Re_o = 1100) and ϕ = 0.20 (Re_{aq} = 620, Re_o = 1000). Top: V_j = 4 m/s, Re_j = 1900, We_j = 1800; Middle: V_j = 8 m/s, Re_j = 3600, We_j = 7300; Bottom: V_j = 12 m/s, Re_j = 5600, We_j = 17000.

Figure 5.11 increases the crossflow velocity from $V_m = 0.2$ m/s to $V_m = 0.4$ m/s while keeping all other properties constant. In contrast to the slower crossflow of Figure 5.10(bottom), the crossflow in Figure 5.11 has a C_1/C_2 ratio that increases between one and three pipe diameter for all aqueous phase fractions. This indicates that the jet is still interacting with the crossflow to lift the aqueous phase between these two positions. Given the lower crossflow takes twice as long to reach the same positions downstream, this suggests that the peak in C_1/C_2 ratio moves downstream with increasing crossflow velocity.

The crossflows have a significant divergence in the C_1/C_2 ratio between different aqueous phase fractions. We again see that lowest aqueous phase fractions have the highest C_1/C_2 ratio while the highest aqueous phase fractions have the lowest C_1/C_2 ratio. In the case of the $\phi = 0.05$ and $\phi = 0.10$ aqueous phase fractions, the C_1/C_2 ratios are well above one, which indicates that a large fraction of the aqueous phase is driven by the jet to the top half of the pipe where it is carried along by the crossflow. Even at a distance of nine pipe diameters, the two crossflows with the lowest aqueous phase fraction still have the C_1/C_2 ratio above one, indicating that the aqueous phase has experienced a little settling in the 1.1 s that the crossflows took to reach this point. The highest aqueous phase fraction has a C_1/C_2 ratio of around one at a distance of $L = 3$ D, indicating that the aqueous phase is well distributed over the measurement plane, while at a distance of $L = 11$ D the C_1/C_2 ratio has again dropped to ≈ 0.8 indicating that the flow is undergoing stratification but remains dispersed.

Figure 5.12(top) presents the C_1/C_2 ratio created by a jet with a velocity of $V_j = 4$ m/s mixing crossflows with a velocity of $V_m = 0.6$ m/s and inlet aqueous fractions of, $\phi = 0.05$, $\phi = 0.10$ and $\phi = 0.20$. Figure 5.12(top) can be compared against Figure 5.10(top) which has a lower crossflow velocity of $V_m = 0.2$ m/s, where at this jet velocity there is a slightly higher degree of mixing for higher the crossflow velocities. The largest increase between Figure 5.12(top) and Figure 5.10(top) occurs for the aqueous phase fraction of $\phi = 0.05$ at a downstream distance of $L = 4$ D. Even still, the mixing is still poor with a C_1/C_2 ratio typically less than 0.4 before a distance of five pipe diameters, and by nine pipe diameters, the C_1/C_2 ratio has dropped to ≈ 0.2 for all three aqueous phase fractions. When compared with Figure 5.10(top) some of the additional mixing seen in Figure 5.12(top) could be caused by the extra energy of the higher velocity crossflow with its wavier liquid-liquid interface layer.

Compared to Figure 5.12(top), Figure 5.12(bottom) increases the jet velocity from V_j = 4 m/s to V_j = 12 m/s, as a result, the C_1/C_2 ratio increases significantly. Indeed, at a distance of L = 3 D, the C_1/C_2 ratios are between 1 and 1.2 for all three aqueous phase fractions. However, at a distance of L = 1 D, the C_1/C_2 ratio is 0.1 which indicates that the jet has not had sufficient time to mix the stratified flow at the higher crossflow velocity of V_m = 0.6 m/s.

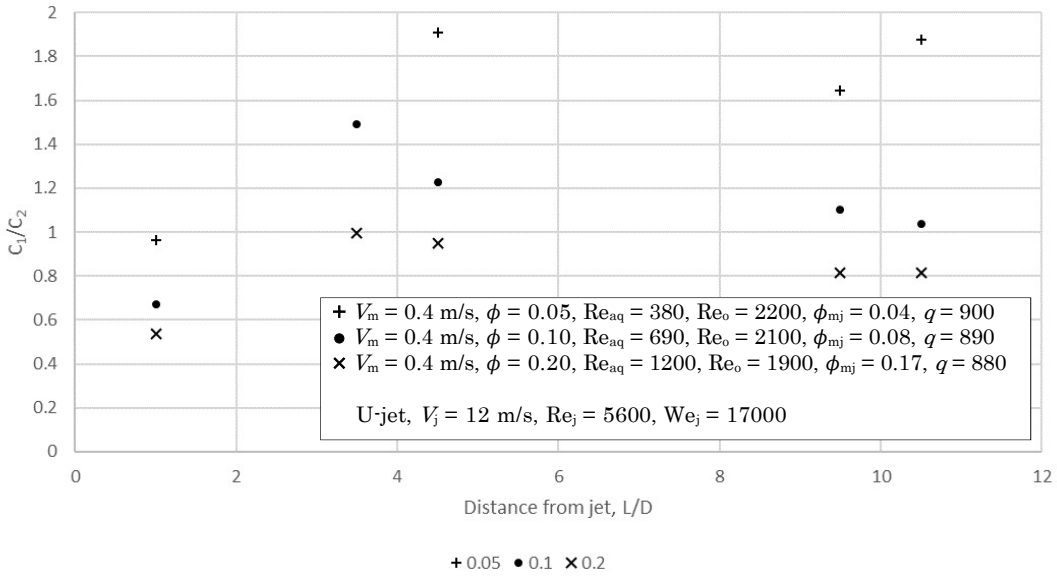


Figure 5.11 C_1/C_2 ratio against distance from jet for the U-jet with a jet velocity of V_j = 12 m/s and Re_j = 5600, We_j = 17000 interacting with a V_m = 0.4 m/s crossflow with inlet aqueous phase fractions of ϕ = 0.05 (Re_{aq} = 380, Re_o = 2200), ϕ = 0.10 (Re_{aq} = 690, Re_o = 2100) and ϕ = 0.20 (Re_{aq} = 1200, Re_o = 1900).

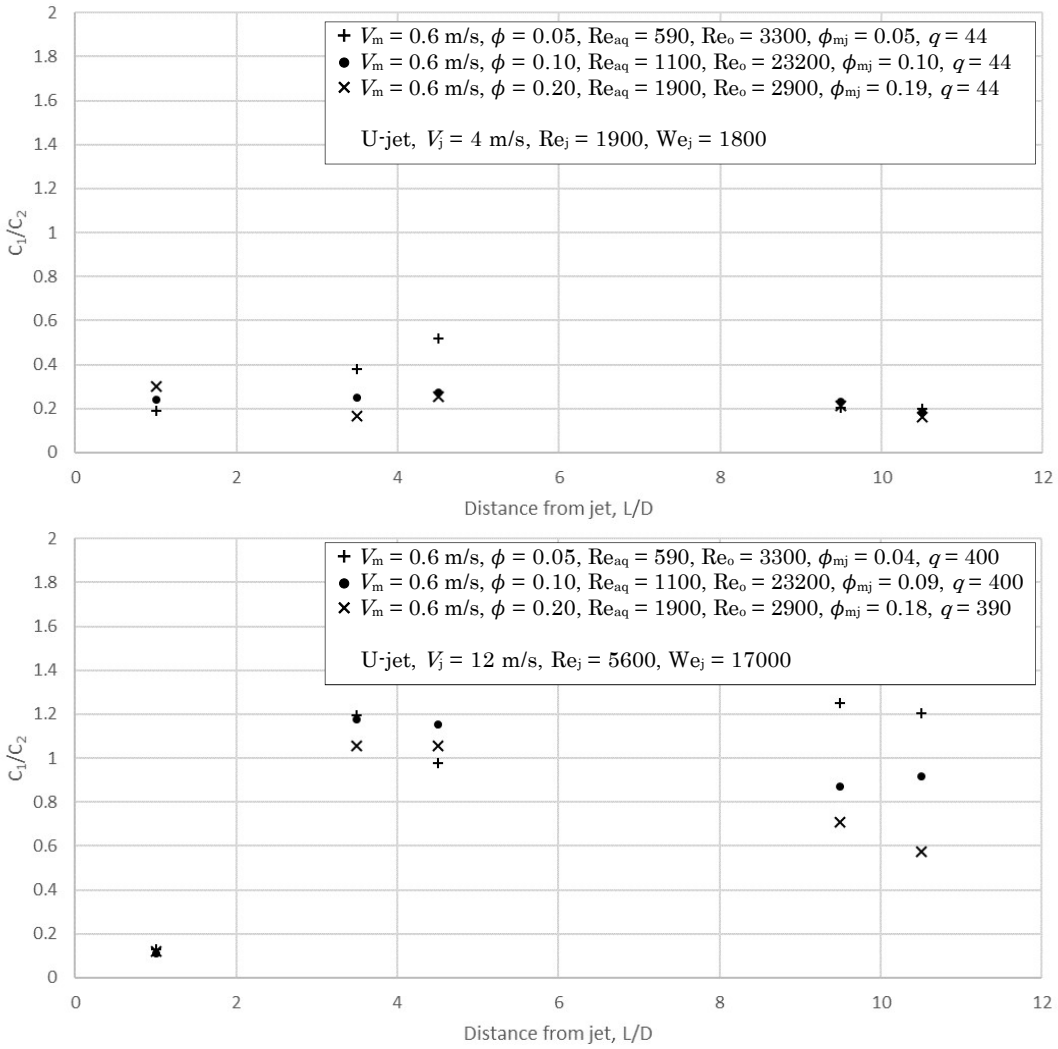


Figure 5.12 C_1/C_2 ratio against distance from jet for the U-jet with a jet interacting with a V_m = 0.6 m/s crossflow with inlet aqueous phase fractions of ϕ = 0.05 (Re_{aq} = 590, Re_o = 3300), ϕ = 0.10 (Re_{aq} = 1100, Re_o = 3200) and ϕ = 0.20 (Re_{aq} = 1900, Re_o = 2900). Top: V_j = 4 m/s, Re_j = 1900, We_j = 1800; Bottom: V_j = 12 m/s, Re_j = 5600, We_j = 17000.

5.2.2 Residence time

This section presents the effect of the residence time following the jet interaction with the crossflow on the C_1/C_2 ratio. This residence time, t_{res}, is dependent on the mixture velocity including the jet flow, V_{mj}, in the test section downstream of the jet and the measurement position L, (Eq. 5.1). The mixture velocity, V_{mj}, is dependent on the mixture flow downstream of the jet, Q_{mj}, and the test sections cross-sectional area, (Eq. 5.2). The mixture flow downstream of the jet is a combination of the input crossflow, Q_m, and jet flow, Q_j, (Eq. 5.3):

$$t_{\mathrm{res}} = \frac{L}{V_{\mathrm{mj}}} \qquad \text{Equation 5.1}$$

$$V_{\mathrm{mj}} = \frac{4Q_{\mathrm{mj}}}{\pi D^2} \qquad \text{Equation 5.2}$$

$$Q_{\mathrm{mj}} = Q_{\mathrm{m}} + Q_{\mathrm{j}} \qquad \text{Equation 5.3}$$

Figure 5.13 plots the C_1/C_2 ratio against the residence time following the jet interaction with the crossflow for distances of three pipe diameters or greater, collating the measurements into three jet velocities of $V_j = 4$, 8 and 12 m/s. The figures vary in inlet aqueous phase fraction where Figure 5.13 top, middle and bottom have aqueous phase fractions of $\phi = 0.05$, $\phi = 0.10$ and $\phi = 0.20$, respectively.

The general trend is for the C_1/C_2 ratio to decrease with time, although, there is considerable scatter when the duration is less than 1.5 s as the jet has had limited time to decay so its influence remains strong. The jet velocity and hence Weber number is correlated with C_1/C_2 ratio where the higher the jet velocity and Weber number the higher the C_1/C_2 ratio is at the beginning. Whilst the gradient of the decay of the C_1/C_2 ratio is inversely correlated with the jet velocity and Weber number, where higher starting jet velocities and Weber numbers correlate with more rapid drops in C_1/C_2 ratio. The aqueous phase fraction affects the starting C_1/C_2 ratio and its gradient, where a higher aqueous phase fraction has a lower initial C_1/C_2 ratio and a lower gradient of decay.

There is considerable spread in the C_1/C_2 ratios presented in Figure 5.13 but the general trends are revealed by applying linear fits. However, given sufficient time these linear fits will pass through zero which is non-physical. In comparison, Figure 5.14 fits exponential trend lines to the same data. These exponential fits will not pass through zero and have improved R^2 values for all cases when compared with the R^2 values of the linear fits of Figure 5.13.

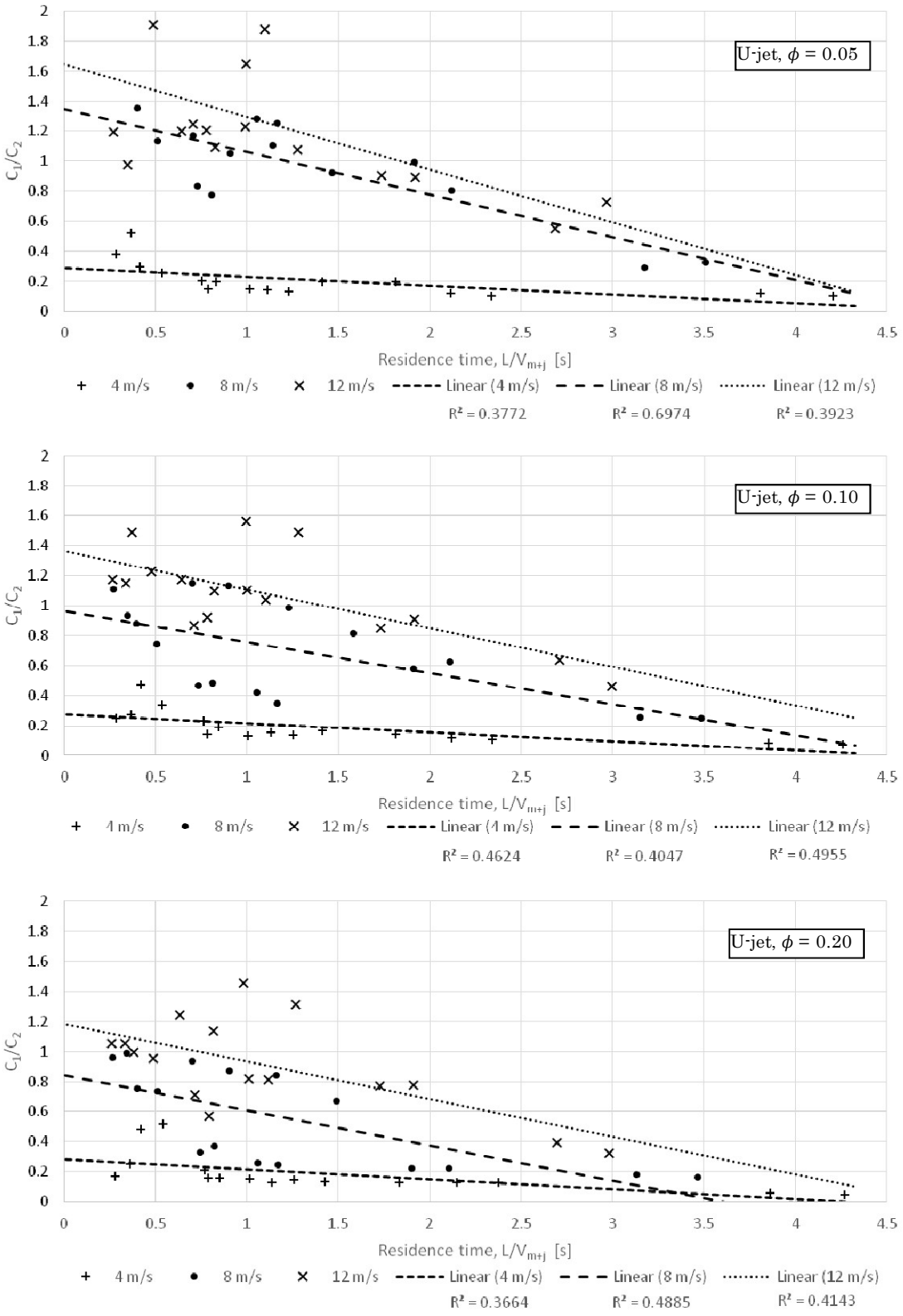


Figure 5.13 C_1/C_2 **ratio against pipeline residence times for the U-jet with jet velocities of** V_j **= 4, 8 and 12 m/s interacting with crossflow velocities between** V_m **= 0.1 – 0.6 m/s with varying inlet aqueous phase fraction. Top:** ϕ **= 0.05; Middle:** ϕ **= 0.10; Bottom:** ϕ **= 0.20. Linear fitting trend lines.**

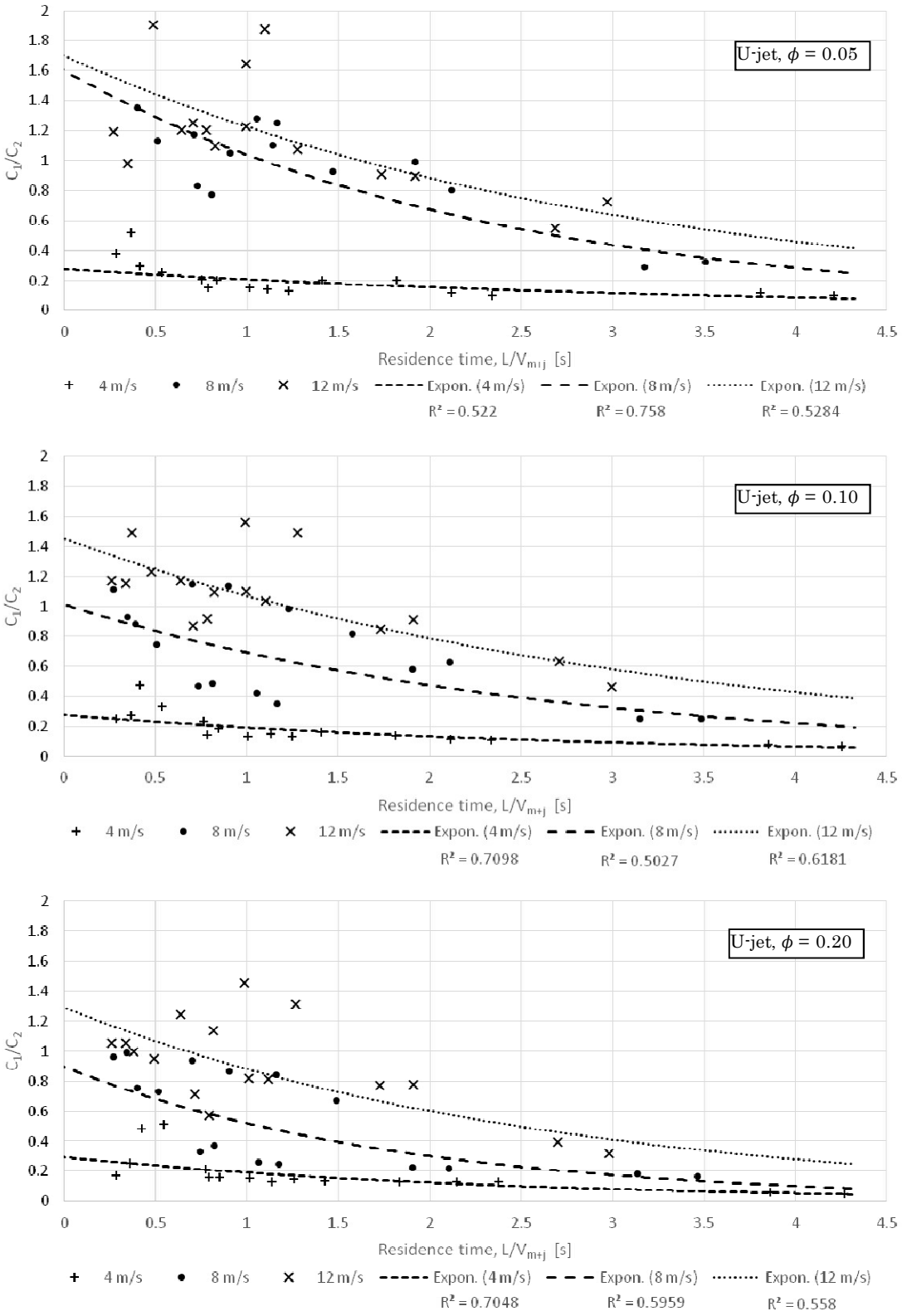


Figure 5.14 C_1/C_2 ratio against pipeline residence times for the U-jet with jet velocities of V_j = 4, 8 and 12 m/s interacting with crossflow velocities between V_m = 0.1 – 0.6 m/s with varying inlet aqueous phase fraction. Top: ϕ = 0.05; Middle: ϕ = 0.10; Bottom: ϕ = 0.20. Exponential fitting trend lines.

5.2.3 Effect of jet type

This subsection presents the C_1/C_2 ratios for the three jet types at a distance of between nine and eleven diameters downstream of the jet exit for jet velocities of $V_j = 4$ m/s, $V_j = 8$ m/s and $V_j = 12$ m/s. Figure 5.15(top row) has a crossflow velocity of $V_m = 0.2$ m/s with an aqueous phase fraction of $\phi = 0.20$. At the lowest jet velocity of $V_j = 4$ m/s, the C_1/C_2 ratios are ≈ 0.2 or lower indicating that all three jet types are poorly mixing. As the jet velocity is increased for both the U-jet and V-jet types the C_1/C_2 ratios increase. However, increasing the jet velocity of the F-jet results in little increase in the C_1/C_2 ratio, suggesting this jet performs poorly in comparison to the other two.

Figure 5.15(middle and bottom rows) increase the crossflow velocity to $V_m = 0.4$ and $V_m = 0.6$ m/s, respectively. In both sets of figures, we see an increase in the level of the C_1/C_2 ratios compared to the crossflow with velocities of $V_m = 0.2$ m/s. This increase can be attributed to the reduction in the residence time and the increase in energy of the higher velocity crossflows. At these higher crossflows, the V-jet is again found to creating the highest C_1/C_2 ratios and hence performs the best, whereas the F-jet again has the lowest C_1/C_2 ratios performing the worst.

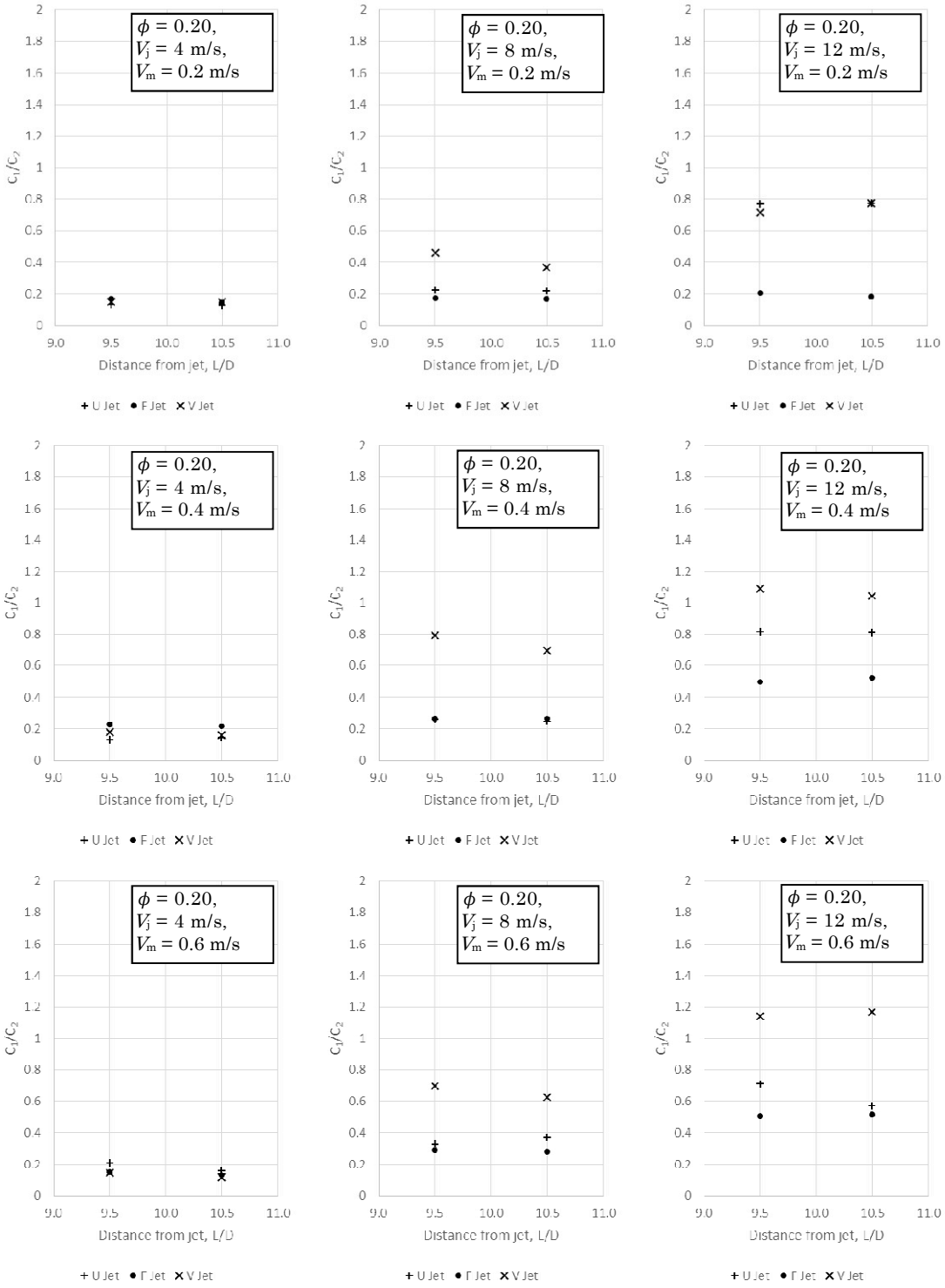


Figure 5.15 C_1/C_2 ratio against distance from jet for the three different jet types interacting with varying crossflow with inlet aqueous phase fractions of $\phi = 0.20$. Left column: $V_j = 4$ m/s; Middle column: $V_j = 8$ m/s; Right columns: $V_j = 12$ m/s. Top row: $V_m = 0.2$ m/s; Middle row: $V_m = 0.4$ m/s; Bottom row: $V_m = 0.6$ m/s.

Figure 5.16 present the C_1/C_2 ratios for the three jet types at a distance of $L = 9.5\ D$ and $L = 10.5\ D$ for crossflows velocities of $V_m = 0.2$, 0.4 and 0.6 m/s where the inlet aqueous phase fraction is $\phi = 0.05$. In all cases where the jet velocity is $V_j = 4$ m/s, the C_1/C_2 ratios are below 0.4, although this is higher than that seen when the aqueous phase fraction was $\phi = 0.20$.

When the crossflow is $V_m = 0.2$ m/s, Figure 5.16(top row), the F-jet again performs the worst with the lowest C_1/C_2 ratio while the other two jet types perform similarly. When the crossflow velocity is $V_m = 0.4$ m/s, Figure 5.16(middle row), and the jet velocity is increased to $V_j = 8$ m/s then all three jets perform better producing higher C_1/C_2 ratios. At a jet velocity of $V_j = 12$ m/s, the V-jet and the F-jet create C_1/C_2 ratios above 1.5 which indicates that these jets are concentrating the aqueous phase above the centre of the pipe. When the crossflow is increased to $V_m = 0.6$ m/s, Figure 5.16(bottom row) the jets are again found to perform poorly at lowest jet velocity. However, as the jet velocities are increased to $V_j = 8$ m/s and above, then all three jets are found to have C_1/C_2 ratios close to the ideal value of one.

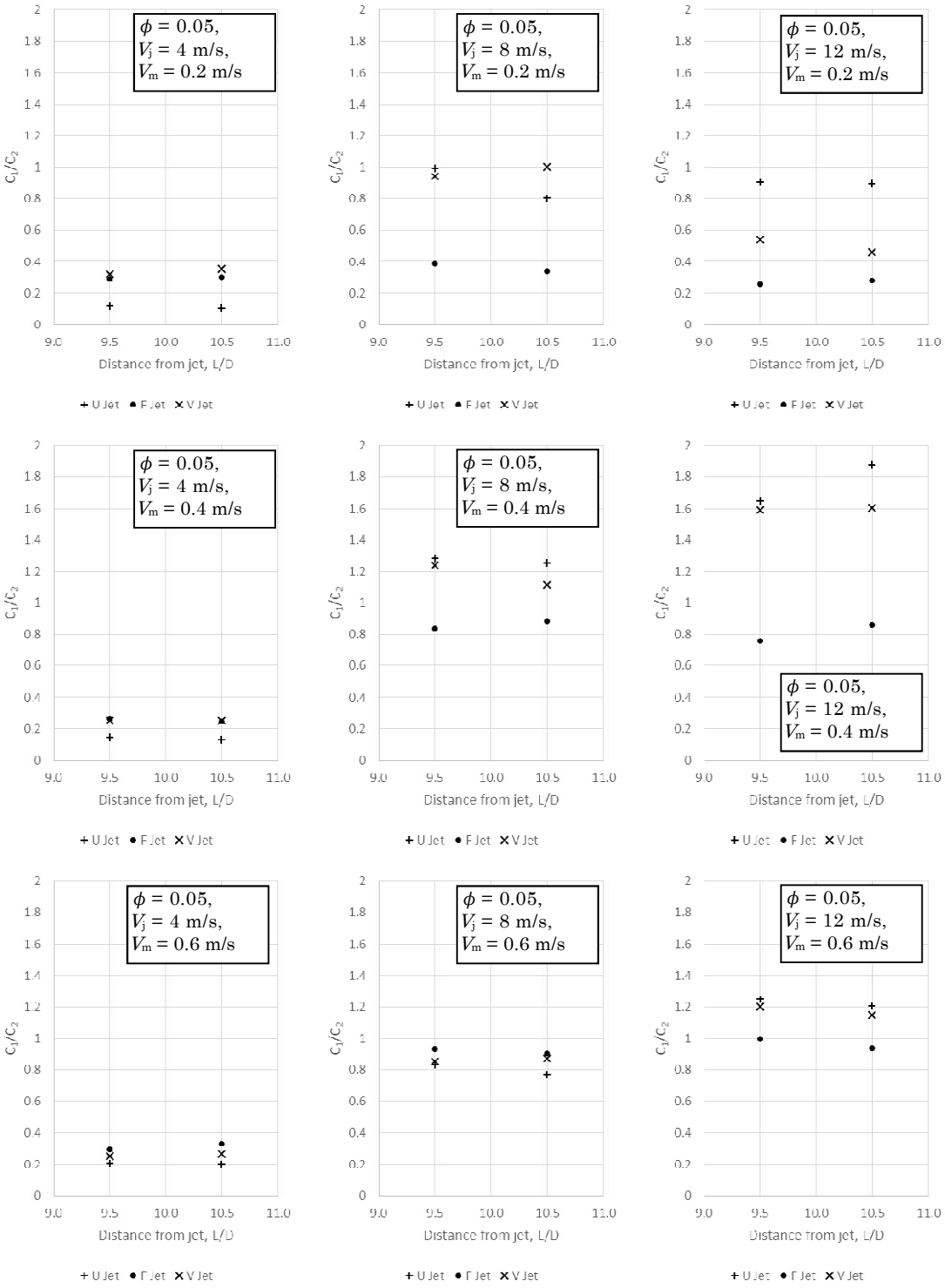


Figure 5.16 C_1/C_2 ratio against distance from jet for the three different jet types interacting with a crossflow with inlet aqueous phase fractions of $\phi = 0.05$. Left column: $V_j = 4$ m/s; Middle column: $V_j = 8$ m/s; Right column: $V_j = 12$ m/s. Top row: $V_m = 0.2$ m/s; Middle row: $V_m = 0.4$ m/s; Bottom row: $V_m = 0.6$ m/s.

5.3 Summary

This chapter presented the measurements of the PLIF concentration profiles and associated industrial C_1/C_2 ratio used for estimating mixing level. Revealing how these measurements change with position, jet velocity, crossflow and aqueous phase fraction and jet type. The key points from this chapter are:

- The concentrations profiles indicate that increasing the jet velocity results in the interface height decreasing while increasing the dispersed aqueous phase for all crossflow velocities and aqueous phase fractions. Similarly, increasing the jet velocity increases the C_1/C_2 ratio as expected for improved mixing.
- The concentration profiles show that, as crossflow velocities increase, the jet velocity must be increased to maintain the same level of mixing. This occurs because the relative energy being input into the crossflow by the jet is reduced as the crossflow velocity increases. However, increasing the crossflow also reduces the residence time, limiting stratification and maintaining an even dispersion over longer distances.
- Measurements of C_1/C_2 ratio reveal that mixing is incomplete at one pipe diameter and may not have completed by three pipe diameters for crossflows at 0.6 m/s. The time needed for a flow to reach a downstream position is inversely proportional to the crossflow velocity. Subsequently, the peak in the C_1/C_2 ratios moves further downstream from the jet exit as the crossflow velocity increases.
- The concentration profiles show that all flows have increased stratification by ten diameters downstream of the jet exit. This indicates that a distance of ten pipe diameters is the upper limit of jet dominance for the conditions tested, beyond which gravitationally-driven separation dominates.

Additional points of interest include:

- The concentration profiles and the C_1/C_2 ratio measurements reveal that increasing the aqueous phase leads to poorer mixing and dispersion as well as more rapid re-stratification. This occurs due to the additional droplet surface that must be created as the aqueous phase fraction is increased.
- The concentrations profiles demonstrate that the height of the interface increases with increasing aqueous phase fraction for any experimental case where a liquid-liquid interface remains.

- Concentration profiles highlight that the jets can lift and concentrate the aqueous phase towards the top of the pipe where it can remain downstream at subsequent measurements. As a result, the concentration in the middle of the pipe can be lower than either the bottom or the top. This results in C_1/C_2 ratio measurements being above one in several of the experimental cases.
- The higher C_1/C_2 ratio measurements of the V-jet indicate that it generally performs better than the other two jet types despite having 70% lower Weber and Reynolds numbers. However, the pressure loss and hence the power requirement of the V-jet is 80% higher. The F-jet generally has the lowest C_1/C_2 ratio measurements and hence is considered to perform the worst.
- Residence time plots of C_1/C_2 ratio measurement generally decreases after 1 to 1.5 seconds from passing the jet exit where the rate of decrease increases with increasing jet velocity and decreases with increasing aqueous phase fraction.
- The C_1/C_2 ratio measurement used by industry provides a reasonable indication of the dispersion of the phase. However, the C_1/C_2 ratio measurement has several issues, firstly, it is prone to large errors in measurement when the dispersed phase fraction is low due to the uncertainty in the measured C_2 denominator. Secondly, it is unable to detect conditions where the concentration is equal in the top and bottom, but different in the middle, as occurs when the jet concentrates the aqueous phase at the pipe top. It is therefore important that vertical concentration profiles are included along with any C_1/C_2 ratio measurements.

Chapter 6

Mixing characteristics: Droplet sizes

This chapter presents the measurement and analysis of droplet chord lengths, including their profiles and distributions. The effect of the distance, crossflow velocity, inlet aqueous fraction, residence time and the jet type are all presented and analysed. The droplet detection method used in this chapter is outlined in Subsection 3.14.6.

6.1 Droplet chord lengths

This section presents various droplet chord length measurements including the mean, D_{10} (Eq. 3.39), the Sauter Mean Diameter, D_{32} (Eq. 3.40), as well as for Dv_{10}, Dv_{50} and Dv_{90}, which corresponds to the droplet chord lengths for 10%, 50% and 90% of the cumulative droplet mass, respectively. The calculation for each of these measurements is outlined in Subsection 3.14.7.

The largest droplet, D_{max}, will settle the fastest due to their higher volume-to-surface ratio when compared with smaller droplets. This makes the maximum droplet size an important measurement for liquid-liquid dispersion and mixing measurements in particular. However, the measurement of the maximum droplet size has a significant amount of scatter and uncertainty, as a result, Dv_{90} is used as a substitute for the maximum droplet chord length.

Table 6.1 presents a small subset of the experimental measurements of droplet chord lengths examined in this analysis. The droplet chord length measurements were performed at the axial position, *L,* stated in column two of Table 6.1. The measurements are spatially averaged over the vertical height of the pipe and horizontally ±0.5D either side of the measurement position, corresponding to an area of 2500 mm^2. The number of drops measured in each experimental case ranges from 2917 to 10597, while the standard deviation in the droplet chord length ranges from 0.16 mm to 0.83 mm. The table reveals that for each measurement $D_{10} < Dv_{10} < D_{32} < Dv_{50} < Dv_{90}$.

Table 6.1 Drop chord length statistics for a subset of the experimental test cases.

Jet type	L [D]	V_j [m/s]	ϕ	V_m [m/s]	N	D_{10} [mm]	Dv_{10} [mm]	D_{32} [mm]	Dv_{50} [mm]	Dv_{90} [mm]	S [mm]
U-jet	10	4	0.05	0.4	3790	0.42	3.39	3.94	8.44	10.11	0.43
U-jet	10	6	0.05	0.4	7067	0.39	0.62	1.93	5.52	8.18	0.30
U-jet	10	8	0.05	0.4	10597	0.35	0.37	0.68	0.72	3.90	0.19
U-jet	10	12	0.05	0.4	5097	0.28	0.28	0.56	0.64	1.88	0.16
U-jet	10	4	0.20	0.4	2917	0.61	2.38	5.20	10.88	15.06	0.71
U-jet	10	8	0.20	0.4	5749	0.50	1.77	3.69	7.41	9.59	0.56
U-jet	10	12	0.20	0.4	6815	0.56	0.92	1.80	2.46	4.61	0.52
U-jet	10	4	0.10	0.4	3732	0.46	0.58	1.31	1.85	6.60	0.30
U-jet	10	8	0.10	0.4	6573	0.43	1.70	3.40	8.20	9.56	0.45
U-jet	10	12	0.10	0.4	7335	0.41	0.58	1.14	1.57	3.45	0.32
U-jet	10	12	0.20	0.1	3545	0.51	2.03	4.67	10.81	12.38	0.54
U-jet	10	12	0.20	0.2	7384	0.54	0.83	2.07	5.38	7.75	0.45
U-jet	10	12	0.20	0.6	3385	0.70	1.87	3.20	4.49	7.56	0.83
U-jet	4	12	0.20	0.1	6025	0.51	0.59	0.92	1.04	1.71	0.32
U-jet	4	12	0.20	0.2	7357	0.52	0.63	1.06	1.34	2.06	0.36
U-jet	4	12	0.20	0.4	4742	0.66	1.03	1.72	2.11	3.15	0.59
U-jet	4	12	0.20	0.6	3695	0.70	1.56	2.42	2.97	4.66	0.75
F-jet	10	12	0.20	0.2	4418	0.47	0.60	1.25	1.57	5.94	0.33
F-jet	10	12	0.20	0.6	6283	0.60	1.51	2.91	4.31	11.17	0.65
V-jet	10	12	0.20	0.2	6918	0.55	0.70	1.39	1.63	6.53	0.39
V-jet	10	12	0.20	0.6	4843	0.86	1.09	2.05	2.45	5.22	0.67

The four plots in Figure 6.1 relate the measured values of D_{32} to that of the other four droplet diameters of D_{10}, Dv_{10}, Dv_{50}, Dv_{90}. The droplet chord length measurements presented in Figure 6.1 are from two axial positions, $L = 4D$ and $L = 10D$. The measurements are spatially averaged over the vertical height of the pipe and horizontally ±0.5D either side of the measurement position, corresponding to an area of 2500 mm^2. A first approximation of the relationship between these five different chords lengths can be expressed by Eqs. 6.1 to 6.4. The relationship between D_{10} and D_{32} is poor with an R-squared value of 0.26 while that of Dv_{90} and D_{32} is arguably the best with an R-squared value of 0.86.

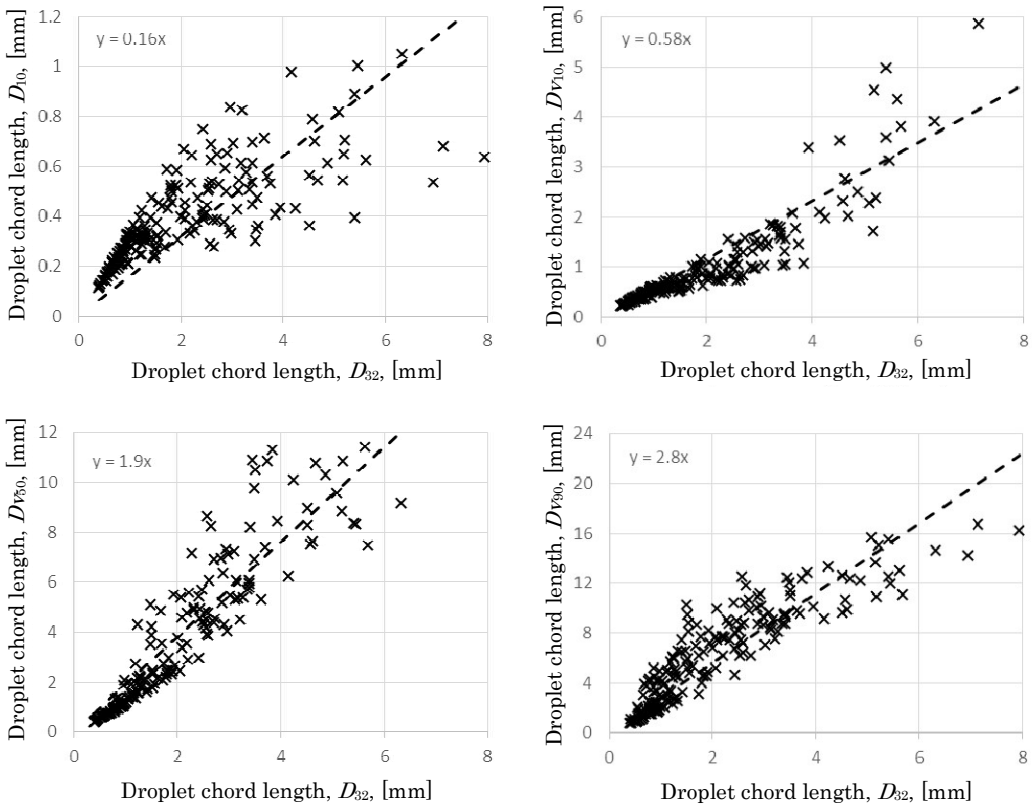


Figure 6.1 Droplet chord lengths relationships: Top left: D_{32} and mean (D_{10}); Top right: D_{32} and Dv_{10}; Bottom left: D_{32} and Dv_{50}; Bottom right: D_{32} and Dv_{90}.

$$D_{10} \approx \frac{D_{32}}{6} \qquad \text{Equation 6.1}$$

$$Dv_{10} \approx \frac{D_{32}}{2} \qquad \text{Equation 6.2}$$

$$Dv_{50} \approx 1.9D_{32} \qquad \text{Equation 6.3}$$

$$Dv_{90} \approx 2.8D_{32} \qquad \text{Equation 6.4}$$

The droplet chord lengths can be expressed as a vertical profile to reveal the variation of chord length with height. The plots in Figure 6.2 present the variation of D_{10}, D_{32} and Dv_{50} for the U-jet with jet velocities ranging from V_j = 4 m/s to V_j = 12 m/s encountering a crossflow with a velocity of V_m = 0.4 m/s and an aqueous phase fraction of ϕ = 0.05 at a downstream distance of L = 10 D. The profiles for the droplet chord lengths were created from 20 equally spaced vertical ranges each being 2.5 mm high. The measurements were spatially averaged over an axial distance of ±0.5D either side L = 10 D. Consequently, the droplet chord lengths

were averaged over an area of 125 mm^2. The left column plots D_{10}, D_{32}, and Dv_{50} simultaneously while the right plots D_{32}, with associated error bars. The jet velocities from top to bottom are V_j = 4 m/s, 6 m/s, 8 m/s and 12 m/s. In all cases, the measurements of D_{10}, D_{32}, and Dv_{50} decrease as the jet velocities, Reynolds and Weber numbers increase. The decrease is due to the higher amount of kinetic energy that is available in the higher velocity jets to break up the incoming stratified flow or equally the increasing dominance of disruptive hydrodynamic forces over the stabilizing force of interfacial tension. This increase in available energy results in an increase in droplet surface area and thus smaller droplets.

The top two plots of Figure 6.2 have a jet velocity of V_j = 4 m/s, a Reynolds number of Re_j = 1900 and a Weber number of We_j = 1800. Under these conditions, significant droplet stratification occurs at the bottom of the pipe appearing as rapid increases in D_{32}, Dv_{50} and D_{10} below $r = -0.4\ R$. In the 2nd row of Figure 6.2 the jet velocity increases to V_j = 6 m/s (Re_j = 2800, We_j = 4100), and under these conditions, the stratification remains present but the height at which the transition occurs is now below $r = -0.8\ R$. The 3rd row of Figure 6.2 has a jet velocity of V_j = 8 m/s (Re_j = 3700, We_j = 7300), and here the droplet stratification is now more gradual. The final row has a jet velocity of V_j = 12 m/s (Re_j = 5600, We_j = 17000) and the droplet diameters continue to increase from top to bottom indicating that at least some limited stratification of the droplet chord lengths is still present.

The plots in Figure 6.3 present the variation in D_{32} with changing jet velocity and inlet aqueous phase for U-jet encountering a crossflow with a velocity of V_m = 0.4 m/s at an axial distance of $L = 10\ D$. The profiles use 20 equally spaced vertical ranges each 2.5 mm high as Figure 6.2. The measurements were spatially averaged over an axial distance of ±0.5D either side of $L = 10\ D$. These plots increase the aqueous phase fraction to $\phi = 0.10$ and $\phi = 0.20$ in the left and right columns of Figure 6.3, respectively. The jet velocity along with Reynolds number and Weber number increase from top to bottom where the top row is V_j = 4 m/s, Re_j = 1900, We_j = 1800, the middle row is V_j = 8 m/s, Re_j = 2800, We_j = 4100 and the bottom row is V_j = 12 m/s, Re_j = 5600, We_j = 17000. Comparing the plots in the left and right columns reveals that as the aqueous phase fraction increases the D_{32} droplet chord lengths increase. In addition, increasing in aqueous phase fraction increases the height at which the chord lengths undergo a rapid increase due to the higher stratification layer at the pipe bottom.

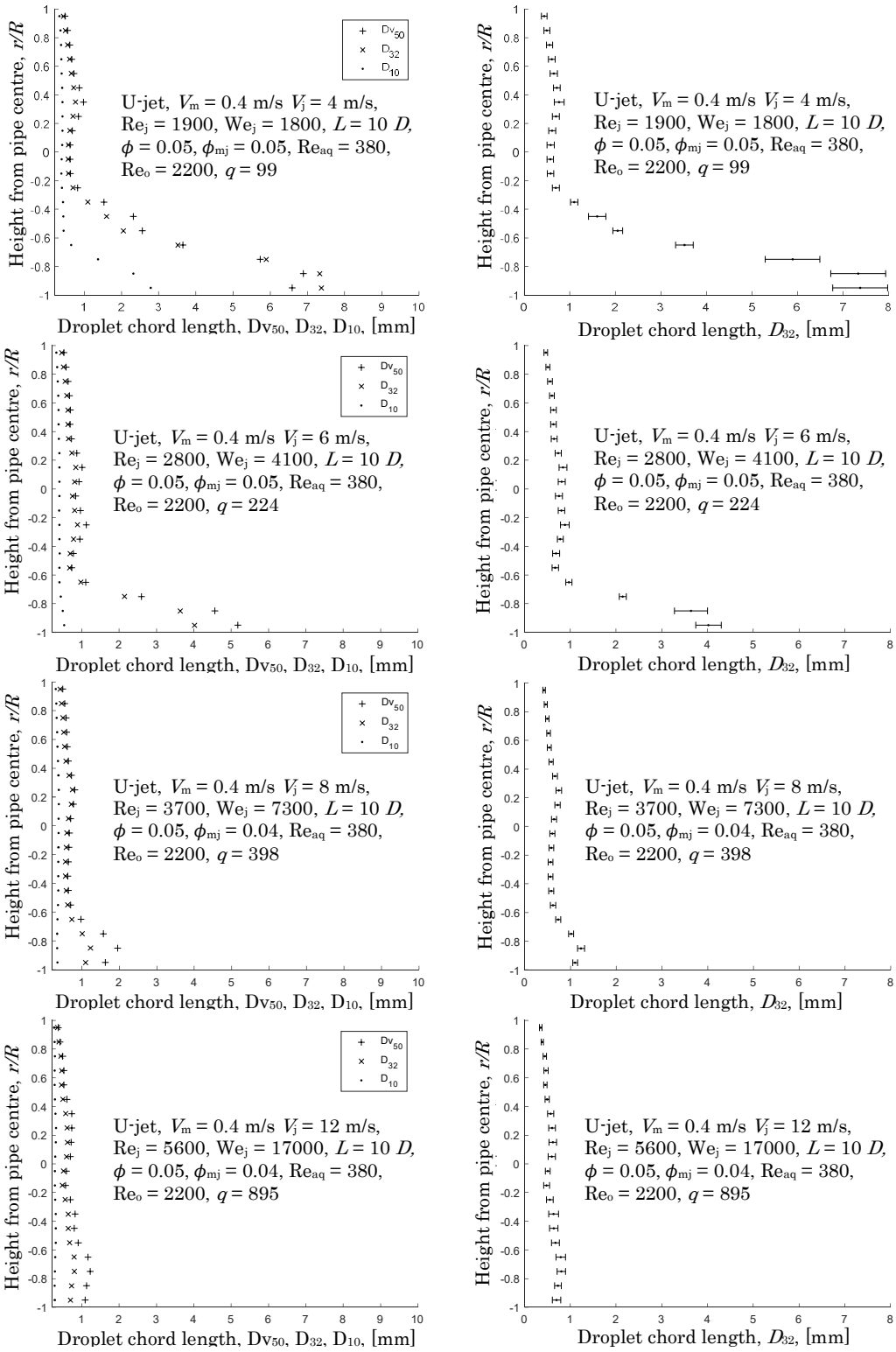


Figure 6.2 Droplet chord lengths against height for a U-jet interacting with a crossflow velocity of V_m = 0.4 m/s and an aqueous phase fraction of ϕ = 0.05 with Reynolds number of Re_{aq} = 380, Re_o = 2200 at a distance of L = 10 D. Left column: D_{10}, D_{32}, Dv_{50}; Right column: D_{32}; Top Row: V_j = 4 m/s, Re_j = 1900, We_j = 1800; 2nd row: V_j = 6 m/s, Re_j = 2800, We_j = 4100; 3rd row: V_j = 8 m/s, Re_j = 3700, We_j = 7300; Bottom row: V_j = 12 m/s, Re_j = 5600, We_j = 17000.

The droplet chord lengths are expressed as probability distributions in the histograms of Figure 6.4. The histograms present the measurements for a U-jet encountering crossflows with a velocity of V_m = 0.4 m/s at an axial distance of L = 10 D. The measurements are spatially averaged over the vertical height of the pipe and horizontally ±0.5D either side of L = 10 D, corresponding to an area of 2500 mm^2. The top row is for aqueous phase fractions of ϕ = 0.05, the 2nd row is for ϕ = 0.10 and the bottom row is for ϕ = 0.20. The left column has jet velocities of V_j = 4 m/s, the middle column V_j = 8 m/s and the right column V_j = 12 m/s. In the top right, the droplet chord length probability distribution contains a well-dispersed flow with small droplets. The probability distribution has a single peak that decays away smoothly as the chord lengths increases. Although, this peak is in the first bin and so it is not possible to determine if the distribution's maximum is visible or below the experimental minimum for droplet chord length of ≈ 0.17 mm (see Subsection 3.14.6).

Moving in either direction away from the top right histogram, by lowering the jet velocity or by increasing the aqueous phase fraction, a second peak at ≈ 0.6 mm appears on the right-hand slope of the probability distributions. Increasing the aqueous phase fraction to ϕ = 0.05 reveals a smaller third peak at ≈ 1.5 mm.

The presence of multiple peaks indicates that there are at least two different droplet size distributions present in most experimental cases. The probability distributions indicate that increasing aqueous phase fraction or decreasing the jet velocity and hence Weber number, leads to the droplet chord length distribution spreading. However, the largest cause of this increased spreading of the distribution is the increase in aqueous phase fraction.

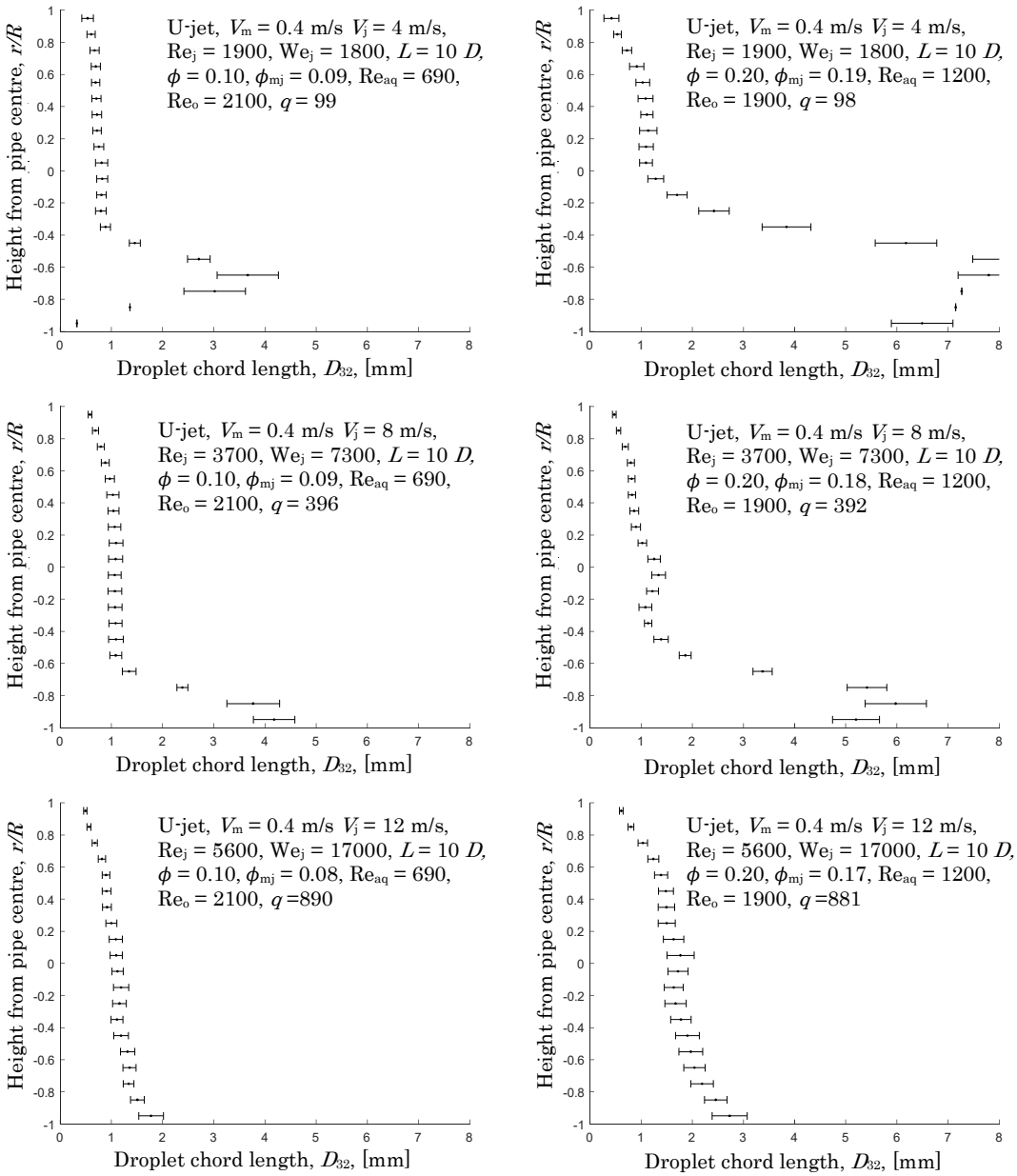


Figure 6.3 D_{32} droplet chord lengths against height for a U-jet interacting with a crossflow velocity of V_m = 0.4 m/s at a distance of L = 10 D where the jet velocities and inlet aqueous phase fractions are varying. Left column: ϕ = 0.10, Re$_{aq}$ = 690, Re$_o$ = 2100; right column: ϕ = 0.20, Re$_{aq}$ = 1200, Re$_o$ = 1900; top row: V_j = 4 m/s, Re$_j$ = 1900, We$_j$ = 1800; 2nd row: V_j = 8 m/s, Re$_j$ = 3700, We$_j$ = 7300; bottom row: V_j = 12 m/s, Re$_j$ = 5600, We$_j$ = 17000.

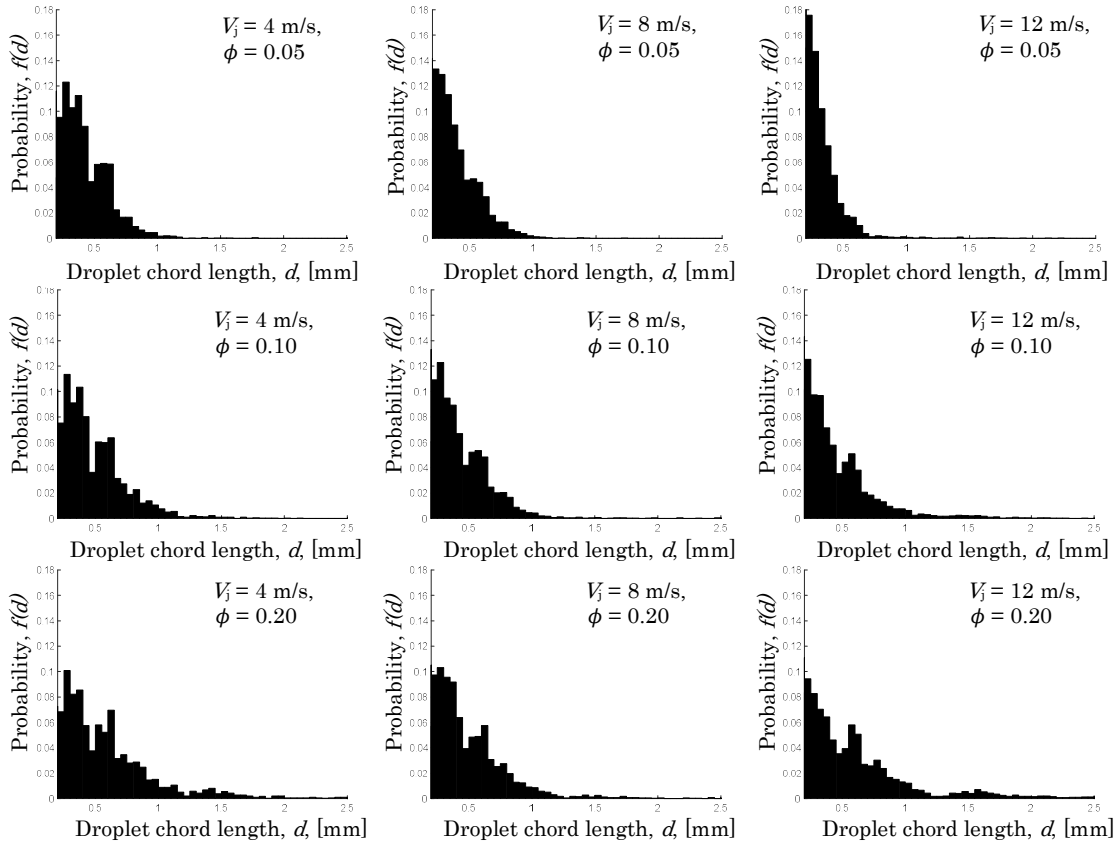


Figure 6.4 Droplet chord length distributions against height for a U-jet interacting with a crossflow velocity of V_m = 0.4 m/s at a distance of L = 10 D where the jet velocities and inlet aqueous phase fractions are varying. Left column: V_j = 4 m/s, Re_j = 1900, We_j = 1800; middle column: V_j = 8 m/s, Re_j = 3600, We_j = 7300; right column: V_j = 12 m/s, Re_j = 5600, We_j = 17000; Top row: ϕ = 0.05, Re_{aq} = 380, Re_o = 2200; 2nd row: ϕ = 0.10, Re_{aq} = 690, Re_o = 2100; bottom row: ϕ = 0.20, Re_{aq} = 1200, Re_o = 1900.

6.2 Evolution of droplet chord lengths

The time-averaged D_{32} and Dv_{90} measurements at two downstream positions from the jet, L = 4 D and L = 10 D, are presented in Table 6.2. These statistics are for a U-jet with a velocity of V_j = 12 m/s, Re_j = 5600 and We_j = 17000 interacting with crossflow velocities of 0.1 to 0.6 m/s and aqueous phase fraction of ϕ = 0.20. The measurements are spatially averaged over the vertical height of the pipe and horizontally ±0.5D either side of the measurement position, corresponding to an area of 2500 mm^2.

The residence times $t_{res,4}$ and $t_{res,10}$, correspond to the time required for the mixed flows to reach downstream distances of L = 4 D and L = 10 D, respectively.

The longest residence time is under three seconds which highlights how rapidly the flow travels from the location of jet interaction to the measurement points.

Even still, in each experimental case, the value of both D_{32} and Dv_{90} increase between $L = 4\ D$ and $L = 10\ D$. This increase indicates that by $L = 10\ D$ any residual effects of the jet are now dominated by the effects of droplet coalescence for these experimental cases.

Furthermore, at $L = 4\ D$ we find that the values of D_{32} and Dv_{90} increase with crossflow, indicating that the jet has either insufficient energy or time to have fully mixed the flow by $L = 4\ D$.

In all cases, the droplet chord lengths increased in size at $L = 10\ D$ from those measured at $L = 4\ D$ revealing that the minimum occurs before $L = 10\ D$. At $L = 10\ D$, the smallest D_{32} and Dv_{90} values occurred when the crossflow velocity was $V_m = 0.4$ m/s. Whilst at $L = 4\ D$ the smallest D_{32} and Dv_{90} values occurred when the crossflow velocity was $V_m = 0.1$ m/s.

Table 6.2 Droplet chord length statistics and associated residence times for a U-jet with a velocity of $V_j = 12$ m/s jet with $Re_j = 5600$ and $We_j = 17000$.

ϕ	V_m [m/s]	Re_{aq}	Re_o	$t_{res,4}$ [s]	$t_{res,10}$ [s]	D_{32} @ 4 D [mm]	D_{32} @ 10 D [mm]	Dv_{90} @ 4 D [mm]	Dv_{90} @ 10 D [mm]
0.2	0.1	290	480	1.12	2.84	0.92	4.67	1.71	12.38
0.2	0.2	620	1000	0.73	1.82	1.06	2.07	2.06	7.75
0.2	0.4	1200	1900	0.44	1.07	1.72	1.80	3.15	4.61
0.2	0.6	1900	2900	0.30	0.75	2.42	3.20	4.66	7.56

These test cases are expressed as vertical profile plots of D_{32} in Figure 6.5. These plots are for a U-jet interacting with a changing crossflow velocity at two downstream positions from the jet $L = 4\ D$ and $L = 10\ D$, corresponding to left and right columns, respectively. In each case, the jet velocity is $V_j = 12$ m/s and inlet aqueous phase fraction is $\phi = 0.20$. The rows increase in crossflow velocity so that the top row is $V_m = 0.1$ m/s, the 2nd row is $V_m = 0.2$ m/s, the 3rd row is $V_m = 0.4$ m/s and the bottom row is $V_m = 0.6$ m/s. The profiles use 20 equally spaced vertical ranges each 2.5 mm high as Figure 6.2. The measurements were spatially averaged over an axial distance of ±0.5D either side $L = 4\ D$ or $L = 10\ D$.

In the left columns of Figure 6.5, at a distance of $L = 4\ D$ from the jet, the droplet chord lengths are almost uniform, increasing slightly from their lowest value

at the top of the pipe. When comparing the left and right columns of Figure 6.5 it is apparent that stratification is occurring at a distance of $L = 10\ D$ where droplets are growing along the bottom of the pipe. In particular, the top two rows display a rapid increase in droplet chord length below $r = -0.8\ R$ when comparing the left to right plots, whereas the 3rd and 4th rows have a more gradual increase in droplet chord length. The plots in Figure 6.5 demonstrate that the flows are undergoing stratification between $L = 4\ D$ and $L = 10\ D$.

Figure 6.6 presents the chord length probability distributions for the same experimental test cases and positions as Figure 6.5. Where in Figure 6.6, the measurements are spatially averaged over the vertical height of the pipe and horizontally ±0.5D either side of the measurement position. In contrast to Figure 6.5, there are few signs of the stratification between $L = 4\ D$ and $L = 10\ D$ in the droplet chord length probability distributions of Figure 6.6. This suggests that larger droplets are better distributed at $L = 4\ D$ than they are at $L = 10\ D$ and that the larger droplets have undergone more stratification when compared to the smaller droplets by $L = 10\ D$.

Further examination of these probability distributions reveals several features. Firstly, there is a higher probability of larger droplets as the mixture velocity increases at both $L = 4\ D$ and $L = 10\ D$. This can be explained due to the decrease in energy of the jet relative to the incoming crossflow, i.e. drops in both the momentum flux ratio and velocity ratio. Secondly, multiple peaks are present, where a secondary peak occurs near 0.6 mm, which decreases in height as the mixture velocity, V_m, increases at a distance of $L = 4\ D$, however at a distance of $L = 10\ D$ this decrease of the secondary peak is not as apparent. While a third peak occurs at 1.5 mm, which is slightly more pronounced at $L = 4\ D$ than at $L = 10\ D$, and this peak increases with mixture velocity, V_m. These multimodal droplet chord length probability distributions indicate that the droplets could be being formed by differing processes.

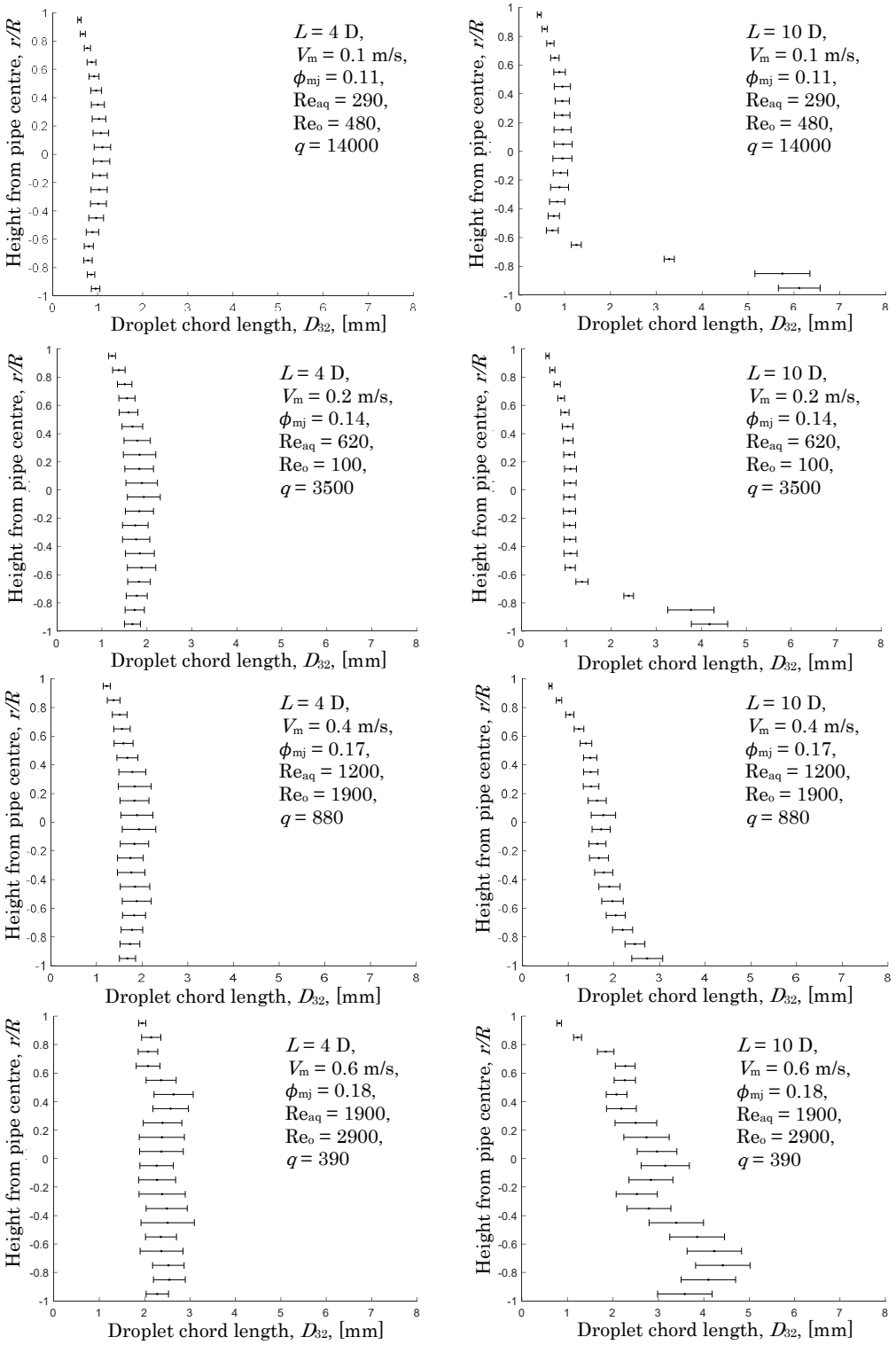


Figure 6.5 D_{32} droplet chord lengths against height for a U-jet interacting with a crossflow of $\phi = 0.20$, a jet velocity of $V_j = 12$ m/s and $Re_j = 5600$, $We_j = 17000$. Left column: $L = 4\ D$; right column: $L = 10\ D$; top row: $V_m = 0.1$ m/s, $Re_{aq} = 290$, $Re_o = 480$; 2nd row: $V_m = 0.2$ m/s, $Re_{aq} = 620$, $Re_o = 1000$; 3rd row: $V_m = 0.4$ m/s, $Re_{aq} = 1200$, $Re_o = 1900$; bottom row: $V_m = 0.6$ m/s, $Re_{aq} = 1900$, $Re_o = 2900$.

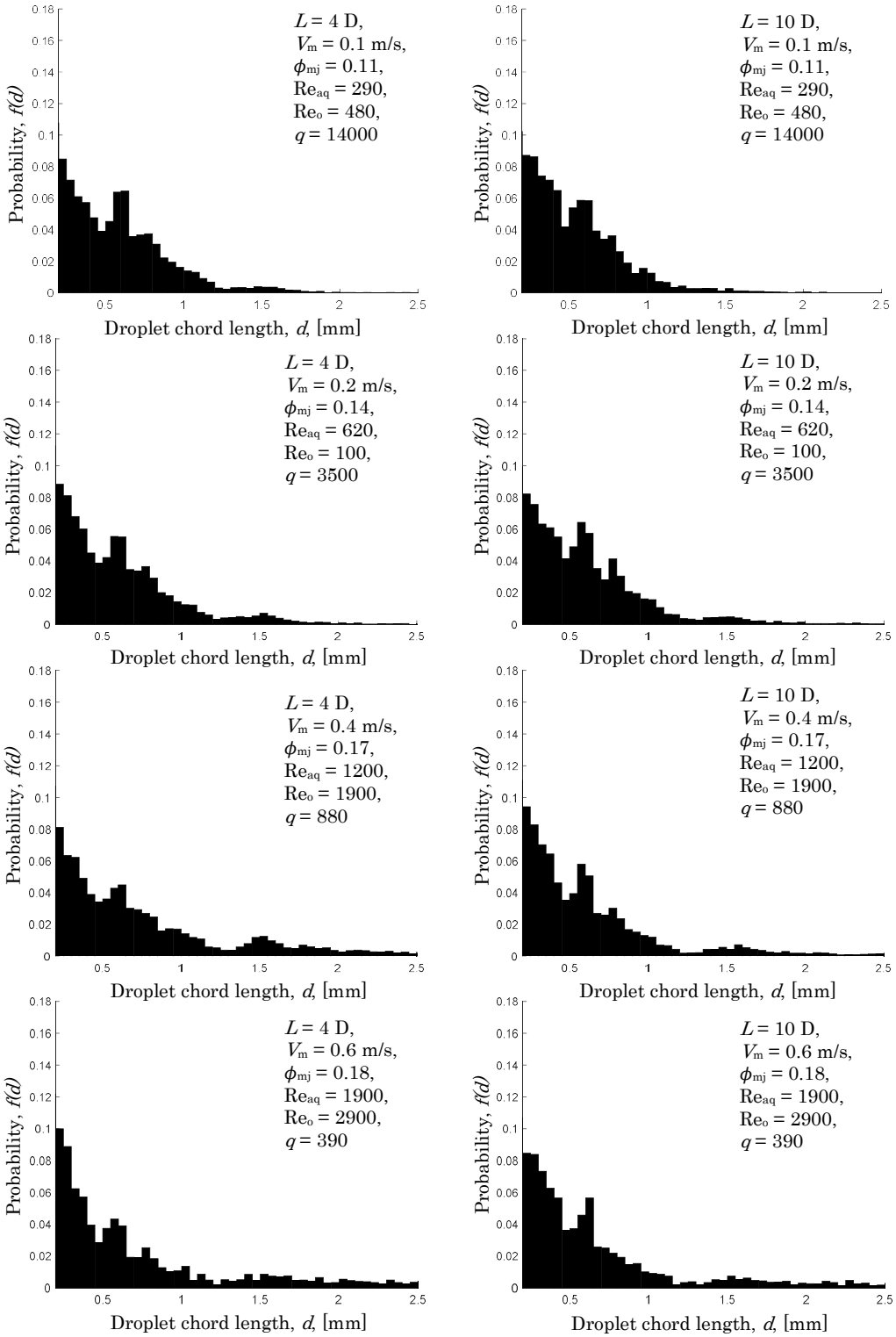


Figure 6.6 D_{32} droplet chord lengths distributions for a U-jet interacting with a crossflow of ϕ = 0.20, a jet velocity of V_j = 12 m/s and Re_j = 5600, We_j = 17000. Left column: L = 4 D; right column: L = 10 D; top row: V_m = 0.1 m/s, V_m = 0.1 m/s, Re_{aq} = 290; 2nd row: V_m = 0.2 m/s, Re_{aq} = 620, Re_o = 1000; 3rd row: V_m = 0.4 m/s, Re_{aq} = 1200, Re_o = 1900; bottom row: V_m = 0.6 m/s, Re_{aq} = 1900, Re_o = 2900.

Further insights into the droplet evolution can be found through separating the droplet chord lengths into three heights ranges, i.e. the top third, middle and the bottom thirds of the pipe's vertical measurement plane. Figure 6.7 presents these probability distributions for a U-jet with a velocity of V_j = 12 m/s interacting with a crossflow with a velocity of V_m = 0.6 m/s and an aqueous phase fraction of ϕ = 0.20. Where the measurements are spatially averaged vertically over the top, middle and the bottom thirds of the pipe and are horizontally ±0.5D averaged either side of the measurement position corresponding to an area of 833 mm^2. The figures are arranged so that the top middle and bottom thirds of the pipe correspond to the top middle and bottom rows, while the left and rights columns correspond to a distance of L = 4 D and L = 10 D, respectively.

The top third of the pipe has the highest probability of having the smallest droplets and the lowest probability of having the largest droplets at both distances. The probability of having larger droplets increases from the top to the bottom at a distance of L = 10 D. In contrast, at a distance of L = 4 D, the probability of the larger droplets appears slightly greater in the middle third of the pipe compared to the bottom third. This would indicate that at a distance of at L = 4 D stratification of the larger droplets has yet to have had a significant effect on the middle and bottom thirds of the pipe.

Larger droplets have a greater volume to the surface area which means drag is less effective at slowing gravitational settling, resulting in the larger droplets falling to the bottom quicker. Further, the side of a droplet closest to the pipe wall experiences a lower velocity over its surface when compared to the side furthest from the wall. This velocity difference results in a pressure differential across the droplet, which creates lift in a direction perpendicular and away from the pipe wall. This lift effect increases with the size of the droplet and hence the larger droplets move further away from the walls, (Voulgaropoulos et al., 2019). The combined effects of gravitational settling and lift result in the largest droplets moving away from the top third of the pipe quicker than the smaller droplets.

When compared to the lower third of the pipe, the middle third appears to have a lower probability for the smallest droplets. This can be explained through an experimental bias in the middle of the pipe, which results in a weighting toward larger droplets in this region. This experimental bias is apparent for the probabilities of the droplet less than $\approx$ 0.25 mm, whereby the middle third of the pipe has a lower probability for these smaller droplets than both the upper and lower pipe thirds.

The experimental bias occurs due to refractive index mismatches of less than 0.0001 between the liquids when combined with the difference in the path length to the camera through the emulsion to the laser plane. A refractive index mismatch results in a small distortion through every droplet interface between the image and camera which results in blurring of the image plane. The greater the number of droplets through which an image plane is viewed the greater the degree of blurring. This blurring results in smaller droplets having a greater probability of becoming indistinguishable from the background noise (predominately the glow of the ETFE pipe). In a circular pipe, the path length through the emulsion to an image plane parallel to the camera is greatest at a height of $r = 0$. Consequently, an image of a droplet needs to pass through to the greatest number of interfaces at $r = 0$. When these effects are combined smaller droplets have a greater probability of being lost to the background noise in the pipe centre creating a bias towards larger droplet sizes.

Figure 6.8 presents the probability distributions for a U-jet with a velocity of V_j = 12 m/s interacting with a crossflow with a velocity of V_m = 0.4 m/s and an aqueous phase fraction of ϕ = 0.20, at the top, middle and bottom thirds of the pipe, the left and rights columns correspond to a distance of $L = 4\ D$ and $L = 10\ D$, respectively. The measurements are spatially averaged vertically over the top, middle and the bottom thirds of the pipe and are horizontally ±0.5D averaged either side of the measurement position. The highest probability for small droplets is again present at the top third of the pipe for both distances. Comparing the histograms at $L = 4\ D$ and $L = 10\ D$ we can see that the ratio of smaller droplets to larger droplets increases at $L = 10\ D$ when compared with $L = 4\ D$ for both the top and middle thirds of the pipe. The bottom third of the pipe also has some increase in smaller droplets but this is less pronounced than in the top third. The systematic bias towards larger droplets in the central third of the pipe is again present.

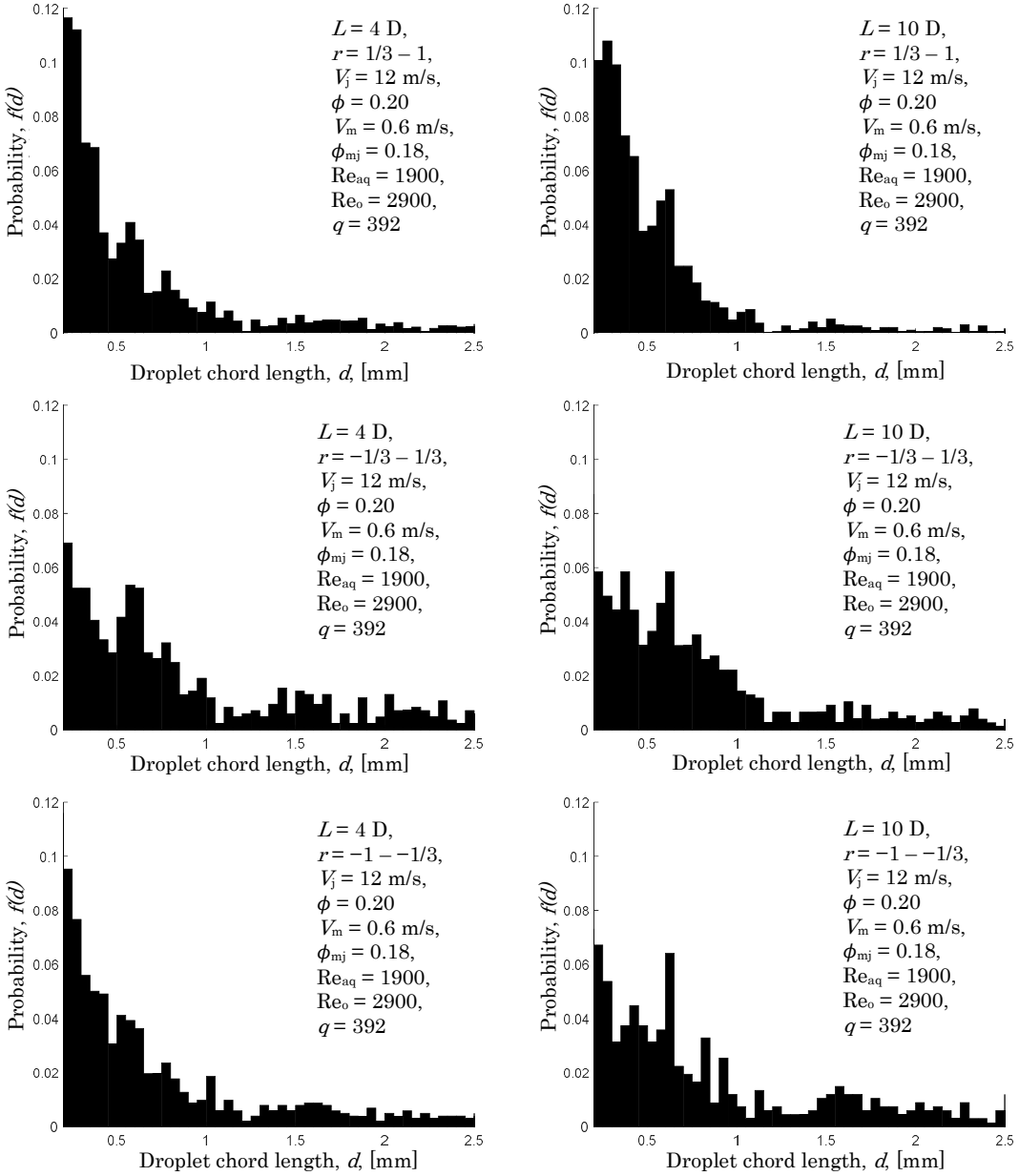


Figure 6.7 D_{32} droplet chord lengths distributions for a U-jet with a velocity of V_j = 12 m/s (Re_j = 5600, We_j = 17000) interacting with a crossflow with a velocity of V_m = 0.6 m/s and an aqueous phase fraction of ϕ = 0.20 (Re_{aq} = 1900, Re_o = 2900). Left top: top 3 rd at 4 D; Right top: pipe top 3 rd at 10 D; Left middle: pipe middle 3rd at 4 D; Right middle: pipe middle 3 rd at 10 D; Left bottom: pipe bottom 3rd at 4 D; Right bottom: pipe bottom 3 rd at 10 D.

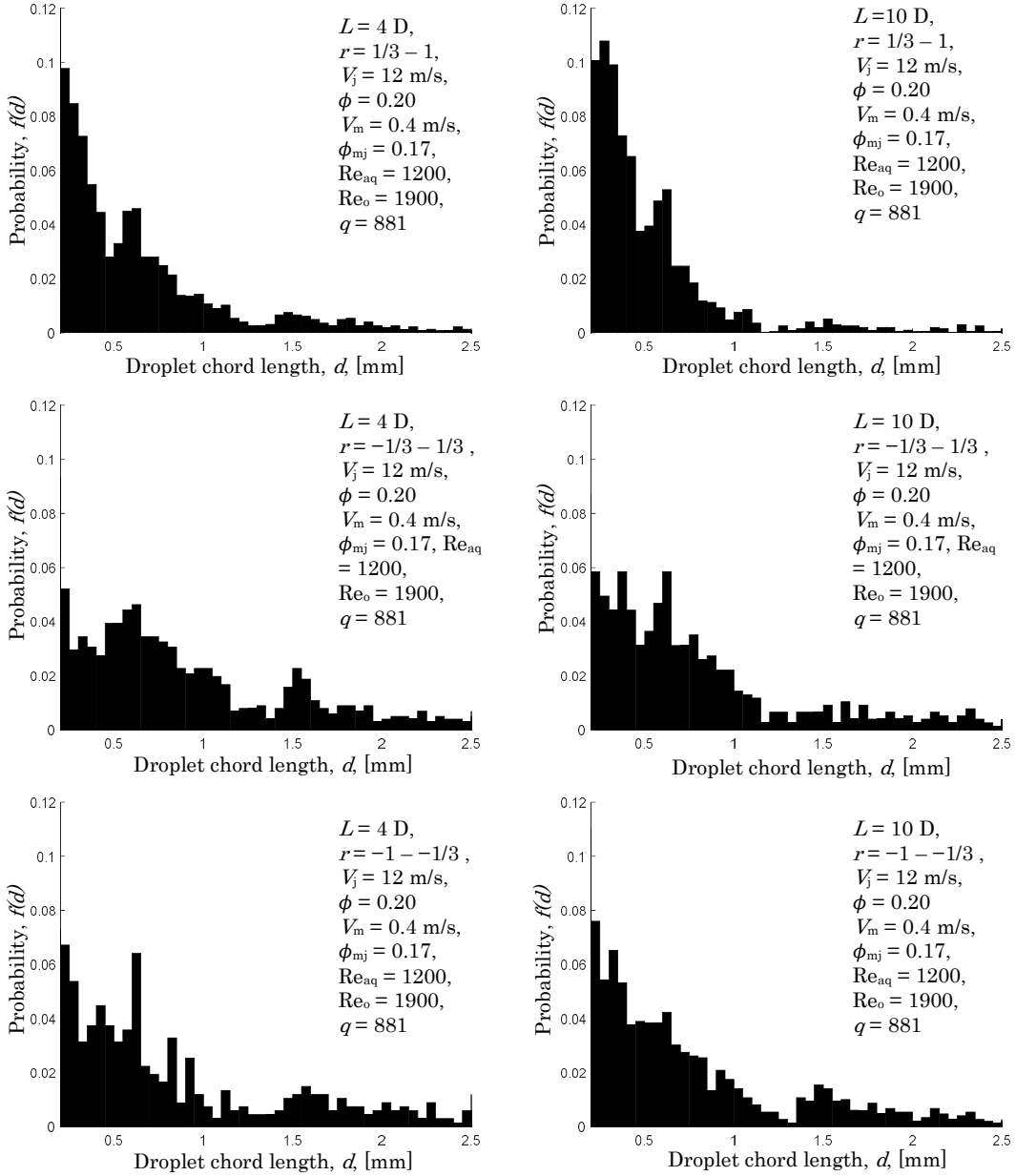


Figure 6.8 D_{32} droplet chord lengths distributions for a U-jet with a velocity of V_j = 12 m/s (Re_j = 5600, We_j = 17000) interacting with a crossflow with a velocity of V_m = 0.4 m/s and an aqueous phase fraction of ϕ = 0.20 (Re_{aq} = 1200, Re_o = 1900). Left top: top 3 rd at 4 D; Right top: pipe top 3 rd at 10 D; Left middle: pipe middle 3rd at 4 D; Right middle: pipe middle 3 rd at 10 D; Left bottom: pipe bottom 3rd at 4 D; Right bottom: pipe bottom 3 rd at 10 D.

Figure 6.9 plots the time-averaged D_{10} measurements against residence time for all experimental cases, where the measurements are separated into three aqueous phase fractions of ϕ = 0.05, ϕ = 0.10 and ϕ = 0.20. Figures 6.9 top, middle and bottom have jet velocities of V_j = 4 m/s (Re_j = 1900, We_j = 1800),

V_j = 8 m/s (Re_j = 3700, We_j = 7300) and V_j = 12 m/s (Re_j = 5600, We_j = 17000), respectively. The measurements are spatially averaged over the vertical height of the pipe and horizontally ±0.5D either side of the measurement position. The linear fits to Figure 6.9 indicate that the longer the residence time the smaller the mean (D_{10}) droplet chord length. This decreasing D_{10} with residence time could be caused by more rapid coalescence of larger droplets which reduce the overall mean droplet chord length. Further investigation is needed to confirm this. In addition, a higher inlet aqueous phase fraction results in a higher droplet chord length for each of the plots. Whilst D_{10} decreases with increasing jet velocity or Weber number, for $\phi < 0.20$. The linear fits presented in Figure 6.9 reveal the trends but have low R^2 numbers, Figure 6.10 applies a second-order polynomials which increase R^2 numbers slightly. Figure 6.10 indicates that D_{10} measurement may increase given residence time but more data is required.

In contrast to the findings of the D_{10} measurements, we find that the D_{32} display differing behaviour at higher jet velocities. Figure 6.11 plots time the averaged D_{32} measurements against residence time for all experimental cases with a jet velocity of V_j = 4 m/s, where each plot separates the experiments into three aqueous phase fractions of ϕ = 0.05, ϕ = 0.10 and ϕ = 0.20, Figures 6.11, top, middle and bottom have jet velocities of V_j = 4 m/s, V_j = 8 m/s and V_j = 12 m/s, respectively. The measurements are spatially averaged over the vertical height of the pipe and horizontally ±0.5D either side of the measurement position. Linear fits are applied to Figure 6.11 to highlight the trends.

When the jet velocity is V_j = 4 m/s, Figure 6.11(top), the D_{32} measurements behave similarly to that of the D_{10} measurements and decrease with residence time. However increasing the jet velocity to V_j = 8 m/s jets, Figure 6.11(middle), results in the trend of the D_{32} measurements for inlet aqueous phase fraction below ϕ = 0.20, reversing so that the D_{32} measurement increase with the residence time. When the jet velocity is V_j = 12 m/s jets, Figure 6.11(bottom) we find that the D_{32} measurements increase for all inlet aqueous phase fractions. Further, we see that the droplet D_{32} measurements are smaller for higher velocity and Weber number jets when the residence time is less than two seconds but that they can be larger when the residence time is longer. Figure 6.12 applies second-order polynomials which increase R^2 numbers compared to Figure 6.11. In the higher jet velocity cases, the trend in Figure 6.12 indicates that D_{32} measurements initially fall with residence

time but then grow. This trend is consistent with a change in dominance between droplet breakup and coalescence at a residence time of about two seconds.

This difference in D_{32} measurements can be explained due to coalescence of the larger droplets into the aqueous layer. The lower velocity jets and highest water fraction crossflows all have an aqueous phase layer by ten pipe diameters downstream. The largest droplets can coalesce and disappear from the statistics into this aqueous layer. In the case of the higher velocity and Weber number jets or lower aqueous phase fractions, the jet completely disperses the aqueous phase and no aqueous layer is present at ten pipe diameters downstream. Thus the largest droplets sink to the bottom of the pipe but remain in the droplet statistics as the aqueous layer has yet to form. Further investigation is needed to establish when this process becomes significant.

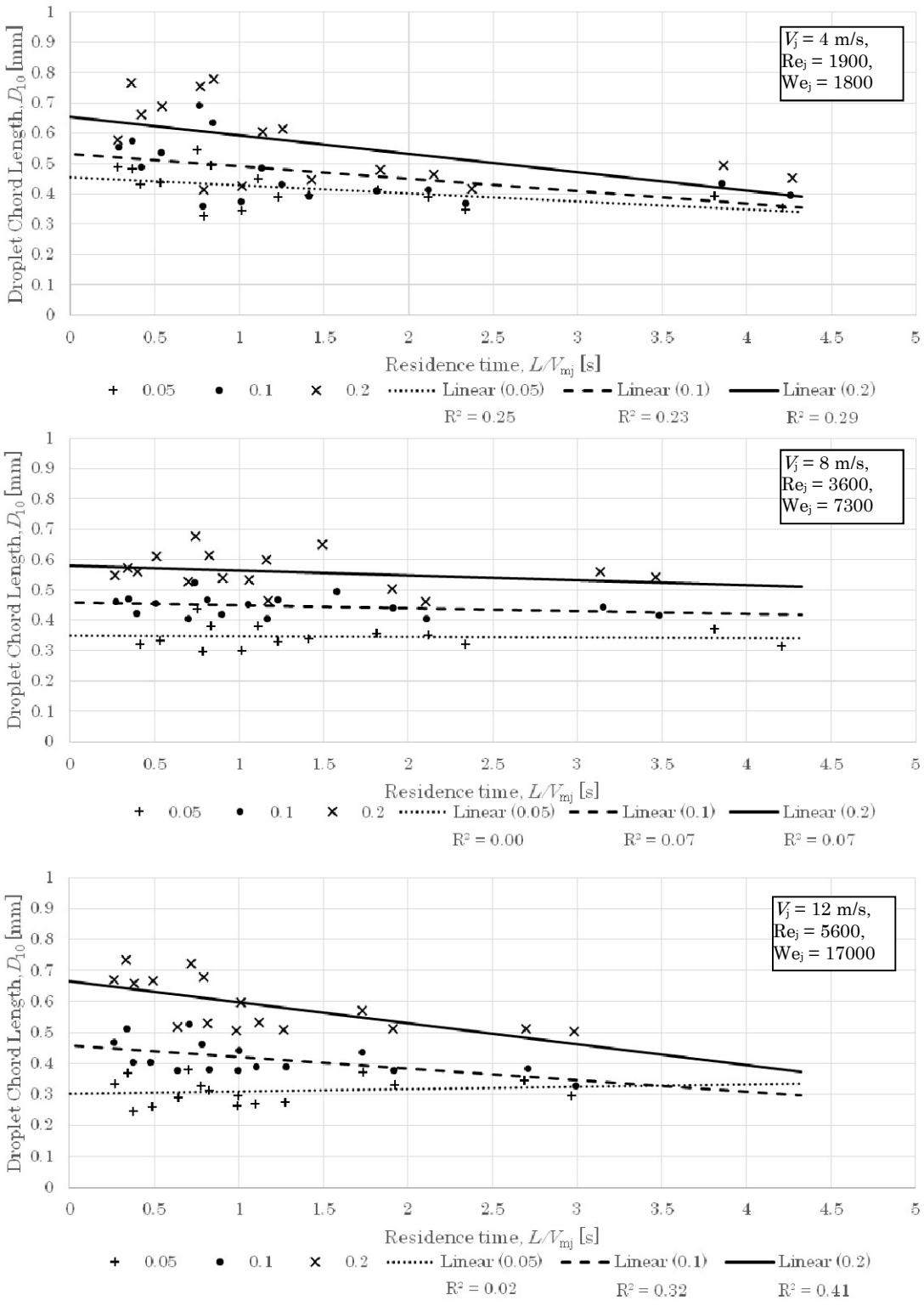


Figure 6.9 D_{10} droplet chord lengths against residence time from a U-jet interacting with crossflows with aqueous phase fractions of $\phi = 0.05$, $\phi = 0.10$ and $\phi = 0.20$, where linear fits have been applied to the data. Top: $V_j = 4$ m/s, Re$_j$ = 1900, We$_j$ = 1800; Middle: $V_j = 8$ m/s, Re$_j$ = 3600, We$_j$ = 7300; Bottom: $V_j = 12$ m/s, Re$_j$ = 5600, We$_j$ = 17000.

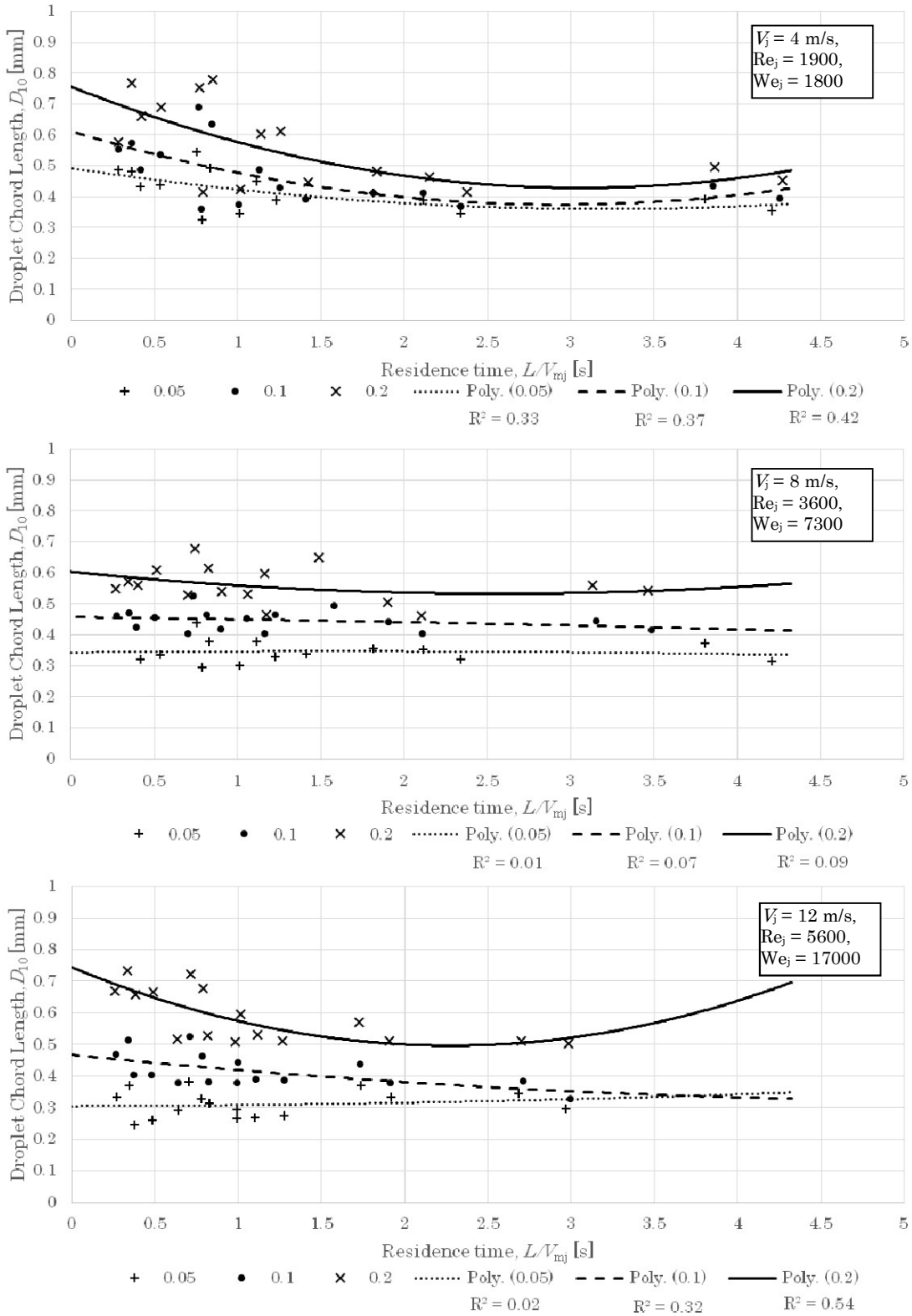


Figure 6.10 D_{10} droplet chord lengths against residence time from a U-jet interacting with crossflows with aqueous phase fractions of $\phi = 0.05$, $\phi = 0.10$ and $\phi = 0.20$, where second-order polynomials have been fitted to the data. Top: $V_j = 4$ m/s, $Re_j = 1900$, $We_j = 1800$; Middle: $V_j = 8$ m/s, $Re_j = 3600$, $We_j = 7300$; Bottom: $V_j = 12$ m/s, $Re_j = 5600$, $We_j = 17000$.

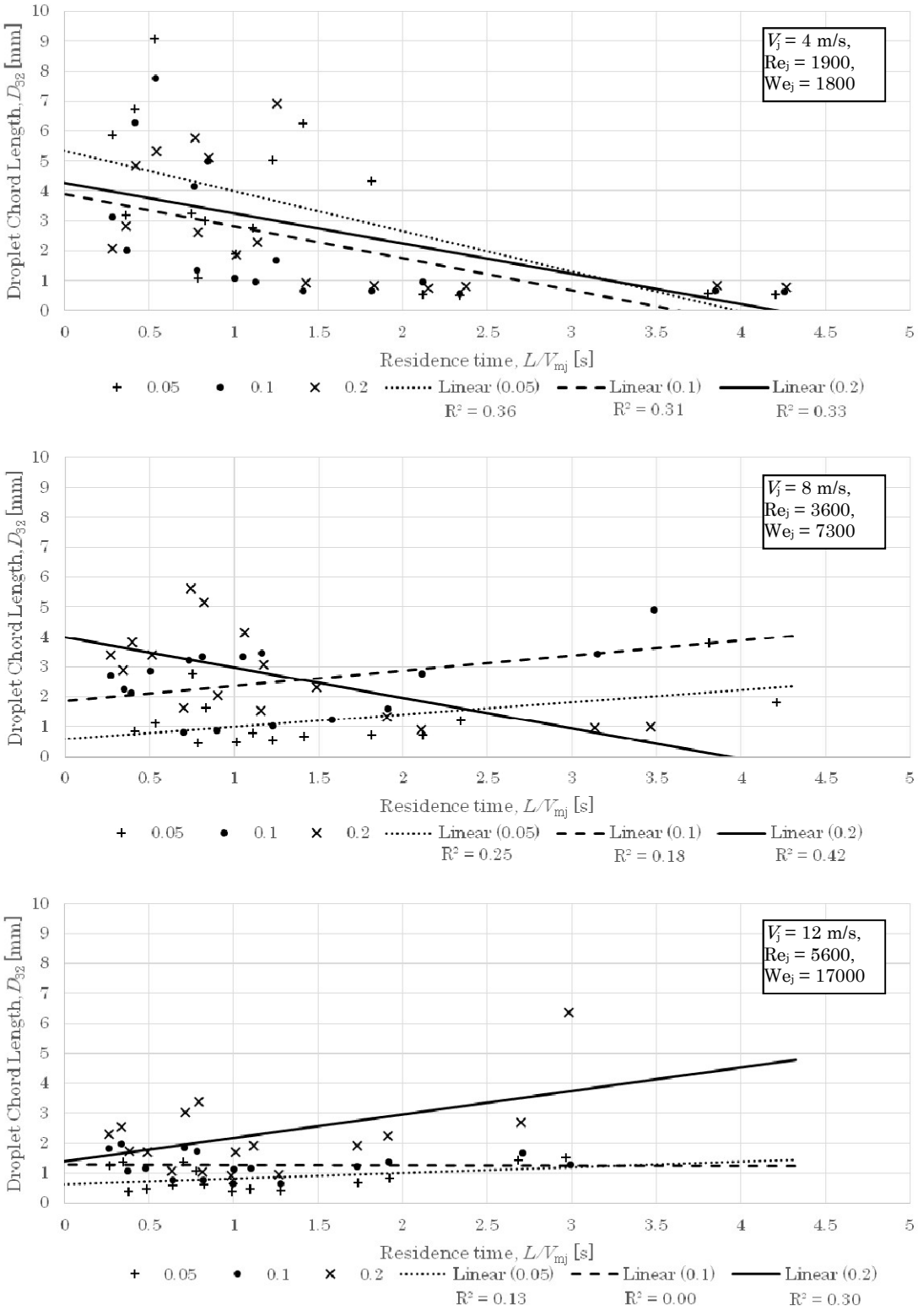


Figure 6.11 D_{32} droplet chord lengths against residence time from the jet for a U-jet interacting with crossflows with inlet aqueous phase fractions of $\phi = 0.05$, $\phi = 0.10$ and $\phi = 0.20$, where linear fits have been applied to the data. Top: $V_j = 4$ m/s, $Re_j = 1900$, $We_j = 1800$; Middle: $V_j = 8$ m/s, $Re_j = 3600$, $We_j = 7300$; Bottom: $V_j = 12$ m/s, $Re_j = 5600$, $We_j = 17000$.

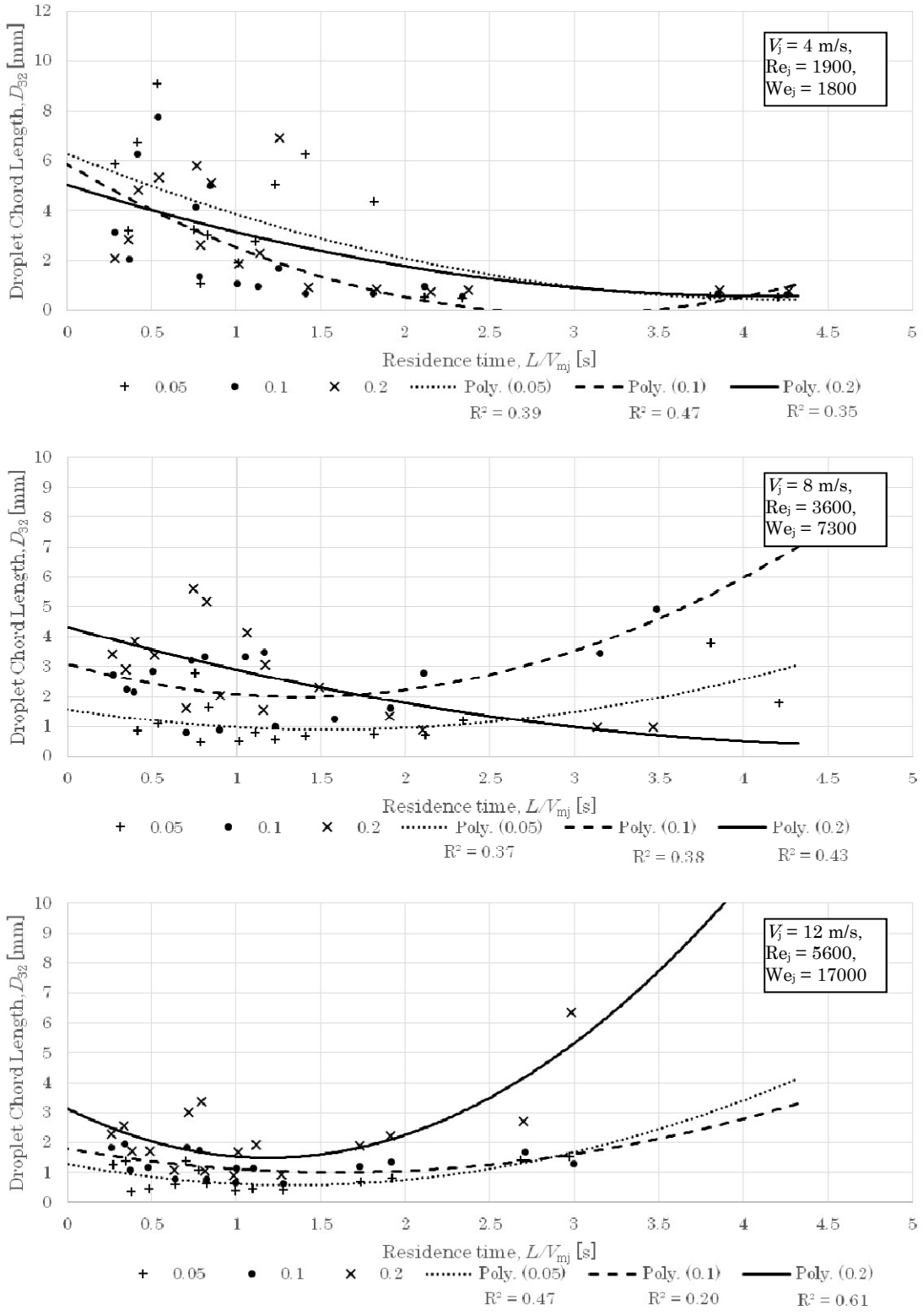


Figure 6.12 D_{32} droplet chord lengths against residence time from the jet for a U-jet interacting with crossflows with inlet aqueous phase fractions of $\phi = 0.05$, $\phi = 0.10$ and $\phi = 0.20$, where second-order polynomials have been fitted to the data. Top: $V_j = 4$ m/s, $Re_j = 1900$, $We_j = 1800$; Middle: $V_j = 8$ m/s, $Re_j = 3600$, $We_j = 7300$; Bottom: $V_j = 12$ m/s, $Re_j = 5600$, $We_j = 17000$.

The plots in figure 6.13 present the time-averaged D_{32} measurement for U-jet with jet velocity V_j = 12 m/s, Re_j = 5600 and We_j = 17000 interacting with three inlet crossflows with inlet aqueous phase fractions of ϕ = 0.05, ϕ = 0.10 and ϕ = 0.20. The measurements are spatially-averaged over the vertical height of the pipe and horizontally ±0.5D either side of the measurement position. In each case, the higher the aqueous phase fraction the larger the D_{32} measurement of droplet chord length. In most cases, the D_{32} measurements are smallest around four pipe diameters downstream from the jet exit and they either remain relatively constant or increase in size as they travel further downstream from the jet.

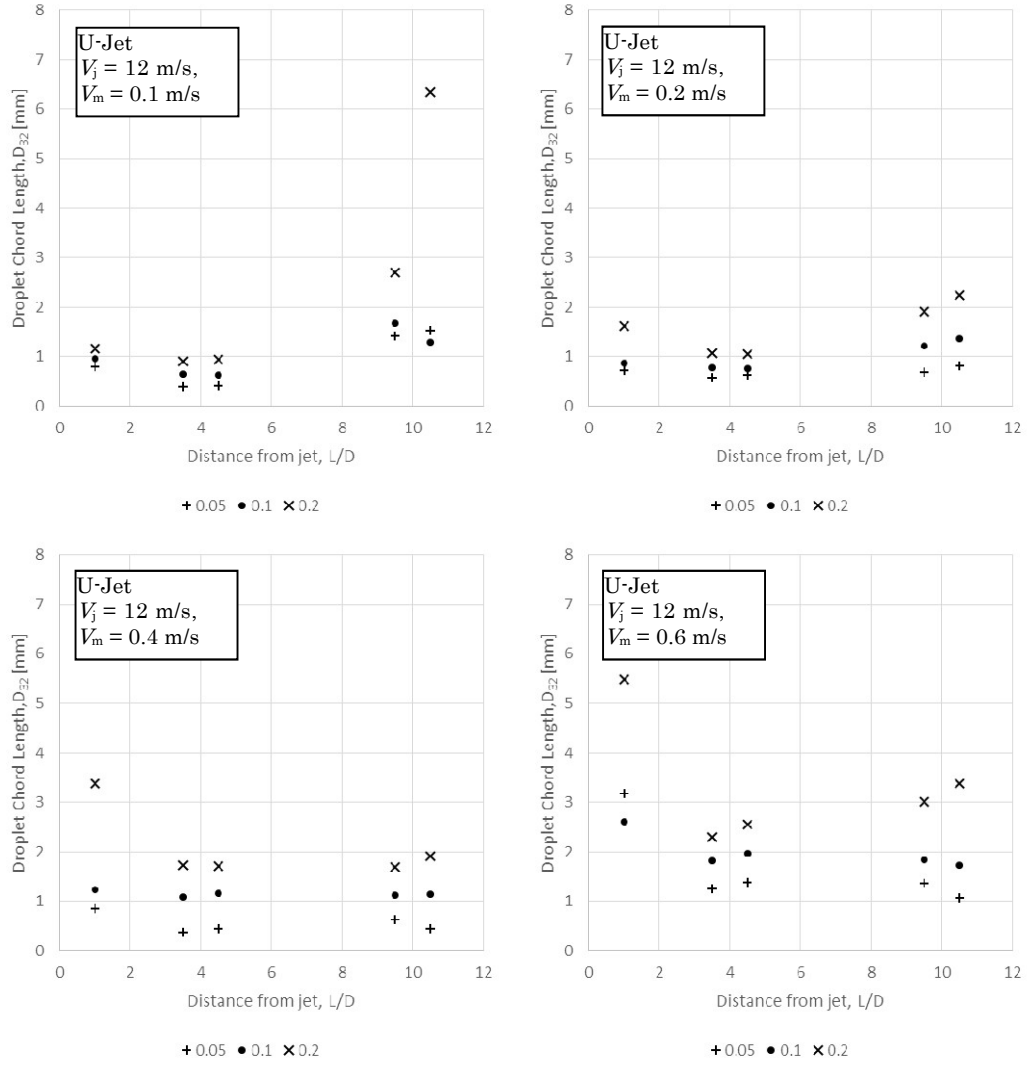


Figure 6.13 D_{32} droplet chord lengths against distance from a U-jet with jet velocity V_j = 12 m/s (Re_j = 5600, We_j = 17000) interacting crossflow with inlet aqueous phase fractions of ϕ = 0.05, ϕ = 0.10 and ϕ = 0.20. Top left: V_m = 0.1 m/s; Top right: V_m = 0.2 m/s; Bottom left: V_m = 0.4 m/s; Bottom right: V_m = 0.6 m/s.

In all cases where the aqueous phase fraction is $\phi = 0.20$, the D_{32} droplet chord length reduces in value after the jet, reaches a minimum and then increases. The lower inlet aqueous phase fractions only appear to have this behaviour at lower crossflow velocities when the residency time is longer. When residence time is on the x-axis rather than the distance, a bathtub shape is formed like that seen in Figure 6.12(bottom). This bathtub-shaped behaviour appears to be present in all cases that do not have a continuous aqueous phase/interface layer at the bottom.

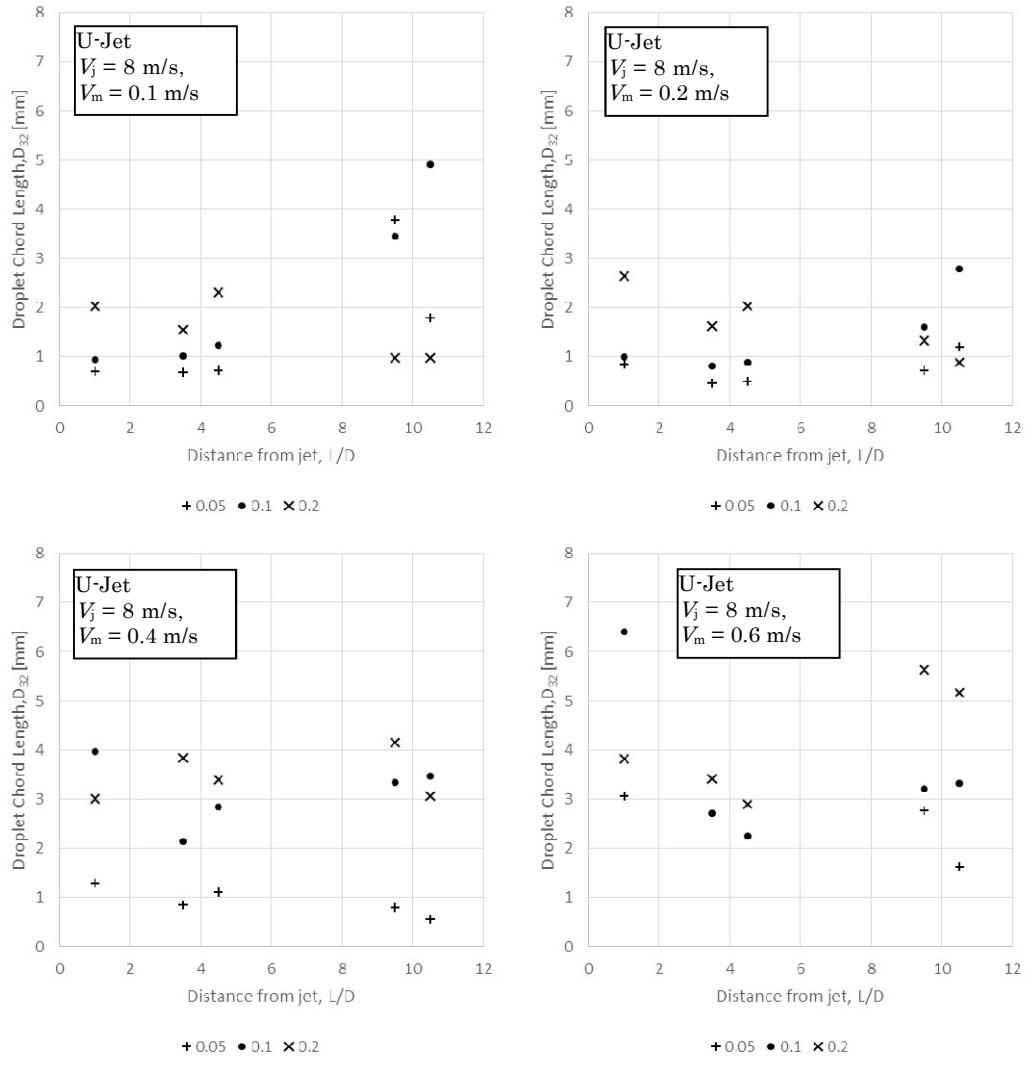


Figure 6.14 D_{32} droplet chord lengths against distance from a U-jet with jet velocity V_j = 8 m/s (Re_j = 3600, We_j = 7300) interacting crossflow with inlet aqueous phase fractions of $\phi = 0.05$, $\phi = 0.10$ and $\phi = 0.20$. Top left: V_m = 0.1 m/s; Top right: V_m = 0.2 m/s; Bottom left: V_m = 0.4 m/s; Bottom right: V_m = 0.6 m/s.

The plots in Figure 6.14 present the time-averaged measurement of D_{32} for U-jet with a velocity of $V_j = 8$ m/s interacting with crossflows that have inlet aqueous phase fractions of $\phi = 0.05$, $\phi = 0.10$ and $\phi = 0.20$. The measurements are spatially averaged over the vertical height of the pipe and horizontally ±0.5D either side of the measurement position. In the case where the aqueous phase fraction is $\phi = 0.20$ and the crossflow velocity is $V_m = 0.2$ m/s or less the D_{32} measurements decrease with distance for the lowest crossflows. These flows frequently have an interface layer at the bottom which allows the largest droplets to coalesce with the aqueous layer's interface and thus be removed from the statistics.

A model to explain these changes in droplet chord length is illustrated in Figure 6.15. In this model, the jet initially causes rapid droplet breakup resulting in the D_{32} droplet size reducing. As the energy of the jet dissipates the droplets begin to coalesce and the D_{32} droplet size increases. The larger the droplet the faster they settle to the bottom of the pipe under gravity, where an interface layer begins to form. As the larger droplets settle they rapidly coalesce with the newly formed interface leaving the remaining smaller droplets entrained within the oil phase, which causes the D_{32} droplet size to again decrease.

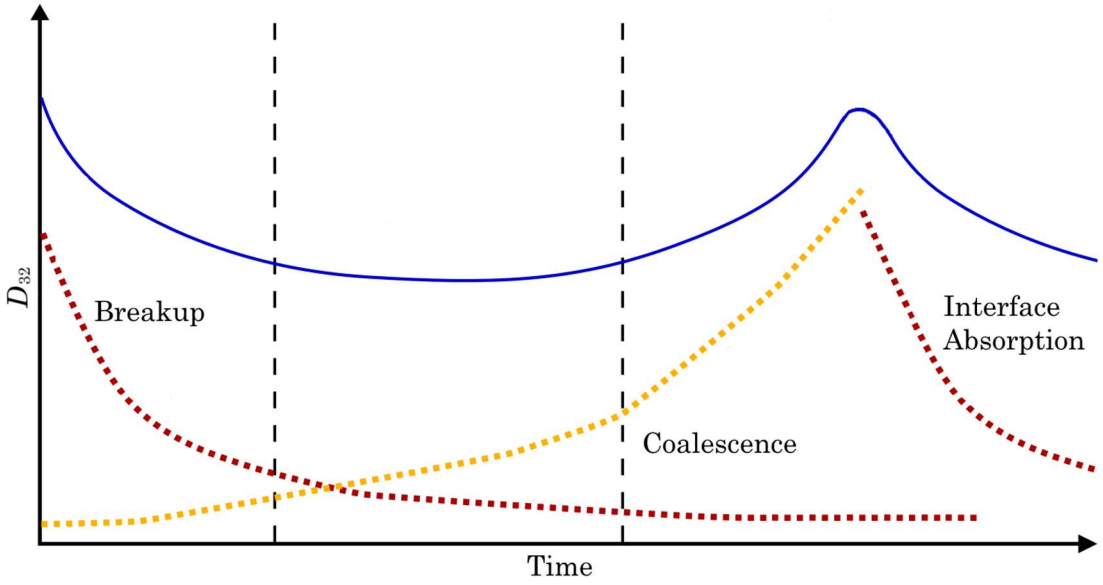


Figure 6.15 D_{32} droplet chord length model including the processes of break up, coalescence and interface absorption.

6.3 Jet type effect on droplet chord length

The D_{32} droplet chord length measurements for the three jet types at a distance of $L = 10\ D$ are presented in the profile plots of Figure 6.16, where jets with a velocity of $V_j = 12$ m/s are interacting with crossflows with an aqueous phase fraction of $\phi = 0.20$ and velocities of $V_m = 0.2$ m/s and $V_m = 0.4$ m/s. The droplet chord lengths profiles are created from 20 equally spaced 2.5 mm high vertical bands ranged over the height of the pipe. These bands are spatially-averaged over an axial distance of ±0.5D either side $L = 10\ D$, and over an area of 125 mm^2. The top, middle and bottom rows present the measurement of the U-jet, F-jet and V-jet, respectively. The D_{32} measurements for the F-jet (middle row) are larger at the bottom of the pipe than the other two jet types, indicating that the F-jet has a higher amount of stratification than the others. Conversely, the V-jet has the smallest droplets towards the bottom of the pipe and has undergone the least stratification.

The droplet chord lengths for different jets are expressed as probability distributions within the histograms of Figure 6.17. The histograms present the measurements for the U-jet encountering crossflows with an aqueous phase fraction of $\phi = 0.20$ and varying velocities at an axial distance of $L = 10\ D$. The measurements are spatially averaged over the vertical height of the pipe and horizontally ±0.5D either side of $L = 10\ D$, corresponding to an area of 2500 mm^2. The top, middle and bottom rows contain results for the U-jet, the F-jet and the V-jet, respectively. The left column has a crossflow velocity of $V_m = 0.1$ m/s, the middle column $V_m = 0.4$ m/s and the right column $V_m = 0.6$ m/s. The V-jet produces a wider distribution of droplet sizes compared to the other two jet types. This difference in droplet size distribution can in part be explained by the different amounts of vertical dispersion of the aqueous phase for each jet type, whereby a more uniform vertical phase distributions results in a wider range of droplet size. The 70% lower Weber number of the V-jet compared to the U-jet and F-jet may also contribute to this wider distribution as the effect of the interfacial tension is marginally greater in the V-jet.

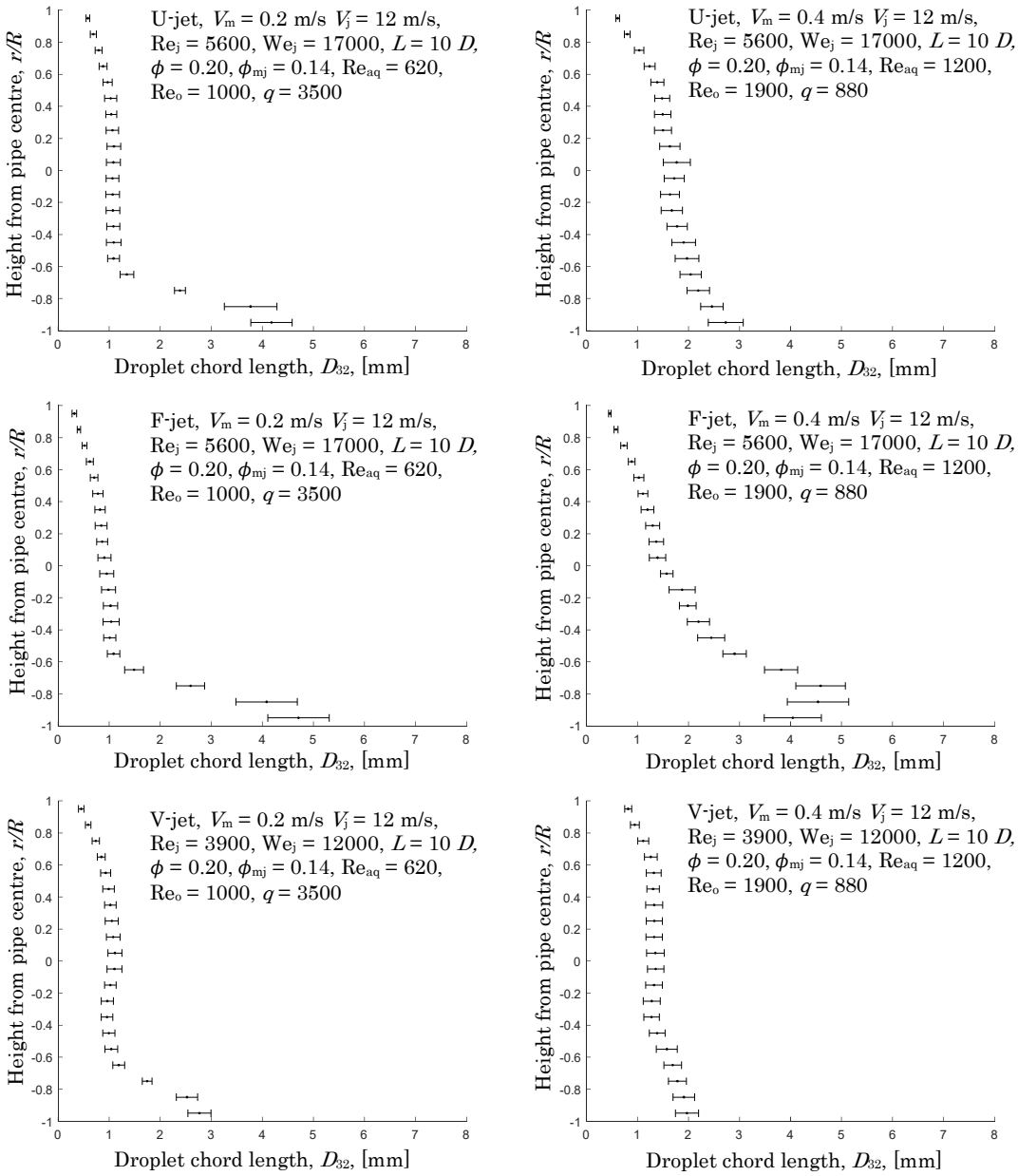


Figure 6.16 D_{32} droplet chord lengths against height for jets interacting with a crossflow of ϕ = 0.20 and a jet velocity of V_j = 12 m/s at a downstream distance of L = 10 D. Left column: V_m = 0.2 m/s, Re$_{aq}$ = 620, Re$_o$ = 1000; right column: V_m = 0.4 m/s, Re$_{aq}$ = 1200, Re$_o$ = 1900; top: U-jet, Re$_j$ = 5600, We$_j$ = 17000; 2nd row: F-jet, Re$_j$ = 5600, We$_j$ = 17000; bottom row: V-jet, Re$_j$ = 3900, We$_j$ = 12000.

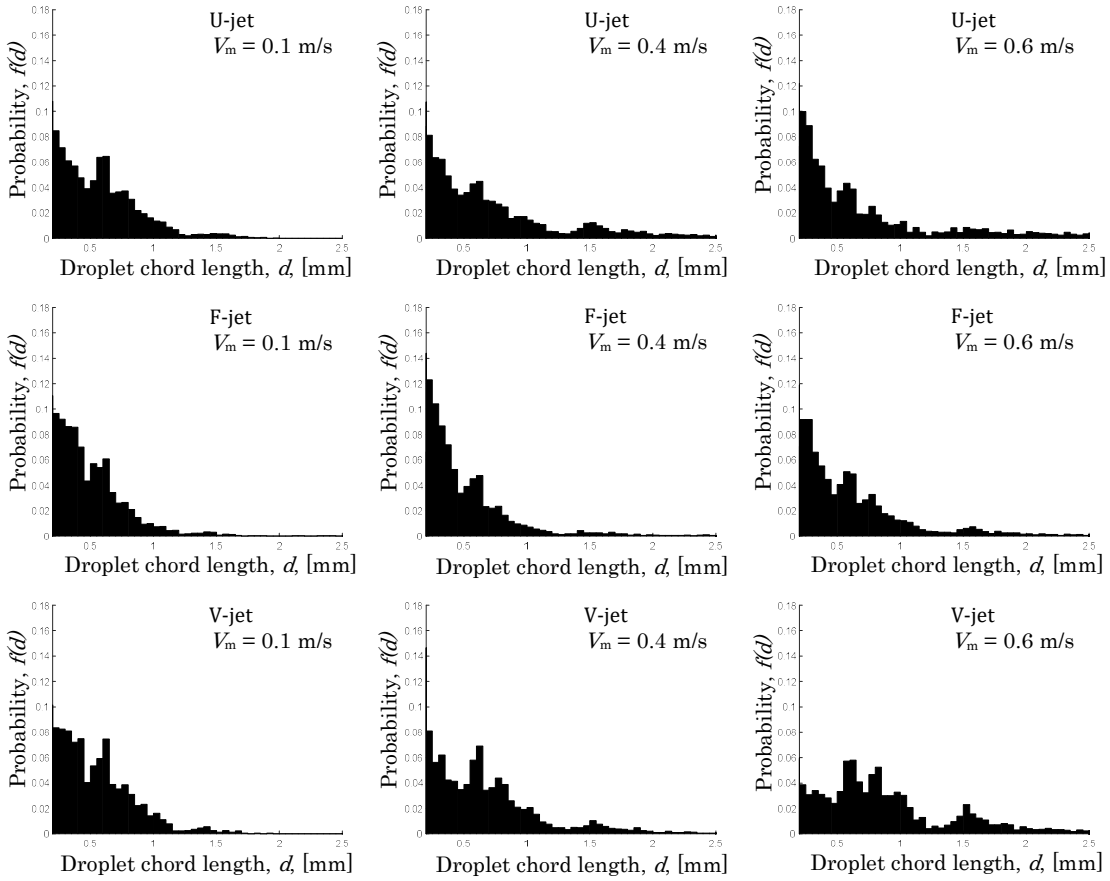


Figure 6.17 D_{32} droplet chord lengths distributions for jets interacting with a crossflow of ϕ = 0.20 and a jet velocity of V_j = 12 m/s at a downstream distance of L = 10 D. Left column: V_m = 0.1 m/s, Re_{aq} = 100, Re_o = 540; middle column: V_m = 0.4 m/s, Re_{aq} = 380, Re_o = 2200; Right column: V_m = 0.6 m/s, Re_{aq} = 590, Re_o = 3300; top row: U-jet, Re_j = 5600, We_j = 17000; 2nd row: F-jet, Re_j = 5600, We_j = 17000; bottom row: V-jet, Re_j = 3900, We_j = 12000.

6.4 Summary

This chapter presented measurements of the droplet chord lengths and how they change with the position, jet velocity, jet type, crossflow velocity and aqueous phase fraction. The key points from this chapter are:

- The probability distribution of D_{32} reveals that for some experimental cases, droplets are still undergoing breakup at four pipe diameters, indicating the influence of the jet can still be significant at this distance.
- The droplet chord lengths increase in size at all distances and stratification occurs more quickly as the input aqueous phase fraction is increased and the jet velocity is decreased.

- Probability distributions exhibit a multimodal distribution of droplet chord lengths in most, if not all, experimental cases. The existence of a multimodal distribution suggests that the droplets are formed through multiple processes. Potential processes listed previously include Kelvin-Helmholtz instabilities and secondary break up of ligaments and sheets formed by the jet during the initial interaction and the second region of jet interaction.
- In all cases, droplets chord lengths were found to have increased at a distance of ten pipe diameters when compared to their lengths at four pipe diameters. This indicates that by ten pipe diameters, coalescence is the dominant process and the energy from the jet has decayed significantly.

Additional points of interest include:

- The relationships between the five droplet chord length measurements of D_{10}, Dv_{10}, Dv_{50} and Dv_{90} to D_{32} were approximated in Eqs. 6.1 to 6.4. Where the D_{max} substitute of Dv_{90} value was found to be ≈ 2.8 times as large as the D_{32}.
- Stratification of the flows is not as apparent in the droplet chord length probability distributions as it is in the vertical profiles of D_{32} or the vertical concentration profiles discussed in Chapter 5.
- Probability distributions reveal that higher velocity jets create smaller droplet distributions. Higher velocity jets add a greater amount of energy into the flow and this additional energy can further counteract interfacial tension and create a greater droplet surface area.
- Vertical droplet chord length profiles have a peak in chord length towards the bottom of the pipe, but not at the bottom. Several processes contribute to this (i) lift effects are produced by the differential pressures created due to different velocities a droplet experience close to a wall causes the largest droplets to move away from the walls; (ii) the combination of gravity and drag causes the largest droplets to settle towards the bottom of the pipe; (iii) high aqueous contact angle keeps the largest droplets further away from the ETFE wall.
- The middle third of the pipe has an experimental bias towards larger droplets due to the increased blurring through a greater number of droplet interfaces to the measurement plane. The blurring occurs due to the slight inevitable mismatch in refractive index between the two closely matched liquids.
- The mean (D_{10}) measurement of droplet chord length was found to decrease with increasing residence time when an interface is present. This can be explained by

the more rapid coalescence of the largest droplets with the interface, which results in reducing the mean of the remaining droplet chord lengths.

- The V-jet was found to produce the most even vertical droplet distribution of the three jet types. However, the V-jet also produced the widest distributions of droplet chord lengths. This difference in droplet chord lengths distribution indicates that the fraction of the processes leading to droplet formation may be different in the V-jet when compared with the other two jet types.

Chapter 7

Velocity field measurements

This chapter presents the PIV and stereo-PIV measurements of the experimental velocity fields for the incoming flows, the area of jet interaction and the resulting dispersions downstream of the jet.

7.1 Incoming velocity fields before jet interaction

This section presents the time-averaged velocity fields of the pipe flow when no jet is present at a position of $L = -2\ D$ upstream of the jet location. Figure 7.1 plots the time-averaged vertical velocity profile for a pipe flow of pure BC10 silicone oil with a velocity of V_m = 0.198 m/s and a Reynolds number of Re = 1380. Averaging was performed over 490 frames which were taken at a speed of 40 Hz. The solid line is the measured flow profile while the dashed line is the measured profile reflected at $r = 0$, and for comparison, the dotted line is the theoretical velocity profile for a laminar flow of the same rate. The velocity profile has an asymmetry of ≈ 3% with the peak in the bottom half of the pipe, while the peak velocity is ≈ 5% below the theoretical for laminar flow.

Initially, the asymmetry in the pipe flow was found to be significantly larger and following an extensive investigation, it was found that the thin and flexible walls of the ETFE pipe were deforming. Gravity caused the pipe cross-sectional to deform, flattening and becoming slightly oval, while the pipe was also found to sag between the pipe supports. Increases in internal pipe pressure caused it to re-inflate and become straighter and circular again. To minimise these deformations the flexible ETFE pipe was encased within a much stronger PVC pipe with the same internal diameter as the ETFE pipe's external diameter. The PVC pipe encased all areas where observations were not being made.

A further effect that may have contributed to flow asymmetry was the density difference between the oil tracer particles of 900 kg/m^3 and the oil itself at 930 kg/m^3. These large particles were found to preferentially rise towards the top of the pipe where they would adhere to the pipe's surface and hence bias the surface roughness of the pipe towards the top when the flows were stopped. The particles were 100 µm in size and this surface roughness would have been of the same order of ≈ 100 µm. However, it should be noted that the flow in figure 7.1 is laminar and thus the effects of surface roughness can be ignored in this example.

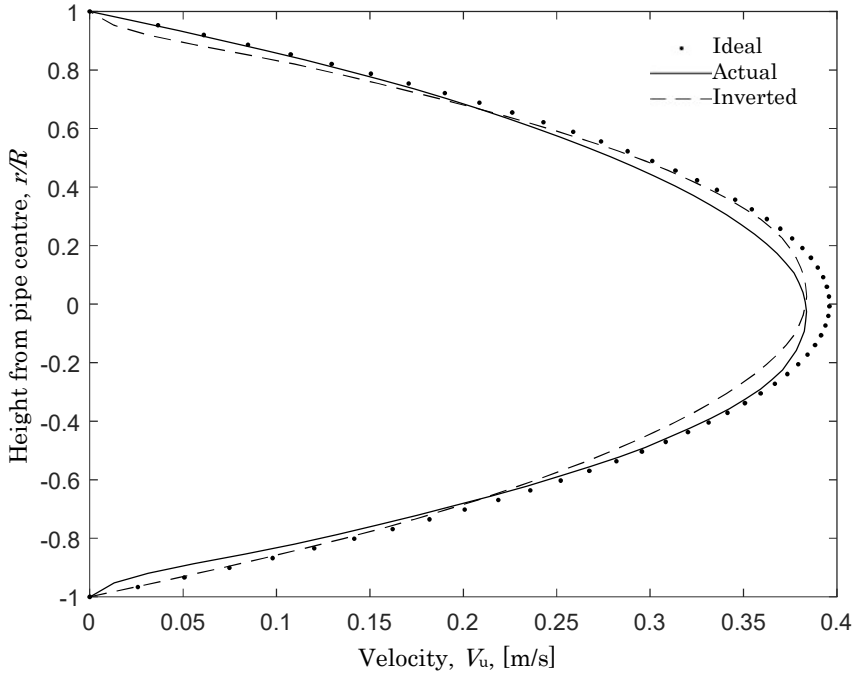


Figure 7.1 PIV measurement of a time-averaged velocity field for a laminar single-phase crossflow velocity of V_m = 0.198 m/s and a Reynolds number of Re = 1380 compared with its reflection in r = 0 and an ideal parabolic laminar flow profile for the same velocity.

Although the velocity profile of Figure 7.1 is not perfectly symmetrical we can integrate this 2-D velocity profile if we make assumptions about the flow outside the measurement plane. To do this we must assume that velocity measured at any point is representative of the semi-annulus of the pipe at the height of the measurement. Figure 7.2 is a stylized example of the method used, the measurement plane passes vertically through the pipe where, in this example, there are eight velocity measurement points. Each point is assumed to be representative of the semi-annuli and semi-circles they are located within. The

flow rate is then calculated by multiplying the measured velocity by the associated area. This method is used to integrate the velocity profile shown in Figure 7.1 to give an oil flow rate of 21.9 L/s. In comparison, the oil flow rate measured by the large oil turbine meter was 23.4 L/s. Therefore, the flow measured between the two methods deviates by 6% and is an indication of the uncertainty of the velocity measurements.

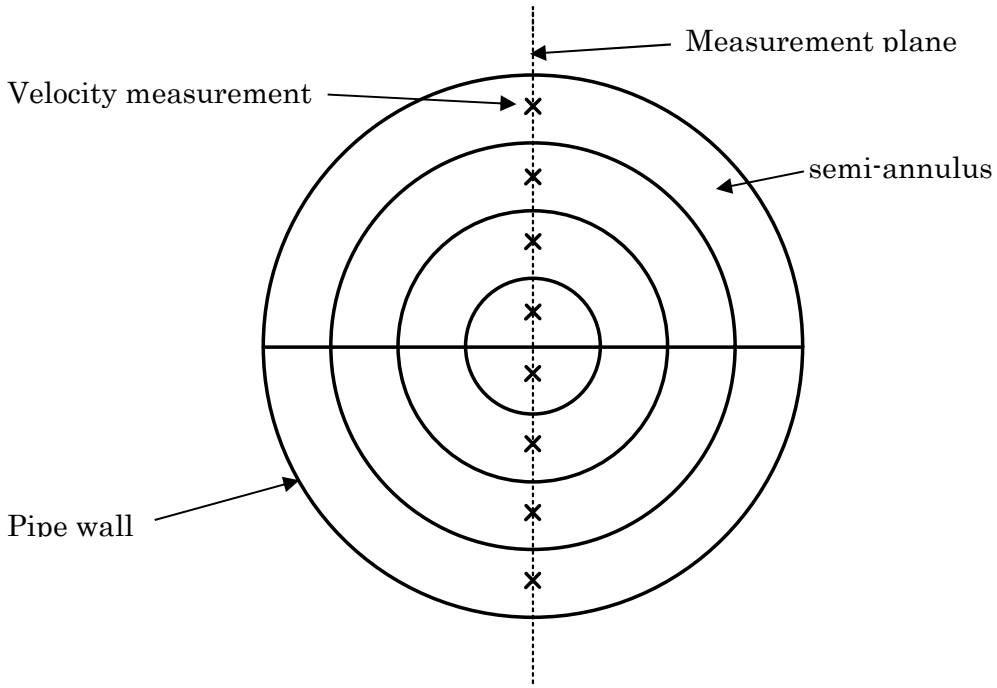


Figure 7.2 Illustration of the method used to integrate the velocity profile of an almost symmetrical laminar flow to calculate the overall flow rate.

Figure 7.3 plots the time-averaged PIV velocity field measurements at a position of $L = -2\ D$ for several two-phase flows with a mixture velocity of $V_m = 0.2$ m/s and aqueous phase fractions of $\phi = 0.05$, $\phi = 0.10$, $\phi = 0.20$ and $\phi = 0.50$. Averaging was performed over 490 frames which were taken at a speed of 40 Hz. The plots indicate that as the fraction of the denser and lower viscosity aqueous phase is increased, the peak in maximum velocity becomes progressively lower in the pipe and consequently closer to the exit of the jet nozzle. No inflection point can be seen at the interface of the liquids although this likely due to similarity in the viscosity of the two phases combined with the spatial resolution of the PIV measurement.

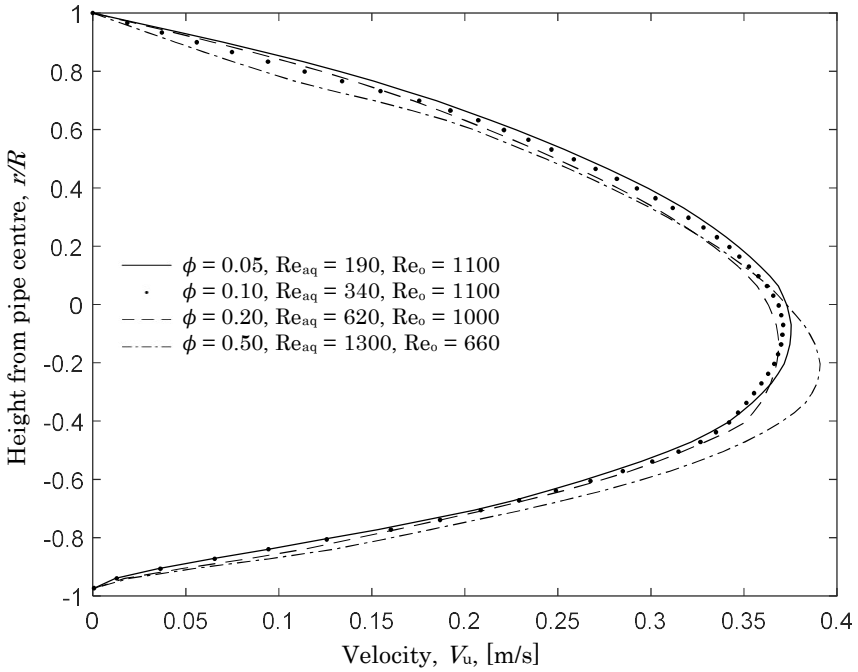


Figure 7.3 PIV measurement of a time-averaged velocity field for a two-phase crossflow with a velocity of V_m = 0.2 m/s and four aqueous phase fractions of ϕ = 0.05, ϕ = 0.10, ϕ = 0.20, and ϕ = 0.50, at a distance of L = −2 D.

7.2 Velocity fields downstream of jet interaction

This section presents a subset of the PIV measurements at a distance of ten pipe diameters downstream of the point of jet interaction (L = 10 D). Comparing the effect of the aqueous phase fraction, inlet velocity and jet velocity on the resultant velocity field.

7.2.1 Aqueous phase fraction effect downstream

Figure 7.4 presents the time-averaged velocity field of the downstream flow following an F-jet with a velocity of V_j = 8 m/s mixing crossflows with a velocity of V_m = 0.2 m/s and aqueous phase fractions of ϕ = 0.05 and ϕ = 0.20. Averaging was performed over 1224 frames which were taken at a speed of 100 Hz.

Comparing the downstream (L = 10 D) velocity profiles of Figure 7.4 with that of the incoming velocity profiles of Figure 7.3, it is apparent that the profiles have a much more rounded appearance which does not follow a laminar flow profile. This indicates that even the worst-performing F-jet is still creating a disturbance at this distance for both crossflow velocities and hence residence times.

The upper third of the two velocity profiles are similar to each other but deviations become apparent in the lower half of the two profiles. The profile for the lower aqueous phase fraction has its velocity peak towards the centre of the pipe whereas the peak for the higher aqueous phase fraction occurs above the centre line at $r \approx 0.2\ R$. The velocity profile of lower aqueous phase fraction decreases slowly until $r \approx -0.4\ R$, where it then decreases rapidly up to the wall. The velocity profile of the higher aqueous phase fraction decreases slowly up until $r \approx -0.9\ R$, where it then decreases more rapidly up to the wall. Instantaneous PLIF images of these flows are presented in Figure 7.5 which reveals that the flow with the higher aqueous phase fraction has managed to form a continuous aqueous layer in contrast to the lower aqueous phase fraction.

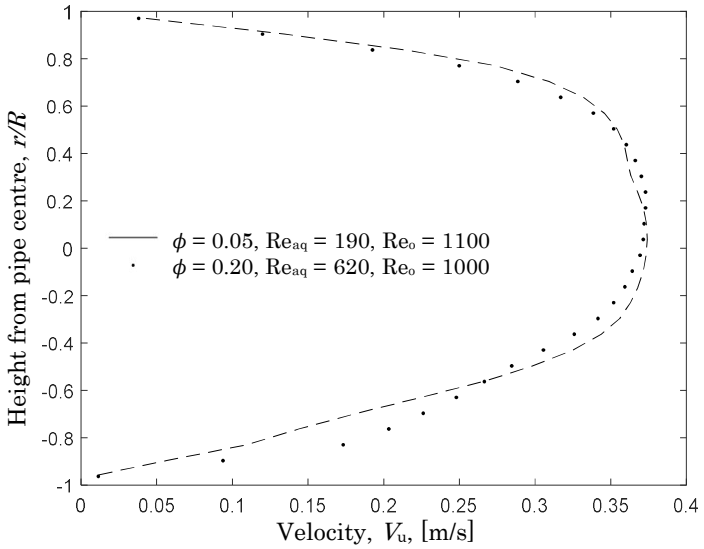


Figure 7.4 Top: PIV measurement of a time-averaged velocity field at a downstream position of $L = 10\ D$ for F-jet with a velocity of $V_j = 8$ m/s and $Re_j = 3600$, $We_j = 7300$ interacting with a crossflow velocity of $V_m = 0.2$ m/s and aqueous phase fractions of $\phi = 0.05$ ($Re_{aq} = 190$, $Re_o = 1100$) and $\phi = 0.20$ ($Re_{aq} = 620$, $Re_o = 1000$).

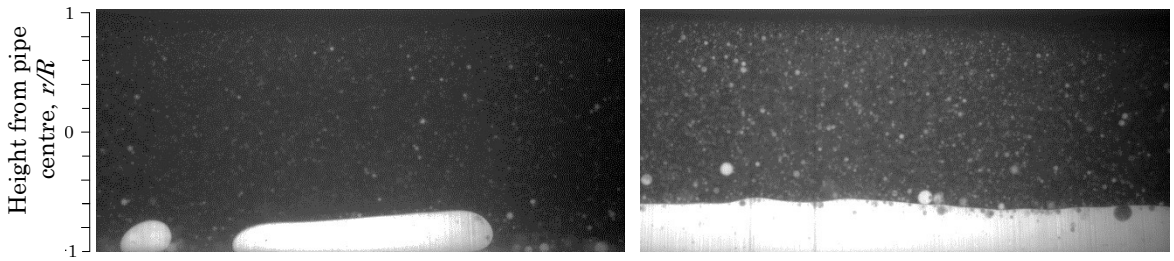


Figure 7.5 PLIF view at a downstream position of $L = 10\ D$ for F-jet with a velocity of $V_j = 8$ m/s and $Re_j = 3600$, $We_j = 7300$ interacting with a crossflow velocity of $V_m = 0.2$ m/s and various aqueous phase fractions. Left: $\phi = 0.05$ ($Re_{aq} = 190$, $Re_o = 1100$); Right: $\phi = 0.20$ ($Re_{aq} = 620$, $Re_o = 1000$).

7.2.2 Crossflow velocity effect downstream

The effect of incoming crossflow velocity on the downstream mixture flow profile are observable in the time-averaged velocity field measurements of Figure 7.6. Figure 7.6 top and bottom correspond to the F-jet and V-jet, respectively. Both profiles were measured at $L = 10\ D$ downstream of the jet and have a jet velocity of $V_j = 8$ m/s. The crossflows have an aqueous phase fraction of $\phi = 0.20$ and velocities of $V_m = 0.2$ m/s and $V_m = 0.6$ m/s.

The velocity profile of the two jet types is relatively similar when the crossflow velocity is $V_m = 0.2$ m/s, but becomes substantially different when the crossflow velocity is increased to $V_m = 0.6$ m/s. This implies that the jet still has a significant effect at ten diameters downstream when the crossflow velocity is $V_m = 0.6$ m/s. This also suggests that the crossflow velocity of $V_m = 0.6$ m/s requires a longer development length than that of the $V_m = 0.2$ m/s crossflow velocity which appears developed at $L = 10\ D$.

In both cases, the peak velocities for the F-jet occurs in the top half of the pipe, occurring at $r = 0.2\ R$ and $r = 0.5\ R$ for crossflow velocities of $V_m = 0.2$ m/s and $V_m = 0.6$ m/s, respectively. Whilst the peak velocities for the V-jet occur lower in the pipe, occurring at $r = 0.0\ R$ and $r = -0.3\ R$ for the crossflow velocities of $V_m = 0.2$ m/s and $V_m = 0.6$ m/s, respectively. Importantly, any remaining stratified aqueous phase would be expected to be present towards the pipe's bottom where the V-jet has higher velocities than that of the F-jet.

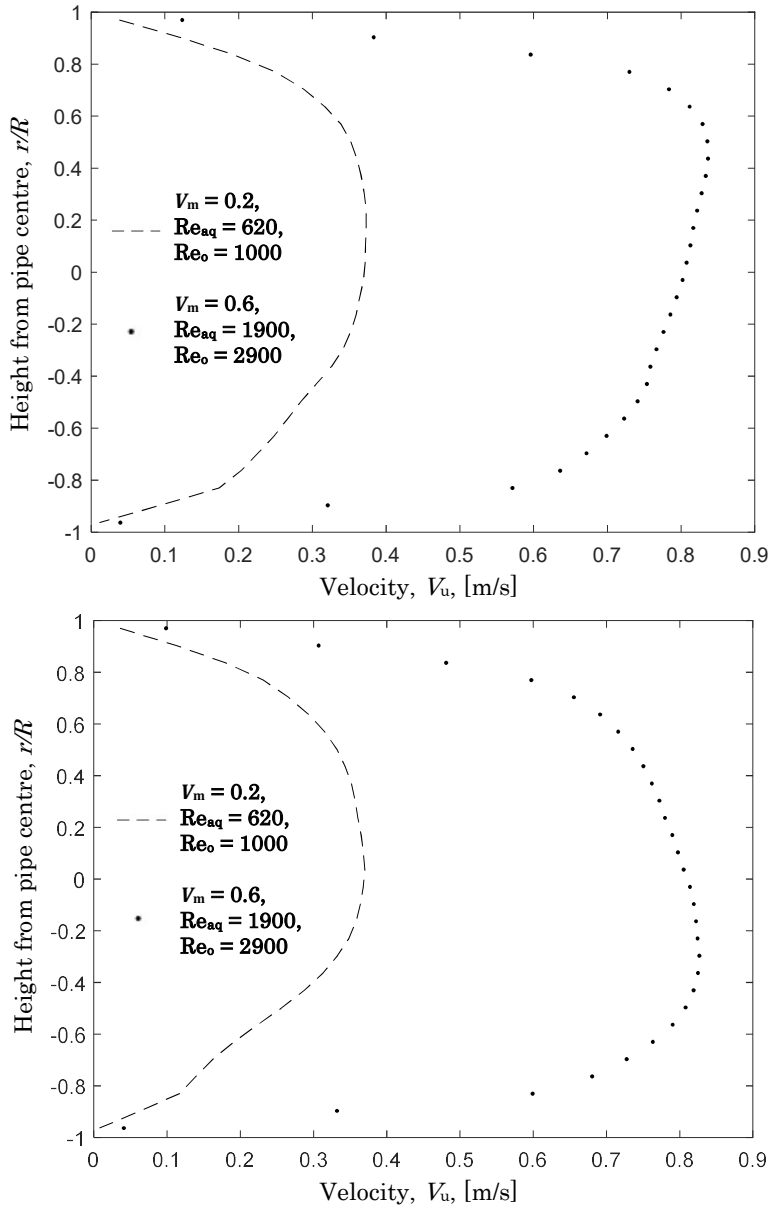


Figure 7.6 PIV measurement of a time-averaged velocity field at $L = 10\,D$ for different jet types with a velocity of $V_j = 8$ m/s interacting with an aqueous phase fraction of $\phi = 0.20$ and two crossflow velocities of $V_m = 0.2$ m/s and $V_m = 0.6$ m/s. Top: F-jet, $Re_j = 3600$, $We_j = 7300$; Bottom: V-jet, $Re_j = 2500$, $We_j = 5100$.

7.2.3 Jet velocity effect downstream

Figure 7.7 presents the measurements of the effect of the jet velocity on the downstream mixture flow profile of a crossflow with a velocity of $V_m = 0.2$ m/s and aqueous phase fraction of $\phi = 0.20$, where the jet velocities are $V_j = 4$ m/s, $V_j = 8$ m/s and $V_j = 12$ m/s. Figure 7.7 top and bottom correspond to the F-jet and V-jet, respectively. The increase

in jet velocity adds to the overall downstream flow at the point of measurement, hence increasing the mixture crossflow velocity as the jet velocity increases.

The velocity profiles of the two jets are broadly similar at jet velocities of $V_j = 8$ m/s and $V_j = 12$ m/s, although the peak in velocity in the F-jet is marginally higher in the pipe when compared to that of the V-jet. The V-jet creates a more evenly vertically distributed velocity profile, especially at the highest jet velocity of $V_j = 12$ m/s.

The two velocity profiles of the F-jet and V-jet diverge more significantly at a jet velocity of $V_j = 4$ m/s where both have a parabolic profile at the top until they diverge at $r = 0.4\,R$. The V-jet continues with a blunted parabolic profile that is similar to that expected for a two-phase stratified flow with a step-change in viscosity at $r \approx -0.4\,R$. The F-jet has a flatter profile between $r = -0.7\,R$ and $r = 0.4\,R$ that decreases in velocity from top to bottom. This is followed by a sharp decrease in velocity to the bottom wall. The cause of the difference at $V_j = 4$ m/s is unclear and needs further investigation.

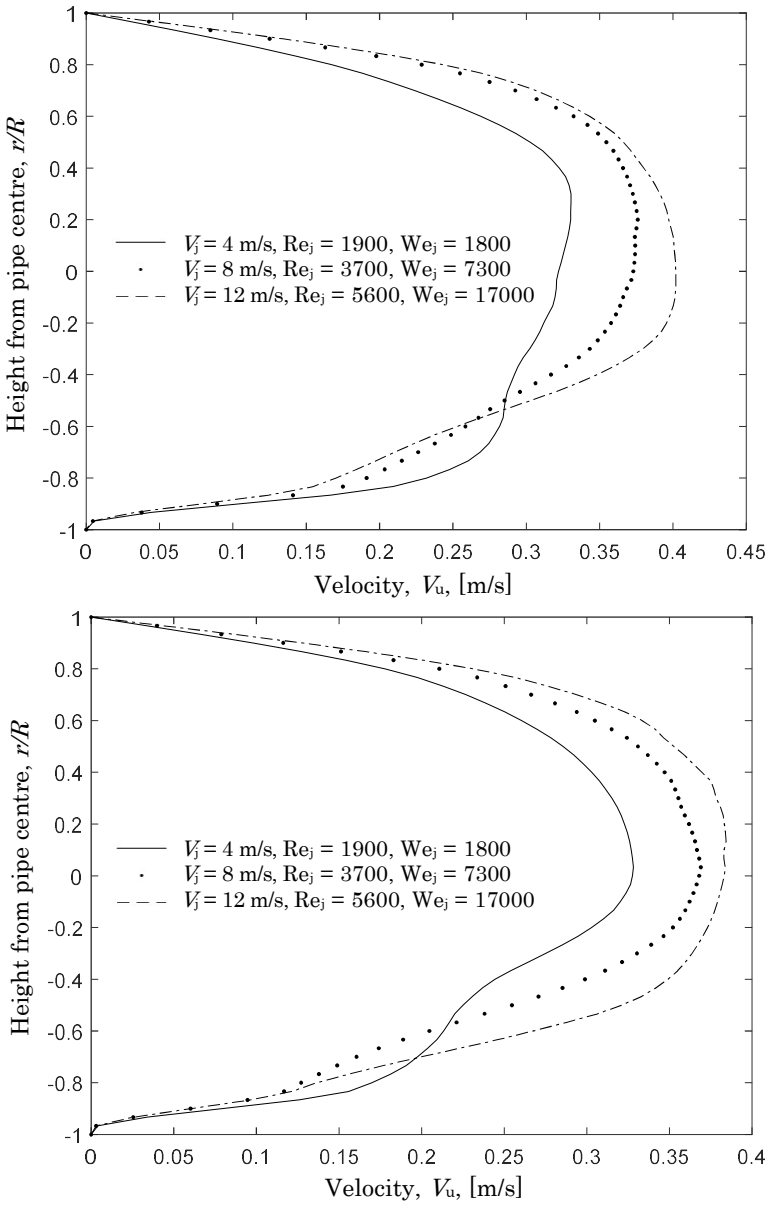


Figure 7.7 PIV measurement of a time-averaged velocity field for different jet types with velocities of V_j = 4 m/s, V_j = 8 m/s and V_j = 12 m/s interacting with a crossflow with a velocity of V_m = 0.2 m/s and an aqueous phase fraction of ϕ = 0.20 with Reynold numbers Re_{aq} = 620, Re_o = 1000. Top: F-jet; Bottom: V-jet.

7.3 Two-component PIV jet velocity fields

This section presents a subset of velocity fields of the flow fields centred on the jet, covering an axial distance of $L = -0.5\ D$ to $L = 1.5\ D$. The two-components of the velocity fields are measured using PIV which uses of a single-camera to make measurements of the axial component, x, and the vertical component, y, in the field of view. Figure 7.8 presents a typical time-averaged velocity field obtained using

these techniques with several of the features present in a typical velocity field. The jet is present on the left of centre and has been turned slightly downstream by the momentum of the crossflow, where the crossflow is travelling from left to right.

The red quadrilateral containing red crosses is a mask covering the jet outlet and the area immediately above the jet where no velocity field is shown. In this masked area, the velocity is at its highest and the PIV algorithms are unable to correlate velocities due to the minimum camera δt between successive frames of 0.5 ms. The velocities in the region range from approximately 0.01 m/s close to the pipe wall to 8 m/s in the core of the jet. Therefore, the relative movement of the particles used for the PIV calculations varies by a factor of ≈ 800. To calculate velocity, the PIV algorithm needs to be able to correlate where a group of particles have moved between successive frames. If the particle movement is too large the algorithm cannot find a correlation, whereas if the particle movement is too small the movement is undetectable. The particles displacement between image frames is dependent on both the fluid's velocity and the duration between the frames. Consequently, PIV techniques are limited by time step between successive images when resolving flows with a wide range of velocities. Current PIV techniques are limited by a dynamic velocity ratio of around 100 to 1 (Schröder et al., 2015), where the dynamic velocity ratio is the ratio of the maximum to minimum resolvable velocities when using an optimal time step between successive frames for the given optical system.

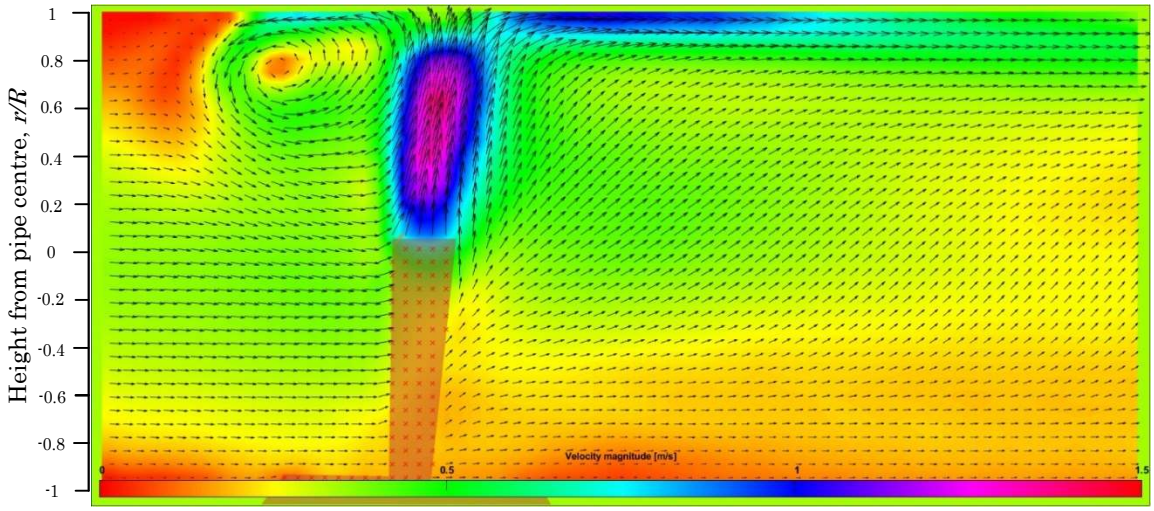


Figure 7.8 PIV measurement of a time-averaged velocity field for a U-jet with a velocity of V_j = 4 m/s and Re_j = 1900, We_j = 1800 interacting with a crossflow of V_m = 0.2 m/s and an aqueous fraction of ϕ = 0.20 with Re_{aq} = 620, Re_o = 1000.

To obtain the velocity field of the jet, the camera frame rate was set to 2kHz due to the high velocities in the regions closest to the jet and the camera's minimum δt between successive frames of 0.5 ms. Averaging of the PIV data was then performed over 4000 frames that were captured over two seconds.

Above the masked-out area in the upper half of the pipe of Figure 7.8 is the highest velocity region which lies at the centre of the jet. The velocity of the jet slows as it approaches the wall, whereupon the jet's flow spreads both upstream and downstream along the top pipe wall at a velocity higher than that of the crossflow. The downstream flow at the top of the pipe slows as it moves away from the jet. Although even at a downstream distance of $L = 1.5\ D$, the jet flow velocity remains higher than the overall downstream mixture's velocity. Consequently, a fraction of the U-jet's energy remains at the top of the pipe where it is unable to interact with any remaining aqueous phase at the bottom. Further, the concentration profiles revealed that the aqueous phase entrained in the jet becomes trapped within this fast flow at the top of the pipe rather than mixing into the bulk of the oil phase.

Upstream of the jet is an anticlockwise rotating vortex which is formed where the jet interacts with the pipe wall and continues to flow upstream into the crossflow, slowing both the upstream jet flow and the crossflow. This upstream crossflow and jet flow are then forced downwards forming the vortex. The interaction of these two flows is chaotic resulting in the vortex moving both vertically and horizontally in time, while the intensity also varies. While not visible in the velocity field presented here, this trapped vortex captures the small vortices created on the upstream side of the jet which adds to its intensity.

Downstream of the jet and to the right of the masked-out area, is in an area with a relatively strong upward velocity component which provides lift to droplets and ligaments and deforms the interface of any remaining aqueous phase layer. Using the information from the downstream velocity field we can infer that a U-jet has a downstream cross-sectional velocity field similar to that illustrated in Figure 7.9. This circulation pattern is formed by the jet flows after the jet impinges the top of the pipe wall, where the flow spread not only upstream and downstream but also around the circumference of the pipe wall. The crossflow then pushes the circumferential flow downstream creating a corkscrew pattern inducing the formation of counter-rotating vortices shown in Figure 7.9. These flows deform any remaining interface, pushing the interface down at the sides while lifting it in the centre, resulting in the aqueous phase

being lifted and stretched into ligaments downstream of the jet. When the jet has sufficient momentum the aqueous phase is penetrated and can be broken up entirely. This inferred cross-section of the velocity profile has also been seen in the preliminary modelling work discussed in the future of modelling work presented in Appendix B.

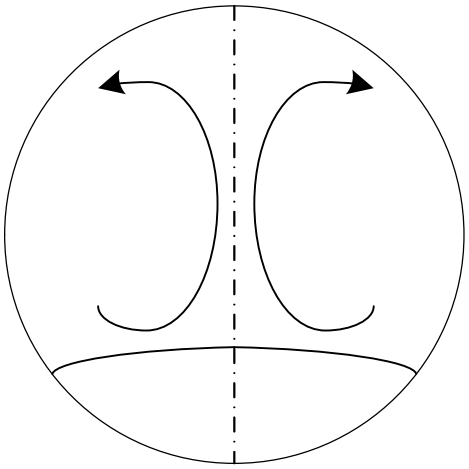


Figure 7.9 Inferred cross-sectional average velocity field of the U-jet, with an aqueous phase layer at the bottom which acts as a barrier to mixing when present.

The lifting of the aqueous phase by the counter-rotating vortices is visible in all of the PLIF images near to the jet, see Figure 4.11, and it can also be seen downstream between $L = 3\ D$ and $L = 5\ D$ in higher velocity crossflows.

7.3.1 Varying aqueous phase fraction

The effect of the aqueous phase fraction on the velocity field is presented in the plots of Figure 7.10. The plots are time-averaged velocity fields of a U-jet with a velocity of $V_j = 4$ m/s interacting with crossflows with a velocity of $V_m = 0.2$ m/s and aqueous fractions of $\phi = 0.05$, 0.20 and 0.50 which correspond to the figures from top to the bottom, respectively. Upstream of the jet, the effect of aqueous phase fraction on the velocity field appears minimal. Downstream of the jet, the vertical upward velocity decreases as the aqueous fraction increases. As a result, the lower aqueous phase fractions have an increased level of vertical lift and hence mixing of the phases.

The PLIF analysis of Chapter 5 established that the height of any remaining aqueous layer increases with aqueous phase fraction. While for the lowest aqueous phase fractions little downstream interface remains and the deformation of the

interface by the circumferential jet flows is relatively deep compared to its height. Combining these PLIF findings with the velocity field data indicates that any downstream aqueous layer provides a barrier to mixing and that as the depth of the aqueous layer increases the degree of secondary mixing decreases.

The effect of the aqueous phase fraction on the vorticity field is presented in the plots of Figure 7.11. The plots are time-averaged vorticity fields for the U-jet with a velocity of $V_j = 4$ m/s interacting with crossflows with a velocity of $V_m = 0.2$ m/s and aqueous fractions of $\phi = 0.05$, 0.20 and 0.50 corresponding to the figures from top to bottom, respectively. In the lower aqueous phase fractions of the first two plots, the large upstream counter-clockwise vortex shows little variation in intensity. However, the vortex intensity weakens once the highest aqueous phase fraction reaches $\phi = 0.50$.

In contrast, around the jet interface, the vorticity increases in intensity as the aqueous phase fraction increases, becoming the most intense at $\phi = 0.50$. This increased vorticity and shear will lead to increased droplet breakup and mixing in the Kelvin-Helmholtz instabilities surrounding the jet. Therefore, increasing the aqueous phase fraction increases the level of mixing near the jet. However, while this increased vorticity around the jet is beneficial for mixing and droplet break up, the PLIF results reveal that any advantage due to increased vorticity is outweighed by the increase in aqueous phase fraction leading to lower overall mixing.

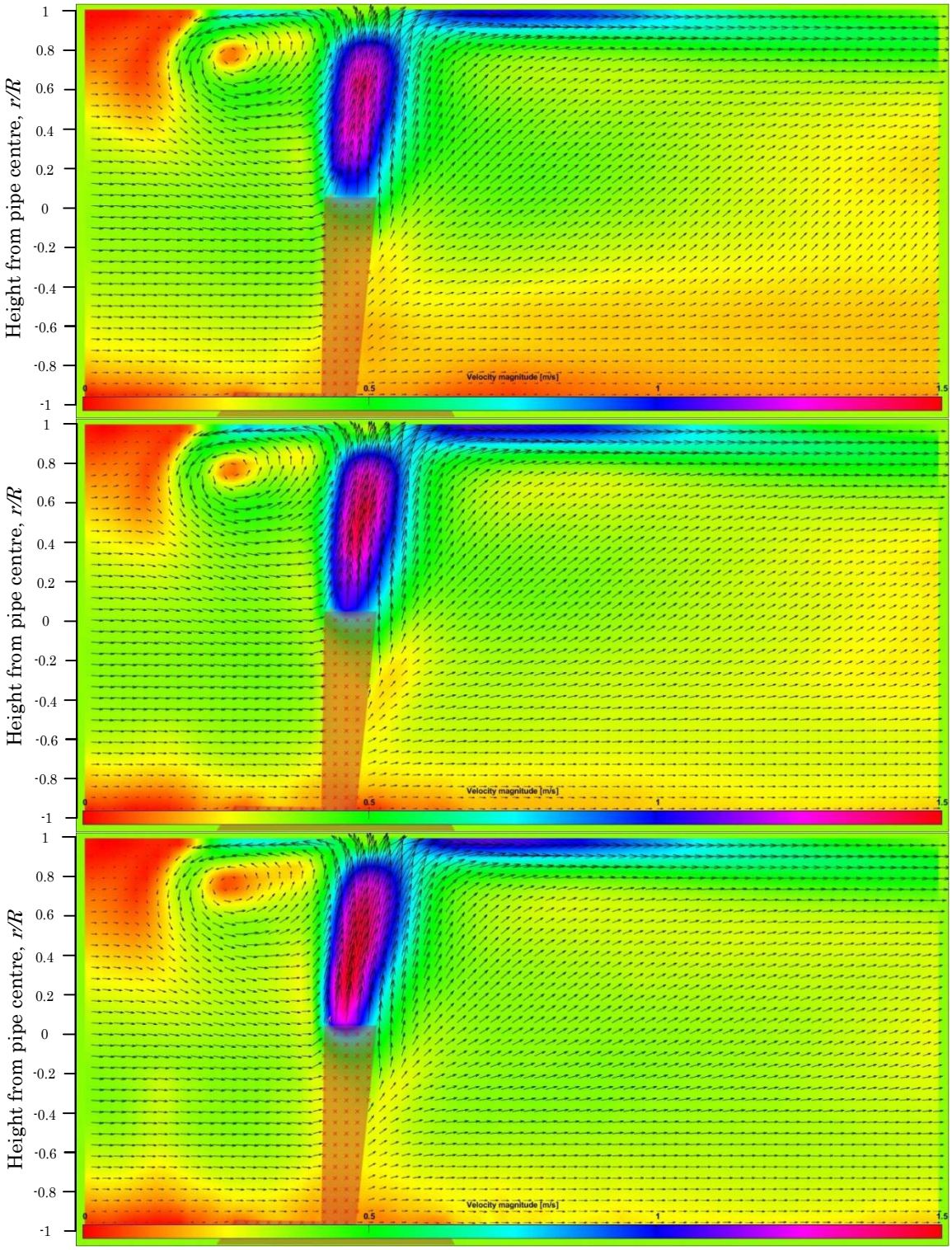


Figure 7.10 PIV measurement of a time-averaged velocity field for jet a with a velocity of V_j = 4 m/s and Re_j = 1900, We_j = 1800 interacting with a crossflow of V_m = 0.2 m/s and a varying aqueous fraction. Top row: ϕ = 0.05, Re_{aq} = 190, Re_o = 1100; Middle row: ϕ = 0.20, Re_{aq} = 620, Re_o = 1000; Bottom row: ϕ = 0.50, Re_{aq} = 1300, Re_o = 660.

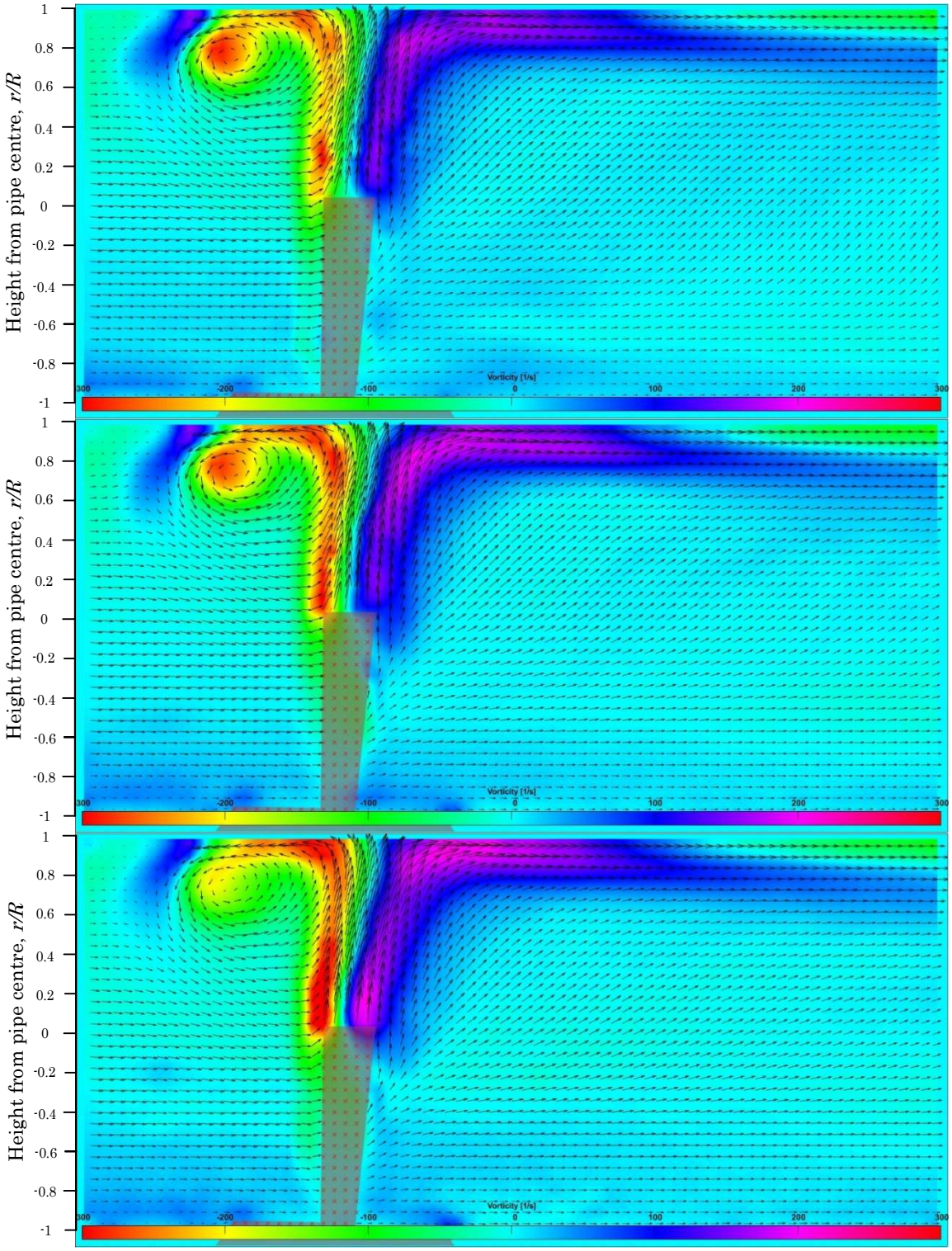


Figure 7.11 PIV measurement of the time-averaged vorticity fields for jet with a velocity of V_j = 4 m/s and Re_j = 1900, We_j = 1800 interacting with a crossflow of V_m = 0.2 m/s and a varying aqueous fraction. Top row: ϕ = 0.05, Re_{aq} = 190, Re_o = 1100; Middle row: ϕ = 0.20, Re_{aq} = 620, Re_o = 1000; Bottom row: ϕ = 0.50, Re_{aq} = 1300, Re_o = 660.

The vorticity fields are presented in the plots of Figure 7.12 as time-space plots. The plots are measured over a 1.5-second period at a distance of $L = 1\ D$ downstream of the jet and are the same three cases as Figures 7.10 and 7.11. The jets have a velocity of $V_j = 4$ m/s and are interacting with crossflows with a velocity of $V_m = 0.2$ m/s and aqueous fractions of $\phi = 0.05$, 0.20 and 0.50 corresponding to the figures from top to bottom, respectively. The most dominant feature is at the top of the pipe, above $r = 0.6\ R$, where there are strong predominantly clockwise vortices that are regularly shed downstream of the jet. The vortices are created on the downstream side of the jet as the jet fluid interacts with the surrounding fluid. These vortices then travel along with the jet to the top of the pipe where they travel along with the faster flow at the top of the pipe. For all these aqueous phase fractions the shedding rate of the clockwise vortices is between 30 Hz and 35 Hz, see Table 7.1.

Table 7.1 Vortex measurements for a jet with $V_j = 4$ m/s velocity, $Re_j = 1900$ and $We_j = 1800$ interacting with $V_m = 0.2$ m/s crossflow of varying aqueous phase fraction.

V_m [m/s]	ϕ	Re_{aq}	Re_o	Anti-Clockwise Vortices	Clockwise Vortices	Period [s]	Clockwise vortex shedding rate [Hz]
0.2	0.05	190	1100	6	52	1.5	35
0.2	0.10	340	1100	7	46	1.5	31
0.2	0.20	620	1000	12	49	1.5	33
0.2	0.50	1300	660	2	45	1.5	30

The top two rows of Figure 7.12 all have similar vorticity intensities below a height of $r = 0.6\ R$, whilst the bottom row, with the highest aqueous phase fraction, appears to be less intense particularly below $r = -0.4\ R$. This decrease in vorticity is similar to the lower intensity seen in the upstream vortex of the last row of Figure 7.11, but this contrasts with the increase in vorticity seen around the jet before it interacts with the pipe wall. Consequently, while the crossflows with higher aqueous phase fraction initially create more localized vorticity around the jet elsewhere the vorticity is lower.

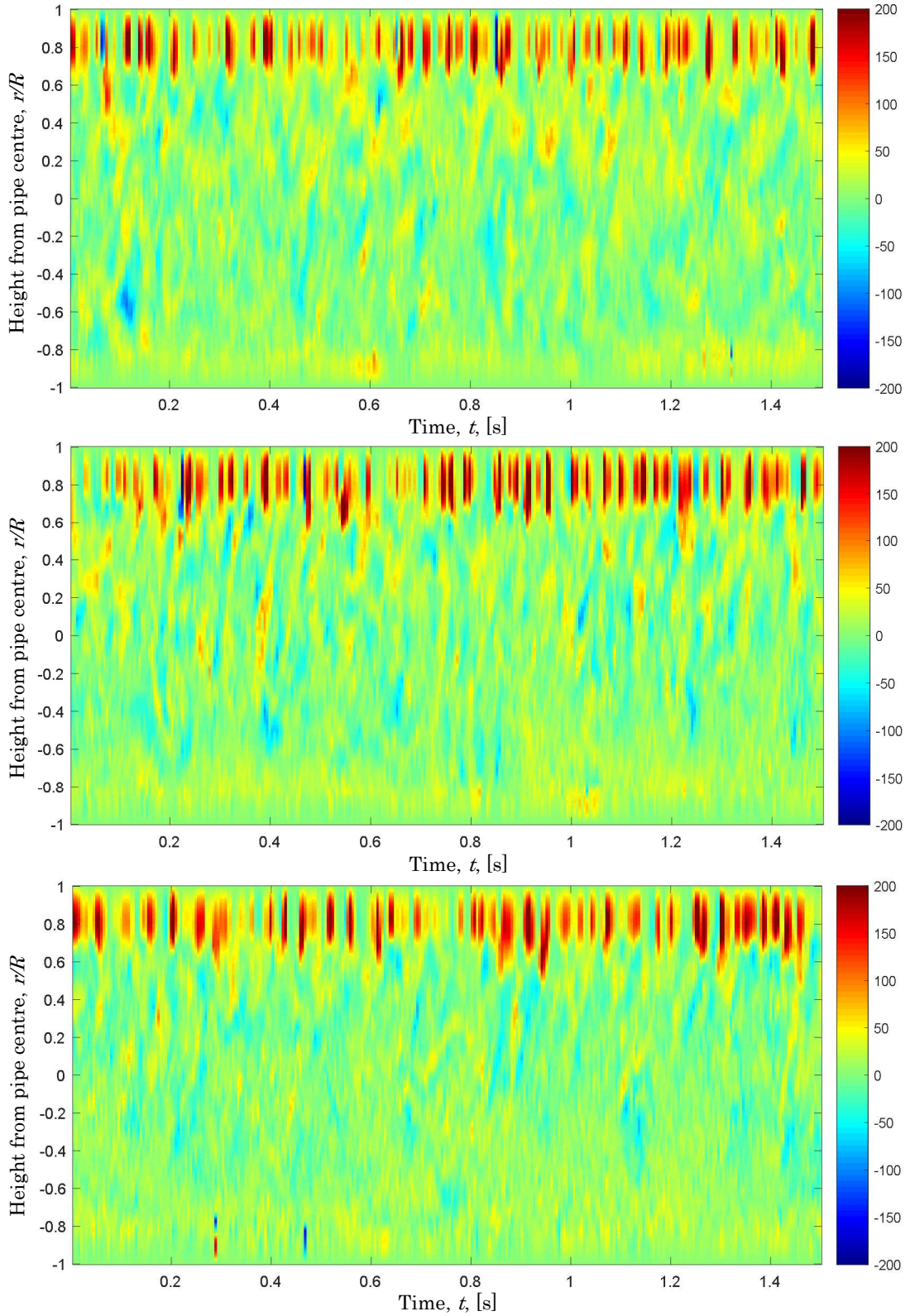


Figure 7.12 PIV measurement a vertical time-space plot of vorticity field for a jet with a velocity of V_j = 4 m/s and Re_j = 1900, We_j = 1800 interacting with a crossflow of V_m = 0.2 m/s and a varying aqueous phase fraction. Top row: ϕ = 0.05, Re_{aq} = 190, Re_o = 1100; Middle row: ϕ = 0.20, Re_{aq} = 620, Re_o = 1000; Bottom row: ϕ = 0.50, Re_{aq} = 1300, Re_o = 660.

It is noticeable that the near-wall vorticity cannot be resolved in Figure 7.12, which could indicate that spatial resolution was not high enough in this region. In addition, the brightness of the ETFE wall may also have made it difficult to detect and correlate tracer particles close to the wall. This highlights an issue with the ETFE that while the liquids and solids are refractive index-matched, the near-wall effects remain difficult to resolve due to the diffusion of the laser and glow created by the ETFE pipe material.

A further time-space plot is presented in Figure 7.13, this shows the horizontal development of the strong vortices as they travel along the top of the pipe at a height of $r = 0.8\ R$ between $L = 0.5$ and 1.0 D. The measurements in Figure 7.13 are of a U-jet with a velocity of $V_j = 4$ m/s interacting with a crossflow with a velocity of $V_m = 0.2$ m/s and an aqueous fraction of $\phi = 0.20$. The intensity of the clockwise vortices can be seen to decrease as they travel downstream, whilst the anticlockwise vortices appear to be maintained and may even grow in intensity.

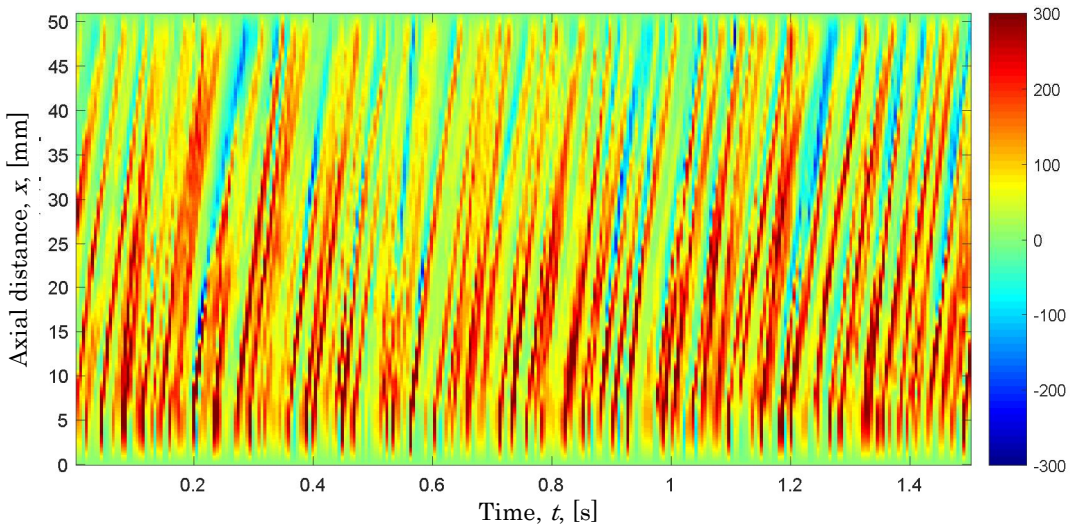


Figure 7.13 PIV measurement the horizontal time-space plot of vorticity field at a height of $r = 0.8\ R$ between a distance of $L = 0.5$ and 1.0 D for a jet with a velocity of $V_j = 4$ m/s and $Re_j = 1900$, $We_j = 1800$ interacting with a crossflow of $V_m = 0.2$ m/s and an aqueous fraction $\phi = 0.20$ and $Re_{aq} = 620$, $Re_o = 1000$.

7.3.2 Varying crossflow velocity

The effect of the crossflow velocity on the average velocity field is presented in the plots of Figure 7.14 and Figure 7.15. Figure 7.14 plots the time-averaged velocity fields for a U-jet with a velocity of $V_j = 4$ m/s interacting with crossflows with an aqueous fraction of $\phi = 0.20$ and velocities of $V_m = 0.1$, 0.2, 0.4 and 0.6 m/s and corresponding to the figures from the top to the bottom, respectively. While Figure 7.15 plots the time-averaged vorticity fields of the same flows.

The jet is increasingly deflected in the direction of crossflow as the crossflow velocity increases, while simultaneously forcing the anticlockwise rotating vortex further downstream and reducing its intensity. Once the crossflow velocity has reached $V_m = 0.6$ m/s the upstream vortex disappears in these time-averaged plots. This occurs because the jet has been deflected so far in the direction of the crossflow that the vortices are no longer trapped by the upward flow created by the jet's interaction with the pipe wall. Any vortices that are created along the upstream side of the jet now escape downstream. Similarly, the area of slow crossflow velocity to the left of the vortex reduces in size and moves downstream as the crossflow increases.

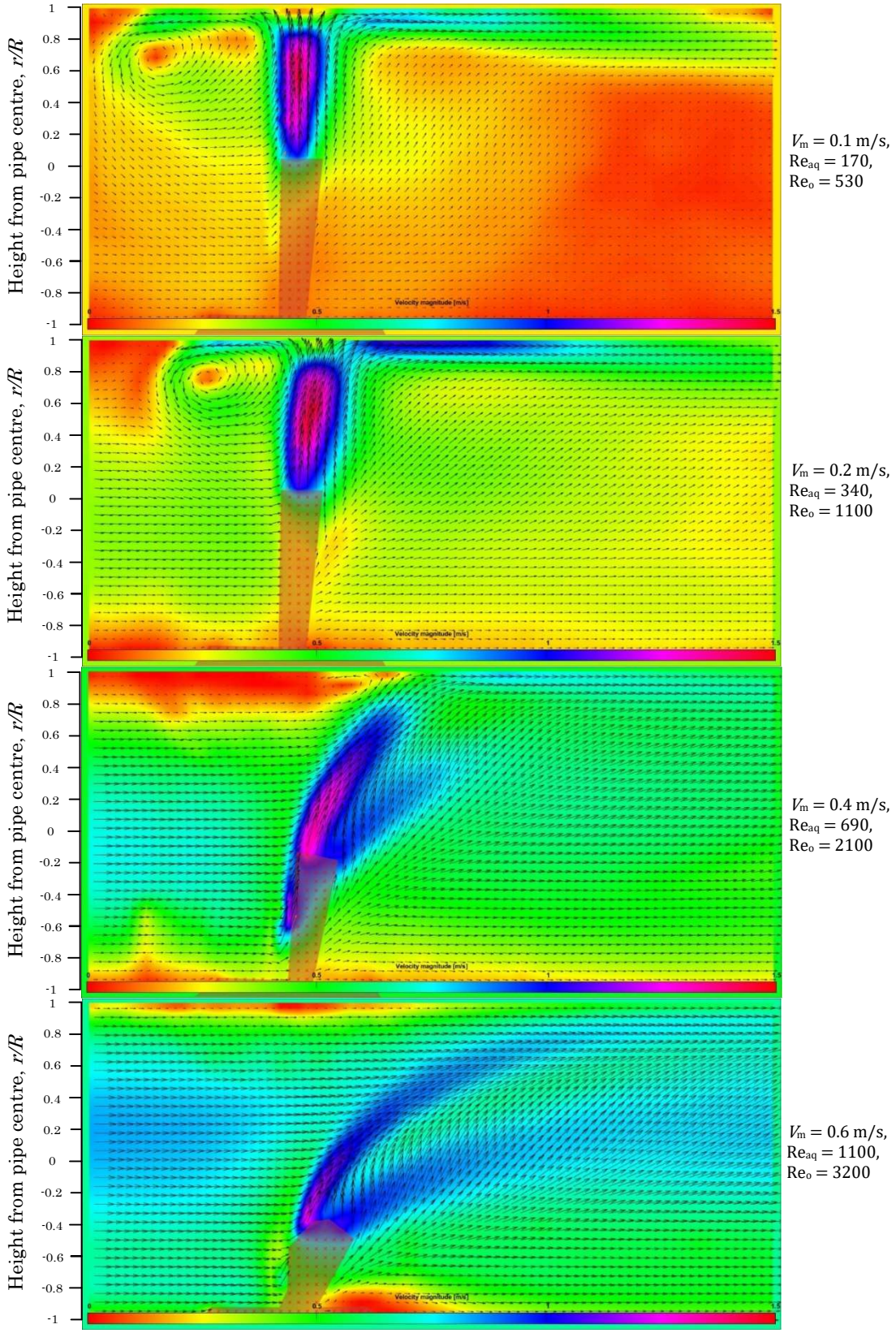


Figure 7.14 PIV measurement of a time-averaged velocity field for jet a with a velocity of V_j = 4 m/s and Re_j = 1900, We_j = 1800 interacting with a varying crossflow velocity with an aqueous phase fraction of ϕ = 0.20. Top row: V_m = 0.1 m/s; 2nd row: V_m = 0.2 m/s; 3rd row: V_m = 0.4 m/s; Bottom row: V_m = 0.6 m/s.

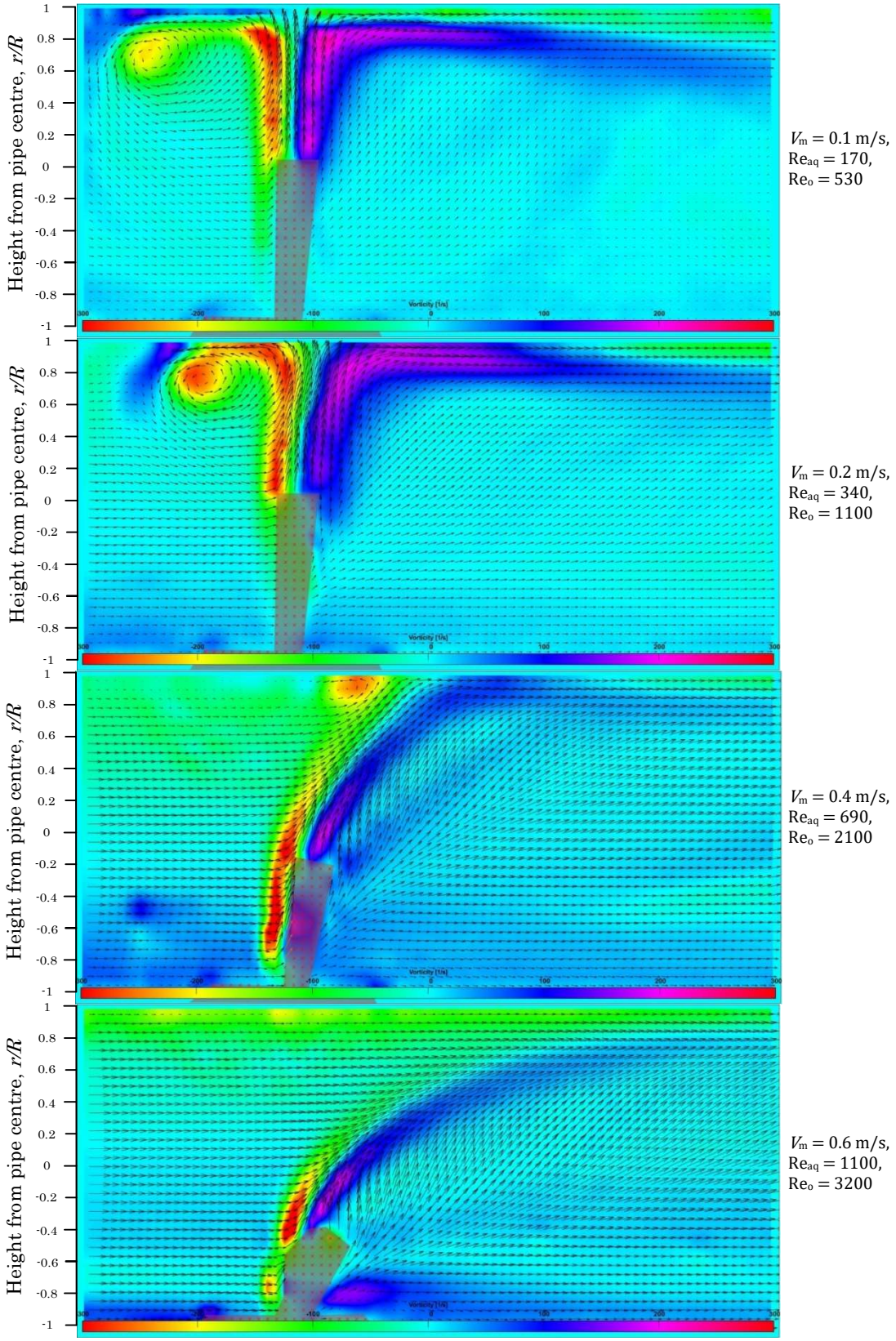


Figure 7.15 PIV measurement of a time-averaged vorticity field for jet a with a velocity of V_j = 4 m/s and Re_j = 1900, We_j = 1800 interacting with a varying crossflow velocity with an aqueous phase fraction of ϕ = 0.20. Top row: V_m = 0.1 m/s; 2nd row: V_m = 0.2 m/s; 3rd row: V_m = 0.4 m/s; Bottom row: V_m = 0.6 m/s.

A second observable phenomenon within the time averages velocity plots is a region of high velocity that becomes visible once the crossflow exceeds a velocity of V_m = 0.4 m/s. This region forms behind and under the jet, wherein Figure 7.14 it appears as if the jet has split into two. The jet is predominately in the upper high-velocity region, however, the jet is occasionally deflected further due to the waviness of the incoming stratified flow. These jet deflections occur after encountering a high amplitude incoming wave at the interface. Figure 7.16 is a PLIF image of a jet about to encounter the peak of an incoming interface wave where the aqueous phase will then cause the jet to be deflected further.

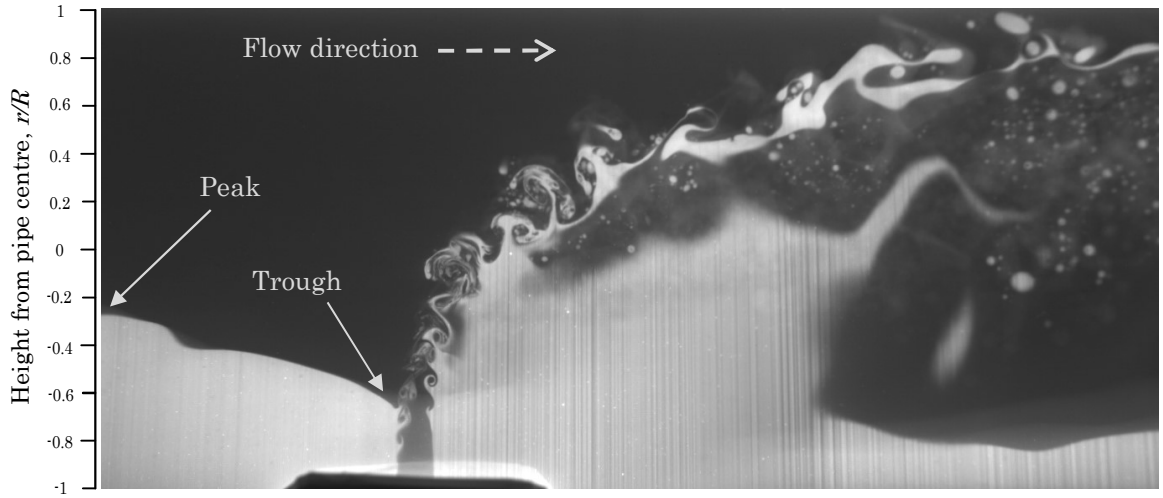


Figure 7.16 PLIF image of an U-jet with a velocity of V_j = 4 m/s and Re_j = 1900, We_j = 1800 interacting with a V_m = 0.6 m/s crossflow velocity and an aqueous phase fraction of ϕ = 0.20 with Re_{aq} = 1900, Re_o = 2900, showing trough followed by a peak of the aqueous layer height of the incoming flow.

This change in jet direction can be seen in the four PLIF snapshots of Figure 7.17, which are for the same experimental conditions as Figure 7.16. The images reveal the extremes of the jet position, where the images on the left have the greatest deflection, while the images on the right have the least deflection. The jets at the lowest angle are generally attached longer to the aqueous layer, while the higher angle jets separate earlier from the aqueous phase. Once the jet attaches to the aqueous phase it is in a semi-stable state that will spontaneously return to the lower-deflection angle at a later time.

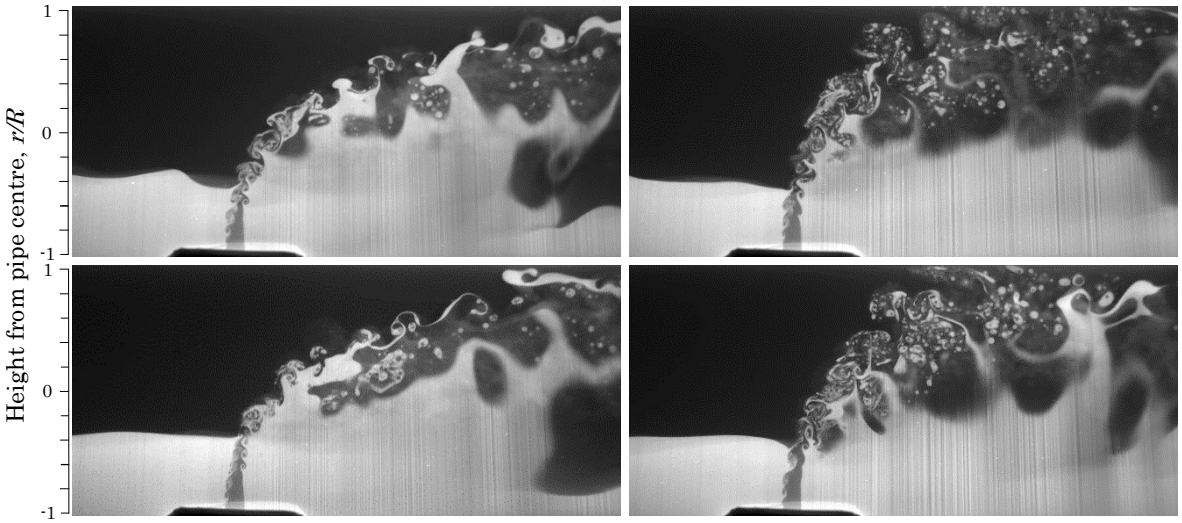


Figure 7.17 PLIF image of a U-jet a with a velocity of V_j = 4 m/s and Re_j = 1900, We_j = 1800 interacting with a V_m = 0.6 m/s crossflow velocity and an aqueous phase fraction of ϕ = 0.20 with Re_{aq} = 1900, Re_o = 2900. Showing several changes in the jet angle of deflection during a single experimental run. Left column: high jet angle of deflection; Right column: low jet angle of deflection.

The vorticity field is presented the time-space plots of Figure 7.18, where the cases for the four plots are the same as those in Figures 7.14 and 7.15. The jet velocity is V_j = 4 m/s and this interacts with crossflows with an aqueous fraction of ϕ = 0.20 and velocities of V_m = 0.1, 0.2, 0.4 and 0.6 m/s which correspond to the figures from the top to the bottom, respectively. The plots are at a distance of L = 1 D from the jet and are measured over a 1.5-second interval.

Strong predominantly clockwise vortices are regularly shed downstream of the jet for all crossflow velocities. These clockwise vortices are formed on the downstream side of the jet and travel to the top of the pipe. The number and shedding rate of the clockwise vortices are detailed in Table 7.2. The clockwise vortices initially increase in number with crossflow velocity but then decrease once the crossflow velocity exceeds 0.2 m/s. It is not clear if this subsequent decrease is due to the smaller vortices passing too quickly to be recorded at the 2 kHz sample rate, therefore, a greater sampling rate would be required to confirm if the shedding rate does decrease. Once the crossflow velocity reaches 0.6 m/s the anticlockwise vortices increase in number. This occurs because at a crossflow velocity of 0.6 m/s the jet is unable to trap the anticlockwise vortices formed on the upstream side of the jet. Hence, these anticlockwise vortices travel downstream along the top of the pipe with the clockwise vortices.

Table 7.2 Vortex measurements for a jet with V_j = 4 m/s velocity, Re_j = 1900 and We_j = 1800 interacting with a varying crossflow with an aqueous fraction ϕ = 0.20.

V_m [m/s]	ϕ	Re_{aq}	Re_o	Anti-clockwise Vortices	Clockwise Vortices	Period [s]	Clockwise vortex shedding rate [Hz]
0.1	0.20	290	480	15	43	1.5	27
0.2	0.20	620	1000	13	50	1.5	33
0.4	0.20	1200	1900	17	33	1.5	22
0.6	0.20	1900	2900	33	30	1.5	20

There is considerable variation in the plots of Figure 7.18 below a height of $r = 0.6\ R$. At a crossflow velocity of V_m = 0.1 m/s large chaotic structures are present above $r = 0\ R$. Increasing the crossflow velocity to V_m = 0.2 m/s results in these structures becoming smaller and present to a depth of $r \approx -0.5\ R$. Once the crossflow reaches a velocity of V_m = 0.4 m/s these vortices and structures seem to disappear, potentially becoming even smaller. In addition, layers appear at $r \approx -0.2\ R$, $r \approx -0.4\ R$ and $r \approx -0.6\ R$, which corresponds to the location of the interface between the oil, large droplets and aqueous phase. Finally, when the crossflow velocity reaches V_m = 0.6 m/s, the structures dramatically change due to the incoming crossflow becoming transitional, with an oil Reynolds number of $Re_o \approx 2900$. Therefore, increasing the crossflow velocity appears to initially reduce vorticity downstream of the jet while the crossflow is laminar, once the crossflow becomes transitional the vorticity increases substantially.

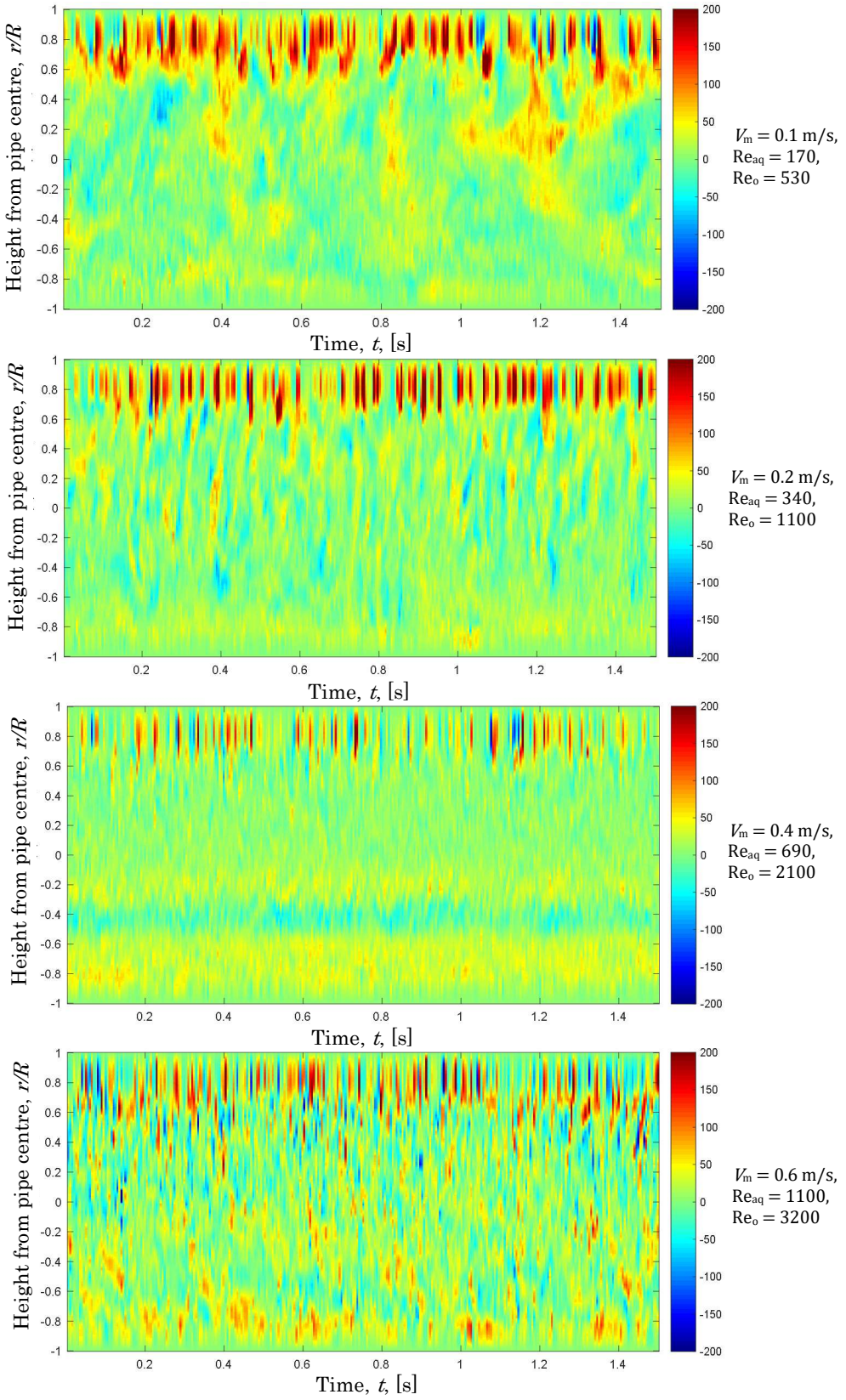


Figure 7.18 PIV measurement of time-space vorticity field for a jet with a velocity of V_j = 4 m/s and Re_j = 1900, We_j = 1800 interacting with a varying crossflow velocity with an aqueous phase fraction of ϕ = 0.20. Top row: V_m = 0.1 m/s; 2nd row: V_m = 0.2 m/s; 3rd row: V_m = 0.4 m/s; Bottom row: V_m = 0.6 m/s.

7.3.3 Varying jet velocity

The effect of the jet velocity on the average velocity field is presented in the plots of Figure 7.19. These time-averaged velocity fields are for a U-jet with velocities of $V_j = 4$, 6 and 8 m/s interacting with a crossflow velocity of $V_m = 0.2$ m/s with an aqueous fraction of $\phi = 0.20$, where the velocity of the jet increases from the top to the bottom.

As the jet velocity increases, the large upstream anticlockwise vortex increases in size and is pushed further upstream of the jet while the downstream flow at the top of the pipe increases significantly. Comparing the velocity of the flow along the top of the pipe relative to the region below reveals that the fraction of flow at the top of the pipe increases as the jet velocity increases. The PLIF analysis of Section 5.1 revealed that a higher aqueous phase fraction is present along the top of the pipe and this increases with increased jet velocity. When these PLIF findings are combined with the higher velocity ratio along the top it revels than an even greater fraction of the aqueous phase is present at the top of the pipe than in the regions below.

Immediately downstream of the jet, we see that the upward v-component of velocity increases in magnitude relative to horizontal axial velocity u-component as the jet velocity increases. This increase in the vertical component is caused by the higher velocity of the jet flow as it travels circumferentially around the pipe wall following impingement, causing the downstream dual vortices to rotate more rapidly.

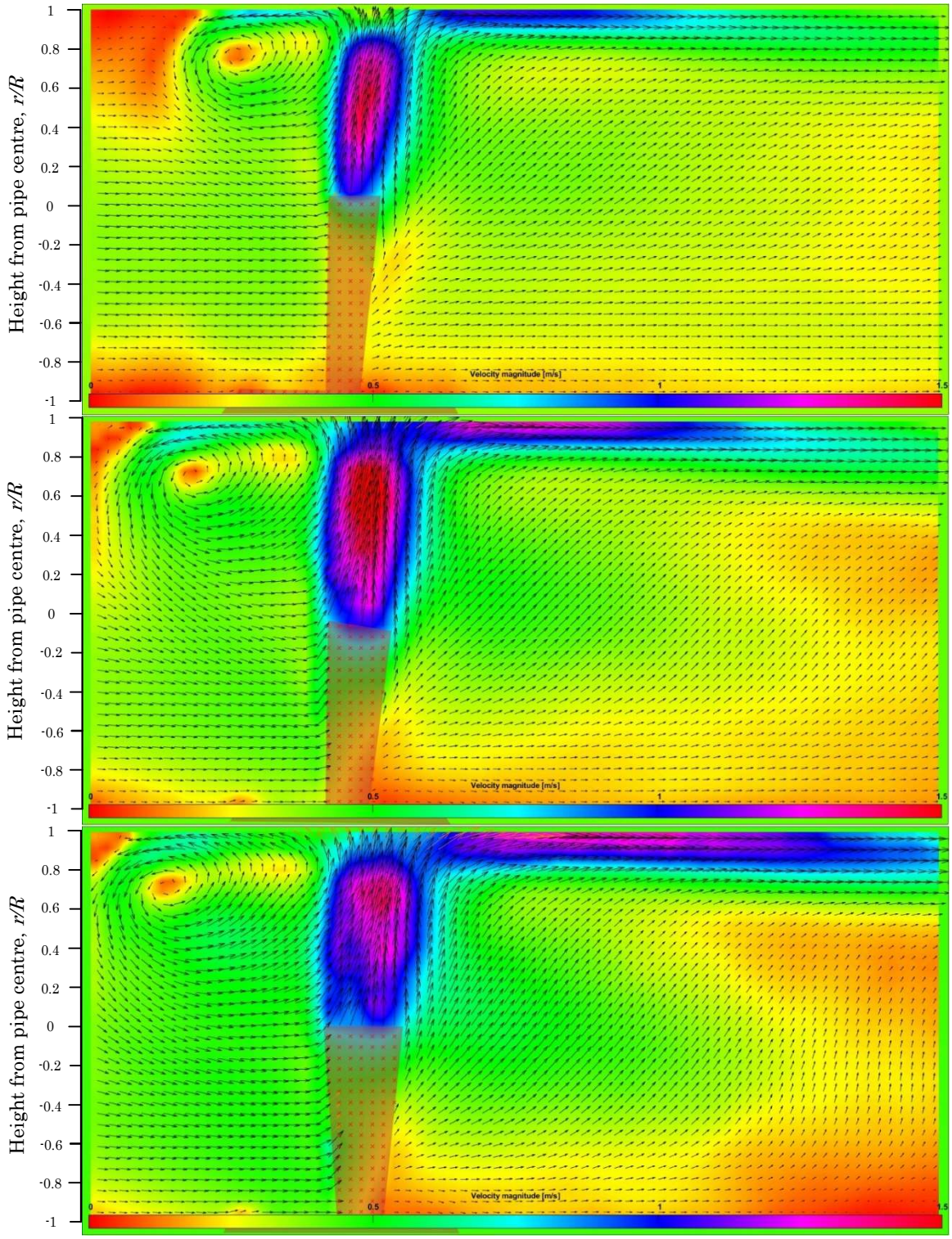


Figure 7.19 PIV measurement of a time-averaged velocity field for a jet with a varying velocity interacting with a crossflow velocity of V_m = 0.2 m/s with an aqueous phase fraction of ϕ = 0.20 with Re_{aq} = 620, Re_o = 1000. Top: V_j = 4 m/s, Re_j = 1900, We_j = 1800; Middle: V_j = 6 m/s, Re_j = 2800, We_j = 4000; Bottom: V_j = 8 m/s, Re_j = 3700, We_j = 7300.

7.4 Three-component stereo-PIV jet velocity fields

The results within this section are a demonstration of what is possible with three-component stereo-PIV measurements which make use of the dual-camera setup to calculate both u- and v-components parallel to the laser sheet as well as the third w-component that is perpendicular to the laser sheet. Results are presented for a single flow condition with a jet with a velocity of $V_j = 4$ m/s interacting with a crossflow with a velocity of $V_m = 0.1$ m/s and an aqueous phase fraction of $\phi = 0.10$. Figure 7.20 presents a time-averaged velocity field averaged over a 1.5-second period. The magnitude of the z-component is displayed as the contour map, where positive velocity values are in the direction that is travelling into the paper.

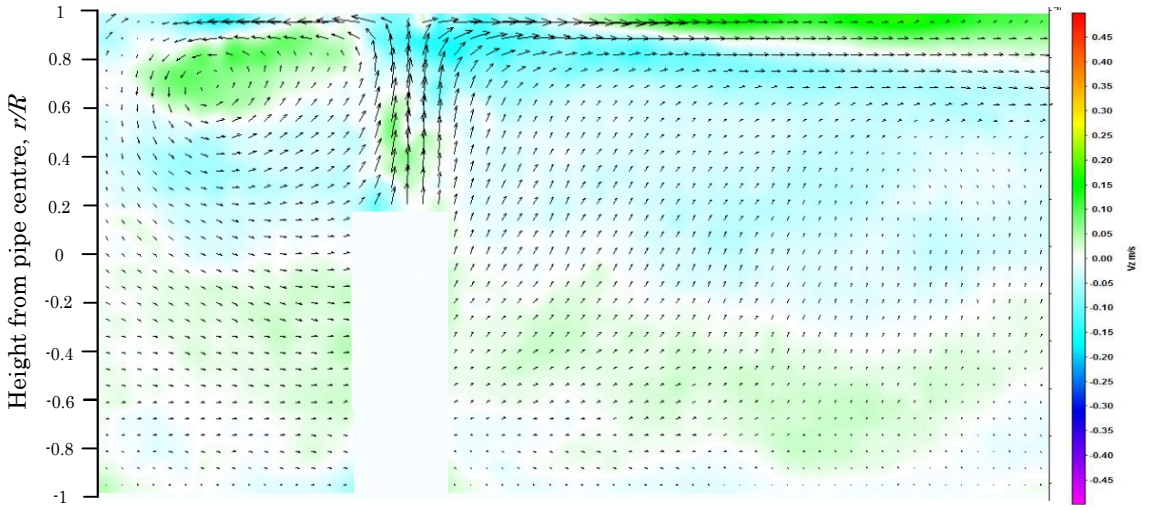


Figure 7.20 Stereo-PIV measurements showing a time-averaged velocity field measurements for a jet with a velocity of $V_j = 4$ m/s and $Re_j = 1900$, $We_j = 1800$ interacting with a crossflow velocity of $V_m = 0.1$ m/s with an aqueous phase fraction of $\phi = 0.10$ with $Re_{aq} = 170$, $Re_o = 530$.

The three velocity components of this flow are split into separate contour maps in Figure 7.21. These plots reveal that the average u- and v-components of velocity have regions which are significantly larger in magnitude than the w-component. Indeed, the w-component should be close to zero if averaged for a sufficiently long period in a fully symmetric incoming flow with perfectly aligned geometry of laser plane, pipe and jet. Indicating that either the laser plane, jet and/or pipe were slightly misaligned or that the incoming crossflow had some asymmetry.

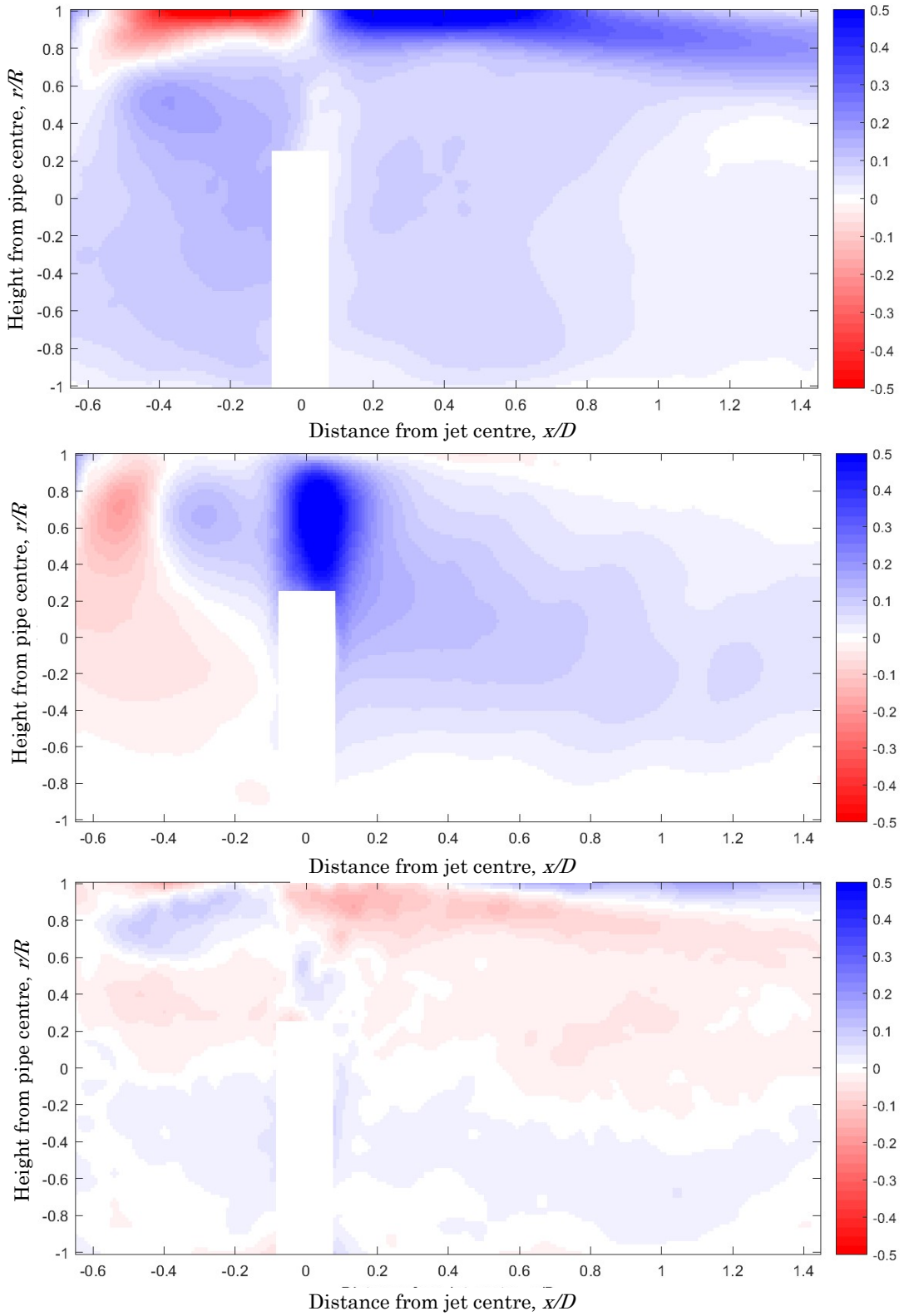


Figure 7.21 Stereo-PIV measurements plotting the contour map of the three separate components of the time-averaged velocity field for a jet with a velocity of V_j = 4 m/s and Re_j = 1900, We_j = 1800 interacting with a crossflow velocity of V_m = 0.1 m/s with an aqueous phase fraction of ϕ = 0.10 (Re_{aq} = 170, Re_o = 530). Top: u-component; Middle: v-component; Bottom: w-component.

Figure 7.22 presents three of the instantaneous velocity fields of the same flow from which Figures 7.20 and Figure 7.21 were created. These instantaneous velocity fields have a significant degree of variation. In particular, the variation in the w-component is large when compared to that of the average velocity fields. Importantly, these changing velocities demonstrate that mixing is occurring chaotically in this 3rd direction and that stereo-PIV is needed to fully understand these complex jet flows.

Detailed examination of the velocity fields highlights that the velocity field around the jet, the impingement region and flow along the top wall undergo the most significant variations in the three spatial directions and the w-component in particular.

The large upstream vortex can be seen to move position whilst changing shape and intensity, while the flows below the vortex change from flowing almost horizontally to becoming deflected downwards.

Downstream of the jet, the flow along the top of the pipe is strong in both the axial u-component and the w-component, indicating that the strong jet flow is indeed travelling both along the top and around the circumference of the pipe walls as predicted by Figure 7.9. This circumferential flow around the pipe wall contributes to the formation of the area below $r = 20$ mm where the v-component lifts the aqueous phase remaining at the bottom of the pipe. The flows in this lower downstream region vary in time, where, in some extreme cases, the velocity field is seen to go against the crossflows, i.e. in the negative axial direction.

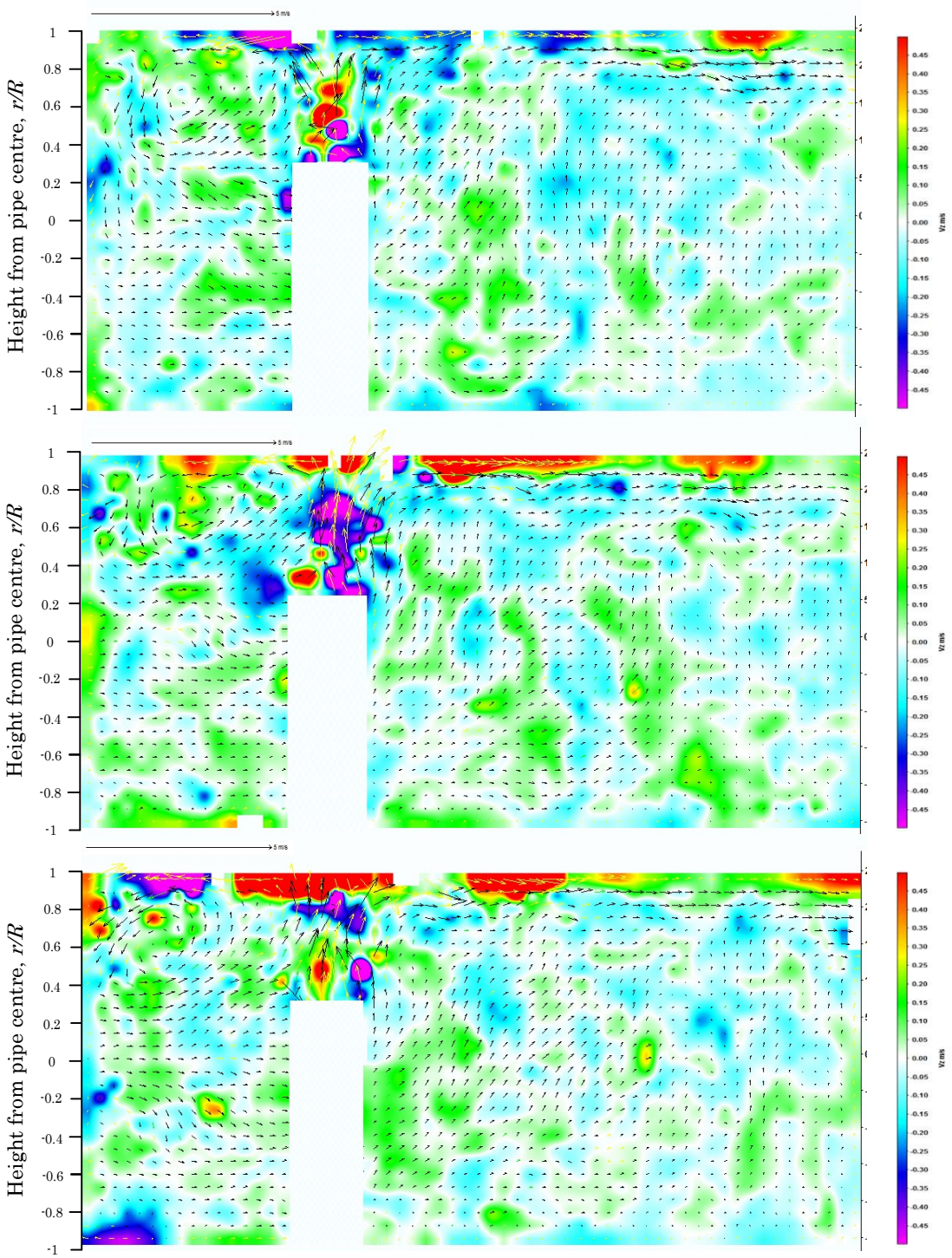


Figure 7.22 Stereo-PIV measurements of three instantaneous velocity field for a jet with a velocity of V_j = 4 m/s and Re_j = 1900, We_j = 1800 interacting with a crossflow velocity of V_m = 0.1 m/s with an aqueous phase fraction of ϕ = 0.10, Re_{aq} = 170, Re_o = 530. The time interval between each of these frames is 300 ms

The kinetic energy can be calculated for these flows using Eq. 7.1 for both PIV and stereo-PIV where M is the number of component vectors (DaVis, 2019). Figure 7.23(top) presents a time-averaged contour plot of the calculated kinetic energy using both u- and v-components of velocity from the flow used in Figures 7.20, 7.21 and 7.22.

$$KE = \sum_{i=1}^{M} \frac{1}{2} V_i^2 \qquad \text{Equation 7.1}$$

In contrast, Figure 7.23(bottom) presents the contour plot of the calculated kinetic energy when using all three velocity components where it is higher than using the u- and v-components towards the top of the jet where the vertical component is slowed as the jet impinges the wall.

$$TKE_{2\text{-}D} = \sum_{i=1}^{2} \frac{3}{4} (V_i - \bar{V}_i)^2 \qquad \text{Equation 7.2}$$

$$TKE_{3\text{-}D} = \sum_{i=1}^{3} \frac{1}{2} (V_i - \bar{V}_i)^2 \qquad \text{Equation 7.3}$$

The turbulent kinetic energy can be calculated for these flows using Eq. 7.2 and 7.3 for PIV and stereo-PIV, respectively (DaVis, 2019). The measurements of TKE for the two- and three-component PIV measurements are presented in Figures 7.24, where these two measurements of TKE are similar.

The results within this section are a demonstration of what is possible with the stereo-PIV configuration. Further work is needed to complete the processing required for the many experimental conditions that were recorded during the experimental campaign.

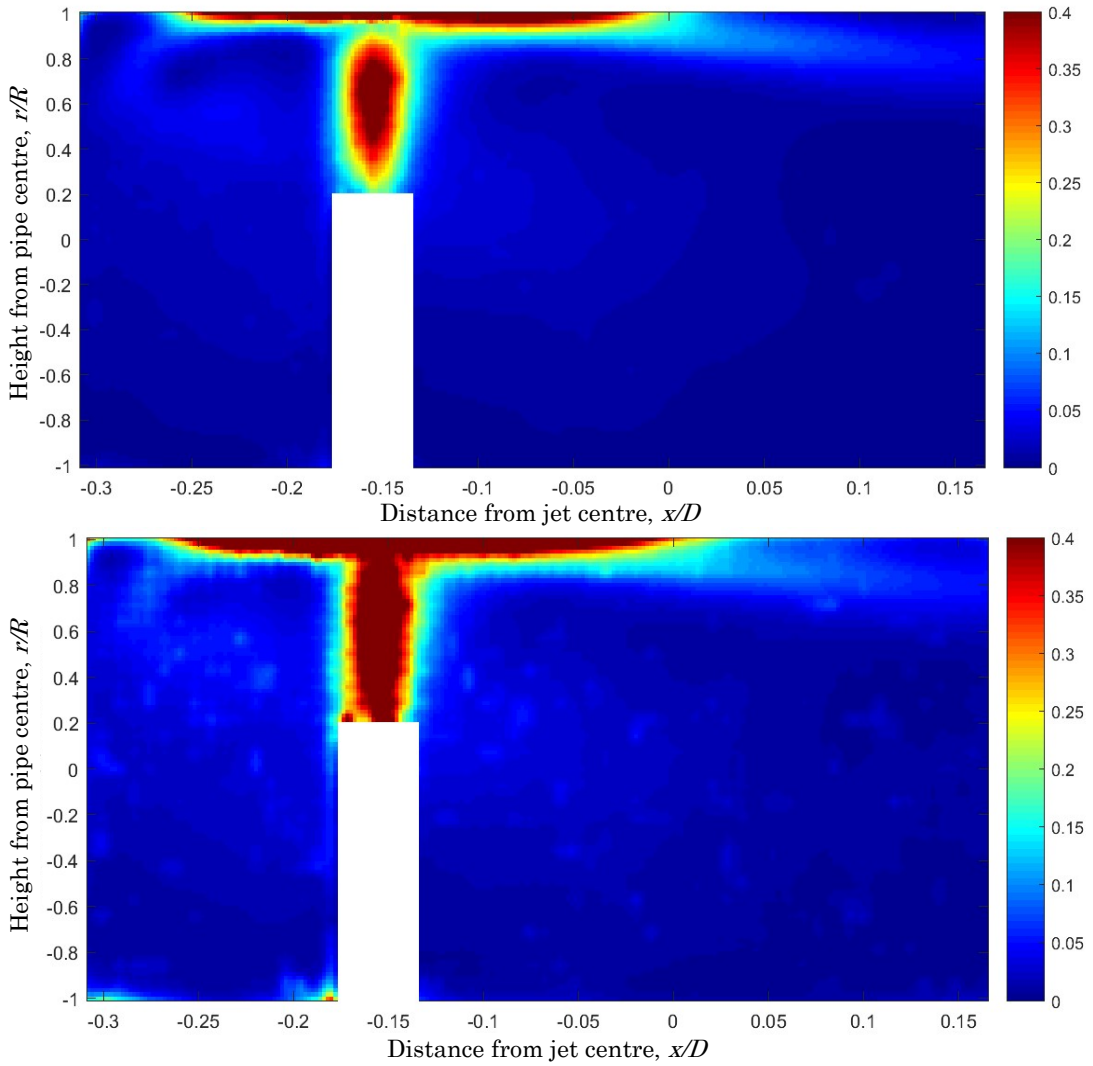


Figure 7.23 Calculation of the kinetic energy for a jet with a velocity of V_j = 4 m/s and Re_j = 1900, We_j = 1800 interacting with a crossflow of V_m = 0.1 m/s and an aqueous fraction ϕ = 0.10 with Re_{aq} = 170, Re_o = 530. Top: 2-component PIV; Bottom: 3-component stereo-PIV.

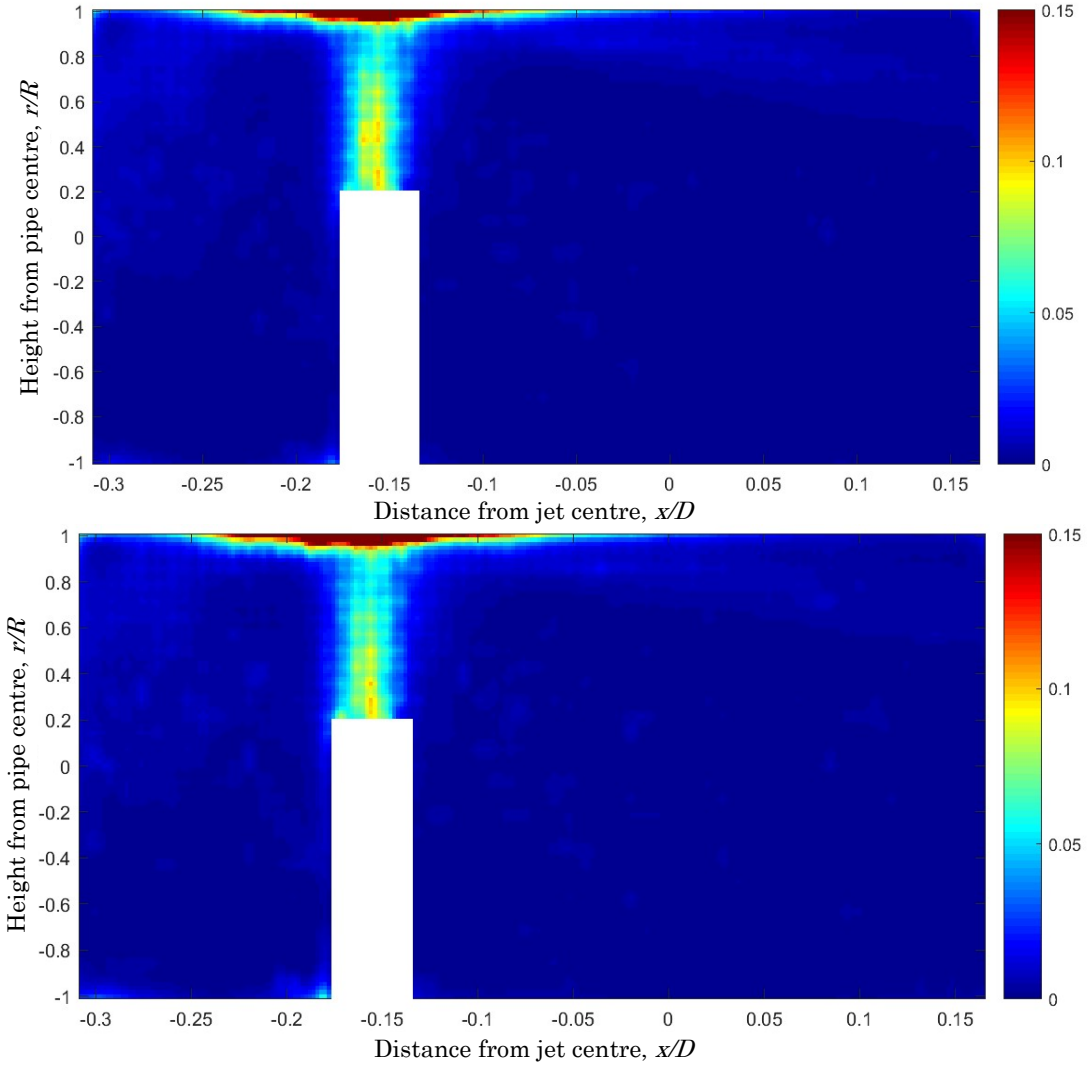


Figure 7.24 Calculation of the turbulent kinetic energy for a jet with a velocity of V_j = 4 m/s and Re_j = 1900, We_j = 1800 interacting with a crossflow of V_m = 0.1 m/s and an aqueous fraction ϕ = 0.10 with Re_{aq} = 170, Re_o = 530. Top: 2-component PIV; Bottom: 3-component stereo-PIV.

7.5 Summary

This chapter presented measurements of the velocity fields of the incoming crossflows, the jet and the resulting dispersion. It discussed how these velocity fields change with position, jet velocity, crossflow, jet type and aqueous phase fraction. The key points from this chapter are:

- The U-jet creates a flow that travels downstream along the top of the pipe. This flow traps some of the aqueous phase that is entrained by the jet at the top of the pipe rather than dispersing it evenly into the bulk. The flow contains a

significant fraction of the remaining jet energy but does not interact significantly with any aqueous phase remaining at the bottom of the pipe.

- The presence of an aqueous layer downstream of the jet provides a barrier to mixing, where an increase in the depth of the downstream aqueous layer decreases the level of secondary mixing that occurs.
- As the waviness on the interface of the incoming stratified flow increases the jet deflection increases. Large-amplitude waves deflect the jet significantly and the jet may not return to its original position immediately.
- The vertical component of velocity downstream of the U-jet is responsible for lifting the aqueous phase at the interface. This upward velocity is a consequence of the dual counter-rotating vortices that are formed as the jet flow impinges the top wall and flows around the circumference of the pipe.
- As the crossflow velocity is increased, the jets are turned into the direction of the crossflow. Eventually, the jet is turned so far that it fails to impinge upon the top of the pipe wall and the large upstream vortex is not resolved in time-averaged velocity fields. In contrast, the downstream anticlockwise vortices increase along the top of the pipe as they are no longer trapped by the jet impinging the top pipe wall.
- The vorticity immediately around the jet increases as the aqueous phase fraction increases. This increase in vorticity and shear around the jet leads to an increase in the Kelvin-Helmholtz instabilities and hence droplet breakup and mixing.

Additional points of interest include:

- PIV measurement for an incoming laminar flow velocity profile follows the theoretical profile where the peak velocity height deviates by ≈ 3% from the theoretical prediction.
- Initial experimental asymmetries in the incoming flows were minimised through encasing the thin flexible ETFE pipe in a hard PVC outer pipe casing. This PVC casing support to the ETFE pipe to maintain its circular shape and horizontal orientation during the subsequent experimental campaign.
- An increase in the aqueous phase fraction leads to an increase in the asymmetry in the incoming laminar flow profiles. This asymmetry is caused by the difference in viscosity between the two liquids.

- The increased asymmetry with increased aqueous fraction remains present at ten diameters downstream of the jet interaction. However, the flow profiles no longer look like a classical laminar flow and have a blunter shape.
- The velocity profiles of the different jets display considerable variation at ten pipe diameters when the crossflow is 0.6 m/s. The velocity of the V-jet is higher in the lower half of the pipe than the other jet types where it can break up any remaining aqueous phase layer.
- The upstream anticlockwise rotating vortex is formed where the jet interacts with the pipe wall and continues to flow upstream into the crossflow, slowing both flows. This upstream crossflow and jet flow are then forced downwards forming the vortex.
- Stereo-PIV measurements demonstrate that the time-averaged w-component of velocity is as expected to be close to zero for the symmetrical system measured in the pipe centre. Whereas the instantaneous velocity field measurements reveal that the w-component is significant on a moment-by-moment basis.
- Instantaneous velocity field measurements reveal that the flow undergoes rapid changes from moment to moment, flow directions can be reversed, the jet curvature can change while the vorticity can ebb and flow.

Chapter 8

Conclusions

This thesis has examined the mixing of a stratified flow of two immiscible liquids using jets. It reveals the complex hydrodynamics effects that occur when mixing these flows. The flows enter a short-lived unstable dispersed state followed by a rapid re-stratification of the two phases. The literature review has highlighted how little work has been completed in this important area for industry and, therefore, the importance of this work. It is believed that these novel results will contribute to the greater understanding of these complex processes and be of benefit in future modelling work.

This chapter presents an overview and the key findings of the experimental work which focused on the extraction of experimental data to obtain a better understanding of jet mixing stratified liquid-liquid flows within pipes. Lastly, recommendations are provided for future work. Suggesting how to enhance the applicability of the experimental methods and test facility, as well as providing proposals for additional studies and modelling work.

8.1 Overview and further discussion

An experimental campaign for the jet mixing of liquid-liquid stratified flows in the laminar to the turbulent flow regimes has been performed. Measurements were conducted using the advanced laser-based techniques of PLIF, PIV and stereo-PIV through the application of refractive index matching of the liquids and solids. Measurements performed include interface heights, aqueous phase fraction profiles, C_1/C_2 ratios, droplet chord lengths and velocity fields.

Mixing occurs in two main zones, the primary and secondary mixing zones. The primary mixing zone occurs during the initial jet interaction and is dominated by Kelvin-Helmholtz instabilities near the jet surface. This primary interaction

creates the smallest visible droplet sizes. The secondary mixing zone occurs downstream of the jet due to the establishment of two counter-rotating vortices formed by the jet flows as they travel around the pipe's circumference following the jets impingement on the pipe wall. These counter-rotating vortices create lift downstream, which distorts any remaining interface and raises the aqueous phase into the oil phase, where it is then broken up and dispersed.

During mixing the flow undergoes rapid changes from moment to moment, where the direction of flows can be reversed, the jet curvature can change and the vorticity can ebb and flow. These rapid changes help to disperse the droplets of aqueous phase throughout the pipe flow.

The momentum of the crossflow turns the jet towards the downstream axial direction where the degree with which the jet is turned is dependent on the ratio of the momentum of the jet to that of the crossflow. When the momentum of the jet is high enough compared to that of the crossflow, the jet impinges upon the top of the pipe wall and continues to flow upstream into the crossflow. This upstream jet flow slows against the crossflow and forms a semi-stationary upstream vortex or recirculation zone. This recirculation zone contributes to the mixing while forcing the crossflow down towards the jet nozzle exit.

In addition to travelling upstream, the jet creates a flow that travels downstream along the top of the pipe. In doing so, the jet traps some of the aqueous phase that was entrained during the primary interaction towards the top of the pipe. This trapped entrained aqueous phase is not dispersed evenly into the bulk of the crossflow. As a result, the concentration in the middle of the pipe can be lower than either the bottom or the top of the pipe as can be seen in the PLIF measurement of the concentration profiles.

An analysis of the flow pattern maps revealed that for the experimental conditions measured that (i) there are positions in the pipe where the jet has had insufficient time to mix close to the jet; (ii) downstream stratification can occur rapidly; (iii) conditions exist where the jet has insufficient energy to mix.

A more detailed analysis of the phase fraction profiles, C_1/C_2 ratios and vertical droplet chord lengths creates a clearer understanding of the effects of the experimental parameters. The aqueous phase becomes more evenly dispersed, with smaller droplet sizes and narrower distributions as the aqueous phase fraction decreases and the jet velocity and hence jet energy increases. Increasing

the amount of aqueous phase to be dispersed requires more jet energy to break up the aqueous layer and counteract interfacial tension. Insufficient jet energy can lead to little mixing and rapid re-stratification.

The concentration profiles make evident that, for any condition where a liquid-liquid interface remains, the height of the interface increases with increasing inlet aqueous phase fraction. While the C_1/C_2 ratios reveal that increasing aqueous phase fraction also leads to a more rapid re-stratification of the flows. Further, increasing the aqueous phase fraction leads to an increase in the asymmetry in the incoming laminar flow. This asymmetry is caused by the difference in viscosity of the two liquids. This increase in asymmetry with increased aqueous fraction remains present at ten diameters downstream of the jet interaction. However, the flow profiles no longer look like a classical laminar flow and have a blunter shape.

Increasing the crossflow velocities increases the distance needed for the flow to develop. The concentration profiles, C_1/C_2 ratios and droplet chord lengths demonstrate that increasing the crossflow velocities can reduce the level of vertical phase distribution. This occurs because, as the crossflow velocity increases, the flow development time and energy relative to the crossflow are reduced while the jet velocity remains constant. However, the reduction in residence time also reduces the time the flow has had to settle once gravity becomes the dominant force.

Increasing the crossflow velocities also increases the waviness of the interface of the incoming stratified flow. This increase in waviness causes the angle of the jet deflection to change, where a large-amplitude wave results in the jet curvature increasing. The resulting position of the jet is semi-stable but eventually returns to the more dominant position.

In regards distance from the jet, at one pipe diameter downstream the mixing of the flow is never complete and droplet breakup is still dominating, at four pipe diameters mixing is transitioning and D_{32} measurements highlighted that the flow can be dominated either by coalescence or jet induced breakup. However, by ten pipe diameters downstream, droplet chord lengths always increase, indicating that coalescence is dominating breakup and thus the energy from the jet has decayed significantly.

Stratification of the downstream flows from the jet is frequently visible in the PLIF results especially at a distance of ten pipe diameters where a stratified layer rapidly forms for the lowest jet velocities and highest aqueous phase

fractions. However, the velocity profiles at ten pipe diameters downstream vary considerably with jet type. Experimental crossflows are currently limited to 0.8 m/s and therefore higher pipeline velocities (or equally lower residence times) may result in mixing still dominate at ten pipe diameters. Higher crossflows velocities are therefore an area for future investigation.

The time needed for a flow to reach a downstream position is dependent on the crossflow and increasing the crossflow reduces the time. This moves the peak in C_1/C_2 further downstream from the jet exit as the crossflow velocity increases. Residence time analysis indicates that the mixed flows undergo rapid changes, where the C_1/C_2 ratio, D_{10} and D_{32} all see measurable trends that show the flow has undergone stratification after five seconds.

The relationships between the five droplet chord length measurements of D_{10}, Dv_{10}, Dv_{50} and Dv_{90} to D_{32} were presented in Eqs. 6.1 to 6.4. Where Dv_{90} (as a substitute for D_{max}) was found to be 2.8 times as large as D_{32}.

Droplets chord lengths appear to go through a bathtub or U shape evolution followed by a long decay. In the first stage, the aqueous phase droplets are still in the process of being broken up by the jet resulting in smaller droplets. Once the jet energy decays sufficiently coalescence starts to dominate, causing the droplet sizes to increase again. Eventually, the largest droplets merge forming a stratified layer and are removed from the statistics. This leaves progressively finer droplets dispersed in the flow resulting in the droplet size decreasing again.

Probability distributions of the droplet chord lengths reveal that most, if not all, experimental cases have a multimodal distribution. The existence of a multimodal distribution indicates that the droplets are formed through multiple processes, where these processes include Kelvin-Helmholtz instabilities and the secondary break up of ligaments and sheets formed by the jet during the initial interaction and the second region of jet interaction.

In the case of flows where the aqueous layer has yet to form, the profile of the aqueous phase fraction has a peak slightly higher than the bottom wall. This occurs through the interaction of several processes; (i) the largest droplets move away from the walls due to the lift effect produced by the differential pressures created due different velocities droplets experience across the near and far surface close to a wall; (ii) gravity causes the largest droplets to settle the fastest;

(iii) the high contact angle of the aqueous phase with the pipe wall in the silicone oil tends to keep some oil below the aqueous droplets.

The chord length measurements reveal that the droplets have a wide range of scales particularly when the jet velocity is low, this differs from static mixers where the range of droplet sizes is more uniform. However, the measurement of the higher velocity jets produces a much narrower range of the droplet chord lengths compared to the lowest jet velocities.

The largest droplets stratify the fastest, and their behaviour is important as they contain a significant fraction of the aqueous phase's volume. However, complex compound drops exist within the experimental flows, which indicates that a calculated droplet settling rate will be higher than the average droplet settling rate due to the lower density difference of the compound droplets. The number, density and subsequent effect of these compound droplets on the flows is an area for future research to provide a reliable calculation of the settling rate of the compound droplets.

In comparing the jet types, measurements show the U-jet has the lowest pressure loss while the pressure losses and power requirements of the F-jet and V-jet are ≈ 10% and ≈ 80% greater, respectively. The flow pattern maps, phase fraction profiles, C_1/C_2 ratios and vertical droplet distributions all indicate that the V-jet produces the evenest dispersions of the three jet types tested, while the F-jet was found to be marginally worse than the U-jet. Significantly, this better mixing is despite the Weber and Reynolds number of V-jet being 70% of the F-jet and V-jet. One difference between these jet is the total surface area, the V-jet has two jets each with a diameter of 2.8 mm with an initial circumference of 8.8 mm each for a total of 17.6 mm, whereas, the F-jet and V-jet have an initial circumference of 12.6 mm. This increased surface area may be the source of increased mixing. The 80% higher pressure loss of the V-jet equates to 80% increase in power requirements to provide the improved mixing which increases the operators running costs. However, no attempt was made to optimize the pressure losses in the design of the nozzle. Future work could therefore investigate if the pattern created by the V-jet nozzle could be created in a more efficient nozzle design to mitigate these losses.

The U-jet was found to create similar if not better performance to the F-jet. However, it would superficially seem that having a jet directed into the incoming flow (F-jet) should increase the level of mixing compared to a jet directed vertically upwards (U-jet). One possibility for this discrepancy is that the point of mixing is

pushed further upstream in the F-jet when compared to the other jet designs. This results in an apparent poorer mixing at the point of comparison ten diameters downstream as the flow has had more time to settle. Indeed, this could be a desirable feature as it would allow a sampling system to be located closer to the jet exit making a design more compact. Further investigation is therefore needed to determine if the measurement is pushed upstream by the forward action of the jet or if the forward angle does result in poorer mixing. Even still, given the forward design increases pressure loss any benefit to mixing seems limited.

The velocity profile at ten pipe diameters downstream shows a considerable variation with jet type when the crossflow is 0.6 m/s, where the velocity of the V jet is higher in the lower half of the pipe where energy is needed to break up any remaining layer of the aqueous phase. Therefore, this concentration of velocity in the lower half could be a contributing factor to the better performance of the V-jet. In contrast, both the U-jet and F-jet create a flow that travels along the top of the pipe which is unable to interact with any remaining aqueous phase at the bottom of the pipe. The V-jet produces a wider droplet size distributions compared to the other jets. This difference in droplet distribution indicates that the proportion of the different processes leading to droplet formation is different in the V-jet when compared with the other two jet types.

Potentially, the mixing effect of the V-jet could have been matched by the U-jet and F-jet through increasing their flow rate. Similarly, the V-jet mixing could have been reduced by lowering its flow rate and power requirements. The lower relative flowrates of the V-jet may then result in smaller line and element sizes which would reduce the systems capital costs.

Importantly, none of the experimental test cases created dispersions that were so fine that the separator was unable to separate the two phases continually. Therefore, the jets were not overmixing and the velocity of all the jets could have been increased further if needed to create finer dispersions.

The measurement of the C_1/C_2 ratio metric used by industry to determine the level of dispersion in a liquid-liquid flow agrees well with the other measurements presented in this thesis. However, the C_1/C_2 ratio metric does suffer from several issues, firstly, it is unable to detect conditions where the concentration is equal in the top and bottom, but different in the middle, as occurs when the jet concentrates the aqueous phase along the top of the pipe. Secondly, the C_1/C_2 measurements go above one in several experimental cases and while this can be valid this can also be

caused by increased uncertainty in the measured C_2 denominator when the dispersed phase fraction is low. It is therefore suggested that phase fraction profiles are included wherever possible when evaluating the performance of a system.

The refractive index matching used within the experimental facility performs well. The PLIF images of incoming stratified flows have clear visible interfaces, although out of plane objects can be seen as dim shadows due to the diffusion of laser light by the ETFE pipe wall. The more complex images of the jets are detailed and clear enough to perform measurements of phase fractions and droplet sizes. Similarly, the refractive index matching providing sufficient clarity to the tracer particles to allow measurements of the velocity fields through PIV and stereo-PIV.

Even still, the middle third of the pipe was found to have an experimental bias towards larger droplets due to the increased blurring through a greater number of droplet interfaces to the measurement plane. The blurring occurs due to the inevitable slight mismatch in refractive index between the two closely matched liquids.

The measured interface heights and pressure drops were found to agree closely with that predicted by the two-fluid model of Taitel and Dukler et al. (1976). Whilst comparing the pressure losses between the first two differential pressure transmitters and two-fluid model also suggests that the flows are well developed by the time they reach the measurement section

8.2 Key findings

The key findings of this work are now listed:

- Droplet chord lengths increase in size at all distances and stratification occurs more rapidly as the input aqueous phase fraction is increased and the jet velocity is decreased relative to the crossflow velocity V_m. The level of mixing increases with the velocity ratio at a given axial position where the interface height decreases and C_1/C_2 ratio increases. As the crossflow velocities increase the jet velocity must be increased to maintain the same level of mixing.
- Increasing the crossflow reduces the residence time, limits stratification and maintains an even dispersion over longer distances while moving the peak in C_1/C_2 downstream. In general, the distance at which a flow remains mixed increases with jet velocity and decreases with aqueous phase fraction.

- Mixing is incomplete at one pipe diameter and for some experimental cases, droplets are still undergoing breakup at four pipe diameters, indicating the influence of the jet can still be significant at this distance.
- A distance of ten pipe diameters is the upper limit of jet dominance for the conditions tested, beyond which gravitational-driven separation dominates and all flows have increased stratification and larger droplets chord lengths.
- The V-jet was the best mixer, producing the greatest number of mixed flow regimes while the F-jet is marginally poorer than that of the U-jet. However, the power requirements of the V-jet are 80% higher than that of the U-jet, which counterbalances its mixing efficiency. Further work is required to optimize the mixing configuration in terms of choice of jets and operating conditions.
- The existence of multimodal distributions suggests that the droplets are formed through multiple processes, which include Kelvin-Helmholtz instabilities and secondary break up of ligaments and sheets formed during the initial jet interaction and the secondary jet interaction zone.
- The U-jet creates a flow that travels downstream along the top of the pipe. This flow traps some of the aqueous phase which was entrained by the jet at the top of the pipe rather than dispersing it evenly into the bulk. The flow contains a significant fraction of the remaining jet energy but does not interact with any aqueous phase remaining at the bottom of the pipe.
- The vertical component of velocity downstream of the U-jet is responsible for lifting the aqueous phase at the interface. This upward velocity is a consequence of the dual counter-rotating vortices that are formed as the jet flow impinges the top wall and flows around the circumference of the pipe.
- The presence of an aqueous layer downstream of the jet provides a barrier to mixing, where an increase in the depth of the downstream aqueous layer decreases the level of secondary mixing that occurs.
- As the waviness on the interface of the incoming stratified flow increases the jet deflections increase. Large-amplitude waves deflect the jet significantly and the jet may not return to its original position immediately.
- As the crossflow velocity is increased, the jet is turned into the direction of the crossflow. Eventually, the jet is turned so far that it fails to impinge upon the top of the pipe wall and the large upstream vortex no longer forms in time-averaged velocity fields.

8.3 Suggestions for future research

The effect of changing the viscosity, density and interfacial tension of the liquids were not tested during this experimental campaign and it is expected these will all affect the behaviour of the processes of breakup, dispersion, coalescence and settling. Similarly, the contact angle of the solid was not investigated. Suggested future work should include the option to test the effect of these fluid and solid properties.

The jet mixing system was tested in a horizontal pipe which is the most common orientation for these systems. However, small inclinations from the horizontal are also common and some jet mixers are located in vertical pipes. The orientation of the pipe is therefore an area for future investigation.

The experiments performed measurements at three points, however, this only provided a snapshot of the development of the flows following mixing. The use of a camera rail would allow the flow development to be captured in more detail and so provide a more detailed understanding of this complex process.

The experimental setup could be improved in several ways as compromises had to be made with the time and equipment available during the project. The use of fluorescent particles would result in smaller but brighter particles. These particles could then be more easily separated from the background glow caused by the diffusion of the laser light by the ETFE pipe through the use of a low pass filter on the cameras so that only particles and dye are captured. However, the cost in purchasing these commercially is prohibitive and while a brief investigation was made into making these particles, project time was too short to accomplish this. Future work could therefore investigate the manufacture of homemade fluorescent particles that could be more generally used in these types of large-scale experiments.

Wider camera angles would lower the uncertainty of the stereo-PIV z-component. This could be accomplished in two ways first the camera perpendicular to the sheet could be moved to increase the angle however this would be at the expense of lower PLIF droplet size measurements as the pixel resolution would decrease on the near side of the image. Ideally, a three-camera setup could be used, where two angled cameras were used for stereo-PIV and a third perpendicular camera is used for PLIF measurements. The Scheimpflug used in the experiments acted like an extension to the lens reducing the angle at which the

lens could be focused. The angle of the stereo-PIV cameras could therefore be increased further through the use of an integral Scheimpflug and lens.

The cameras are synchronized together and control the timing of the laser pulse, however, the cameras are limited to 2 kHz, while the laser has a minimum rate of 200 Hz. These constraints limit the camera frame rate to between 200 Hz and 2 kHz and hence the time step between frames, so restricting the range of the velocities that can be measured using PIV. Ideally, cameras that are capable of being controlled from an external synchronizer would allow a wider range of timing between PIV measurement frames and hence allow a more in-depth analysis of the flow fields.

The ETFE pipe material is difficult to work with on several levels. It has to be thin to allow sufficient visibility through the wall for the experiments. However, ETFE is a soft material and so thin walls deform easily. Early experimentally asymmetries in the incoming flows were minimised through encasing the thin flexible ETFE pipe in a hard PVC outer pipe casing. This provided sufficient support to the ETFE pipe to maintain its circular shape during the subsequent experimental campaigns. The thin ETFE walls make hydraulic sealing difficult in this non-stick Teflon like material, especially when this flexibility is combined with creep caused by the low surface tension of the silicone oil. Finally, the ETFE diffuses the laser and this contributes to the background noise making the analysis difficult for both PLIF and PIV. It is therefore suggested that future experimentalists again try to seek for an alternative solid with a refractive index around 1.40 to match the liquids.

List of future experimental work:

- Continue with the processing of the PIV and stereo-PIV results created during this project.
- Investigate the effect of viscosity, density and interfacial tension and contact angles on the mixing process.
- Investigate the effect of crossflow velocities greater than 0.8 m/s on the effect of mixing and subsequent stratification of the flows.
- Investigate why the V-jet provides better mixing, is it the increased surface area of the jets?
- Investigate if the pattern created by the V-jet could be created in a more efficient nozzle design.

- Investigate the effect of jet mixer orientation on the mixing process, i.e. inclined and vertical flows.
- Investigate the creation of cost-effective fluorescent particles for use in large scale experimental systems.
- Implementation of a camera rail or similar to watch the flows develop as they travel along the pipe.
- Implement a wider separation angle for stereo-PIV, possibly using three cameras and integrated Scheimpflug and lens.
- Seek a stiffer solid with a refractive index close to 1.40 with an opacity that is lower than that of ETFE. This solid should also be chemically compatible with silicone oil.
- Investigate compound droplets to discover the effects on the settling rate of droplets within the flows.
- Examine the effect of the jet angle in more detail to discover if forward faced jets push the mixing upstream.
- Investigate the effects of scaling on the results to establish the applicability of the results to large pipe diameters.
- Investigate mixing through the cross section of the pipe to obtain a better understanding of the 3-D character of the mixing processes.

References

Abbas MA, Crowe CT (1987). Experimental study of the flow properties of a homogenous slurry near transitional Reynolds numbers. Int J Multiph Flow 13:357–364

Abbott JR (1991). Experimental observations of particle migration in concentrated suspensions: Couette flow. J Rheol 35:773–795

Ackerson BJ, Pusey PN (1988). Shear-induced order in suspensions of hard spheres. Phys Rev Lett 61:1033–1036

Agrawal Y, Talbot L, Gong K (1978). Laser anemometer study of flow development in curved circular pipes. J Fluid Mech 85: 497–518

Akinci A, Cobanoglu E (2009). Coating of Al mould surfaces with polytetrafluoroethylene (PTFE), fluorinated ethylene propylene (FEP), perfluoro-alkoxy (PFA) and ethylene-tetrafluoroethylene (ETFE). E Polym 33:1–7

Alahyari A, Longmire EK (1994). Particle image velocimetry in a variable density flow: Application to a dynamically evolving microburst. Exp Fluids 17:434–440

Alahyari AA, Longmire EK (1997). Concentration measurements in experimental microbursts. AIAA J 35:569–571

Albuquerque L, Ventura C, Gonçalves R (1996). Refractive indices, densities, and excess properties for binary mixtures containing methanol, ethanol, 1,2-ethanediol, and 2-methoxyethanol. J Chem Eng Data 41:685–688

Allen E, Triantaphillidou S, (2011). The Manual of Photography, 10th edition, Focal press, Taylor and Francis, Oxford, UK

Amatya DM, Longmire EK (2010). Simultaneous measurements of velocity and deformation in flows through compliant diaphragms. J Fluids Struct 26:218–235

Amini N, Hassan YA (2009). Measurements of jet flows impinging into a channel containing a rod bundle using dynamic PIV. Int J Heat Mass Transf 52:5479–5495

Amini N, Hassan YA (2012). An investigation of matched index of refraction technique and its application in optical measurements of fluid flow. Exp Fluids 53:2011–2020

Amundsen L (2011). An experimental study of oil-water flow in horizontal and inclined pipes. PhD thesis, Norwegian Univeristy of Science and Technology, Trondheim, Norway

Angeli P. (1996). Liquid-liquid dispersed flows in horizontal pipes. PhD thesis, Imperial College London (University of London), London, UK

Angeli P, HEWITT GF (1999). Pressure gradient in horizontal liquid-liquid flows. Int J Multiph Flow 24:1183–1203

Arago D, Biot J (1806) Mémoire sur les affinités des corps pour la lumière, et particulièrement sur les forces réfringentes des différens gaz. Académie des Sciences, Paris, France

Atherton TJ, Kerbyson DJ (1999). Size invariant circle detection. Image Vis Comput 17(11):795–803

ASTM 2010. Manual of Petroleum Measurement Standards (MPMS), Chapter 8.2. Standard Practice for Automatic Sampling of Petroleum and Petroleum Products. ASTM International, 100 Barr Harbor Drive, PO Box C700, West Conshohocken, PA 19428–2959, United States

Augier F, Morchain J, Guiraud P, Masbernat O (2003). Volume fraction gradient-induced flow patterns in a two-liquid phase mixing layer. Chem Eng Sci 58:3985–3993

Augier FDR, Guiraud P, Masbernat O (2007). Fluctuating motion in a homogeneous liquid-liquid dispersed flow at high phase fraction. Phys Fluids 19:057105

Averbakh A, Shauly A, Nir A, Semiat R (1997). Slow viscous flows of highly concentrated suspensions – Part I: Laser-Doppler velocimetry in rectangular ducts. Int J Multiph Flow 23:409–424

Aziza ARA, Wong KFV (2003). Velocity measurements across fluid-porous medium interface using particle image velocimetry. Int J Model Simul 23:179–186

Bai K, Katz J (2014). On the refractive index of sodium iodide solutions for index matching in PIV. Exp Fluids 55:1704

Bailey BC, Yoda M (2003). An aqueous low-viscosity density- and refractive index-matched suspension system. Exp Fluids 35:1–3

Baker RC (1986). Sampling Water-in-oil: A Critical Assessment of the Validity of ISO/DIS 3171 Annex A for the Estimation of Water-in-oil Dispersion, Cranfield University Press.

Baker RC (1988). Computational method to assess concentration of water in crude oil downstream of a mixing section. ARCHIVE: Proceedings of the Institution of Mechanical Engineers, Part A: Power and Process Engineering 1983–1988 (vols 197–202), 202, 117–127

Bakker A, Laroche RD (2000). Modeling of the Turbulent Flow in HEV Static Mixers.

Baldwin JT, Tarbell JM, Deutsch S, Geselowitz DB (1989). Mean flow velocity patterns within a ventricular assist device. ASAIO J 35:429–432

Bale-Glickman J, Selby K, Saloner D, Savas O (2003). Experimental flow studies in exact-replica phantoms of atherosclerotic carotid bifurcations under steady input conditions. J Biomech Eng 125:38–48

Baragi JG, Aralaguppi MI, Aminabhavi TM, Kariduraganavar MY, Kittur AS (2005). Density, viscosity, refractive index, and speed of sound for binary mixtures of anisole with 2-chloroethanol, 1,4-dioxane, tetrachloroethylene, tetrachloroethane, DMF, DMSO, and diethyl oxalate at (298.15, 303.15, and 308.15) K. J Chem Eng Data 50:910–916

Beall JH (2014). A Review of Astrophysical Jets. Acta Polytechnica CTU Proceedings, 1, 259–264

Begolo, S, Colas G, Viovy JL, Malaquin L (2011). New family of fluorinated polymer chips for droplet and organic solvent microfluidics. Lab Chip 11:508–512

Bell JH, Mehta RD (1989). Design and calibration of the mixing layer and wind tunnel. Stanford University: Stanford University

Benjamin T (2001). Eductor pumps: the calculations. World Pumps 413:233–246

Berard LR, Raessi M, Bauer MT, Friedman PD, Codyer SR (2013). An investigation on the breakup of underwater buoyant oil jets: Computational simulations and experiments. At Sprays 23:981–1000

Bhatia SC, Bhatia R, Dubey GP (2009). Refractive properties and internal pressures of binary mixtures of octan-1-ol with chloroform, 1,2-dichloroethane and 1,1,2,2-tetrachloroethane at 298.15 and 308.15 K. J Mol Liq 145:88–102

Blanchette F, Bigioni TP (2000). Dynamics of drop coalescence at fluid interfaces. J Fluid Mech, 620:333–352

Bordoloi AD, Longmire EK (2012). Effect of neighboring perturbations on drop coalescence at an interface. Phys Fluids 24:062106

Borrero-Echeverry D, Morrison BCA (2016). Aqueous ammonium thiocyanate solutions as refractive index-matching fluids with low density and viscosity. Exp Fluids 57:123

Bovendeerd PHM, Steenhoven AAV, Vosse FNVD, Vossers G (1987). Steady entry flow in a curved pipe. J Fluid Mech 177:233–246

Bowman, CL (1998). Quantifying the cleanliness of glass capillaries. Cell Biochem Biophys 29:203–223

Braun MJ, Canacci VA, Hendricks RC (1991). Flow visualization and quantitative velocity and pressure measurements in simulated single and double brush seals. Tribol Trans 34:70–80

Brauner N, Moalem Maron D (1989). Two-phase liquid-liquid stratified flow. Physico Chem Hydrodynam 11: 487–506

Brauner N, Moalem Maron D, Rovinsky J (1998) A two-fluid model for stratified flows with curved interfaces. Int J Multiph Flow 24: 975–1004

Bravo L, Kweon CB (2014). A Review of Liquid Spray Models for Diesel Engine Computational Analysis. Army Res Lab, ARL-TR-6932

Breedveld LVA (2000). Shear-induced self-diffusion in concentrated suspensions. PhD thesis, Universiteit Twente, Enschede, Netherlands

Breedveld V, Van Den Ende D, Bosscher M, Jongschaap RJJ, Mellema J (2001). Measuring shear-induced self-diffusion in a counterrotating geometry. Phys Rev E 63:021403

Breedveld V, Van Den Ende D, Bosscher M, Jongschaap RJJ, Mellema J (2002). Measurement of the full shear-induced self-diffusion tensor of noncolloidal suspensions. J Chem Phys 116:10529

Breedveld V, Van Den Ende D, Tripathi A, Acrivos A (1998). The measurement of the shear-induced particle and fluid tracer diffusivities in concentrated suspensions by a novel method. J Fluid Mech 375:297–318

Brown ML, Parsheh M, Aidun CK (2006). Turbulent flow in a converging channel: effect of contraction and return to isotropy. J Fluid Mech 560:437

Brown GO (2002). The history of the Darcy-Weisbach equation for pipe flow resistance. ASCE Civil Engineering Conference and Exposition 2002 3rd–7th November, Washington D.C., United States.

Buckingham E (1914). On Physically Similar Systems; Illustrations of the Use of Dimensional Equations. Phys Rev, 4:345–376

Buchmann NA, Atkinson C, Jeremy MC, Soria J (2011). Tomographic particle image velocimetry investigation of the flow in a modeled human carotid artery bifurcation. Exp Fluids 50:1131–1151

Buchmann NA, Yamamoto M, Jermy M, David T (2010). Particle image velocimetry (PIV) and computational fluid dynamics (CFD) modelling of carotid artery haemodynamics under steady flow: A validation study. J Biomech Sci Eng 5:421–436

Budwig R (1994). Refractive index matching methods for liquid flow investigations. Exp Fluids 17:350–355

Budwig R, Elger D, Hooper H, Slippy J (1993). Steady flow in abdominal aortic aneurysm models. J Biomech Eng 115:418–423

Burdett ID, Webb DR, Davies GA (1981). A new technique for studying dispersion flow, holdup and axial mixing in packed extraction columns. Chem Eng Sci 36:1915–1919

Burgmann S, Grosse S, Schröder W, Roggenkamp J, Jansen S, Gräf F, Büsen M, (2009). A refractive index-matched facility for fluid–structure interaction studies of pulsatile and oscillating flow in elastic vessels of adjustable compliance. Exp Fluids 47:865–881

Butscher D, Hutter C, Kuhn S, Rudolf Von Rohr P (2012). Particle image velocimetry in a foam-like porous structure using refractive index matching: A method to characterize the hydrodynamic performance of porous structures. Exp Fluids 53:1123–1132

Byron ML, Variano EA (2013). Refractive-index-matched hydrogel materials for measuring flow-structure interactions. Exp Fluids 54:1456

Cadillon J, Saksena R, Pearlstein AJ (2016). Transparent, immiscible, surrogate liquids with matchable refractive indexes: Increased range of density and viscosity ratios. Phys Fluids 28:127102

Cameron (2013) JISKOOT CoJetix Sampling System. Cameron, Tunbridge Wells, Kent, UK.

Carpenter CP, Kinkead ER, Geary DL, Sullivan LJ, King JM (1975). Petroleum hydrocarbon toxicity studies. Toxicol Appl Pharm 32:282–297

Cenedese A, Viotti P (1996). Lagrangian analysis of nonreactive pollutant dispersion in porous media by means of the particle image velocimetry technique. Water Resour Res 32:2329–2343

Cerne G, Petelin S, Tiselj I (2001). Coupling of the Interface Tracking and the Two-Fluid Models for the Simulation of Incompressible Two-Phase Flow. J Comp Phys, 171:776–804

Chaudhuri P, Gao Y, Berthier L, Kilfoil M, Kob W (2008). A random walk description of the heterogeneous glassy dynamics of attracting colloids. J Phys: Condens Matter 20:244126

Charogiannis A, Denner F, van Wachem BGM, Kalliadasis S, Markides CN (2017). Detailed hydrodynamic characterization of harmonically excited falling-film flows: A combined experimental and computational study. Phys Rev Fluids

Chen B, Mikami, F, Nishikawa N (2005). Experimental studies on transient features of natural convection in particles suspensions. Int J Heat and Mass Transf 48:2933–2942

Chen RC, Fan LS (1992). Particle image velocimetry for characterizing the flow structure in three-dimensional gas-liquid-solid fluidized beds. Chem Eng Sci 47:3615–3622

Chen RC, Kadambi JR (1990). LDV measurements of solid-liquid slurry flow using refractive index matching technique. Part Sci Technol 8:97–109

Chen RC, Kadambi JR (1995). Discrimination between solid and liquid velocities in slurry flow using laser Doppler velocimeter. Powder Technol 85:127–134

Chen RC, Reese J, Fan LS (1994). Flow structure in a three-dimensional bubble column and three-phase fluidized bed. AIChE J 40:1093–1104

Cho JS, Han S, Kim KH, Beag YW, Koh SK (2003). Surface modification of polymers by ion-assisted reaction. Thin Solid Films 445:332–341

Clift R, Grace JR, Weber ME (2005). Bubbles, drops and particles, 31st East 2nd Street, Mineola, New York 11501, Dover Publications Inc.

Conan C, Masbernat O, Décarre S, Liné A (2007). Local hydrodynamics in a dispersed-stratified liquid–liquid pipe flow. AIChE J 53:2754–2768

Colebrook CF (1939). Turbulent flow in pipes, with particular reference to the transition region between smooth and rough pipe laws. J I Civil Eng 11(4):133-156

Corino ER, Brodkey RS (1969). A visual investigation of the wall region in turbulent flow. J Fluid Mech, 37:1–30

Cui MM, Adrian RJ (1997). Refractive index matching and marking methods for highly concentrated solid-liquid flows. Exp Fluids 22:261–264

Curran SJ, Black RA (2004). Quantitative experimental study of shear stresses and mixing in progressive flow regimes within annular-flow bioreactors. Chem Eng Sci 59:5859–5868

Daviero GJ, Roberts PJW, Maile K (2001). Refractive index matching in large-scale stratified experiments. Exp Fluids 31:119–126

De Silva IPD, Fernando HJS (1998). Experiments on collapsing turbulent regions in stratified fluids. J Fluid Mech 358:29–60

Das PK, Legrand J, Morançais P, Carnelle G (2005). Drop breakage model in static mixers at low and intermediate Reynolds number. Chem Eng Sci 60:231–238

DaVis, (2017). Product manual: FlowMaster 8.4 Software. 14 September 2017, LaVision GmbH, Anna-Vandenhoeck-Ring 19, D-37081 Göttingen, Germany.

DaVis, (2019). Product manual: DaVis 8.4 Software. 12 July 2019, LaVision GmbH, Anna-Vandenhoeck-Ring 19, D-37081 Göttingen, Germany.

Dibble CJ, Kogan M, Solomon MJ (2006). Structure and dynamics of colloidal depletion gels: Coincidence of transitions and heterogeneity. Phys Rev E 74:041403

Dietze GF, Al-Sibai F, Kneer R (2009). Experimental study of flow separation in laminar falling liquid films. J Fluid Mech 637:73–104

Dijksman JA, Rietz F, Lorincz KA, Van Hecke M, Losert W (2012). Invited article: Refractive index matched scanning of dense granular materials. Rev Sci Instrum 83:011301

Dogăn N, Dogăn İ (2010) Determination of the number of bins/classes used in histograms and frequency tables: a short biography. J Stat Res 7(2):77–86

Downie H, Holden N, Otten W, Spiers AJ, Valentine TA, Dupuy LX (2012). Transparent soil for imaging the rhizosphere. PLoS One 7:e44276

Drobny JG (2006). Rapra review report 184: Fluoroplastics. Rapra Technology Ltd, Shrewsbury, UK

Duffy DC, McDonald JC, Schueller OJ, Whitesides GM (1998). Rapid prototyping of microfluidic systems in poly(dimethylsiloxane). Anal Chem 70:4974–4984

Duncan DD, Bargeron CB, Borchardt SE, Deters OJ, Gearhart SA, Mark FF, Friedman MH (1990). The effect of compliance on wall shear in casts of a human aortic bifurcation. J Biomech Eng 112:183–188

Durst F, Jovanovic J, Sender J (1995). LDA measurements in the near-wall region of a turbulent pipe flow. J Fluid Mech 295:305–335

Durst F, Loy T (1985). Investigations of laminar flow in a pipe with sudden contraction of cross sectional area. Comput Fluids 13:15–36

Durst F, Müller R, Jovanovic J (1988). Determination of the measuring position in laser-Doppler anemometry. Exp Fluids 6:105–110

Ebnesajjad S, Khaladkar PR (2005). Fluoropolymers applications in chemical processing industries—The definitive user's guide and databook. William Andrew Inc, New York, NY, USA

Egelhoff CJ, Budwig RS, Elger DF, Khraishi TA, Johansen KH (1999). Model studies of the flow in abdominal aortic aneurysms during resting and exercise conditions. J Biomech 32:1319–1329

Eggers J, Villermaux E (2008). Physics of liquid jets. Rep Prog Phys 71:036601

Eykman JF (1895). Recherches réfractométriques (suite). Rec Trav Chim 14:185–202

Eyring H, Jhon MS (1969). Significant Liquid Structures. John Wiley & Sons, New York, NY, USA

Fernando LM (1990). Jet mixing of water in crude oil pipelines. PhD Doctoral, Cranfield University.

Fernando LM, Lenn CP (1990). Jet mixing of water in crude oil pipelines for representative sampling. Anal Chim Acta 238:251–256

Fitzgerald SD, Holley ER (1979). Jet Injections for Optimum Mixing in Pipe Flow. Washington, DC: Final Research Report Office of Water Research and Technology.

Forliti D (2012). Trajectory and Mixing Scaling Laws for Confined and Unconfined Transverse Jets

Fort C, Fu CD, Weichselbaum NA, Bardet PM (2015). Refractive index and solubility control of para-cymene solutions for index-matched fluid–structure interaction studies. Exp Fluids 56:210

Fort T (1964). The wettability of a homologous series of nylon polymers. Adv Chem 43:302–309

Forziati AF (1950). Refractive index as a function of wavelength for sixty API-NBS hydrocarbons. J Res Natl Bur Stand 44:RP2085

Fradette L, Tanguy P, Li HZ, Choplin L (2007). Liquid/Liquid Viscous Dispersions with a SMX Static Mixer. Chem Eng Res Des 85:395–405

Fries RJ, Han K, Ko CM (2016). Jet Hadronization via Recombination of Parton Showers in Vacuum and in Medium. Nucl Phys A 956:601–604

Frish MB, Webb WW (1981). Direct measurement of vorticity by optical probe. J Fluid Mech 107:173–200

Freeman PI (1980). Report on Tests on a jet flow conditioning system for the department of energy's petroleum engineering directorate. NEL, Scotland ENER/11

Galeazzo FCC, Donnert G, Habisreuther P, Zarzalis N, Valdes RJ, Krebs W (2011). Measurement and Simulation of Turbulent Mixing in a Jet in Crossflow. J Eng Gas Turb Power 133:061504.

Gao Y, Kilfoil ML (2007). Direct imaging of dynamical heterogeneities near the colloid-gel transition. Phys Rev Lett 99:078301

Geoghegan PH, Buchmann NA, Spence CJT, Moore S, Jermy M (2012). Fabrication of rigid and flexible refractive-index-matched flow phantoms for flow visualization and optical flow measurements. Exp Fluids 52:1331–1347

Georgalas I, Ladas I, Tservakis I, Taliantzis S, Gotzaridis E, Papaconstantinou D, Koutsandrea C (2011). Perfluorocarbon liquids in vitreoretinal surgery: a review of applications and toxicity. Cutan Ocul Toxicol 30:251–62

Geyer A, Phillips JC, Mier-Torrecilla M, Idelsohn SR, Oñate E (2011). Flow behaviour of negatively buoyant jets in immiscible ambient fluid. Exp Fluid 52:261–271

Ghatage SV, Peng Z, Sathe MJ, Doroodchi E, Padhiyar N, Moghtaderi B, Joshi JB, Evans GM (2014). Stability analysis in solid–liquid fluidized beds: Experimental and computational. Chem Eng J 256:169–186

Gijsen FJH, Palmen DEM, Van Der Beek MHE, Van De Vosse FN, Van Dongen MEH, Janssen JD (1996). Analysis of the axial flow field in stenosed carotid artery bifurcation models – LDA experiments. J Biomech 29:1483–1489

Gladstone JH, Dale TP (1863). XIV Researches on the refraction, dispersion and sensitiveness of liquids. Phil Trans Royal Soc Lond 153:317–343

Goharzadeh A, Khalili A, Jo/rgensen BB (2005). Transition layer thickness at a fluid-porous interface. Phys Fluids 17:057102

Gómez E, González B, Calvar N, Tojo E, Domínguez Á (2006). Physical properties of pure 1-ethyl-3-methylimidazolium ethylsulfate and its binary mixtures with ethanol and water at several temperatures. J Chem Eng Data 51:2096–2102

Graham AL (1991). NMR imaging of shear-induced diffusion and structure in concentrated suspensions undergoing Couette flow. J Rheol 35:191–201

Graham AL, Bird RB (1984). Particle clusters in concentrated suspensions. 1. Experimental observations of particle clusters. Ind Eng Chem Fundam 23:406–410

Gülan U, Lüthi B, Holzner M, Liberzon A, Tsinober A, Kinzelbac W (2012). Experimental study of aortic flow in the ascending aorta via particle tracking velocimetry. Exp Fluids 53:1469–1485

Gutmark EJ, Ibrahim IM, Murugappan S (2008). Circular and nocirlcular subsonic jets in cross flow. Phys Fluids 20:075110

Haam SJ, Brodkey RS (2000). Motions of dispersed beads obtained by particle tracking velocimetry measurements. Int J Multiph Flow 26:1419–1438

Haam SJ, Brodkey RS, Fort I, Klaboch L, Placnik M, Vanecek V (2000). Laser Doppler anemometry measurements in an index of refraction matched column in the presence of dispersed beads. Int J Multiph Flow 26:1401–1418

Hager WH (2003). Blasius: A life in research and education. Exp Fluid 34:566–571

Ham JM, Homsy GM (1988). Hindered settling and hydrodynamic dispersion in quiescent sedimenting suspensions. Int J Multiph Flow 14:533–546

Hannoun I (1985). Matching the refractive index in density stratified flows. California Institute of Technology

Hannoun IA, Fernando HJS, List EJ (1988). Turbulence structure near a sharp density interface. J Fluid Mech 189:189–209

Harrington M, Lin M, Nordstrom KN, Losert W (2014). Experimental measurements of orientation and rotation of dense 3D packings of spheres. Granul Matter 16:185–191

Hassan YA, Dominguez-Ontiveros EE (2008). Flow visualization in a pebble bed reactor experiment using PIV and refractive index matching techniques. Nucl Eng Des 238:3080–3085

Hayes WM (Ed.) (2015). CRC Handbook of Chemistry and Physics, 96th Edition. CRC Press, Boca Raton, FL, USA

Hayward P (1983). Conditions hydrauliques minimales pour l'echnatillonnage automatique. Petrole et Techniques 295:64–668

Heller W (1945). The determination of refractive indices of colloidal particles by means of a new mixture rule or from measurements of light scattering. Phys Rev 68:5–10

Hendriks F, Aviram A (1982). Use of zinc iodide solutions in flow research. Rev Sci Instrum 53:75–78

Hewitt GF, Jayanti S, Hope CB (1990). Structure of thin liquid films in gas-liquid horizontal flow. Int J Multiph Flow 16:951–957

Hibberd DJ, Mackie AR, Moates GK, Penfold R, Watson AD, Barker GC (2007). Preparation and characterisation of a novel buoyancy and refractive index matched oil-in-water emulsion. Colloid Surf A 301:453–461

Hinze JO (1955). Fundamentals of the hydrodynamic mechanism of splitting in dispersion processes. AIChE J, 1:289–295

Hirsch D, Graff EC, Pereira F, Gharib M (2015). Influence of common transparent materials on the accuracy of image-based velocimetry. Meas Sci Technol 26:087002

Hirschberg S, Koubek R, Moser F, Schöck J (2009). An improvement of the Sulzer SMX™ static mixer significantly reducing the pressure drop. Chem Eng Res Des 87:524–532

Hopkins LM, Kelly JT, Wexler AS, Prasad AK (2000). Particle image velocimetry measurements in complex geometries. Exp Fluids 29:91–95

Hosseinzadeh M, Ghaemi A, Shirvani M (2017) Hydrodynamic performance evaluation of a novel eductor liquid–liquid extractor using CFD modeling. Chem. Eng. Res. Des. 201:205–213

Hosseinzadeh M, Shirvani M, Ghaemi A (2018) A study on mean drop size and drop size distribution in an eductor liquid–liquid extractor. Sep. Purif. Technol. 201:205–213

Huang AYL, Huang MYF, Capart H, Chen RH (2008). Optical measurements of pore geometry and fluid velocity in a bed of irregularly packed spheres. Exp Fluids 45:309–321

Huang AYL, Huang MYF, Chen RH, Capart H (2009a). Influence of aspect ratio on the distribution of porosity and velocity in columns of spheres. J Chin Inst Eng 32:421–426

Huang MYF, Huang AYL, Chen RH, Capart H (2009b). Automated tracking of liquid velocities in a refractive index matched porous medium. J Chin Inst Eng 32:877–882

Hussain SA (2004). Experimental and computational studies of liquid-liquid dispersed flows. Doctoral, Imperial College London (University of London)

Hwang RR, Chiang TP (1986). Buoyant jets in a crossflow of stably stratified fluid. Atmos Environ 20:1887–1890

Hydraulic-Institute (1979). Hydraulic institute engineering data book, Cleveland, OH, USA

Ibarra RJ, Markides CN, Matar OK (2014). A Review of Liquid-Liquid Flow Patterns in Horizontal and Slightly Inclined Pipes. Multiph Sci Techol 26:171–19

Ibarra RJ. 2017. Horizontal and low inclination oil/water flow investigations using laser-based diagnostic techniques. PhD, Imperial College London.

Im S, Heo GE, Jeon YJ, Sung HJ, Kim SK (2013). Tomographic PIV measurements of flow patterns in a nasal cavity with geometry acquisition. Exp Fluids 55:1644

Imao S, Itoh M, Harada T (1996). Turbulent characteristics of the flow in an axially rotating pipe. Int J Heat Fluid F 17:444–451

Isehunwa SO, Olanisebe EB, Ajiboye OO, Akintola SA (2015). Estimation of the refractive indices of some binary mixtures. Afr J Pure Appl Chem 10:58–64

ISO 1999. Petroleum liquids—Automatic pipeline sampling. rue de Stassart, 36. B-1050 Brussels: International organization for standardization.

Jacobs DA, Jacobs CW, Andereck CD (1988). Biological scattering particles for laser Doppler velocimetry. Phys Fluids 31:3457–3461

Jan DL, Shapiro AH, Kamm RD (1989). Some features of oscillatory flow in a model bifurcation. J Appl Physiol 67:147–159

Jana SC (1995). Apparent wall slip velocity coefficients in concentrated suspensions of noncolloidal particles. J Rheol 39:1123–1132

Johnston W, Dybbs A, Edwards R (1975). Measurement of fluid velocity inside porous media with a laser anemometer. Phys Fluids 18:913–914

Jiskoot JJ (1979) Liquid sampling system. GB2030963A

Jiskoot JJ (1986) Pipeline sampling system. GB2164021A

Jiskoot MA (2001) Mixing oil in a transfer line prior to sampling. GB2357710A

Jiskoot MJ, Baker JM, Potten GM (2018) Apparatus for mixing of fluids flowing through a conduit. US10058828B2

Kang JH, Lee KJ, Nam JH, Kim CJ, Park HS, Lee S, Kwang I (2010). Visualization of invasion-percolation drainage process in porous media using density-matched immiscible fluids and refractive-index-matched solid structures. J Power Sources 195:2608–2612

Kapoor B, Acrivos A (2006). Sedimentation and sediment flow in settling tanks with inclined walls. J Fluid Mech 290:39–66

Karabelas AJ (1977). Vertical distribution of dilute suspensions in turbulent pipe flow. AIChE Jl 23:426-434

Karabelas AJ (1978a). Droplet size spectra generated in turbulent pipe flow of dilute liquid/liquid dispersions. AIChE J 24:170–180

Karabelas AJ (1978b). Recent studies improve velocity criteria used for bs&w sampling. Oil Gas J 76(17 Apr1978):98–100

Karnis A, Goldsmith HL, Mason SG (1966). The kinetics of flowing dispersions I: Concentrated suspensions of rigid particles. J Colloid Interf Sci 22:531–553

Kaufman LJ, Weitz DA (2006). Direct imaging of repulsive and attractive colloidal glasses. J Chem Phys 125:074716

Kaur S, Leal LG (2010). Drop deformation and break-up in concentrated suspensions. J Rheol 54:981–1008

Kefayati S, Poepping TL (2013). Transitional flow analysis in the carotid artery bifurcation by proper orthogonal decomposition and particle image velocimetry. Med Eng Phys 35:898–909

Kegel WK, Van Blaaderen A (2000). Direct observation of dynamical heterogeneities in colloidal hard-sphere suspensions. Sci 287:290–293

Khattab IS, Bandarkar F, Fakhree MAA, Jouyban A (2012). Density, viscosity, and surface tension of water+ethanol mixtures from 293 to 323K. Korean J Chem Eng 29:812–81

Kim J, Longmire EK (2009). Investigation of binary drop rebound and coalescence in liquids using dual-field PIV technique. Exp Fluids 47:263–278

Koh CJ, Hookham P, Leal LG (1994). An experimental investigation of concentrated suspension flows in a rectangular channel. J Fluid Mech 266:1–32

Kohnen C, Bohnet M (2001). Measurement and simulation of fluid flow in agitated solid/liquid suspensions. Chem Eng Technol 24:639–643

Kollhoff RT, Kelemen K, Schuchmann HP (2015). Local multiphase flow characterization with micro particle image velocimetry using refractive index matching. Chem Eng Technol 38:1774–1782

Kondyurin A, Gan BK, Bilek MMM, Mizuno K, McKenzie DR (2006). Etching and structural changes of polystyrene films during plasma immersion ion implantation from argon plasma. Nucl Instrum Methods Phy Res Sect B Beam Interact Mater Atoms 251:413–418

Kong XZ, Holzner M, Stauffer F, Kinzelbach W (2010). Time-resolved 3D visualization of air injection in a liquid-saturated refractive-index-matched porous medium. Exp Fluids 50:1659–1670

Krishnan GP, Beimfohr S, Leighton DT (1996). Shear-induced radial segregation in bidisperse suspensions. J Fluid Mech 321:371–393

Kumar S, Kusakabe K, Fan LS (1993). Heat transfer in three-phase fluidized beds containing low-density particles. Chem Eng Sci 48:2407–2418

Kurban APA (1997). Stratified liquid-liquid flow. PhD Doctoral, Imperial College London (University of London)

Kurtz SS, Ward AL (1936). The refractivity intercept and the specific refraction equation of Newton. I. Development of the refractivity intercept and comparison with specific refraction equations. J Frankl Inst 222:527–646

Lakshmanan S, Holland D, Sederman A, Gurevich M, Maru W (2015). Multiphase flow quantification using Computational Fluid Dynamics and Magnetic Resonance Imaging. 33rd North Sea flow measurement workshop 2015, 20th–23rd October 2015, Tønsberg, Norway

Lakshmanan S, Huang J, Maru W, Thomas A (2017a). Measurement of an oil–water flow using magnetic resonance imaging. Flow Meas Instrum 53:161–171

Lakshmanan S, Huang J, Maru W, Thomas A (2017b). Quantifying mixing efficiency in Automatic Pipeline Sampling. 35th North Sea flow measurement workshop 2017, 24th–27th October 2017, Tønsberg, Norway

Le TB, Troolin DR, Amatya D, Longmire EK, Sotiropoulos F (2013). Vortex phenomena in sidewall aneurysm hemodynamics: experiment and numerical simulation. Ann Biomed Eng 41:2157–2170

Legrand J, Morançais P, Carnelle G (2001). Liquid-Liquid Dispersion in an SMX-Sulzer Static Mixer. Chem Eng Res Des 79:949–956

Leighton D, Acrivos A (1987). Measurement of shear-induced self-diffusion in concentrated suspensions of spheres. J Fluid Mech 177:109–131

Leis AP, Schlicher S, Franke H, Strathmann M (2005). Optically transparent porous medium for nondestructive studies of microbial biofilm architecture and transport dynamics. Appl Environ Microbiol 71:4801–8

Lemenand T, Valle D, Zellouf Y, Peerhossaini H (2003). Droplets formation in turbulent mixing of two immiscible fluids in a new type of static mixer. Int J Multiph Flow 29:813–840

LemenandT, Dupont P, Valle, D, Peerhossaini H (2005). Turbulent Mixing of Two Immiscible Fluids. J Fluid Eng 127:1132

Lenn CP, Hemp J, Baker RC, Hayes ER, Harper AD (1993). A study of flow downstream of a t-junction and the implications of its effect (in crude oil flow) on water droplet size and distribution. ARCHIVE: Proceedings of the Institution of Mechanical Engineers, Part E: J Process Mech Eng 207:123–132

Lenoble M, Snabre P, Pouligny B (2005). The flow of a very concentrated slurry in a parallel-plate device: Influence of gravity. Phys Fluids 17:073303

Leron RB, Soriano AN, Li MH (2012). Densities and refractive indices of the deep eutectic solvents (choline chloride + ethylene glycol or glycerol) and their aqueous mixturesat the temperature ranging from 298.15 to 333.15 K. J Taiwan Inst Chem Eng 43:551–557

Li C (2009). Effect of Corrosion Inhibitor on Water Wetting and Carbon Dioxide Corrosion In Oil-Water Two-Phase Flow. PhD Doctoral, Ohio University

Li Y, Li, SN, Zhai Q, Marcilla A, Jiang Y, Hu M (2013). Solubility, density, refractive index, and viscosity for the polyhydric alcohol + CsBr + H2O ternary systems at different temperatures. J Chem Eng Data 58:1577–1588

Lichtenecker K (1926). Die dielektrizitätskonstante natürlicher und künstlicher mischkörper. Phys Z 27:115–158

Lichtenecker K, Rother K (1931). Die Herleitung des logarithmischen mischungsgesetzes aus allgemeinen prinzipien der stationären strömung. Phys Z 32:255–260

Liu CH, Nouri JM, Whitelaw JH, Tse DGN (1989). Particle velocities in a swirling, confined flow. Combust Sci Technol 68:131–145

Liu CH, Vafidis C, Whitelaw JH, Margary R (1990). Flow in the coolant passages of an internal combustion engine cylinder head. Exp Fluids 10:50–54

Liu L (2005). Optical and computational studies of liquid-liquid flows. PhD thesis, Imperial College London, London, UK

Liu L, Matar OK, Hewitt GF (2006a). Laser-induced fluorescence (LIF) studies of liquid-liquid flows. Part II: Flow pattern transitions at low liquid velocities in downwards flow. Chem Eng Sci 61:4022–4026

Liu L, Matar OK, Lawrence CJ, Hewitt GF (2006b). Laser-induced fluorescence (LIF) studies of liquid-liquid flows. Part I: Flow structures and phase inversion. Chem Eng Sci 61:4007–4021

Liu S, Hrymak AN, Wood PE (2005). Drop Breakup in an SMX Static Mixer in Laminar Flow. Can J Chem Eng 83:793–807

Lobry E, Theron F, Gourdon C, Le Sauze N, Xuereb C, Lasuye T (2011). Turbulent liquid-liquid dispersion in SMV static mixer at high dispersed phase concentration. Cheml Eng Sci 66:5762–5774

Longmire EK, Bordoloi AD (2015). Drop penetration through a constriction: Effect of surrounding fluid. Procedia IUTAM, 15:194–200

Longmire EK, Norman TL, Gefroh DL (2001). Dynamics of pinch-off in liquid/liquid jets with surface tension. Int J Multiph Flow 27:1735–1752

Lopez-Gejo JL, Kunjappu J, Turro NJ, Conley WE (2007). Amplification of the index of refraction of aqueous immersion fluids with crown ethers. J Micro Nanolithogr MEMS MOEMS 6:013002

Lowe ML, Kutt PH (1992). Refraction through cylindrical tubes. Exp Fluids 13:315–320

Lovick J, Angeli P (2004). Experimental studies on the dual continuous flow pattern in oil–water flows. Int J Multiph Flow 30:139–157

Lorentz HA (1906) Theory of electrons and its appications to the phenomena of light amd radint heat. GE Stechert & Co, New York, NY, USA

Lyon MK, Leal LG (1998a). An experimental study of the motion of concentrated suspensions in two-dimensional channel flow. Part 1. Monodisperse systems. J Fluid Mech 363:25–56

Lyon MK, Leal LG (1998b). An experimental study of the motion of concentrated suspensions in two-dimensional channel flow. Part 2. Bidisperse systems. J Fluid Mech 363:57–77

Majumdar A, Graham AL, Roco MC, Stroeve P (1987). Experimental study on solid particle dynamics in shear flow. Powder Technol 49:217–226

Malitson IH (1963). A redetermination of some optical properties of calcium fluoride. Appl Opt 2:1103

Mandava S, Kolla N, Chagarlamudi K, Anne SB, Abbineni R (2015). Refractive properties for binary mixtures containing DEC + o-xylene or m-xylene or p-xylene. Int J Innov Res Sci Eng Technol 4:12598–12612

Markides CN, Mathie R, Charogiannis A (2016). An experimental study of spatiotemporally resolved heat transfer in thin liquid-film flows falling over and inclined heated foil. Int J Heat and Mass Transf 93:872–888

Maru W, Lakshmanan S (2018) Automatic pipeline sampling in flow measurement for custody transfer application "The Elephant in the room". 36th North Sea flow measurement workshop 2018, 22nd–24th October 2018, Aberdeen, Scotland

Maru W, Rathwell G, Sherman RE (2018) Water-in-oil analysis uses controlled vortices. Control Mag

Maru W, Waters JR (2018) Smart entrainment and atomisation mixing system. US2018/0290115A1

Maru W, Lakshmanan S, Singh N, Thomas A (2019) Oil-Water Flow Measurement for Custody Transfer Applications. Flowmek 2019 18th international flow measurement conference, 26th–28th June 2019, Lisbon, Portugal

Maruyama T, Susuki S, Mizushina T (1981). Pipeline mixing between two fluid streams meeting at a T-Junction. I cheml eng 21:205–212

Mathews IM (1914) Refractive index and density. J Franklin I 177(6):673-686

Mathie R, Nakamura H, Markides CN (2013) Heat transfer augmentation in unsteady conjugate thermal systems – Part II: Applications. Int J Heat and Mass Transf 56:819–833

McCafferty E, Wightman JP (1999). Determination of the acid-base properties of metal oxide films and of polymers by contact angle measurements. J Adhes Sci Technol 13:1415–1436

McDougall TJ (1979). On the elimination of refractive-index variations in turbulent density-stratified liquid flows. J Fluid Mech 93:83–96

Mcilroy HM, Mceligot DM, Pink RJ (2010). Measurement of turbulent flow phenomena for the lower plenum of a prismatic gas-cooled reactor. Nucl Eng Des 240:416–428

Mehra R (2003). Application of refractive index mixing rules in binary systems of hexadecane and heptadecane withn-alkanols at different temperatures. J Chem Sci 115:147–154

Mehta M, Kadambi JR, Sastry S, Sankovic JM, Wernet MP, Addie G, Visintainer R (2007). Particle velocities in the rotating impeller of a slurry pump. 5th Joint ASME/JSME Fluids Engineering Conference, San Diego, California, USA

Merrington AC, Richardson EG (1947). The break-up of liquid jets. Proc Phys Soc 59:1–13

Mier-Torrecilla M, Geyer A, Phillips JC, Idelsohn SR, Oñate E (2012). Numerical simulations of negatively buoyant jets in an immiscible fluid using the Particle Finite Element Method. Int J Num Meth Fluid 69:1016–1030

Middleman S (1974). Drop Size Distributions Produced by Turbulent Pipe Flow of Immiscible Fluids through a Static Mixer. Ind Eng Chem Proc Des Dev 13:78–83

Mikami F, Chen B, Nishikawa N (2001). Visualization and PTV study of natural convection in particle suspensions. Simultaneous measurements of velocity, temperature and interface between particle-free fluid and suspension. JSME Int J Ser B 44:30–37

Miller P, Danielson K, Moody G, Slifka A, Drexler E, Hertzberg J (2006). Matching index of refraction using a diethyl phthalate/ethanol solution for in vitro cardiovascular models. Exp Fluids 41:375–381

Mohamed-Kassim Z, Longmire EK (2003). Drop impact on a liquid–liquid interface. Phys Fluids 15:3263–3273

Mohamed-Kassim Z, Longmire EK (2004). Drop coalescence through a liquid/liquid interface. Phys Fluids 16:2170–2181

Mohajer (2013). Apparatus and method for maintiaing consistent fluid velocity and homgeneity in a pipeline. US20130036800A1

Mondy LA, Graham AL, Majumdar A, Bryant LE (1986). Techniques of measuring particle motions in concentrated suspensions. Int J Multiph Flow 12:497–502

Moreira R, Chenlo F, Legall D (2009). Kinematic viscosity and refractive index of aqueous solutions of ethanol and glycerol. Ind Eng Chem Res 48:2157–2161

Morgan RG (2012). Studied of Liqui-Liquid Two-Phase Flows using Laser-Based Methods. PhD Doctoral thesis, Imperial College London

Morgan RG, Markides CN, Hale CP, Hewitt GF (2012). Horizontal liquid-liquid flow characteristics at low superficial velocities using laser-induced fluorescence. Int J Multiph Flow 43:101–117

Morgan RG, Markides CN, Zadrazil I, Hewitt GF (2013). Characteristics of horizontal liquid-liquid flows in a circular pipe using simultaneous high-speed laser-induced fluorescence and particle velocimetry. Int J Multiph Flow 49:99–118

Morgan RG, Ibarra R, Zadrazil I, Matar OK, Hewitt GF (2016). On the role of buoyancy-driven instabilities in horizontal liquid-liquid flow. Int J Multiph Flow, accepted, in press

Moroni M, Cushman JH (2001). Three-dimensional particle tracking velocimetry studies of the transition from pore dispersion to Fickian dispersion for homogeneous porous media. Water Resour Res 37:873–884

Morsi SA, Alexander AJ (1972). An investigation of particle trajectories in two-phase flow systems. J Fluid Mech 55:193-208

Najjari MR, Hinke JA, Bulusu KV, Plesniak MW (2016). On the rheology of refractive-index-matched, non-Newtonian blood-analog fluids for PIV experiments. Exp Fluids 57:96

Narrow TL, Yoda M, Abdel-Khalik SI (2000). A simple model for the refractive index of sodium iodide aqueous solutions. Exp Fluids 28:282–283

NEL 1980. ENER/11 Tests on a jet flow-conditioning system. In: DIRECTORATE, D. O. E. S. P. E. (ed.). National Engineering Laboratory Flow Measurement Divison

Newton I (1704). Opticks: Or, a treatise of the reflexions, refractions, inflexions and colours of light. Willliam Innys, London, UK

Ng KM, Davis HT, Scriven LE (1978). Visualization of blob mechanics in flow through porous media. Chem Eng Sci 33:1009–1017

Ng TS (2002). Interfacial structure of stratified pipe flow, Chemical Engineering and Chemical Technology, Imperial College London. PhD Thesis.

Nguyen TT, Biadillah DY, Mongrain R, Brunette J, Tardif JC, Bertrand OF (2004). A method for matching the refractive index and kinematic viscosity of a blood

analog for flow visualization in hydraulic cardiovascular models. J Biomech Eng 126:529–535

Ni WJ, Capart H (2015). Cross-sectional imaging of refractive-index-matched liquid-granular flows. Exp Fluids 56:163

Nicolai H, Herzhaft B, Hinch EJ, Oger L, Guazzelli E (1995). Particle velocity fluctuations and hydrodynamic self-diffusion of sedimenting non-Brownian spheres. Phys Fluids 7:12–23

Nicolai HLN, Guazzelli E (1995). Effect of the vessel size on the hydrodynamic diffusion of sedimenting spheres. Phys Fluids 7:3–5

Nicolai HLN, Peysson Y, Guazzelli EL (1996). Velocity fluctuations of a heavy sphere falling through a sedimenting suspension. Phys Fluids 8:855–862

Ninomiya N, Yasuda K (2006). Visualization and PIV measurement of the flow around and inside of a falling droplet. J Vis 9:257–264

Northrup MA, Kulp TJ, Angel SM (1991). Fluorescent particle image velocimetry: Application to flow measurement in refractive index-matched porous media. Appl Opt 30:3034–3040

Nouri JM, Whitelaw JH, Yianneskis M (1987). Particle motion and turbulence in dense two-phase flows. Int J Multiph Flow 13:729–739

Ortiz-Dueñas C, Kim J, Longmire EK (2010). Investigation of liquid–liquid drop coalescence using tomographic PIV. Exp Fluids 49:111–129

Ottewill RH, Williams NSJ (1987). Study of particle motion in concentrated dispersions by tracer diffusion. Nat 325:232–234

Oster G (1948). The scattering of light and its applications to chemistry. Chem Rev 43:319–365

Ovdat H, Berkowitz B (2006). Pore-scale study of drainage displacement under combined capillary and gravity effects in index-matched porous media. Water Resour Res 42:W06411

Overmars EFJ, Warncke NGW, Poelma C, Westerweel J (2010). Bias errors in PIV: the pixel locking effect revisited. 15th Int Symp on Applications of Laser Techniques to Fluid Mechanics 5th–8th July 2010, Lisbon, Portugal

Pacák P, Kodejš Z (1988). Molar volumes and refractivities of highly concentrated solutions of ammonium and potassium thiocyanates in water and dimethylsulphoxide. Can J Chem 66:2244–2249

Pai MG, Bermejo-Moreno I, Desjardins O, Pitsch H (2009). Role of Weber number in primary breakup of turbulent liquid jets in crossflow. Center for Turbulence Research Annual Research Briefs 2009

Paul EL, Atiemo-Obeng VA, Kresta SM (2004). Handbook of industrial mixing: science and practice, Hoboken, N.J., Wiley-Interscience

Park JT, Mannheimer RJ, Grimley TA, Morrow TB (1989). Pipe flow measurements of a transparent non-Newtonian slurry. J Fluids Eng 111:331–336

Parker J, Merati P (1996). An investigation of turbulent Taylor-Couette flow using laser Doppler velocimetry in a refractive index matched facility. J Fluids Eng 118:810–818

Pashtrapanska M, Jovanović J, Lienhart H, Durst F (2006). Turbulence measurements in a swirling pipe flow. Exp Fluids 41:813–827

Patil VA, Liburdy JA (2010). Refractive index matching with distortion measurements in a bed of irregularly packed spheres. In: Proceedings of ASME 3rd Joint US-European Fluids Engineering Summer Meeting and 8th International Conference on Nanochannels, Microchannels, and Minichannels, Montreal, Canada

Patil VA, Liburdy JA (2012). Optical measurement uncertainties due to refractive index mismatch for flow in porous media. Exp Fluids 53:1453–1468

Patil VA, Liburdy JA (2013). Turbulent flow characteristics in a randomly packed porous bed based on particle image velocimetry measurements. Phys Fluids 25:043304

Peerless SJ, Jiskoot MA (1978). A unique pipeline conditioning system to evenly distribute and finely disperse non-homogeneous pipeline contents (F.I. Crude oil) prior to extraction to ensure true representatively—interim report Sept '78. Imperial College London

Peerless SJ, Walker SP (1985). Theoretical analysis and modelling of jet mixers. Imperial College London. Unpublished

Perktold K, Hofer M, Rappitsch G, Loew M, Kuban BD, Friedman MH (1997). Validated computation of physiologic flow in a realistic coronary artery branch. J Biomech 31:217–228

Peterson DA, Tankin R, Bankoff SG (1987). Bubble behavior in a three-phase fluidized bed. Int J Multiph Flow 13:477–491

Peurrung LM, Rashidi M, Kulp TJ (1995). Measurement of porous medium velocity fields and their volumetric averaging characteristics using particle tracking velocimetry. Chem Eng Sci 50:2243–2253

Pielhop K, Klaas M, Schröder W (2012). Analysis of the unsteady flow in an elastic stenotic vessel. Eur J Mech B Fluids 35:102–110

Polling BE, Prausnitz JM, O'Connell JP (2001). The properties of gases and liquids. McGraw-Hill Inc, New York, NY, USA

Pouplin A, Masbernat O, Décarre S, Liné A (2011). Wall friction and effective viscosity of a homogeneous dispersed liquid-liquid flow in a horizontal pipe. AIChE J 57:1119–1131

Potten GA, Wright SF (2014) Methods of Determining and Verifying Fiscal Sampling System Uncertainty by Analysing 25 Years of Real Field Proving Data and Laboratory Tests Compared with International Acceptance Criteria. 32nd North Sea flow measurement workshop 2014, 21st–24th October 2014, Aberdeen, Scotland

Prasad V, Brown K, Tian Q (1991). Flow visualization and heat transfer experiments in fluid-superposed packed beds heated from below. Exp Therm Fluid Sci 4:12–24

Rama Rao NV, Baird MHI, Hrymak AN, Wood PE (2007). Dispersion of high-viscosity liquid-liquid systems by flow through SMX static mixer elements. Chem Eng Sci 62:6885–6896

Rashidi M, Peurrung L, Tompson AFB, Kulp TJ (1996). Experimental analysis of pore-scale flow and transport in porous media. Adv Water Resour 19:163–180

Ravelet F, Delfos R, Westerweel J (2007). Experimental studies of liquid-liquid dispersion in a turbulent shear flow. 11th EUROMECH European Turbulence Conference, Porto, Portugal

Reddy RK, Sathe MJ, Joshi JB, Nandakumar K, Evans GM (2013). Recent developments in experimental (PIV) and numerical (DNS) investigation of solid-liquid fluidized beds. Chem Eng Sci 92:1–12

Reis JC, Lampreia IM, Santos AF, Moita ML, Douheret G (2010). Refractive index of liquid mixtures: theory and experiment. Chemphyschem 11:3722–3733

Richards JR, Scheele GF (1985). Measurement of laminar jet velocity distributions in liquid-liquid systems using flash photolysis. Chem Eng Commun 36:73–92

Saarinen V, Karesoja M, Kallio T, Paronen M, Kontturi K (2006). Characterization of the novel ETFE-based membrane. J Membr Sci 280:20–28

Saksena R, Christensen KT, Pearlstein AJ (2015). Surrogate immiscible liquid pairs with refractive indexes matchable over a wide range of density and viscosity ratios. Phys Fluids 27:087103

Saleh S, Thovert JF, Adler PM (1992). Measurement of two-dimensional velocity fields in porous media by particle image displacement velocimetry. Exp Fluids 12:210–212

Satake SI, Aoyagi Y, Unno N, Yuki K, Seki Y, Enoeda M (2015). Three-dimensional flow measurement of a water flow in a sphere-packed pipe by digital holographic PTV. Fusion Eng Des 98–99:1864–1867

Schäfer M, Höfken M, Durst F (1997). Detailed LDV measurements for visualization of the flow field within a stirred-tank reactor equipped with a rushton turbine. Chem Eng Res Des 75:729–736

Schmidt FW, Kulakowski B, Wang DF (1984). Evaluation of the effect of variable refraction index on the path of a laser beam. Exp Fluids 2:153–158

Schmitt GA, Stradmann N (1998). Wettability of Steel Surfaces at CO2 Corrosion Conditions. I. Effect of Surface Active Compounds in Aqueous and Hydrocarbon Media. CORROSION 98. San Diego, California: NACE International

Schröder A, Schanz D, Geislet R, Gesemann S, Willert C (2015). Near-wall turbulence characterization using 4D-PTV Shake-The-Box. 11th international symposium of particle image velocimetry. 14th–16th September 2015, Santa Barbara, California, United States.

Scholz P, Reuter I, Heitmann D (2012). PIV measurements of the flow through an intake port using refractive index matching. 16th Int Symp on Applications of Laser Techniques to Fluid Mechanics 9th–12th July 2012, Lisbon, Portugal

Segev A (1984). Mechanistic model for estimating water dispersion in crude oil flow. (1984) Annual Meeting—American Institute of Chemical Engineers. San Francisco, CA, USA

Sembira AN, Merchuk JC, Wolf D (1986). Characteristics of a motionless mixer for dispersion of immiscible fluids—I. A modified electroresistivity probe technique. Chem Eng Sci 41:445–455

Sembira AN, Merchuk JC, Wolf D (1988). Characteristics of a motionless mixer for dispersion of immiscible fluids—III. Dynamic behaviour of the average drop size and dispersed phase hold-up. Chem Eng Sci 43:373–377

Sharma S, Patel PB, Patel RS, Vora JJ (2007). Density and comparative refractive index study on mixing properties of binary liquid mixtures of eucalyptol with hydrocarbons at 303.15, 308.15 and 313.15 K. E J Chem 4:343–349

Shauly A, Averbakh A, Nir A, Semiat R (1997). Slow viscous flows of highly concentrated suspensions – Part II: Particle migration, velocity and concentration profiles in rectangular ducts. Int J Multiph Flow 23:613–629

Shuib AS, Hoskins PR, Easson WJ (2010). Flow regime characterization in a diseased artery model. World Acad Sci Eng Technol 4:87–91

Sirignano WA, Mehring C (2000). Review of theory of distortion and disintegration of liquid streams. Prog Energy Combust Sci 26:609–655

Slater BG (1983) Mixing device. GB 2129696A

Smedley G, Coles D (1990). Some transparent immiscible liquid pairs. J Colloid Interface Sci 138:42–60

Soleimani A (1999). Phase Distribution and Associated Phenomena in Oil-Water Flows in Horizontal Tubes. PhD Doctoral, Imperial College London

Soranna F, Chow YC, Uzol O, Katz J (2008). Turbulence within a turbomachine rotor wake subject to nonuniform contraction. AIAA J 46:2687–2702

Stephenson JL, Stewart WE (1986). Optical measurements of porosity and fluid motion in packed beds. Chem Eng Sci 41:2161–2170

Stöhr M, Roth K, Jähne B (2003). Measurement of 3D pore-scale flow in index-matched porous media. Exp Fluids 35:159–166

Stoots C, Becker S, Condie K, Durst F, Mceligot D (2001). A large-scale matched index of refraction flow facility for LDA studies around complex geometries. Exp Fluids 30:391–398

Sturges HA (1926). The choice of a class interval. J Am Stat Assoc. 21 (153):65–66

Sun JZ, Erickson MCE, Parr JW (2005). Refractive index matching and clear emulsions. J Cosmet Sci 56:253–265

Svensson FJE, Rasmuson A (2004). LDA-measurements in a stirred tank with a liquid-liquid system at high volume percentage dispersed phase. Chem Eng Technol 27:335–339

Svensson FJE, Rasmuson A (2006). PIV measurements in a liquid-liquid system at volume percentages up to 10% dispersed phase. Exp Fluids 41:917–931

Tabrizi SS (2012). Effect of Mechanical Abrasion on Oil/water Contact Angle in Metals. MSc Masters, University of Wisconsin-Milwaukee

Taitel Y, Dukler AE (1976). A theoretical approach to the Lockhart–Martinelli correlation for stratified flows. Int J Multiph Flow 2:591–595

Takamura K, Fischer H, Morrow NR (2012). Physical properties of aqueous glycerol solutions. J Petrol Sci Eng 98–99:50–60

Tang X, Richter S, Nesic S (2009). Study of wettability of different mild steel surfaces. Ohio University.

Tasić AZ, Djordjevic BD, Grozdanic, DK, Radojkovic N (1992). Use of mixing rules in predicting refractive indexes and specific refractivities for some binary liquid mixtures. J Chem Eng Data 37:310–313

Thakur RK, Vial C, Nigam KDP, Nauman EB, Djelveh G (2003). Static Mixers in the Process Industries—A Review. Chem Eng Res Des 81:787–826

Theron F, Sauze NL (2011). Comparison between three static mixers for emulsification in turbulent flow. Int J Multiph Flow 37:488–500

Theron FL, Le Sauze N, Ricard A (2010). Turbulent Liquid-Liquid Dispersion in Sulzer SMX Mixer. Ind Eng Chem Res 49:623–632

Thormahlen I, Straub J, Grigull U (1985). Refractive index of water and its dependence on wavelength, temperature and density. J Phys Chem Ref Data 14:933–945

Tidhar M, Merchuk JC, Sembira AN, Wolf D (1986). Characteristics of a motionless mixer for dispersion of immiscible fluids—II. Phase inversion of liquid-liquid systems. Chem Eng Sci 41:457–462

Thielicke W, Stamhuis E (2014) PIVlab-towards user-friendly, affordable and accurate digital particle image velocimetry in MATLAB. J Open Res Softw 2(1):e30

Timberlake BD, Morris JF (2002). Concentration band dynamics in free-surface Couette flow of a suspension. Phys Fluids 14:1580–1589

Tindal MJ, Cheung RS, Yianneskis M (1988). Velocity characteristics of steady flows through engine inlet ports and cylinders. SAE Tech Pap Ser 880383:1–19

Tomac MN, Gregory JW (2014). Internal jet interactions in a fluidic oscillator at low flow rate. Exp Fluids 55:1730

Trallero JL (1995). Oil-Water Patterns in Horizontal Pipes. PhD Doctoral, University Tulsa.

Trallero JL, Sarica C, Brill JP (1997). A Study of Oil-Water Flow Patterns in Horizontal Pipes. SPE Prod Facil 12:165–172

Tropea C, Yarin AL, Foss JF (2007). Springer handbook of experimental fluid mechanics. Springer, Berlin

Transportation Research Board (2004). Transmission Pipelines and Land Use: A Risk-Informed Approach -- Special Report 281. Washington, DC: The National Academies Press. https://doi.org/10.17226/11046.

Unno N, Nakata S, Satake S-I, Taniguchi J (2016). Three-dimensional particle tracking around microstructures in water via total internal reflection fluorescence microscopy and refractive-index-matching method. Exp Fluids 57:120

Uzol O, Brzozowski D, Chow YC, Katz J, Meneveau C (2007). A database of PIV measurements within a turbomachinery stage and sample comparisons with unsteady RANS. J Turbul 8:N10

Uzol O, Chow YC, Katz J, Meneveau C (2002). Unobstructed particle image velocimetry measurements within an axial turbo-pump using liquid and blades with matched refractive indices. Exp Fluids 33:909–919

Varty RL (1984). A new system for index-matched laser-anemometer measurements. J Phys E Sci Instrum 17:1124–1126

Vazquez G, Alvarez E, Navaza JM (1995). Surface tension of alcohol water + water from 20 to 50 °C. J Chem Eng Data 40:611–614

Verloop EM, Verloop PC, (2010a) A device for homogenizing fluids. NL2001803C2

Verloop EM, Verloop PC, (2010b) Device and method for homogenizing fluids. EP2145676A1

Verloop EM, Verloop PC, (2012) A method and system for at least temporarily homogenizing a fluid flow in a pipeline. EP2447698B1

Verloop E, Verloop P, Dods J, Sveinsvoll E, Øverbø S (2019) Evaluation of new mixing method for pipeline sampling at NEL flow facility. 37th North Sea flow measurement workshop 2019, 22nd–25th October 2019, Tønsberg, Norway.

Voulgaropoulos V, Angeli P (2017). Optical measurements in evolving dispersed pipe flows. Exp Fluids 58.

Voulgaropoulos V, Jamshidi R, Mazzei L, Angeli P (2019). Experimental and numerical studies on the flow characteristics and separation properties of dispersed liquid-liquid flows. Phys Fluids 31:073304

Walker JD, Tiederman WG, Phillips WM (1989). Effect of tilting disk, heart valve orientation on flow through a curved aortic model. J Biomech Eng 111:228

Wang DC, Khalili A (2002). Flow visualization and quantitative measurements inside porous media by particle image velocimetry. In: Proceedings of SPIE optical technology and image processing for fluids and solids diagnostics, Beijing, China

Wang P, Song C, Briscoe C, Makse HA (2008). Particle dynamics and effective temperature of jammed granular matter in a slowly sheared three-dimensional Couette cell. Phys Rev E 77:061309

Weitzman JS, Samuel LC, Craig AE, Zeller RB, Monismith SG, Koseff JR (2014). On the use of refractive-index-matched hydrogel for fluid velocity measurement within and around geometrically complex solid obstructions. Exp Fluids 55:1862

Wiederseiner S, Andreini N, Epely-Chauvin G, Ancey C (2011). Refractive-index and density matching in concentrated particle suspensions: A review. Exp Fluids 50:1183–1206

Wiener O (1910). Zur theorie der refraktionskonstanten. Ber Verh Koniglich Saechs Ges Wiss Leipzig, Math-Phys Kl 62:256–277

Wildman DJ, Ekmann JM, Kadambi JR, Chen RC (1992). Study of the flow properties of slurries using the refractive index matching technique LDV. Powder Technol 73:211–218

Wright SF, Potten GA, Moreau JFA (2020). Real-time Composition Measurement for Fiscal, Allocation and Process Optimization. 2020 Offshore Technology Conference. May 2020, Houston, Texas, USA. SPE OTC 30727-MS.

Wright SF, Zadrazil I, Markides CN (2017). A review of solid-fluid selection options for optical-based measurements in single-phase liquid, two-phase liquid-liquid and multiphase solid-liquid flows. Exp Fluids 58

Wright SJ (1977). Effects of ambient crossflows and density stratification on the characteristic behavior of round turbulent buoyant jets.

Wright SJ (1984). Buoyant Jets in Density-Stratified Crossflow. J Hydraul Eng 110:643–656

Wu H, Miorini RL, Tan D, Katz J (2012). Turbulence within the tip-leakage vortex of an axial waterjet pump. AIAA J 50:2574–2587

Wu Y, Liu S, Yuan H, Shao J (2011). PIV measurement on internal instantaneous flows of a centrifugal pump. Sci China Technol Sci 54:270–276

Wu Y, Yuan H, Shao J, Liu S (2009). Experimental study on internal flow of a mini centrifugal pump by PIV measurement. Int J Fluid Mach Syst 2:121–126

Yagi T, Sato A, Shinke M, Takahashi S, Tobe Y, Takao H, Murayama Y, Umezu M (2013). Experimental insights into flow impingement in cerebral aneurysm by stereoscopic particle image velocimetry: Transition from a laminar regime. J Royal Soc Interface 10:20121031

Yamamoto T, Kawasaki H, Kumazawa H (2007). Relationship between the Dispersed Droplet Diameter and the Mean Power Input for Emulsification in Three Different Types of Motionless Mixers. J Chem Eng JPN 40:673–678

Yang WC, Hwang RR (2001). Vertical Buoyant Jets in a Linearly Stratified ambient cross-stream. Envir Fluid Mech 1:235–256

Yarlagadda AP, Yoganathan AP (1989). Experimental studies of model porous media fluid dynamics. Exp Fluids 8:59–71

Yousif MY, Holdsworth DW, Poepping TL (2010). A blood-mimicking fluid for particle image velocimetry with silicone vascular models. Exp Fluids 50:769–774

Yuan HJ, Shao J, Wu YL, Liu SH (2012). Experiment of a centrifugal pump during changing speed operation. IOP Conf Ser Earth Environ Sci 15:62–65

Yuki K, Hasegawa S, Sato T, Hashizume H, Aizawa K, Yamano H (2011). Matched refractive-index PIV visualization of complex flow structure in a three-dimentionally connected dual elbow. Nucl Eng Des 241:4544–4550

Yuki K, Okumura M, Hashizume H, Toda S, Morley NB, Sagara A (2008). Flow visualization and heat transfer characteristics for sphere-packed pipes. J Thermophys Heat Transf 22:632–648

Zachos A, Kaiser M, Merzkirch W (1996). PIV measurements in multiphase flow with nominally high concentration of the solid phase. Exp Fluids 20:229–231

Zadrazil I, Bismarck A, Hewitt GF, Markides CN (2012). Shear layers in the turbulent pipe flow of drag reducing polymer solutions. Chem Eng Sci 72:142–154

Zadrazil I, Markides CN (2014). An experimental characterization of liquid films in downwards co-current gas-liquid annular flow by particle image and tracking velocimetry. Int J Multiph Flow 67:42–53

Zadrazil I, Matar OK, Markides CN (2014). An experimental characterization of downwards gas-liquid annular flow by laser-induced fluorescence: Flow regimes and film statistics. Int J Multiph Flow 60:87–102

Zerai B, Saylor BZ, Kadambi JR, Oliver MJ, Mazaheri AR, Ahmadi G, Bromhal GS, Smith DH (2005). Flow characterization through a network cell using particle image velocimetry. Transp Porous Medium 60:159–181

Zhang J, Li J, Han Y (2004). Superhydrophobic PTFE surfaces by extension. Macromol Rapid Commun 25:1105–1108

Zhu W, Knapp Y, Deplano V (2016). Low hazard refractive index and density-matched fluid for quantitative imaging of concentrated suspensions of particles. Exp Fluids 57:68

Zisselmar R, Molerus O (1979). Investigation of solid-liquid pipe flow with regard to turbulence modification. Chem Eng J 18:233–239

Appendix A:

Refractive index matching systems

This appendix summarises solid-liquid flow systems that have previously been utilized in RIM experiments, i.e., matching the RI of a particular solid with either a pure liquid, a mixture of liquids or additive solutions. Solid-liquid systems can be understood here as a suspension of particles in a liquid continuum (e.g., the flow of a sand slurry) or a single-phase flow (e.g., an external flow over a solid obstacle or an internal flow within a pipe or conduit).

A.1 Common plastics

Plastics are a common material for conducting RIM experiments. Many plastics are transparent or translucent when in the amorphous state, while the transparency of plastics in the crystalline state can sometimes be improved through transitioning to a more transparent amorphous state through heating above the melting temperature and quenching (Wiederseiner et al., 2011). Plastics are also readily available, affordable and can be easily manufactured in many different shapes and sizes. Consequently, they are preferentially chosen for the study of flows in complex geometries, e.g., biological systems, moving machinery, etc. (Soranna et al., 2008; Bale-Glickman et al., 2003).

Two manufacturing processes are commonly used for the production of plastic components (e.g., test-sections) that are commonly employed in scientific studies, namely extrusion and casting; more recently, rapid prototyping and 3-D printing processes have allowed an even greater range of components to be made from suitable plastics. Depending on the process, plastic components often bear different physical properties, despite their identical chemical composition. Plastic pipes are frequently produced via extrusion processes, which can result in a ribbed-effect on the pipe walls and a variability (and asymmetry) in the pipe diameter. Nevertheless, plastic pipes typically have a roughness of the order of ≈ 1 µm, which is much

smoother than steel pipes frequently installed in industrial (e.g., the oil-and-gas) systems that have roughness's in the order of 10s of μm (Hydraulic-Institute, 1979).

Plastics vary widely in chemical composition and, as a result, important properties like air-water-solid contact angles can span a wide range of values. For example, Nylon 6 has $\theta = 70°$ (Fort, 1964), while the highly hydrophobic fluorocarbon polytetrafluoroethylene (PTFE) has $\theta = 118°$ (Zhang et al., 2004).

Plastics also vary in chemical resistance, so compatibility with contacting fluids should be checked carefully since any incompatibility can lead to damage to the test-section or other components in the flow loop. Dijksman et al. (2012) found that poly(methyl methacrylate) (PMMA) can develop micro-cracks when washed and dried after being in contact with Triton X100. Nevertheless, the chemical resistance of plastics can in some cases be improved. In the case of micro-cracks in PMMA, this can be done by reducing internal stresses through annealing after cutting (Hendriks and Aviram, 1982). Further chemical compatibility issues encountered in the literature are discussed in the corresponding material section. Apart from chemical damage, physical damage can also occur from lasers, and this can occur at relatively low laser powers in some plastics, such as polycarbonate and PMMA (e.g., compared to glass, Hirsch et al. (2015)). While this is mainly a consideration when using high-powered lasers, it should still be reviewed for a given experiment, especially if high luminosities are required.

This section focuses on solid-liquid matched RI systems, where the solid phase consists of a plastic material. The following plastics are considered, in order of increasing RI: fluorinated ethylene propylene (FEP), poly(vinyl acetate) (PVA), PMMA, nylon and polystyrene (PS). In addition, previously unused, but common, plastics that could be utilized in future RIM experiments are included, namely: tetrafluoroethylene-hexafluoropropylene-vinylidene fluoride (THV), ethylene-tetrafluoroethylene (ETFE) and polyvinylidene difluoride (PVDF). Collated data of a number of possible solid-liquid RIM combinations, together with the known density and viscosity values of pure or fluid mixtures, can be found in Table A.1.

Table A.1 List of plastics and polymer-based refractive index-matched systems including FEP, THV, ETFE, PVDF, PVA, PMMA, Nylon and PS.

Solid	n_S	Density [kg/m³]	Liquid	n_L	Density [kg/m³]	Dynamic viscosity* [mPa s]	Phase	References
FEP	1.340	2150	water	1.330	998	1 @ 20 °C	Aq.	Hewitt et al. (1990) Amini and Hassan (2009) Amini and Hassan (2012) Hassan and Dominguez-Ontiveros (2008) Zadrazil et al. (2014) Zadrazil and Markides (2014) Satake et al. (2015)
THV	1.355	1970						Drobny (2006)
ETFE	1.403	1710						Ebnesajjad and Khaladkar (2005)
PVDF	1.420	1780						Ebnesajjad and Khaladkar (2005)
PVA	1.466 – 1471	1190	Ucon oil 50-HB-5100 (polyglycol oil) 4 vol.% tetrabromohethane	1.467	1139	2460	Org.	Karnis et al. (1966)
			cis-decalin trans-decalin	1.471			Org.	Ottewill and Williams (1987)
PMMA	1.486 – 1.491	1180	Dow Corning 550 fluid (silicone oil) Dow Corning 200 fluid (silicone oil)				Org.	Johnston et al. (1975)
			84 wt.% Dow Corning 550 (silicone oil) 16 wt.% Dow Corning 556 (silicone oil)	1.490	1050	99.8	Org.	Stöhr et al. (2003)
			73 wt.% Dow Corning 550 (silicone oil) 27 wt.% Union Carbide L42 (silicone oil)	1.491	1060		Org.	Northrup et al. (1991)
			83 wt.% Dow Corning 550 (silicone oil) 17 wt.% Dow Corning 556 (silicone oil) phenyl-tris(trimethylsilyloxy)silane	1.489 – 1.491	887	53.2	Org.	Peurrung et al. (1995) Rashidi et al. (1996) Braun et al. (1991)
			Dow Corning 550 (silicone oil)					Ng et al. (1978)
			silicone fluid	1.490	988	40.35 @ 25 °C	Org.	Prasad et al. (1991)
			sodium salicylate water	1.490			Aq.	Prasad et al. (1991)
			69.2 vol.% turpentine oil 30.8 vol.% tetralin	1.489	894	1.53	Org.	Tindal et al. (1988)
			68.2 vol.% turpentine oil 31.8 vol.% tetralin	1.489	894	1.46	Org.	Liu et al. (1989) Liu et al. (1990) Nouri et al. (1987)
			62.9 wt.% turpentine oil 37.1 wt.% tetralin	1.491	890	1.47	Org.	Kapoor and Acrivos (2006)
			2,2 thiodiethanol phosphate-buffered saline glycerol	1.489				Zhu et al. (2016)

Solid	n_S	Density [kg/m³]	Liquid	n_L	Density [kg/m³]	Dynamic viscosity* [mPa s]	Phase	References
			para-cymeme (p-cymeme)	1.489 – 1.490	853 – 860	0.5 – 1.195 0.741 @ 25 °C	Org.	Frish and Webb (1981) Haam et al. (2000) Haam and Brodkey (2000) Hassan and Dominguez-Ontiveros (2008) Huang et al. (2008) Huang et al. (2009a) Huang et al. (2009b) Amini and Hassan (2012) Ni and Capart (2015)
			98.4% – 99.2% p-cymene 0.8% – 1.6% cinnamaldehyde					Fort et al. (2015)
			Ethyl and benzyl alcohol mixture					Hassan and Dominguez-Ontiveros (2008)
			dibutylphthalate	1.490	1046 – 1118	15 – 20.71 16.583 @ 25 °C	Org.	Ng et al. (1978) Frish and Webb (1981) Hendriks and Aviram (1982) Aziza and Wong (2003) Ovdat and Berkowitz (2006) Amini and Hassan (2012)
			14.07 wt.% 1,1,2,2 tetrabromoethane 35.66 wt.% polyalkylene glycol oil (UCON H-90000) 50.27 wt.% Triton X100 0.1 wt.% Tinuvin 328 (in TBE)	1.491	1182—1185	495 @ 21.5 °C 495 @ 23.2 °C		Abbott (1991) Graham (1991) Shauly et al. (1997)
			1,1,2,2 tetrabromoethane polyalkylene glycol oil (UCON H-450) Triton X100 Tinuvin 328	1.491	1175			Averbakh et al. (1997)
			14.07 wt.% 1,1,2,2 tetrabromoethane 35.66 wt.% polyalkylene glycol oil (UCON HB-9500) 50.27 wt.% Triton X100 0.1 wt.% Tinuvin 328 (in TBE)	1.491	1182	103 @ 23.25 °C		Abbott (1991)
			33.7 wt.% polyalkylene glycol oil 41.8 wt.% terpineol 24.4 wt.% 1,1,2,2 tetrabromohethane 0.1 wt.% Tinuvin					Mondy et al. (1986) Majumdar et al. (1987)
			Shellflex 214 BG oil kerosene			10 @ 40 °C	Org.	Bovendeerd et al. (1987)
			62 wt.% polyalkylene glycol oil (UCON 50-HB-5100) 38 wt.%1,1,2,2 tetrabromoethane	1.491	1387 @ 22 °C	2830 @ 21.6 °C		Graham and Bird (1984)

Solid	n_S	Density [kg/m³]	Liquid	n_L	Density [kg/m³]	Dynamic viscosity* [mPa s]	Phase	References
			50% Triton X100 23% 1,6 dibromohexane 13.5% UCON 75-H-90000 oil 13.5% UCON 75-H-450 oil	1.487	1185 – 1190	480 @ 20 °C		Lyon and Leal (1998a) Lyon and Leal (1998b)
			23 wt.% UCON oil 75-H-90 000 77 wt.% DER 331 liquid epoxy resin.	1.489	1104	3000		Kaur and Leal (201)
			hexadecane microscope oil (Sigma-Aldrich S150)		890	25 @ 25 °C	Org.	Lenoble et al. (2005)
			Triton X100	1.489	1070	240 @ 23 °C		Jana (1995) Harrington et al. (2014)
			60—64 wt.% NaI 36—40 wt.% water	1.485 – 1.500	1690 – 1840	1.382 @ 28.9 °C 1.382 @ 29 °C 1.47 @ 26.7 °C 1.98	Aq.	Parker and Merati (1996) Uzol et al. (2002) Uzol et al. (2007) Soranna et al. (2008) Hassan and Dominguez-Ontiveros (2008) Yuki et al. (2008) Yuki et al. (2011) Mehta et al. (2007) Amatya and Longmire (2010) Tomac and Gregory (2014) Wu et al. (2009) Wu et al. (2011) Wu et al. (2012) Scholz et al. (2012)
			74 vol.% NaI 21 vol.% glycerol 5 vol.% water	1.485	1700	5.4	Aq.	Zerai et al. (2005)
			79 vol.% saturated sodium iodide water solution 20 vol.% glycerol 1 vol.% water	1.490	1750	6.65 @ 25 °C	Aq.	Baldwin et al. (1989) Baldwin et al. (1994)
			60 wt.% ZnI 40 wt.% water	1.487			Aq.	Hendriks and Aviram (1982)
			ammonium thiocyanate water				Aq.	Budwig et al. (1993) Egelhoff et al. (1999)
			44.8% ammonium thiocyanate 30% glycerol 25.2% water	1.442 – 1.490	1180 – 1230	4.99 @ 22.5 °C 17.9	Aq.	Bailey and Yoda (2003) Jan et al. (1989)
			potassium thiocyanate water glycerol	1.490	1230	2.2	Aq.	Jan et al. (1989)
			71 wt.% potassium thiocyanate 39 wt.% water	1.491		2.02 @ 36 °C [mm²/s]	Aq.	Gijsen et al. (1996) Budwig et al. (1993)
			85.5 vol.% diethylphthalate 14.5 vol.% ethanol	1.486		3.327 @ 16.7 °C [mm²/s]		Nguyen et al. (2004)
			40.67 wt.% glycerol 22.82 wt.% ethylene glycol 36.51 wt.% styrene glycol		1178	280		Leighton and Acrivos (1987)
			glycerol water					Agrawal et al. (1978)

Solid	n_S	Density [kg/m³]	Liquid	n_L	Density [kg/m³]	Dynamic viscosity* [mPa s]	Phase	References
			77.38 wt.% Triton X100 13.39 wt.% zinc-II-chloride 9.23 wt.% water	1.491	1172	3400 @ 23 °C		Breedveld et al. (1998) Breedveld (2000) Breedveld et al. (2001) Breedveld et al. (2002)
			76 wt.% Triton X100 16.2 wt.% zinc chloride 7.8 wt.% water	1.491	1180	16000 @ 23 °C		Timberlake and Morris (2002)
			77.93 wt.% Triton X100 9.01 wt.% zinc chloride 13.06 wt.% water		1172	3700 @ 27 °C		Krishnan et al. (1996)
			decalin tetralin cyclohexyl bromide					Gao and Kilfoil (2007) Chaudhuri et al. (2008)
			decalin tetralin carbon tetrachloride					Kegel and van Blaaderen (2000)
			decalin tetralin (3.06:1 by weight)	1.510				Ackerson and Pusey (1988)
			65.6% cyclohexyl bromide 34.4% decalin			2.06 @ 25 °C		Dibble et al. (2006)
			74 wt.% cyclohexyl bromide 26 wt.% decalin	1.490	1190			Wang et al. (2008)
			cyclohexyl bromide decalin tetrabutyl-ammonium chloride					Kaufman and Weitz (2006)
			sunflower oil	1.473		9.8 @ 26 °C	Org.	Curran and Black (2004)
Nylon	1.514	1150	Pale 4 oil (oxidized castor oil) tetrabromoethane	1.514	1138	1360	Org.	Karnis et al. (1966)
PS	1.590 – 1.600	1050	67.7 wt.% 1-methylnaphthalene 10.4 wt.% 1-chloronaphthalene 21.9 wt.% polyalkylene glycol	1.586 — 1.600	1052	124 @ 20 °C	Org.	Koh et al. (1994)
			28 vol.% 1-methylnaphthalene 31 vol.% 1-chloronaphthalene 41 vol.% tetralin	1.590	1050	2.547	Org.	Cui and Adrian (1997)

* Temperature for viscosity is provided when stated, otherwise it is assumed this is in ambient laboratory conditions between 20 °C and 25 °C.

Referring to Table A.1, we proceed here to provide details relating to the various solid plastic materials, along with dedicated examples of their use in RIM systems. FEP is a hydrophobic fluoropolymer with an RI of 1.338, a density of 2150 kg/m3, an air-water contact angle of $\theta = 102.1°$ (Akinci, 2009), and has high chemical resistance. At optical wavelengths, FEP is translucent rather than clear, yet despite this, clear

images can still be taken through FEP walls a few mm thick. Importantly, the RI of FEP is close to that of water (1.333), and as a result, FEP has been implemented extensively as a RIM solid with water. For example, Satake et al. (2015) performed holographic PTV measurements in a sphere-packed pipe using a RIM system with water as the test-fluid, an FEP pipe (RI = 1.338) and spheres were made from MEXFLON resin (RI = 1.330). The pipe was located in a square observation section filled with water (correction box) to reduce distortions from the outside pipe wall.

PVA is a rubbery polymer with an RI of ≈ 1.470, a density of 1190 kg/m3 and an air-water contact angle of $\theta = 60.6°$ (McCafferty and Wightman, 1999). A fluid mixture of Pale 4 oil (oxidized castor oil) and tetrabromoethane was created by Karnis et al. (1966) to match the RI of PVA discs with RI = 1.467. This RIM system was used for the optical study of dilute, disc-shaped particle suspensions in Couette and Poiseuille flows. The authors reported satisfactory results with PVA in their application.

PMMA, which is also known by the trade names Perspex, Plexiglas or acrylic glass, is the most commonly employed solid in RIM experiments with an RI of ≈1.490, a density of 1180 kg/m3 and an air-water contact angle of $\theta = 59.3°$ (Stöhr et al., 2003). It is optically clear and is easily machined, although it is also brittle and prone to cracking. It has been used for optical measurements in RIM systems with complex geometries, e.g.: a model of abdominal aortic aneurysms (Budwig et al., 1993; Egelhoff et al., 1999); a column containing dispersed beads (Haam and Brodkey, 2000; Haam et al., 2000); an axial turbo-pump (Uzol et al., 2002; Uzol et al., 2007); or highly concentrated (50%) spherical suspensions (Breedveld et al., 1998; Breedveld, 2000; Breedveld et al., 2001; Breedveld et al., 2002).

PMMA can, however, be attacked by a number of chemicals, hence liquid compatibility must be carefully considered. Chemicals including ethanol (and other alcohols), dimethylsulfoxide (DMSO), and Triton X100 can all cause PMMA to form microcracks (Dijksman et al., 2012). In a related study, Liu et al. (1990) found that stress cracks and crazing created in PMMA by a mixture of 68.2 vol.% turpentine oil and 31.8 vol.% Tetralin (RI = 1.489) could be removed by a careful casting, machining and subsequent annealing treatment. Similarly, Jana (1995) treated PMMA with a silicon-based hard coating to increase its chemical resistance to Triton X100, which despite causing crazing is a close RI match to PMMA. Terpineol also attacks PMMA over long time scales, as observed Mondy et al. (1986) who matched PMMA to a mixture of 33.7 wt.% polyalkylene glycol oil, 41.8 wt.% terpineol, 24.4

wt.% 1,1,2,2-tetrabromohethane and 0.1 wt.% Tinuvin. Further, Dijksman et al. (2012) noted that PMMA is known to absorb water and found that it will also absorb Triton X100 as well as dimethylsulfoxide, and that this absorption leads to changes in the RI of PMMA, while Lyon and Leal (1998a) found that the RI of their quaternary liquid mixture was affected due to the differential absorption of the 1,6-dibromohexane mixture component into PMMA particles. Numerous liquids have been utilized for the matching of PMMA's RI, including aqueous salt solutions, and binary and ternary mixtures. A list of PMMA RIM systems along with density and viscosity information can be found in Table A.1.

Nylon is translucent plastic, like FEP, with an RI of ≈ 1.510, a density of ≈ 1150 kg/m3 and has an air-water contact angle of $\theta = 70°$ (Fort, 1964). Our literature search has shown that Nylon has rarely been used in RIM experiments. Nevertheless, Nylon rods with an RI = 1.514 have been matched to a blend of Pale 4 oil (oxidized Castor oil) and tetrabromoethane in order to study optically dilute rod-shaped particle suspensions in Couette and Poiseuille flows (Karnis et al., 1966).

Polycarbonate (PC) is another common clear hard plastic with an RI of ≈ 1.580, a density of ≈ 1210 kg/m3 and an air-water contact angle of $\theta = 78°$ (Cho et al., 2003). Its high RI means that combinations with aqueous solutions are rare and, as a result, no PC RIM experimental systems were found in the literature. Hendriks and Aviram (1982) however showed that a ZnI2 solution could be created to match PC. Even still, Hirsch et al. (2015) found distortions through polycarbonate windows lead to lower accuracy position measurements than with PMMA or glass, and that polycarbonate was also damaged by lower laser powers than PMMA and glass. As a result of these findings, Hirsch et al. (2015) recommended that polycarbonate should not be used for optical measurements.

Finally, referring to Table A.1, PS is a transparent plastic with a RI between 1.590 and 1.600, a density of ≈ 1050 kg/m3 and an air-water contact angle of $\theta = 90°$ (Kondyurin et al., 2006). Of note is the fact that PS is vulnerable to several chemicals, such as cyclohexyl bromide and decalin (Dibble et al., 2006), and its use as a RIM solid in the literature is rare. However, one application example by Koh et al. (1994) had particles made from PS with divinylbenzene cross-linkage that were both density and RI (1.600) matched to a mixture of 1-methylnaphthalene, 1-chloronaphthalene and polyalkylene glycol. It was suspected, however, that the PS particles slowly absorbed both the 1-methylnaphthalene and

1-chloronaphthalene causing the RIs of both the solids and liquids to vary over time (Koh et al., 1994). The high RI of PS restricts the available fluid RIM options. Although no matching aqueous systems found in the literature, Hendriks and Aviram (1982) showed that a ZnI2 aqueous-solution can match PS.

Several additional commercially available transparent or translucent solids of interest can be found on the market that have not yet been employed in RIM experiments to the best of the authors' knowledge. These include THV, ETFE and PVDF, which are all hydrophobic fluoropolymers with RIs of 1.350, 1.403 and 1.420, densities of 1970, 1730 and 1780 kg/m3, and air-water contact angles of $\theta = 99^{o}$ (Begolo et al., 2011), $\theta = 99.2^{o}$ (Akinci, 2009), $\theta = 94^{o}$ (Saarinen et al., 2006), respectively. ETFE and PVDF are optically translucent rather than clear in the visible part of the electromagnetic spectrum (although slightly less clear than FEP), whereas THV is transparent. Both ETFE and PVDF are relatively stiff fluoropolymers allowing thin-walled tubes and other sections with adequate optical transparency to be constructed. Similarly to other fluoropolymers, like FEP, these materials have excellent chemical resistance. Of course, even with the mention of these plastics this is not a complete list, especially since new materials are constantly emerging. Further plastic RIM options have been suggested by Wiederseiner et al. (2011) including: polyetheretherketone (PEEK), polyethyleneterephthalate (PET), polyvinylchloride (PVC), styrene/acrylonitrile copolymer (SAN), polychlorotrifluoroethylene (PCTFE), polyformaldehyde (POM), with RIs of 1.650 – 1.770, 1.575, 1.540, 1.570, 1.435 and 1.410, respectively.

A.2 Silicone and urethane rubbers

Silicone rubbers are elastomers composed of a silicon-containing polymer. They typically have RIs in the range 1.410 – 1.440, while the air-water contact angle of PDMS silicone rubber is 108^{o} (Duffy et al. 1998). The density of silicone rubber varies widely based on its exact composition, however, it is usually in the range of 1100 – 2300 kg/m3. Flexibility makes silicone rubbers particularly useful for compliant models of flows through flexible structures or membrane-like tissues, e.g., in RIM models for blood-flow experiments and, as a result, have been frequently employed in such systems (Duncan et al., 1990; Perktold et al., 1997; Bale-Glickman et al., 2003; Burgmann et al., 2009;

Shuib et al., 2010; Yousif et al., 2010; Gülan et al., 2012; Pielhop et al., 2012; Geoghegan et al., 2012; Im et al., 2013; Kefayati and Poepping, 2013).

Sylgard 184, manufactured by Dow Corning, has been identified as a silicone rubber of particularly interest (Duncan et al., 1990; Perktold et al., 1997; Hopkins et al., 2000; Yousif et al., 2010; Shuib et al., 2010; Buchmann et al., 2010; 2011; Geoghegan et al., 2012 and Kefayati and Poepping, 2013). Although a common choice, Hopkins et al. (2000) cautioned that the effects of mixing and curing on Sylgard 184 can result in RI variations between models, and the care must therefore be taken in matching liquid RIs to individual models.

It should be noted, that silicone rubbers are known to absorb some liquids, including silicone oils and methlcyclohexane, and this can lead to significant swelling of the material (100% or more) while also potentially affecting the RI (Burdett et al., 1981). This is important in the practical deployment of these materials, as silicone oils are a close RI match for silicone rubbers but are unlikely to be suitable in most cases. An example of the use of silicone rubber is given in Im et al. (2013), where silicone rubber was RI matched to a glycerol solution in order to perform tomographic PIV measurements through a model of a nasal cavity.

Although rarely used, urethane is another transparent rubber that can be employed to study flows in compliant geometries. Le et al. (2013) matched urethane rubber with a RI of 1.490 to an aqueous-solution of NaI and glycerol in order to study a model of an aneurysm. The different liquids identified as having been used in RIM experiments featuring rubbers are shown in Table A.2.

Table A.2 List of rubber-based refractive index-matched systems.

Solid	n_S	Density [kg/m³]	Liquid	n_L	Density [kg/m³]	Dynamic viscosity* [mPa s]	Phase	References
silicone elastomer (silicone rubber) (PDMS)	1.410 – 1440	1100 – 2300	36.3 vol.% diethylphthalate 63.7 vol.% ethanol	1.410		1.818 @ 23 °C		Miller et al. (2006)
			55.6 vol.% diethylphthalate 44.4 vol.% ethanol	1.440		3.327 @ 16 °C [mm²/s]		Nguyen et al. (2004)
			methylcylohexane	1.422	772		Org.	Burdett et al. (1981)
			67.9 wt.% glycerol 32.1 wt.% water	1.422	1173	19.3	Aq.	Burdett et al. (1981)
			60.7 wt.% glycerol 39.3 wt.% water	1.406			Aq.	Burgmann et al. (2009)
			water 40 wt.% glycerol sodium iodide	1.406			Aq.	Burgmann et al. (2009)
			59 vol.% glycerol 41vol.% water	1.430		6.55 @ 27.5 °C [mm²/s]	Aq.	Hopkins et al. (2000)
			glycerol water				Aq.	Pielhop et al. (2012)
			60 wt.% glycerol 40 wt.% water	1.410	1160	5.4 @ 37 °C	Aq.	Yagi et al. (2013)
			61 vol.% glycerol 39vol.% water	1.417	1150	11.7 @ 20 °C 12.7 @ 20 °C	Aq.	Buchmann et al. (2010) Buchmann et al. (2011)
			61 vol.% glycerol 39vol.% water	1.430	1140	10.6	Aq.	Geoghegan et al. (2012)
			59% water 41% glycerol	1.430		9.82 [mm²/s]	Aq.	Im et al. (2013)
			47.38 wt.% water 36.94 wt.% glycerol 15.68 wt.% sodium iodide	1.410	1244	4.31 @ 22.2 °C	Aq.	Yousif et al. (2010)
			47.9 wt.% water 37.1 wt.% glycerol 15.0 wt.% sodium chloride	1.410	1080	6.23 @ 20 °C	Aq.	Shuib et al. (2010)
			47.38 wt.% water 36.84 wt.% glycerol 15.68 wt.% sodium iodide	1.414		4.31	Aq.	Kefayati and Poepping (2013)
			70 vol.% isopropyl alcohol 30 vol.% glycerol	1.410	930	13.95 @ 25 °C		Bale-Glickman et al. (2003)

			sodium thiocyanate water	1.414		1.3 @ 30 °C [mm²/s]	Aq.	Duncan et al. (1990) Perktold et al. (1997)
urethane rubber	1.490		54.3 wt.% NaI 20.8 wt.% glycerol 24.9 wt.% water	1.490	1780	17.8	Aq.	Le et al. (2013)

* Temperature for viscosity is provided when stated, otherwise it is assumed this is in ambient laboratory conditions between 20 °C and 25 °C.

A.3 Custom polymers, resins and hydrogels

Optically clear resins have been developed with a wide range of customized RIs (covering the range 1.31 – 1.60), and are currently available commercially from companies such as MY Polymers and Addison Clear Wave Inc. There are over 50 different types of optically clear resins on the market with varying composition, compatibility and, of course, RI. Resins are frequently moulded into complex geometries and can be found in optical equipment including lenses, optical adhesives and fibre optics. The main advantage of using optically clear resins is that their RIs can be tuned in a similar way to that of a mixture of liquids, however, the cost of these custom-made resins is relatively high and may prove prohibitive, especially for large-scale experiments. In one successful implementation, Butscher et al. (2012) performed PIV measurements in a foam-like porous test-section that was entirely made of the epoxy resin WaterShed XC 11122, which was RI matched to the liquid anisole at an RI of 1.515. In another example, Leis et al. (2005) examined the fluoropolymer-copolymer Nifion as RIM combination with water for studying biofilms. Importantly, Nifion is an atypical hydrophilic fluoropolymer with RI = 1.336 – 1.343 when water wetted.

Hydrogels comprise networks of polymer chains that contain large amounts of water (>90%), leading typically to RIs in the range 1.333 – 1.349. They have been used as particles in flows but are less likely to be suitable for use as rigid walls as they possess a degree of flexibility. The most common hydrogels include those based on polyacrylamide or agarose (Byron and Variano, 2013). Weitzman et al. (2014) explored the use of copolymers of polyacrylamide and sodium acrylate in creating hydrogels that were RI matched to water while being readily available at low cost and easily moulded. In another successful application, hydrogel spheres and water were also RI matched by Kang et al. (2010) in order to perform visualization experiments showing

the invasion drainage of porous media with density-matched immiscible liquids. The second liquid phase in these tests, an organic phase consisting of a mixture of soybean oil and carbon tetrachloride, was intentionally unmatched in RI so that it could be easily identified and observed. The custom polymers, resins and hydrogels identified in the literature as having been used in RIM experiments are listed in Table A.3.

Table A.3 List of custom-polymer, resin and hydrogel refractive index-matched systems.

Solid	n_S	Density [kg/m³]	Liquid	n_L	Density [kg/m³]	Dynamic viscosity* [mPa s]	Phase	References
MEXFLON resin	1.330		water	1.330			Aq.	Satake et al. (2015) Unno et al. (2016)
hydrogel agarose (0.4%) water (99.6%)	1.333	1007	water	1.330	998	1 @ 20 °C	Aq.	Byron and Variano (2013)
hydrogel 0.3 wt.% polyacrylamide 0.7 wt.% sodium acrylate trace N, N-methylene-bis-acrylamide 99.0 wt.% water	1.333		water	1.332			Aq.	Weitzman et al. (2014)
Nafion (fluoropolymer-copolymer)	1.336 – 1.343 (wet)		water				Aq.	Leis et al. (2005)
Nafion (fluoropolymer-copolymer)	1.340		water	1.330			Aq.	Downie et al. (2012)
hydrogel (8 vol.%) polyacrylamide/bis (0.5 vol.%) ammonium persulphate (92%) water	1.349	1024	water	1.330	998	1 @ 20 °C	Aq.	Byron and Variano (2013)
Sumikagel		1010	water		998	1 @ 20 °C	Aq.	Kumar et al. (1993)
hydrogel			water		998	1 @ 20 °C	Aq.	Kang et al. (2010)
Smooth-On Inc. Crystal Clear	1.498		65.0 wt.% NaI 35.0 wt.% water	1.499			Aq.	Bai and Katz (2014)
Forecast3D UOPTIC 2	1.499		65.0 wt.% NaI 35.0 wt.% water	1.499			Aq.	Bai and Katz (2014)

Renshape SL7870	1.508		66.8 wt.% NaI 33.2 wt.% water	1.507			Aq.	Bai and Katz (2014)
Watershed XC 11122	1.512		Anisole	1.515	989	0.992 @ 25 °C		Butscher et al. (2012)

* Temperature for viscosity is provided when stated, otherwise it is assumed this is in ambient laboratory conditions between 20 °C and 25 °C.

A.4 Glasses

Many glasses are readily available with a wide range of RIs (1.45 – 1.51). Glasses are of interest for RIM experiments as they are optically transparent and provide high chemical resistance, making them compatible with a variety of aqueous and organic fluids. Importantly, glasses can tolerate significantly higher laser powers than plastics before undergoing damage, which may be an important factor when higher illumination levels are required (Hirsch et al., 2015), and they can also withstand higher stresses without significant deformation (e.g., due to pressure). On the other hand, glasses are not as easily machined and are typically more brittle than plastics. Glasses are typically hydrophilic and tend to be water wetted, e.g., in liquid-liquid water-oil flows. Common (clean) polished quartz and borosilicate glasses have contact angles in the range 10° to 20° (Bowman 1998). Furthermore, glasses have a surface roughness of typically ≈ 1 µm, which is the same as that of plastics pipes but smoother than metal pipes.

The RI of glass components varies slightly depending on their manufacturing process and composition. In the context of RIM experiments, RI variations should be established to ascertain their effect on measurement accuracy. Dijksman et al. (2012) found that different batches of glass beads had RIs that varied by up to 0.01. Similarly, the type of glass can affect optical accuracy. Hirsch et al. (2015) found that optical glass was, unsurprisingly, best suited for optical measurements but also that annealed-normal-glass had only slightly worse optical performance. Our RIM literature search revealed three common glass types: fused-quartz; borosilicate; and soda-lime glass. RIM systems featuring these glasses can be found in Table A.4, along with silica gel.

Table A.4 List of glass-based refractive index-matched systems including fused-quartz, silica-gel, borosilicate and soda-lime glass, as the solid phase.

Solid	n_S	Density [kg/m³]	Liquid	n_L	Density [kg/m³]	Dynamic viscosity* [mPa s]	Phase	References
Fused-quartz	1.450 – 1.460	2203	tetraethylene glycol	1.459	1125	47.4 @ 23.5 °C		Stephenson and Stewart (1986)
			Tetrahydropyran-2-methanol	1.458	1027	11.4 @ 20 °C		Stephenson and Stewart (1986)
			90 vol.% cyclooctane 10 vol.% cyclooctene	1.458	834	2.42 @ 20 °C		Stephenson and Stewart (1986)
			83.11 wt.% dimethylsulfoxide (DMSO) 16.89 wt.% water	1.462	1098	2.85 @ 25.2 °C		Dietze et al. (2009)
			90.98 wt.% glycerol 9.02 wt.% water	1.462	1231	93.77 @ 32.6 °C	Aq.	Dietze et al. (2009)
			Penreco Drakeol #5 (light mineral oil)	1.459			Org.	Stoots et al. (2001) McIlroy et al. (2010)
			70.3 vol.% diethylphthalate (DEP) 29.7 vol.% ethanol	1.459		3.499 @ 23 °C		Miller et al. (2006)
			63 wt.% calcium chloride (dihydrate) 37 wt.% water	1.458		17 @ 30 °C	Aq.	Amini and Hassan (2012)
			98 wt.% Dow Corning 556 fluid (silicone oil) 2% wt.% Dow Corning 200 fluid (silicone oil)	1.460	970	20.37	Org.	Stöhr et al. (2003)
			58 wt.% $ZnCl_2$ 42 wt.% water	1.460	1700	6.8	Aq.	Stöhr et al. (2003)
			60 wt.% Soddard solvent* 40 wt.% mineral oil	1.445	812	4.1	Org.	Park et al. (1989)
			92 wt.% glycerol 8 wt.% water	1.456			Aq.	Park et al. (1989)
silica gel	1.452		45 vol.% benzyl alcohol 55 vol.% ethyl alcohol	1.452	974	2.0 @ 20 °C		Cui and Adrian (1997)
			chloroform water					Abbas and Crowe (1987)
			50% sodium iodide 50% water	1.443	1550	1.145 @ 25 °C	Aq.	Wildman et al. (1992) Chen and Kadambi (1990) Chen and Kadambi (1995)

Solid	n_S	Density [kg/m³]	Liquid	n_L	Density [kg/m³]	Dynamic viscosity* [mPa s]	Phase	References
borosilicate glass	1.470 – 1.474	2230	trichloroethylene	1.474				Corino and Brodkey (1969)
			48.5 wt.% Dow Corning 556 (silicone oil) 51.5 wt.% Dow Corning 550 (silicone oil)	1.474		59 @ 25 °C	Org.	Yarlagadda and Yoganathan (1989)
			68.9 vol.% Dow Corning 556 (silicone oil) 31.1 vol.% Dow Corning 550 (silicone oil)	1.474	1006	42.76	Org.	Wang and Khalili (2002)
			67.8 vol.% Dow Corning 556 (silicone oil) 32.2 vol.% Dow Corning 550 (silicone oil)	1.474	1006	42.76 @ 23 °C	Org.	Goharzadeh et al. (2005)
			ESSO MARCOL 82 oil PRIMOL 352 oil	1.474			Org.	Saleh et al. (1992)
			55 wt.% NaI 45 wt.% water	1.474			Aq.	Chen and Fan (1992) Chen et al. (1994)
			60 wt.% NaI 40 wt.% water	1.470	1770	1.805	Aq.	Jacobs et al. (1988)
			58.5 wt.% NaI 41.5 wt.% water	1.472			Aq.	Ghatage et al. (2014)
			54.5 wt.% NaI 45.5 wt.% water	1.470			Aq.	Narrow et al. (2000)
			55 wt.% NaI 45 wt.% water	1.475			Aq.	Reddy et al. (2013)
			81.1 vol.% diethylphthalate 18.9 vol.% ethanol	1.474		4.862 @ 23 °C		Miller et al. (2006)
			glycerol	1.470		954 @ 23 °C	Aq.	Cenedese and Viotti (1996) Moroni and Cushman (2001)
			78.7 vol.% tetrechloroethylene 21.3 vol.% Freon 113	1.471	1610	0.844		Varty (1984)
			turpentine ethereal oil xylene	1.470			Org.	Cenedese and Viotti (1996)
			ZnCl water	1.470			Aq.	Cenedese and Viotti (1996)
			decalin	1.470				Cenedese and Viotti (1996)

Solid	n_S	Density [kg/m³]	Liquid	n_L	Density [kg/m³]	Dynamic viscosity* [mPa s]	Phase	References
			diesel oil mixture			4.3 @ 20 °C [mm²/s] 3.9 @ 20 °C [mm²/s]	Org.	Durst et al. (1995) Pashtrapanska et al. (2006)
			ammonium thiocyanate water				Aq.	Patil and Liburdy (2010) Patil and Liburdy (2012) Patil and Liburdy (2013)
			45 wt.% ammonium thiocyanate 55 wt.% water	1.470			Aq.	Reddy et al. (2013)
			potassium thiocyanate glycerol water	1.482			Aq.	Walker et al. (1989)
			White Oil (FC 2012W)	1.473			Org.	Schäfer et al. (1997)
			parafin oil light	1.465			Org.	Reddy et al. (2013)
			42 wt.% potassium thiocyanate 58 wt.% water	1.460			Aq.	Reddy et al. (2013)
			benzene with turpentine	1.470				Reddy et al. (2013)
			turpentine chloronaphthalene	1.465				Reddy et al. (2013)
			turpentine benzyl alcohol	1.470				Reddy et al. (2013)
			68% turpentine 32% tetralin	1.467	915	1.20		Reddy et al. (2013)
			turpentine tetralin parafin oil light	1.465 – 1.467	855 – 915	1.2 – 10.1		Reddy et al. (2013)
			66% Dipropylene glycol monomethyl ether 33% diphenyal ether	1.474				Peterson et al. (1987)
			oil (Pharma 5, DEA) light protective liquid (Eusolex, Merck)				Org.	Kohnen and Bohnet (2001)
soda-lime glass	1.504 – 1.519	2520	isopropyl alcohol methylnaphthalene	1.504				Hassan and Dominguez-Ontiveros (2008)
			heating oil (Diesel) palationol					Durst and Loy (1985) Durst et al. (1988)

Solid	n_S	Density [kg/m³]	Liquid	n_L	Density [kg/m³]	Dynamic viscosity* [mPa s]	Phase	References
			diethylphthalate	1.504	1180	12 @ 20 °C		Hassan and Dominguez-Ontiveros (2008) Nguyen et al. (2004)
			28wt.% tetralin 72wt.% TSF 451-1000 (silicone oil)	1.500	975	19.62	Org.	Mikami et al. (2001) Chen et al. (2005)
			methyl benzoate	1.510				Zisselmar and Molerus (1979)
			Santicizer 278 (Monsanto)	1.510 – 1.519	1080 – 1090	912.6 @ 24 °C 1300 @ 22 °C		Ham and Homsy (1988) Nicolai and Guazzelli (1995) Nicolai et al. (1995) Nicolai et al. (1996)
			tetralin clear coal oil	1.513		2 @ 20 °C	Org.	Zachos et al. (1996)
			60 wt.% NaI 40 wt.% water	1.500			Aq.	Chen and Fan (1992)

* Temperature for viscosity is provided when stated, otherwise it is assumed this is in ambient laboratory conditions between 20 °C and 25 °C.

Fused-quartz is high-purity silicon oxide (SiO_2) in amorphous (i.e., non-crystalline) form with a density of 2203 kg/m^3. It has both a lower coefficient of thermal expansion (5.5×10^{-7} K^{-1}) and a lower RI (1.450 – 1.460) compared to both borosilicate and soda-lime glasses, although its purity results in it being more expensive than these glasses. Fused-quartz has featured in numerous RIM systems, including a RIM facility described by Stoots et al. (2001) for the purposes LDA flow studies around complex geometries for which the fused-quartz observational sections of the facility were RI matched at 1.459 to a light mineral oil ("Penreco Drakeol #5"). McIlroy et al. (2010) then employed this flow system to study the turbulent flow in a gas-cooled reactor part using tomographic PIV.

Silica gel is a form of SiO_2 which is often in the form of granules or a porous material with a density of approximately 2210 kg/m^3 and a RI of 1.452. Silica gel is highly hydroscopic with a specific surface area of ≈ 800 m^2/g. Once it becomes saturated with water it can be regenerated by heating to 120 °C for 1 to 2 hours. Silica gel has been used in a few RIM systems including that of Abbas and Crowe (1987) who

used beads of silica gel that were RI matched to a mixture of chloroform and water to perform LDA measurements on homogenous slurry near transitional Reynolds numbers. Chloroform was selected in this study as it was considered reasonably priced, non-toxic, non-flammable, chemically stable, optically clear and colourless.

Borosilicate glass, also known as Pyrex and Duran glass, is a laboratory glass with a RI in the range 1.470 – 1.474, a density of 2230 kg/m^3, and a thermal expansion coefficient of 3×10^{-6} K^{-1} which is generally lower than soda-lime glass but higher than fused-quartz. The literature indicates that borosilicate glass is the second most common solid in RIM experiments behind PMMA. The wide use of borosilicate glass in RIM experiments has resulted in the identification of many liquid-phase matching substances (aqueous and organic). Similarly to PMMA, borosilicate glass has been used for optical measurements in complex geometries, e.g., an aortic model (Walker et al., 1989) and flow through a porous medium (Cenedese and Viotti, 1996).

Reddy et al. (2013) created a solid-liquid fluidized bed for PIV measurements, where the solid bed was made from borosilicate glass spheres with a RI of 1.470 and the column was made from PMMA. A number of liquids were examined as matches to borosilicate spheres. A 55 wt.% NaI solution (RI = 1.475) was RI matched but was considered too corrosive. A 42 wt.% KSCN solution (RI = 1.460) and a 45 wt.% ammonium thiocyanate (NH_4SCN) solution (RI = 1.470) were also considered reasonable RI matches, but were also regarded too toxic and corrosive. Three further mixtures of benzene and turpentine (mixture RI = 1.470), turpentine and chloronaphthalene (RI = 1.465), and turpentine and benzyl alcohol (RI = 1.470) were close RI matches for the borosilicate glass, but attacked the PMMA test-section. A mixture of 68% turpentine and 32% tetralin (RI = 1.467) was found to RI match the borosilicate spheres, while also being compatible with the PMMA column. Finally, a light paraffin oil with a RI of 1.465 was also found to be a close RI match for borosilicate glass, whilst being compatible with the PMMA. This light paraffin oil was then added to adjust the viscosity of the 68% turpentine and 32% tetralin mixture used as the base experimental liquid.

Soda-lime is the most common form of glass with a density of approximately 2520 kg/m^3. It is more brittle than both borosilicate and fused-quartz, but has a lower cost. It is predominantly composed of silicon dioxide (SiO_2) along with other oxides including those of sodium (Na_2O), calcium (CaO), aluminium (Al_2O_3), potassium (K_2O), titanium (TiO_2), magnesium (MgO), iron (Fe_2O_3), sulphur (SO_3), and other

impurities. The exact composition varies with the manufacturing process, which also affects the RI of the material between batches and suppliers. A search of the literature has shown that soda-lime glass typically has RI values between 1.50 and 1.52 due to this compositional variation. The relatively wide range soda-lime glass RIs means that care must be taken when matching liquid(s) to solid components. Chen and Fan (1992) used two NaI solutions to match the RI of soda-lime and borosilicate glasses, in their study of 3-D flow structures in a solid-liquid-gas fluidized-bed system. The soda-lime glass beads (RI = 1.500) of the fluidized bed were matched to a 60 wt.% NaI solution, while the borosilicate cylindrical walls were enclosed in a box filled with a 55 wt.% NaI solution that matched the RI of borosilicate (1.474). It is not clear why different glasses were selected for the beads and cylindrical walls, as the selection of the same glass would have led to a closer RI-matched system.

The lowest RI of the aforementioned glasses is that of fused quartz (RI = 1.450), nevertheless, the RI of calcium fluoride (CaF_2) glass is even lower at 1.434 (Malitson, 1963). Given this RI, as well as its insolubility in water, CaF_2 appears as excellent RIM candidate for use in aqueous-based liquid-liquid systems, however, the authors have been unable to find examples of CaF_2 employed in this way in the literature. The mineral form of CaF_2, fluorite, is often fluorescent under ultraviolet light, and as a result care should be taken when selecting the purity of the CaF_2 glass as well as the wavelength of any light-source/laser.

A.5 Liquid-liquid systems

Transparent single-component immiscible liquid-liquid pairs, where one liquid was hydrophobic and the other hydrophilic, were experimentally studied by Smedley and Coles (1990). In all, they collated 121 compatible systems, of which 13 had a RI match of 0.001 or less, and a further 20 had RI differences of 0.005 or less. Given that all 121 systems were a single component and therefore not tuned in RI, it seems likely that many of these systems could be significantly improved upon through blending or additives. The 13 closest RIM pairs of Smedley and Coles (1990) are included within Table A.5. It is worth noting that none of the RIM systems in Smedley and Coles (1990) involve the commonly used RIM fluids of water, glycerol or silicone oil. These liquids can, however, be found in many other liquid-liquid RIM systems included in Table A.5.

The RI's of the matched liquid-liquid systems span the range from 1.322 – 1.460, with the majority of actual experimental flow systems being near a value of 1.40.

Table A.5 List of selected liquid-liquid refractive index-matched systems.

n_L	Phase	Material	Density [kg/m³]	Dynamic viscosity* [mPa s]	Interfacial tension [mN/m]	References
1.322 – 1.335	Org.	57.9 wt.% FC-72 39.1 wt.% hexane 3.0 wt.% F_6H_6				Hibberd et al. (2007)
	Aq.	98.5 wt.% water 0.4 wt.% Brij-35 0.3 wt.% NaN_3 0.8 wt.% PEO				
1.385	Org.	n-heptane	684	0.4 @ 29 °C	31 @ 29 °C	Pouplin et al. (2011)
	Aq.	43 vol.% glycerol 57 vol.% water	1102	3.2 @ 29 °C		
1.391	Org.	heptane	684	0.45 @ 29 °C	31 @ 29 °C	Conan et al. (2007)
		50 wt.% glycerol 50 wt.% water	1123	4.2 @ 29 °C		
1.395 – 1.436	Aq.	water CsBr 1,2-propanediol				Saksena et al. (2015)
	Org.	LSO (5 mm²/s silicone oil) HSO (50 mm²/s silicone oil) 1-bromooctane				
1.382 – 1.436	Aq.	water CsBr 1,2-propanediol				Cadillon et al. (2016)
	Org.	LSO (1 mm²/s silicone oil) HSO (1000 mm²/s silicone oil) 1-bromooctane				
1.395	Org.	n-heptane	684	0.45 @ 29 °C	31 @ 29 °C	Augier et al. (2003) Augier et al. (2007)
	Aq.	50 wt.% glycerol 50 wt.% water	1180	6 @ 29 °C		
1.396	Org.	62.4 wt.% Freon 37.6 wt.% octanol				Budwig (1994)
	Aq.	37.8 wt.% sucrose 62.2 wt.% water				
1.399 – 1.403	Org.	silicone oils (6 mm²/s)	925	5.4@ 20 °C		Ninomiya and Yasuda (2006)
	Org.	silicone oils (20 mm²/s)	950	18.32 @ 20 °C		
	Aq.	50 wt.% glycerol 50 wt.% water	1130	6.7 @ 20 °C		
1.400	Org.	Dow Corning 200 (20 mm²/s silicone oil)	949	19	29.1	Mohamed-Kassim and Longmire (2003) Mohamed-Kassim and Longmire (2004)
	Aq.	45 vol.% glycerol 55 vol.% water	1128	6.3		
1.401	Org.	Wacker AK 100 silicone oil		96 @ 25 °C		Kollhoff et al. (2015)
	Aq.	20.19 wt.% NaCl 18.75 wt.% sucrose 61.06 wt.% DI water		3.7 @ 25 °C		
	Org.	11 mPa s silicone oil	940	1.4		

n_L	Phase	Material	Density [kg/m³]	Dynamic viscosity* [mPa s]	Interfacial tension [mN/m]	References
1.399 – 1.401	Aq.	30 wt.% NaI 70 wt.% water	1340	11		Svensson and Rasmuson (2004) Svensson and Rasmuson (2006)
1.401	Org	silicone oil (50 mm²/s)	960	48	29.1 – 29.5	Bordoloi and Longmire (2012) Longmire and Bordoloi (2015)
	Aq.	48 vol.% glycerol 52 vol.% water	1130	6.7 – 7		
	Org	silicone oil (20 mm²/s)	950	19	25.7	Longmire and Bordoloi (2015)
	Aq.	48 vol.% glycerol 52 vol.% water	1130	7		
1.401	Org.	Dow Corning 200 (50 mm²/s silicone oil)	960	48	29.1 – 29.5	Mohamed-Kassim and Longmire (2003) Mohamed-Kassim and Longmire (2004) Kim and Longmire (2009) Ortiz-Dueñas et al. (2010)
	Aq.	46 vol.% glycerol 54 vol.% water	1131	6.7		
1.394 – 1.407	Org.	Dow Corning 200 (5 mm²/s silicone oil)	970	4.85	29.5	Longmire et al. (2001)
	Org.	Dow Corning 200 (50 mm²/s silicone oil)	960	48		
	Aq.	56 wt.% glycerol 44 wt.% water	1140	8.33		
1.431 – 1.432	Org.	diethyl pimelate	994	4.0 @ 20 °C		Smedley and Coles (1990)
	Aq.	ethylene glycol	1109	19.9 @ 20 °C		
1.431 – 1.432	Org.	diprpyl adipate	979			Smedley and Coles (1990)
	Aq.	1,2-propanedoil	1036	56.0 @ 20 °C		
1.431 – 1.432	Org.	ethyl laurate	862	3.4 @ 20 °C		Smedley and Coles (1990)
	Aq.	1,2-propanedoil	1036	56.0 @ 20 °C		
1.431 – 1.432	Org.	diprpyl adipate	979			Smedley and Coles (1990)
	Aq.	ethylene glycol	1109	19.9 @ 20 °C		
1.431 – 1.432	Org.	ethyl laurate	862	3.4 @ 20 °C		Smedley and Coles (1990)
	Aq.	ethylene glycol	1109	19.9 @ 20 °C		
1.432	Org.	methyl laurate	870	3.1 @ 20 °C		Smedley and Coles (1990)
	Aq.	1,2-propanedoil	1036	56.0 @ 20 °C		
1.432	Org.	methyl laurate	870	3.1 @ 20 °C		Smedley and Coles (1990)
	Aq.	ethylene glycol	1109	19.9 @ 20 °C		
1.432	Org.	glycerol tripropanoate	1098	14.3 @ 20 °C		Smedley and Coles (1990)
	Aq.	ethylene glycol	1109	19.9 @ 20 °C		
1.438	Org.	Exxsol D80	803	1.62 @ 25 °C	19 @ 20 °C	Liu (2005) Liu et al. (2006a) Liu et al. (2006b)
	Aq.	39 wt.% $CaCl_2$ 61 wt.% water	1442	11.84 @ 25 °C		
	Org.	silicone oil (0.65 mm²/s)		0.65 [mm² s]	43	Berard et al. (2013)
	Org.	silicone oil (5 mm²/s)		5 [mm² s]		
	Org.	silicone oil (20 mm²/s)		20 [mm² s]		
	Aq.	glycerol solution				

n_L	Phase	Material	Density [kg/m³]	Dynamic viscosity* [mPa s]	Interfacial tension [mN/m]	References
1.440 – 1.441	Org.	2-bromopentane	1208			Smedley and Coles (1990)
	Aq.	1,3-propanedoil	1060	46.6 @ 20 °C		
1.440	Org.	1-bromobutane	1276	0.64 @ 20 °C		Smedley and Coles (1990)
	Aq.	1,3-propanedoil	1060	46.6 @ 20 °C		
1.444	Org.	Exxsol D80	803	1.9 @ 20 °C	25	Morgan et al. (2012) Morgan et al. (2013) Morgan et al. (2016)
	Aq.	81.7 wt.% glycerol 18.3 wt.% water	1213	82.3 @ 20 °C		
1.446	Org.	Shell Macron EDM110 oil	800	3.0 @ 20 °C	45	Ravelet et al. (2007)
	Aq.	510 g/L NaI water solution	1500	2.0 @ 20 °C		
1.447	Org.	bis(2-ethylhexyl) adipate	922	13.3 @ 20 °C		Smedley and Coles (1990)
	Aq.	formanide	1133	3.85 @ 20 °C		
1.447 – 1.448	Org.	1-bromohexane	1174	1.1 @ 20 °C		Smedley and Coles (1990)
	Aq.	diethylene glycol	1116	35.7 @ 20 °C		
1.448 – 1.449	Org.	1-bromohexane	1174	1.1 @ 20 °C		Smedley and Coles (1990)
	Aq.	1,5-pentanedoil	992	128.1 @ 20 °C		

* Temperature for viscosity is provided when stated, otherwise it is assumed this is in ambient laboratory conditions between 20 °C and 25 °C.

A.6 Organic liquids

A wide range of organic liquids have been employed in RIM systems, including pure hydrocarbons, hydrocarbon mixtures, mineral or silicone oils, fluorocarbons, etc. A selection of such fluids is listed in Table A.6, covering an RI range from 1.251 to 1.631. The table forms a guide for the selection of potential components for tuning organic mixtures. For instance, high RI organic chemicals like tetralin (RI = 1.541) can be added to increase the RI of another organic phase, while similarly low RI liquids like tetradecafluorohexane can be added to lower the RI. Table A.6 also provides water solubility as well as PMMA compatibility information that has been obtained principally via supplier datasheets and should be regarded as approximate guidance only.

Table A.6 List of organic liquids previously in refractive index-matched experiments, with their RI, surface tension, dynamic viscosity and density.

Liquid	n_S	Density [kg/m^3]	Dynamic viscosity* [mPa s]	Surface tension [mN/m]	Water solubility	PMMA compatibility	References
tetradecafluorohexane	1.251	1680	0.635 @ 25 °C	12.23 @ 25 °C	immiscible		Hibberd et al. (2007)
Freon-113	1.356				poor		Varty (1984)
n-hexane	1.375 — 1.381	659	0.3 @ 25 °C	18.4 @ 20 °C	immiscible	good	Hibberd et al. (2007) Blanchette and Bigioni (2009)
isopropyl alcohol	1.378	785	2.038 @ 25 °C	20.93 @ 25 °C	miscible	poor	Hassan and Dominguez-Ontiveros (2008) Hayes (2015)
heptane	1.395	684	0.45 @ 29 °C	19.66 @ 25 °C	immiscible	poor	Augier et al. (2003) Hayes (2015)
Dow Corning 200 (silicone oil)	1.375 — 1.404	978	0.65 – 1,000,000 @ 25 °C	19.7 — 21.6	immiscible	good	Dow Corning datasheets
Exxsol D60	1.434	785	1.64 @ 15 °C		immiscible	good	Amundsen (2011)
Stoddard solvent	1.438	789			immiscible	poor	Carpenter et al. (1975)
chloroform	1.441	1472	0.537 @ 25 °C	26.67	slightly	poor	Bhatia et al. (2009) Hayes (2015)
Exxsol D80	1.444	796	2.3 @ 21 °C		immiscible	good	Morgan et al. (2012)
carbon tetrachloride	1.453	1580	0.9	45	immiscible	poor	Tidhar et al. (1986) Rheims et al. (1997)
UCON H-450 (polyalkylene glycol oil)	1.457	1084	120		miscible	poor	Averbakh et al. (1997)
Exxsol D140	1.459	828	6 @ 25 °C	27.6	immiscible	good	Lovick and Angeli (2004)
Dow Corning 556 (silicone oil)	1.460	980	22.5 @ 23 °C		immiscible	good	Goharzadeh et al. (2005)
UCON 75-H-90000 (polyalkylene glycol oil)	1.464	1094	51100 @ 20 °C		miscible	poor	Koh et al. (1994) Kaur and Leal (2010)
turpentine	1.464	850	1.43		immiscible	good	Kapoor and Acrivos (2006)
decalin (decahydronaphthalene)	1.470	897	2.2 @ 25 °C		immiscible	poor	Miller et al. (2006) Hayes (2015)
Triton X100	1.487	1055	280 @ 28 °C		miscible	poor	Averbakh et al. (1997)
para-cymeme (p-cymeme)	1.489	855	1.023		immiscible		Ni and Capart (2015)
dibutylphthalate (DBP)	1.49	1049	16.6 @ 25 °C		immiscible	poor	Aziza and Wong (2003) Hayes (2015)
xylene	1.493	860	0.6 @ 26 °C	29.76 @ 25 °C	immiscible	poor	Richards and Scheele (1985) Hayes (2015)
Dow Corning 550 (silicone oil)	1.494	1068	125 @ 23 °C	24.5	immiscible	good	Goharzadeh et al. (2005) Stöhr et al. (2003)
cyclohexyl bromide	1.495				immiscible		Dijksman et al. (2012)
diethylphthalate (DEP)	1.504	1180	12		immiscible	poor	Nguyen et al. (2004)
tetrachloroethylene	1.504	1615	0.861 @ 25 °C		poor	poor	Baragi et al. (2005)
anisole	1.515	989	0.992 @ 25 °C	35.10	immiscible		Baragi et al. (2005) Hayes (2015)
methyl salicylate	1.526	1180	4.09	35	poor	poor	Nguyen et al. (2004) Merrington and Richardson (1947)

Dow Corning 710 (silicone oil)	1.533	1110	500	28.5	immiscible	good	Stöhr et al. (2003)
benzyl alcohol	1.540	1045	2 @ 20 °C	27.89 @ 75 °C	slightly	poor	Cui and Adrian (1997) Hayes (2015)
tetralin (tetrahydronaphthalene)	1.546	967 – 970	2.2 @ 20 °C	33.17 @ 25 °C	immiscible		Cui and Adrian (1997) Hayes (2015)
methylnaphthalene	1.616	1017	3.29 @ 20 °C		immiscible	poor	Koh et al. (1994)
tetrabromoethane (TBE)	1.624	2943	1		poor		Averbakh et al. (1997)
chloronaphthalene	1.631	1191	3.42 @ 20 °C		poor		Koh et al. (1994)

* Temperature for viscosity is provided when stated, otherwise it is assumed this is in ambient laboratory conditions between 20 °C and 25 °C.

Generally, the RI of hydrocarbons within a given chemical class generally increases with the size/weight or complexity of their chemical structure. Fluorocarbons have relatively low RIs, and importantly, many fluorocarbons have RIs that are lower than water. This proximity in their RI to that of water makes fluorocarbon-based blends suitable as organic liquid candidates for solid-liquid-liquid RIM systems with water and FEP as the aqueous and solid phases, respectively. Although sourcing fluorocarbons in both reasonable quantities and cost may in some cases prove difficult, especially for a large system (Saksena et al., 2015). Hibberd et al. (2007) reported using tetradecafluorohexane and n-hexane with RIs of 1.251 and 1.378, respectively, to prepare a water-based RIM emulsion. Of importance, in this case, is the flammability and relatively low boiling points of tetradecafluorohexane (< 61 °C) and n-hexane (< 69 °C), which introduce the need to apply caution when handling these fluids outside of controlled, closed environments. Longer chain fluorocarbons are potentially even more suitable for experimental systems, e.g., Vitreon (perfluoroperhydrophenanthrene) has RI = 1.335 (close to water) and is both non-toxic and non-volatile (Georgalas et al., 2011). Therefore, a combination of FEP, water and perfluoroperhydrophenanthrene appears to be a promising triply matched RI system.

Silicone oils are another group of organic liquids worth mentioning. In general, they are non-toxic and have wide ranges of both RIs and viscosities which makes them ideal candidates for tuning the viscosity of organic mixtures. Dow Corning 200 silicone (polydimethylsiloxane) oils, which is the most common silicon oil family, cover kinematic viscosities in the range $6.5\times10^{-7} – 1$ m^2/s, but have associated RIs in the relatively narrow range 1.375 – 1.404 as shown in Figure A.1 Viscosity and RI tuning can then be achieved through mixing with a range of

available miscible higher-RI silicone oils like Dow Corning 550 (RI = 1.490 – 1.500, viscosity 1.0×10^{-4} – 1.50×10^{-4} m²/s), Dow Corning 556 (RI = 1.46, viscosity 2.25×10^{-5} m²/s) or Dow Corning 710 (RI = 1.533, viscosity 5×10^{-3} m²/s).

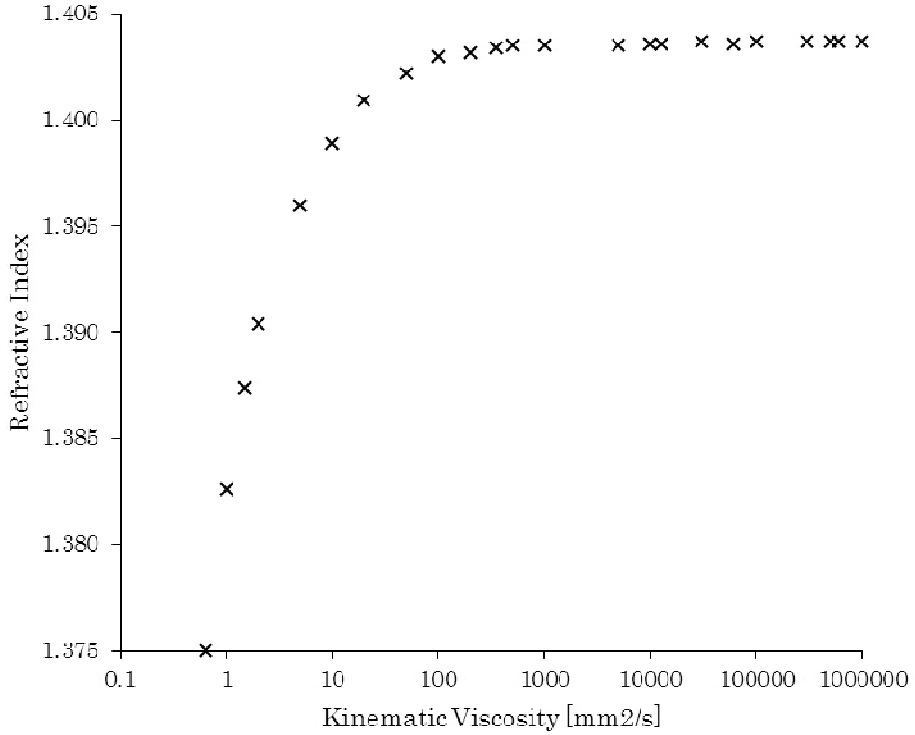


Figure A.1 Variation of refractive index with viscosity for Dow Corning 200 (polydimethylsiloxane) silicone oils (Dow Corning datasheets).

Finally, solubility in water (indicated in Table A.6) and in other organic solvents should be checked when considering a liquid-liquid RIM system. Hassan and Dominguez-Ontiveros (2008) matched the RI of soda-lime glass to two different organic systems: (i) diethylphthalate; and (ii) a mixture of isopropanol and methylnaphthalene. Isopropanol, however, is fully soluble in water and therefore, organic mixtures that include isopropanol cannot be used when water is the aqueous-phase in a liquid-liquid system. UCON polyalkylene glycol-based oils are also widely found in RIM-based experimental literature but these are again miscible with water.

A.7 Aqueous and hydrophilic liquids

Aqueous systems are comprised of water, which has a relatively low RI (of 1.333). This means that RI matching to the majority of available and commonly used solids

and organic liquids, which have considerably higher RIs (hydrogels, FEP and fluorocarbons being exceptions), is a challenge and requires significant amounts of tuning with mixing or additives. An increase in the RI of an aqueous-phase is often achieved through the addition of glycerol (Bailey and Yoda, 2003; Takamura et al., 2012). Glycerol has a relatively high RI (of 1.473) and thereby allows a range of RI values to be spanned based on the water-glycerol ratio. The effect on the RI of different glycerol solution concentrations over the entire range of mole fractions for temperatures between 25 °C and 60 °C is reported in a comprehensive study by Leron (2012), see Figure A.2.

The dynamic viscosity of pure glycerol is 1.412 Pa·s, so the addition of glycerol to water (0.89 mPa·s) is also accompanied by a significant increase in viscosity. Glycerol's increase in viscosity can be undesirable when studying liquid-liquid flows that mimic real flow systems, as the water-to-oil viscosity ratios can be significantly altered (Morgan et al., 2013; 2016). In such cases, glycerol solutions can be further combined with alcohols in ternary systems (Moreira et al., 2009) or salts so that density, viscosity or surface tension can be independently controlled. Baldwin et al. (1989) created a mixture of 79 vol.% saturated NaI solution, 20 vol.% glycerol and 1 vol.% water which matched the RI of PMMA, while also having approximately the same viscosity of blood.

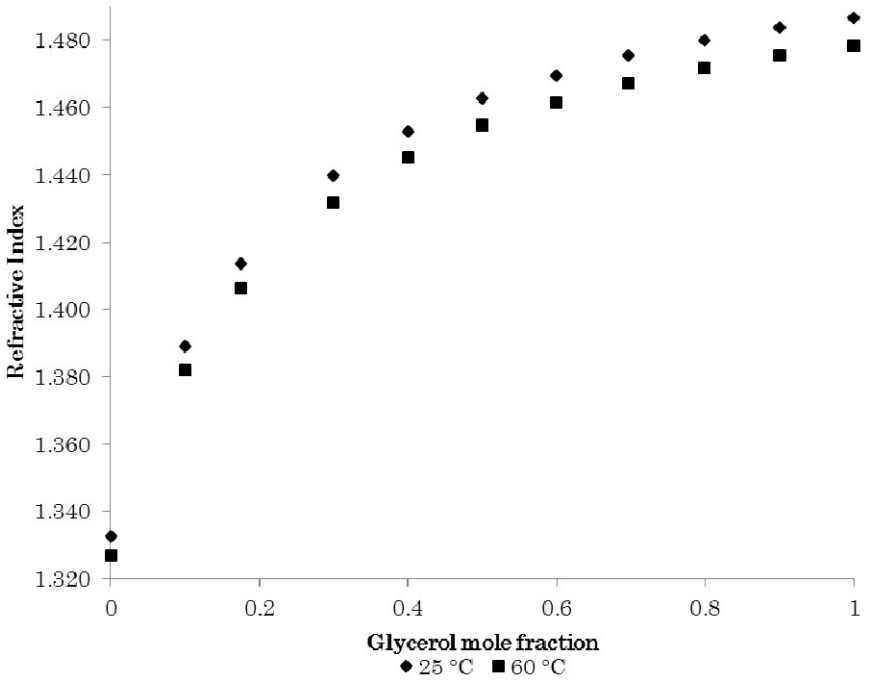


Figure A.2 Refractive index variation for two temperatures of 25 °C and 60 °C over a full range of glycerol solutions; data from Leron (2012).

The density and surface tension of glycerol solutions can also be modified via the addition of certain alcohols, e.g., ethanol, which has a significantly lower surface tension and density ($\sigma = 23.4\times10^{-3}$ N/m; $\rho = 789$ kg/m^3) but similar viscosity and RI ($\mu = 1.2\times10^{-3}$ Pa·s; $n = 1.361$) compared to water (Vazquez et al., 1995; Khattab et al., 2012; Mathie et al., 2013; Markides et al., 2016). Nevertheless, ethanol is known to attack some plastics (e.g., PMMA) so chemical compatibly should be checked at the experiment design stage.

Table A.7 lists common liquids suitable for the RI tuning of aqueous solutions, where we have again included PMMA compatibility data that has been collated from supplier datasheets.

Table A.7 Hydrophilic liquids previously used in refractive index-matched experiments, with their refractive index, surface tension, dynamic viscosity and density.

Liquid	n_L	Density [kg/m³]	Dynamic viscosity* [mPa·s]	Surface tension [mN/m]	PMMA compatibility	References
water	1.333	998	1.04 @ 20 °C	72.5	good	Takamura et al., (2012)
methanol	1.327	789	0.544 @ 25 °C	22.07	poor	Hayes (2015) Albuquerque et al. (1996)
ethanol	1.360	785	1.082 @ 25 °C	27.1	poor	Gómez et al. (2006) Hayes (2015)
1,2 propanedoil	1.432	1036	56.0 @ 20 °C		good	Smedley and Coles (1990)
ethylene glycol	1.432	1109	19.9 @ 20 °C		good	Smedley and Coles (1990)
dipropylene glycol	1.440	1021	76.2 @ 20 °C		good	Smedley and Coles (1990)
1,3 propanedoil	1.440	1060	46.6 @ 20 °C		good	Smedley and Coles (1990)
diethylene glycol	1.447	1116	35.7 @ 20 °C		good	Smedley and Coles (1990)
formamide	1.447	1133	3.85 @ 20 °C		good	Smedley and Coles (1990)
1,5 pentanedoil	1.449	992	128.1 @ 20 °C		good	Smedley and Coles (1990)
triethylene glycol	1.453	1124	49.0 @ 20 °C		good	Smedley and Coles (1990)
tetraethylene glycol	1.459	1125	47.4			Stephenson and Stewart (1986)
glycerol	1.474	1231	1500 @ 20 °C	63.5	good	Takamura et al., (2012)
dimethylsulfoxide (DMSO)	1.477	1095	1.984 @ 25 °C	42.92 @ 25 °C	poor	Baragi et al. (2005) Hayes (2015)

* Temperature for viscosity is provided when stated, otherwise it is assumed this is in ambient laboratory conditions between 20 ºC and 25 ºC.

Salts are commonly added in order to increase the RI of aqueous RIM systems (see Table A.8). The ability of salts to increase RI is usually limited by their solubility in the solvent, so the RI of a given solution can be modified from that of the pure liquid (e.g., water with RI of 1.333) up to that achieved by the saturated salt solution. Nevertheless, this solubility can be altered by further additives, such as crown ethers (Lopez-Gejo et al., 2007). On the other hand, the introduction of salts also leads to an increase in the density and viscosity of the resulting aqueous-solution, as well as an increase in the risk of corrosion (e.g., electrochemical oxidation of metals), and therefore, care must be taken when selecting the materials to be used in any experimental campaign (e.g., plastics and, in particular, metals). The typical criteria

for the selection of a given salt additive are: (i) increase in the RI with concentration; (ii) salt solubility; (iii) increase in the viscosity with concentration; (iv) increase in the density with concentration; (v) compatibility and corrosion potential; and (vi) stability of a given salt solution. All these criteria are temperature sensitive making temperature control important especially in saturated systems where drops in temperature can lead to salts leaving the solution.

Table A.8 List of solids used for refractive index tuning of aqueous solutions.

Liquid	Solubility [g/100 g @ 20 °C]	n_L	PMMA compatibility	References
KH_2PO_4	>10	1.330 – 1.345		Alahyari and Longmire (1994)
NaCl	35.9	1.330 – 1.380	good	Hayes (2015)
CsBr	123 [@ 25 °C]	1.330 – 1.405		Li et al. (2013)
$CaCl_2$	74.5	1.330 – 1.442	good	Hayes (2015)
$ZnCl_2$	395	1.330 – 1.470	good	Stöhr et al. (2003)
NaSCN	139	1.330 – 1.480		Budwig (1994)
KSCN	224	1.330 – 1.490		Jan et al. (1989)
sodium salicylate ($C_7H_5NaO_3$)	125	1.330 – 1.490	good	Prasad et al. (1991)
sucrose ($C_{12}H_{22}O_{11}$)	≈ 2000	1.330 – 1.490	good	Dijksman et al. (2012)
NaI	178	1.330 – 1.499	good	Bai and Katz (2014)
NH_4SCN	170	1.330 – 1.503	good	Borrero-Echeverry and Morrison (2016)
sodium polytungstate ($Na_6[H_2W_{12}O_{40}]$)	>1000	1.330 – 1.550	good	Dijksman et al. (2012)
ZnI_2	432	1.330 – 1.620	good	Hendriks and Aviram (1982)

Referring to Table A.8, the present review of the literature has revealed that NaI is the most widely employed salt in RIM experiments. Typical NaI solutions matching the RI of PMMA have concentrations in the range of 60.0 – 64.8 wt.%, yielding an RI in the range 1.485 – 1.491 (Imao et al., 1996; Parker and Merati, 1996; Uzol et al., 2002; Mehta et al., 2007; Uzol et al., 2007; Soranna et al., 2008; Yuki et al., 2008; Wu et al., 2009; Amatya and Longmire, 2010; Wu et al., 2011; Yuki et al., 2011; Wu et al., 2012; Yuan et al., 2012; Tomac and Gregory, 2014). A detailed study of the use of NaI for RI matching (aimed at PIV measurements) over an even wider RI range (1.330 – 1.510) was performed by Bai and Katz (2014), who also matched NaI solutions to three optical solids formed from resins with RIs in the range 1.495 – 1.508. NaI solutions with RIs >1.499 could only be reached at temperatures >23 °C. Of interest in the context of RI matching is a useful study by Narrow et al. (2000), who developed a model for predicting the RI of NaI solutions for a known temperature and concentration. At the same time, the addition of NaI to water does

not significantly affect the liquid solution's viscosity. NaI solutions have kinematic viscosities of ≈ 1.1×10^{-6} m^2/s, which is only slightly higher than that of water that has a viscosity of 1.0×10^{-6} m^2/s at 20 °C (Uzol et al. (2002); Uzol et al. (2007)).

NaI, like many iodides, undergoes photodissociation, oxidizing in the presence of light (Chen and Fan, 1992). This can, however, be counteracted through the addition of 0.1 g of sodium thiosulfate ($Na_2S_2O_3$) per L (Ghatage et al., 2014; Narrow et al., 2000; Parker and Merati, 1996). The precipitation of iodide can also be reduced by the addition of 20 mg of ascorbic acid per cm^3 of salt solution (Jacobs et al., 1988).

NH_4SCN is the second most common salt reported in RIM systems and was examined in detail in the context of RIM experiments by Borrero-Echeverry and Morrison (2016). This study reported an RI value of 1.503 for a 62.6 wt.% aqueous-NH_4SCN solution, also with a relatively low kinematic viscosity of 1.7 mm^2 s and a density of 1140 kg/m^3. NH_4SCN is, like other thiocyanates, toxic if inhaled or ingested and it must be handled with care and suitable protective clothing.

Hendriks and Aviram (1982) investigated the use of ZnI_2 in RIM systems. It was shown that ZnI_2 can form aqueous solutions with a high RI (1.620) at 81 wt.%, with a kinematic viscosity of 5×10^{-6} m^2/s at 21 °C, and that for a less concentrated 60 wt.% solution the viscosity falls to 2×10^{-6} m^2/s, whilst matching the RI of PMMA at 1.490. Hence, ZnI_2 solutions have the potential to be utilized as aqueous RIM systems matching all solids from FEP to PS in RI. Nevertheless, ZnI_2, like many salts, is hygroscopic and so the accurate measurement of the weight of a given salt requires the salt to be dried first (Hendriks and Aviram, 1982).

The material compatibility and corrosion issues associated with the use of salts have been addressed by several investigators. Cenedese and Viotti (1996) noted that $ZnCl_2$ corrodes aluminium and so opted instead to use glycerol in their RIM experiments. Similarly, Reddy et al. (2013) considered a 55wt.% NaI solution too corrosive, while a solution of 42 wt.% KSCN and a solution of 45% NH_4SCN were both considered too corrosive and too toxic. Borrero-Echeverry and Morrison (2016) found that NH_4SCN solutions were compatible with 6061 aluminium alloy, anodized aluminium, 316 stainless steel, common plastics and glass but corroded plain steel and 304 stainless steel. Furthermore, Stöhr et al. (2003) showed a 58 wt.% concentration of $ZnCl_2$ has a pH of ≈ 2 and is therefore incompatible with PMMA and many fluorescent dyes. Bailey and Yoda (2003) were successful in creating a ternary mixture of NH_4SCN, water and glycerol that was compatible with plastics including

PMMA, PC and PVC. However, it corroded many metals, with the exception of 304 stainless steel and some aluminium alloys. In a couple of other approaches of interest, Dijksman et al. (2012) noted that sodium polytungstate is a relatively non-toxic salt, forming solutions with RIs up to 1.550 which are compatible with most plastics and metals, with the exception of aluminium, while Prasad et al. (1991) matched sodium salicylate solution to PMMA in static conditions. Sodium salicylate, however, was not deemed suitable for flow experiments, as it required high concentrations, was expensive and changed colour over time.

Appendix B:

Preliminary modelling work

A significant area of future work is the modelling of these flows. Some preliminary modelling work was carried out using ANSYS Fluent 15.0.7 and STAR CCM+ 12.02.010 using the volume of a fluid (VOF) approach to model the breakup of an oil-water laminar stratified flow using a few jet configurations. Theses simulations used a pipe diameter of 50 mm and a jet diameter of 4 mm, a mixture velocity of V_m = 0.1 m/s, a jet velocity of V_j = 4 m/s and an aqueous phase fraction of ϕ = 0.20. The simulations were broken into the three sections of Figure B.1. The upstream section is the development of the liquid-liquid stratified flow. The interaction section models the breakup of the stratified flow by the jet. The downstream section models the development of the dispersion after the jet's influence has decayed.

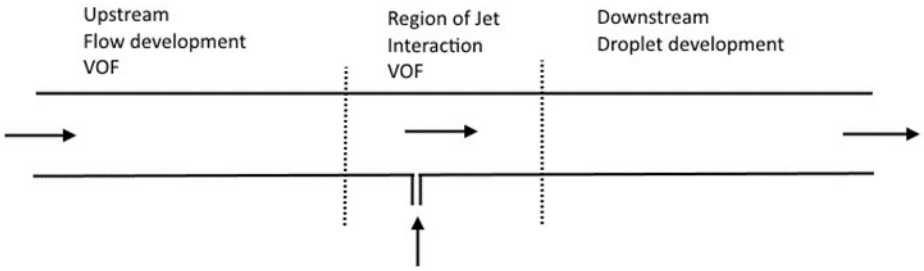


Figure B.1 Upstream, interaction and downstream modelling sections.

Figure B.2(left) shows a side view of a simulation of a single jet in crossflow, the water-oil interface is in green and the aqueous phase fraction is shown on the *y-z* plane. Interestingly, the oil jet does not have the water sheath seen in the experimental PLIF images of Chapter 4 and by Fernando (1990) in static conditions (Figure 2.18). In the simulation, the water is found to be principally entrained downstream of the jet. The downstream counter-rotating vortices are present in this simulation where the aqueous phase can be seen to rotate and break up while the interface is distorted and lifted by the jet flows around the wall.

Figure B.2(right) shows a simulation looking downstream for two jets in crossflow impinging head-on where the interface between water and oil is shown in green. With the dual impinging jets, the water breakup mostly occurs up in the centre of the pipe where the jets meet whereas for the single jet the water is mostly broken up when the jet impinges the walls.

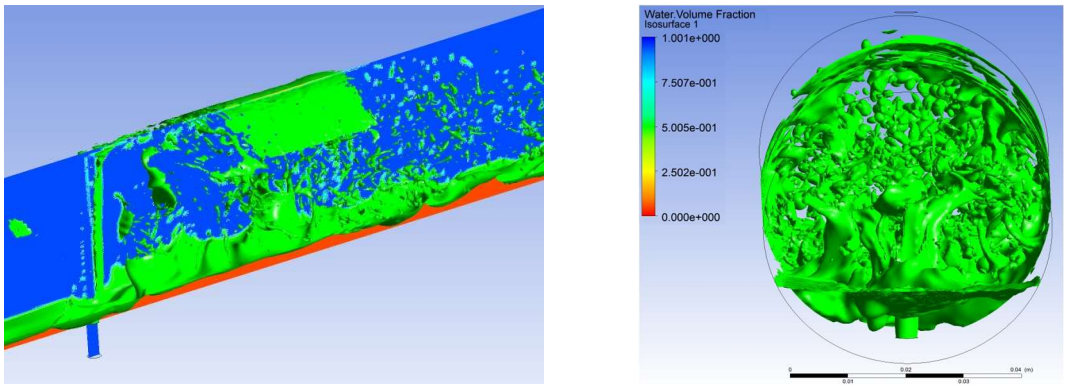


Figure B.2 CFD Simulations showing water-oil crossflow being mixed by jets. Left: single vertically upward jet; Right: twin impinging jets, one arranged vertically up and the other vertically down.

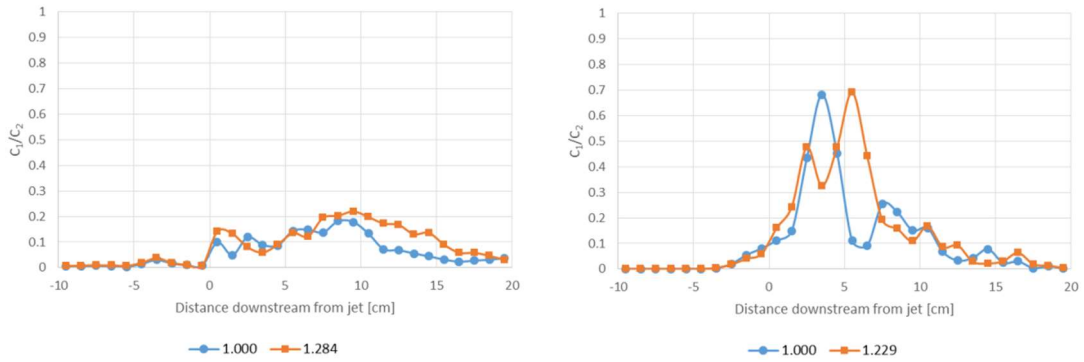


Figure B.3 The C_1/C_2 ratio against distance from jet. Left: single upward jet C_1/C_2 at 1.000 s and 1.284 s.; Right: two vertically impinging jets at 1.000 s and 1.229 s.

The simulations calculate the C_1/C_2 ratio as it varies along the axis of the pipe. Figure B.3(left) presents results for the single jet at time 1.000 s and 1.284 s and Figure B.3(right) presents the results for the dual impinging jet at time 1.000 s and 1.229 s. The dual impinging jets manages to lift significantly more water than the single jet but that this water falls back to the bottom half of the pipe more rapidly, whereas the single jet manages to suspend smaller droplets of water for longer.

Future work will be to continue to investigate if these simulations can reproduce the behaviour of these flows and in particular the behaviour of the largest droplets in the flows.

These simulations highlighted a few issues, the VOF model was too computationally intensive at the current time to simulate these flows for industrial purposes. The simulations were limited in both time and memory to a mesh size of 500 µm and so ≈ 6 million cells. However, the mesh size needs to be on the order of ten times smaller than the droplet diameter to be correctly simulated and the experimental results have found that many droplets are smaller than 500 µm. If the simulations were limited to droplet sizes of 500 µm and so a mesh size of 50 µm was used, this would still require a simulation with a 1000 times as many cells and a time step of a tenth as long. This results in current VOF simulations needing three to four orders of magnitude more processing power and memory and outside the ability of hardware commonly available at this time

Future work should therefore investigate the most suitable models for these complex flows. In particular, hybrid Eulerian and VOF models appear interesting in the context of modelling the complex transitions that occur as these systems transition from a stratified flow to a disperse flow and back again. These hybrid models could incorporate population balance models so that droplet size can also be calculated. Comparison of the performance, usability and modelling capabilities different software packages should also be undertaken due to the industry importance to perform these calculations quickly on inexpensive hardware. These models can then be compared with the experimental results contain within this thesis to see how well they can replicate the flow pattern transitions that have been witnessed.

List of future modelling work:

- Perform detailed modelling of these flows to compare with the experimental results presented in this thesis.
- Investigate new models, in particular hybrid Eulerian and VOF models which include population balance models.
- Test commercial packages for performance in the simulating these flows.